Blast Attenuation in Cohesive Soils

Arthur Van Lerberghe MEng

Thesis submitted to the

University of Sheffield
Department of Civil & Structural Engineering

and

Defence Science Technology Laboratory (Dstl)

July 2024

Papa, Maman
Auguste, Bertille, Louison
Merci de votre soutien durant cet incroyable chapitre de ma vie!

"Once we accept our limits, we go beyond them." – Albert Einstein

Abstract

Soil-filled wire and geotextile gabions are essential components of defensive infrastructure in military bases, leveraging the attenuating properties of soils to safeguard personnel and critical assets against blast and fragmentation effects. Understanding the behaviour of cohesive soils under extreme loading conditions opens new avenues for design engineers, enabling the development of robust soil constitutive models to address evolving threats effectively.

This study investigates the response of cohesive soils, focusing primarily on kaolin clay due to its homogeneity, widespread availability, and consistent properties. Initially, quasi-static tests were conducted using a triaxial compression (TXC) and an oedometer apparatus to validate how moisture content influences cohesive soil behaviour at low-strain-rates and to gain insight into the dynamic behaviour of cohesive soils under such conditions. High-strain-rate experimental testing was then conducted on approximately 150 kaolin clay specimens using the split-Hopkinson pressure bar (SHPB) apparatus. These tests were performed under both unconfined and confined conditions across varying moisture contents, from unsaturated to fully saturated states. The analysis of the experimental results reveals the strain rate dependence of cohesive soils and identifies distinct phase behaviour for transmitted and radial stresses, influenced by factors such as strain rate, moisture content and confinement.

Utilising LS-DYNA and the finite element method (FEM), SHPB tests are modelled for comparison against experimental findings. While LS-DYNA, supplemented by smooth particle hydrodynamics (SPH) node modelling, offers valuable insights, significant disparities between modelled and practical results underscore the challenges inherent in accurately simulating the phase behaviour of cohesive soils. This comprehensive exploration of cohesive soil's high-strain-rate behaviour yields critical insights for engineers, enabling them to effectively adapt defensive strategies to diverse threats and loading scenarios.

Furthermore, by harnessing cutting-edge machine learning models such as the Proper Orthogonal Decomposition (POD) and sparse Proper Generalised Decomposition (sPGD), data-driven parametric models were developed using SHPB test data. These models provide precise predictions of cohesive soil behaviour under specified strain rates and moisture content levels, empowering engineers to swiftly anticipate soil responses to emerging threats and ground conditions.

Résumé

Les gabions en fil métallique et en géotextile remplis de terre sont des composants essentiels de l'infrastructure défensive dans les bases militaires, exploitant les propriétés d'atténuation des sols pour protéger le personnel et les actifs critiques contre les effets des explosions et de la fragmentation. Comprendre le comportement des sols cohésifs sous des conditions de charge extrême ouvre de nouvelles voies pour les ingénieurs en conception, leur permettant de développer efficacement des modèles constitutifs robustes pour répondre aux menaces évolutives.

Cette étude examine la réponse des sols cohésifs, en se concentrant sur l'argile kaolin en raison de son homogénéité, disponibilité et propriétés constantes. Des tests quasi-statiques ont été réalisés avec un appareil de compression triaxiale (TXC) et un oedomètre pour valider l'influence de la teneur en eau sur le comportement des sols cohésifs à faible taux de déformation. Des essais à haute vitesse de déformation ont été menés sur environ 150 spécimens d'argile kaolin à l'aide de barres de pression Hopkinson divisées (SHPB), sous des conditions non confinées et confinées, avec des niveaux de teneur en eau variés, de non saturé à complètement saturé. L'analyse des résultats révèle la dépendance des sols cohésifs au taux de déformation et identifie des comportements de phase distincts pour les contraintes axiales et radiales, influencés par le taux de déformation, la teneur en eau et le confinement des échantillons.

En utilisant LS-DYNA et la méthode des éléments finis (FEM), les tests SHPB sont modélisés pour être comparés aux résultats expérimentaux. Bien que LS-DYNA, complété par la modélisation nodale de la dynamique des particules lisses (SPH), offre des perspectives précieuses, d'importantes disparités entre les résultats modélisés et pratiques soulignent les défis inhérents à la simulation précise du comportement des phases des sols cohésifs. Cette exploration approfondie du comportement à grande vitesse de déformation des sols cohésifs offre des perspectives critiques aux ingénieurs, leur permettant d'adapter efficacement les stratégies défensives à diverses menaces et scénarios de charge.

De plus, grâce à l'utilisation de modèles de machine learning tels que la Proper Orthogonal Decomposition (POD) et la sparse Proper Generalised Decomposition (sPGD), des modèles paramétriques basés sur les données des tests SHPB ont été développés. Ces modèles permettent de prédire avec précision le comportement des sols cohésifs sous différents taux de déformation et niveaux d'humidité, offrant ainsi aux ingénieurs la capacité d'anticiper rapidement les réponses des sols face aux menaces émergentes et aux conditions du sol.

Acknowledgements

It gives me great pleasure to acknowledge all the people who have helped make this possible.

First and foremost, thank you to my supervisor, Professor Sam D. Clarke, whose support and friendship have made this research project a truly entertaining and fulfilling experience. Few students are lucky enough to have a supervisor so invested in their work and committed to their development as a person. His guidance and advice powered me through long months away from my family. I am also grateful to my second supervisor, Dr. Andrew D. Barr, for his support and insightful feedback over the years.

To the "Heartspace gang", I extend my heartfelt gratitude for the countless lunches, moments of laughter and cherished memories shared throughout the years. Oswald, your friendship has made this journey truly enjoyable. Without you, the early drives to Buxton, the months spent in the bunker conducting tests and the long analysis discussions would undoubtedly have made this more challenging. Thank you for being an indispensable part of this experience.

I am thankful to the Blast and Impact Dynamics group for their guidance, insights, and many productive conversations. Thanks also to the technical staff at Blastech and at the University of Sheffield, who assisted and aided me in completing my experimental work.

I am also grateful to my collaborators Paco, Babs, Angelo and Sebastian from ENSAM, France and CNRS@CREATE, NUS, Singapore for their support, insights, and guidance in the field of machine learning, highlighting its incredible potential.

My project was sponsored by the Defence Science and Technology Laboratory (Dstl), and I am thankful for their trust in me to thrive and explore. Their contribution has enabled me to achieve my goals, create long-lasting partnerships, and develop invaluable skills for my career.

Thank you to the Sheffield University Rowing Club (SURC) for introducing me to the beautiful, challenging, and intensely passionate sport that is rowing. It has truly helped in providing me with a peaceful mindset during my research journey.

This has been an incredible chapter of my life, I am immensely grateful to my family and friends for their support.

Arthur Van Lerberghe
July 2024

Contents

List of Figures

List of Tables

Chapter 1

Introduction

1.1 Background

Understanding how structures respond to explosions or high-velocity projectiles is of profound global importance. In a world where terrorism and geopolitical tensions are escalating, there is an urgent need to develop robust methods to minimise the impact of these threats. Therefore, evaluating the suitability of different geomaterials from a military defence perspective becomes paramount.

This Dstl-sponsored research project serves as a cornerstone within the Force Protection Engineering (FPE) programme, focusing on fundamental soil research crucial for military fortification engineers (Warren et al. 2013). At its core, the FPE research initiative strives to deepen the understanding of how materials perform under diverse loading conditions. Presently, FPE structures are engineered through a synergy of traditional testing, numerical modelling and experimental assessments.

Such tests, albeit time-consuming and costly, are indispensable for grasping real-life scenarios. One of the primary goals of the FPE programme is to gain a comprehensive understanding of the relative performance of protective materials. This understanding is essential for developing robust numerical models and devising effective solutions to counter future threats swiftly and cost-efficiently.

Fortification engineers face a daunting challenge: ensuring the resilience of defensive structures worldwide. Soil-filled wire and geotextile gabions, exemplified by Hesco Concertainers, stand as stalwart solutions, offering protection against the destructive forces of blast and fragmentation. The versatility and availability of soil make it an attractive defence material, facilitating the rapid and cost-effective construction of robust-barriers. However, despite its ubiquity, the high-strain-rate behaviour of soil remains enigmatic, especially in the context of emerging threats and evolving landscapes.

As conflicts shift from sandy terrains to regions where sand may not be readily available, the need to understand and harness the potential of cohesive soils such as clay and silt becomes imperative. These materials, found across the globe, constitute the terrestrial and aquatic strata, presenting a promising alternative for fortifications in diverse settings.

1.2 Scope & objectives

In navigating unfamiliar terrain, fortification engineers require precise data to assess the performance of local soils and adapt their designs accordingly. The development of constitutive models capable of accommodating new soils and emerging threats necessitates comprehensive studies on soil behaviour under extreme loading conditions. In this regard, the focus on kaolin clay, a well-researched and representative soil, provides a foundation for quantitative insights into the mechanical response of cohesive soils. By preparing kaolin clay samples at varying moisture contents and testing them under both unconfined and confined conditions using the SHPB apparatus, this study aims to elucidate the effects of strain rate, moisture content and confinement on cohesive soils.

Venturing into the realm of blast attenuation in cohesive soils unveils uncharted territory. The unique characteristics of cohesive soils, including their undrained behaviour, variable saturation states, and very fine particle size, pose significant challenges in evaluating their response at high strain rates. Unlike cohesionless soils, like sand, which have been extensively studied under high-strain-rates conditions as seen in papers by Ross et al. (1986), Veyera (1994), Gray III (2000), Bragov et al. (2008), Luo et al. (2014) and Barr (2016*b*), cohesive soils, particularly kaolin clay, remain largely unexplored in this context. This study aims to bridge this gap, paving the way for more resilient and adaptive fortification designs.

By harnessing physics-informed insights from high-strain-rate tests, this research project aims to save considerable time and cost through the utilisation of machine learning programmes and experimental test data, in order to create data-driven parametric models. These models will be able to predict the high-strain-rates behaviour of cohesive soils by mapping their complete response under different strain rate, moisture content and confinement conditions, thereby providing fortification engineers with fast, dependable, and accurate information. Ultimately, this ensures civilian and military assets are protected faster and more efficiently.

This thesis is primarily concerned with the effect of strain rate, moisture content and confinement on the high-strain-rate compaction behaviour of kaolin clay through one-dimensional compression tests. Using the experimental results, numerical models are evaluated using existing FEM software, such as LS-DYNA, which are then scrutinised to validate them against the tests conducted. Cutting-edge machine learning programmes are then used to predict the high-strain-rate behaviour of kaolin clay using the performed tests. The thesis can be structured into three key sections: Test, Model, and Predict.

The main objectives of this thesis are therefore to:

1. Verify the impact of moisture content on the undrained shear strength behaviour of cohesive soils, at low strain rates;
2. Investigate the high-strain-rate behaviour of cohesive soils, with regard to their strain rate, moisture content and confinement conditions;
3. Evaluate current constitutive finite element models in LS-DYNA to assess their effectiveness in modelling the high-strain-rate behaviour of cohesive soils; and
4. Develop data-driven parametric models using high-strain-rate tests on cohesive soils to predict their behaviour under various strain rate, moisture content and confinement scenarios.

1.3 Thesis outline

The remainder of this thesis is organised into the following chapters:

Chapter 2: Literature review

This chapter presents an overview of the published literature relevant to the study of blast attenuation in cohesive soils. The main variables affecting the quasi-static and high-strain-rate behaviour of the most commonly researched cohesive soils under one-dimensional compression are identified. Quasi-static as well as high-strain-rate testing methods are introduced, with a discussion on the triaxial, oedometer and split-Hopkinson pressure bar (SHPB) apparatus. Existing constitutive numerical models of dynamic events on cohesive soils are also evaluated. Furthermore, background information on parametric modelling programmes is provided.

Chapter 3 - Material characterisation, specimen preparation, and test programme

In Chapter 3, the material characterisation of the selected cohesive soil, kaolin clay, is detailed. Kaolin clay was chosen due to its global abundance, well-researched nature, and representative behaviour of cohesive soils. A comprehensive material characterisation of the selected soil is conducted, covering particle density, shape, size distribution, mineralogy and the Atterberg limits. The sample preparation methodology for both quasi-static and high-strain-rate testing is then presented. This process involves preparing specimens with moisture contents that cover the entire range of saturation levels: unsaturated, partially saturated, and fully saturated. This chapter concludes with a detailed test programme, outlining the quasi-static and high-strain-rate tests performed in this research project.

Chapter 4 - Strain rate dependence in cohesive soils

In Chapter 4, experiments are conducted to investigate the effect of strain rate, confinement and moisture content on kaolin clay samples. These experiments include both high-pressure quasi-static tests, utilising the triaxial and oedometer apparatus, as well as high-strain-rate tests, employing the SHPB apparatus where samples are examined under both unconfined and confined conditions. The results are analysed to assess the compressibility of the soil under quasi-static loading, the influence of strain rate, the impact of moisture content, and the effects of confinement on the strain-rate sensitivity of kaolin clay.

Chapter 5 - Numerical modelling of high-strain-rate SHPB tests on cohesive soils

Chapter 5 utilises the quasi-static test results from Chapter 4 to provide high-pressure compaction data for calibrating finite element models in LS-DYNA. The data generated from high-strain-rate SHPB tests on kaolin clay samples is then used to evaluate the quality of soil models in LS-DYNA. Validation experiments are carried out by comparing the numerical models in LS-DYNA to the SHPB test results. Modelling optimisation is performed by evaluating model limitations, with the aim of creating a comprehensive cohesive soil model that accurately represents the experimental findings.

Chapter 6 - Data-driven parametric modelling of SHPB tests on cohesive soils

Chapter 6 focuses on building a parametric model using the data collected from the SHPB tests performed on kaolin clay samples under both unconfined and confined conditions, as evaluated in Chapter 4. Utilising the SHPB tests conducted on the kaolin clay samples in Chapter 4, a fast, dependable and accurate machine learning model is created to predict their behaviour within the range previously investigated. Key parameters such as strain rate, confinement and moisture content guide the design of this physics informed parametric model. The background mathematics behind the developed programme is introduced before presenting the methodology used to create the data-driven parametric models.

Chapter 7: Summary, conclusions & future work

This final chapter summarises the main findings of the current work completed, highlights the key conclusions, and identifies the most promising opportunities for future research.

1.4 Publications

The research presented in this thesis has undergone rigorous evaluation and dissemination through publication at international conferences and in peer-reviewed academic journals. The list of these publications is provided below:

Papers published at international conferences:

Paper A: Van Lerberghe, A., Barr, A. D., Clarke, S. D., and Kerr, S. L., (2022), Blast attenuation in cohesive soils.
- ICILSM3 2022, Trondheim, Norway.

Paper B: Van Lerberghe, A., Barr, A. D., Clarke, S. D., and Kerr, S. L., (2023), High strain rate testing of cohesive soils.
- ICPS6 2023, Auburn, Alabama, USA.

Papers submitted to academic journals for publication as lead author:

Paper 1: Van Lerberghe, A., Li, K. S. O., Barr, A. D., Clarke, S. D., (2024), An open-source algorithm for correcting stress wave dispersion in split-Hopkinson pressure bar experiments.
- submitted to the MDPI Journal Sensors.

Paper 2: Van Lerberghe, A., Li, K. S. O., Barr, A. D., Clarke, S. D., (2024), High strain rate behaviour of cohesive soils.
- accepted in the International Journal of Impact Engineering.

Paper 3: Van Lerberghe, A., Pasquale, A., Rodriguez, S. I., Barr, A. D., Clarke, S. D., Baillargeat, D., Chinesta, F., (2024), Data-driven parametric modelling of split-Hopkinson pressure bar tests on cohesive soils.
- resubmitted to the International Journal of Impact Engineering after minor corrections added.

Papers submitted to academic journals for publication, with contributions as a secondary author:

Paper 4: Li, K. S. O., Van Lerberghe, A., Barr, A. D., Clarke, S. D., (2024), Split-Hopkinson pressure bar testing of water, with partial lateral confinement.
- resubmitted to the Journal of Experimental Mechanics after minor corrections added.

Paper 5: Li, K. S. O., Van Lerberghe, A., Barr, A. D., Clarke, S. D., (2024), Impact of partial lateral confinement on high strain rate behaviour of cohesive soils.
- submitted to the Journal of Experimental Mechanics, awaiting corrections.

It is important to clarify that this work was done in collaboration with O. Li, who recently published a thesis, with some common experimental test data and numerical modelling. However, each thesis was written independently, presenting unique narratives that reflect our individual perspectives and analyses. To avoid any confusion, the papers we have contributed to are clearly delineated above, with specific mention of those where we each took the lead as the primary author, as these relate closely to our respective thesis objectives. This ensures transparency regarding our individual contributions to the research.

Thesis chapter	*Published in*
Chapter 3 - Material characterisation, specimen preparation, and test programme	Paper 2
Chapter 4 - Strain rate dependence in cohesive soils	Paper 1 & 2
Chapter 5 - Numerical modelling of high-strain-rate SHPB tests on cohesive soils	Paper 2, 4 & 5
Chapter 6 - Data-driven parametric modelling of SHPB tests on cohesive soils	Paper 3

Table 1.1: Overview of thesis chapters and associated publications.

Chapter 2

Literature Review

2.1 Introduction

This chapter provides a comprehensive overview of the published literature pertinent to the investigation of blast attenuation in cohesive soils. It begins by delineating the key variables influencing the quasi-static and high-strain-rate behaviour of cohesive soils under one-dimensional (1D) compression. Subsequently, it presents an analysis of the most commonly investigated cohesive soils and compiles the variables collected in experimental testing into a tabular format. The discussion then extends to various strain rate regimes, accompanied by illustrative examples and associated testing methodologies. Further examination explores the main experimental testing methods used in quasi-static and high-strain-rate scenarios, with specific emphasis on the methodologies, theories and limitations of triaxial, oedometer, and split-Hopkinson pressure bar (SHPB) testing apparatuses. This analysis is complemented by a thorough review of experimental testing applications on cohesive soils, particularly in scenarios involving high strains and stresses. Additionally, the chapter explores the utilisation of numerical modelling to develop and apply material models for cohesive soils under high-strain-rate conditions, with a particular focus on the finite-element software LS-DYNA. Notable instances of application drawn from the literature are examined. It also introduces parametric and hybrid twin modelling methods, discussing their background, theory, and illustrative examples. Finally, the chapter culminates in a summary that synthesises the state-of-the-art insights from the literature with the ongoing research efforts.

2.2 Material characterisation

Soil particles span a broad range of sizes, from fractions of a micrometre to over a metre (Table 2.1). This study focuses on cohesive soils, where the majority of particles measure below 0.063 mm in diameter. Despite this small size range, these particles exhibit significant variations in size distribution, shape and surface roughness.

Soils are typically categorised into two main categories: cohesionless soils and cohesive soils. Cohesionless soils, such as gravel and sand, consist of coarse particles and derive their strength from particle friction. In contrast, cohesive soils, such as silt and clay, are easily deformable fine sticky soils, whose strength is determined by the surface tension of capillary water.

Soil type	*Fraction*	*Subfraction*	*Particle size, mm*
Very coarse soil	Boulders	Large boulder	> 630
		Boulder	200 – 630
	Cobbles		63 – 200
Coarse soil	Gravel	Coarse gravel	20 – 63
		Medium gravel	6.3 –20
		Fine gravel	2.0 – 6.3
	Sand	Coarse sand	0.63 – 2.0
		Medium sand	0.2 – 0.63
		Fine sand	0.063 – 0.2
Fine soil	Silt	Coarse silt	0.02 – 0.063
		Medium silt	0.0063 – 0.02
		Fine silt	0.002 – 0.0063
	Clay		$\leq$ 0.002

Table 2.1: Particle size fractions, from EN ISO 14688–1:2002.

This research focuses specifically on cohesive soils, which are defined as follows:

- Silt primarily consists of silica, with quartz $[SIO_2]$, the most common mineral constituent. Silica-based clay minerals such as kaolinite, illite and montmorillonite are also present (Powrie 2018).
- Clay is essentially composed of layers containing two or three alternating sheets of silica and either brucite $[Mg_3(OH)_6]$ or gibbsite $[Al_2(OH)_6]$. Common mineral constituents in clay include kaolinite, quartz, illite and montmorillonite (Powrie 2018).

In soil mechanics, understanding a sample's drained and undrained behaviour is crucial because it directly influences the water-solid relationship within the sample. Drained soils are those from which water can easily drain away. Typically, these soils consists of coarse particles and are categorised as cohesionless, such as gravel and sands. In contrast, undrained soils are those in which water cannot readily flow into or out of the soil. These soils are generally cohesive and fine soils, such as silt and clay.

Mineral particles in soil are surrounded by void spaces typically filled with air, water, or a combination of both. The void ratio is a useful measure of soil compaction. When the void ratio reaches 0, all void spaces are closed, and the density matches that of the mineral (Figure 2.1).

The composition of this three-phase system can be expressed using soil properties such as void ratio e, saturation ratio S_r, and moisture content w, as shown below in Equations (2.1), (2.2) and (2.3):

$$\text{Void ratio, } e = \frac{\text{Volume of voids}}{\text{Volume of solids}} = \frac{\mathrm{V}_v}{\mathrm{V}_s} \tag{2.1}$$

$$\text{Saturation ratio, } S_r = \frac{\text{Volume of water}}{\text{Volume of voids}} = \frac{\mathrm{V}_w}{\mathrm{V}_v} \tag{2.2}$$

$$\text{Moisture content, } w = \frac{\text{Mass of water}}{\text{Mass of solids}} = \frac{\mathrm{M}_w}{\mathrm{M}_s} \tag{2.3}$$

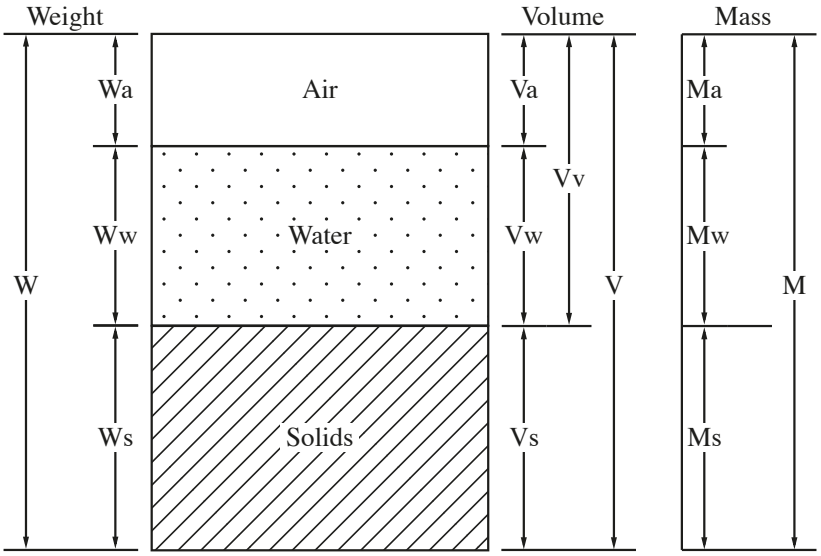

Figure 2.1: Soil-phase relationship diagram (weights, volumes and masses of phases) (Venkatramaiah 1995).

The terms 'unsaturated', 'partially-saturated' and 'fully saturated' describe the saturation ratio, S_r, of a soil sample. In an unsaturated sample, $S_r = 0$, indicating that the voids are filled with air. In a partially-saturated sample, $S_r < 1$, indicating that the voids are filled with both air and water. In a fully saturated sample, $S_r = 1$, indicating that all voids are filled with water.

The particle density, ρ_s, represents the density of the solid mineral particles and is combined with the bulk dry density, ρ_d, to determine the void ratio of a soil using the relation in Equation (2.4):

$$\text{Void ratio, } e = \frac{\rho_s}{\rho_d} - 1 \tag{2.4}$$

where the particle density, ρ_s, is

$$\rho_s = \frac{\text{Mass of solids}}{\text{Volume of solids}} = \frac{\mathrm{M}_s}{\mathrm{V}_s}$$

and the bulk dry density, ρ_d, is

$$\rho_d = \frac{\text{Mass of solids}}{\text{Total volume}} = \frac{\mathrm{M}_s}{\mathrm{V}}$$

The Atterberg limits, originating from the work of Albert Atterberg in 1911 on clay plasticity, and further refined by Casagrande (Bauer 1960), consists of three key parameters: the liquid limit, LL, plastic limit, PL, and plastic index, PI. Engineers commonly employ these limits to gauge the plastic characteristics of materials, particularly clay (White 1949). They are defined as follows in Equations (2.5) and (2.6):

$$\text{Plastic index, PI} = \text{Liquid limit} - \text{Plastic limit} = \text{LL} - \text{PL} \tag{2.5}$$

$$\text{Liquid index, LI} = \frac{\text{Moisture content – Plastic limit}}{\text{Plastic index}} = \frac{w - \text{PL}}{\text{PI}} \tag{2.6}$$

The liquid limit, LL, represents the moisture content, expressed as a percentage by weight of the dry soil, at which the soil will just begin to "flow slightly"; and the plastic limit, PL, represents the lowest moisture content, also expressed as a percentage by weight of the dry soil, at which the soil can be rolled into "thin 1/8 inch (3.2 mm) threads" without breaking (White 1949). Given the undrained conditions of the samples, moisture content significantly influences the behaviour of cohesive soils, making the Atterberg limits particularly pertinent to this study.

2.2.1 Cohesive soils

The cohesive soils most commonly tested in the published literature include kaolin, adobe, London clay and silt, each with distinct characteristics:

- Kaolin: Derived from the Chinese ‘kau ling’ meaning high ridge, the name of a hill in Jauchau Fu, China where it was mined centuries ago (Jamo and Abdu 2014). Kaolin is a soft very fine white silty CLAY (C), with a particle size of ≤ 0.002 mm. Its main mineral constituent is kaolinite.
- Adobe: A term of Spanish/Arabic origin, commonly used to describe "mud bricks". It is among the earliest building materials used by man. Adobe is a soft brown sandy CLAY (C) (Calatan et al. 2017) often reinforced with vegetation or animal fibres (Brown and Clifton 1978).
- London clay: A stiff, overconsolidated brown marine CLAY (C), deposited across the London and Hampshire Basins of south-east England, reaching depths up to 150 m (King et al. 1981). Although often referred to as a uniform material, variations in strength, stiffness and consolidation properties exist due to its depositional history (Pantelidou and Simpson 2007).
- Silt: Composed mainly of quartz and kaolinite, silt (S) is composed of coarse, medium or fine particles, ranging from 0.002 to 0.063 mm (EN ISO 14688–1:2002). It is often tested in combination with other materials, such as sand and/or clay, making it difficult to compare with experimental test data.

The material properties evaluated in this project, as displayed in Table 2.2, include the primary mineral, particle angularity, particle density (ρ_s), particle size distribution (D_{50}), dry density (ρ_d), moisture content (w), and Atterberg limits (LL, PL, PI) of the tested cohesive soils. These properties are gathered from experimental test data in published literature, reflecting a wide array of testing environments.

The extensive testing on kaolin clay soils, as evident in Table 2.2, provides detailed material property data. This abundance of data is attributed to global availability, idealised structure and easy procurement of kaolin clay. Consequently, kaolin clay emerges as an excellent candidate for further experimentation, given its wealth of comparable soil properties in the literature.

Reference	*Primary mineral*	*Particle angularity*	ρ_s $Mg.m^{-3}$	D_{50} μm	ρ_d $Mg.m^{-3}$	w %	*LL* %	*PL* %	*PI* %
Kaolin clay									
Yoshinaka and Kazama (1973)	Kaolinite	SR–SA*	2.69	–	1.350	28.0	70.5	33.6	36.9
Mohd Yusoff et al. (2015)	Kaolinite	–	2.47	7.0*	1.410	27.0	71.0	37.4	33.6
Abbey et al. (2019)	Kaolinite	SR–SA*	2.60	5.5	1.500	17.0	58.0	30.0	28.0
Oluwatuyi et al. (2020)	Kaolinite	SR–SA*	2.65	1.0<	–	–	45.2	24.2	21.0
Adobe clay									
Degirmenci (2008)	Quartz	–	2.44	–	1.364	37.7	56.4	35.71	20.7
Sharma et al. (2016)	–	–	2.67	–	1.880	12.5	23.3	17.8	5.5
Kafodya et al. (2019)	Quartz	–	2.70	–	1.761	17.0	40.0	21.00	19.0
Muñoz et al. (2020)	Quartz	SR–SA*	–	1.69	1.800	–	–	–	–
London clay									
Ward et al. (1959)	–	–	2.68	–	–	22.0	66.0	28.0	38.0
Monroy et al. (2010)	Illite	SR–SA*	2.70	–	1.384	23.6	83.0	29.0	54.0
Gasparre et al. (2011)	Illite	SR–SA*	2.74	1.0<	–	26.0	66.0	29.0	37.0
Bagheri and Rezania (2021)	Quartz	–	2.67	–	–	29.0	70.0	19.0	51.0
Silt									
Nowamooz and Masrouri (2008)	Quartz	–	2.71	–	1.270	–	52.0	15.0	37.0
Christ and Kim (2009)	–	–	2.50	15.0*	1.530	19.8	39.5	28.1	11.4
Oka et al. (2010)	Kaolinite	–	2.60	15.0*	1.300	–	–	–	–
Chow et al. (2020)	–	–	2.71	–	–	–	67.0	39.0	28.0

[– Data not reported * Estimated from data provided]

Table 2.2: Overview of cohesive soil properties tested in published literature.

2.3 Strain rate

In order to accurately predict material response during blast and impact events, it is crucial to comprehend their behaviour across a broad spectrum of strain rates. This is because the rate of deformation can include different modes of material response. For instance, metals such as copper, aluminium, and magnesium exhibit a notable increase in yield strength at high-strain-rates (Davies and Hunter 1963).

Figure 2.2 provides a visual representation of various strain-rate regimes, along with examples and tests applicable to soils within this range. Throughout this literature review, strain-rate regimes will be referred to using these defined categories.

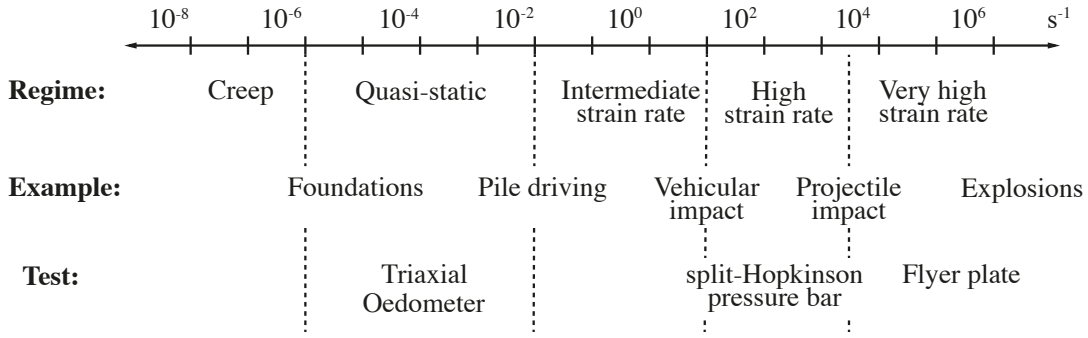

Figure 2.2: Strain rate regimes, examples of phenomena & tests in soils.

The majority of civil engineering soil applications are situated in the creep and quasi-static strain-rate regimes ($<10^{-1}$ s^{-1}), where the system tends to maintain stress equilibrium. Low-velocity consolidation, characteristic of this regime, allow for precise measurements using triaxial or oedometer apparatuses, facilitating accurate assessments of stress and strain.

In contrast, testing at high-strain-rates, prevalent in blast and impact events, demands specialised experimental methods due to the extreme test conditions and transient loading. High-strain-rate environments (10^2 s^{-1} to 10^4 s^{-1}) necessitate stress wave propagation through the material, a challenge addressed experimentally through the split-Hopkinson pressure bar (SHPB) apparatus.

Other methods to measure the high-strain-rate response of materials include cyclic testing (Doygun and Brandes 2020), drop hammers (Shibusawa and Oida 1992), and custom triaxial testing apparatuses (Veyera 1994). However, while these methods can achieve strain rates of 10^{-1} s^{-1}, they cannot ensure the high-stress conditions necessary for applications in blast or ballistics engineering, making them impractical for these contexts.

For even higher strain-rates ($> 10^4$ s^{-1}), flyer plate tests for example become essential, where the intense impact of a high-velocity flyer generates shock waves within the specimen.

The subsequent sections of this literature review will delve into the investigation of quasi-static and high-strain rate one-dimensional compression testing methods. Shock loading and flyer plate testing are beyond the scope of this thesis and therefore will not be examined.

2.4 Quasi-static testing

Quasi-static testing methods, such as the triaxial compression (TXC) test and oedometer test, are essential tools to understand soil behaviour at low strain rates. Delving into the methodology, theory and limitations of each apparatus, the expected findings of TXC and oedometer testing on cohesive soils are showcased to present the current understanding of quasi-static soil behaviour. Additionally, high-stress and high-strain-rate applications of these testing methods on cohesive soils are examined.

2.4.1 Triaxial compression test

The triaxial compression apparatus has a rich history dating back to its development by von Karman in 1910, initially aimed at studying the behaviour of brittle rocks, such as Carrara marble and Mutenberg sandstone. Significant advancements were made in 1930 by Casagrande, who suggested loading the apparatus vertically to obtain the material sample's strength properties (Lade 2016). This innovation was pivotal in understanding principles such as effective stresses, pore water pressure and consolidation's influence on shear strength, during a time when these concepts were still being questioned (Skempton 1960, De Boer 2005). Further technical developments and experiments utilising the triaxial test have been published by Bishop and Henkel (1957), Head and Epps (1980) and Donaghe et al. (1988) outlining its advances. In the upcoming sections, the methodology, theory and limitations of the TXC test are examined, along with its applications on cohesive soils at high-stresses or high-strain-rates.

2.4.1.1 Methodology & theory

The TXC test assesses the mechanical properties of the tested soil sample, requiring a homogeneous and representative specimen from the field. It primarily yields stress-strain relations, pore pressure behaviour, and the shear strength of the soil sample. Additional parameters such as the soil's compressibility, earth pressure coefficient, permeability, coefficient of consolidation, creep and stress relaxation can be derived (BS 1377–8:1990). The TXC test is performed on cylindrical specimens, as depicted in Figure 2.3.

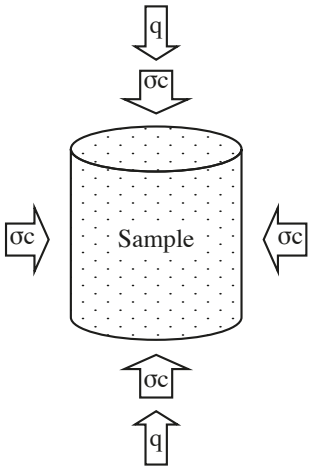

Figure 2.3: Specimen stress state during TXC testing (σ_c: confining stress, q: deviator stress) (BS 1377–8:1990).

A confining stress, σ_c, also called σ_3 is applied along the radial direction of the specimen by pressuring the cell fluid. The deviator stress, q, is generated by applying an axial strain to the soil, acting in addition to the confining stress in the axial direction. Together, these stresses are equal to the axial stress or major principal stress σ_1. The stress applied externally to the sample in the axial direction is represented as

$$\sigma_1 = q + \sigma_c$$

and therefore as

$$\sigma_1 = q + \sigma_3$$

In the general case, three principal stress σ_1, σ_2 and σ_3 may act on a soil element in the field. However, the triaxial test can only apply two different principal stress to the specimen. The intermediate principal stress σ_2, has the following potential values:

$$\sigma_2 = \sigma_3 : \text{Triaxial compression}$$

or,

$$\sigma_2 = \sigma_1 : \text{Triaxial extension}$$

To induce triaxial extension, negative stress differences are applied to the specimen, reducing compression in the extension direction without causing tension. The stress state is isotropic when σ_1=σ_3, and anisotropic when $\sigma_1 \neq \sigma_3$.

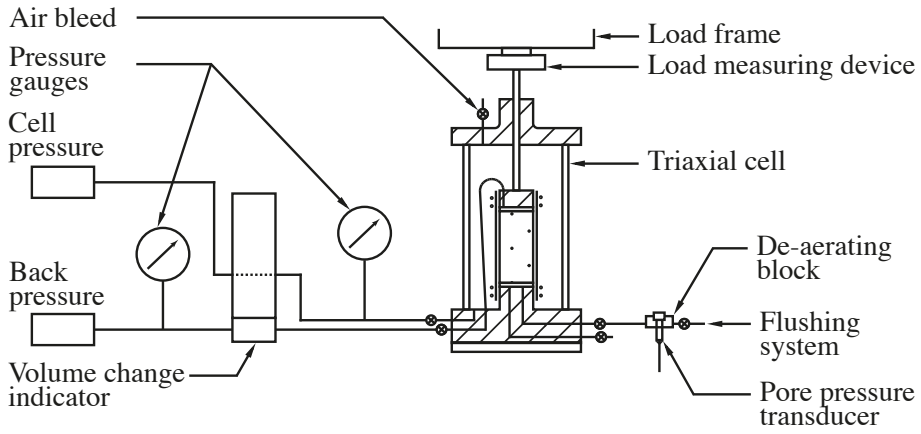

Figure 2.4: Essential features of a typical triaxial cell (BS 1377–8:1990).

The test is carried out using a triaxial apparatus, depicted in Figure 2.5. The specimen, typically ranging from 38 mm to 100 mm in height with 2:1 height-to-diameter ratio, is enclosed by a cap, a base and a membrane. Placed within a triaxial cell, the specimen undergoes hydrostatic confinement from the cell pressure, which remains uniform in all directions. Axial load is applied through a load cell, with vertical deformation detected by a dial attached to the piston. Drainage lines facilitate volume change measurements during the test, allowing for pore pressure measurement via a transducer. Standard measurements during a TXC test include confining pressure, vertical load, axial deformation and pore water pressure serving as the basis for calculating additional values such as stress differential and strain.

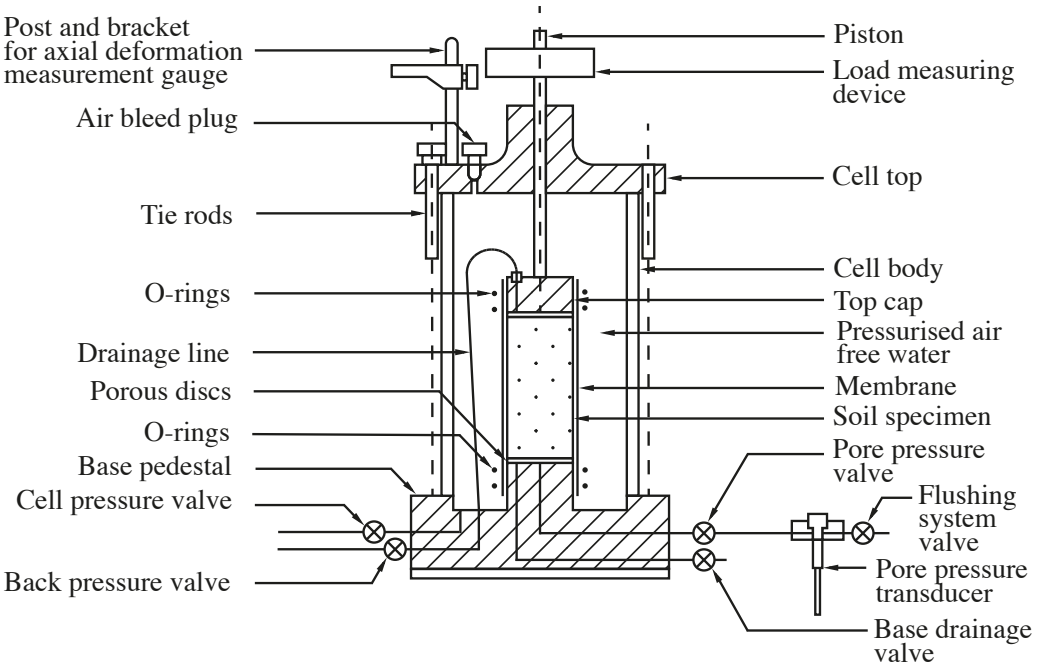

Figure 2.5: Typical general arrangement of a triaxial test (BS 1377–8:1990).

The TXC test consists of two stages, consolidation and shearing, and are defined as follows:

Consolidation: First, the soil's initial condition is established in terms of effective stresses and stress history. Stresses applied mimic those acting on the soil element in the field, including those overlaying soil strata and other existing materials or structures. Sufficient time is allowed for consolidation to occur under the applied stresses, establishing the triaxial specimen's state (BS 1377–8:1990).

Shearing: In this second stage, additional stress is applied to reach the peak failure and beyond under relevant drainage conditions. The additional stress applied should closely correspond to changes in stress on the field element due to new overall field loading situation. These changes may involve vertical stress increases or decreases (e.g. addition of a structure or excavation of overlaying soil strata) or a horizontal stress changes (e.g. similar to vertical stress changes). TXC test can simulate various combinations of vertical and horizontal stress changes (BS 1377–8:1990).

The three TXC test conditions on clay—unconsolidated undrained (UU), consolidated undrained (CU), and consolidated drained (CD)—are defined as follows (BS 1377–8:1990), along with their Mohr circles:

- UU TXC test (Figure 2.6): A total stress test, characterised by the absence of saturation or consolidation stages during testing, focusing only the shear stage. Stress is rapidly applied without pore water drainage, making it an efficient method for characterising a soil's mechanical properties.

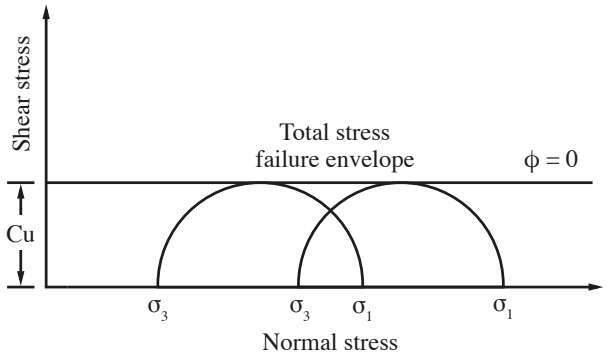

Figure 2.6: UU TXC Mohr circle test results on clay.

In Figure 2.6, the total stress failure envelope is horizontal, indicating that the angle of friction (ϕ) is zero. The circles represent different stress conditions, showing that shear failure occurs at constant undrained shear strength (Cu), without accounting for pore pressure effects. This test does not allow water drainage, so only total stress is recorded.

- CU TXC test (Figure 2.7): The sample is saturated before testing, and excess pore pressure, u, is allowed to dissipate during consolidation to reach equilibrium conditions. While excess pore pressure dissipation is not permitted during the shear stage, it is measured to determine effective stresses in the specimen, reflecting the soil's natural environment.

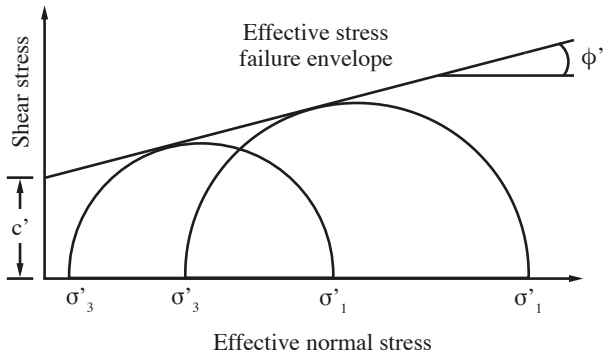

Figure 2.7: CU TXC Mohr circle test results on clay.

In Figure 2.7, the effective stress envelope is inclined, showing that the material has an angle of internal friction (ϕ'). Consolidation occurs prior to testing, allowing pore pressure to dissipate, but during shearing, drainage is not allowed, so effective stress is considered. This results in larger stress circles compared to the UU test, reflecting realistic soil conditions.

- CD TXC test (Figure 2.8): Similar to a CU TXC test, it starts with a saturation stage, proceeds to a prolonged consolidation stage, and concludes with a gradual shear stage. It is crucial to prevent pore pressure buildup in the sample and allow it to disperse. The measurement of the sample volume change, ΔV, is essential. Long-term geotechnical problems are best addressed through CD TXC tests.

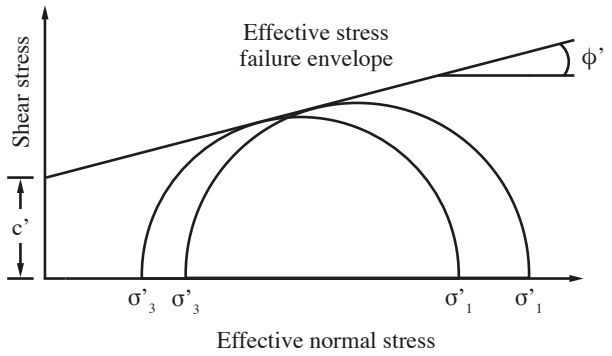

Figure 2.8: CD TXC Mohr circle test results on clay.

In Figure 2.8, the effective stress failure envelope is inclined, indicating frictional strength with an internal friction angle (ϕ'). Since drainage is allowed throughout the test, the effective stress controls the behaviour, providing a more accurate reflection of long term-soil behaviour. This test is critical for understanding soil volume change (ΔV) over time, making it suitable for assessing long-term geotechnical problems.

In the shear stage of a TXC test, the deviator stress, q, is plotted against the axial strain ε_a, to monitor the specimen's response until either failure or a predetermined value is reached. While a UU TXC test only records a specimen's stress-strain behaviour, CU and CD TXC tests also track excess pore pressure and specimen volume change, respectively.

Figure 2.9 and 2.10 depict the behaviour of a normally consolidated and over consolidated clay for UU, CU and CD TXC test conditions.

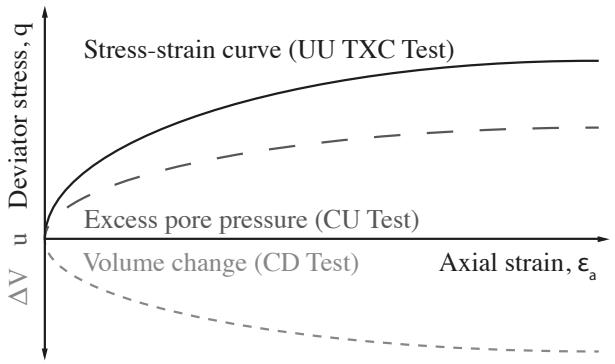

Figure 2.9: Typical TXC test response diagram of a normally consolidated clay.

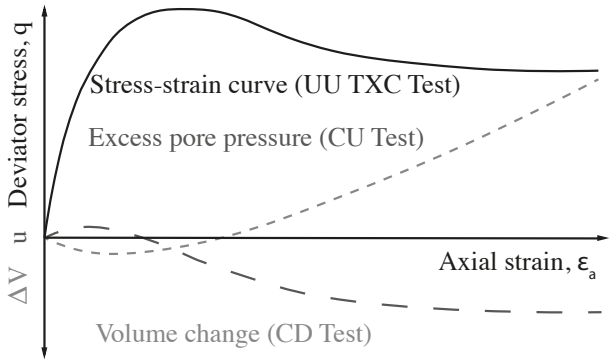

Figure 2.10: Typical TXC test response diagram of an over consolidated clay.

2.4.1.2 Limitations of the TXC test

The TXC test has several limitations, outlined below (BS 1377–8:1990):

1. Stress concentrations due to friction between specimen and end plates (cap and base) can lead to nonuniform strains and stresses, resulting in inconsistent stress-strain, volume change, or pore pressure responses.
2. Specimens can only be subjected to axisymmetric stress conditions, while most field problems involve plane strain or general three-dimensional conditions with principal stress rotation.
3. TXC tests cannot provide all the necessary data to characterise the behaviour of an anisotropic or a cross-anisotropic soil deposit.
4. While the axisymmetric principal stress condition is limited, applying adequate shear stresses or tension to a soil in simple tests is more challenging.

Remediation methods exist: the first limitation listed above can be addressed by lubricating the ends of the specimen to ensure homogeneous strains and stresses, therefore achieving a more accurate soil response (Lade 2016).

2.4.1.3 TXC testing on cohesive soils

TXC testing on cohesive soils has been extensively documented in the works of Nakase and Kamei (1983), Germaine and Ladd (1988), Gasparre (2005), Anantanasakul et al. (2012) and Lade (2016). This study aims to investigate the quasi-static behaviour of cohesive soils at high-stresses using the TXC apparatus and compare it with high-stress, high-strain-rate tests. Standard TXC tests on cohesive soils are typically limited to a maximum stress of 1 MPa and a strain rate of 10^3 s^{-1}.

To achieve higher stresses, specialised TXC rigs have been developed. Akers et al. (1986), Martin et al. (2013), Williams et al. (2006) and Barr (2016*b*) have utilised innovative triaxial cell designs to measure the high-stress behaviour of sand, concrete, dry clayey sand and quartz sand specimens up to stresses of 70, 125, 500 MPa and 1 GPa, respectively. However, since these specialised TXC rigs are rare and their application on cohesive soils is non-existent, extrapolation of data will be necessary to compare quasi-static stress results with those from high-strain-rates.

2.4.2 Oedometer test

In 1919, Karl von Terzaghi began his research on consolidation, which led to the establishment of his consolidation theory after a series of experiments. By 1923, Terzaghi's hypothesis was formalised and published, marking the creation of the first oedometer testing instrument. The term 'oedometer' derives from the ancient greek οιδεω, 'oideo', meaning to swell and $\mu\varepsilon\tau\rho\text{ον}$, 'metron', meaning to measure. Casagrande expanded on Terzaghi's work in the 1920s, developing a method still used today to estimate the pre-consolidation pressure of natural soil samples along a logarithmic time scale. Taylor continued the research during the 1940s, introducing Taylor's method, which is akin to Casagrande's approach but along a square root time scale (Skempton and Terzaghi 1960). Standardisation of the apparatus is detailed in BS 1377–5:1990. The subsequent sections delve into the methodology, theory, and limitations of the oedometer test, exploring its applications on cohesive soils at high-stresses or high-strain-rates.

2.4.2.1 Methodology & theory

To grasp the purpose of the oedometer apparatus, it is essential to define key terms such as shock, impact, compaction, and consolidation:

Shock: In mechanical terms, shock refers to a transient physical excitation characterised by exceptionally high rates of force over time, as seen in impacts or explosions.

Impact: Contrastingly, impact denotes the sudden application of extreme force or shock when two bodies collide, resulting in significant impulsive forces to be exerted between them. Examples include a hammer striking a nail or a bat striking a ball.

Compaction: Within geotechnical engineering, soil compaction describes the process whereby stress is applied to a soil, leading to the densification of soil particles by displacing air from the voids between them.

Consolidation: Similarly, soil consolidation in geotechnical engineering occurs when stress is applied to soil, causing densification of soil particles by displacing water or another liquid from between the voids of the soil.

The purpose of the oedometer test is to determine the consolidation properties of the soil sample being tested. The oedometer test is performed on cylindrical specimens (Figure 2.11), where the soil specimen examined needs to be homogeneous and representative of the material in the field (BS 1377–5:1990).

A confining stress σ_c, also called σ_1 along the vertical direction, is applied to the specimen, resulting in a dominant axial stress:

$\sigma_c = \sigma_1$: Axial compression

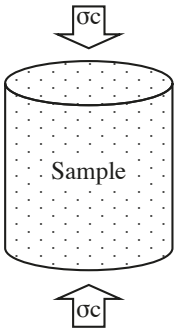

Figure 2.11: Specimen stress state during oedometer testing (σ_c: confining stress) (BS 1377–8:1990).

During the oedometer test, radial stresses are absent. The consolidation test, conducted with an oedometer apparatus (Figure 2.12), involves submerging the specimen in a water bath within a steel ring. The cell dimensions typically ranging from 75mm to 35mm in diameter (Figure 2.13), accommodate the tested sample. Vertical deformation is measured using an electronic dial gauge atop the apparatus at specific intervals. Consolidation process is conducted through staged loading, with load doubling every 24 hours. Generally starting at 25 kPa, loading increments to 50, 100, 200, 400, 800, reaching the apparatus's weight capacity limit (BS 1377–5:1990). This setup facilitates the understanding of a material's behaviour at low stresses and low strains.

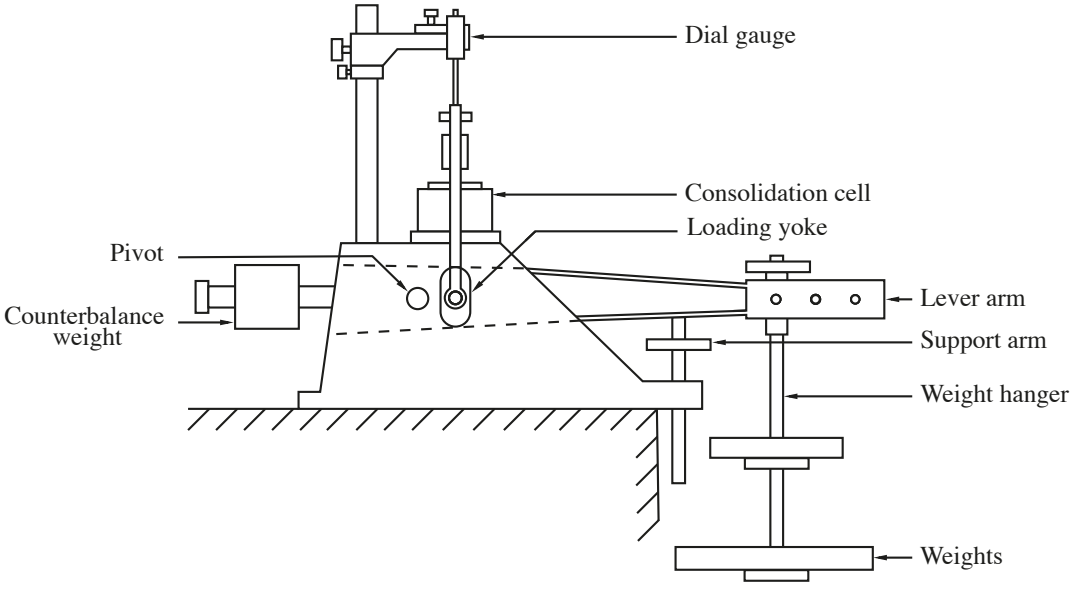

Figure 2.12: Typical general arrangement of the oedometer apparatus.

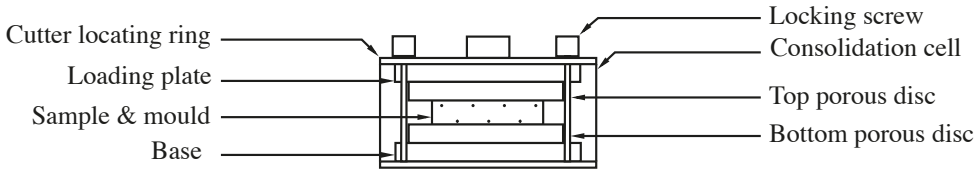

Figure 2.13: Typical general arrangement of the oedometer load cell.

2.4.2.2 Limitations of the Oedometer test

The oedometer test offers valuable insights into a soil's consolidation properties, yet it comes with limitations outlined in BS 1377–5:1990. One issue lies in the loading mechanism, particularly in older versions of the apparatus that relied on weights to increase the consolidation pressure on the sample. This method limited the maximum pressure applied when sufficient weights were unavailable. Additionally, the small sample sizes used in testing may mischaracterise the soil's environment. Furthermore, the omission of pore pressure measurements during testing poses another constraint. To address these limitations, weight-based loading systems were replaced with load cells, and data recording was digitised using computers, simplifying and standardising the testing process.

2.4.2.3 Oedometer testing on cohesive soils

Numerous studies feature extensive experimental tests on cohesive soils conducted using the oedometer apparatus under static conditions. Samples such as kaolin clay, adobe clay, London clay and silt have undergone thorough examination in various projects, as evidenced by works such as Davison and Atkinson (1990), Gasparre et al. (2011), Casini et al. (2012) and Aubert et al. (2013).

Figure 2.14a illustrates typical void ratio versus axial stress compression and swelling curves obtained during oedometer tests on cohesive soils. A physics-based depiction of cohesive soils' consolidation behaviour, along with water, is presented in Figure 2.14b. This representation is widely used in physics to illustrate the dynamic behaviour of materials, as seen in Arlery et al. (2010), which investigates the dynamic behaviour of dry and water-saturated sand under planar shock conditions.

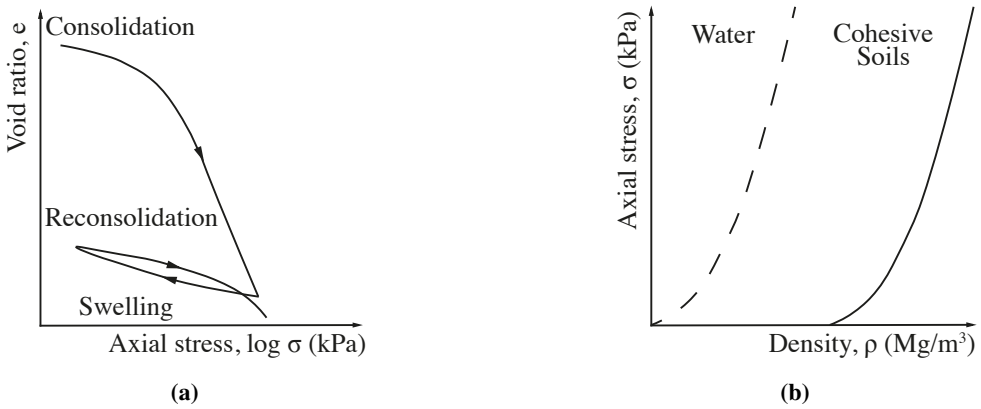

Figure 2.14: (a) Typical oedometer test response diagram of void ratio vs axial stress for cohesive soils, (b) Typical oedometer test response diagram of axial stress vs density for cohesive soils and water.

2.5 High-strain-rate testing

2.5.1 Split Hopkinson pressure bar test

The contemporary split-Hopkinson pressure bar (SHPB), named after Bertram Hopkinson, originated from his method to measure the pressure generated by bullet impacts or explosive detonations (Hopkinson 1914). Initially, the Hopkinson pressure bar consisted of a long steel bar transmitting pressure from the impact, with a shorter bar serving as a momentum trap, allowing inference of pressure wave magnitude and duration. Later, Davies (1948) expanded the theory of stress wave propagation in bars to account for dispersive effects (see §2.5.1.3). Herbert Kolsky (1949) expanded upon this design by incorporating two bars in series, separated by a material specimen. This configuration facilitated recording of stress pulses in each bar, enabling calculation of the dynamic stress-strain response of the specimen.

Modern compression SHPB configurations replace condenser units with semiconductor strain gauges, but the fundamental setup of two Hopkinson pressure bars, or the Split Hopkinson pressure bar or Kolsky bar, remains unchanged. In the following sections, the methodology of the SHPB test, how data from the test is processed and analysed, and the experimental assumptions upon which this analysis is based upon are discussed. This technique's experimental testing applications on cohesive soils are also investigated.

2.5.1.1 Methodology & theory

Key components and methodology of the SHPB test

In the idealised SHPB test illustrated in Figure 2.16, the specimen is positioned between two long cylindrical bars, termed the incident and transmitter bars, which are mounted on linear bearings. A stress pulse is induced by striking the end of the incident bar with a shorter striker bar. To ensure that only elastic waves are generated, care is taken not to exceed the proportional limit of the pressure bars.

Strain gauges affixed on the bars are connected to a Wheatstone bridge circuit, and the resulting output is captured by an oscilloscope to measure longitudinal stress waves generated throughout the test. The length of the bars and the placement of the strain gauges are carefully chosen to prevent stress pulses from overlapping at the recording point.

The SHPB test is segmented into distinct stages, as delineated in Figure 2.16. It is assumed that all bars in the SHPB, are made of the same material, and both the bars and specimen have the same diameter.

1. When the striker bar collides with the end of the incident bar, a compressive stress wave is created, which propagates to the right in the incident bar, and to the left in the striker bar. When the striker bar's left-going stress wave reaches the free surface at its left face, it is reflected as a tension wave of equal magnitude, reducing the stress in the bar to zero and alleviating the compressive contact between striker and incident bars. As a result, a right-going compressive stress pulse double the length of the striker bar is produced.

2. The strain gauge detects the compressive pulse as it travels down the incident bar. This is the incident wave σ_i.

3. When the incident wave reaches the interface between the incident bar and the specimen, a portion of the wave continues into the specimen and the remainder is reflected as the surface tension. These are the transmitted wave, σ_t, and reflected wave, σ_r, respectively. The magnitudes of the transmitted and reflected waves are determined by the relative impedance, ρc_0, of the bars and specimen. The stress wave will also reverberate within the tested specimen.

4. The transmitted wave proceeds through the specimen and into the transmitted bar, where the stress wave is measured by the strain gauge.

5. The reflected wave travels back down to the incident bar and is detected by the strain gauge.

6. All of the information required for the experiment has been gathered at this point, though the stress waves will continue to oscillate up and down the bars.

Using one-dimensional elastic wave theory, which assumes that the stress waves in the bar propagate as longitudinal waves with velocity, $c_0 = \sqrt{E/\rho}$ (Kolsky 1963), the stress pulses measured in the bar during the experiment can be used to deduce stress and strain histories of the two ends of the specimen.

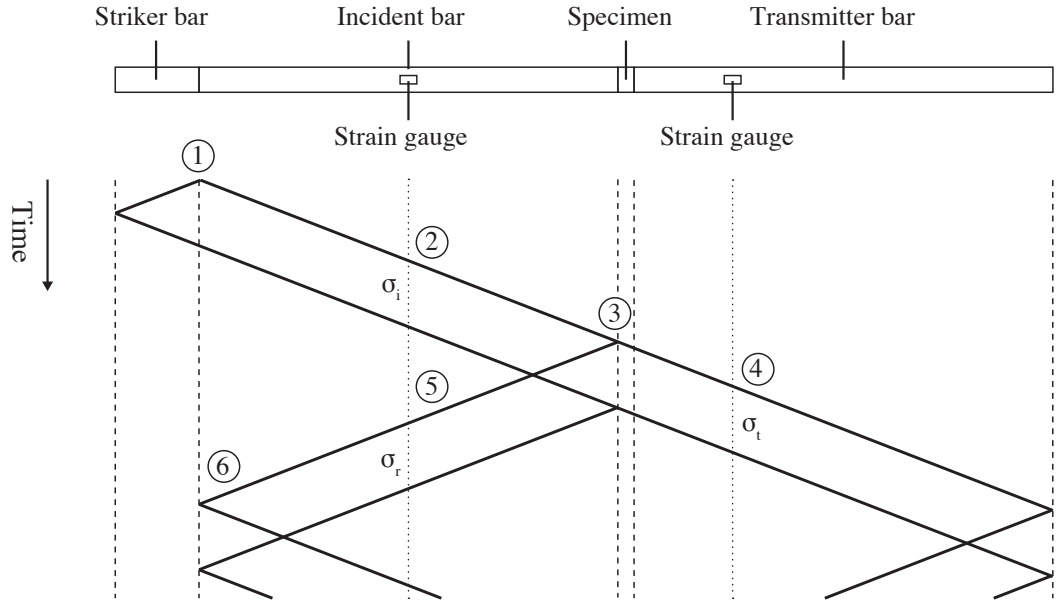

(a)

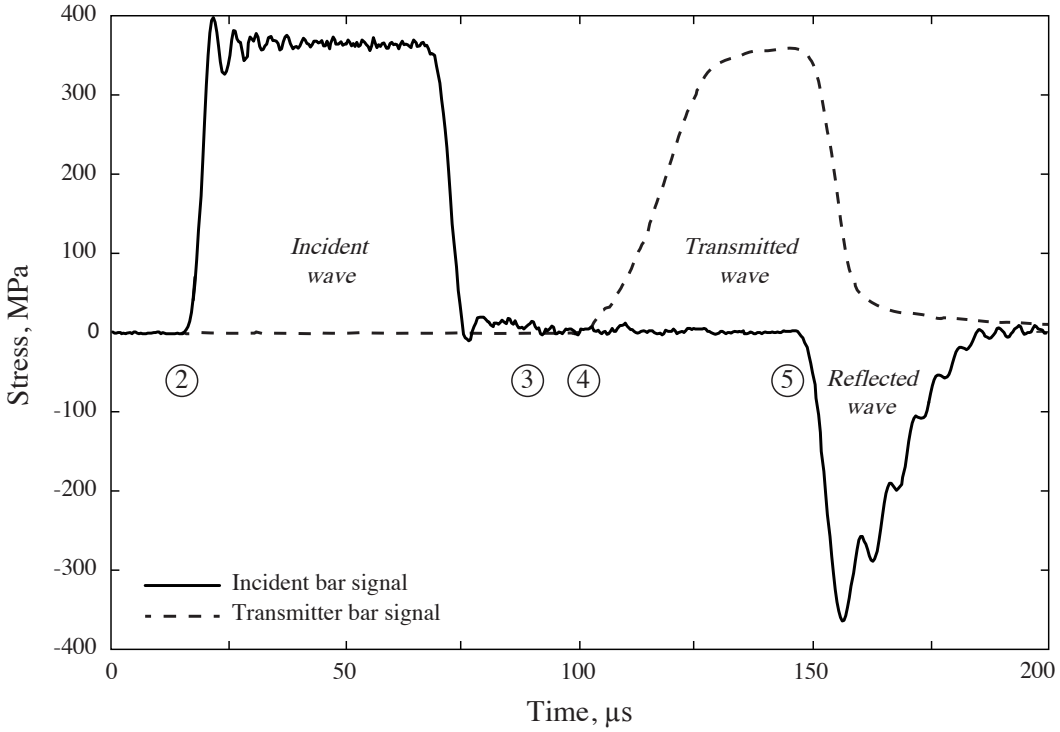

(b)

Figure 2.16: Stress waves in SHPB test: (a) Lagrange diagram of wave propagation and interactions, (b) typical strain gauge signals for a SHPB test on sand (Barr 2016*b*).

Application of one-dimensional wave theory in SHPB analysis

As demonstrated by Kolsky (1963), consider the propagation of an elastic stress wave along a dimension x in a bar with density ρ and Young's modulus E. Taking a small length of the bar, δx, if the stress on one face is σ_x the stress on the other face will be $\sigma_x + (\partial \sigma_x / \partial x)\delta x$.

If the resulting displacement is u, Newton's second law of motion is applied

$$A\frac{\partial \sigma_x}{\partial x}\delta x = \rho A \delta x \cdot \frac{\partial^2 u}{\partial t^2} \tag{2.7}$$

Since the bar behaves elastically, Equation (2.7) can be rearranged to obtain the 1D wave equation

$$\rho\frac{\partial^2 u}{\partial t^2} = E\frac{\partial^2 u}{\partial x^2}$$

Given that all waves are assumed to travel at velocity $c_0 = \sqrt{E/\rho}$, this equation can also be written as

$$\frac{\partial^2 u}{\partial t^2} = {c_0}^2\frac{\partial^2 u}{\partial x^2}$$

The general solution to the partial differential equation is as follows:

$$u = f\,(\,x + c_0 t\,) + \; g\,(\,x - c_0 t\,)$$

where f and g are functions corresponding to waves travelling with negative and positive velocity, respectively. Using a wave travelling in the direction of decreasing x, as an example, $u = f\,(\,x + c_0 t\,)$, and differentiating with respect to x and t:

$$\frac{\partial u}{\partial x} = f\,'\,(\,x + c_0 t\,) \tag{2.8}$$

$$\frac{\partial u}{\partial t} = c_0 f\,'\,(\,x + c_0 t\,) \tag{2.9}$$

and so, combining Equations (2.8) and (2.9),

$$\frac{\partial u}{\partial t} = c_0 \frac{\partial u}{\partial x} \tag{2.10}$$

Equation (2.10) can be expressed in terms of stress, since $\partial u / \partial x$ refers to elastic strains:

$$\frac{\partial u}{\partial t} = c_0 \left(\frac{\sigma_x}{E} \right) = \frac{\sigma_x}{\rho c_0}$$

where it is shown that particle velocity varies linearly with stress. The displacement of the bar is then provided by the time integral of this expression:

$$u = \frac{1}{\rho c_0} \int_0^t \sigma_x \, dt \tag{2.11}$$

To determine the stresses acting at the bar ends, the strain gauges signals are translated along the time axis by a time factor

$$t_{shift} = \frac{l_{offset}}{c_0}$$

where l_{offset} denotes the distance between the strain gauge and the specimen end of the bar. The stress in the bar can be determined at the incident bar-specimen interface by superimposing the incident and reflected waves

$$\sigma_1 = \sigma_i + \sigma_r$$

whereas at the interface of the specimen and the transmitter bar, the stress in the bar is solely determined by the transmitted wave

$$\sigma_2 = \sigma_t$$

The mean axial stress along the length of the specimen is then

$$\sigma_s = \frac{\sigma_1 + \sigma_2}{2}$$

From Equation (2.11) the displacements of the incident and transmitter bars at the specimen interfaces are

$$u_1 = \frac{1}{\rho c_0} \int_0^t (\sigma_i + \sigma_r) dt$$

$$u_2 = \frac{1}{\rho c_0} \int_0^t \sigma_t dt$$

Since the specimen is restricted between the two bars, the mean axial strain along the length of the specimen can be calculated as

$$\varepsilon_s = \frac{u_1 - u_2}{l_{s,0}}$$

where $l_{s,0}$ is the original length of the specimen. There is now enough information to describe the axial stress-axial strain response of the specimen.

2.5.1.2 Limitations of SHPB testing method

After presenting the experimental setup, it is crucial to acknowledge the assumptions made during data interpretation. In practice, the uniform distribution of stresses and strains across a specimen's length is hindered by axial and radial inertia, which impedes stress wave propagation. Soil's comparatively low wave speed, around 300 m.s^{-1}, significantly slower than the 5000 m.s^{-1} for steel pressure bars, exacerbates this issue, potentially leading to major stress discrepancies along the specimen (Felice 1986).

To mitigate this, reducing the specimen length ensures a shorter transit time for stress waves, allowing for stress equilibrium within the specimen. Studies by Song and Chen (2004) and Felice et al. (1985) demonstrated improved stress uniformity with shorter specimen lengths, suggesting a length-to-diameter aspect ratio of 0.2 as adequate for soil testing (Figure 2.17).

Alternatively, modifying the incident pulse's shape, such as employing thin metallic discs to plasticise the leading edge, can achieve a more gradual stress increase (Nemat-Nasser et al. 1991, Frew et al. 2005). Additionally, the presence of friction between pressure bars and specimens affects test outcomes, particularly in uniaxial compression tests, where friction can artificially stiffen the specimen (Gray III 2000). Lateral restraint also plays a significant role, potentially causing specimen barrel distortion rather than uniform deformation. While lateral restraints such as rigid cylinders or rings prevent barrel distortion, they may introduce friction, as seen in confined SHPB tests done by Felice et al. (1985), on clayey silty sand samples. However, their results indicate minimal friction effects at a specimen aspect ratio of 0.2.

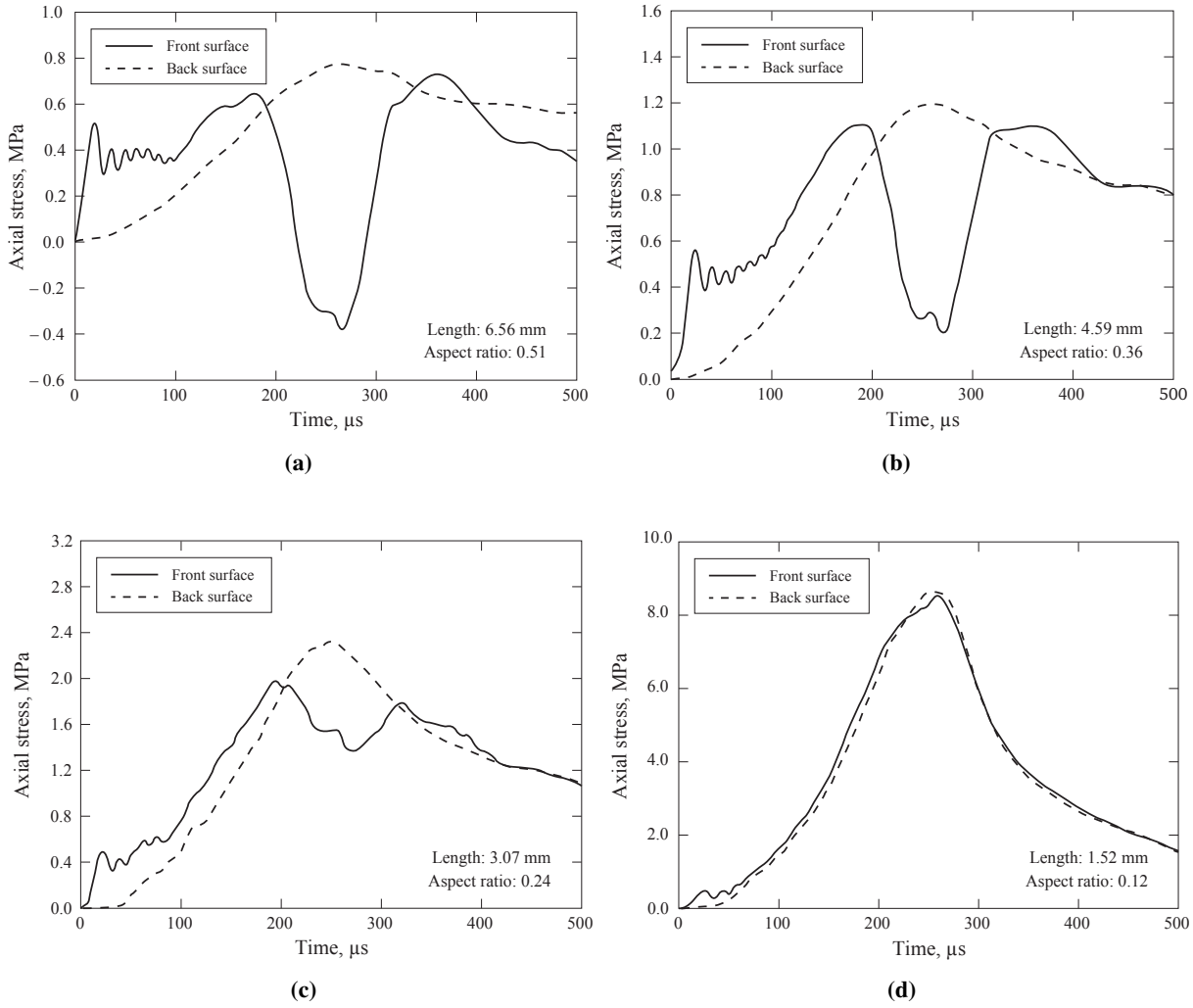

Figure 2.17: Effect of specimen length on stress equilibration in SHPB tests on silicone rubber (Song and Chen 2004).

2.5.1.3 Limitations of one-dimensional wave theory

In one-dimensional wave theory, longitudinal waves propagate uniformly at a velocity, c_0, along the bar, while transverse sections of the bar remain plane. However, due to radial expansion and contraction caused by compressive and tensile axial strains in accordance with the bar's Poisson ratio, the distribution of stresses over the cross-section becomes altered, resulting in distorted plane sections (Kolsky 1963).

Three-dimensional wave equations, initially derived by Pochhammer (1876) and Chree (1889), were later applied to the case of longitudinal waves in a cylindrical bar by Bancroft (1941). These equations reveal that longitudinal waves do not propagate uniformly at a velocity of c_0, but rather at a specific phase velocity c_ω, which is determined by various factors including wave length, bar diameter, one-dimensional wave speed, and Poisson's ratio, as seen in Equation (2.12):

$$(x-1)^2\varphi(ha)-(\beta x-1)[x-\varphi(\kappa a)]=0 \tag{2.12}$$

where

$$\begin{aligned}\beta &= (1-2\nu)/(1-\nu)\\ x &= (c_\omega/c_0)^2(1+\nu)\\ h &= \gamma(\beta x-1)^{\frac{1}{2}}\\ \kappa &= \gamma(2x-1)^{\frac{1}{2}}\\ \varphi(y) &= yJ_0(y)/J_1(y)\end{aligned}$$

c_ω – Phase velocity
c_0 – One-dimensional elastic wave velocity
a – Bar radius
ν – Poisson's ratio
γ – Wave number, $2\pi/\lambda$
λ – Wave length
$J_n(y)$ – Bessel function of the first kind, of order n

This equation has an infinite number of roots, each corresponding to a different mode of propagation in the bar. The first three modes are shown in Figure 2.18. Notably, while low-frequency waves propagate at approximately c_0, the phase velocity decreases as frequency increases, especially when the wavelength approaches the bar's diameter.

The complex waveforms generated during SHPB experiments encompass a broad spectrum of frequency components. Due to this frequency dependency, stress waves disperse as they travel along the bar. Figure 2.19 displays the dispersion of a trapezoidal wave in stainless steel pressure bar, wherein high-frequency wave components associated with the 'sharp' features become rounded, and previously linear elements exhibit oscillations.

The frequency-dependent fluctuation in stress and strain across the bar's cross-section accompanies the dispersion of the stress pulse (Davies 1948). As depicted in Figure 2.20, an increase in the forcing function's frequency results in reduced strains measured on the bar's surface compared to those measured at the axis. At high frequencies, surface axial strains become negligible, and at even higher frequencies, they become opposite in sign to the strains at the bar's axis. This phenomenon thereby limits the frequencies that can be accurately measured using surface strain gauges.

Methods have been developed to correct pressure bar signals due to inaccuracies in characterising specimen reactions when recording signals on the bar's surface at a distance from the specimen. The Fast Fourier Transform (FFT) was employed by Gorham (1983) to translate strain signals into the frequency domain. Then, based on the phase velocity derived from the Pochhammer-Chree equations, the phase angle of each Fourier component could be corrected. Extending this approach, Tyas and Watson (2000) introduced an additional correction to the amplitude of each Fourier component to account for stress variation across the bar-cross. While these corrections currently assume all waves propagate in the first mode, they have been shown to significantly improve timeshifting signals over frequency-independent assumptions established in one-dimensional wave theory (Tyas and Pope 2005).

More recently, studies by Rigby, Barr and Clayton (2018) and Barr et al. (2020) delve into pulse-shaping techniques, Pochhammer-Chree dispersion in Hopkinson bar, and innovative approaches to ensure uniform strain rates in SHPB tested samples. These investigations underscore the importance of dispersion correction in validating SHPB test results.

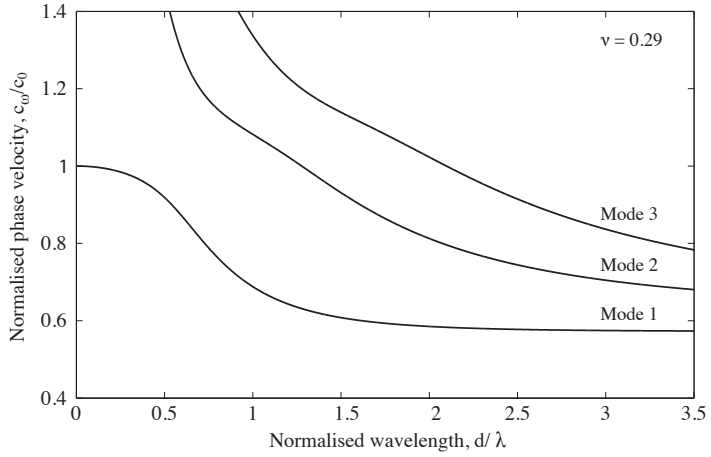

Figure 2.18: Relationship of phase velocity to wavelength for the first three modes of propagation of a longitudinal wave in a cylindrical bar, for $\nu = 0.29$ (Barr 2016*b*).

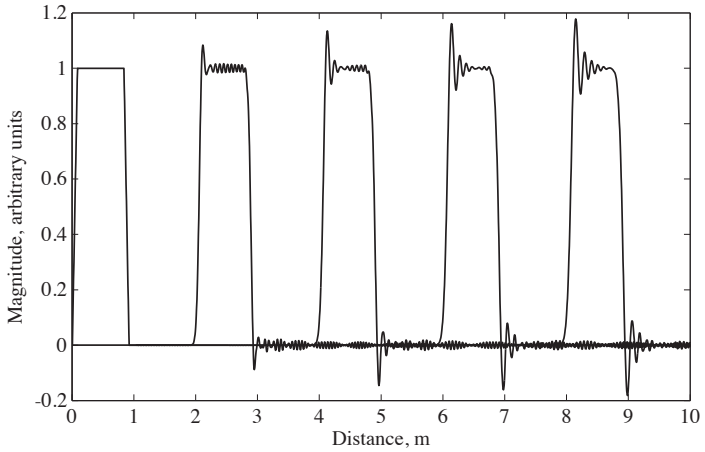

Figure 2.19: Dispersion of a trapezoidal wave in cylindrical steel pressure bar. Recordings are shown at 2m increments (Barr 2016*b*).

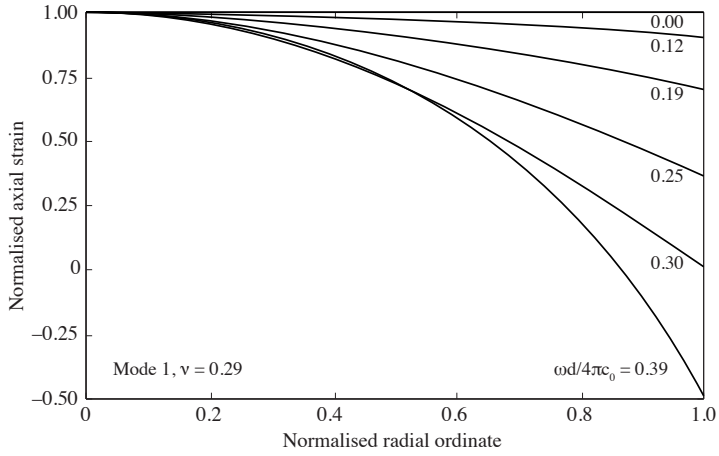

Figure 2.20: Distribution of axial strain over a stainless-steel ($\nu = 0.29$) bar cross section for an infinite duration single frequency forcing function (Tyas and Watson 2000).

2.5.1.4 SHPB testing on cohesive soils

High-strain-rate SHPB testing on cohesive soils is rare, with only four papers employing this apparatus to study this material. Table 2.3 summarises the key testing parameters and results from of each paper.

Bragov et al. (1996) modifies the well-known Kolsky method to explore the dynamic compressibility of soft soils, such as plasticine and clay. A rigid steel jacket considerably limits the specimen's radial stress, revealing a significant decrease in clay compressibility under dynamic loading compared to static loading. Consequently, it recommends adding strain gauges on the jacket for future SHPB testing to measure the specimen's overall radial strain deformation.

Ma (2010) investigates the dynamic mechanical properties of artificial frozen clay from Alaska, USA, using a SHPB equipped with a refrigerating attemperator. Assessing temperature, strain rate, and soil-water mixture combinations reveals increased brittleness with lower temperatures and higher strain rates. However, artificially freezing reduces the sample's cohesive properties, making it behave as a solid.

Yang et al. (2017) studies the high-strain-rate properties of a clay from a Beijing subway tunnel using a SHPB combined with a high-pressure consolidation apparatus. Consolidated to 3.2 MPa, the clay is tested at varying strain rates under unconfined conditions, revealing that higher strain rates lead to increased peak failure stress and strain.

Konstantinov et al. (2022) conducts an experimental study and dynamic deformation model identification of dry clay at strain rates up to 2500 s^{-1}. Dry clay samples with moisture contents ranging from of 0 to 10% are tested using a SHPB apparatus under confined conditions with an elastic cage and strain gauge. Results show varied compressibility behaviour at different strain rates, informing the development of an LS-DYNA model for comparison with experimental results.

Reference	ρ_d, $Mg.m^{-3}$	*w, %*	*Peak strain rate,* s^{-1}	*Peak stress, MPa*
Bragov et al. (1996)	1.560	–	10^4	200*
Ma (2010)	1.710	21.4	10^3	21
Yang et al. (2017)	1.870	17.3	10^2	3.8
Konstantinov et al. (2022)	–	0 – 10	10^3	250*

[– Data not reported * Estimated from data provided]

Table 2.3: Key testing parameters and results of high-strain-rate SHPB testing on cohesive soils, in the literature.

Studies from Bragov et al. (1996), Ma (2010), Yang et al. (2017) and Konstantinov et al. (2022) utilise the SHPB apparatus to investigated the high-strain-rate behaviour of cohesive soils, with tests conducted up to 2500 s^{-1}, under both unconfined and confined conditions. However, these studies lacked detailed material characterisation and sample preparations of their chosen cohesive soil. This included factors such as moisture content, particle size distribution and Atterberg limits, which hindered reproducibility and the validity of their findings.

For instance, SHPB tests conducted on dry clay samples provided limited insights into the effects of moisture content on cohesive soils at high-strain-rates (Bragov et al. 1996, Yang et al. 2017, Konstantinov et al. 2022). Moreover, artificially frozen clay samples compromised the inherent properties of moisture content in cohesive soils, rendering the results incomparable with other SHPB tests on cohesive soils (Ma 2010).

Confined SHPB tests on dry clay samples were conducted, with jackets of different thicknesses (Bragov et al. 1996), and utilising gauged elastic cylindrical cages (Konstantinov et al. 2022). Nevertheless, these results provided limited information on the effect of confinement, as the material deformed too easily due to inadequate rigidity to restrict the sample. Furthermore, comparison with unconfined SHPB tests on the same soil samples to understand the effect of confinement was absent.

In contrast, high-strain-rate SHPB testing on cohesionless soils is more comprehensive, with clearly defined material properties prior to investigating the impact of strain rate, moisture content and lateral confinement, as depicted in Ross et al. (1986), Veyera (1994), Gray III (2000), Bragov et al. (2008), Luo et al. (2014), Barr (2016*b*). This further underscores the untapped potential of novel research in comprehensively addressing the behaviour of cohesive soils at high strain rates, an area that remains largely unexplored.

2.6 Numerical modelling at high strain rates

2.6.1 Overview of high-strain-rate numerical modelling techniques

Full scale trials of blast and ballistic events entail considerable costs and time investments. Consequently, numerical techniques serve as invaluable tools for modelling these events. Explosions, blast effects, and impacts are commonly simulated using dynamic software such as LS-DYNA, which incorporates the Finite Element Method (FEM). In FEM, a complex problem is divided into *parts*, each representing a material with defined mechanical properties. These parts are segmented into *elements* using a *mesh*, and explicit time integration is utilised to compute the solution across each element at small time intervals (Hallquist et al. 2007). The precision of the solution depends on factors such as geometry, mesh resolution, and the handling of connections between *parts*. Ultimately, each *part* behaves according to its constitutive model.

The reliability and accuracy of material models are paramount and must be verified against experimental data (Church et al. 2014). Typically, this involves developing a material model based on experimental properties and then comparing the results obtained from physical experiments to those of more complex simulations. Discrepancies between the experimental and modelled data indicate inaccuracies in the material model. Adjusting the inputs until the outputs align with experimental data is not a viable solution, as the model may fail to predict future material responses under different test configurations.

The Discrete Element Method (DEM), pioneered by Cundall and Strack (1979), has gained prominence in modern numerical techniques, where material behaviour is governed by the interactions between individual particles. DEM tracks the motion of each spherical particle and assesses interactions, including particle-particle and particle-wall collisions, to predict material behaviour (Karajan et al. 2014). However, effectively utilising DEM demands a nuanced understanding of particle contact effects, such as friction and particle fracture, and modelling large-scale DEM models, particularly for fine soils, presents significant computational challenges.

In FEM-based modelling, soil is often treated as a continuum with homogeneous bulk properties (Cundall and Strack 1979). Since individual particles are not explicitly modelled in continuum approaches, constitutive models are employed to capture crucial bulk properties, which are typically derived from geotechnical tests (O'Sullivan 2015).

LS-DYNA offers various modelling approaches to create constitutive numerical models for dynamic impacts on soils. These include Lagrangian with material erosion and/or mesh adaptivity, Arbitrary Lagrangian-Eulerian (ALE), and Smooth Particle Hydrodynamics (SPH) modelling (Hallquist et al. 2007). Additionally, LS-DYNA provides a range of built-in material cards for simulating soil behaviour, from basic models with compressibility curves and yield surfaces to more complex models incorporating pore water effects, strain softening & hardening, and strain effects (Hallquist et al. 2007).

Other software, such as Autodyn and ABAQUS, offer alternative FEM solutions for modelling soils. For example, Fiserova (2006) utilised Autodyn to model sand, while Liu et al. (2019) employed ABAQUS to model saturated clays. However, due to limited access to these software packages because of licensing restrictions and sponsor requirements, the focus was exclusively on LS-DYNA.

While most finite element studies using LS-DYNA in the literature focus on buried explosives, only a small number address SHPB modelling of soils, with an even smaller subset dedicated to cohesive soils. These articles will be scrutinised, focusing on the design of the models, their geometry, and the material cards employed to numerical represent the soil in these experiments.

2.6.2 Material models for soil simulation in LS-DYNA

The LS-DYNA documentation manuals identify several constitutive material models appropriate for soil modelling (LSTC 2021). To facilitate comparisons, several models adopt similar methodologies for defining the equation of state (EOS) and material failure surface. As a result, material models tailored for soil simulation were categorised, as presented in Table 2.4.

Group	*Models*	*Material card No.*
Soil and Foam	*Soil and Foam**	*MAT_005
	Soil and Foam with Failure	*MAT_014
	*Pseudo-Tensor**	*MAT_016
	Soil and concrete	*MAT_078
Mohr-Coulomb	*FHWA Soil Model*	*MAT_147
	*Mohr-Coulomb**	*MAT_173
	Drucker-Prager	*MAT_193
Cap Models	*Geological Cap**	*MAT_025
	Schwer-Murray Cap	*MAT_145
Nested Surface	*Hysteric Soil**	*MAT_079

[* Material model selected for group representation.]

Table 2.4: Grouping of similar LS-DYNA material soil models for comparison.

To compare and validate the use of LS-DYNA soil material models for high-strain-rate compression, the models have been categorised as shown in Table 2.4. The following sections provide a brief overview of the required parameters and theoretical background for each representative model, along with an assessment of their suitability for modelling cohesive soils in LS-DYNA.

Soil and Foam

The *Soil and Foam* model (*MAT_SOIL_AND_FOAM) is a simple, pressure-dependent model designed for simulating the behaviour of foams and soils confined within a structure (LSTC 2021). Key input parameters for this material model, as listed in Table 2.5, include a compressibility curve, shear strength function, bulk modulus, and tensile cut-off.

Figure 2.21 illustrates the comparison between experimental and numerical behaviour of sand using the *Soil and Foam* model, focusing on axial stress and dry density (Barr 2016*b*). The numerical specimen exhibits lower stiffness compared to experimental results from both quasi-static and high-strain-rate tests, indicating that this material model is not well-suited for representing sands. Figure 2.22 shows the compressibility curve, derived from quasi-static test data. However, the numerical model experiences pressures exceeding 400 MPa, indicating insufficient resistance to shear forces.

While the *Soil and Foam* model is straightforward to populate with experimental data, its fixed shear modulus leads to significant deviations from expected soil behaviour with large changes in bulk modulus. This makes it unsuitable for modelling soil behaviour at high pressures. Moreover, since the pressure-volume behaviour is derived from quasi-static tests, the dynamic behaviour of cohesive soils complicates the determination of a compressibility curve that can be accurately extrapolated to high-stress conditions.

Variables	*Description*
`ro`	Initial density, kg.m^{-3}.
`g`	Elastic shear modulus, Pa.
`bulk`	Bulk modulus (to define unloading response), Pa.
`pc`	Tensile pressure cut-off, Pa.
`eps1` − `eps10`	Volumetric strain values corresponding to pressure `p1` − `p10` and is given by natural log of relative volume. Values are negative in compression.
`p1` − `p10`	Pressure values corresponding to volumetric strains `eps1` − `eps10`, Pa. Values are positive in compression.
`a0,a1,a2`	Constants to create quadratic yield function within J_2-P space.
`vcr`	Volumetric crushing option (boolean): 0 for "on", 1 for loading and unloading defined by pressure strain curve.
`ref`	Use reference geometry to initialise pressure (boolean): 0 for "off", 1 for "on".

Table 2.5: LS-DYNA variables for *Soil and Foam*.

Pseudo-Tensor

The *Pseudo-Tensor* model (*MAT_PSEUDO_TENSOR) is originally designed for concrete applications (LSTC 2021) but can be adapted for soils by excluding inputs related to steel reinforcement, aligning it closely with the soil and Foam model while explicitly defining Poisson's ratio. The required input parameters for this model are listed in Table 2.6.

Similar to *Soil and Foam*, *Pseudo-Tensor* allows for explicit Poisson's ratio definition and variation of shear modulus during simulations. However, it has been observed that the Poisson's ratio varies during computation, which affects the accuracy of axial stiffness representation compared to experimental data.

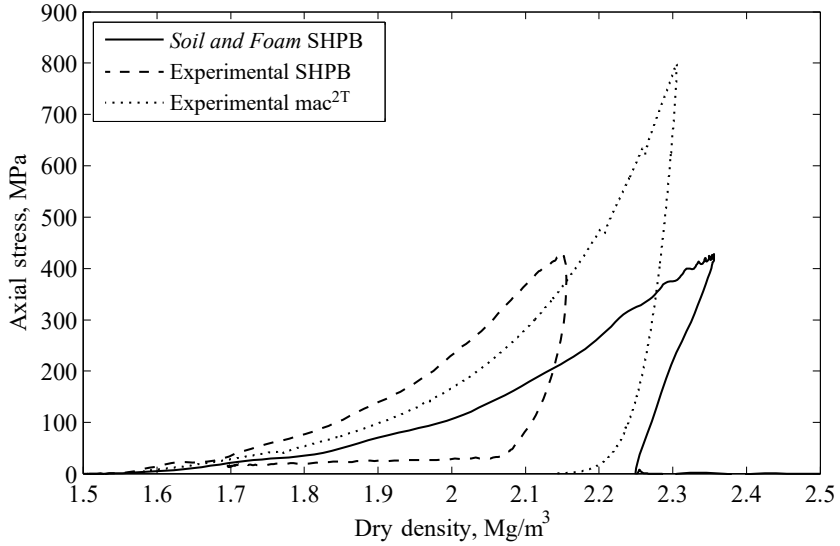

Figure 2.21: Axial stress-dry density behaviour of *Soil and Foam* SHPB specimen compared to mean experimental data (Barr 2016*b*).

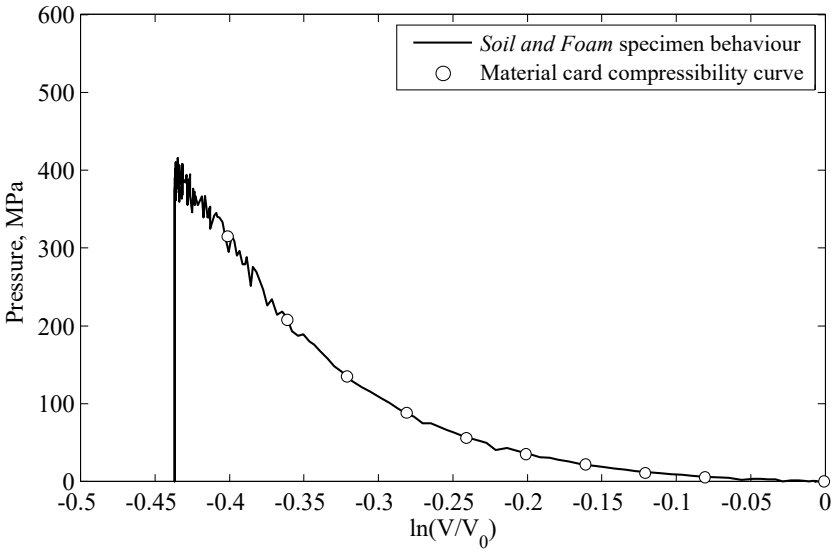

Figure 2.22: Pressure-volume behaviour of *Soil and Foam* SHPB specimen, and defined compressibility curve (Barr 2016*b*).

Additionally, Barr (2016*b*) utilised quasi-static tests with the mac^{2t} apparatus to gather compressibility data, but this apparatus is unsuitable for cohesive soils due to its inability to simulate multi-axial compression adequately.

Variables	*Description*
`ro`	Initial density, kg.m^{-3}.
`g`	Shear modulus, Pa.
`pr`	Poisson's ratio.
`sigf`	Tensile cut-off, Pa.
`x1` − `x10`	Yield surface: pressures, Pa.
`ys1` − `ys10`	Yield surface: yield stresses, Pa.

Table 2.6: LS-DYNA variables for *Pseudo-Tensor* in Mode 1.

Mohr-Coulomb

The *Mohr-Coulomb* model (*`MAT_MOHR_COULOMB`) utilised the Mohr-Coulomb constitutive model for soils, where the yield criterion can be expressed as:

$$\tau = \sigma' \tan\phi' + c'$$

where τ is the shear strength, σ is the effective normal stress, ϕ is the angle of friction resistance, and c is the intercept of the yield surface with τ axis. The required parameters for defining the yield function and plastic potential function of this model are shown in Table 2.7, with only the variables relevant to soils listed (LSTC 2021). However, the *Mohr-Coulomb* model encountered issues with negative volume error at low stresses in the SHPB model. This is because of its inability to respond to compaction, causing it to behave in a linear-elastic manner throughout the loading process (Barr 2016*b*).

Variables	*Description*
`ro`	Initial density, kg.m^{-3}.
`gmog`	Elastic shear modulus, Pa.
`rnu`	Poisson's ratio.
`phi`	Angle of shearing resistance, rad.
`cval`	Cohesion, Pa.
`psi`	Dilation angle, rad.

Table 2.7: LS-DYNA variables for *Mohr-Coulomb*.

The *Mohr-Coulomb* material model primarily requires commonly determined geotechnical parameters and offers the flexibility to explicitly define the Poisson's ratio, making it an attractive option for modelling soil behaviour. However, its limitation lies in its inability to accurately represent compaction response, particularly at high pressures, due to its simplistic nature. Nevertheless, this simplified material behaviour enhances its adaptability to represent various types of soils effectively.

Konstantinov et al. (2022) observed from high-strain-rate tests on dry clay that the shear resistance of dry clays could be described by the Mohr-Coulomb law. This finding suggests that despite the material model's limitations due to its simplicity, it can be adapted to represent cohesive soil behaviour effectively.

Cap Models

The *Geological Cap* model (*MAT_GEOLOGICAL_CAP) is a two-invariant cap model composed of yield, cap and tension cut-off surfaces, requiring the parameters listed in Table 2.8. This model simulates plastic compaction through a hardening law when interacting with cap surfaces (LSTC 2021). However, due to the need for a hardening function, this model is unsuitable for cohesive soils, as the required curve values are difficult to obtain. Similarly, the Schwer-Murray Cap model (*MAT_SCHWER_MURRAY_CAP_MODEL) also relies on an exponential hardening function and is therefore excluded for its inability to replicate high levels of compaction behaviour.

Variables	*Description*
ro	Initial density, kg.m^{-3}.
k	Initial bulk modulus, Pa.
g	Initial shear modulus, Pa.
alpha	Failure envelope parameter, α.
theta	Failure envelope linear coefficient, θ.
gamma	Failure envelope exponential coefficient, γ.
beta	Failure envelope exponent, β.
r	Cap surface axis ratio, r.
d	Hardening law exponent, d.
w	Hardening law coefficient, w.
x0	Hardening law exponent, x_0).
toff	Tension cut-off, t (< 0).

Table 2.8: LS-DYNA variables for *Geological Cap*.

Nested Surface

The *Hysteretic Soil* model (*MAT_HYSTERETIC_SOIL) is a sophisticated nested-surface model that incorporates up to ten elastic-perfectly-plastic surfaces, enabling the representation of hysteretic soil behaviour. As shear stress increases, these nested yield surfaces are sequentially activated, resulting in a material behaviour that reflects the combined effects of these active surfaces. Both bulk and shear moduli are pressure-sensitive and determine the material's response to compaction. The model's parameters are detailed in Table 2.9.

Barr (2016*b*) used the least squares method to fit experimental data to the necessary parameters. However, it was found that the *Hysteretic Soil* model was inadequate for representing the compressibility of sands at stresses exceeding 100 MPa, rendering it unsuitable for high-stress SHPB tests.

Variables	*Description*
ro	Initial density, kg.m^{-3}.
k0	Initial bulk modulus, Pa.
p0	Cut-off/datum pressure, Pa.
b	Exponent for pressure-sensitive moduli.
a0, a1, a2	Yield function constants.
df	Damping factor.
rp	Reference pressure, Pa.
lcid	Load curve id defining shear stress against shear strain.
sfld	Scale factor to apply to shear stress in lcid.
dil_a − dil_d	Dilation parameters, A, B, C, D.
gam1 − gam5	Shear strains, γ_1 - γ_5 (alternative to lcid).
tau1 − tau5	Shear stresses, τ_1 - τ_5 (alternative to lcid).

Table 2.9: LS-DYNA variables for *Hysteretic Soil*.

Summary

All the material models discussed above have intrinsic limitations that hinder their ability to accurately depict high-strain-rate soil behaviour, particularly in simulating soil compaction. The key limitations include lack of compaction mechanism, reliance on an exponential mechanism instead of a logarithmic one, or the inability to model the effects of shear modulus or Poisson's ratio.

Despite these limitations, simplifying material behaviour allows for the optimisation of numerical models to simulate SHPB tests on cohesive soils. While Barr (2016*b*) found the *Pseudo-Tensor* model most reliable for sands, its inability to handle multi-axial compression tests on cohesive soils limits its effectiveness. However, the simplicity of the *Mohr-Coulomb* model offers a reasonably accurate depiction of soil behaviour, making it suitable for coupling with experimental testing to fully characterise soil responses. Further development and optimisation of material models for numerical modelling in LS-DYNA will be discussed in Chapter 5.

2.6.3 Current methods for modelling geometries in LS-DYNA

2.6.3.1 Comparison between 2D and 3D models

In finite element analysis, shell elements are represented as extremely thin sections, significantly reducing computational time by minimising the number of mesh elements. While shell elements simplify solid elements by focusing solely on the outer "shell" of the material, they have limitations. Their hallow definition restricts the consideration of stresses through the thickness of the shell, potentially leading to inaccuracies in simulating shear deformation. Despite this drawback, modelling 2D with shell elements offers advantages, particularly in creating axisymmetric models where only half of the structure needs to be analysed due to assumed symmetry along an axis. This approach substantially decreases computational demands without sacrificing simulation accuracy (L'Eplattenier and Caldichoury 2016). Consequently, when developing comprehensive models, both 3D and 2D representations are often utilised to compare the accuracy and reliability of simulation results.

2.6.3.2 Arbitrary Lagrangian-Eulerian (ALE) modelling

The ALE technique integrates elements of both the Lagrangian and Eulerian formulations. While the Lagrangian method tracks individual particle movements in space over time, the Eulerian method characterises material behaviour at specific spatial and temporal coordinates. ALE combines these approaches, enabling individual particle tracking akin to the Lagrangian method while allowing no mesh movement similar to the Eulerian methods. This flexibility facilitates more accurate modelling of complex motion or deformation (Krayterman 2022). Busch and Tarefder (2017) applied this technique to simulate blast scenarios in LS-DYNA, where significant deformation is anticipated. Although the modelled crater did not precisely match the physical crater, it exhibited a deformation and scatter pattern consistent with experimental observations.

Similarly, Rigby, Fuller and Tyas (2018) employed the ALE method to simulate near-field blast loading with LS-DYNA, incorporating an ALE air domain and explosive charge. The numerical model effectively monitored blast wave propagation through the air domain, with qualitative comparisons indicating strong agreement between numerical predictions and experimental findings.

2.6.3.3 Smooth particle hydrodynamics (SPH) node modelling

The SPH method, a meshless Lagrangian approach, is often chosen for its ability to handle large deformations or fragmentation elements (Colagrossi and Landrini 2003). Unlike Lagrangian mesh methods where elements move as a fixed structure, SPH represents elements as a collection of particles interacting with each other, making it suitable for modelling complex geometries and boundary conditions.

This technique has found application in blast modelling, where significant deformation is expected. Chen and Lien (2018) employed the SPH method to model sand behaviour in TNT explosions, demonstrating its capability to simulate large deformations and problems with high density ratios. In SPH, interactions between particles are governed by interpolation functions, smoothing particle properties over a certain spatial distance known as the smoothing length. However, when SPH particles with different densities interact, inaccurate density and mass values can arise due to overlapping smoothing lengths. This can lead to errors in fluid behaviour characterisation, as illustrated by Ihmsen et al. (2011) in their SPH modelling of air-water interactions, where unnatural particle acceleration near SPH boundaries was observed.

2.6.4 Existing LS-DYNA modelling of high-strain-rate SHPB tests on cohesive soils

There have been attempts to numerically model SHPB experiments on cohesive soils using LS-DYNA. However, limited research on the high-strain-rate behaviour of cohesive soils has created a significant gap in the development of accurate FEM numerical models for SHPB experiments on materials prone to extreme deformation, such as cohesive soils.

Konstantinov et al. (2022) utilised LS-DYNA to model 3D axisymmetric SHPB tests on dry clay samples, incorporating a confining ring made from a rigid elastic element. SHPB tests at different strain rates (1400, 1800 and 2500 s^{-1}) provided the input data for the model. Based on the pressure data from these experiments, shear stress was estimated using the Mohr-coulomb approach before being inputted into the model. The experimental data is then compared to LS-DYNA model findings from *Soil and Foam* (`*MAT_005`). The stress vs time plots showed some degree of similarity between experimental and numerical modelling results.

Eremeyev et al. (2023) adopted a similar approach, comparing the friction coefficients of experimental SHPB cone penetration tests on dry clay with the material model *Soil and Foam* (*MAT_005) from LS-DYNA, utilising the MM-ALE technique. The comparison between the experimental and numerical results displayed significant differences.

The studies by Konstantinov et al. (2022) and Eremeyev et al. (2023) encompass the entire spectrum of high-strain-rate modelling on cohesive soils. They underscore several critical issues: the lack of clear material characterisation of the investigated cohesive soil, the absence of soil shear strength data at high pressures during modelling, and significant limitations in accurately modelling the behaviour of cohesive soils at all three saturation levels—unsaturated, partially saturated, and fully saturated.

Furthermore, SPH modelling, an innovative meshless Lagrangian numerical technique for modelling fluid equations of motion under high-strain-rate effects, has never been utilised in LS-DYNA for modelling cohesive soils samples in SHPB experiments. Given the dynamic nature of SHPB tests and the complex material behaviour of cohesive soils, this presents an ideal opportunity for exploration.

2.7 Parametric modelling

2.7.1 Background & key concepts

Fortification engineers rely on soil-filled barriers like Hesco Concertainers for blast protection, yet cohesive soil's high-strain-rate behaviour remains elusive despite its widespread availability. Understanding cohesive soils such as clay and silt is crucial for the design of fortifications, due to their global presence and potential as alternatives where sandy soils are less common.

Precise data on local soils are vital for fortification engineers to adapt designs, urging comprehensive studies on soil behaviour under extreme loading conditions. Focusing on kaolin clay offers a foundation for understanding its response to strain rate, moisture, and confinement variations through SHPB tests. The complexities of cohesive soils, including their undrained behaviour and fine particle size, pose challenges compared to cohesionless soils such as sand (Bragov et al. 2008, Luo et al. 2014, Barr 2016*b*), necessitating new research to inform resilient fortification designs and bridge existing knowledge gaps.

Various machine learning algorithms can be utilised for regression tasks. Linear regression assumes a relationship between input features and the target variable, while polynomial regression extends this concept by considering polynomial relationships. Regularised regressions, such as Ridge and Lasso, add penalty terms to prevent overfitting and induce sparsity in models (Hastie et al. 2001). Support vector Regression (SVR) (Smola and Schölkopf 2004) extends support vector machines (SVMs) for regression tasks, while decision trees (Leo Breiman 1984) and random forest regression (Breiman 2001) split the data and combine trees to improve accuracy. Gradient boosting (Friedman 2001) builds weak learners sequentially, correcting errors, and deep learning techniques (Goodfellow et al. 2016), like artificial neural networks, learn complex relationships for regression.

Model Order Reduction (MOR) is a branch within computational science dedicated to simplifying intricate mathematical models, often represented by systems of differential equations or transfer functions, while preserving their fundamental behaviour. MOR aims to reduce the computational burden associated with simulating or analysing such models by generating simplified versions, known as reduced-order models (ROMs), that adequately represent the system's dynamics with sufficient accuracy (Benner et al. 2017, Rozza et al. 2020*a*,*b*).

Through the reduction of degrees of freedom in the model, MOR facilitates faster simulations, optimisation, and control design, all while maintaining fidelity. This proves advantageous for systems characterised by high-dimensional or parametric descriptions encountered in scientific environments.

In polynomial regressions, addressing the challenges of high-dimensional parametric problems has led to the development of novel techniques such as the Proper Generalised Decomposition (PGD) (Ibáñez Pinillo et al. 2018, Sancarlos et al. 2023, Champaney, Chinesta and Cueto 2022). PGD, a tensor-based method, represents high-dimensional data by utilising separable representations and a greedy iterative algorithm for adaptive basis construction. It finds applications across various engineering and scientific fields, such as blast and impact dynamics in this case.

Polynomial regression techniques, employed in computational mechanics (Pasquale et al. 2022*a*) and structural deformation (Champaney, Pasquale, Ammar and Chinesta 2022*a*), have yet to be applied in the field of blast and impact dynamics. This section introduces key concepts of parametric modelling that will be employed in this study, along with examples of their applications. Further details on the polynomial regression technique used, and its application in this project are provided in Chapter 6.

2.7.2 Case studies in parametric modelling applications

This section presents the parametric modelling methodology of the PGD polynomial regression technique through its application to two case studies. Papers by Pasquale et al. (2022*a*) and Champaney, Pasquale, Ammar and Chinesta (2022*a*) employ this method, and are evaluated to examine the methodology, results, and benefits of its use for this research project.

2.7.2.1 Case study 1

In the paper by Pasquale et al. (2022*a*), a parametric metamodel is developed based on experiments from a full frontal rigid barrier crash test. In the automotive industry, building parametric surrogate models is a fundamental tool for evaluating the performance of newly designed car components in real time. These models allow for significant gains in terms of manufacturing costs and time delays during the investigation phase, where multiple parameters can be evaluated simultaneously using these models.

This work primarily focuses on snapshots-based reduced order modelling (Benner et al. 2020), particularly the Proper Orthogonal Decomposition (POD) and the sparse Proper Generalised Decomposition (sPGD). Extensive reviews and investigations on these techniques can be found in the referenced literature (Borzacchiello et al. 2019, Chinesta, Leygue, Bordeu, Aguado, Cueto, González, Alfaro, Ammar and Huerta 2013, Chinesta, Keunings and Leygue 2013, Chinesta et al. 2017, Ibáñez et al. 2018, Ibánez et al. 2019, Champaney, Pasquale, Ammar and Chinesta 2022*b*, Chinesta et al. 2022).

In this case study, the test data is split into training and tests sets before applying the POD and sPGD regression models. The predicted versus true values are then evaluated to assess the model's accuracy. Furthermore, this paper also investigates clustering, multi-regression models, and data classification methods, all of which are highly useful tools that could be employed in our research project.

For a comprehensive representation of the parametric analysis conducted in this case study, refer to the plots in Pasquale et al. (2022*a*).

2.7.2.2 Case study 2

In the paper by Champaney, Pasquale, Ammar and Chinesta (2022*a*), the background methodology and theory of the parametric modelling techniques are initially discussed, followed by the design of the POD and sPGD regression models. The application of these models is then illustrated through two computational mechanics problems. First, a parametric analysis of a tension-loaded dog bone specimen is conducted. Subsequently, another parametric analysis is performed on a notched dog bone specimen, also subjected to tension.

For the design of the parametric model, the same approach as in Case study 1 (Section 2.7.2.1) was employed. This case study required a more careful investigation into data alignment and uncertainty propagation due to the variation in displacement behaviour of the dog bone sample.

In the first case, test results from the tension loaded dog bone specimen showed that the observed response during testing could be divided into two zones. Parametric modelling analysis was therefore conducted separately on each zone before performing curve reconstruction and alignment.

In the second case, the notched dog bone specimen loaded in tension exhibited a distinct behaviour across different zones based on the notch position. Consequently, a confidence interval of 0.95 was applied, and parametric model enrichment was employed through numerical modelling to further characterise its behaviour across the different zones. Real-time calibration, using data alignment and clustering, was conducted to categorise the observed behaviours. After classifying the data, curve reconstruction was performed. The model predictions were then compared with the training and test data.

2.7.2.3 Summary

In summary, the case studies discussed in Sections 2.7.2.2 and 2.7.2.2 both utilise the POD and sPGD parametric modelling methods in different environments. These methods provide efficient mathematical tools to rapidly and effectively predict the physical behaviour of unknown tests with a high level of accuracy, using collected experimental data. This polynomial regression approach technique is used in this research project, and the details of its application are provided in Chapter 6.

2.8 Summary

Material characterisation

This chapter begins by defining key material characterisation terminology in geotechnical engineering, followed by an introduction to prevalent cohesive soils in testing, such as kaolin clay, adobe clay, London clay and silt. To underscore the extensive research conducted on cohesive soils, material parameters are juxtaposed across various literature sources. Given the considerable variability of cohesive soils, the project's focal point gravitates towards a meticulously studied, archetypal soil: kaolin clay.

Quasi-static testing

Following an evaluation of the TXC and oedometer testing apparatuses, commonly used for exploring the quasi-static behaviour of cohesive soils under one-dimensional compression, insights were gained into how soil material properties affect strain-rate. Nonetheless, it is important to note that these testing methods are limited to low-strain and low-stress conditions.

Conducting UU TXC tests helps characterise the undrained behaviour of cohesive soils at low-strain rates. Additionally, oedometer testing has proven reliable in applying sustained loads to soil samples under similar conditions, providing vital geotechnical variables. This highlights the importance of conducting quasi-static tests, as they establish a foundation for understanding cohesive soil behaviour at low-strain rates, which can then be compared with high-strain-rate tests. Furthermore, these tests provide essential parameters for future numerical modelling developments.

High-strain-rate testing

The importance of the SHPB in studying material behaviour at high-strain-rates has been underscored, particularly in the context of testing soils. Experimental factors critical to SHPB testing of soils include careful selection of specimen length-to-diameter ratios to minimise lateral inertia and boundary friction effects. However, dispersive effects can become significant, violating the assumptions of one-dimensional wave theory for high-frequency stress pulses. Methods for correcting these frequency-dependent effects have been proposed, such as timeshifting signals with high-frequency components or dispersion correction.

High-strain-rate SHPB testing on cohesive soils is limited, with only a few studies exploring the individual impacts of moisture content, confinement, and temperature. These factors have been shown to significantly influence soil behaviour. Clear opportunities exist to enhance our understanding of cohesive soils through comprehensive studies varying these factors. The SHPB, leveraging one-dimensional wave theory, is a valuable tool for investigating high-strain-rate behaviour. While extensive work has been done on coarser-grained soils such as sands, research on cohesive soils remains sparse due to their tendency to extrude laterally, posing challenges in experimental setups and interpretations.

Numerical modelling

Turning to numerical FEM, LS-DYNA has emerged as a valuable asset for predicting dynamic events in soils, including blast and ballistic scenarios. It enables the acquisition of parameters such as deflection and stress state across the entire field of interest, contingent upon robust material models defining the behaviour of model parts. Numerical modelling, combined with experimental data, is crucial for effectively characterising soil behaviour and developing a robust constitutive model. While several common soil material models have been evaluated, each has intrinsic limitations that prevent a complete depiction of cohesive soil behaviour under high-strain-rates. Nonetheless, simplistic models such as *Mohr-Coulomb* can still offer valuable insights. The absence of high-pressure shear strength data in cohesive soils, was identified as a source of error in many existing studies. Furthermore, the lack of numerical modelling of SHPB tests using SPH for large dynamic deformations presents an avenue for further exploration.

The development of numerical models, when used alongside experimental testing, provides a robust method for reaching meaningful conclusions. This combined approach can help optimise simulations and improve the understanding of cohesive soil behaviour under various loading conditions.

Parametric modelling

Various machine learning algorithms for conducting regression tasks were evaluated, with a focus on Model Order Reduction (MOR) and Proper Generalised Decomposition (PGD) polynomial regression techniques. PGD was selected for this research project due to its mathematical rigour and physics-based design approach. The application of the PGD in different sectors was also examined through two case studies to inform its implementation in this study.

Research aim

The aim of this study will be to investigate how moisture content, strain rate, and confinement conditions affect the behaviour of kaolin clay across different loading conditions, from quasi-static to high-strain-rates. This research will involve characterising the material quasi-statically at various moisture contents using the TXC, oedometer apparatus. Additionally, cohesive soil samples with varying moisture contents will undergo SHPB testing at different strain rates, and different confinement conditions. Leveraging the parameters gathered from testing, constitutive material models in LS-DYNA will be evaluated. These models will compare experimental findings with numerical simulations, assessing their alignment and validating the model's predictive capabilities in simulating the behaviour of cohesive soils at high strain rates. Finally, parametric models will be developed based on the POD and sPGD methods using SHPB test results conducted on cohesive soils samples. These tests vary in moisture content, strain rate and confinement conditions. They will be used to accurately and rapidly predict the behaviour of cohesive soil samples with parameters that have not yet been tested.

Chapter 3

Material characterisation, specimen preparation, and test programme

3.1 Introduction

This chapter starts by presenting the material characterisation of the selected cohesive soil, kaolin clay, covering particle density, shape, size distribution, mineralogy and the Atterberg limits. The sample preparation methodology for testing is then presented, and concludes with a detailed test programme, outlining the quasi-static and high-strain-rate tests performed in this research project. The findings from this chapter have been published, and the article is available in Appendix A.5.

3.2 Material characterisation

The soil selected is defined using EN ISO 14688–1:2002, as white fine CLAY (CL). For brevity, it is referred to as 'kaolin clay'. Table 3.1 provides an overview of the kaolin clay material properties, which are derived using the methods described in Sections 3.2.1, 3.2.2, 3.2.3, 3.2.4 and 3.2.5.

Soil properties	*Units*	*Value*
Primary mineral	–	Kaolinite
Particle density, ρ_s	$Mg.m^{-3}$	2.65
Liquid Limit, LL	%	40
Plastic Limit, PL	%	25
Plastic Index, PI	%	15
D_{50}	μm	0.74
Particle sphericity	–	Low–Medium
Angularity	–	Subrounded–Subangular
Surface texture	–	Smooth

Table 3.1: Overview of the kaolin clay material properties.

3.2.1 Particle density

The particle density, denoted as ρ_s, represents the density of the solid mineral particles. It is used with the bulk dry density, ρ_d, to determine the void ratio of a soil using the following relationship:

$$e = \frac{\rho_s}{\rho_d} - 1$$

The particle density, ρ_s, of the kaolin clay was calculated to be 2.65 $Mg.m^{-3}$, using the method described in BS 1377–2:1990 §8.2, which is the density of kaolinite.

3.2.2 Particle size distribution

The particle size distribution (PSD) of the kaolin clay is determined using the data sheet provided by the supplier, IMERYS, due to the limitations with in-house equipment, including material clumping and difficulty measuring very fine particle sizes in cohesive soils. Figure 3.1 depicts the cumulative PSD of the kaolin clay. The D_{50} of this well-graded impermeable soil is 0.74 μm, and the clay and silt contents are calculated to be 80 % and 20 %, respectively. The soil is therefore characterised as CLAY (CL).

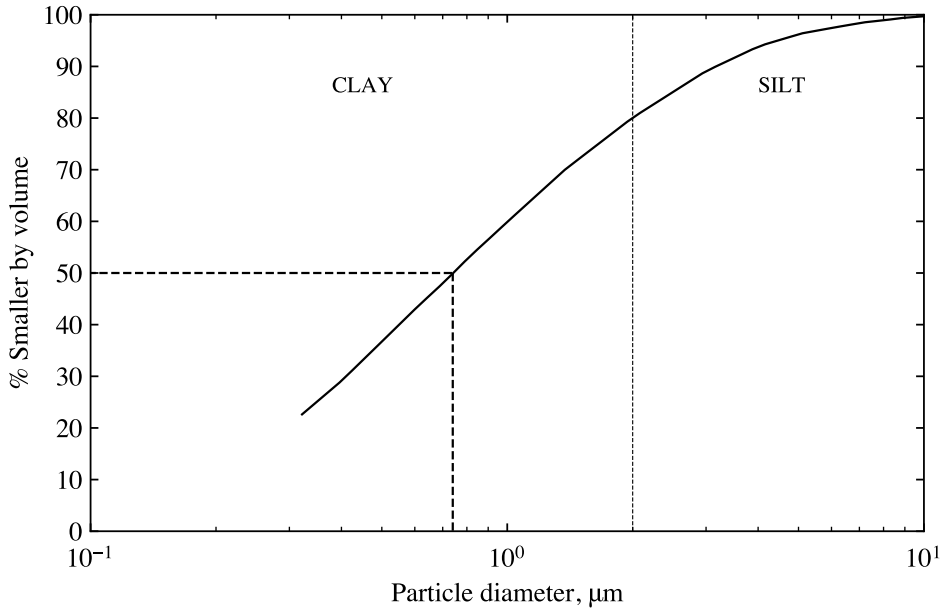

Figure 3.1: Cumulative particle size distribution of the kaolin clay soil (IMERYS data sheet).

3.2.3 Atterberg limits

For consistency, Atterberg limits must be uniform across all soil samples. The fall cone test was used to obtain consistent Atterberg limit values for the different kaolin clay samples (BSI 1990*a*). The liquid limit, LL, plastic limit, PL, and plastic index, PI are 40 %, 25 % and 15 %, respectively. The values of which are above the A-line (Casagrande 1948), confirming the soil selected is a CLAY (CL).

3.2.4 Particle mineralogy

X-ray diffraction (XRD) was carried out on the kaolin clay to establish the constituent minerals. In XRD an incident X-ray beam undergoes diffraction due to the regular atomic structure of a crystalline specimen. By measuring the intensity of diffraction at different incident angles, θ, a distinct diffraction pattern is obtained. This pattern can be compared to a database of known patterns to identify the phases present in the specimen. Phase analysis was carried out using a PANalytical Aeris diffractometer and the ICDD's Diffraction File (PDF-4+). Figure 3.2 shows the diffraction pattern of the kaolin clay. As expected, kaolinite is the primary mineral, followed by quartz. The cohesive soil used in this investigation is composed of 70% kaolinite and 30% quartz.

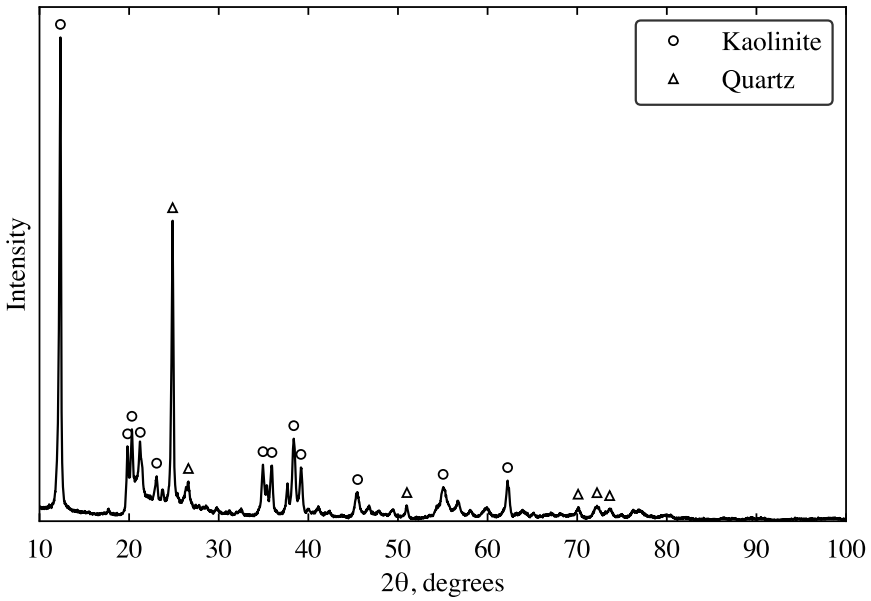

Figure 3.2: X-ray diffraction data of kaolin clay soil.

3.2.5 Particle shape

The shape of the kaolinite-sized particles in the soil are assessed qualitatively with a scanning electron microscope (SEM), using the descriptors provided in EN ISO 14688–1:2002 ISO (2002):

- Sphericity indicates how closely a particle's shape resembles a sphere, with low-sphericity particles being elongated along one axis;
  [low < medium < high]
- Angularity characterises the shape of particle edges and corners, irrespective of overall regularity;
  [well rounded < rounded < subrounded < subangular < angular]
- Surface texture describes the texture of particle faces.
  [rough/smooth]

Kaolin clay soil was gold (Au) coated before SEM insertion. Images were captured using secondary electron (SE) signals with a high voltage of 5.00 kV. Using Figure 3.3, kaolin clay particles vary from low to medium sphericity, are subrounded to subangular, and have smooth surface texture.

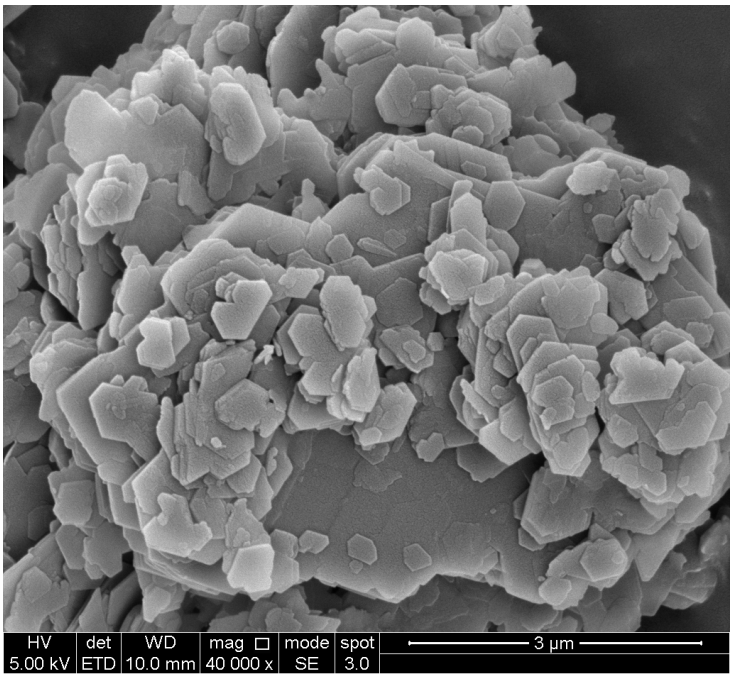

Figure 3.3: SEM imagery of kaolin clay particles.

Material characterisation tests on kaolin clay have been conducted in existing literature, as discussed in Section 2.2. Comparison of obtained values indicates consistency with existing kaolin clay tests.

3.3 Specimen preparation

Kaolin clay samples were prepared by mixing powdered Speswhite kaolin clay with water at a 1:1 ratio by weight to create a kaolin slurry. This slurry was then placed in a pressurised cylindrical Rowe cell and consolidated to three different pressures: 400, 500 or 600 kPa. The resulting kaolin clay wheels were 250 mm in diameter and 110 mm in height, with moisture contents of 41, 42 or 44 %, respectively. The moisture content was determined through material characterisation tests by comparing the wet and dry masses of samples taken from these wheels.

3.3.1 Specimen preparation for quasi-static testing

For the triaxial compression (TXC) tests, kaolin clay specimens were prepared using the large kaolin clay wheels. Samples measuring 38 mm in diameter and 76 mm in length were extracted using a steel cylinder to fit perfectly in the triaxial cell.

For the oedometer tests, kaolin clay specimens were also prepared using the large kaolin clay wheels. Samples measuring 75 mm diameter and 20 mm in length were extracted using a cutter ring, before being inserted into the confining cell of the oedometer apparatus.

3.3.2 Specimen preparation for high-strain-rate testing

Utilising the kaolin clay wheels previously prepared, a controlled drying procedure was employed to investigate the effect of moisture content on kaolin clay samples at high-strain-rates using the SHPB apparatus. Specimens with moisture content levels ranging from 0 to 44 % were prepared, covering all saturation levels: unsaturated, partially-saturated and fully saturated. The kaolin clay samples used for both unconfined and confined SHPB testing are prepared using the following procedure:

1. Cylindrical kaolin clay samples with varying moisture content are made using a 25 mm stainless-steel cylinder slicer. The specimens have a nominal length of 5 mm and a diameter of 25 mm. The initial weight of the kaolin clay specimen is recorded immediately after it has been sliced.
2. Samples are air dried in a temperature-controlled setting at 20ºC, and weighed at regular intervals to measure their current moisture content based on their initial wet weight and current weight. To prepare the unsaturated dry samples, the specimens are oven-dried for 12 hours.
3. Cut and air-dried samples are wrapped in polyvinylidene chloride to minimise changes in moisture content between sample preparation and testing. The samples are prepared and tested in different laboratories, hence they are stored in sealed plastic bags for 24 hours maximum, until required for testing.

Experimental trials showed that the thin, 5 mm thick cylindrical kaolin clay samples allowed for consistent air-drying, making it the primary method for producing specimens with varying moisture contents.

3.4 Test programme

The test programme outlined in Table 3.2 summarises the experiments conducted in this research project on kaolin clay. It includes information on the targeted strain rate amplitudes of the tests, the moisture contents of the specimens evaluated and the total number of tests performed. The aim of this research project is to assess how kaolin clay responds to significant changes in strain rate, investigate the impact of varying moisture content on its behaviour, and analyse how confinement affects its overall behaviour. Each test type is described in detail alongside key research inquiries and properties of interest.

Testing apparatus	*Strain rate, s^{-1}*	*Moisture content, %*	*Number of tests*
TXC	10^{-3}	41, 42 & 44	9
Static oedometer	10^{-3}	41, 42 & 44	3
Dynamic oedometer	10^{-3}	41, 42 & 44	3
Unconfined SHPB	10^{3}	From 0 to 44	98
Confined SHPB	10^{3}	From 0 to 44	46

Table 3.2: Test programme overview for the research project.

Only samples with moisture contents of 41%, 42%, and 44% were tested using the TXC and Oedometer apparatus, as even minor variations in moisture content significantly impact stress and strain behaviour at low strain rates.

3.4.1 Quasi-static test programme

3.4.1.1 TXC test programme

Three quasi-static one-dimensional unconsolidated undrained (UU) TXC tests were conducted on each sample, with a moisture content of 41, 42 and 44 %, at an initial confining pressure of 100, 200 & 300 kPa (Table 3.2). The aim of these tests is to record the stress, strain and undrained shear strength of the sample to validate the impact of moisture content on the kaolin clay's behaviour under quasi-static testing conditions.

3.4.1.2 Oedometer test programme

Three quasi-static oedometer tests were performed on kaolin clay samples at consolidation pressures ranging from 0 to 3200 kPa (Table 3.2). The stress, void ratio and density data of the sample are collected to confirm the influence of moisture content on the kaolin clay's sample behaviour.

In addition, three dynamic oedometer tests were carried out on kaolin clay samples with moisture contents of 41, 42 and 44 %, consolidated directly to 3200 kPa (Table 3.2). The objective is to analyse the stress, void ratio and density changes to understand the dynamic compression behaviour of the sample at low strain rates, and compare this behaviour against high-strain-rate tests. Indicative boundaries for water and kaolinite were added to the dynamic oedometer plots to aid with comparison.

3.4.2 High-strain-rate test programme

3.4.2.1 Unconfined SHPB test programme

High-strain-rate unconfined SHPB tests were conducted on kaolin clay samples with moisture contents ranging from 0 to 44 %, as shown in Table 3.3. The tests were performed at speeds of 8, 12 and 16 m/s, resulting in maximum average strain rates of 1200, 1900 and 2800 s^{-1}, respectively. Additional tests were performed at 18, 20 and 22 m/s to evaluate its behaviour at higher strain rates. The specimen's axial stress and strain are measured to understand how varying moisture content affects kaolin clay's high-strain-rate behaviour. Figure 3.4 provides a detailed breakdown of the tested speeds, moisture contents, and corresponding number of unconfined SHPB tests.

Speed, m/s	*Moisture content, %*	*Number of tests*
8	0, 5, 10, 15, 20, 25, 30, 41, 42 & 44	37
12	0, 5, 10, 15, 20, 25, 30, 35, 41 & 44	27
16	0, 10, 15, 20, 25, 30, 25 & 41	27
18	0, 20 & 41	3
20	0 & 20	2
22	20 & 25	2
Total		98

Table 3.3: High-strain-rate unconfined SHPB test programme for this research project.

3.4.2.2 Confined SHPB test programme

High-strain-rate confined SHPB tests are performed on kaolin clay samples with moisture contents ranging from 0 to 44 %, as outlined in Table 3.4. Initial tests were performed at 12 m/s to facilitate behavioural comparison with unconfined SHPB tests. Subsequent tests were carried out at 18, 20 and 22 m/s, resulting in maximum average strain rates of 2600, 2800 and 3100 s^{-1}, respectively. The axial and radial stresses and strains of the specimen are measured to assess the effect of confinement on cohesive soils at high strain rates. Figure 3.5 provides a detailed breakdown of the tested speeds, moisture contents, and corresponding number of confined SHPB tests.

Speed, m/s	*Moisture content, %*	*Number of tests*
12	0, 21 & 41	9
18	0, 10, 20, 25, 30, 35 & 41	20
20	0, 20 & 41	7
22	0, 10, 20, 30 & 41	10
Total		46

Table 3.4: High-strain-rate confined SHPB test programme for this research project.

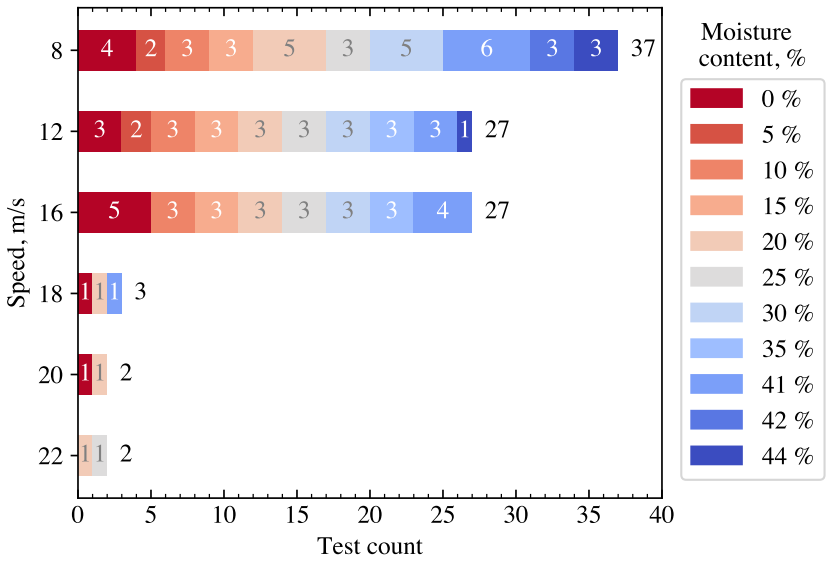

Figure 3.4: Unconfined SHPB test programme breakdown of the number of tests for each moisture content.

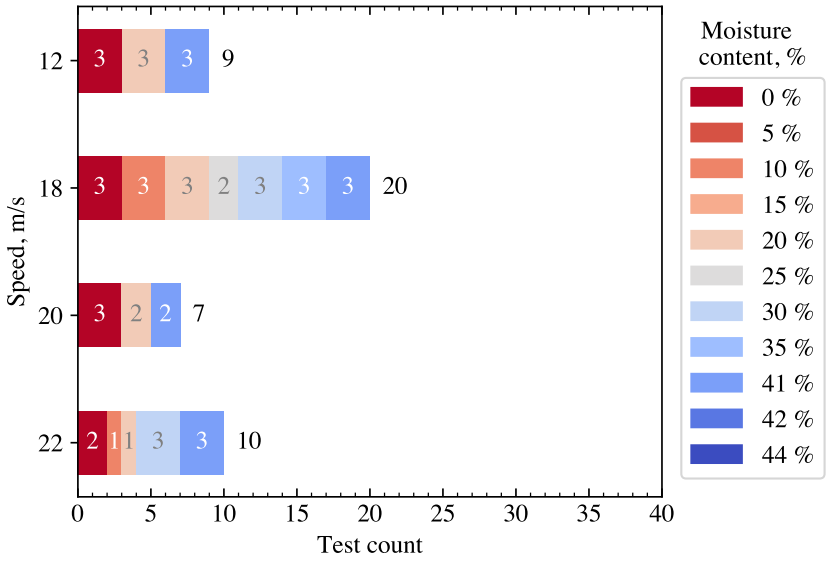

Figure 3.5: Confined SHPB test programme breakdown of the number of tests for each moisture content.

3.5 Summary

This chapter presents a comprehensive examination of kaolin clay as the cohesive soil under investigation, outlining its detailed characterisation through various material tests. These tests ensure the reproducibility of the results and facilitate comparison with existing literature on the properties of the kaolin clay. Material characterisation tests were conducted to gather data on the particle density, particle shape, particle size distribution, particle mineralogy and the Atterberg limits of the kaolin clay used in experimental testing.

A detailed sample preparation and test programme was developed for both quasi-static and high-strain-rate experimental tests, aligning with the main objectives outlined in this thesis and addressing the key research gaps in cohesive soil behaviour. These objectives include verifying the influence of moisture content on the undrained shear strength behaviour of cohesive soils at low-strain-rates, and investigating the high-strain-rate behaviour of cohesive soils with regard to moisture content, strain rate and confinement.

Chapter 4

Strain rate dependence in cohesive soils

4.1 Introduction

This chapter presents the experiments conducted to investigate the effect of strain rate, confinement and moisture content on kaolin clay samples. These experiments include both high-pressure quasi-static tests, utilising the triaxial and oedometer apparatus, as well as high-strain-rate tests, employing the SHPB apparatus where samples are examined under both unconfined and confined conditions. The results are analysed to assess the compressibility of the soil under quasi-static loading, the influence of strain rate, the impact of moisture content, and the effects of confinement on the strain-rate sensitivity of kaolin clay.

4.2 TXC testing methodology

The quasi-static TXC tests were conducted on kaolin clay samples with varying moisture contents of 41, 42 or 44 %, each measuring 38 mm in diameter and 76 mm in length. These tests were performed under unconsolidated undrained (UU) conditions, with initial confining pressures of 100 kPa, 200 kPa & 300 kPa. The objective of these tests was to assess the stress, strain and undrained shear strength of the samples to confirm the influence of moisture content on the clay's behaviour at low strain rates. Further details regarding specimen preparation and the test programme are provided in Sections 3.3.1 and 3.4.1.1, respectively.

4.2.1 Experimental setup

The general arrangement of the triaxial apparatus used is shown in Figure 4.1. Prior to commencing the testing procedure, each feature of the triaxial cell underwent thorough inspection. Pressure valves were manually controlled, while load application and data acquisition were automatically handled by the computer. Tests were conducted at 20ºC to ensure consistent testing conditions. Further discussion on the methodology, theory and limitations of this apparatus can be found in Section 2.4.1.

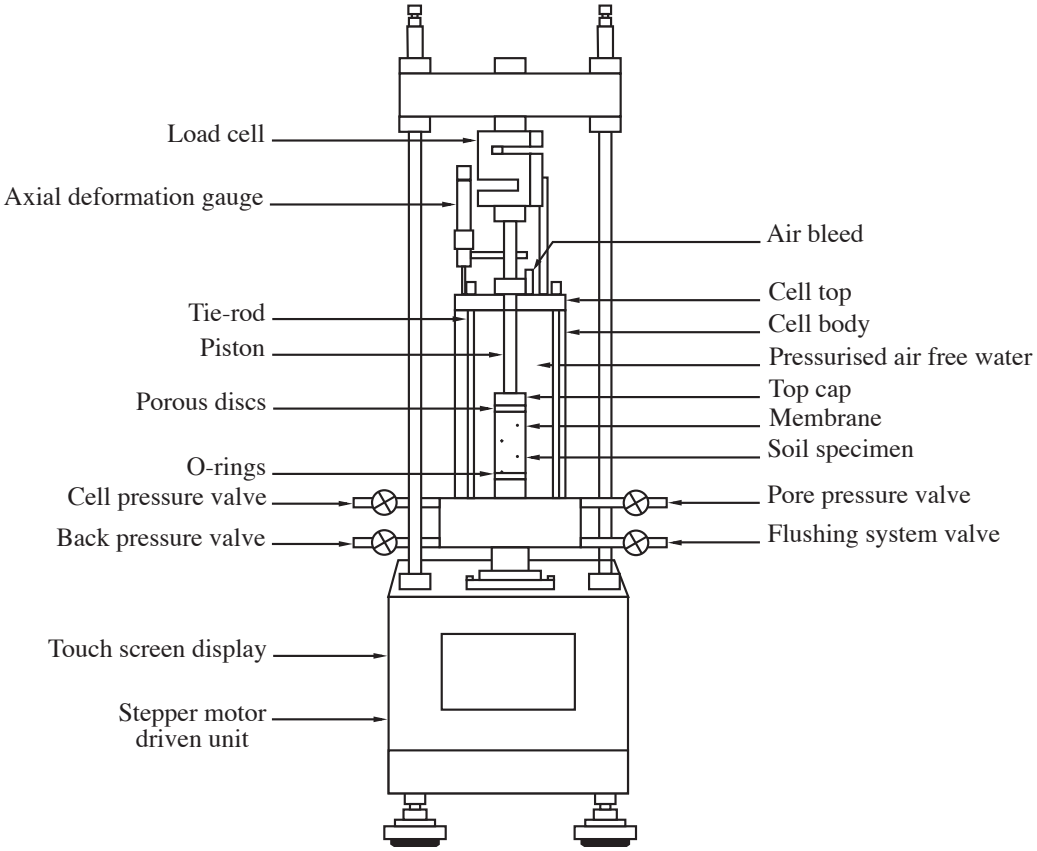

Figure 4.1: Schematic diagram of the TXC experimental setup.

4.2.2 Testing procedure

Samples from Section 3.3.1 were installed in the TXC apparatus (Figure 4.1) as follows:

1. Saturated porous discs were placed above and below the prepared samples, on the base pedestal in the triaxial cell, and fitted with a latex rubber membrane sealed with o-rings to prevent air entrapment.

2. O-rings were placed around the drainage line connected to the top cap and around the base pedestal. The back pressure valve was briefly opened to moisten the top cap and ensure a tight seal without air entrapment. Vertical alignment of the specimen was verified.

3. The cell body was assembled with the loading piston well above the specimen's top cap. Alignment was checked by slowly sliding the piston until it contacts the top cap's bearing surface. De-aerated water was slowly filled into the triaxial cell.

4. The first cell pressure increment was applied to initiate the testing procedure of the TXC test.

Once the sample has been installed inside the TXC apparatus, the testing procedure can commence. The compression stage marks the beginning of the test, during which the load cell in the TXC apparatus applies a shear force on the kaolin clay specimen at a constant rate of axial deformation until failure, a process known as strain-controlled compression. Given that UU TXC tests were conducted, drainage was not permitted, ensuring that the moisture content remained constant throughout the tests.

The testing procedure for the TXC test using the apparatus depicted in Figure 4.1 is as follows:

1. The machine platen was adjusted until the cell loading piston was brought within a short distance of the specimen top cap. The reading of the force-measuring device was recorded as the initial reading.
2. The compression machine was adjusted to have an accurate rate of axial displacement based on the specimen's properties.
3. Adjustments were made to bring the loading piston just into contact with the seating on the top cap of the specimen. The piston was checked to be properly seated and in correct alignment, ensuring the axial load applied to the specimen was as small as possible, then set at zero.
4. The axial deformation gauge was secured to measure the vertical deformation of the specimen length; it was initially set at zero.
5. The back pressure valve was closed, and both the cell pressure valve and pore pressure valve were opened.
6. The confining pressure of the TXC apparatus was first set to 100 kPa, then 200 kPa and then 300 kPa, for each of the three tests conducted for each moisture content sample.
7. Initial readings of date, time, deformation gauge reading, force device reading, pore pressure and cell pressure were taken numerically. Starting the compression of the kaolin clay specimen simultaneously launched the timer.
8. Recordings of the deformation gauge and force device were made numerically at set intervals during testing to obtain a clear stress-strain curve for the sample as it approached failure.
9. The TXC test continued until either the maximum deviator stress, maximum effective principal stress ratio, or a constant shear stress and constant pore pressure were reached, ending the test.

4.3 Oedometer testing methodology

Static and dynamic quasi-static oedometer tests were carried out on kaolin clay samples with varying moisture contents of 41, 42 or 44 %. Samples were 75 mm in diameter and 20 mm in length. The tests were conducted to confining pressure of 3200 kPa. In static tests, stress, void ratio and density data were directly measured using the apparatus to verify the influence of moisture content on the behaviour of the samples. Dynamics tests aim to analyse changes in stress, void ratio and density to understand the dynamic compression behaviour of the sample at low-strain-rates, and compare it against high-strain-rate tests. Additional details regarding specimen preparation and the test programme can be found in Sections 3.3.1 and 3.4.1.2, respectively.

4.3.1 Experimental setup

The general arrangement of the oedometer used is depicted in Figure 4.2. Before initiating the test sequence, each essential feature of the oedometer underwent thorough inspection. Load application and data acquisition were automatically handled by a computer. Tests were conducted at 20ºC to ensure consistent testing conditions. For further details on the methodology, theory and test limitations refer to Section 2.4.2.

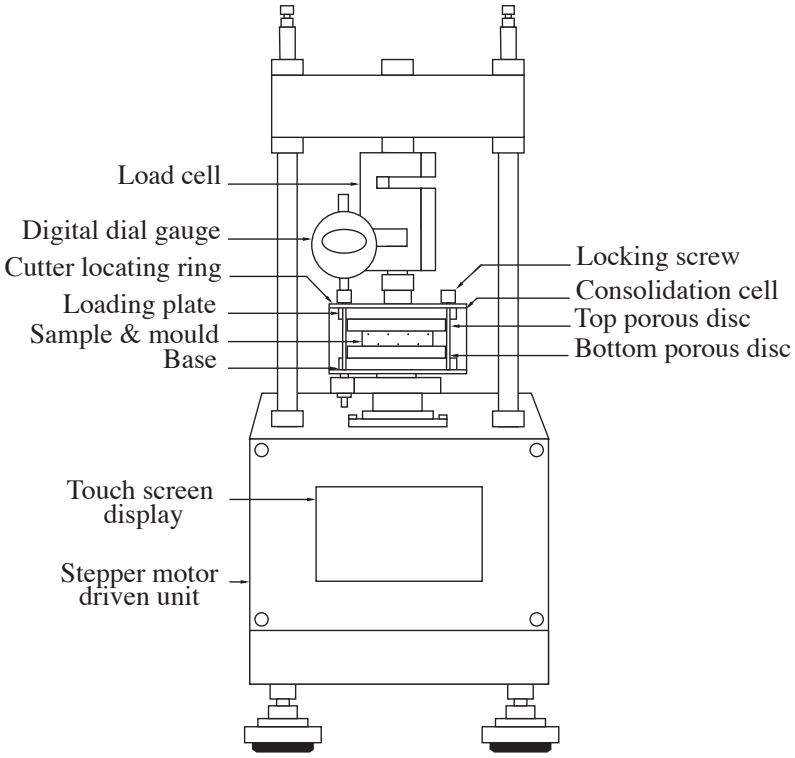

Figure 4.2: Schematic diagram of the oedometer experimental setup.

4.3.2 Testing procedure

Once samples from Section 3.3.1 were installed in the oedometer apparatus (Figure 4.2), they were tested using the following testing procedure:

1. The bottom porous plate was centrally placed in the consolidation cell, supporting the specimen along with its consolidation ring, while the top porous plate and loading cap were centrally positioned on the specimen and secured with bolts.
2. The consolidation cell was positioned on the bed of the VJ tech ACONS Pro motorised automatic consolidation system.
3. After ensuring the top of the loading frame was level, it was securely bolted in place.
4. The piston is put into contact with the consolidation cell which has been topped up with water, and the vertical displacement gauge is set to zero, ready to start the test.
5. For static oedometer tests, the initial confining pressure is set at 25 kPa and doubles every 24 hours until the maximum allowable pressure of the apparatus is reached, which includes the following increments: 50, 100, 200, 400, 800, 1600, and 3200 kPa (BS 1377–5:1990). For dynamic oedometer tests, the samples were directly consolidated to 3200 kPa at a rate of 10.00 mm/min.
6. Upon test completion, the specimen was unloaded by reducing the pressure using the 'UNLOAD' button on the VJ tech ACONS Pro motorised automatic consolidation system.
7. To disassemble the confining cell and retrieve the sample, the cell was removed, the water drained, the bolts unscrewed, and the top porous plate and loading cap removed to extract the sample.

4.4 Split-Hopkinson pressure bar testing methodology

High-strain-rate split-Hopkinson pressure bar tests were performed on kaolin clay samples with moisture contents ranging from 0 to 44 %, under both unconfined and confined conditions. The samples, measuring 25 mm in diameter and 5 mm in length, underwent high-strain-rate unconfined SHPB testing at speeds of 8, 12 and 16 m/s, for an average peak strain rate of 1200, 1900 and 2800 s^{-1}, respectively. Additional tests were conducted at 18, 20 and 22 m/s to evaluate its behaviour at higher strain rates. Confined SHPB tests were carried out at 12 m/s for behavioural comparison with unconfined SHPB tests, followed by subsequent tests at 18, 20 and 22 m/s, for an average peak strain rate of 2600, 2800 and 3100 s^{-1}, respectively. The axial and radial stresses and strains of the specimens were measured to evaluate the impact of strain rate, moisture content and confinement on the behaviour of cohesive soils at high-strain-rates. The test log for all SHPB experiments conducted in this study is in Appendix B. Further details on specimen preparation and the test programme are available in Sections 3.3.2 and 3.4.2. The findings presented in this section were published in the International Journal of Impact Engineering (Van Lerberghe, Li, Barr and Clarke 2024*a*), with the full paper available in Appendix A.5.

4.4.1 Experimental setup

4.4.1.1 Initial setup

The initial SHPB setup shown in Figure 4.3 had notable limitations: gas gun leakage, outdated balance box design, no signal amplification, absence of a speed trap, and the use of a brass diaphragm and piston instead of a pressure valve, leading to repeatability issues. This necessitated a complete redesign.

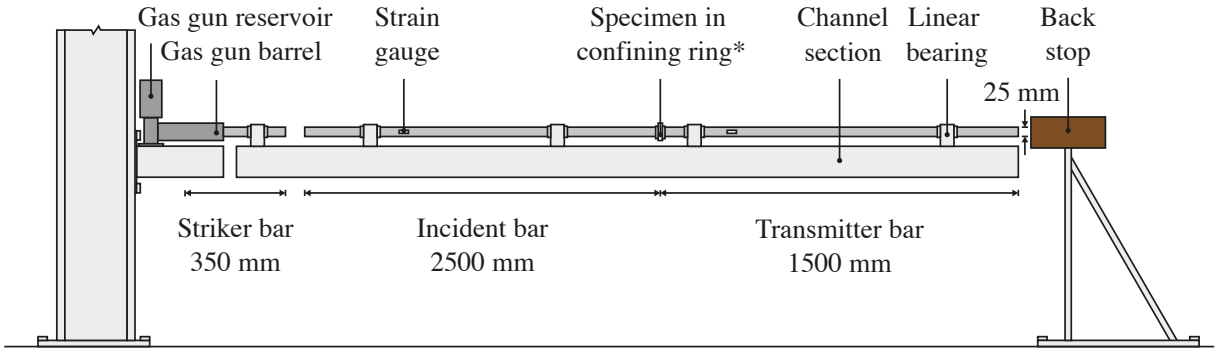

Figure 4.3: Diagram of the initial SHPB test setup with the confining ring [* removed for unconfined SHPB tests].

4.4.1.2 New setup

The new SHPB experimental set up comprises of a typical pressure bar arrangement, consisting of three EN24T steel bars: a striker bar, an incident bar and a transmitter bar, each measuring 25 mm in diameter and 350 mm, 2500 mm and 1500 mm in length, respectively. A kaolin clay sample is sandwiched between the incident and transmitter bar for testing, as represented in Figure 4.4. Additionally, for confined tests, a stainless steel confining ring is incorporated into the experimental setup. The strain gauges are positioned 500 mm from the sample on the incident bar and 1000 mm on the transmitter bar.

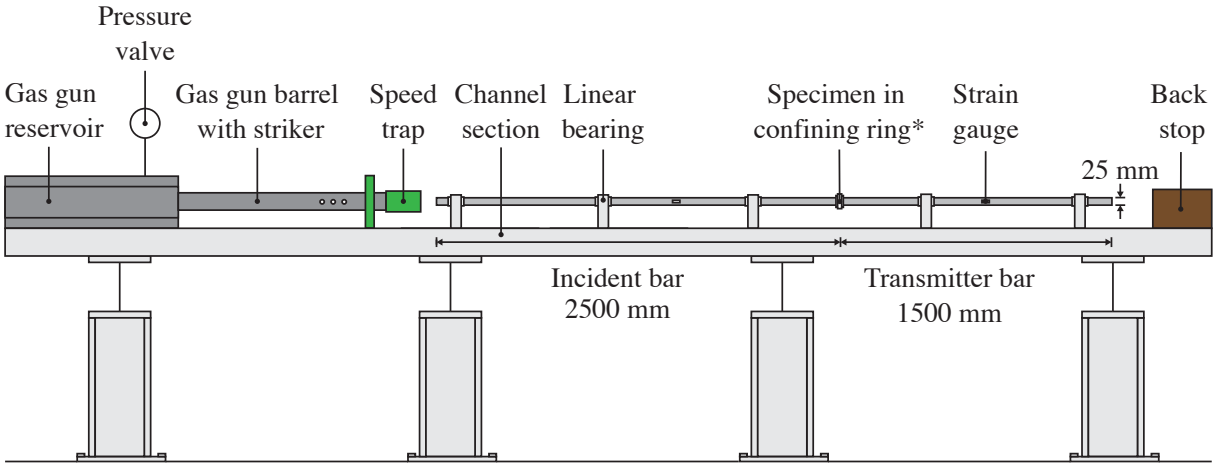

Figure 4.4: Diagram of the new SHPB test setup with the confining ring [* removed for unconfined SHPB tests].

This new setup was used for all SHPB tests in this research project. It includes improvements identified from the design flaws of the initial setup, along with expert recommendations.

To initiate the test, a compressive stress pulse is generated by striking the incident bar from one end with a steel striker bar fired by a gas gun. Strain gauges positioned on the incident and transmitter bars and the steel confining ring record this pulse and its reflections, enabling the response of the test specimen to be recorded. Linear bearings are employed to maintain alignment of the incident, transmitter and striker bars, mounted on an aluminium channel. The striker bar's acceleration is controlled by a gas gun with a pressure valve, and the transmitter bar's movement is restricted by a back stop. The striker bar velocity is calculated by timing its movement between two laser detectors spaced 50 mm apart in a speed trap.

To achieve the diverse striker speeds needed for high-strain-rate testing, it was essential to determine the appropriate combination of gas gun reservoir pressure, measured in PSI, and striker depth in the gas gun barrel, measured in mm. This is a crucial upgrade from the initial setup. Comprehensive speed tests were conducted (Appendix C), evaluating striker depths and gas gun reservoir pressures with accuracies of 5 mm and 1 PSI, respectively. These accuracies stem from the ruler and pressure valve unit measurements. Striker speeds were then recorded within an accuracy of 0.1 m/s. Table 4.1 summarises the combinations of striker depths and gas gun reservoir pressures required to achieve the desired striker speeds.

Striker bar speed, m/s	*Striker bar depth, mm*	*Gas gun reservoir pressure, PSI*
8 ± 0.1	600 ± 5	14 ± 1
12 ± 0.1	600 ± 5	28 ± 1
16 ± 0.1	600 ± 5	48 ± 1
18 ± 0.1	600 ± 5	60 ± 1
20 ± 0.1	600 ± 5	72 ± 1
22 ± 0.1	600 ± 5	86 ± 1

Table 4.1: Striker bar depths and gas gun reservoir pressure combinations for attaining targeted striker velocities.

To calibrate the individual bars, the incident signal from the impact of a striker of known velocity was compared with the theoretical strain in the bar given by Equation (4.1):

$$\varepsilon_b = \frac{v_s}{2c_0} \tag{4.1}$$

where ε_b is the longitudinal strain in the bar, v_s is the velocity of the striker bar on impact and c_0 is the longitudinal wave speed in the bar. The wave speed can be found using Equation (4.2):

$$c_0 = \frac{2l}{t} \tag{4.2}$$

where l is the distance between the strain gauge and the specimen end of the bar and t is the time between the incident and reflected pulses. Gauge factor, F is calculated from Equation (4.3), as the ratio of voltage across the gauge's Wheatstone bridge and strain in the bar:

$$F = \frac{2V_o}{\varepsilon V_i} \tag{4.3}$$

where V_i and V_o are the input and output voltages across the Wheatstone bridge. Table 4.2 summarises the pressure incident and transmitter bar parameters in the new SHPB setup.

	Wave speed, m/s	*Density, kg.m^{-3}*	*Gauge factor*
Incident bar	5376	7666	123
Transmitter bar	5305	7677	127

Table 4.2: Pressure bar testing parameters.

4.4.2 Confining ring

For confined SHPB testing, an additional stainless steel ring is integrated into the experimental setup, as depicted in Figure 4.5. Kaolin clay specimens are enclosed within the confining ring with a 25 mm internal diameter and 35 mm external diameter, spanning a length over 5 mm, as illustrated in Figure 4.6a. Locating flanges, each 1 mm thick are positioned on both sides of the ring to facilitated installation on the pressure bars and prevent soil loss (Figure 4.6b). The circumferential strain of the ring was measured using a strain gauge located on its exterior surface. Using thick walled pipe theory, expression (4.4) correlates the average internal pressure in the sample to the circumferential strain:

$$P_i = \frac{r_o^2 - r_i^2}{2r_i^2} E\varepsilon_\theta \tag{4.4}$$

where P_i represents the internal radial pressure exerted on the specimen by the confining ring, E denotes the Young's modulus of the ring, ε_θ indicates the circumferential strain measured on the outside of the ring, and r_o and r_i stand for the outer and inner radii of the ring, respectively (Stephens 2013). For the current arrangement, $P_i = 0.48\ E\varepsilon_\theta$. This formulation allows for recording both axial and radial stresses and strains within the sample. The strain relationships are shown in Equation (4.5), (4.6) & (4.7):

$$\varepsilon_\theta = \frac{1}{E}(\sigma_\theta - \nu(\sigma_r + \sigma_z)) \tag{4.5}$$

$$\varepsilon_r = \frac{1}{E}(\sigma_r - \nu(\sigma_\theta + \sigma_z)) \tag{4.6}$$

$$\varepsilon_z = \frac{1}{E}(\sigma_z - \nu(\sigma_\theta + \sigma_r)) \tag{4.7}$$

where ε_θ, ε_r and ε_z are the circumferential, radial and axial strain, σ_θ, σ_r and σ_z are the circumferential, radial and axial stress, E is the Young's modulus and ν the Poisson's ratio.

During the test, as the incident bar end of the sample begins to move while the transmitted bar end remains stationary, the strain gauge's position changes relative to the specimen's midpoint. In a representative test scenario where the confining ring remains stationary during sample loading, the sample's centre moves approximately 1 mm relative to the strain gauge. Moreover, the 5 mm thickness of the confining ring's wall distributes the load applied to one surface across a broader area on the other. This allows the strain gauge to measure radial stress as an average over several millimetres inside the ring. As a result, any movement of the sample relative to the strain gauge has a reduced effect, and the stress recorded by the gauge provides a good indication of the stress experienced on the radial surface of the kaolin clay samples.

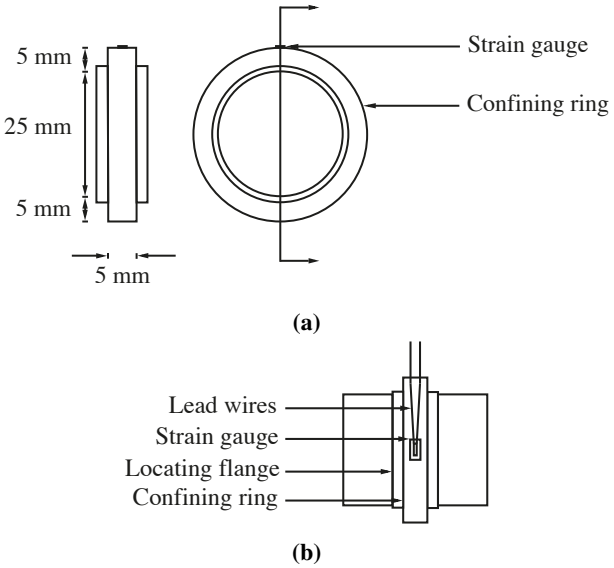

Figure 4.5: (a) Gauged steel confining ring, and (b) strain gauge installation on a confining ring.

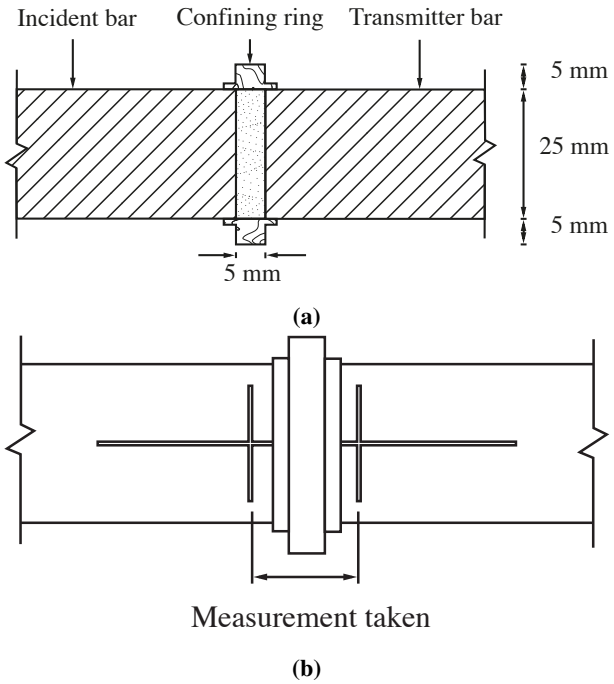

Figure 4.6: Steel confining ring: (a) axial section and (b) axial elevation with sample measurement markings.

4.4.3 Testing procedure

This experimental testing procedure was employed on prepared samples of kaolin clay to demonstrate the SHPB's capability in testing cohesive soils under unconfined and confined conditions. Additionally, it aimed to validate the reliability of the chosen design set up in producing accurate measurements.

Before conducting the tests, the samples underwent precise measurements. Their weight was recorded to three decimal places using an RS Pro weighing scale with an accuracy of 0.001 g. The thickness of the samples was measured at three different locations using a digital calliper and averaged to account for inconsistencies in measurements and variations in sample shape, with an accuracy of 0.01 mm. These measurements were crucial for data processing.

For unconfined SHPB testing on kaolin clay samples, the following procedure was followed:

1. The supports surrounding the incident and transmitter bars were securely bolted down to the channel of the SHPB experimental setup.
2. A kaolin clay sample, 5 mm in nominal length and 25 mm in diameter, was positioned and held in between the incident and transmitter bars, inside a glass polymer containment box.
3. The lid of the containment box is closed in preparation for testing.

For confined SHPB testing, a similar procedure was followed. The confining ring was inserted onto the incident bar before the prepared specimen is gently placed in between the incident and transmitter bars. Subsequently, the confining ring is slid back over the specimen, ready for testing.

In both cases, loading was achieved by impacting the incident bar with a steel striker bar discharged from a gas gun at varying speeds, to achieve different strain rates. These speeds were measured using a speed trap at the exit of the gas gun barrel.

4.4.4 Instrumentation and signal processing

Figure 4.7 shows a diagrammatic representation of the instrumentation used for SHPB testing. The material's axial stress response is monitored using a pair of Kyowa KSP-2-120-E4 strain gauges mounted on the incident and transmitter bars, the details of which are listed in Table 4.3. A single gauge was affixed on the surface of the confining ring (Figure 4.9a), while two gauges were positioned on each bar (Figure 4.8a), ensuring the exclusion of bending strains and the sole measurement of longitudinal strains.

The signals from the pressure bar strain gauges are recorded using a TiePie Handyscope four-channel digital oscilloscope, boasting a 14-bit A-D resolution, a sample frequency of 1 MHz, and a record length of 131.072 kSa. These strain gauge signals are collected from the incident and transmitter bars through a half Wheatstone bridge configuration, illustrated in Figure 4.8b. The signal from the confining ring's strain gauge is obtained via a quarter Wheatstone bridge configuration, depicted in Figure 4.9b.

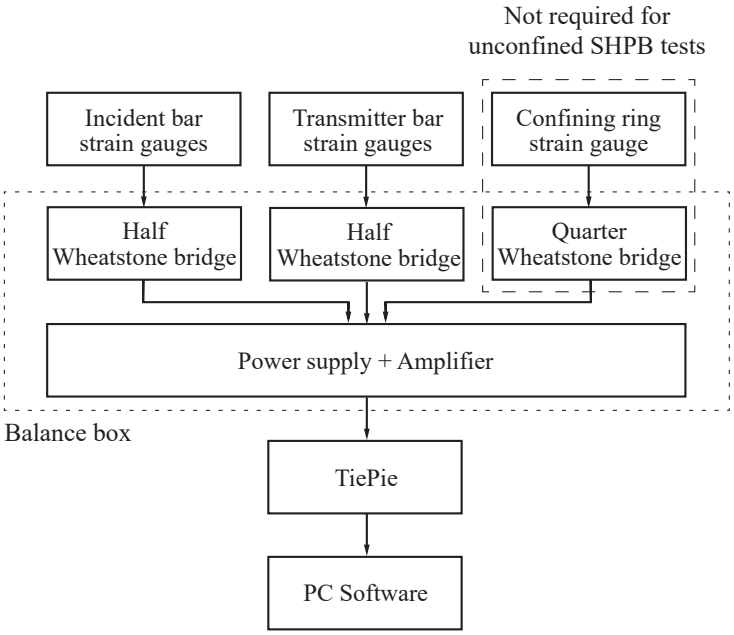

Figure 4.7: Instrumentation for signal processing during SHPB tests.

Property	*Value*
Gauge pattern	Uniaxial
Resistive material	P-type silicon
Gauge length	2 mm
Gauge factor	Approx 120 (Table 4.2)
Gauge resistance	120 Ω
Base size	7.7 x 4 mm
Base material	Paper, phenol-epoxy

Table 4.3: Properties of Kyowa KSP-2-120-E4 semiconductor strain gauge.

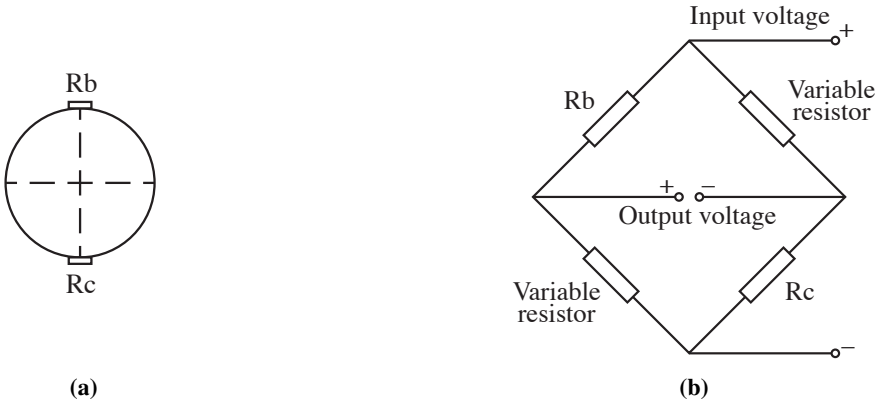

Figure 4.8: Pressure bars (a) strain gauge arrangement, and (b) half Wheatstone bridge configuration.

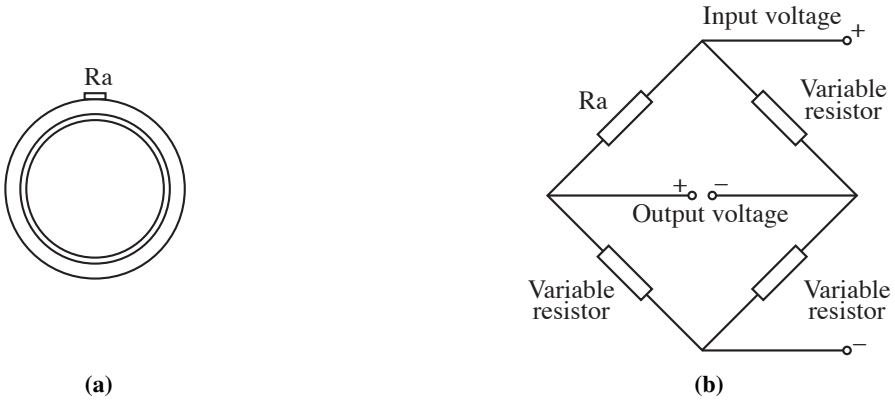

Figure 4.9: Confining ring (a) strain gauge arrangement, and (b) quarter Wheatstone bridge configuration.

Each set of strain gauges is integrated into their respective Wheatstone bridge configuration, generating an analogue voltage signal. Prior to commencing testing, the variable resistors within each Wheatstone bridge configuration are adjusted to balance the bridge, as illustrated in Figure 4.10. Variable resistors will maintain a steady resistance throughout testing.

Encased in a sturdy grey aluminium steel case, the balance box processes signals from the SHPB tests using the Wheatstone bridge architecture depicted in Figures 4.8 and 4.9. On each circuit board, 16-pin SOIC Instrumentation amplifiers, specifically NA110KU from Texas instruments, are incorporated. During confined SHPB tests involving the confining ring, all three boards are utilised. However, during unconfined SHPB tests, the board dedicated to the confining ring is omitted as it serves no purpose.

A detailed diagram illustrating the internal circuit board layout, measuring 200 x 432 mm, is provided in Figure 4.11. Additionally, schematic representations of the individual 58 x 64 mm circuit boards for the incident bar, transmitter bar and confining ring can be found in Figures 4.12 and 4.13. Each of the three circuit boards is dedicated to processing input signals from the incident bar, the transmitter bar and the confining ring, respectively.

Using Equations (4.8) & (4.9), the recorded output voltages were used to calculate the strain in the pressure bars and ring:

$$\varepsilon_{bar} = 2\frac{V_o}{FV_i} \tag{4.8}$$

$$\varepsilon_{ring} = 4\frac{V_o}{FV_i} \tag{4.9}$$

where V_i is the input voltage, V_o is the output voltage, and F is the gauge factor.

A dispersion-correction method was implemented to process the strains in order to find the response of the soil specimen. Data processing using one-dimensional wave theory introduced large false oscillations in the stress at the front face of the specimen, preventing calculation of a representative mean axial stress.

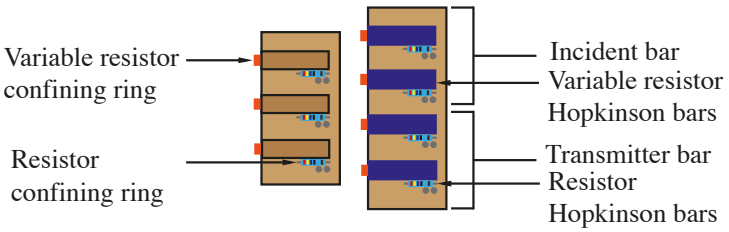

Figure 4.10: Variable resistor boards, top view.

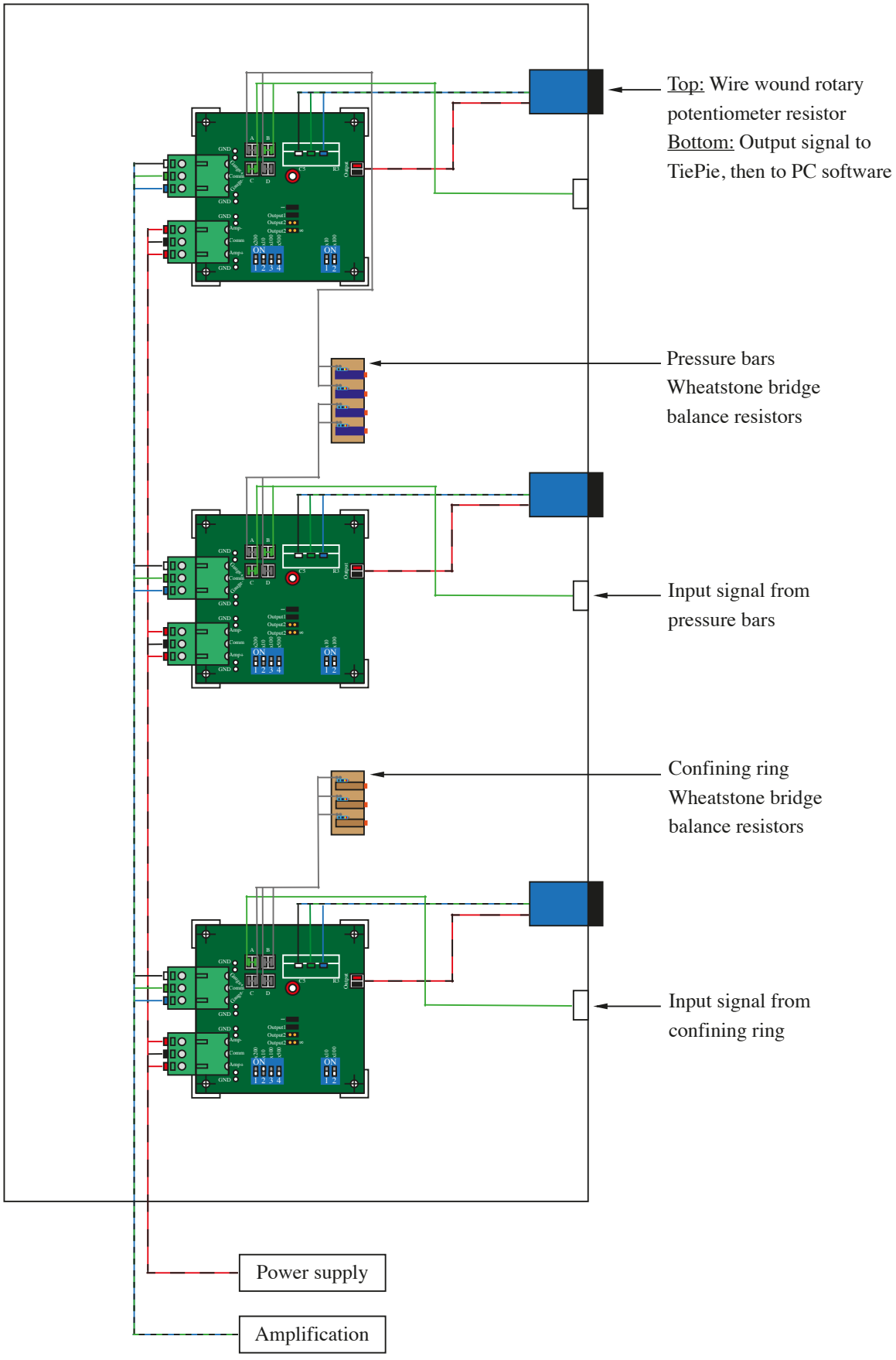

Figure 4.11: Balance box internal layout.

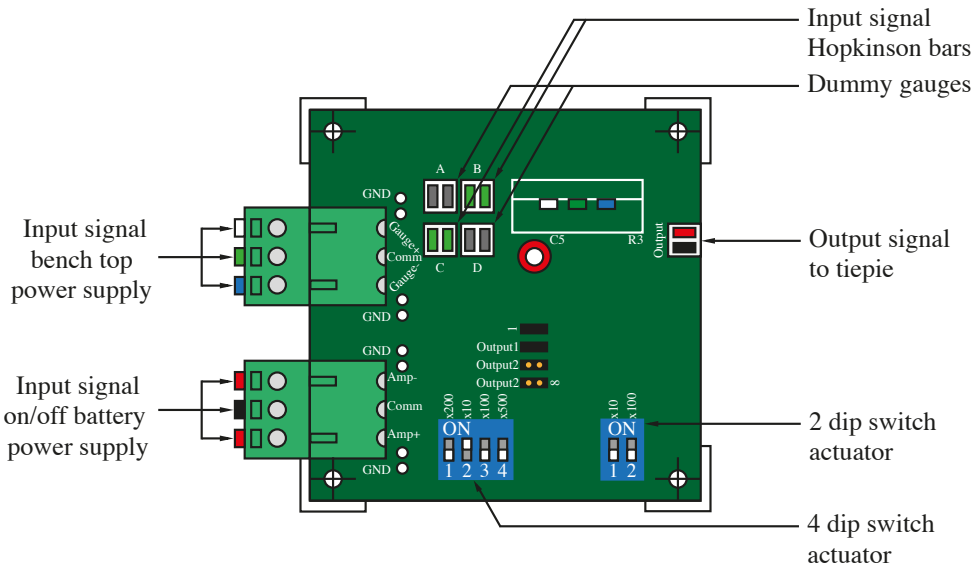

Figure 4.12: Pressure bars board, top view.

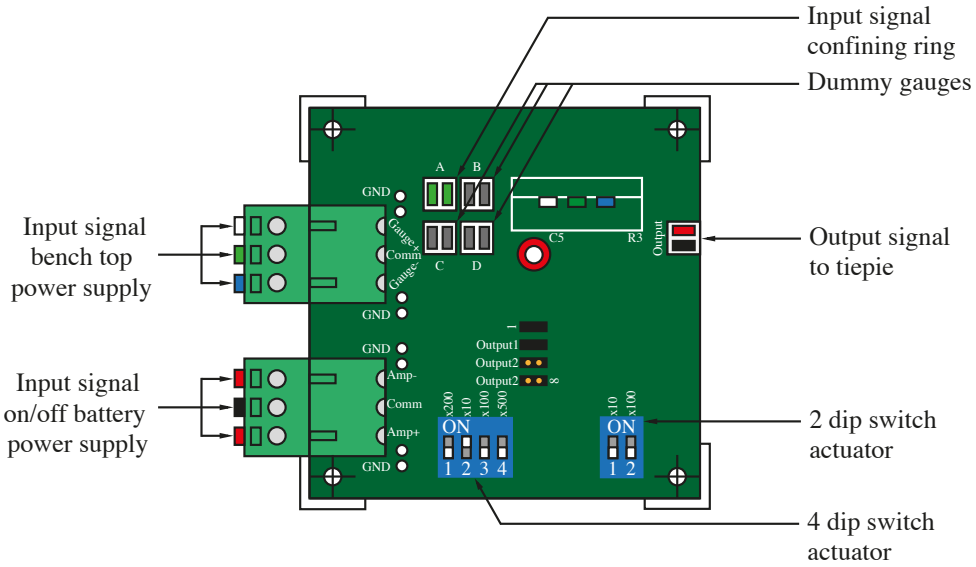

Figure 4.13: Confining ring board, top view.

4.4.5 Dispersion correction in SHPB experiments

This section addresses the sources of error related to dispersion encountered during SHPB experiments, with a focus on their impact on axial stress and strain measurements.

As detailed in Section 2.5.1.3, dispersion correction in SHPB test results is necessary due to several factors, including:

1. Signal dispersion caused by variations in phase velocity with frequency, resulting in changes to the phase angle of frequency components;
2. Response inconsistencies across the bar cross-section due to radial inertia effects, affecting the amplitude of frequency components; and
3. Variation in the axial stress to axial strain ratio both across the bar cross-section and with frequency, which affect the amplitude of frequency components.

The second item above points to radial inertia effects as the cause of the inconsistencies, while the third item discusses the variation in stress-to-strain behaviour as the main issue. Both affect the amplitude of frequency components, but for different reasons: one due to inertia, the other due to material deformation properties under different stresses and frequencies.

The details regarding correction methods to mitigate dispersion effects in SHPB experiments are provided in a paper submitted to the journal of Experimental Mechanics (Van Lerberghe, Li, Barr and Clarke 2024*b*), available in Appendix A.4. The following sections are extracted from this paper.

For frequencies higher than a/$\lambda > 0.05$ (where a is the bar radius and λ the wavelength), the mentioned errors above become significant, but they can be mitigated through the approach outlined by Tyas and Pope (2005). This method involves adjusting the amplitudes and phase angles of each frequency components of the signal.

4.4.5.1 Phase angle correction

The first correction made to the SHPB signals is the adjustment of the phase angle to account for the dispersion of each frequency component over the distance between the strain gauge and the bar end. This is accomplished, according to Gorham (1983) and Follansbee and Frantz (1983), by computing the phase velocity c_ω, of each component using Bancroft's equation (Equation (2.12) in Section 2.5.1.3) and then applying a phase shift, θ'_ω , as seen in Equation (4.10):

$$\theta'_\omega = \left(\frac{c_0}{c_\omega} - 1\right)\frac{\omega z}{c_0} \tag{4.10}$$

where ω is the component's angular frequency, and z is the distance over which the correction is performed, positive in the direction of wave propagation. In this study, it is assumed that waves propagate solely in the first mode. Bancroft's equation demonstrates that high modes propagate at normalised frequencies greater than $f\,a/c_0 \approx 0.23$ (92 kHz in the current setup).

Numerical simulations conducted by Barr et al. (2020) aimed to understand how energy is distributed among higher modes of propagation, concluding that the frequency content in typical SHPB experiments only requires consideration of the first mode of propagation.

4.4.5.2 Amplitude correction

The second correction to the SHPB signals involves applying factors to the amplitude of the frequency components. These factors, denoted as M_1 and M_2, were introduced by Tyas and Watson (2001) to account for the radial variation of strain and Young's modulus, respectively. These factors were derived from Davies' (1948) examination of radial effects. By employing these factors, the strain measurement obtained on the bar's surface can be used to calculate the mean axial stress and strain acting over the entire cross-section. The factors are defined in Equations (4.11) and (4.12) as follows:

$$M_1 = \frac{2\left(1+\frac{1-\beta x}{x-1}\right)}{\varphi(ha)+\frac{1-\beta x}{x-1}\varphi(\kappa a)} \tag{4.11}$$

$$M_2 = E\left(\frac{c_\omega}{c_0}\right)^2 \tag{4.12}$$

where

$$\beta = (1-2\nu)/(1-\nu)$$
$$x = (c_\omega/c_0)^2(1+\nu)$$
$$h = \gamma(\beta x-1)^{\frac{1}{2}}$$
$$\kappa = \gamma(2x-1)^{\frac{1}{2}}$$
$$\varphi(y) = yJ_0(y)/J_1(y)$$

c_ω – Phase velocity
c_0 – One-dimensional elastic wave velocity
a – Bar radius
ν – Poisson's ratio
E – Young's modulus
γ – Wave number, $2\pi/\lambda$
λ – Wave length
$J_n(y)$ – Bessel function of the first kind, of order n

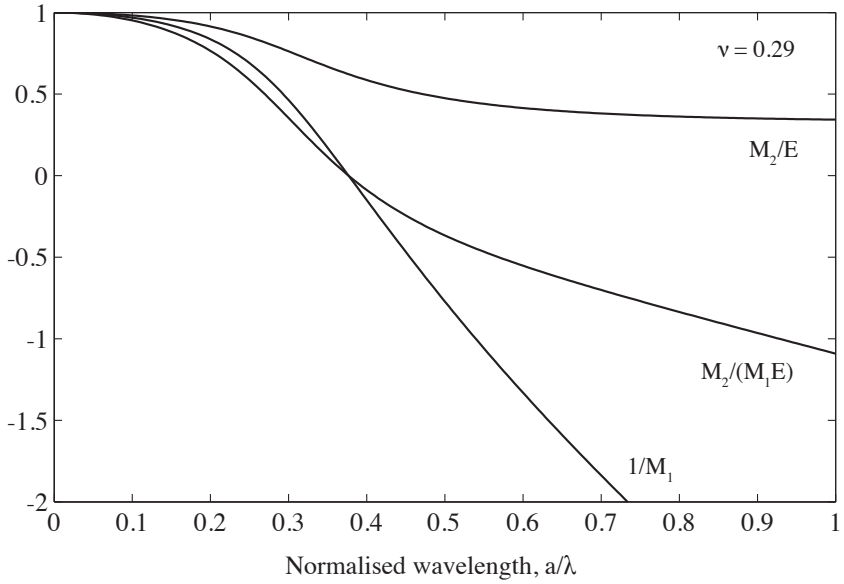

Figure 4.14: Variation of factors M_1 and M_2 in a cylindrical stainless-steel bar for $\nu = 0.29$ (Barr 2016*b*).

Figure 4.14 illustrates the fluctuation of M_1 and M_2 with normalised wavelength for a stainless-steel bar with a Poisson's ratio of 0.29.

Due to the discontinuity in M_1 at $a/\lambda = 0.375$, corresponding to the point where the recorded strain on the bar's surface falls to zero, the reciprocal of M_1 is shown; at even higher frequencies, the recorded strain exhibits an opposite sign compared to the mean cross-sectional response. At $a/\lambda = 0.375$, the adjustments necessitate multiplying a signal of low-magnitude by a significantly large correction factor, making it susceptible to noise in the signal and potentially compromising the accuracy of the result. This essentially sets an upper limit on the frequency range that can be corrected: as per Tyas and Watson (2001), the methods can be effectively applied at normalised wavelengths below $a/\lambda \approx 0.3$, which is equivalent to 94 kHz in the current experiments.

4.4.6 SHPB_Processing.py

This section presents the open-source Python algorithm `SHPB_Processing.py` employed for high-strain-rate SHPB signal processing. This function includes a key subroutine titled `dispersion.py` that is optimised to process raw signal strain data using dispersion correction, and is discussed in depth in Section 4.4.7.

Further details regarding this algorithm are provided in a paper submitted to the journal of Experimental Mechanics (Van Lerberghe, Li, Barr and Clarke 2024*b*), available in Appendix A.4. The following sections are extracted from this paper.

This function, SHPB_Processing.py, is designed to take strain gauge input data from high-strain-rate SHPB tests and, by specifying the additional input variables defined in Table 4.4, determine axial and radial (if confinement specified) stress developments of the sample, its strain and strain rate history variations through impact, and other related parameters derived from these output variables.

The following command line is necessary to run this algorithm:

SHPB_Processing (csv_path, sample_data, confinement, signal_channels, signal_amp, disp_correction, alignment, speedtrap)

The optimal approach to running this function is detailed below, with Figure 4.15 depicting this as a concise flowchart:

1. Calculate stress wave speed and gauge factors of the cylindrical bars used for SHPB testing using the gauge_factor.py script, available on GitHub and ORDA (Van Lerberghe and Li 2023).

2. Use phase_velocity.py to calculate the dispersion factors required to perform the dispersion correction of the collected SHPB signals using dispersion.py based on the material properties of the cylindrical bar used for SHPB testing. The algorithm phase_velocity.py is available on GitHub and ORDA (Van Lerberghe and Barr 2023*b*).

3. The algorithm SHPB_Processing.py is ready to be run, with the subroutine dispersion.py, to effectively process the SHPB test data with dispersion correction, based on the input parameters chosen. The results are returned in a designated processed data folder. Dispersion.py is available on GitHub and ORDA (Van Lerberghe and Barr 2023*a*).

The full source code for SHPB_Processing.py and all its associated subroutines is available on GitHub and ORDA (Li, Van Lerberghe and Barr 2024).

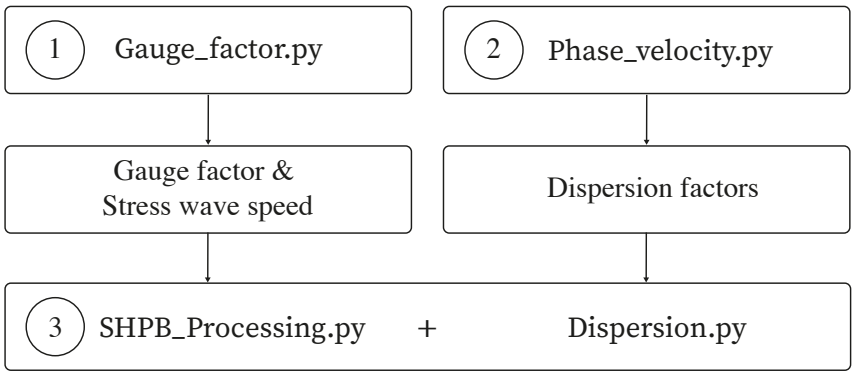

Figure 4.15: Flowchart illustrating the steps to run SHPB_Processing.py efficiently.

Inputs	*Description*
`csv_path`	File directory containing CSV file with raw test data.
`sample_data`	Array containing the initial length, mass and dry mass of the sample i.e. [initial length, mass, dry mass].
`confinement`	Confinement mechanism applied i.e. 'None', 'Ring' or 'Reservoir'.
`signal_channels`	Oscilloscope channel numbers used to record raw data i.e. [in_bar_gauge_channel, out_bar_gauge_channel, ring_gauge_channel or reservoir_gauge_channel].
`signal_amp`	Strain gauge amplification applied to strain gauge measurement i.e. [in_bar_gauge_amp, out_bar_gauge_amp, ring_gauge_amp].
`disp_correction`	Apply dispersion correction or simple time shift processing for signal data. i.e 'True' for dispersion correction using `dispersion.py`.
`alignment`	Specify alignment mode for aligning stress waves at sample interfaces i.e. 'start' aligns the start of incident and transmitted pulse, 'end' aligns the end, and 'mid' aligns the median time of the pulse. Integer/float values greater than 1 aligns the peaks of the incident and transmitter pulse to specific times. Float values between 0 and 1 aligns the incident and transmitted pulse on a specific fraction of the max value.
`speedtrap`	Specify speed trap data to determine striker bar velocity i.e 'True' for speed trap velocity calculation.
Outputs	*Description*
Processed data folder	Folder with all the csv processed data files, and test log for history monitoring.

Table 4.4: Input and output variables used in `SHPB_Processing.py`.

The function's operation can be summarised as follows:

1. The oscilloscope data from SHPB strain gauges are read.
2. The striker bar velocity is determined based on raw speed trap data.
3. The raw data file prepared for correction and confinement analysis via pulse detection and signal reformatting.
4. The correction ('True' for dispersion correction, or 'False' for simple time shift) and confinement ('None', 'Ring' or 'Reservoir') requirements are applied on strain data collected based on input specifications.
5. The incident, reflected and transmitted pulses are detected using the trigger and wave speed propagation in the bars used during SHPB testing.
6. The pulse end is marked when the sample strain reaches its maximum.
7. The dispersion-corrected stresses and strains for each wave are calculated using `dispersion.py`, details of which are present below. For simple timeshifting, simple signal restructuring is conducted.
8. The axial stresses and strains in the specimen are calculated using the incident, reflected and transmitted wave signals.
9. Based on strain gauge strain, the sample strain is determined from the displacement of the pressure bars.
10. Based on the confinement type selected, 'None', 'Ring' or 'Reservoir', the following will happen:
    a. For a SHPB test with 'None' as the confinement type, no radial stresses or strains are calculated for the specimen.
    b. For a SHPB test with 'Ring' as the confinement type, using thick-walled pipe theory, the radial stress and strain in the specimen is calculated from the circumferential strain in the ring.
    c. For a SHPB test with 'Reservoir' as the confinement type, pressure data collected from the gauge in the reservoir is used to calculate the specimen's radial stress and strain.
11. The specimen density and dry density are calculated for 'Ring' and 'Reservoir' confinement types.
12. All the results are saved into the Processed data folder as csv files, along with the test log.

4.4.7 Dispersion.py

In this section the open-source Python algorithm `dispersion.py` is presented. This script has been developed to automate the application of phase angle and amplitude corrections to SHPB signals collected during testing as part of the main processing of `SHPB_Processing.py`. This substitutes basic time shifting of signals with manipulation of individual frequency components. The capabilities of this function are described in this section, with the complete source code for `dispersion.py` and its accompanying subroutine available on GitHub and ORDA (Van Lerberghe and Barr 2023*a*). This algorithm was inspired by a MATLAB script created by Barr (2016*a*).

Further details regarding this algorithm are provided in a paper submitted to the journal of Experimental Mechanics (Van Lerberghe, Li, Barr and Clarke 2024*b*), available in Appendix A.4. The following sections are extracted from this paper.

4.4.7.1 Frequency domain in Python

The fast Fourier transform (FFT) is an algorithm used to convert a signal into the frequency domain. This technique portrays a signal as the sum of a sequence of sinusoidal waves of varying frequencies and amplitudes. FFT is implemented in Python using the `numpy` library and `fft` function, which takes any regularly-sampled signal and returns amplitude and phase information with frequency as a matrix of complex vectors of the form $z = z_r + iz_i$. At a given frequency, the amplitude, A (Equation (4.13)), and phase angle, θ (Equation (4.14)), of the Fourier component are calculated as:

$$A = \sqrt{z_r^2 + z_i^2} \tag{4.13}$$

$$\theta = \tan^{-1}\left(\frac{z_i}{z_r}\right) \tag{4.14}$$

These relationships are illustrated in Figure 4.16a, where z and its complex conjugate $\bar{z}$ are represented in the complex plane, and in Figure 4.16b, where these values are utilised to represent the amplitude and phase angle of a specific sinusoid.

The Fourier component can be reconstituted using the relationship in Equation (4.15) once suitable corrections have been applied to the amplitude and phase angle, as seen below:

$$z = A\cos(\theta) + iA\sin(\theta) = Ae^{i\theta} \tag{4.15}$$

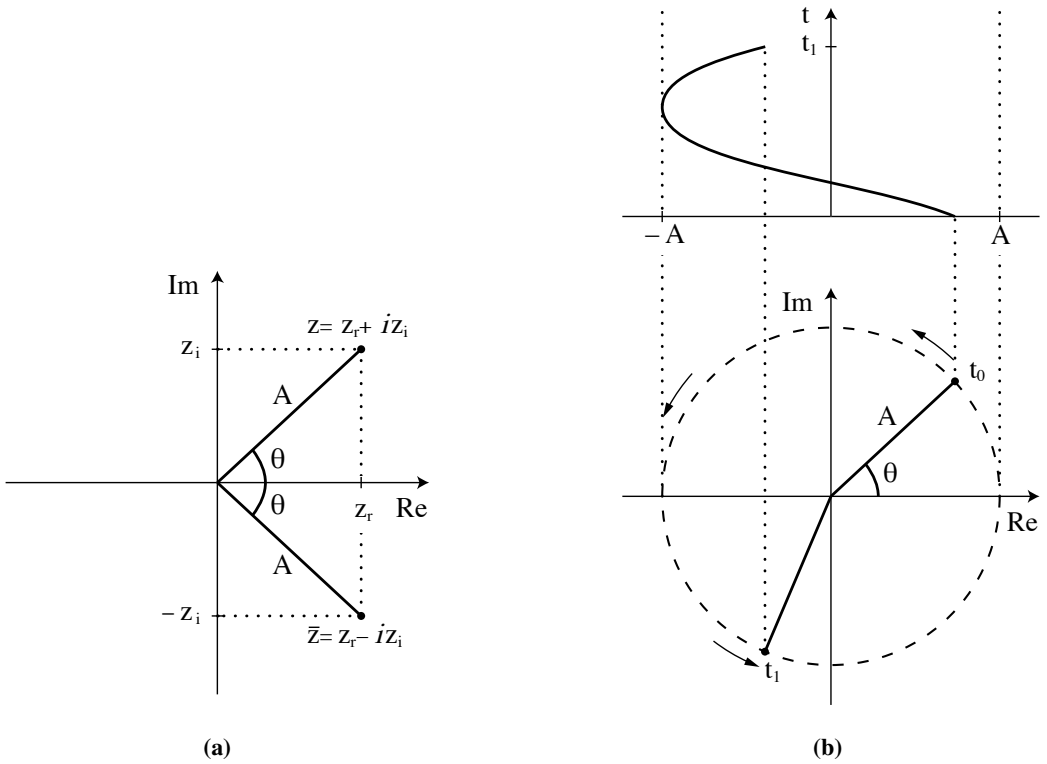

Figure 4.16: A Fourier component z in the complex plane with (a) relationship to amplitude and phase angle and (b) description of a sinusoid (Barr 2016*b*).

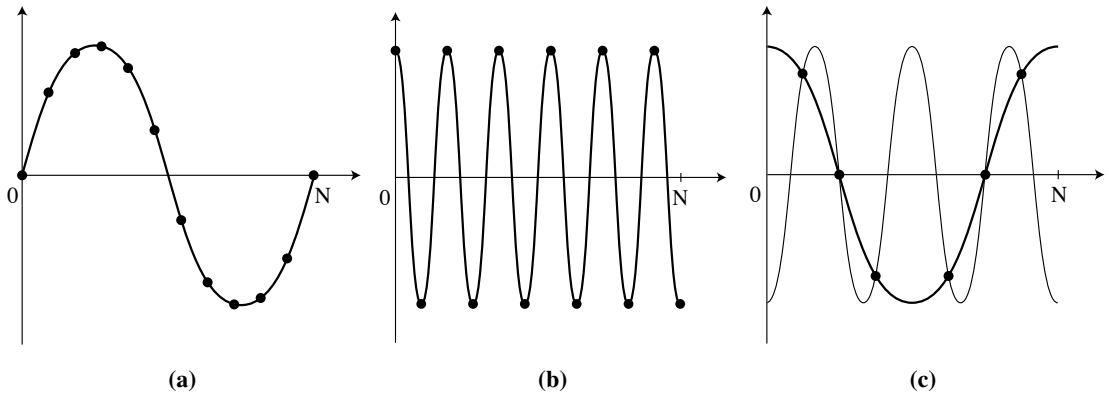

Figure 4.17: Frequency limitations in the FFT with (a) minimum frequency and (b) maximum frequency for a signal where $N = 12$ and (c) aliasing at higher frequencies (Barr 2016*b*).

4.4.7.2 Correction bandwidth

The FFT is a discrete form of the Fourier transform, components are only calculated at discrete frequency values that depend on the original signal's sampling rate and length. If a signal is sampled N times at a frequency f, the lowest readable frequency is equal to f/N, describing a single wave occupying the sampling window (Figure 4.17a). Higher frequencies are multiples of the fundamental frequency, all the way up to the highest readable frequency, or Nyquist frequency, which equates to $f/2$ (Figure 4.17b). This limit is set because at least two samples are necessary for each period to prevent aliasing, as shown in Figure 4.17c. Due to undersampling, two different sinusoids can be fitted to the sample data. The oscilloscope's sample rate ($f/2$ = 500 kHz in the current tests) limits the highest readable frequency, although the frequency resolution can be improved by raising N, either by increasing the recording duration, or by zero-padding the input signal.

The `fft` function will generate an N-length frequency domain vector $X(\omega)$, given an N-length time-domain vector *x(t)*. As a result of the aliasing explained above, the second half of $X(\omega)$ is the complex conjugate of the first half, reflected about the Nyquist frequency, as seen in Figure 4.18. This means that modifications only need to be individually applied to the first $N/2 + 1$ bins in $X(\omega)$, which may then be reflected to complete the vector.

As stated in Section 4.4.5.2, the very low strain signals measured on the surface of the bar at wavelengths below $a/\lambda \approx 0.3$, impose an additional frequency limit. For example, for a 25 mm diameter stainless-steel bar, adjustments can only be successfully made between 39 μHz and 94 kHz in the current SHPB set up. Figure 4.19 depicts a frequency-domain portrayal of a typical experimental incident pulse in the form of a modified periodogram. Power is measured in logarithmic units, with a change of 10 dB denoting an order of magnitude shift in the power of the signal. The periodogram, as explained above, indicates that the power of the signal recorded on the surface of the bar rapidly decreases to zero between 94 kHz and 110 kHz. Since dispersion correction can only be implemented at frequencies below 94 kHz, for this setup, the signal is sent through a low-pass filter to remove the higher frequencies. In Figure 4.20, the power at these frequencies is orders of magnitude smaller, and so little information is lost in filtering.

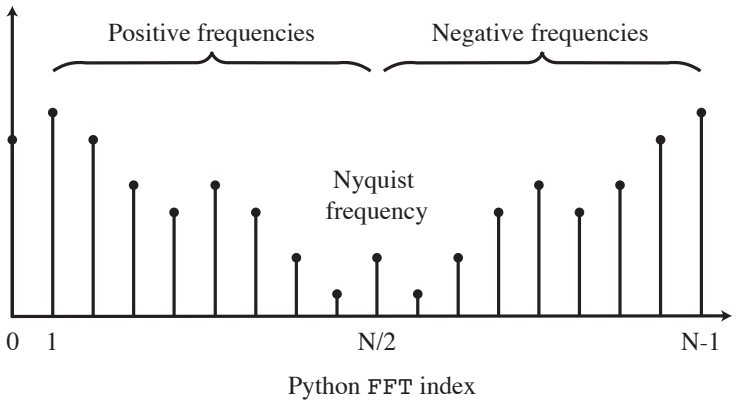

Figure 4.18: Composition of the frequency-domain vector produced by `fft` in Python (Barr 2016*b*).

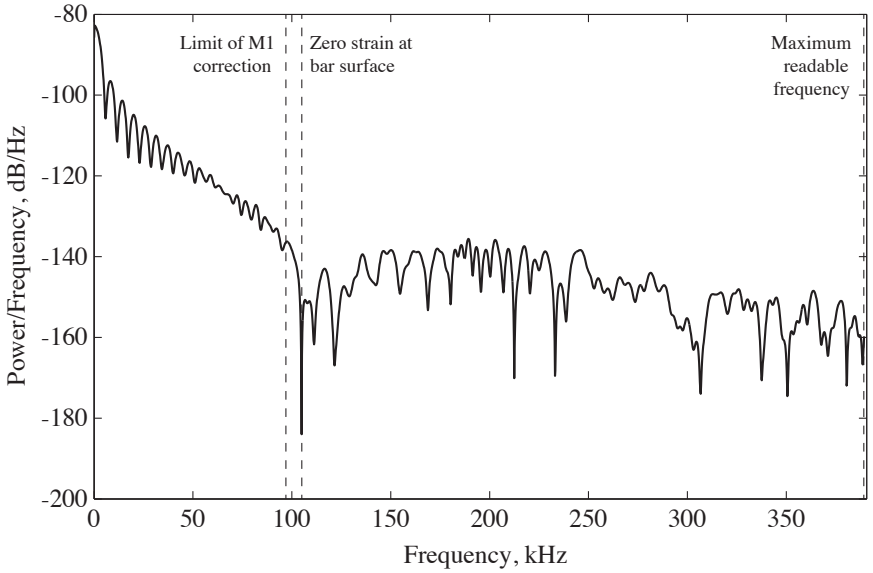

Figure 4.19: Power spectral density for experimental incident wave, from a 25 mm stainless-steel bar with a Poisson's ratio of 0.29, and maximum frequency limits imposed by the strain gauge data and FFT (Barr 2016*b*).

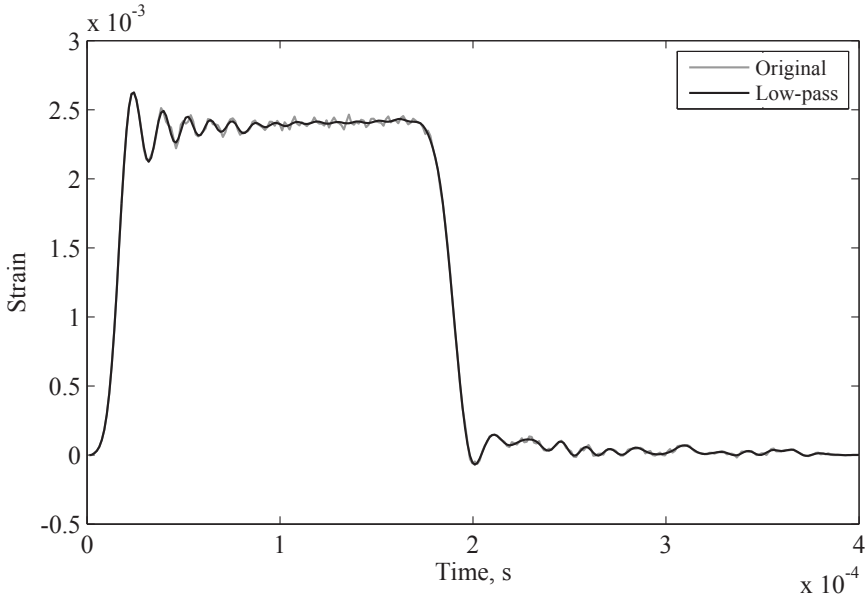

Figure 4.20: This experimental setup's incident wave and result of low-pass filtering of frequencies above 94 kHz (Barr 2016*b*).

4.4.7.3 Operation of dispersion.py

When the option for dispersion correction is selected in `SHPB_Processing.py`, the open-source Python algorithm `dispersion.py` is called as a subroutine during the processing of the SHPB signals collected from testing.

The function `dispersion.py` was created to automate the application of phase angle and amplitude correction factors generated by `dispersion_factors.py`, to SHPB pressure bar signals obtained from the experiments, manipulating frequency components and correcting the effects of dispersion over a specified propagation length.

The programme `dispersion_factors.py` is a mandatory subroutine of `dispersion.py`.

After isolating the incident, reflected, and transmitted waves, `dispersion.py` is used to infer the stress and strains at the bar-specimen interface for each wave using the following command, which includes input and output variables defined in Table 4.5.

The following command line is necessary to run this algorithm:

`dispersion(x, fs, a, c0, E, z)`

Inputs	*Description*
`x`	Zero-padded strain signal in time domain (1xN numeric).
`fs`	Sampling frequency, Hz.
`a`	Bar radius, m.
`c0`	One-dimensional wave velocity of the bar, m/s.
`E`	Young's modulus of the bar, GPa.
`z`	Distance to apply correction over, positive in direction of propagation, m.

Outputs	*Description*
`x_strain`	Dispersion-corrected strain signal.
`x_stress`	Dispersion-corrected stress signal, MPa

Table 4.5: Input and output variables used in in `dispersion.py`.

This subroutine adapts Tyas and Pope (2005) dispersion-correction approach to ensure that the inferred axial stress and strain data accurately depicts the specimen behaviour.

The function's operation can be summarised as follows:

a) FFT is used to convert the strain signal to a frequency-domain signal.

b) The frequency components above the M_1 correction cut-off are removed using an ideal low-pass filter.

c) Below the Nyquist frequency, for each of the remaining components:

   i) The `disperion_factors.py` function is used to calculate the required phase shift as well as the factors M_1 and M_2. To reduce computation time, this method employs a pre-calculated, normalised look-up table generated by `phase_velocity.py`.

   ii) Equation (4.15), factors M_1 and the phase angle correction θ'_ω are used to rebuild a dispersion-corrected strain component, as shown below in Equation (4.16):

$$z_\varepsilon = M_1 A e^{i(\theta - \theta'_\omega)} \tag{4.16}$$

   where A is the original amplitude of the component and θ is the original phase angle.

   iii) A dispersion-corrected stress component is similarly reconstructed using factors M_1 and M_2, as well as the phase angle correction, θ'_ω, as illustrated in Equation (4.17) below:

$$z_\sigma = M_1 M_2 A e^{i(\theta - \theta'_\omega)} \tag{4.17}$$

d) Frequency components above the Nyquist frequency are formed by taking the complex conjugate of these adjusted stress and strain components.

e) The frequency-domain stress and strain signals are transformed back to the time domain using the inverse FFT, `ifft()`, from the numpy library, and returned as output variables `x_strain` and `x_stress`.

These corrected pressure bar stresses and strains are then used in `SHPB_Processing.py` to infer the behaviour of the SHPB specimen.

4.4.7.4 Operation of dispersion_factors.py

The Python algorithm, `dispersion_factors.py`, is a subroutine of the programme `dispersion.py`.

The dispersion factors utilised in this script are calculated using the algorithm `phase_velocity.py`, with a Poisson's ratio of 0.29, which is based on the property of the Hopkinson bars used for testing in this case. Afterwards, `dispersion_factors.py` loads the four dispersion factor files, `m1`, `m2`, `norm_freqs` and `v_ratios`, before calculating the amplitude and phase angle corrections required to account for dispersion at a specific frequency.

The following command line is necessary to run this algorithm, with details of the input and output variables outlined in Table 4.6:

`dispersion_factors(f,a,c0,z)`

Inputs	*Description*
`f`	Frequency, Hz.
`a`	Bar radius, m.
`c0`	One-dimensional wave velocity of the bar, m/s.
`z`	Distance to apply correction over, m.
Outputs	*Description*
`angle_mod`	Phase angle correction, rad.
`m1`	Correction for variation in response across bar cross-section.
`m2`	Correction for variation in ratio of axial stress and axial strain (dynamic Young's modulus).

Table 4.6: Input and output variables used in `dispersion_factors.py`.

The corrected `angle_mod`, `m1` and `m2` factors are then used in `dispersion.py` to apply the appropriate signal phase shift to obtain the adjusted strain and stress. This algorithm was inspired by a MATLAB script created by Barr (2016*a*).

4.4.7.5 Operation of phase_velocity.py

The independent open-source function `phase_velocity.py` is available on GitHub and ORDA (Van Lerberghe and Barr 2023*b*). Its aim is to determine the first root of Bancroft's (1941) equation using the bisection method, for a defined Poisson's ratio, and over a defined range of normalised wavelength (d/L). The result is the normalised phase velocity, c_p/c_0, representing the first mode of propagation for longitudinal waves in an elastic cylindrical bar. Additionally, normalised wavelengths are converted into normalised frequency, fa/c_0. These normalised phase velocities are then used to compute Tyas and Watson (2001) factors M_1 and M_2, which account for wavelength-dependent radial variations in strain and Young's modulus, respectively.

In this study, stainless steel bars with a Poisson's ratio of 0.29 were used to perform these SHPB experiments. A normalised look up table containing phase velocity factors, denoted as `m1`, `m2`, `norm_freqs` and `v_ratios`, were computed and then stored in four separate .pickle files, within a directory named `dispersion_factors`, corresponding to the chosen Poisson's ratio (Table 4.7). This programme enables the generation of additional tables for any cylindrical bar utilised during testing, based on its corresponding Poisson's ratio.

The following command line is required to run this algorithm, with details regarding input and output variables provided in Table 4.7:

`phase_velocity(nu, l_ratios)`

Inputs	*Description*
`nu`	Poisson's ratio of bar material used for SHPB tests.
`l_ratios`	Normalised wavelength range to calculate the first root of Bancroft's (1941) equation.
Outputs	*Description*
`dispersion_factors`	Folder which includes 4 .pickle files containing the dispersion factors `m1`, `m2`, `norm_freqs` and `v_ratios`.

Table 4.7: Input and output variables used in `phase_velocity.py`.

Variables `m1`, `m2`, `norm_freqs` and `v_ratios` are used in `dispersion_factors.py` and `dispersion.py` by association, to facilitate the dispersion correction of the collected SHPB signals, as a functionality of the the main processing script `SHPB_Processing.py`. This algorithm was inspired by a MATLAB script initially created by Barr (2023).

4.4.8 Comparison with one-dimensional wave theory

To demonstrate the advantages of dispersion correction through the `dispersion.py` subroutine within the main algorithm `SHPB_Processing.py`, Figures 4.21 and 4.22 depict the front and back sample stresses obtained from an SHPB test conducted on kaolin clay with 0 % moisture content under unconfined testing conditions. These stresses are computed using one-dimensional wave theory and the frequency-domain method outlined above. In Figure 4.21a, the incident and reflected stress waves recorded at the incident bar strain gauge maintain their shapes as they are translated along the time axis. Conversely, in Figure 4.21b, the dispersion associated with 1000 mm of travel in the bar is introduced to the incident wave and removed from the reflected wave, taking the frequency dependence of phase velocity into account.

The dispersion correction notably diminishes the pronounced fluctuations observed in the front stress calculated using one-dimension wave theory, as depicted in Figure 4.21c. This reduction is attributed to adjustments made to the initial gradient of the stress waves, along with the modifications to the position and magnitude of the Pochhammer-Chree oscillations, resulting in improved alignment of these characteristics in both incident and reflected waves.

For clarity, 'front' stress refers to the stress at the incident bar-sample interface, while 'back' stress corresponds to the sample-transmitter bar interface.

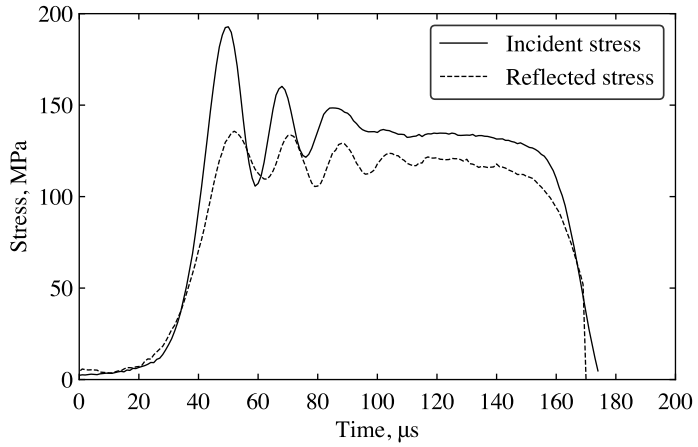

(a)

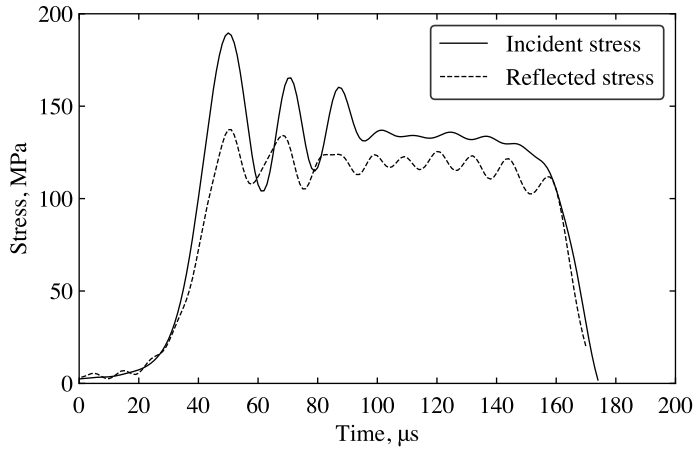

(b)

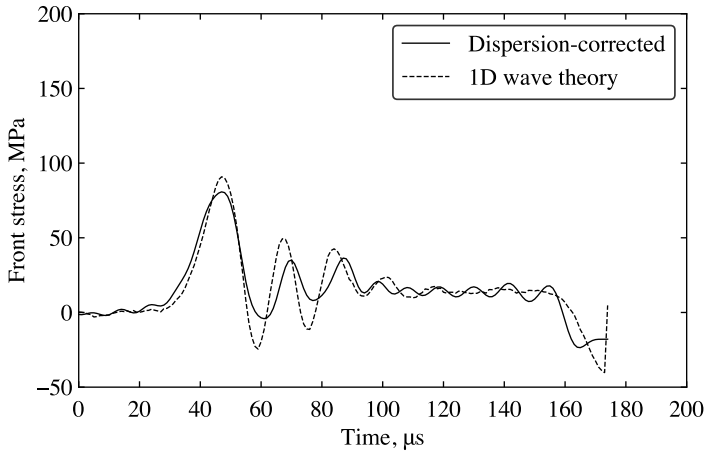

(c)

Figure 4.21: Comparison of incident and reflected waves using (a) one-dimensional wave theory and (b) dispersion-corrected analysis, and (c) calculation of sample front stress using each method.

As the specimen front stress is calculated by the superposition of the incident and reflected waves, the inferred front stress is greatly improved as a result. In contrast, the dispersion correction exerts minimal influence on the calculated back stress illustrated in Figure 4.22. This is because the transmitted wave contains few high-frequency features and is measured only 500 mm from the specimen interface.

This improved processing method has been implemented across all SHPB experiments discussed in this thesis, allowing for the calculation of a more representative axial stress to be calculated from the mean of the front and back specimen stresses. Application of dispersion correction to incident and reflected waves results in significantly reduced spurious oscillations in the inferred sample front stress. This leads to improved accuracy in axial stress data and a deeper understanding of specimen behaviour.

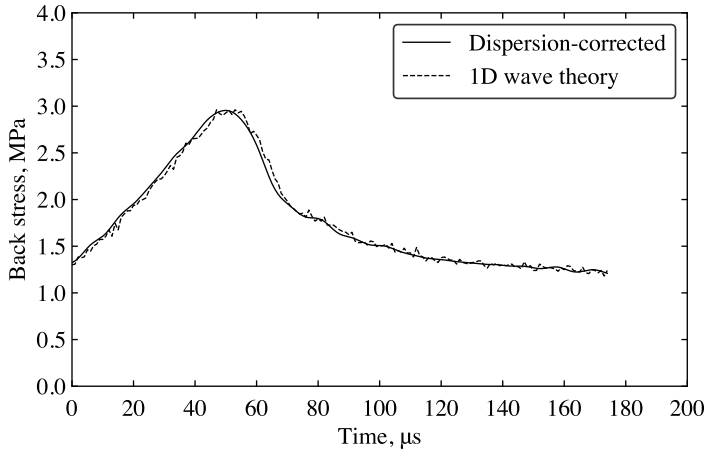

Figure 4.22: Comparative analysis of specimen back stress computed using dispersion-correction and one-dimensional wave theory.

4.4.9 Stress equilibrium

Figures 4.23 and 4.24 illustrate the normalised stress difference between the front and back stress for an unconfined and confined SHPB tests on a kaolin clay sample. Although stress equilibrium is not reached `SHPB_Processing.py` functions effectively and yields accurate results.

In ideal conditions, stress equilibrium is achieved during SHPB testing, indicated by equal pulse lengths detected at the specimen's front and back bar interfaces (i.e. front and back stresses). However, this equilibrium is not always attained, particularly when stress waves fail to fully propagate through the sample, resulting in considerable lateral propagation.

Stress equilibrium during a SHPB test can be represented by Equation (4.18), provided that the deformation of the specimen is uniform and that the axial propagation of the stress wave has been taken into account.

$$\varepsilon_i(t) = \varepsilon_r(t) + \varepsilon_t(t) \tag{4.18}$$

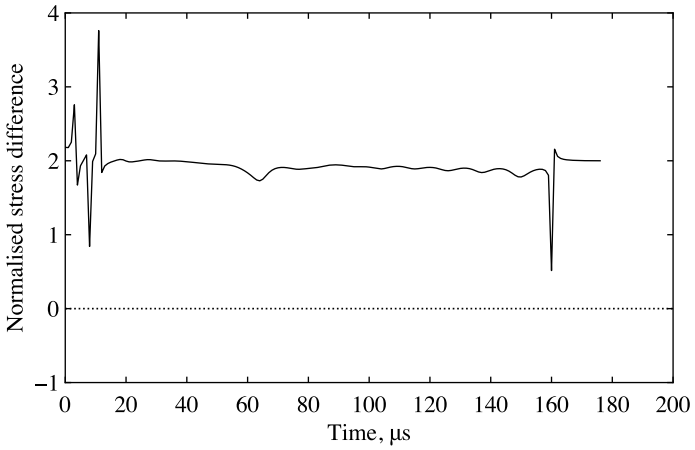

Figure 4.23: Normalised stress difference of front and back stresses for an unconfined SHPB test on kaolin clay.

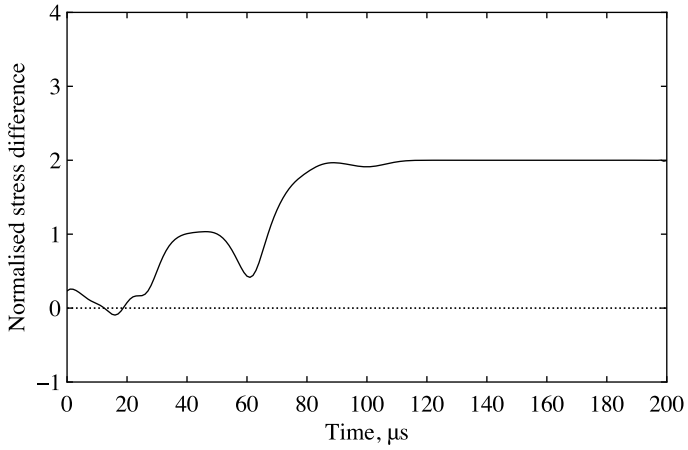

Figure 4.24: Normalised stress difference of front and back stresses for a confined SHPB test on kaolin clay.

The normalised stress difference, plotted in Figure 4.23 and 4.24 to evaluate the stress equilibrium during the SHPB tests, is represented by Equation (4.19).

$$\text{Normalised stress difference} = \frac{\sigma_{\text{front}} - \sigma_{\text{back}}}{\sigma_{\text{mid}}} \tag{4.19}$$

The ability in `SHPB_Processing.py` to set an alignment to manage the front and back stresses means this function is able to account for cases where stress equilibrium may not be fully obtained, but an estimation of the axial stress can still be determined, though with the caveat that it should be coupled with further experimental testing or numerical modelling in order to be utilised for material characterisation.

The SHPB tests carried out in this project deviate from traditional SHPB tests due to the absence of stress equilibrium. Instead, they are impact dynamic loading tests aimed at evaluating the dynamic behaviour of cohesive soils, specifically kaolin clay, under both unconfined and confined conditions.

4.4.10 Electromagnetic effects in SHPB experiments

This section discusses the electromagnetic sources of error observed during SHPB experiments and the techniques employed to mitigate electromagnetic interference around the confining ring.

Research by Barr (2016*b*) demonstrated that pressure bars are the primary source of electromagnetic noise in SHPB experiments, as confirmed by experiments using an induction coil (Figure 4.25a). The positioning of leadwires significantly affects the electromotive force (EMF) generated in the strain gauge circuit (Figure 4.25b), making automated correction of these EMFs would be challenging in the current testing configuration. Consequently, a consistently position twisted pair of gauge leadwires were adopted during high-strain-rate SHPB testing to minimise the impact of EMF.

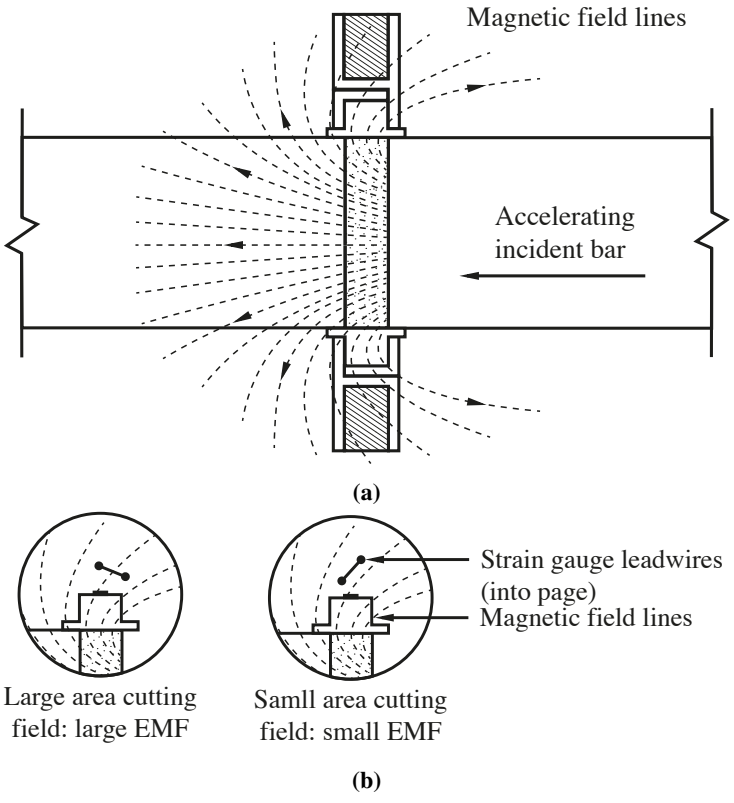

Figure 4.25: An example of the field around a magnetised incident bar in relation to (a) the induction coil, and (b) the leadwires on the confining ring strain gauge (Barr 2016*b*).

4.5 Results and discussion

The experimental research programme in this project examines the influences of three key parameters: strain rate, moisture content, and confinement. The quasi-static and high-strain-rate test results will undergo analysis for each parameter. Initially, the soil's response will be assessed through quasi-static one-dimensional compression analysis. This evaluation focuses on validating the impact of moisture content on the compressibility behaviour of kaolin clay under quasi-static loading conditions. Next, the signals generated by the experimental SHPB setup will be scrutinised. This validation process ensures the accurate detection of incident, reflected and transmitted signals in the absence of any sample - a test commonly referred to as 'bar-to-bar'. This step is to confirm that the signals captured during material testing originate solely from the material being tested. Subsequently, the material properties of the prepared specimens obtained from pre-testing will be thoroughly examined. Following this, the results of both unconfined and confined SHPB tests will be analysed. This evaluation aims to assess the effects of strain rate, moisture content and confinement on kaolin clay samples under high-strain-rates conditions.

4.5.1 Quasi-static compressibility

A set of three unconsolidated undrained (UU) one-dimensional TXC tests were conducted for each kaolin clay sample prepared at moisture contents of 41, 42 and 44 %. Before each test, the cell consolidation pressure was set at 100, 200 and 300 kPa, respectively, for each moisture content. In total, nine UU TXC tests were performed on the prepared kaolin specimens. Further details on specimen preparation and the test programme are available in Sections 3.3.1 and 3.4.1.1.

The deviatoric stress versus axial strain results of the TXC tests are depicted in Figure 4.26, along with their associated Mohr circle behaviour for each kaolin clay sample at moisture contents of 41, 42 and 44 %, as illustrated in Figure 4.27. The maximum average deviatoric and shear stresses are in Table 4.8.

Moisture content, %	*Maximum average deviatoric stress, kPa*	*Maximum average shear stress, kPa*
41	115.41	57.70
42	96.06	48.03
44	85.99	42.99

Table 4.8: TXC test results: maximum average deviatoric and shear stress results for different moisture contents.

The deviatoric stress, $\sigma_d = \sigma_1 - \sigma_3$, represents the difference between axial and confining stresses in the TXC test and is responsible for inducing plastic deformation, causing shape distortion without altering the material's volume. The shear stress, $\tau = \frac{\sigma_1 - \sigma_3}{2}$, is the component of deviatoric stress acting parallel to the material's surface, causing soil particles to slide over each other and leading to failure through shape change. In UU TXC tests, the maximum average deviatoric and shear stress can be computed as the sample is tested without drainage, meaning no volume change occurs during shear.

The results show a clear trend: as moisture content increases, both maximum average deviatoric stress and shear stress decrease. These independent parameters are influenced by the moisture content of the kaolin clay sample, confirming its impact on the strength of cohesive soils under quasi-static loading conditions.

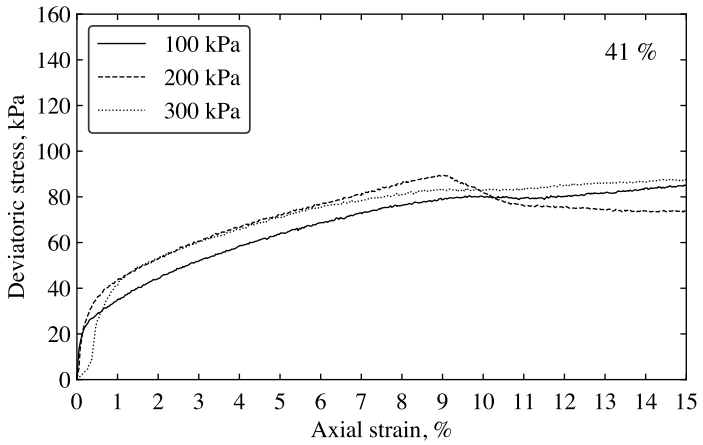

(a)

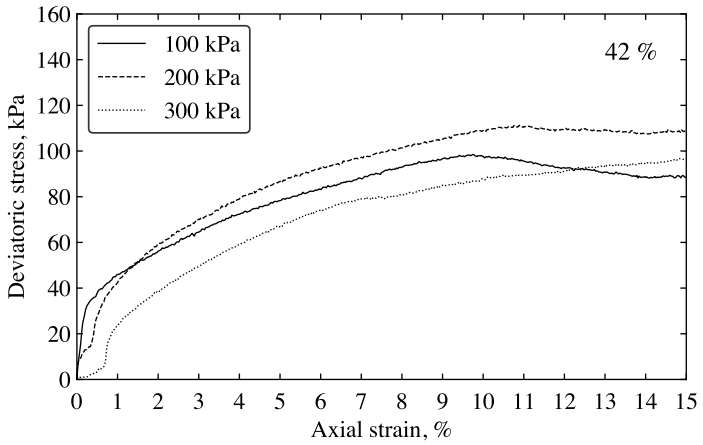

(b)

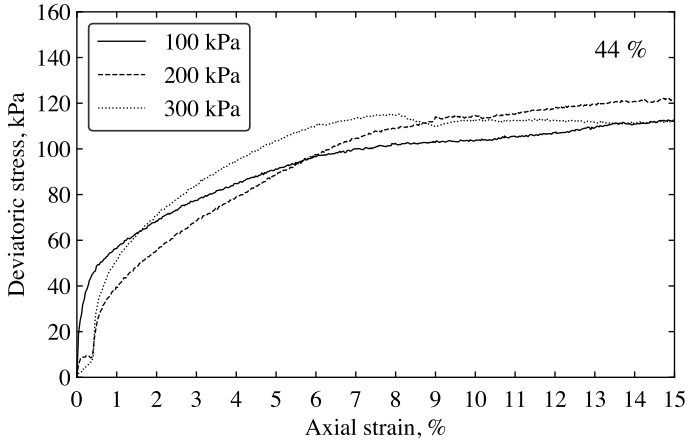

(c)

Figure 4.26: Deviatoric stress vs axial strain behaviour for kaolin clay samples at a moisture content of (a) 41 %, (b) 42 % and (c) 44%.

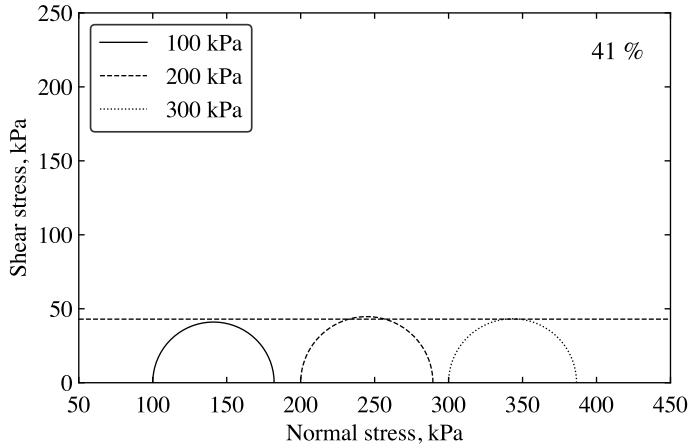

(a)

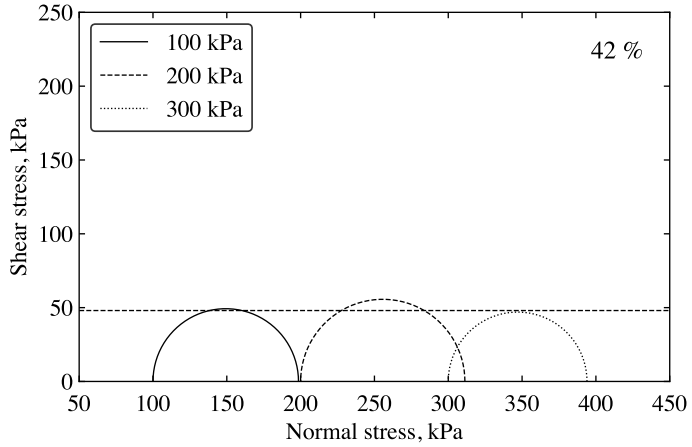

(b)

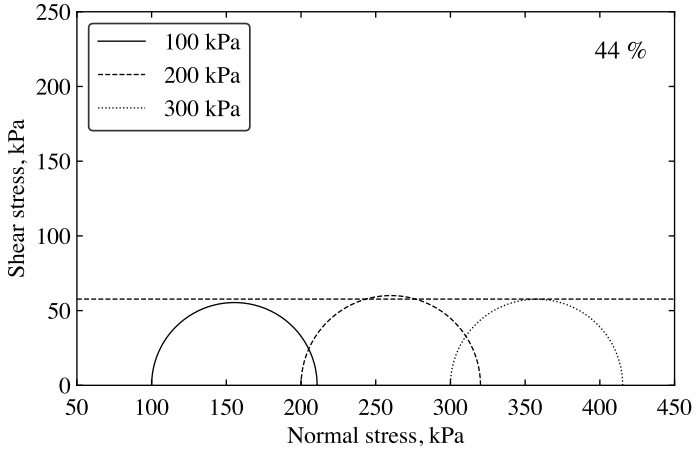

(c)

Figure 4.27: Mohr circles for kaolin clay samples at a moisture content of (a) 41 %, (b) 42 % and (c) 44%.

The static and dynamic oedometer tests were conducted on kaolin clay samples with moisture contents of 41%, 42%, and 44%. Detailed information on sample preparation and the test programme is available in Sections 3.3.1 and 3.4.1.2. Figure 4.28 presents the axial stress versus dry density behaviour, while Figure 4.29 shows the void ratio versus axial stress behaviour under both static and dynamic testing conditions. A comparison between static oedometer tests, where consolidation pressure was gradually increased over time, and dynamic oedometer tests, where a pressure of 3200 kPa was applied directly at a rate of 1 mm/min, revealed significant differences in the behaviour of kaolin clay.

Figure 4.29, shows dynamic tests with no density increase during consolidation, as evidenced by the visible extrusion of kaolin clay from the consolidation cell during testing. This behaviour mirrors SHPB tests where lateral extrusion rather than consolidation occurs. Water, represented in blue in Figure 4.29, similarly shows zero change in dry density under stress, similar to the behaviour of kaolin clay. This suggests that during consolidation at low-strain-rates, the behaviour of the kaolin clay specimen is primarily influenced by the sample's moisture content, as the clay particles have little effect on its dynamic response.

The permeability of cohesive soils, such as kaolin clay, plays a crucial role in their behaviour, particularly their inability to dissipate pore water quickly. The small particle size and tight packing of clay particles restrict water movement, causing increased pore pressure during rapid loading. This delays consolidation, reduces shear strength, and amplifies the soil's fluid-like response under stress. Consequently, during dynamic loading, it is the moisture content of the kaolin clay, rather than the clay particles themselves, that predominantly governs the material's behaviour. This is reflected in Figure 4.29, where the static curve approaches the kaolinite particle density trendline (in red), while the dynamic curve remains parallel to the water density trendline (in blue).

The application of axial stress to kaolin clay induces lateral pressure, exhibiting behaviour similar to that of a fluid. This response arises from the material's limited resistance to axial loading. Such fluid-like characteristics are evident not only in dynamic oedometer testing but also in SHPB experiments, where lateral extrusion occurs under both unconfined and fully confined conditions, resembling fluid dynamics (see Sections 4.5.4 and 4.5.5 for further details).

Figure 4.29 further illustrates the behaviour of kaolin clay under both static and dynamic conditions. Under static conditions, as axial stress increases, the void ratio decreases progressively, reflecting the clay's consolidation. This results in a trendline that becomes increasingly vertical with higher axial stresses, indicating a steady reduction in void space. In contrast, under dynamic conditions, the trendline remains horizontal as axial stress increases, suggesting a rapid compression phase with minimal void reduction due to the clay's inability to dissipate pore water quickly under high strain rates. This distinction underscores the different consolidation mechanisms at play in static versus dynamic loading scenarios.

In conclusion, the comparison between static and dynamic oedometer tests on kaolin clay reveals distinct behavioural differences influenced primarily by moisture content and the rate of applied stress. While static conditions result in gradual consolidation and a steady reduction in void ratio, dynamic conditions show minimal consolidation due to the clay's inability to dissipate pore water quickly under high strain rates. This fluid-like behaviour, particularly under dynamic loading, highlights the significant role of moisture content in governing the material's response. The observed differences between static and dynamic testing underscore the complexity of modelling cohesive soils, particularly under varying loading conditions, and emphasise the need for further research to refine our understanding of their behaviour under high-strain-rates.

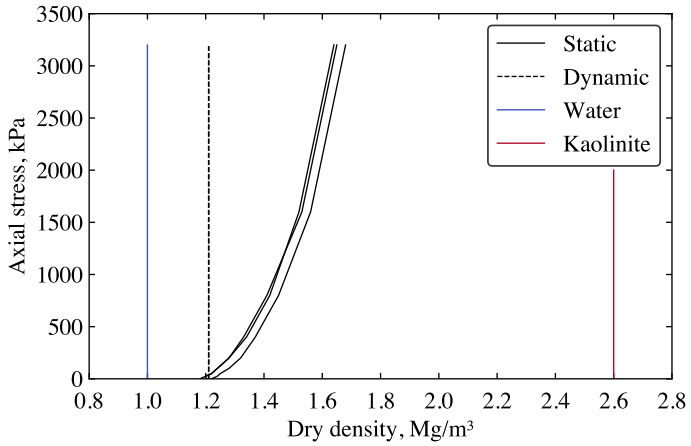

Figure 4.28: Axial stress-dry density behaviour for kaolin clay at a moisture content of 41, 42 and 44 %, tested using an oedometer under both static and dynamic conditions.

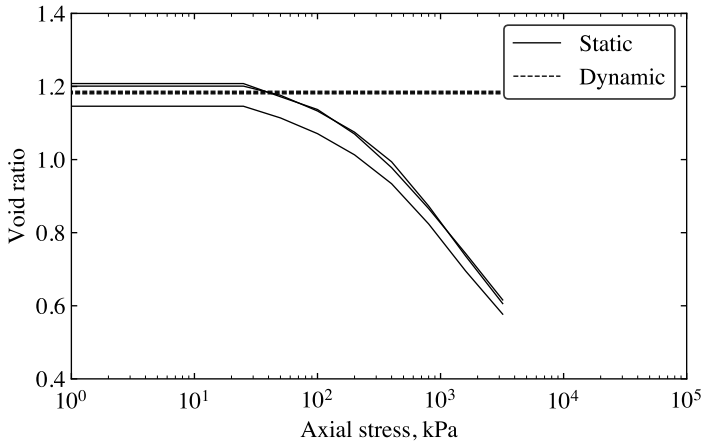

Figure 4.29: Void ratio-axial stress behaviour of kaolin clay at a moisture content of 41, 42 and 44 %, tested using an oedometer under both static and dynamic conditions.

4.5.2 Signal setup calibration

Before subjecting the prepared kaolin clay samples to testing on the split-Hopkinson pressure bar apparatus, a calibration test is performed to confirm the signals recorded by the strain gauges on the incident and transmitter bar is as expected. This validation test aims to accurately record the incident, reflected and transmitted signals by the strain gauges on the incident and transmitter bars in the absence of any sample - a test commonly referred to as 'bar-to-bar'. This step's aim is to ensure that the signals recorded during material testing originate exclusively from the material under examination. Figure 4.30 depicts the calibration test, showing the incident and transmitted wave signals. The near-perfect transmission of the stress pulse from the incident to the transmitter bar is evident, as expected in the absence of a sample.

Given the direct contact between the two stainless steel pressure bars, the incident pulse's amplitude should be directly transferred to the transmitter bar as the transmitted pulse. Any observed discrepancies in the reflected pulse should ideally remain minimal, possibly stemming from imperfections at the pressure bars' end. These imperfections could arise due to repeated testing or issues with the gauges or balance box. Nonetheless, the results meet the condition for stress equilibrium, where the superposition of incident and reflected pulses equals the transmitted pulse.

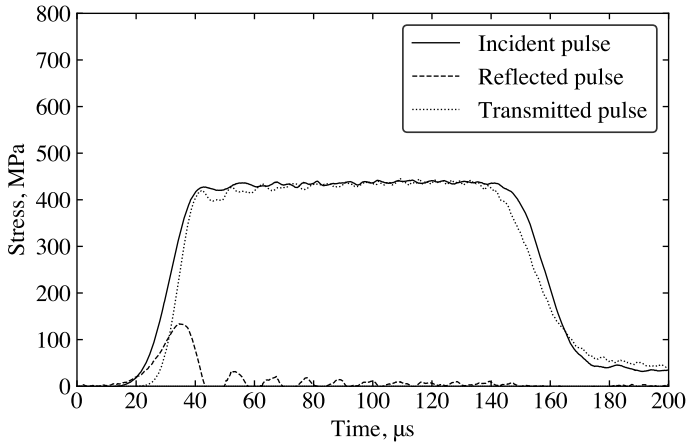

Figure 4.30: SHPB 'bar-to-bar' calibration test.

All plots have a fixed y-axis limit for clarity and ease of comparison. Although all plots start at 0, this may not be immediately visible as the x-axis blends with the first few data points.

To aid comparison of the waveforms, stress wave signals were all truncated to match the point where the sample reached its maximum strain, after being aligned at their peak at 50 microseconds. Outside the plotted range, the stress pulses naturally start and end at 0 as expected.

Alignment based on peak stress was performed specifically for this scenario, considering the tested strains, selected material, and its non-equilibrium stress conditions. Aligning based on peak stress at smaller strains would obscure the data.

4.5.3 Sample material properties

Prior to conducting the unconfined and confined SHPB tests, key sample properties were calculated to understand the evolution of air, water, and soil in the kaolin clay sample during testing. These properties, which include the volume of air (V_{air}), volume of water (V_{water}), and total volume (V), are crucial for interpreting the material's behaviour under dynamic loading conditions.

To obtain these essential material properties, the first step involved measuring the sample's diameter, thickness, wet mass, and dry mass. Using these values, the moisture content was calculated, followed by determining the total volume (V) of the sample. Next, the volume of water (V_{water}) was calculated by subtracting the dry mass from the wet mass and dividing by the density of water (ρ_w). The volume of solids (V_{solids}) was then determined by dividing the dry mass by the product of specific gravity and ρ_w. This process allowed us to calculate the volume of voids (V_{voids}) as $V - V_{solids}$ and the volume of air (V_{air}) as $V_{solids} - V_{water}$.

These calculated volumes were then used to derive the air volume ratio and water volume ratio. The air volume ratio is obtained by dividing the volume of air (V_{air}) by the total sample volume (V), as shown in Equation (4.20).

$$\text{Air volume ratio} = \frac{V_{air}}{V} \tag{4.20}$$

Similarly, the water volume ratio is determined by dividing the volume of water (V_{water}) by the total sample volume, as shown in Equation (4.21):

$$\text{Water volume ratio} = \frac{V_{water}}{V} \tag{4.21}$$

In addition to these ratios, a key objective of this study is to examine the high-strain-rate behaviour of kaolin clay across various moisture contents, including different saturation levels. The saturation ratio, S_r, links moisture content (w) to the clay's behaviour under high-strain-rate loading. This relationship, expressed in Equation (4.22), helps us understand the distribution of water relative to the voids in the sample, which is critical for interpreting the clay's consolidation and shear response under dynamic loading.

$$\text{Saturation ratio, } S_r = w \times k \tag{4.22}$$

where k represents a coefficient calculated as the specific gravity, Gs, divided by the void ratio, e.

To summarise, these material properties—total volume, individual volumes of air, water, and solids, along with the derived volume ratios and saturation ratio—are essential for understanding the physical behaviour of kaolin clay under dynamic high-strain-rate testing conditions. These properties were carefully determined for each sample before testing, using Equations (4.20), (4.21), and (4.22) as analytical tools.

4.5.4 Unconfined SHPB test results

4.5.4.1 Signal processing

The signals collected during an unconfined SHPB test are processed using `SHPB_Processing.py`. Included as inputs are the material properties of the sample, setup parameters and processing requirements. For further sample details refer to Appendix B. The following command line was utilised to process the test data for an unconfined SHPB test on a kaolin clay sample with a moisture content of 0 %:

$$\texttt{SHPB\_Processing}\,(\texttt{csv\_path} = \text{“}\texttt{test0\_kaolin0\_600mm\_14psi.csv}\text{”},\ \texttt{sample\_data} = [5.633, 3.175, 3.175], \texttt{confinement} = \text{“}\texttt{None}\text{”}, \texttt{signal\_channels} = [3, 4],\ \texttt{signal\_amp} = [10, 100], \texttt{disp\_correction} = \texttt{True}, \texttt{alignment} = 50, \texttt{speedtrap} = \texttt{True})$$

This test was conducted without confinement, signal amplification was set at 10 for the incident bar and 100 for the transmitter bar, dispersion correction was applied, signals were set to align at an assigned peak value of 50 MPa, and the velocity of the striker bar was recorded.

4.5.4.2 Experimental results

Unconfined SHPB tests were performed on kaolin clay samples with moisture content levels ranging from 0 to 44 %, to cover all saturation stages: dry, partially-saturated and fully saturated. Initially, the samples were tested at 8, 12, 16 m/s, corresponding to strain rates of 1200, 1900 and 2800 s^{-1}. The sample's strain rate, strain, front, back and mid stresses were determined using the signal processing algorithms in Sections 4.4.6 and 4.4.7. The corresponding peak average strain rate for each relative test speed is represented in Figure 4.31a.

Figures 4.31b, 4.32a, 4.32b and 4.32c show that in a typical unconfined SHPB test at a moisture content of 0 %, increasing the strain rate correlates with higher material strain, front, back and mid stresses. Figure 4.31c portrays kaolin clay's strain rate dependency. A crucial discovery in our understanding of the high-strain-rate behaviour of cohesive soils.

When comparing front and back stresses in Figures 4.32a and 4.32b, a significant amplitude difference is evident. The front stress, indicating the stress at the incident bar-sample interface, is ten times greater than the back stress, which represents the sample-transmitter bar interface. This suggests that instead of the stress wave transmitting purely axially through the sample, it is reasonable to assume that the stress wave predominantly propagates laterally. This highlights the substantial stress-dampening properties of the kaolin clay. Hence, stress equilibrium is not conventionally achieved. Therefore, the method outlined in Section 4.4.9 was used to evaluate the front, back, and mid-stress of the specimen (where the mid-stress is the average of the front and back stresses).

At the same strain rate, the material's strain and front stress behaviour are consistent across all moisture contents. However, the back stress behaviour is dependent on the strain rate and moisture content of the tested kaolin clay sample, where it exhibits four distinct phase behaviours, as displayed in Figure 4.34. This means that the material's mid-stress at a specific strain rate and moisture content is primarily determined by the resulting back stress.

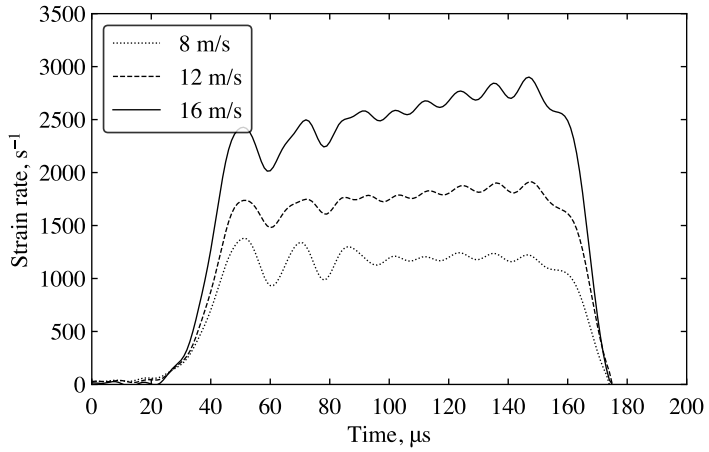

(a)

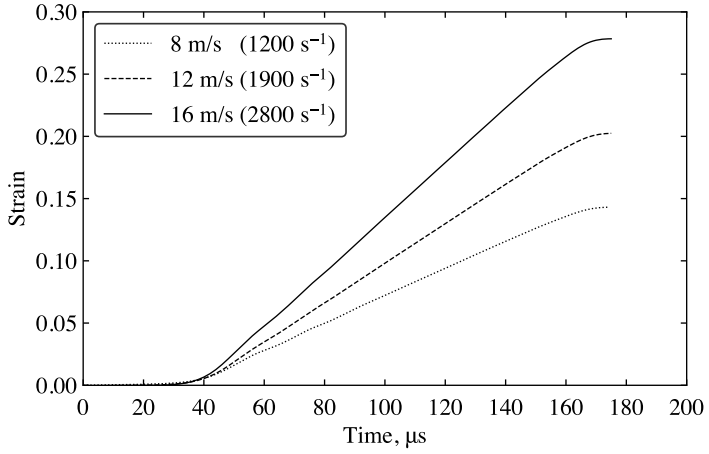

(b)

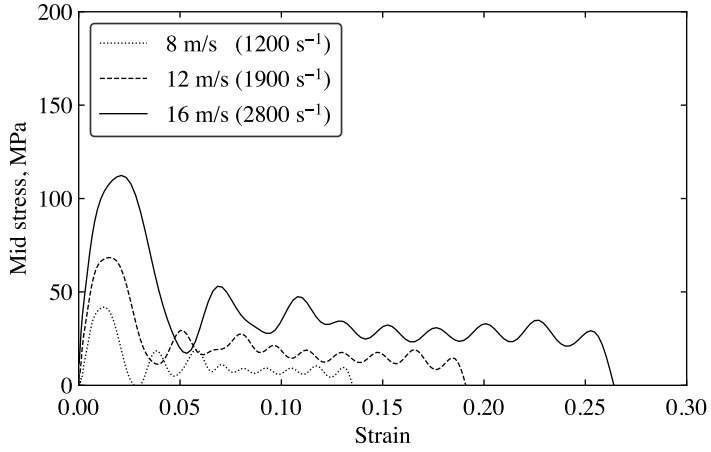

(c)

Figure 4.31: Typical behaviours for an unconfined SHPB test on kaolin clay, at a moisture content of 0 % and different strain rates: (a) peak average strain rates (b) strain vs time, and (c) mid stress vs strain.

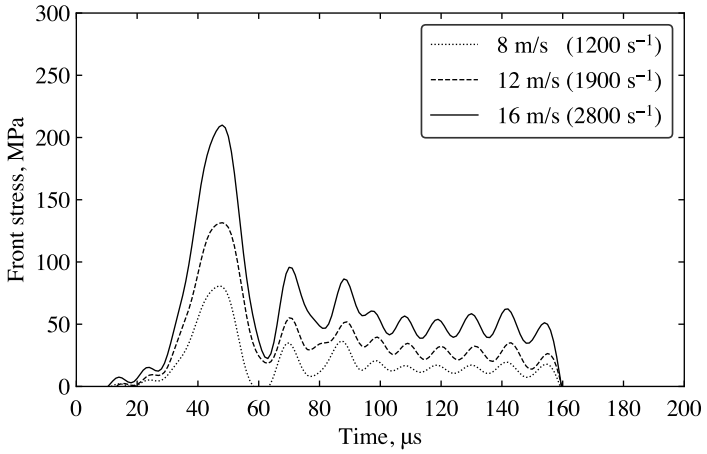

(a)

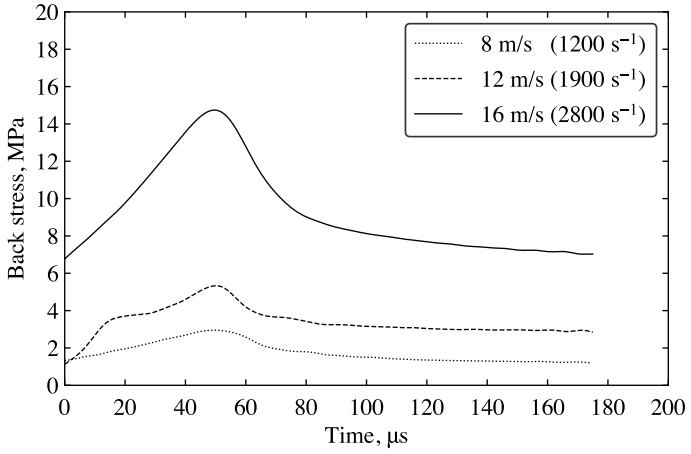

(b)

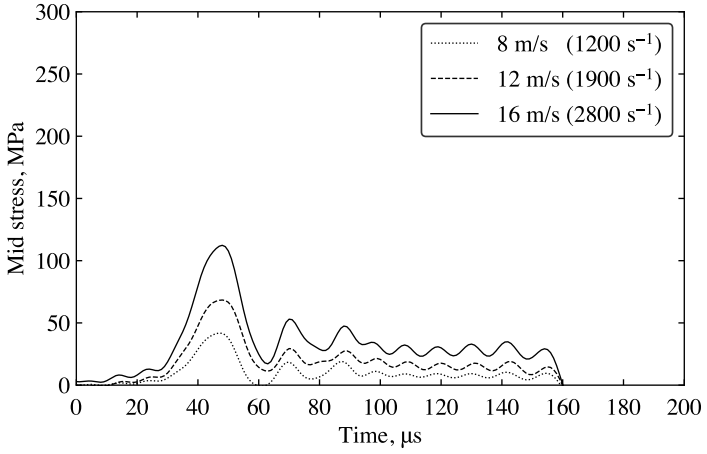

(c)

Figure 4.32: Typical behaviours for an unconfined SHPB test on kaolin clay, at a moisture content of 0 % and different strain rates: (a) front stress vs time, (b) back stress vs time, and (c) mid stress vs time.

4.5.4.3 Steps for developing the phase behaviour diagram in unconfined SHPB testing

Step 1: Axes

- **X-axis:** Represents the moisture content of the kaolin clay samples tested under unconfined SHPB conditions. This parameter is measured prior to testing and is illustrated in Figure 4.33a.
- **Y-axis:** Represents the material properties of the kaolin clay sample. This includes the air volume ratio and water volume ratio, computed before testing under unconfined SHPB conditions. These properties are detailed in Section 4.5.3 and visualised in Figure 4.33a.

Step 2: Plotting the material properties

- **Material property data:** The air and water volume ratios are plotted against the moisture content for each specimen tested under unconfined SHPB conditions, as shown in Figure 4.33b.
- **Trendlines:** Trendlines are drawn from the plotted data, representing the overall behaviour of each material property under unconfined SHPB conditions, as illustrated in Figure 4.33b.

Step 3: Intersection Point A - Phase 0 and Phase 1

- **Intersection point A:** The point where the trendlines of the air volume ratio and water volume ratio intersect, labeled as Point A, is shown in Figure 4.33c.
- **Delimitation of Phase 0 and Phase 1:** Point A marks the right boundary of Phase 1, with its left boundary defined by the y-axis. Phase 0 corresponds to specimens with 0% moisture content, represented as the y-axis (Figure 4.33c).

Step 4: Max experimental strain of the sample

- **Max experimental strain of the sample:** Measured during unconfined SHPB testing, this parameter indicates the maximum strain experienced by the kaolin clay sample at a given strain rate. It is represented as a red line in Figure 4.33d.

Step 5: Intersection Point B - Phase 2 and Phase 3

- **Intersection point B:** The intersection of the maximum experimental strain line and the trendline of the air volume ratio, designated as Point B, is depicted in Figure 4.33e.
- **Delimitation of Phase 2 and Phase 3:** Point B defines the right boundary of Phase 2 and the left boundary of Phase 3. The ranges of Phases 2 and 3 depend on the maximum experimental strain of the sample. Generally, higher strain rates lead to higher maximum experimental strains, expanding Phase 3 while reducing the size of Phase 2. These boundaries are illustrated in Figure 4.33e.

This section outlines the methodology for constructing the phase behaviour diagram based on experimental data collected and analysed from SHPB tests. The diagram is derived from trends in material responses, which were categorised according to sample parameters and interpreted through their physical properties. This systematic analysis offers insights into the material behaviour under varying conditions. A definition of the four distinct phases identified in the SHPB tests is provided in Section 4.5.4.4.

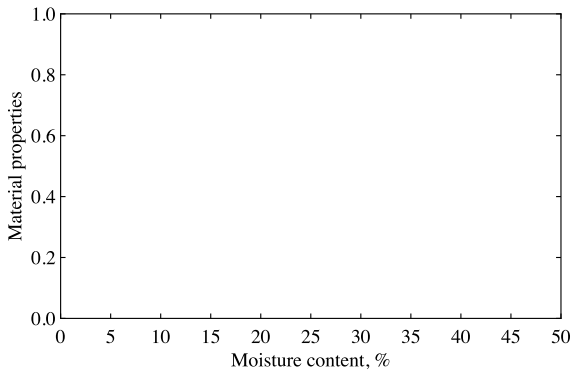

(a) Step 1: Axes.

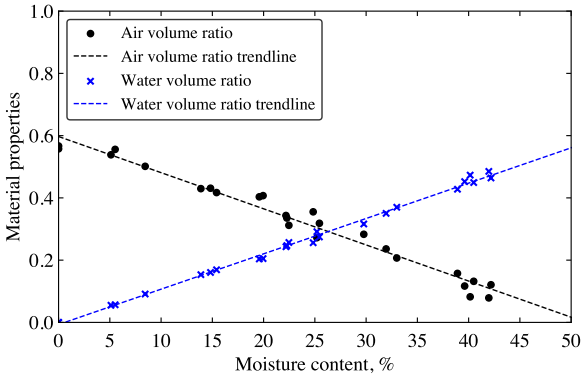

(b) Step 2: Plotting the material properties.

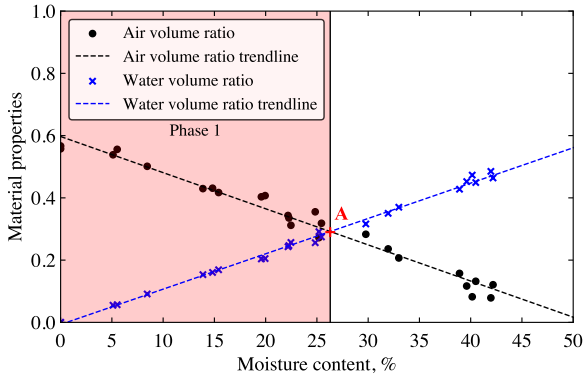

(c) Step 3: Intersection Point A - Phase 0 and Phase 1.

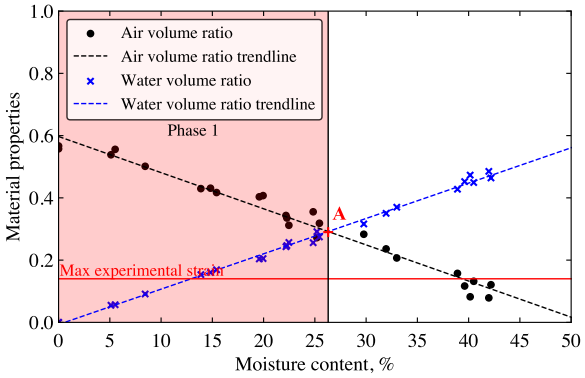

(d) Step 4: Max experimental strain of the sample.

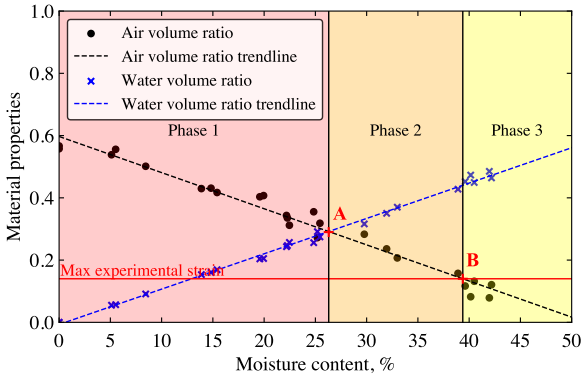

(e) Step 5: Intersection Point B - Phase 2 and Phase 3.

Figure 4.33: Steps for developing the phase behaviour diagram in SHPB testing for cohesive soils.

4.5.4.4 Phase behaviour in unconfined SHPB testing

To facilitate the analysis of experimental data collected from SHPB tests, trends in material response based on the sample's material properties were categorised, each associated with representative phase behaviours depicted in Figures 4.34a, 4.34b and 4.34c. The four phases identified can be defined as follows:

- **Phase 0:** This phase includes the tests located on the y-axis of Figures 4.34a, 4.34b and 4.34c. Samples are dry, with a moisture content of 0 %. The sample no longer contains any water; it is dry, consisting mainly of air and kaolin clay. Since there is no moisture to encourage lateral extrusion of the sample in this phase, the back stress is the highest, and a larger proportion of the stress wave travels axially towards the transmitter bar. The back stress does not return to zero because the sample consolidates, leaving a thin dry kaolin disk between the bars (Figure 4.34d).
- **Phase 1:** This phase is shown in red in Figures 4.34a, 4.34b and 4.34c. Samples in this phase are partially-saturated throughout the test, and the soil pores are primarily filled with air. It encompasses tests with a moisture content above 0 % and the intersection of the air and water volume trendlines (Point A). The back stress during this phase has a distinct shape, with a magnitude significantly lower than in phase 0, and returns close to zero after reaching its peak as the sample almost entirely extruded during testing. In phase 1, moisture content has no effect on the back stress behaviour of the kaolin clay samples (Figure 4.34e).
- **Phase 2:** This phase is shown in orange in Figures 4.34a, 4.34b and 4.34c. Samples in this phase are partially-saturated throughout the test but the soil pores are primarily filled with water. The range of this phase varies depending on the strain rate of the tests and correlated between the theoretical and final experimental strains. This phase spans from Point A to the intersection of the air volume ratio and the maximum experimental strain experienced by the sample during testing (Point B). In phase 2, moisture content has no effect on the back stress behaviour of the kaolin clay samples (Figure 4.34f).
- **Phase 3:** This phase is shown in yellow in Figures 4.34a, 4.34b and 4.34c. Samples in this phase become fully saturated during testing. This phase includes tests with a moisture content higher than the intersection of the air volume ratio and the maximum experimental strain experienced by the sample during testing (Point B). During this phase, the back stress first consists of an initial peak before levelling off and gradually decreasing back down to zero. This is due to the fast extrusion of the kaolin clay sample, which is behaving as a fluid. Within phase 3, moisture content has no effect on the back stress behaviour of the kaolin clay samples (Figure 4.34g).

Figures 4.34a, 4.34b and 4.34c show that as strain rate rises, phase 1 and 3 increase, while phase 2 decreases. This is due to the increase in the max experimental strain the sample experiences during unconfined SHPB testing. Additional tests performed at 18, 20 and 22 m/s have phase 2 disappearing, as the max experimental strain achieved a strain of 0.29, at the intersection of the two trendlines (Point A).

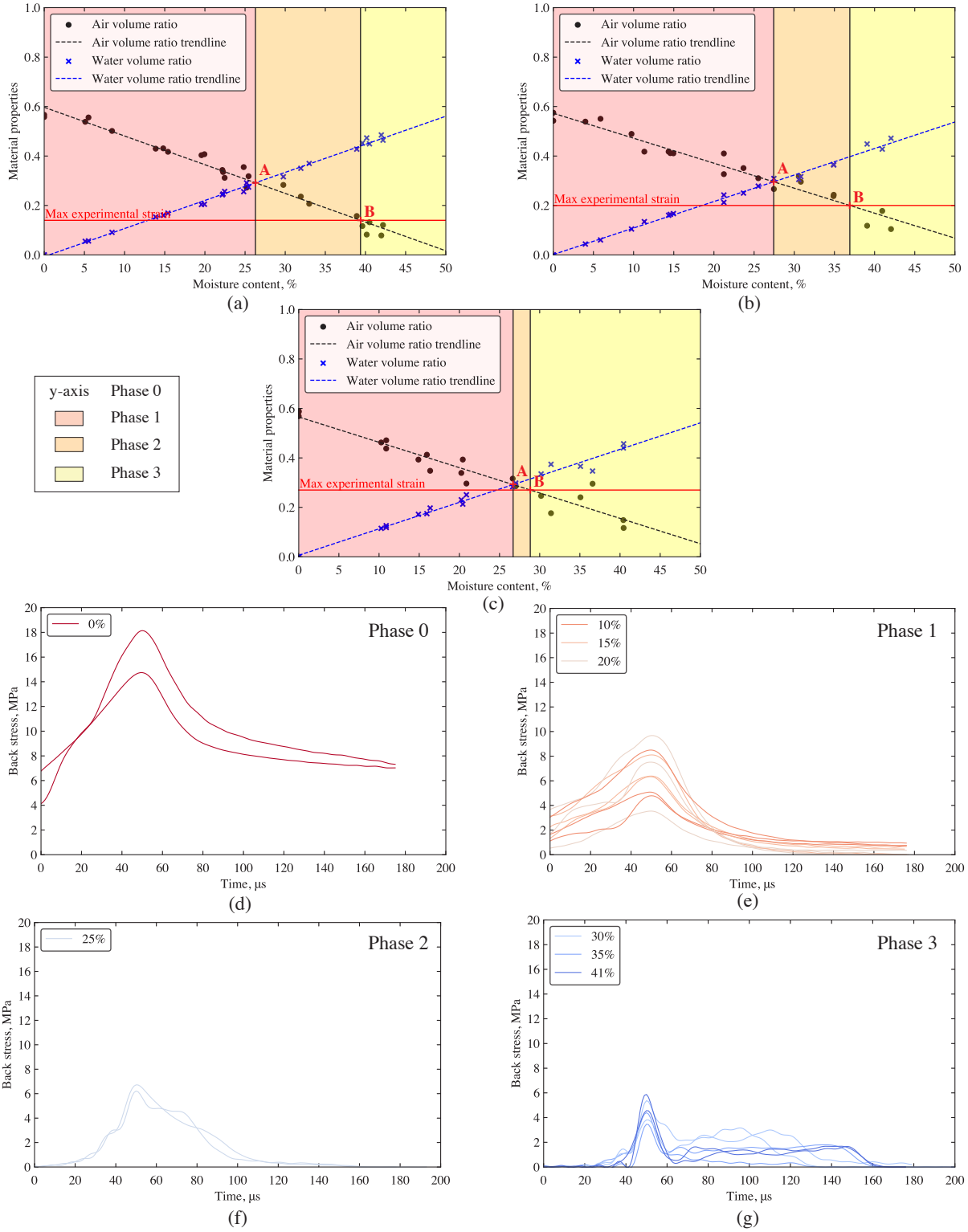

Figure 4.34: Unconfined SHPB testing of kaolin clay with (a) the phase behaviour at 8 m/s (1200 s^{-1}), (b) phase behaviour at 12 m/s (1900 s^{-1}) and (c) phase behaviour at 16 m/s (2800 s^{-1}), as well as the associated back stress at 16 m/s (2800 s^{-1}) for (d) Phase 0, (e) Phase 1, (f) Phase 2 and (g) Phase 3.

4.5.4.5 Effect of strain rate

To understand the high-strain-rate behaviour of kaolin clay samples fully, it is essential to explore how strain rate affects phase boundaries alongside moisture content. The tests conducted at three striker velocities (8, 12 and 16 m/s) reveal four distinct phases, with phases 1 and 3 showing increased magnitude and phase 2 decreasing due to higher induced strains on the specimen, caused by the striker bar.

To underscore the strain rate dependency of the material, plots of strain rate versus strain and strain rate versus stiffness results were generated, as illustrated in Figures 4.35 and 4.36. The stiffness of the sample was calculated as the ratio of the maximum axial stress to the corresponding strain, averaged over the entire range of the sample. This property is not a direct measurement due to the inherent limitations of the SHPB test, which cannot isolate parameters such as stiffness. An exponential trendline, represented by Equation (4.23), was utilised to depict this relationship. The R^2 value for the exponential trendline is 0.67, implying significant correlation between strain rate and stiffness as depicted by this trendline.

$$\text{Strain rate} = 588.12 \times e^{(0.00026 \times \text{Stiffness})} \tag{4.23}$$

A similar method was employed to examine the behaviour of strain versus strain rate, utilising a linear trendline to represent its relationship, shown in Equation (4.26). The R^2 value for the linear trendline is 0.9929, signifying a high correlation between strain rate and strain, as depicted by this equation:

$$\text{Strain rate} = 10344.83 \times \text{Strain} \tag{4.24}$$

The boundaries defining the four phases in Figures 4.34a, 4.34b and 4.34c are determined by the known material properties of the sample and the sample's strain response during testing. The increase in maximum experimental strain (Figure 4.31b) resulting from higher striker speeds directly impacts the position of the boundary between phases 2 and 3. The boundaries between phases 0 and 1, as well as between phases 1 and 2, remain consistent due to the stable material properties of the samples, which are unaffected by the test parameters. In contrast, the boundary between phases 2 and 3 decreases with higher strain rates, since it depends on the maximum experimental strain the sample reaches during testing. Consequently, the suitable range of moisture content within phase 2 narrows and eventually disappears as the strain rate increases.

Unconfined SHPB tests were also conducted at higher striker bar velocities of 18, 20 and 22 m/s to further investigate the behaviour of phase 2 under increased strain rates. These velocities correspond to average peak strain rates of 2800, 3000 and 3300 s^{-1}, respectively, as shown in Figure 4.37. The strain for each test velocity was plotted, with the maximum experimental strain being recorded at the point where the sample has fully strained, as shown in Figure 4.38 (0.29). Based on the linear relationship between strain and strain rate in Figure 4.36, a maximum experimental strain of 0.29 is required for phase 2 to completely disappear, as this is the maximum strain achievable during testing.

This corresponds to a strain rate of 3000 s^{-1}, which is equivalent to a striker velocity of approximately 20 m/s. This observation is supported by Figure 4.38. Equation (4.26) confirms that a strain rate of 3000 s^{-1} is required for phase 2 to completely disappear, given a maximum experimental strain of 0.29. Hence:

$$\text{Strain rate} = 10344.83 \times \text{Strain} = 10344.83 \times 0.29 = 3000\ s^{-1} \tag{4.25}$$

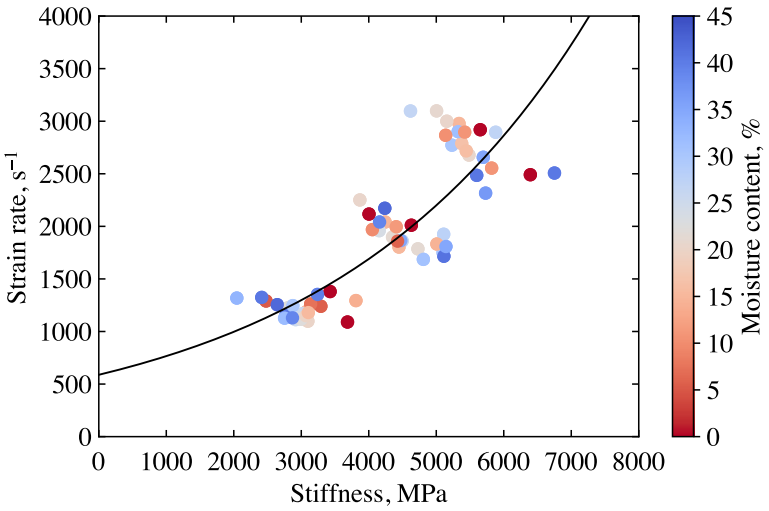

Figure 4.35: Stiffness-strain rate response of unconfined SHPB tests at different striker bar velocities (grouped at velocities of 8, 12 and 16 m/s), with its associated trendline.

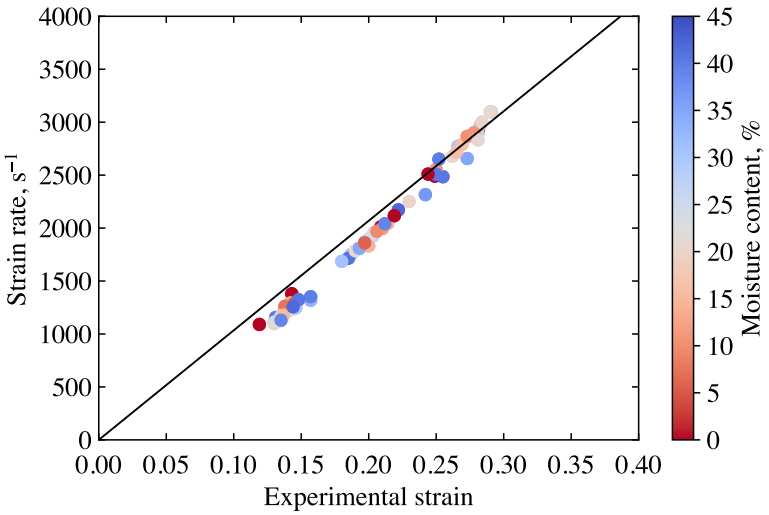

Figure 4.36: Strain-strain rate response of unconfined SHPB tests at different striker bar velocities (8, 12 and 16 m/s), with its associated trendline.

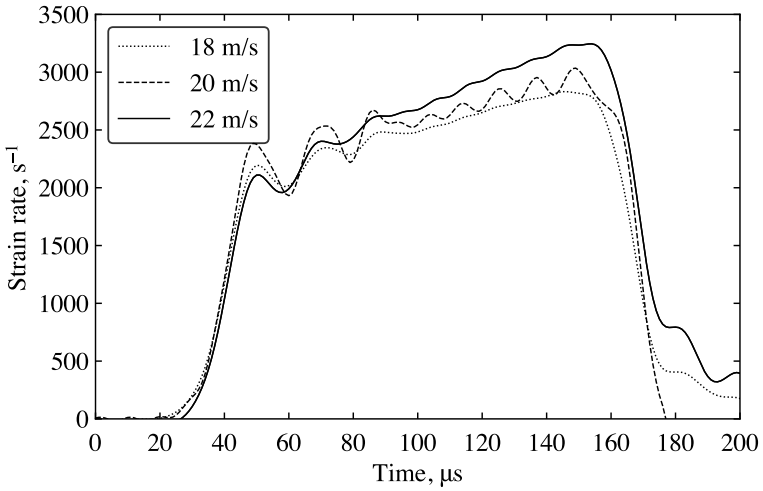

Figure 4.37: Typical peak average strain rate for an unconfined SHPB test on kaolin clay, at a moisture content of 0 %, and striker velocities of 18, 20 and 22 m/s.

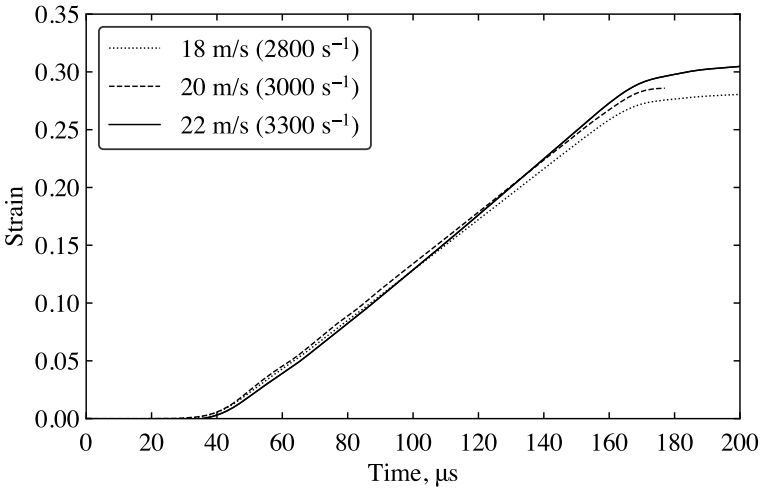

Figure 4.38: Typical strain behaviours for an unconfined SHPB test on kaolin clay, at a moisture content of 0 %, and striker velocities of 18, 20 and 22 m/s.

4.5.5 Confined SHPB test results

4.5.5.1 Signal processing

Similar to unconfined SHPB tests, signals collected during a confined SHPB test are processed using `SHPB_Processing.py`. For sample details see Appendix B. The following command line was utilised to process the test data for a confined SHPB test on a kaolin clay sample with a moisture content of 0 %:

$$\texttt{SHPB\_Processing}\,(\texttt{csv\_path} = \text{“}\texttt{test0\_kaolin0\_600mm\_60psi\_con.csv}\text{”},\ \texttt{sample\_data} = [6.760, 3.257, 3.257], \texttt{confinement} = \text{“}\texttt{Ring}\text{”}, \texttt{signal\_channels} = [7, 8, 5],\ \texttt{signal\_amp} = [10, 10, 5], \texttt{disp\_correction} = \texttt{True}, \texttt{alignment} = 50, \texttt{speedtrap} = \texttt{True})$$

This test was conducted with confinement, signal amplification was set at 10 for the incident and transmitter bar and 5 for the confining ring, dispersion correction was applied, signals were set to align at an assigned peak value of 50 MPa, and the velocity of the striker bar was recorded.

4.5.5.2 Experimental results

Applying the same processing methodology used for unconfined SHPB tests (detailed in Sections 4.4.6 and 4.4.7), the sample's stress and strain data from the confined SHPB tests can be obtained. The confining ring is employed to investigate the effects of strain rate and moisture content and determine if the previously observed phase behaviour in unconfined testing persists under lateral confinement.

Confined SHPB testing was conducted at velocities of 18, 20 and 22 m/s, revealing peak average strain rates of 2600, 2800 and 3100 s^{-1}, respectively, as depicted in Figure 4.39a.

Figures 4.39b, 4.39c, 4.40a, 4.40b, 4.40c and 4.41 display the strain, radial, front, back and mid stresses for a typical confined SHPB test on kaolin clay, with 0 % moisture content at different strain rates. These figures illustrate how the stress and strain responses of the sample increase with higher strain rates, while the moisture content remains constant. At a given strain rate, strain and front stress remain consistent regardless of the moisture content of the sample. However, radial and back stresses vary depending on the sample's moisture content, directly impacting the mid stress response (Figure 4.40c). The mid stress versus strain response is displayed in Figure 4.41. This confirms earlier findings from unconfined SHPB tests, highlighting the strain rate and moisture content dependence of cohesive soils (see Section 4.5.4).

In contrast to unconfined SHPB tests, a more pronounced variation in back stress magnitude is observed, particularly in saturated kaolin clay samples. This is due to their enhanced stress propagation capabilities under confinement. While unconfined SHPB tests lead to lateral extrusion of saturated kaolin clay, the confining ring restricts lateral stress flow, acting as a barrier.

As a result, with lateral movement constrained, the lateral stress is redirected axially toward the back end of the sample. This redirection causes the material to extrude at the edge of the confining ring, forcing it to deform along the axis. The increased axial force leads to a higher recorded back stress, as the confined sample cannot dissipate stress laterally. This effect is particularly noticeable in saturated cohesive soils such as kaolin clay, which exhibit enhanced stress propagation under lateral confinement, further amplifying the recorded back stress.

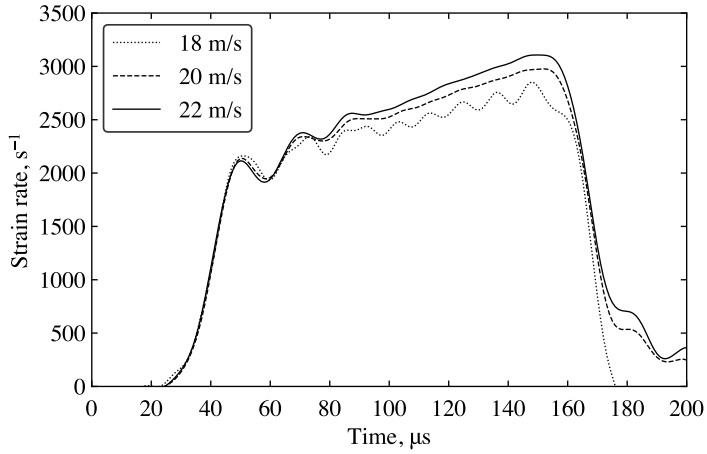

(a)

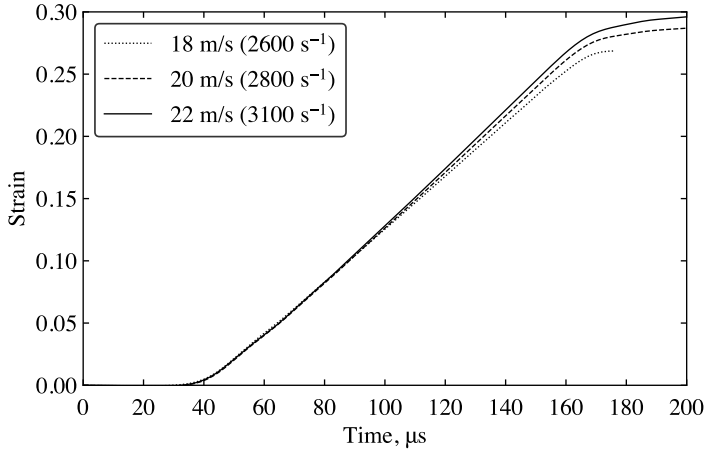

(b)

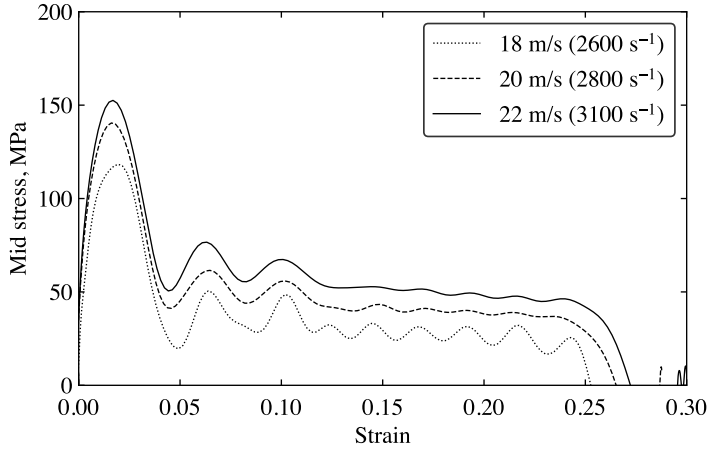

(c)

Figure 4.39: Typical behaviours for an confined SHPB test on kaolin clay, at a moisture content of 0 % and different strain rates: (a) peak average strain rate (b) strain vs time, and (c) mid stress vs strain.

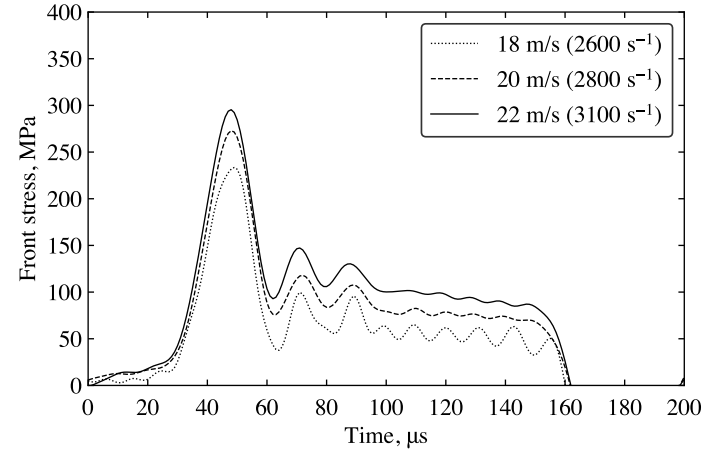

(a)

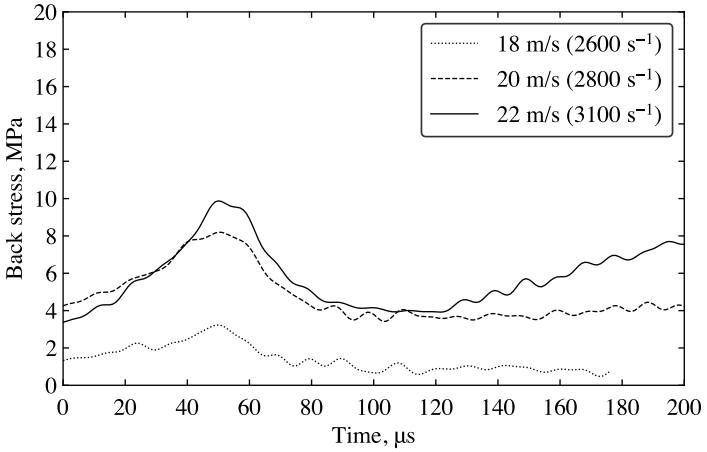

(b)

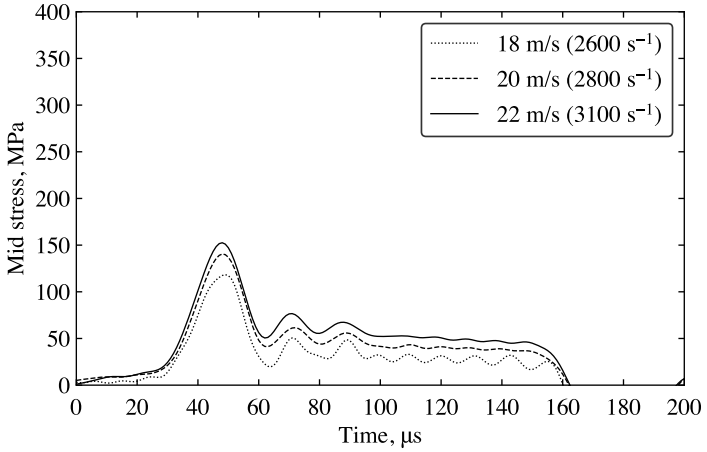

(c)

Figure 4.40: Typical behaviours for a confined SHPB test on kaolin clay, at a moisture content of 0 % and different strain rates: (a) front stress vs time, (b) back stress vs time, and (c) mid stress vs time.

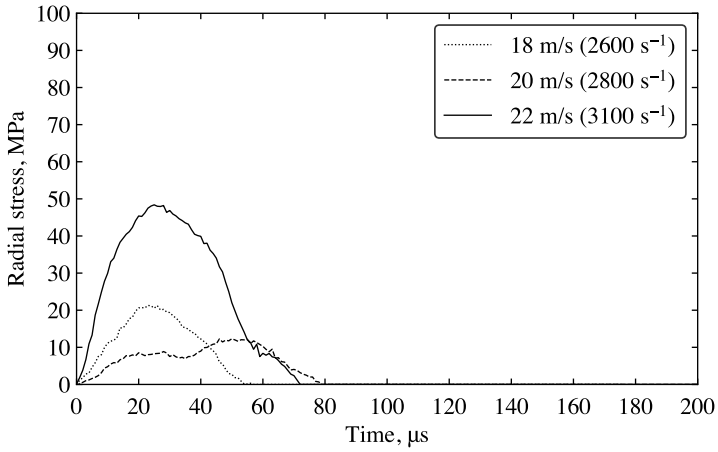

Figure 4.41: Typical radial stress behaviour for a confined SHPB test on kaolin clay, at a moisture content of 0 % and different strain rates.

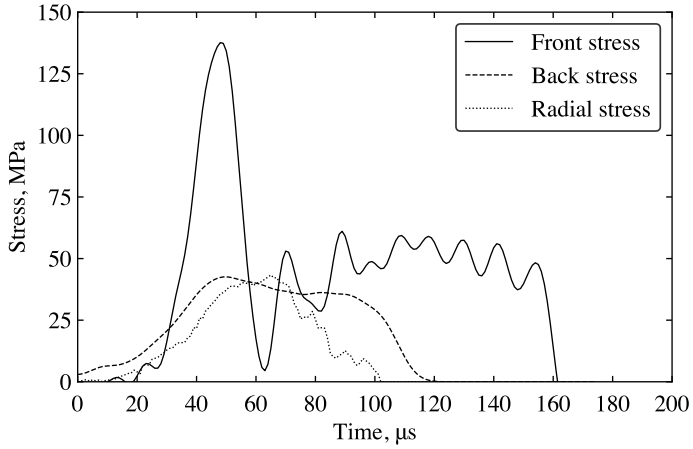

Figure 4.42: Front, back and radial stresses for a confined SHPB test at 12 m/s (1600 s^{-1}), on a saturated kaolin clay sample, with at a moisture content of 41 %.

By analysing the curves in Figure 4.42, the onset of extrusion can be identified by examining the front and radial stress curves. The point at which the front and radial stresses begin to increase marks the start of the extrusion of the sample from the confining ring. In this case at it occurs at 10 μs.

Figure 4.42 shows that the radial and back stress pulses have similar amplitudes, supporting the hypothesis that lateral stress is redirected axially. This redirection causes the lateral stress recorded by the confining ring to transfer axial stress to the back of the specimen and onto the transmitter bar. This mechanism is critical for understanding how confinement influences stress distribution and material deformation during high-strain-rate testing, further emphasising the role of the confining ring in controlling material behaviour under dynamic loading conditions.

4.5.5.3 Phase behaviour in confined SHPB testing

Confined SHPB tests exhibit four phases at a striker speed of 18 m/s (2600 s^{-1}) and three phases at higher speeds of 20 and 22 m/s (2800 and 3100 s^{-1}, respectively), as shown in Figures 4.43a, 4.43b, and 4.43c. In phases 0 and 1, the back and radial stresses follow similar patterns: the back stress starts at zero, rises to a peak, and then gradually decreases without returning to zero (Figures 4.43d and 4.43e). Meanwhile, the radial stress reaches a similar maximum but returns to zero after 50 μs (Figures 4.43g and 4.43h).

This behaviour in phases 0 and 1 is due to the volume of water in the sample being less than the combined volume of air and soil. During testing, the significant air voids in the sample are compacted upon impact, creating a shock absorption effect that dampens the stress wave. As a result, only a fraction of the stress wave propagates through the sample to the transmitted bar interface. The confining ring plays a key role by providing lateral confinement, forcing the sample to consolidate. This results in high radial stress and a fully compacted sample at the end of testing.

Under unconfined conditions, achieving the same strain rate (2700 s^{-1}) requires a striker speed of 12 m/s. This highlights that speed is specific to the test setup, whereas strain rate reflects the sample's response during testing. This distinction underscores the significant influence of material impedance on the relationship between applied velocity and strain rate. Materials with lower impedance require lower striker speeds to achieve equivalent strain rates, emphasising the role of mechanical properties in determining test outcomes.

Phase 2 appears only in confined SHPB tests at a striker speed of 18 m/s (2600 s^{-1}). However, it vanishes when the sample's maximum experimental strain reaches 0.27, corresponding to a strain rate of 2700 s^{-1} (where Point B equals Point A), as empirically validated through SHPB testing. Consequently, phase 2 is absent at higher velocities of 20 and 22 m/s (2800 and 3100 s^{-1}), as shown in Figures 4.43a, 4.43b, and 4.43c. Figures 4.43f and 4.43i further illustrate the distinct back and radial stress behaviours associated with phase 3.

For fully saturated kaolin clay samples, a Poisson's ratio of 0.5 is calculated from confined SHPB test results, decreasing as the sample's moisture content reduces. The Poisson's ratio, calculated as $\nu = -\epsilon_{\text{lateral}}/\epsilon_{\text{axial}}$, where $\epsilon_{\text{lateral}}$ is the strain perpendicular to the loading direction and ϵ_{axial} is the strain along the loading direction, highlights the role of deformation in determining material response. As the phase behaviour transitions from four to three phases (Figure 4.43), the confining ring becomes unable to completely seal the sample, allowing some extrusion.

Similar to unconfined experiments, once the sample exceeds the moisture threshold for full saturation, the water content ratio dictates the sample's behaviour, resulting in complete lateral extrusion. Although the confining ring is designed to seal the sample and prevent extrusion, kaolin clay particles still extrude beyond a certain strain rate due to the significant impact forces. The confining ring's role in stress wave propagation is influenced by the cohesive soil's intrinsic properties, such as moisture content and strain rate.

As seen in Figure 4.43, moisture content impacts the high-strain-rate behaviour of back and radial stresses, similar to findings from unconfined SHPB tests. The lateral confinement provided by the ring restricts lateral stress propagation, redirecting stress axially. This effect highlights the critical interaction between phase behaviour, stress wave propagation, and the mechanical properties of the sample.

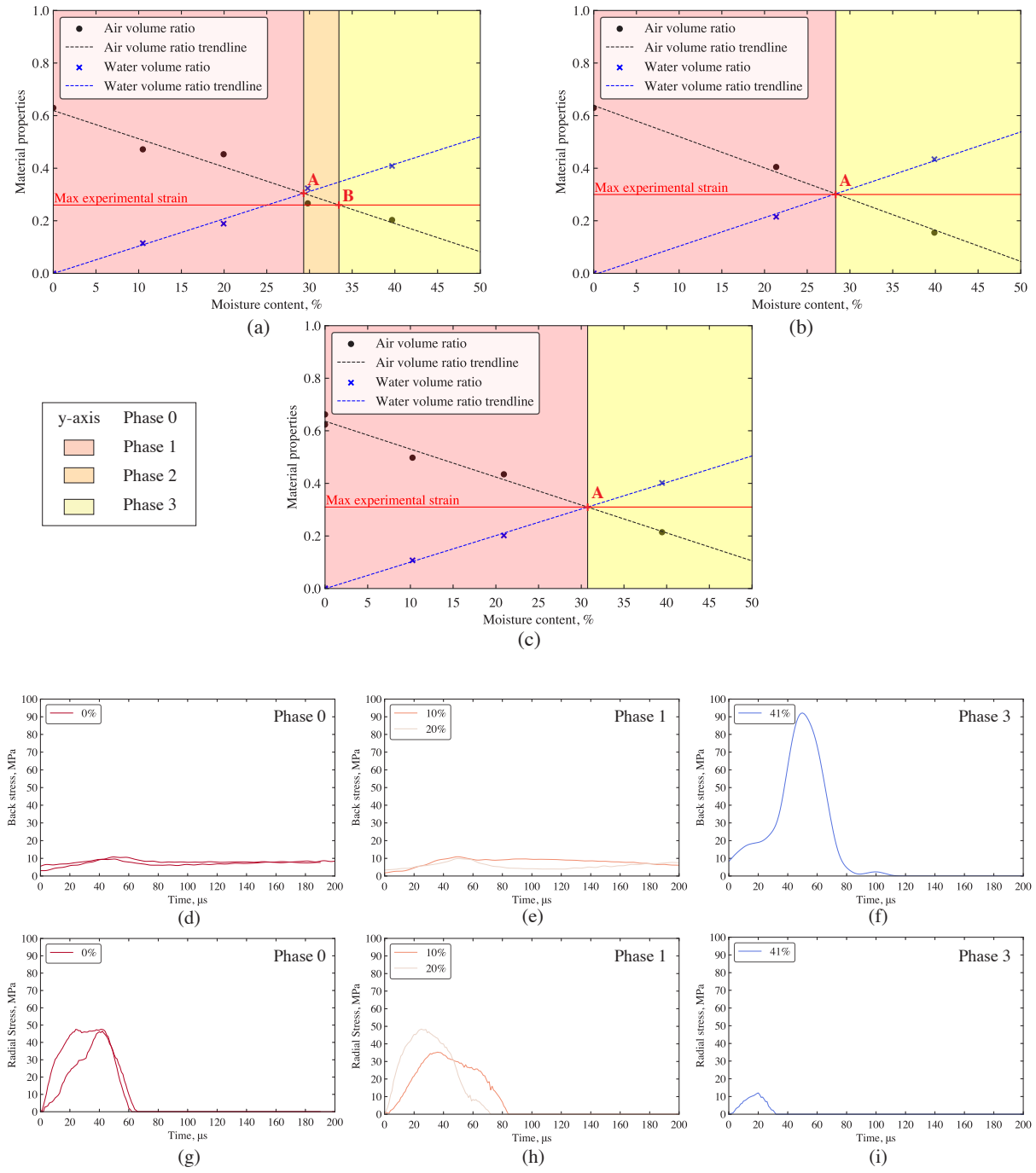

Figure 4.43: Confined SHPB testing of kaolin clay with (a) phase behaviour at 18 m/s (2600 s^{-1}), (b) phase behaviour at 20 m/s (2800 s^{-1}) and (c) phase behaviour at 22 m/s (3100 s^{-1}), as well as the associated back stress at 20 m/s (2800 s^{-1}) for (d) Phase 0, (e) Phase 1, and (f) Phase 3, and radial stress at 20 m/s (2800 s^{-1}) for (g) phase 0, (h) phase 1, and (i) phase 3.

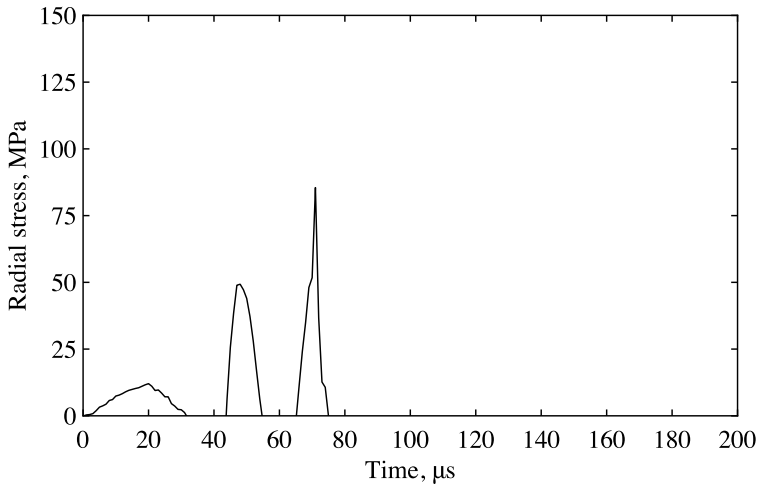

Figure 4.44: Complete radial stress response during confined SHPB testing of a fully saturated kaolin clay sample at 41 %, with a striker velocity of 22 m/s (3100 s^{-1}).

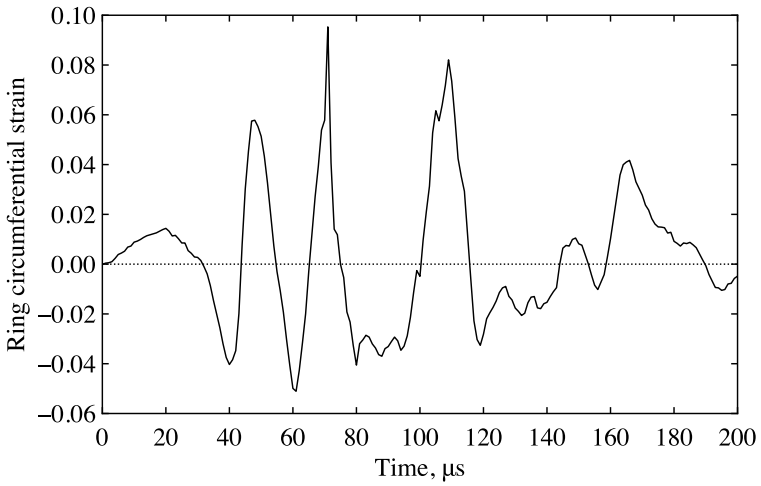

Figure 4.45: Confining ring typical circumferential strain history during SHPB testing.

For fully saturated kaolin clay samples tested using the SHPB apparatus under full confinement, multiple radial stress peaks are recorded. The initial radial stress peak is small, and corresponds to the first impact of the sample from the incident bar (Figure 4.43i). Subsequently, as illustrated in Figure 4.44, two additional radial stress peaks are recorded, increasing in magnitude. This occurs because during the first impact, moisture in the fully saturated sample extrudes, leading the sample to consolidate inside the confining ring. Then, on the second impact, a sample with lower moisture content is tested, resulting in a higher radial stress with significantly less sample extrusion. This process repeats until the sample completely extrudes from the confining ring. The duration of this radial stress pulse corresponds precisely to the duration of the back stress pulse, 80 μs, a correlation evident from the comparison of Figure 4.43f and Figure 4.44. Consequently, the behaviour observed in Figure 4.44, along with the increasing amplitude of subsequent radial peaks in Figure 4.43i, is due to sample extrusion and volume loss.

In addition to volumetric loss caused due to sample extrusion, physical limitations linked with the material composition of the confining ring mean that the resultant radial stress pulse experiences multiple oscillations due to vibration upon impact. Figure 4.45 displays the complete circumferential strain history of the confining ring from the moment of impact, providing insight into the significant oscillations that persist after the stress wave has traversed the sample. In Figure 4.45, the circumferential strain of the sample oscillates between extrusion and contraction, influenced by the sample's physical composition and the external pressure exerted by the bars. This behaviour highlights the sample's mechanical response during testing. Moreover, incidental contact between the confining ring and the pressure bars introduces slight contributions to circumferential strain measurements from the strain gauge. These factors underscore the necessity for numerical modelling to facilitate the interpretation of confinement effects.

4.5.5.4 Effect of strain rate

In contrast to unconfined SHPB tests, there was no discernible correlation between strain rate and stiffness of the samples. However, examining the radial stress-strain rate behaviour shown in Figure 4.46 of the kaolin clay samples at varying moisture contents, it was evident that samples with the highest moisture content exhibited the highest radial stress. The higher radial stress at greater moisture contents is attributed to the sample's high water content, which renders it incompressible. In phase 3, the peak radial stress response occurs as a result of significant moisture extrusion, followed by sample consolidation.

The strain-strain rate response of confined SHPB tests at various striker bar velocities is depicted in Figure 4.47, along with its corresponding linear trendline. The high correlation between strain rate and strain for confined SHPB tests is highlighted by the R^2 value of 0.9971, indicating a strong relationship portrayed by this trendline:

$$\text{Strain rate} = 10000 \times \text{Strain}$$

Graphically, based on the phase diagrams in Figure 4.43, the maximum experimental strain at which phase 2 disappears completely is 0.27. According to Equation (4.26), this corresponds to a strain rate value of 2700 s^{-1}, which falls between the strain rate of the striker velocities of 18 and 20 m/s. Therefore:

$$\text{Strain rate} = 10000 \times \text{Strain} = 10000 \times 0.27 = 2700\ s^{-1} \tag{4.26}$$

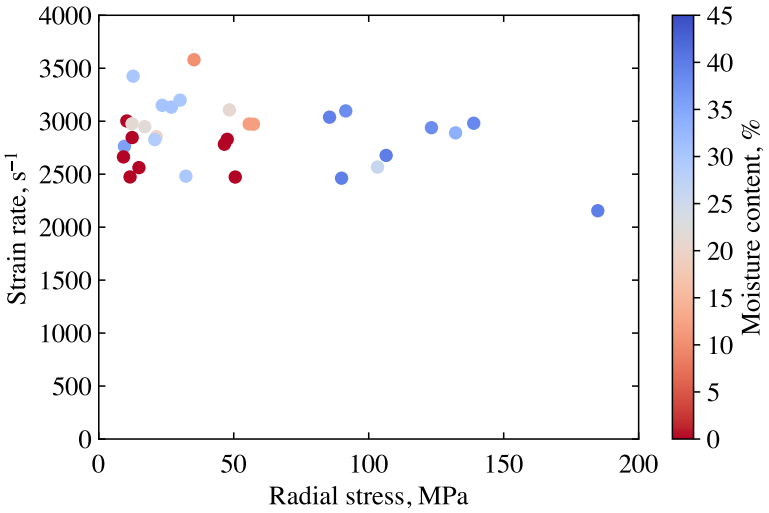

Figure 4.46: Radial stress-strain rate response of confined SHPB tests at different striker bar velocities (18, 20 and 22 m/s).

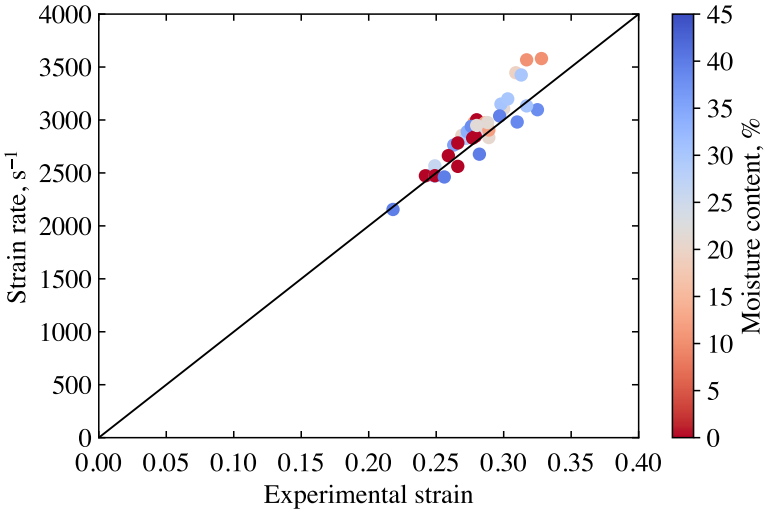

Figure 4.47: Strain-strain rate response of confined SHPB tests at different striker bar velocities (18, 20 and 22 m/s), with its associated trendline.

4.6 Summary

This chapter introduces two types of tests conducted on kaolin clay specimens: quasi-static and high-strain-rate one-dimensional compression tests. These tests involved specimens created with varying moisture contents ranging from 0 to 44 %. Quasi-static tests were performed using the TXC and oedometer apparatus, while high-strain-rate tests were carried out using the SHPB apparatus under both unconfined and confined conditions. The primary objective of the quasi-static tests was to validate the impact of moisture content on kaolin clay samples. Conversely, the high-strain-rate tests aimed to investigate the effects of strain rate, moisture content and confinement on these samples.

Unconsolidated undrained (UU) TXC tests were performed on kaolin clay samples, complemented by standard static oedometer tests to confirm the consolidation behaviour of cohesive soils at low strain rates. The results indicated that kaolin clay samples at 41, 42 and 44 % behaved as expected, showcasing different stress-strain responses. Specifically, samples with lower moisture content exhibited higher axial and shear stresses.

Dynamic oedometer tests were also conducted to assess the dynamic behaviour of cohesive soils at low strain rates. There results from these quasi-static tests highlighted the challenge cohesive soil face in dissipating pore pressure, with the moisture content playing a pivotal role in governing their response under dynamic loading conditions. This observation is crucial as it signifies that cohesive soils such as kaolin clay display fluid-like behaviour even at low strain rates when subjected to dynamic loading.

Given the pivotal role moisture content has in governing the behaviour of cohesive soils at low strain rates, a comprehensive specimen preparation and testing programme was developed for SHPB tests. This aimed not only to elucidate the influence of moisture content but also to assess the effects of strain rate and confinement on the material.

At high-strain-rates, the effect of moisture content on the behaviour of cohesive soils was thoroughly investigated through SHPB tests conducted under both confined and unconfined conditions, revealing an inherent phase behaviour. This phase behaviour significantly impacts the use of cohesive soils, as moisture content directly affects the material's ability to propagate stress. Moisture content levels in phase 1 yielded the most effective results in preventing stress wave propagation in confined test cases, while in unconfined test cases, phase 4 was the most effective.

In unconfined SHPB testing, phase 4 sees the behaviour of the material governed by the water volume in the specimen. In unconfined testing scenarios, stress propagation through the material is primarily limited by moisture content, while any remaining stress propagates laterally as the specimen extrudes. However, implementing this in practice poses challenges due to the difficulty in transporting and moulding the material into specific structures.

In confined SHPB testing, phase 1 sees the material's physical behaviour dictated by the soil, as the volume of soil in the sample exceeds that of water. In contrast to other phases, where the water volume ratio is either nonexistent (phase 0) or dominant (phases 2 and 3), phase 1 sees the water volume in the sample aiding to the material's strengthening. In cases where a confining ring restricts lateral propagation, stress is redirected axially, resulting in an increase in axial stress, as seen in phase 4 for confined SHPB tests. When phase 2 disappears, radial stresses decrease. This occurs because of the incident bar's high velocity, which causes lateral extrusion of the sample from the confining ring and simultaneously redirects the stresses axially.

Furthermore, when the sample is fully saturated, an initial small radial stress peak is followed by two successive peaks, each increasing in amplitude. This behaviour is attributed to repeated impacts from the incident bar, which drive further extrusion from the confining ring. These findings indicate that the confining ring cannot fully contain the sample at such high-strain-rate levels. Additionally, differences in speed and strain rate between unconfined and confined SHPB tests highlight the significant influence of confinement on the high-strain-rate behaviour of kaolin clay. Stress-strain analysis further confirms a clear strain rate dependence of the material under high-strain-rate conditions.

In conclusion, the ability of cohesive soils to limit stress propagation is strongly influenced by moisture content and confinement. The back stress derived from the SHPB tests reflects the extent of stress propagation through the sample, with moisture content acting as a dampener that restricts lateral stress flow. Confinement further limits lateral extrusion, redirecting radial stress axially and impacting overall stress transmission. Future investigations will focus on high-strain-rate numerical modelling of cohesive soils, aiming to replicate the phase behaviour observed in this chapter. These simulations will be compared with the experimental results to validate and extend the findings.

Chapter 5

Numerical modelling of high-strain-rate SHPB tests on cohesive soils

5.1 Introduction

The main objective of this chapter is to evaluate current constitutive finite element models in LS-DYNA and assess their effectiveness in modelling the high-strain-rate phase behaviour of cohesive soils developed in Chapter 4. To support this objective, this chapter utilises quasi-static triaxial and oedometer test results from Chapter 4 to provide high-pressure compaction data for calibrating finite element models in LS-DYNA. Validation is carried out by comparing the numerical models in LS-DYNA to the SHPB test results collected. Model optimisation is achieved by assessing the limitations of existing models, with the goal of developing a comprehensive cohesive soil model that accurately reflects the high-strain-rate phase behaviour observed in the test results. The results, developments, and research processes discussed in this chapter have been published in Van Lerberghe, Li, Barr and Clarke (2024*a*), Li, Van Lerberghe, Barr, Clarke and Dennis (2024), Li, Van Lerberghe, Barr and Clarke (2024), available in Appendix A.5, A.7, A.8, respectively.

5.2 Overview of model design

In this section, a flowchart outlining the overall conceptual LS-DYNA model design is presented in Figure 5.1. It illustrates the evolution of the thought process behind the design of the unconfined and confined SHPB numerical models in LS-DYNA. This diagram indicates the iterations which either successfully replicated or failed to replicate the behaviour observed in testing. It also showcases the selected LS-DYNA model configuration used for comparative analysis with experimental test data. Subsequent Sections (5.3 and 5.4) delve into the specifics of the model design used to emulate the SHPB apparatus. The final model design is presented in Section 5.5. The aim of this final LS-DYNA model is to accurately represent the high-strain-rate phase behaviour of cohesive soils, as identified in Chapter 4.

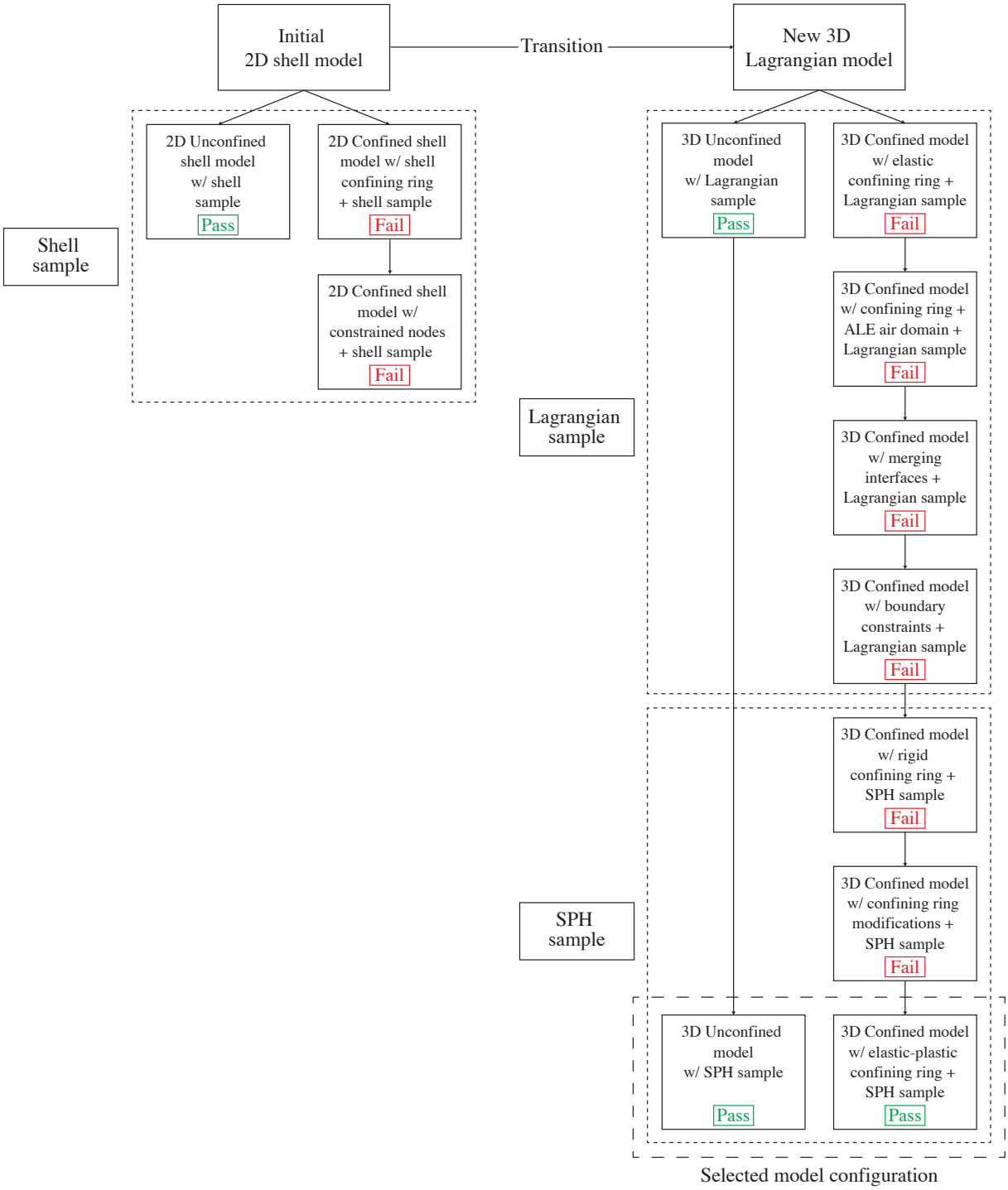

Figure 5.1: Overview of SHPB numerical model design in LS-DYNA.

5.3 Initial 2D shell model

Initially, the SHPB apparatus was configured in LS-DYNA using 2D axis-symmetric shell elements. All components were modelled as Lagrangian shell solids, following the dimensions of the experimental setup, as illustrated in Figure 5.6. The striker bar, transmitter bar, and incident bar were represented as elastic material elements with specific properties: a density of 7666 kg.m^{-3}, a Young's modulus of 168 GPa, and a Poisson's ratio of 0.29. For further details on the material card used in the numerical model, refer to Appendix D, Table D.1. Mesh generation was facilitated through a MATLAB script developed by Dr. Sam Rigby (Personal communication, 2021). Dr. Sam Rigby conducted sensitivity studies to determine the appropriate mesh for the material model of the two steel pressure bars, and for a sample with a thickness of 5 mm, as seen in Figures 5.3 and 5.4 (2.5 mm and 0.625 mm, respectively).

For simplicity and given the limited contact interfaces, an automatic contact model was employed: *CONTACT_2D_AUTOMATIC_SINGLE_SURFACE. This model automatically identifies interfaces between the 2D Lagrangian elements and establishes contact interactions based on material parameters and geometrical configuration.

The striker bar was initially set to a velocity of 16 m/s, consistent with the experimental setup. The constitutive model results were collected at specific distances from the specimen bar interface to ensure they mirrored the locations where strain gauge data were obtained in the experiments. Therefore, model data was recorded at 1000 mm away from the incident bar-sample interface and 500 mm away from the transmitted bar-sample interface.

Initially, due to the material's dynamic behaviour resembling that of water, the sample was modelled using the *MAT_NULL, material card, typically employed for simulating fluids such as water, with a density set at 1000 kg.m^{-3}. Since this material card necessitates an equation of state (EOS), the following EOS for water based on a linear polynomial model type was employed, defined in LS-DYNA by the equation:

$$P = C_0 + C_1\mu + C_2\mu^2 + C_3\mu^3 + (C_4 + C_5\mu + C_6\mu^2)E$$

where C_0, C_1, C_2, C_3, C_4, C_5, C_6 are constants, $\mu = \rho/\rho_0$ - 1, ρ and ρ_0 are the current and initial densities of the fluid, and E is the specific internal energy of the fluid. The parameters utilised to formulate the EOS are derived from prior studies on water modelling in blast and high impact engineering (Shin et al. 1998). This material card serves as a validation of the SHPB geometrical setup, while alternative material cards suitable for modelling kaolin clay are explored in Section 5.6. The complete LS-DYNA material card, *MAT_NULL, and its associated EOS are provided in Appendix D, Tables D.2 and D.9.

The stress behaviour observed in experimental testing is mirrored in the data retrieved from specific points on each pressure bar, corresponding to strain gauge locations. The numerical model demonstrates a similar phenomenon to that observed in experimental testing, where a significant amount of sample is extruded as depicted in Figure 5.5. However, while a minor transmitted pulse is evident, the majority of the stress wave fails to propagate through to the transmitter bar.

Figure 5.2: Initial 2D shell SHPB model with confining ring [confining ring removed for unconfined modelling].

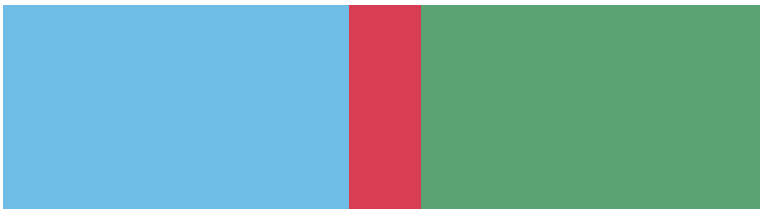

Figure 5.3: Zoom-in on initial 2D unconfined SHPB model.

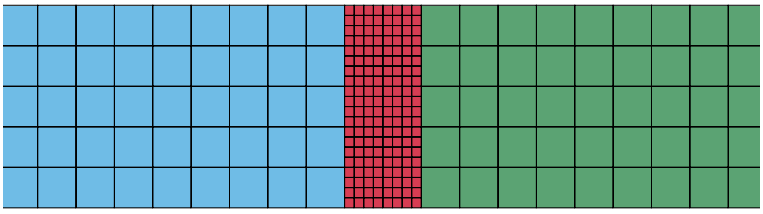

Figure 5.4: Zoom-in on initial 2D unconfined SHPB model with element meshes.

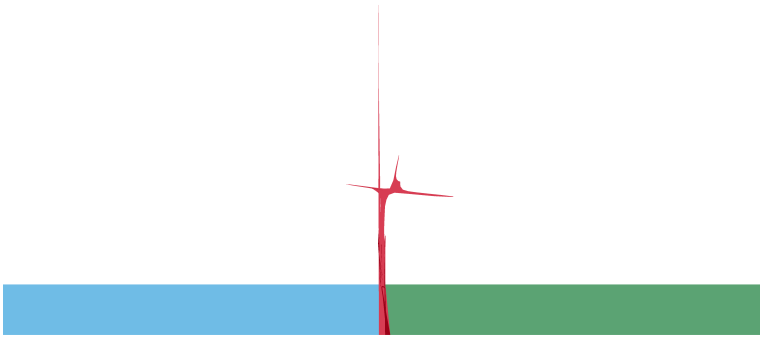

Figure 5.5: Final time state for initial 2D unconfined SHPB model.

5.3.1 Confining ring

This model is then tailored for fully confined SHPB testing conditions, where a stainless steel confining ring is placed on the edge of the sample as illustrated in Figure 5.6. The same contact model applied in the unconfined SHPB test, *CONTACT_2D_AUTOMATIC_SINGLE_SURFACE, is utilised between the ring and other model components. However, this approach presented substantial design challenges, primarily associated to negative volume errors resulting from sample extrusion in confined SHPB test modelling.

Figure 5.7 illustrates the state of the sample just before termination, depicting its condition prior to extrusion from the edge of the confining ring. As the pressure bars and confining ring are modelled as elastic steel members, they deform under stress. Consequently, when the ring experiences changes in lateral stress, it deforms, permitting the soil sample to protrude beyond the confines of the confining ring, ultimately leading to model failure. Recognising the inadequacy of this model design, alternative options had to be explored. The high-impact nature of the experiments induced significant deformation in the sample, exceeding its handling capacity.

The design of the confining ring model aims to resolve the computational issue of negative volume error, thereby enabling a more effective evaluation of current constitutive finite element models in LS-DYNA for modelling the high-strain-rate phase behaviour of cohesive soils, as discussed in Section 5.3.2 below.

5.3.2 Constrained nodes

To replicate the effect of the steel confining ring in the 2D shell model, an alternative solution was developed: a boundary constraint was applied along the nodes on the sample's edge to prevent lateral displacement, as depicted in Figure 5.8. Consequently, all nodes along the sample's edge were designated as boundary nodes. This implementation required specifying the degrees of freedom with restricted movement for these nodes. Since the objective was to restrict lateral displacement while permitting translational movement of the sample along the y-axis, all rotational axes and translational movement in the x-axis were restricted.

Despite these efforts, challenges persisted with negative volume errors, as the boundary constraints were insufficient to prevent lateral extrusion of the sample. While the boundary on the sample's edge might delay lateral extrusion, the pressure bars inevitably deform when the stress wave passes through. Therefore, the sample cannot be fully constrained, leading to negative volume errors when it extrudes through any gaps caused by the deformation of the pressure bars.

All viable confinement options in 2D shell modelling underwent testing, revealing persistent challenges with negative volume errors. Hence, transitioning to a 3D Lagrangian model became imperative to explore alternative LS-DYNA modelling techniques such as Arbitrary Lagrangian Eulerian (ALE) and Smooth Particle Hydrodynamics (SPH).

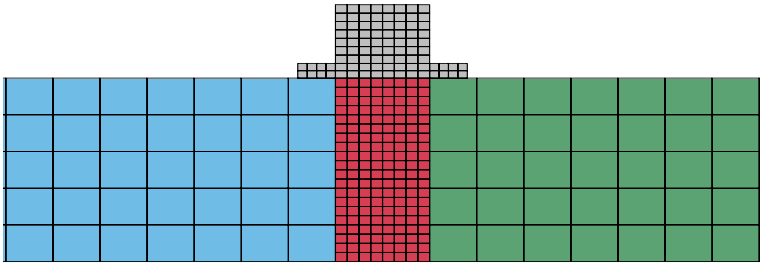

Figure 5.6: Zoom-in on 2D confined SHPB model with confining ring (grey) and element meshes.

Figure 5.7: Zoom-in on final time state of 2D confined SHPB model before negative volume error.

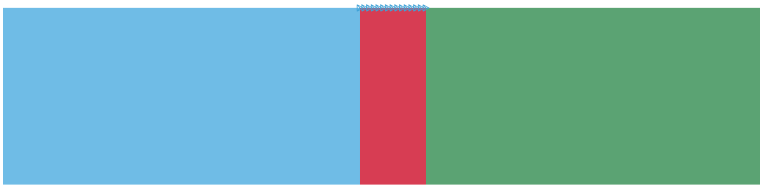

Figure 5.8: Zoom-in on 2D confined SHPB model with boundary constraints on nodes at edge of sample.

5.4 Transition to 3D Lagrangian model

While a 2D axisymmetric model offers computational advantages by reducing processing time, its design simplicity limits the application of certain numerical methods. Therefore, the development of a 3D Lagrangian model became essential to explore effective techniques for addressing the persistent negative volume error observed in Section 5.3.1 and 5.3.2. The ultimate goal, as outlined at the beginning of this chapter in Section 5.1, is to accurately model the high-strain-rate phase behaviour of cohesive soils.

The 3D model's dimensions were aligned with those of the experimental SHPB apparatus. Instead of 2D shell elements, the striker bar, incident bar, transmitter bar, and sample were modelled as 3D Lagrangian solids, as seen in Figure 5.9. Using the LS-DYNA Block Mesher, butterfly blocks were generated to form a cylindrical mesh with suitable dimensions and mesh size, as outlined in Table 5.1. Maintaining a consistent element mesh size radially across all cylindrical elements, as depicted in Figure 5.10, minimised the risk of improper axial stress transfer along the elements.

Block Mesher input parameters	*Value*
Density of cylinder perimeter	10
Radius of cylinder	0.0125
Number of elements in radial direction	8

Table 5.1: Input parameters for cylindrical mesh.

Contact interactions were manually defined for each interface. The `*CONTACT_AUTOMATIC_SURFACE_TO_SURFACE` contact card was assigned to the following surface interfaces: striker bar-incident bar, incident bar-sample, and sample-transmitter bar. Detailed information on the contact card used can be found in Appendix D, Table D.7.

The unconfined SHPB model constructed in 3D with Lagrangian elements was developed to validate its functionality, showcasing its state upon normal termination in Figure 5.11. These results mirror the physical behaviour observed in experimental testing of cohesive soils.

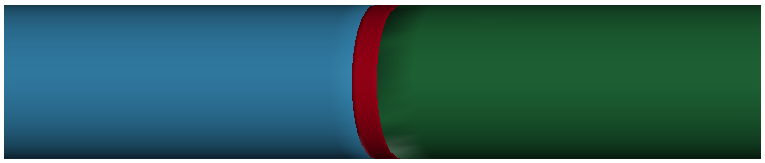

Figure 5.9: 3D unconfined SHPB model.

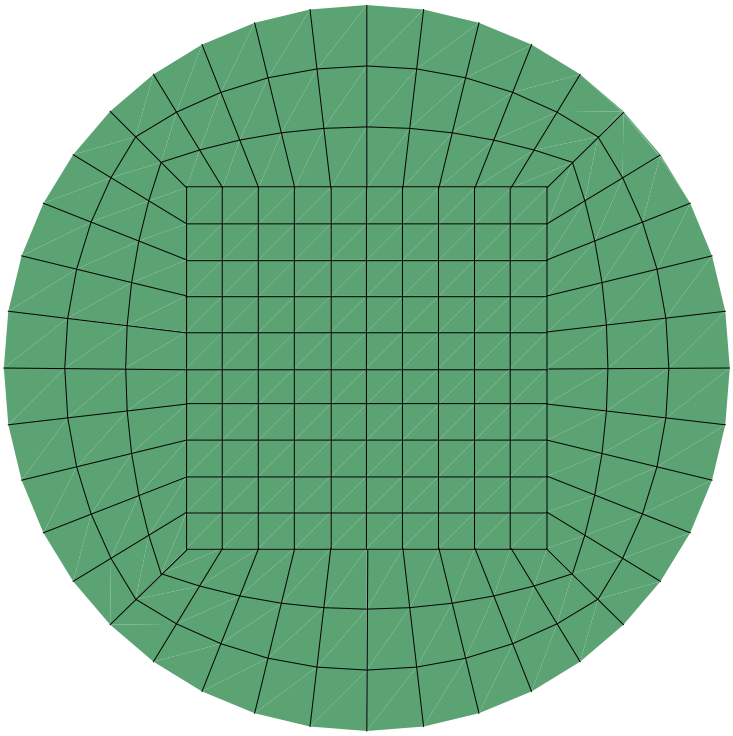

Figure 5.10: Top view of the radial meshing for the cylindrical elements in the 3D SHPB model for: striker bar, incident bar, sample, and transmitter bar.

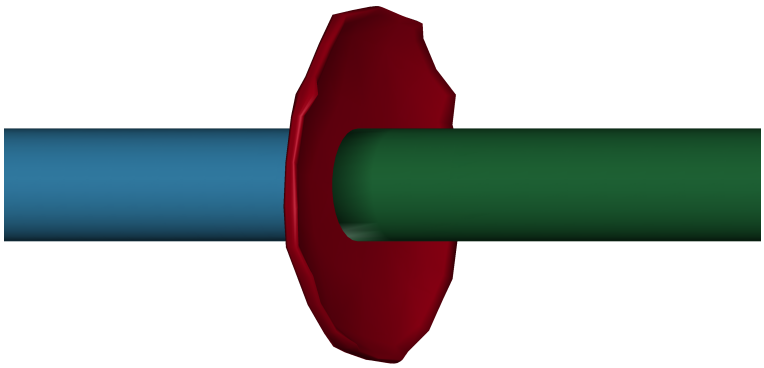

Figure 5.11: Final time state for the 3D unconfined SHPB model.

5.4.1 3D Lagrangian confining ring

To create the confining ring for the fully confined SHPB numerical model in LS-DYNA, the same Block Mesher employed to create a tubal butterfly block mesh was used, with its parameters detailed in Table 5.2. The 3D model with the confining ring is depicted in Figure 5.12. Unfortunately, without restrictions to control substantial sample deformation during extrusion, the negative volume error persisted. Figure 5.13 shows the large volume change of the sample, where small gaps forming during the model's progression caused a rapid increase in internal pressure, resulting in unrealistic extrusion in both scale and shape. The confining ring design was simplified to a single ring, as flanges introduced unnecessary vibrations that affected the radial stress signal.

Block Mesher input parameters	*Value*
Density of cylinder perimeter	10
Outer radius of cylinder	0.0175
Inner radius of cylinder	0.0125
Number of elements in radial direction	3

Table 5.2: Input parameters for tubal ring mesh.

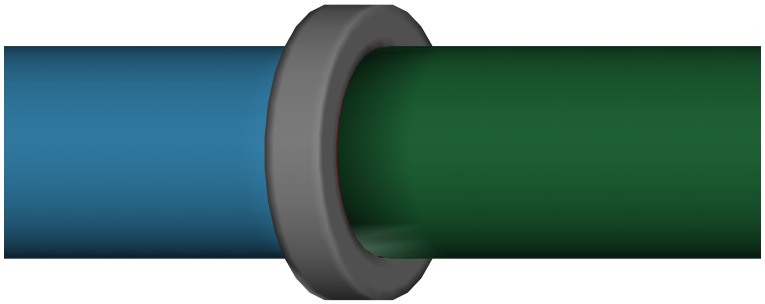

Figure 5.12: 3D confined SHPB model with confining ring.

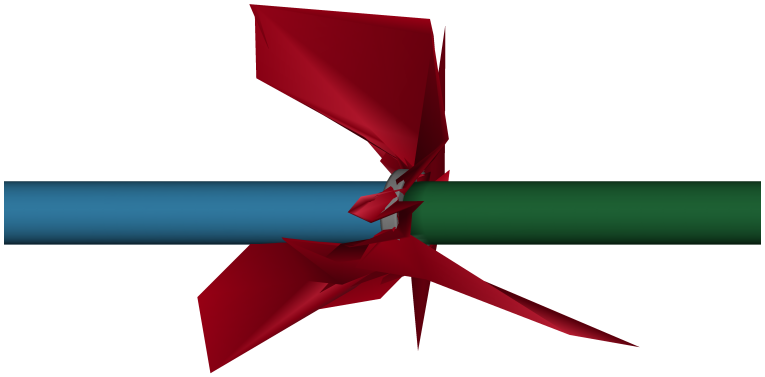

Figure 5.13: Final time state of 3D confined SHPB model before computation fails due to negative volume error.

5.4.2 ALE air domain

The shift to a 3D model was not solely about enhancing accuracy beyond the limitations of the 2D axisymmetric model; it also aimed to address challenges related to negative volume error. Creating an ALE air domain around the sample, confining ring, and pressure bars was intended to form a containment, restricting sample extrusion within the confines of this domain. This transition to a 3D Lagrangian model facilitates the proper application of ALE meshing, overcoming initial issues encountered with 2D axisymmetric shell elements.

A 100 mm cubic box was created with a mesh size of 2 mm and modelled as an ALE solid, utilising the *MAT_NULL, material model. This material card, intended to simulate fluids, features a density set to 1.225 kg.m^{-3} to represent atmospheric pressure. Information on the material card and EOS can be found in Appendix D, Tables D.3 and D.9, respectively. The ALE air domain can be visualised in Figure 5.14.

Despite confining the sample within the ALE domain, the rapid volume change during the sample's extrusion still triggered the negative volume error, as depicted in Figure 5.15. Consequently, although the extruded sample's volume remains within the ALE domain, the abrupt, substantial volume change led to premature termination of the model, preventing the collection of useful data.

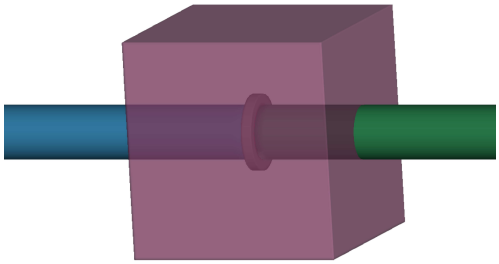

Figure 5.14: Confined SHPB 3D model with surrounding ALE air domain.

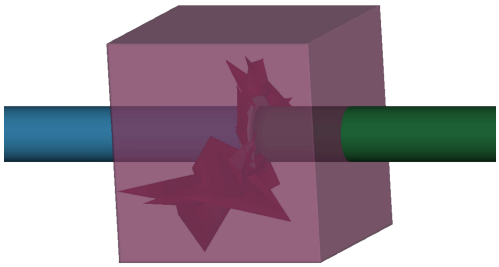

Figure 5.15: Final time state of confined SHPB 3D model with surrounding ALE air domain before model failure.

5.4.3 Merging interfaces

The negative volume error arose due to the abrupt volume change during sample extrusion. To address this, specific combinations of duplicate nodes at interfaces were merged to constrain volume loss and mitigate the error. The aim was to create a scenario where the ring and pressure bars are permanently connected by their interface, theoretically preventing any significant sample extrusion, in order to replicate the high-strain-rate phase behaviour observed in experimental testing.

Table 5.3 reveals that the majority of combinations still produced the negative volume error due to abrupt sample extrusion. Only the last two combinations, numbers 4 and 5, resulted in partial transmitter signals. Complete merging of all interfaces allowed the model to run smoothly without visible sample extrusion, as seen in Figure 5.16, where a transmitted signal was obtained from the transmitter bars.

No.	*Location of duplicated nodes at merged interface*	*Extrusion Yes/No*	*Model Pass/Fail*
1	Sample - Transmitter bar	Yes	Fail
2	Sample - Incident bar	Yes	Fail
3	Sample - Confining ring	Yes	Fail
4	Sample - Incident, Sample - Transmitter	Yes	Fail
5	Sample - Incident, Sample - Transmitter, Sample - Ring	No	Pass

Table 5.3: Combinations of tested merged interfaces.

To validate this model approach, the stresses in the input bar, ring, and transmitter bar must closely match those obtained during confined SHPB experimental testing, as shown in Chapter 4, Section 4.5.5. As a result, stress comparisons were made at three points: the incident bar, the ring, and the transmitter bar. The stresses on the incident bar match those obtained experimentally. However, the stress patterns on the ring mirror those found directly adjacent to the sample interface on the transmitter bar. This suggests that the recorded stresses primarily reflect the stiffness of the ring rather than the sample itself. In essence, the stress wave propagates through the ring instead of the sample, rendering this method invalid.

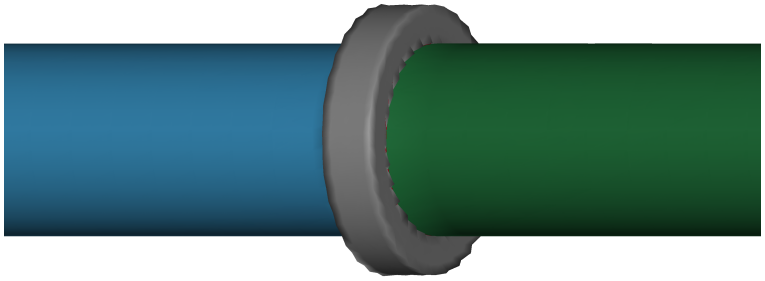

Figure 5.16: Final time state of 3D confined SHPB model with all sample interfaces merged before computation fails due to negative volume error.

5.4.4 Boundary constraints

The efficacy of employing boundary constraints to prevent lateral displacement is reexamined in light of the transition to a 3D model. In this iteration, the nodes surrounding the sample were constrained on five of the six degrees of freedom, with only the translational y-axis left unrestricted to accommodate axial movement. The model featuring these boundary constraints is depicted in Figure 5.17.

Despite these efforts, the persistent negative volume error can be attributed, as illustrated in Figure 5.18, to the rapid and large deformation of the specimen caused by the incident pressure bar. Additionally, under stress, the pressure bars deform, creating gaps that allow the sample to extrude beyond the boundary surface, which in turn enables significant deformation of the sample. The Lagrangian solid mesh, from which the sample is constructed, is unable to adapt to the large stresses impacting the sample. This suggests that the fluid-like behaviour of the kaolin clay may not be effectively addressed through conventional Lagrangian solid meshes.

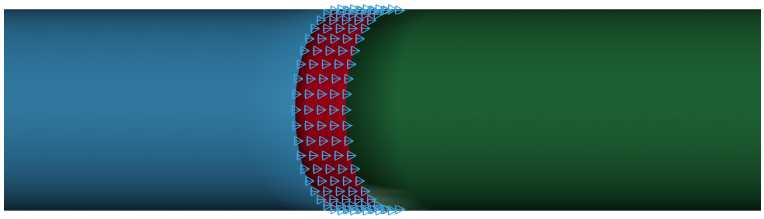

Figure 5.17: 3D confined SHPB model with boundary constraints on nodes at edge of sample.

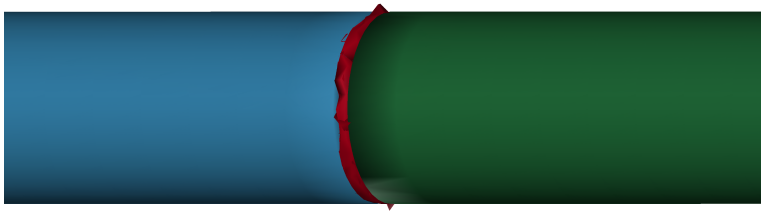

Figure 5.18: Final time state of the 3D confined SHPB model with all sample interfaces merged before model computation fails due to negative volume error.

5.4.5 Smooth particle hydrodynamics (SPH)

Ultimately, smooth particle hydrodynamics (SPH) was chosen to model the cohesive soil sample, an innovative meshless Lagrangian numerical method. This technique is frequently employed to simulate fluid deformations and continuum media under high loading conditions. It operates by interpolating individual particles instead of utilising the conventional mesh-based approach found in traditional Lagrangian solids. Despite its limited use in SHPB testing, as discussed in Section 2.5.1.4, SPH modelling is particularly well-suited for simulating the high-strain-rate behaviour of cohesive soils, such as kaolin clay, due to the dynamic loading conditions inherent in SHPB testing.

SPH's lack of a solid mesh makes it ideal for scenarios involving extreme deformation, as it dynamically generates connectivity between particles. Given kaolin clay's tendency for lateral deformation and significant volumetric loss, SPH is a suitable method for addressing the negative volume error associated with these deformations.

An SPH model was created by transforming the existing solid mesh of the sample while preserving its volume and material properties. This transformation results in the representation of the sample with 1205 SPH nodes, as depicted in Figure 5.19. With contacts no longer occurring between the surfaces of solid meshes, it becomes necessary to redefine contact interactions for interactions between SPH nodes and Lagrangian solids. For this model, `*CONTACT_AUTOMATIC_NODES_TO_SURFACE` was selected to model the contact between SPH nodes and the incident bar and transmitter bar surfaces. Details of this contact card are available in Appendix D, Table D.6.

The placement of SPH nodes and the meshing arrangement were carefully designed to ensure seamless connections between the SPH and Lagrangian elements, specifically between the specimen, pressure bars, and confining ring. Nodes were positioned precisely at the intersections of the Lagrangian elements. The mesh and SPH node design were kept simple, as the primary goal was to establish an LS-DYNA model capable of representing the high-strain-rate behaviour of cohesive soils identified in Chapter 4.

Validating the unconfined SHPB model before progressing to the fully confined version was essential to building a reliable foundation. Figures 5.20 and 5.21 display the initial and final time states of the unconfined model, confirming its functionality. This validation underscores SPH's suitability for modelling cohesive soils prone to substantial deformations under high-strain-rate loading conditions, accommodating sudden volumetric changes without compromising mesh integrity.

The inclusion of the confining ring necessitated a redefinition of the contacts between the confining ring and the SPH nodes, employing once more the `*CONTACT_AUTOMATIC_NODES_TO_SURFACE` contact card. This choice simplifies the designation of contacts between interfaces, albeit at the expense of increased computational time. The confined SHPB 3D model incorporating the SPH sample is in Figure 5.22.

The utilisation of SPH for the sample effectively mitigated the occurrence of the negative volume error. However, the lateral deformation of the sample induced immense vibrational movement on the confining ring, leading to pronounced deformation of the confining ring (Figure 5.23). This vibration phenomenon mirrors observations from experimental testing detailed in Chapter 4. Nevertheless, the numerical model, by creating a perfect seal that entirely restricts sample extrusion, amplifies the reflections arising from vibrations, thereby introducing more noise compared to test results and compromising the reliability of the outcomes. Significant noise was seen in the stresses on the incident and transmitter bars, due to the deformation of the ring, which resulted in unrealistic radial stress patterns.

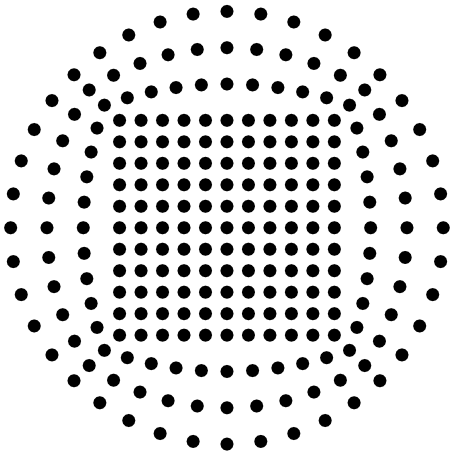

Figure 5.19: Top view of the SPH node arrangement for the sample in LS-DYNA.

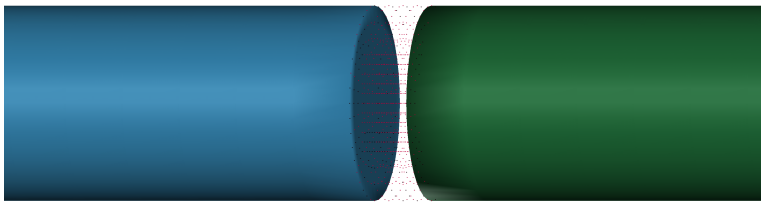

Figure 5.20: Unconfined SHPB model with sample modelled using SPH nodes.

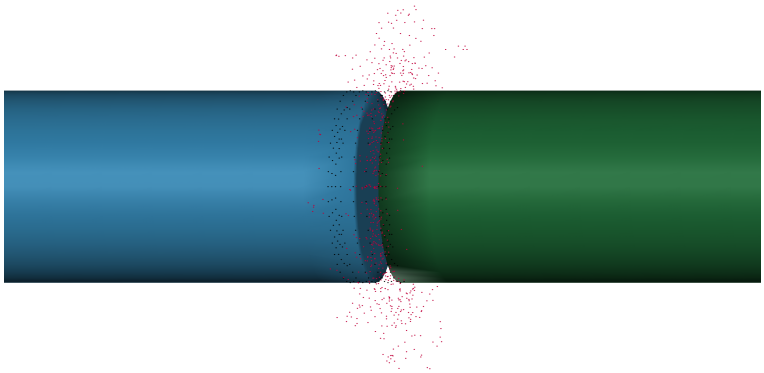

Figure 5.21: Final time state of unconfined SHPB model with sample modelled using SPH nodes.

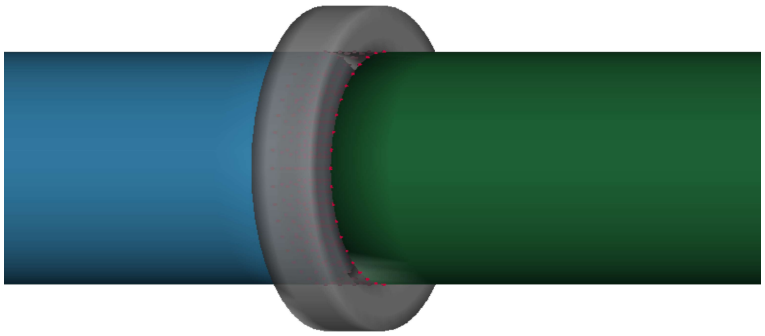

Figure 5.22: Unconfined SHPB model with sample modelled using SPH nodes.

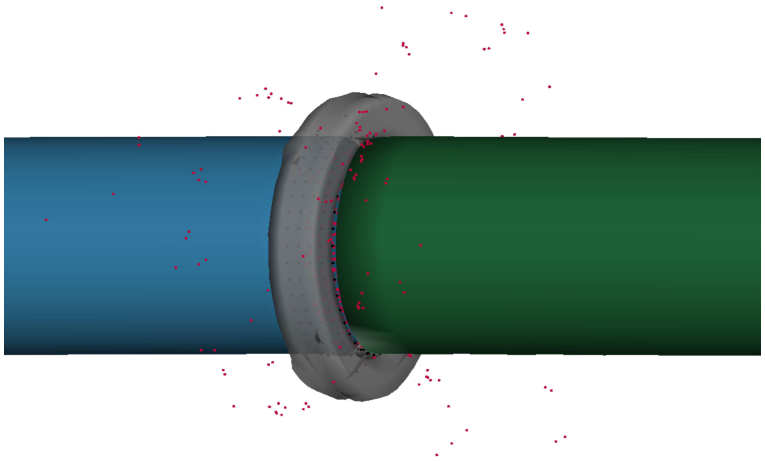

Figure 5.23: Final time state of unconfined SHPB model with sample modelled using SPH nodes.

5.4.6 Rigid confining ring

This section focuses on evaluating the overall design of the experiment. Confirming that the cause of the problems in modelling the high-strain-rate phase behaviour of cohesive soils is due to the design of the confining ring and its interaction with the specimen and its design.

The resolution to the negative volume error involved employing SPH nodes to simulate the sample behaviour in SHPB tests. However, despite this adjustment, the extreme deformation of the confining ring continued to render the results unviable. Therefore, modifications to the confining ring design became imperative to curtail its deformation.

To achieve this, the material model *MAT_RIGID was used. This model facilitates the restriction of material degrees of freedom, with details on its structure outlined in Appendix D, Table D.5. In the updated SPH model, the material of the ring was altered to a model with constrains in the x and z translational directions, as well as x, y, and z rotational directions. This configuration prevented the ring from deforming while still allowing translation along the y-axis of the pressure bars.

This model effectively captured stress propagation through the sample onto the transmitter bar with minimal interference. However, there is notable difference between the stress directly adjacent to the sample on the ring and the stress on the sample itself, suggesting that the ring's stiffness is not being measured. While the sample is prevented from experiencing lateral deformation, this constraint impedes stress propagation through the ring material. Hence, radial stress readings cannot be recorded, thereby precluding a comparison between radial stresses from the numerical model and experimental results.

This still offers valuable validation of cohesive soil behaviour under fully confined conditions. With the ring acting as a rigid boundary, preventing lateral displacement and extrusion of the sample, there is noticeable axial stress propagation through the sample. However, despite accurately depicting the sample's tendency to propagate stress primarily in the lateral direction under high-strain-rate loading, there is still a disparity between the back stresses in the numerical and experimental models. Yet, this disparity aligns with the limitations of the confining ring. Deformation of the ring prompts substantial lateral extrusion and volumetric loss, contributing to the observed differences.

Incorporating this design step into the design of the experiment ensured that the overall setup was robust, allowing the primary focus to be on the confining ring and the specimen's high-deformation response to the stress wave from the incident bar.

5.4.7 Modifications to confining ring design

Although the rigid confining ring was able to replicate the general experimental behaviour of cohesive soil under high-strain-rate conditions, it remains advantageous to develop a numerical model that permits radial stress development on the confining ring. This ensures the development of a numerical model capable of validating experimental behaviour with the current setup.

Introducing an elastic element to the confining ring, which *MAT_RIGID currently lacks, theoretically enables the ring to resist extreme deformation while facilitating the propagation of radial stresses through this singular elastic component. Integrating both elastic and rigid elements within the confining ring aims to minimise the vibrational movement of the elastic components while preserving the restrictive characteristics of the rigid ring in Section 5.4.6.

The initial approach to optimise the design of the confining ring focused on optimising the number of elastic elements. This was achieved by separating elements along the same radial axis as the confining ring (Figure 5.24) and assigning them the same elastic steel material properties as the original fully elastic confined model discussed in Section 5.4.5. However, this approach created a potential scenario where stress could travel through the three elements on the 'column' to the edge of the confining ring (the same location of the strain gauge on the physical confining ring).

Despite these adjustments, the radial stresses recorded from the elastic element on the edge of the modelled ring remained at zero. This suggests that the elements are still resisting the propagation of radial stress, likely due to their close proximity to other rigid elements. Since the nodes of the elastic elements are merged with those of the rigid elements in nearly all directions, each elastic element is essentially fixed in place on all eight edges, rendering it incapable of deformation. This explains why configurations No. 2 & 3 failed to record any radial stress.

Other modifications to the confining ring have been tested, albeit with limited success in accurately simulating a radial stress pulse. A summary of the methods tested is presented in Table 5.4. This suggests that a larger volume of elastic elements is necessary, ensuring that the elements through which radial stresses propagate are not directly adjacent to fully rigid elements. The final combination (No. 5 in Table 5.4) proved most successful in achieving a balance between radial stress propagation and minimising vibrational noise (Figure 5.25). The mesh used in the final iteration of the confining ring design (No. 5) is depicted in Figure 5.26, with nodes at the boundaries between the rigid and elastic materials merged to ensure the entire ring functions as a single model part.

Incident and transmitter stresses are recorded similarly to when the confining ring was fully rigid. However, upon examining the radial stress readings from the elastic element directly adjacent to the sample in the final ring configuration (Figure 5.25), radial stress was of a considerable magnitude.

No.	*Modifications*	*Radial stress*	*Findings*
1	Fully elastic ring with 4 rigid 'columns'	Yes	Radial stress was obtained, but limited rigid elements failed to contain extreme vibration and deformation of the ring, resulting in high radial stresses.
2	Fully rigid ring with 4 elastic 'columns'	No	Similar results were observed as the one 'column' scenario. Rigid material restricted elastic elements.
3	Fully rigid ring with 8 elastic 'columns'	No	Freedom of elastic elements remained mostly restricted. Small levels of radial noise were observed.
4	All inner radius elements as elastic material	Yes	Approach prompted the development of radial stress. However, all elements in inner ring radius had 4 of their 8 nodes restricted by rigid elements.
5	Only radius elements as rigid material	Yes	Configuration yielded the highest radial stress, since stress was able to propagate radially, while the outer layer minimising noise from vibrational movement.

Table 5.4: Configurations tested in LS-DYNA for the design of the confining ring, and their respective findings.

This design process aimed to evaluate model configurations suited to represent the unconfined and confined high-strain-rate behaviour of cohesive soils. A trial-and-error approach was used to address model challenges, including confining ring design, negative volume error, sample deformation, and meshing.

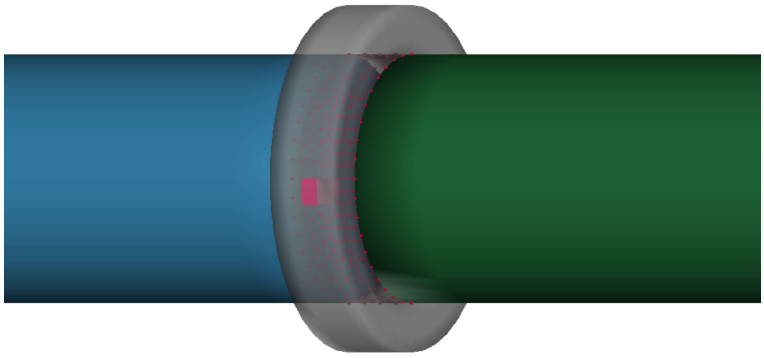

Figure 5.24: Confined SHPB model with one 'column' of elastic elements in the confining ring modelled as an elastic material (pink) with the rest of the confining ring modelled as a rigid material (grey).

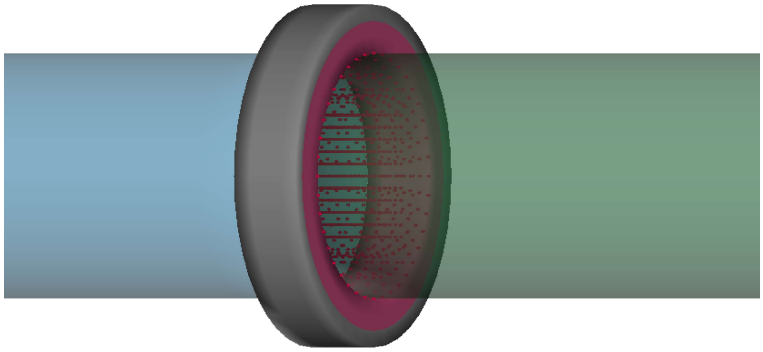

Figure 5.25: Confined SHPB model with half rigid, half elastic confining ring, and SPH sample.

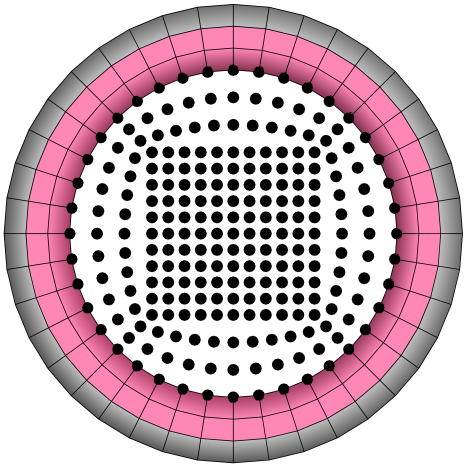

Figure 5.26: Top view of confining ring with outer radius made of a rigid material (grey) and two inner radial layers made of an elastic material (pink).

5.5 Final model setup

The final LS-DYNA numerical model of the setup used is shown in Figure 6.5. It was created using the FEM software LS-DYNA, in order to compare numerical and experimental SHPB test results on kaolin clay samples. The striker (yellow), incident (blue) and transmitter (green) bars are modelled as 3D solid Lagrangian meshes. The confining ring (pink and grey) is also modelled this way. The confining ring is modelled using a combination of rigid (*MAT_RIGID), and elastic elements (*MAT_ELASTIC), as discussed in Section 5.4.7, while all the stainless-steel pressure bars are built as elastic elements (*MAT_ELASTIC). SPH node modelisation was used for the kaolin clay sample and shown in red.

Figure 5.28a depicts the 5 mm SPH kaolin clay sample section numerically simulated between the incident and transmitter bars. A more detailed representation of the confining ring with the SPH sample slotted inside is illustrated in Figure 5.28b. A fixed sample length of 5 mm was chosen, and the model's bulk density was changed to match the precise sample length tested using the SHPB apparatus.

When examined at high strain rates, kaolin clay exhibits high deformation and fluid-like behaviour, hence SPH is chosen as the most suitable option over traditional Lagrangian meshing procedures. This modelling approach effectively resolves issues with excessive distortion and negative volume errors.

The contact interface between the SPH-modelled kaolin clay sample and the two Lagrangian pressure bars (i.e. incident and transmitter bar) was represented in LS-DYNA using the *CONTACT_AUTOMATIC_NODES_TO_SURFACE. The contact interface between the SPH-modelled kaolin clay sample and the inside of the confining ring was modelled in this similar manner. On the other hand, the contact interface between the pressure bars was modelled using *CONTACT_AUTOMATIC_SURFACE_TO_SURFACE. Details of these contact cards are available in Appendix D, Tables D.6 and D.7.

Figure 5.27: LS-DYNA SHPB model with confining ring [confining ring removed for unconfined modelling].

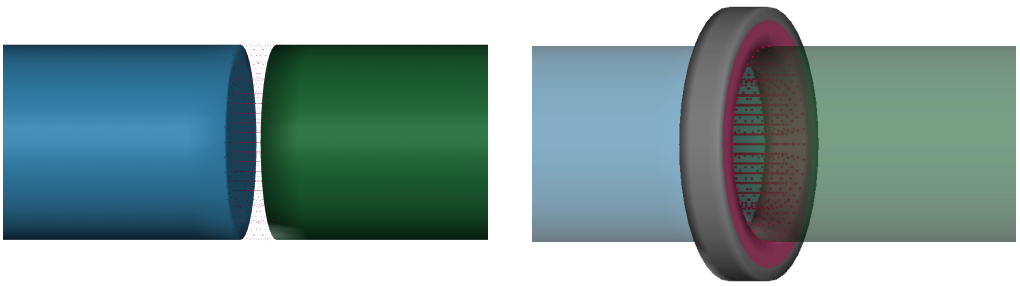

(a) **(b)**

Figure 5.28: Zoom-in on the (a) unconfined SHPB, and (b) confined SHPB modelling setup in LS-DYNA.

5.6 Assessment of LS-DYNA material models for cohesive soils

The LS-DYNA documentation identifies several constitutive models suitable for soil modelling (LSTC 2007). These models vary from basic compressibility curves and perfectly-plastic yield surfaces to more sophisticated ones incorporating pore water effects, dilatancy, hardening and strain-rate effects. Below is a brief overview of each model, and Table 5.5 presents a comparison of their key features.

Soil and Foam (*MAT_005**):** This simple pressure-dependent model simulates crushing through volumetric deformation. It features a pressure-dependent quadratic yield surface in J_2–P space, and unloads elastically to a tensile cut-off.

Soil and Foam with Failure (*MAT_014**):** Similar to *Soil and foam*, this model incorporates a failure pressure, indicating the point where an element loses its ability to carry tension.

Pseudo Tensor (*MAT_016**):** Originally designed for concrete applications, this model, when excluding parameters for reinforcement material, can also be applied to soils, resembling the behaviour of *Soil and foam*. Compressibility is determined through tabulated equations of state or tabulated compaction curve. Yield surfaces are presented in $(\sigma_1 - \sigma_3)$–P space, with the option to incorporate strain-rate dependence through yield stress multiplier.

Geological Cap (*MAT_025**):** This is a two-invariant cap model featuring kinematic hardening. The yield surface is defined in $\sqrt{J_2}$–J_1 space and includes both tension cut-off and cap surfaces. The hardening function is customisable, and the model assumes an associated flow rule.

Schwer-Murray Cap (*MAT_145**):** This cap model is derived from the geological cap and incorporates strain rate dependence through viscoplasticity and strain softening.

FHWA Soil Model (*MAT_147**):** The modified Mohr-Coulomb yield surface extends to include parameters for excess pore pressure, viscoplasticity, strain softening, kinematic hardening, and removal of distorted elements.

Mohr-Coulomb (*MAT_173**):** The Mohr-Coulomb yield surface is characterised by cohesion and the angle of friction. It incorporates a dilation angle to establish a nonassociated flow rule, with both ϕ and ψ subject to variation with plastic strain.

Drucker-Prager (*MAT_193**):** The modified Drucker-Prager yield surface is defined by cohesion and the angle of friction. It employs a dilation angle to establish a nonassociated flow rule, with both ϕ and ψ subject to variation with plastic strain. Additionally, the yield surface can be altered using a shape factor.

*MAT_	*Model name*	*Failure surface space*	*Failure surface definition*	*Pressure dependent*	*Strain-rate dependent*	*Hardening criteria*	*Dilatency*	*Compressibility control*
005	*Soil and Foam*	J_2–P	Quadratic	Yes	No	None	No	P–ε_v, tabulated
014	*Soil and Foam with Failure*	J_2–P	Quadratic	Yes	No	None	No	P–ε_v, tabulated
016	*Pseudo-Tensor (I)*	q–p	Tabulated	Yes	Shear strength scale factor	None	No	Defined EOS
025	*Geological Cap*	$\sqrt{J_2}$–I_3	Coefficients	Yes	No	Associated, kinematic	Yes	Cap surface
145	*Schwer-Murray Cap*	$\sqrt{J_2}$–I_3	Coefficients	Yes	Viscoplasticity	Nonassociated, kinematic	Yes	Cap surface
147	*FHWA Soil Model*	p, J_2, J_3	ϕ, c coefficients	Yes	Viscoplaticity	Associated	Yes	No
173	*Mohr-Coulomb*	τ, σ	ϕ, c	Yes	No	Nonassociated	Yes	No
193	*Drucker-Prager*	τ, σ	ϕ, c	Yes	No	Nonassociated	Yes	No

Table 5.5: Comparison of LS-DYNA soil models (modified from Barr (2016*b*)).

While the *MAT_NULL material model served its purpose in testing the model geometry and its design, it does not reflect the material properties of kaolin clay. Therefore, to develop a model that accurately represents cohesive soil behaviour, an investigation into potential material models in LS-DYNA was conducted. Each material model is assessed based on the following criteria:

1. Ease of model calibration, particularly with regard to utilising quasi-static experimental data on kaolin clay specimens.
2. Model performance in comparison with experimental SHPB data; and
3. Possibilities for optimisation and recommendations for improving accuracy in representing experimental SHPB data for kaolin clay.

To streamline comparisons, many models share similar approaches to defining the equation of state (EOS) and material failure surface. Hence, models from Table 5.5 were grouped, as shown in Table 5.6.

Group	*Models*	*Material card No.*
Soil and Foam	*Soil and Foam*	*MAT_005
	Soil and Foam with Failure	*MAT_014
	Pseudo-Tensor	*MAT_016
Mohr-Coulomb	*FHWA Soil Model*	*MAT_147
	Mohr-Coulomb	*MAT_173
	Drucker-Prager	*MAT_193
Cap Models	*Geological Cap*	*MAT_025
	Schwer-Murray Cap	*MAT_145

Table 5.6: Grouping of similar material soil models.

Firstly, examining the 'Soil and Foam' group, all soil models within this category - namely, *Soil and Foam*, *Soil and Foam with Failure* and *Pseudo-Tensor* - mandate the use of an EOS for the LS-DYNA model to function properly. However, given the strain dependence of the investigated material, no EOS could be computed to map the complete behaviour of the soil, hence, none of these models can be utilised.

Similarly, all the models in the 'Cap Models' group face the same limitations, while also requiring additional parameters, which could not be acquired for our material due to its cohesive properties. Therefore, these models were not employed in the modelling of our kaolin clay in LS-DYNA.

Examining the 'Mohr-Coulomb' group, the *FHWA Soil Model* necessitates parameters that are unattainable through testing for our cohesive material, as this model is primarily designed for solid elements, making it impractical for our purposes. On the other hand, the *Mohr-Coulomb* material model appears promising, as it was developed to simulate sandy soils and other granular materials. The required parameters for its successful implementation can be obtained through testing, rendering it a viable option.

The *Drucker-Prager* model shares similar parameter requirements with the *Mohr-Coulomb* model. However, it is not recommended for cohesive soils as it does not account for the tensile behaviour, and therefore it was not employed in the LS-DYNA simulations.

Other material models were evaluated, including *Cohesive mixed mode*, *Cohesive General*, *Arup adhesive* and *Null*. These models proved unsuitable for modelling cohesive soils at high-strain-rates due to their unobtainable parameters and poor performance for representing the behaviour of cohesive soils.

In conclusion, several material models have been explored to assess their suitability for simulating the behaviour of kaolin clay. However, many were disregarded due to challenges in obtaining specific model parameters. Table 5.7 summarises the material models commonly used for modelling soils or cohesive behaviour, as well as other recently developed models, which were found unsuitable for accurately modelling kaolin clay under high-strain-rate conditions.

*MAT_ *No.*	*Models*	*Viability*
*MAT_005	*Soil and Foam*	Requires an EOS.
*MAT_014	*Soil and Foam with Failure*	Requires an EOS.
*MAT_016	*Pseudo-Tensor*	Requires an EOS.
*MAT_147	*FHWA Soil Model*	Designed for road based soil models, requires viscoplastic parameters.
*MAT_173	*Mohr-Coulomb**	Suitable for cohesive soils and parameters obtainable.
*MAT_193	*Drucker-Prager*	Similar parameters to *Mohr-Coulomb*, but does not account for tensile behaviour within cohesive soils.
*MAT_025	*Geological Cap*	Requires a hardening function, parameters can not be obtained for cohesive soils.
*MAT_145	*Schwer-Murray Cap*	Requires unobtainable parameters for cohesive soils.
*MAT_138	*Cohesive mixed mode*	Cohesive model but not optimised for cohesive soil modelling at high-strain-rates.
*MAT_186	*Cohesive General*	Not optimised for cohesive soil behaviour.
*MAT_169	*Arup adhesive*	Models cohesion but for adhesive bounding between aluminium members.
*MAT_009	*Null*	Designed for fluids, no cohesion parameters, suitable only as a reference.

[* Material model selected for LS-DYNA modelling.]

Table 5.7: Summary of material soil models considered to models cohesive soils in LS-DYNA and their viability.

As a result, *Mohr-Coulomb* was the sole material model capable of modelling cohesive soils and assessing the accuracy of LS-DYNA models in simulating SHPB tests on kaolin clay samples.

5.7 Evaluation of LS-DYNA models for modelling SHPB tests on kaolin clay

In this section, the LS-DYNA numerical models representing the SHPB tests on kaolin clay under both unconfined and confined conditions are evaluated. The aim is to ensure that the numerical model accurately reflects the physical behaviour of the material observed during testing. To begin, the calibration of the material used to represent the kaolin clay specimen and its associated variables are described. The numerical models are then compared against their respective test results.

5.7.1 Material model calibration

The stainless-steel pressure bars are modelled as linear elastic using the *MAT_ELASTIC, with a density, Young's modulus and Poisson's ratio of ρ = 7666 kg.m^{-3}, E = 222 GPa and ν = 0.29, respectively. To mirror experimental SHPB tests, the model's striker bar velocity was set to the associated striker speed used in experimental testing: 8, 12, 16 m/s for unconfined tests and 18, 20, 22 m/s for confined tests.

The confining ring used for SHPB testing is made of stainless-steel. It was initially modelled as linear elastic using *MAT_ELASTIC, however, this led to a lot vibration and noise interference with the numerical data. A fully rigid confining ring was modelled using the *MAT_RIGID to remove these interferences associated with the contact between the pressure bars and the confining ring. This resulted in no radial stress data being recorded. Therefore, a combination of rigid and elastic elements were utilised to model the confining ring to be able to collect radial stress data (orange and pink in Figure 5.28b).

The material model *MAT_MOHR_COULOMB implements the Mohr-Coulomb constitutive model for soils, characterised by a yield criterion of the form

$$\tau = \sigma' \tan\phi' + c'$$

where τ is the shear strength, σ' is the effective normal stress, ϕ' is the angle of shearing resistance and c' is the intercept of the yield surface with the y axis. Variables for joint definition in rocks and depth-dependent properties have been omitted from Table 5.8.

Variable	*Description*
ro	Initial density, kg m^{-3}.
gmod	Elastic shear modulus, Pa.
rnu	Poisson's ratio.
phi	Angle of friction, rad.
cval	Cohesion, Pa.
psi	Dilation angle, rad.

Table 5.8: LS-DYNA variables for *MAT_MOHR_COULOMB.

The kaolin clay sample, simulated using *MAT_MOHR_COULOMB, incorporates essential parameters including initial density (ro), elastic shear modulus (gmod), Poisson's ratio (rnu), angle of friction (phi) and cohesion factor (cval), as depicted in the calibrated LS-DYNA material card in Table 5.9.

*MAT_MOHR_COULOMB								
Kaolin clay sample								
$#	mid	ro	gmod	rnu		phi	cval	psi
	X	x1	1.3E7	x2		0.08075	55759.4	0.0
$#		nplanes		lccpdr	lccpt	lccjdr	lccjt	lcsfac
		0		0	0	0	0	0
$#	gmoddp	gmodgr	lcgmep	lcphiep		lcgmst	cvalgr	aniso
	0.0	0.0	0.0	0.0		0.0	0.0	1.0
	[x1 and x2 are adjusted based on the material properties of the sample tested.]							

Table 5.9: Material card for *MAT_MOHR_COULOMB, calibrated to represent kaolin clay.

These values were established through the following processes:

1. The angle of friction, phi, can be found by plotting the Mohr's circles of stress using the data in Section 4.5.1. Despite conducting UU TXC tests on the kaolin clay samples at moisture contents of 41, 42 and 44 %, an estimated value of phi can be obtained. To achieve this, the stress envelope is modestly inclined to cover the top of the plotted Mohr circles, rather than remaining completely horizontal. This approach is necessary because the model fails when phi equals zero. The values for phi and cval are slightly exaggerated to ensure the model runs effectively. This analysis provided a value of phi equal to 4.62º, which is equivalent to 0.08075 rad.

2. Given that kaolin clay is a cohesive soil, a cohesion factor, cval, can be determined from the same Mohr circle plots described above. This analysis yields a value of cval equal to 55759.4 Pa.

3. Elastic shear modulus, gmod, was determined using the quasi-static test data presented in Section 4.5.1, giving a value of gmod = 1.3E7 Pa.

4. The initial density, ro, and Poisson's ratio, rnu, will vary depending on the moisture content of the kaolin clay sample under examination. These values are adjusted for each LS-DYNA specimen model. To make these adjustments, the specimen's moisture content and Poisson's ratio are input based on its calculated material properties during testing. They are labeled as x1 and x2 in Table 5.9 above.

5.7.2 Comparison between unconfined SHPB tests and corresponding LS-DYNA numerical models

The material card *MAT_MOHR_COULOMB includes parameters such as bulk density, ρ, and Poisson's ratio, ν, specific to the moisture content sample being modelled, denoted as x1 and x2, as seen in Table 5.9. Table 5.10 provides a comprehensive overview of the inputs utilised in LS-DYNA to model the unconfined SHPB tests, along with the corresponding results, specifically the maximum front and back stresses within the model.

Striker speed, m/s	*Moisture content, %*	ρ (ro) *kg.m*$^{-3}$	ν (rnu)	*Max front stress, MPa*	*Max back stress, MPa*	*Max radial stress, MPa*
8	0	934	0.40-0.49	27.0	2.4	–
8	20	1087	0.40-0.49	27.0	2.4	–
8	41	1296	0.40-0.49	27.0	2.4	–
12	0	934	0.40-0.49	41.2	3.4	–
12	20	1087	0.40-0.49	41.2	3.4	–
12	41	1296	0.40-0.49	41.2	3.4	–
16	0	934	0.40-0.49	54.1	2.4	–
16	20	1087	0.40-0.49	54.1	2.4	–
16	41	1296	0.40-0.49	54.1	2.4	–

Table 5.10: Summary of the LS-DYNA modelling inputs and outputs for the unconfined SHPB numerical model.

To optimise the material model for specific moisture content conditions, adjustments were attempted on the bulk density and Poisson's ratio within the *MAT_MOHR_COULOMB material card. Utilising the known physical properties of kaolin clay at different moisture levels, varying levels of bulk density were set to correspond to specific moisture contents. For instance, bulk densities of 934, 1087 and 1296 kg.m^{-3} were selected to represent moisture contents of 0 %, 20 %, and 41 % respectively. Table 5.10 presents a summary of the tests conducted at these different bulk densities across all three striker bar velocities.

It is well-established that the Poisson's ratio of fully saturated kaolin clay tends to approach 0.5 under high-strain-rate conditions. However, despite this understanding, attempts to define the Poisson's ratio as 0.5 led to computational failure. Even after exploring variations of Poisson's ratio from 0.40 to 0.49, efforts to modify its values and assess their impact on model behaviour yielded no observable changes.

As depicted in Table 5.10, altering the bulk density failed to induce any variations in the front and back stresses. This represents a significant drawback of the numerical model, indicating that different moisture content levels do not yield any discernible changes, which contradicts experimental findings. This limitation is primarily due to the current material model's inability to accurately simulate high-strain-rate flows and challenges in correctly modelling the sample's moisture behaviour. The *MAT_MOHR_COULOMB material model, being a simplified approach, may not be optimal for modelling these complex soil behaviours.

As the striker bar speed increased, higher strain rates were induced, resulting in elevated front and back stresses in the numerical model, aligning with expectations based on experimental testing. Figure 5.29 illustrates a direct comparison between numerical and experimental back stresses from unconfined SHPB tests on saturated kaolin clay. Notably, both the magnitude and shape of the back stress pulse exhibited noticeable similarity.

When examining the front stress (a combination of incident and reflected pulses) at the designated striker bar speed, as depicted in Figure 5.30, the numerical front stress remains nearly zero throughout the pulse duration. This suggests that a substantial portion of the stress is reflected back from the sample interface on the incident bar (Figure 5.31). Conversely, in experimental tests, although the initial peak is similar, the experimental front stress wave effectively propagates through, as evidenced by the non-zero front stress before returning to zero.

The observed phenomenon stems from the absence of a cohesive mechanism within the material model employed to characterise the numerical sample. Consequently, when the stress wave reaches the sample interface, it triggers an instantaneous displacement of the SPH particles. In actuality, internal cohesive properties play a vital role in binding the sample material together, mitigating lateral deformation to some degree. This phenomenon explains why minimal changes are observed when altering moisture content: limited stress is able to effectively transmit through the material despite variations in moisture levels. While the numerical model adeptly captures qualitative behaviour, the absence of cohesive properties to unite individual particles during high-strain-rate loading renders precise stress values unreliable.

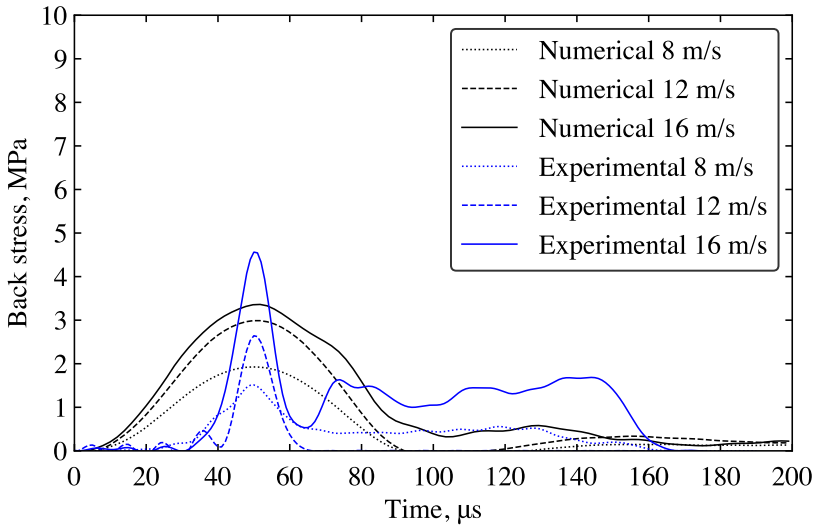

Figure 5.29: Comparison of back stress from the experimental unconfined SHPB tests and corresponding numerical LS-DYNA models on fully saturated kaolin clay samples, at different strain rates.

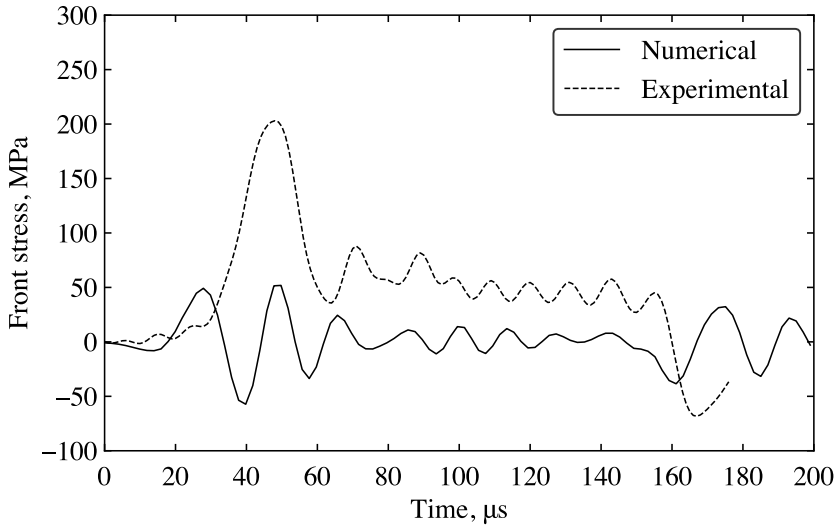

Figure 5.30: Comparison of the experimental and numerical model's front stresses for an unconfined SHPB test on a fully saturated kaolin clay sample at 16 m/s.

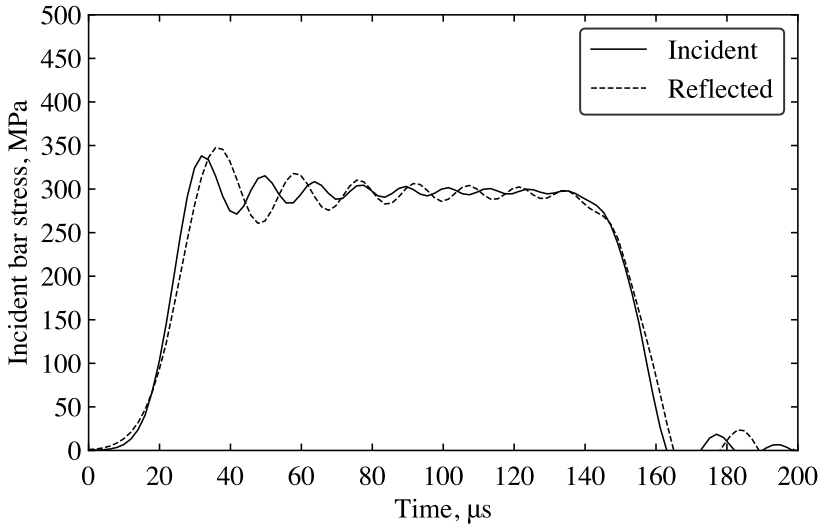

Figure 5.31: Typical incident and reflected stresses from an unconfined SHPB numerical model at 16 m/s.

5.7.3 Comparison between confined SHPB tests and corresponding LS-DYNA numerical models

Similarly to the unconfined SHPB models, Table 5.11 provides an overview of the inputs utilised in LS-DYNA to model the confined SHPB tests, along with the corresponding outputs. Findings detailed in Table 5.11, echo the findings of unconfined SHPB models, confirming that Poisson's ratio does not influence the results, with the model failing to run for a Poisson's ration of 0.5. Furthermore, adjustments in moisture content through variations in bulk density, do not alter the material's behaviour in the model.

Striker speed, m/s	*Moisture content, %*	ρ (ro) *kg.m*$^{-3}$	ν (rnu)	*Max front stress, MPa*	*Max back stress, MPa*	*Max radial stress, MPa*
18	0	934	0.40-0.49	329.0	289.2	509.0
18	20	1087	0.40-0.49	329.0	289.2	509.0
18	41	1296	0.40-0.49	329.0	289.2	509.0
20	0	934	0.40-0.49	365.2	322.2	624.0
20	20	1087	0.40-0.49	365.2	322.2	624.0
20	41	1296	0.40-0.49	365.2	322.2	624.0
22	0	934	0.40-0.49	407.6	369.2	674.0
22	20	1087	0.40-0.49	407.6	369.2	674.0
22	41	1296	0.40-0.49	407.6	369.2	674.0

Table 5.11: Summary of the LS-DYNA modelling inputs and outputs for the confined SHPB numerical model.

Figure 5.32 depicts the incident and reflected pulses in the numerical model. The front stress behaviour in the LS-DYNA numerical model resembles that observed in the SHPB tests (Figure 5.33), albeit with a higher magnitude, due to sample containment from the seal of the numerical model design of the confining ring (Table 5.11).

Although altering moisture content was unfeasible, the base model captured changes in strain rate. The confined model, minimised lateral displacement of the sample. As a result, stress translation from lateral to axial on the transmitter bar became evident. Notably, significant lateral stresses were recorded on the confining ring due to lateral displacement and impact from SPH nodes (Figure 5.34). Simultaneously, a large amount of back stress was recorded (Figure 5.35). The numerical model's characteristic prevention of extrusion and volumetric loss ensured that all stress from the sample was propagated either laterally towards the confining ring or axially towards the transmitter bar. Naturally, this resulted in much higher back and radial stress readings in the numerical model compared to the test data.

In Figure 5.35, the back stress for the fully saturated kaolin clay specimens tested under confined conditions at different strain rates (striker velocities) decrease in amplitude, whereas in the model, they increase. This disparity arises because in the numerical model, the sample's SPH node particles cannot extrude, a limitations more pronounced at higher striker velocities.

The confinement mechanism facilitated the transfer of stress into the sample in the numerical model, as evidenced by a higher magnitude of front stress displayed by the model (Figure 5.33). Despite the incident stress remaining consistent due to the uniform initial striker bar velocity, the reflected stress exhibits a notably lower value (Figure 5.32). This situation mirrors instances of stress equilibrium, where there is evident axial stress propagation. Consequently, traditional one-dimensional wave theory was employed to equate the superposition of incident and reflected pulses with the back stress.

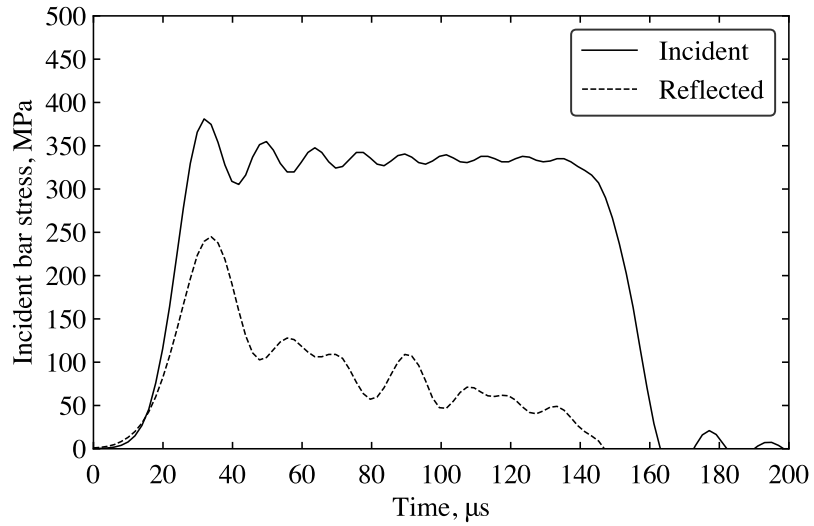

Figure 5.32: Typical incident and reflected stresses from a confined SHPB numerical model at 18 m/s.

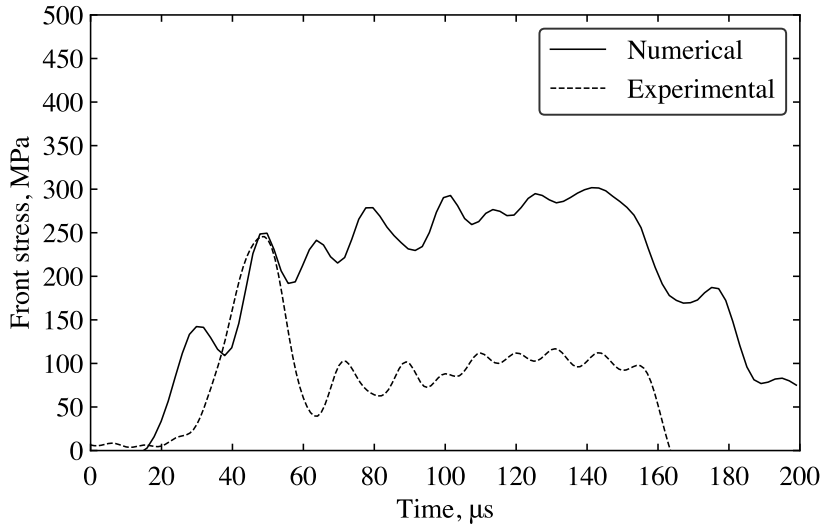

Figure 5.33: Comparison of the experimental and numerical model's front stresses for a confined SHPB test on a fully saturated kaolin clay sample at 18 m/s.

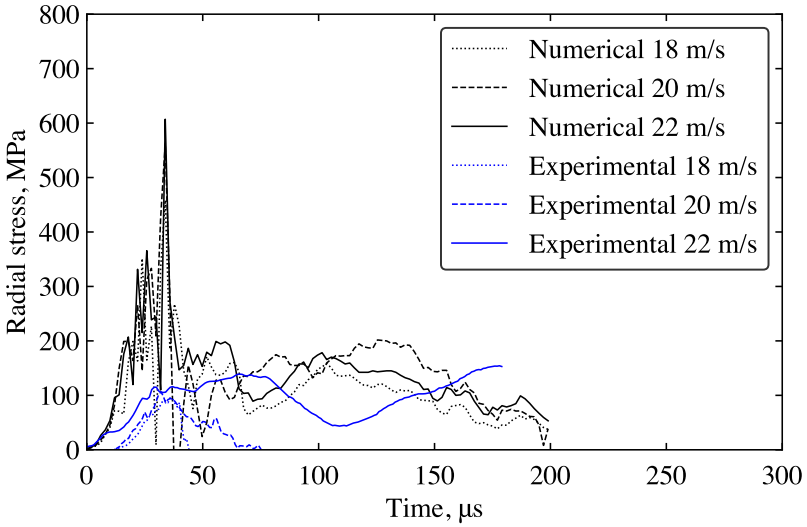

Figure 5.34: Comparison of radial stress from the experimental confined SHPB tests and corresponding numerical LS-DYNA models on fully saturated kaolin clay samples, at different strain rates.

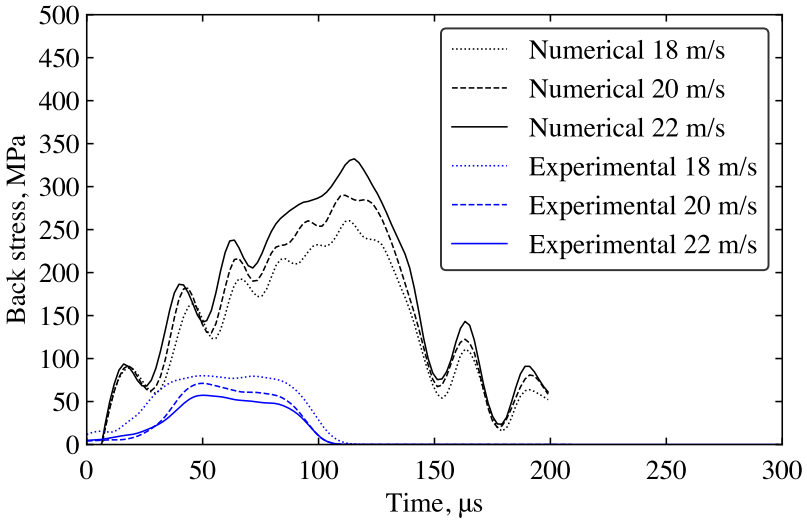

Figure 5.35: Comparison of back stress from the experimental confined SHPB tests and corresponding numerical LS-DYNA models on fully saturated kaolin clay samples, at different strain rates.

When the sample is fully saturated, with a Poisson's ratio of 0.5, the model fails to run due to limitations of *MAT_MOHR_COULOMB, necessitating the used of *MAT_NULL to model the fluid-like behaviour of the material. Since there is no sample extrusion in the numerical model, the front, back and radial stress results show higher values than in the experimental SHPB tests (Table 5.11). The perfect seal of the ring in the model alters the sample's radial stress behaviour, as there is no inertia effect from the incident bar impacting the sample.

5.7.4 Sensitivity analysis of material card parameters

A sensitivity analysis of material card parameters in *MAT_MOHR_COULOMB, influencing the Mohr - Coulomb curve response such as phi, cval, and psi (representing angle of friction, cohesion, and dilation angle respectively), was conducted. Ideally, one would anticipate different parameter values would be implemented in the material model based on the moisture content of the tested sample. However, for this study, fully saturated conditions were uniformly applied across all parameters, using the quasi-static test data collected in Section 4.5.1. This choice stems from the practical difficulty in experimentally obtaining quasi-static data from tests on this material at low moisture contents.

Despite this limitation, the sensitivity analysis revealed minimal impact on results. It became evident that at high-strain-rates, speed of the striker bar predominantly governs the material behaviour when using this material model, overshadowing the influence of material parameter variations. Consequently, the limitations of the material model became apparent, as adjusting these parameters failed to produce any discernible change in material response.

5.8 Analysis of internal stress behaviour in numerical models

Apart from strain gauge locations corresponding to the experimental setup, the numerical model offers the advantage of recording stresses at various other points. As validated through comparisons with experimental testing, current numerical models can reasonably reflect the physical effects of high-strain-rate loading on kaolin clay, albeit with specific limitations. This implies that besides measuring radial stresses from the location on the confining ring, internal lateral stresses and stress propagation from the sample's centre can be monitored by tracking stress variations at each individual SPH node. The internal stress distribution across three of the five sample node layers has been identified and utilised for analysis. These layers correspond to the central, front (incident-sample interface), and back (sample-transmitted interface) layers, as depicted in Figure 5.36.

For more insights into the findings discussed in this section, refer to the paper by Li, Van Lerberghe, Barr and Clarke (2024) in Appendix A.8.

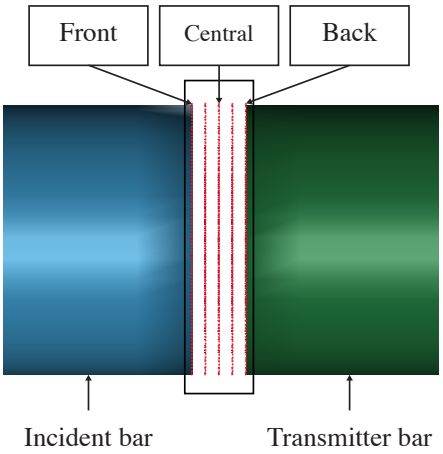

Figure 5.36: Location of front, central and back layers of SPH sample used for measuring internal radial stresses.

5.8.1 Internal radial stress distribution

5.8.1.1 Unconfined test condition

Figure 5.37a illustrates the time frame when all radial stresses (z-stress) are at zero for all SPH nodes along the z-axis within the central layer of the sample. Figure 5.37b depicts the time frame when the maximum radial stress is recorded along the z-axis within the central layer of the specimen. A z-displacement of zero indicates the sample's centre. Although LS-DYNA cannot directly calculate circumferential stresses in a polar coordinate system, stresses along the z-axis portray the propagation of lateral stresses from the sample's centre to its edge. The stresses of the sample nodes along the x-axis yielded nearly identical distributions, suggesting a level of rotational symmetry along the loading axis (y-axis).

As anticipated, the centre of the sample encounters the lowest maximum lateral stress, since it theoretically experiences the highest axial stress. The distribution depicts a gradual escalation of lateral stress from the centre towards the vicinity of the outermost radius of SPH nodes. The layer just before the outermost radius is significant, because it indicates that the initial stress propagation from the centre triggers a displacement effect of these nodes. In unconfined conditions, the outermost radius shows no radial stress because the particles will have extruded. Consequently, when the maximum stress wave reaches the sample's edge, most nodes are already displaced, leading to a clear contrast in stress distributions.

5.8.1.2 Confined test condition

A similar internal stress distribution is obtained for the SPH nodes in the fully confined SHPB model as depicted in Figures 5.38a and 5.38b. The gradual increase in maximum lateral stress can be observed from the centre to the edge of the sample. However, owing to the presence of a fully rigid confinement to prevent extrusion of the outer nodes, the stress wave fully propagates through to the edge of the sample. Remarkably, the magnitude of this initial internal wave is observed to be similar to its unconfined counterpart, even without the presence of any confinement mechanism.

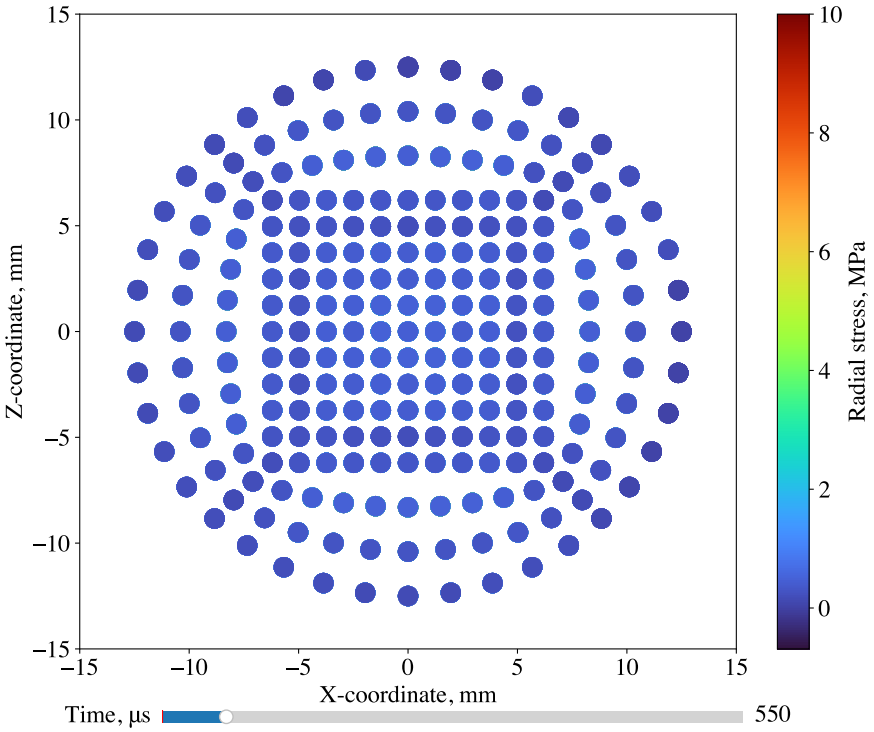

(a)

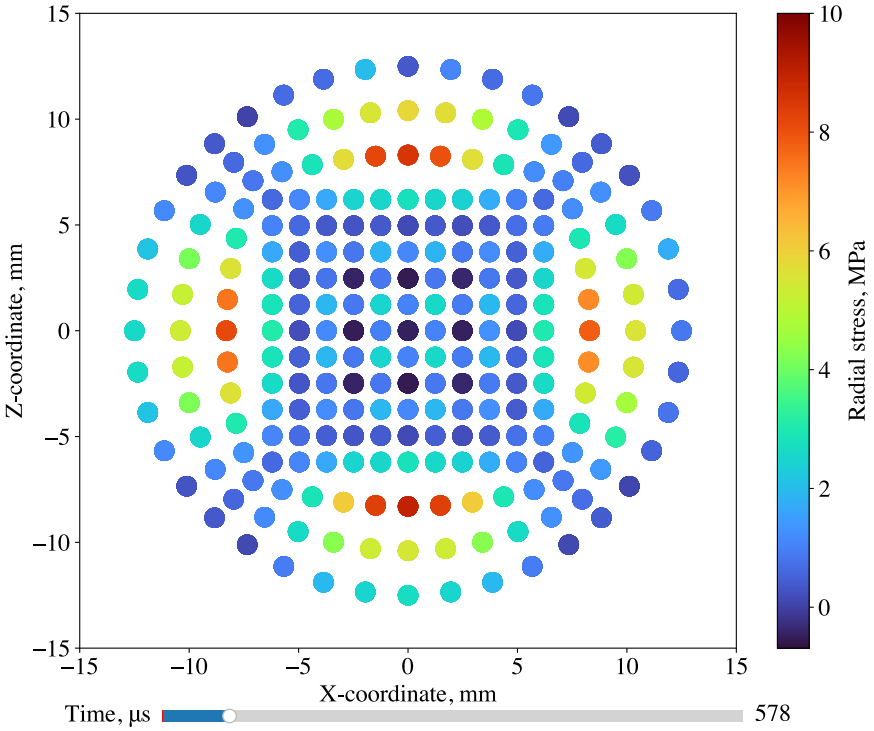

(b)

Figure 5.37: Internal radial stress distribution in the sample's central layer for the unconfined SHPB numerical model: (a) radial stresses at zero, and (b) maximum radial stress recorded.

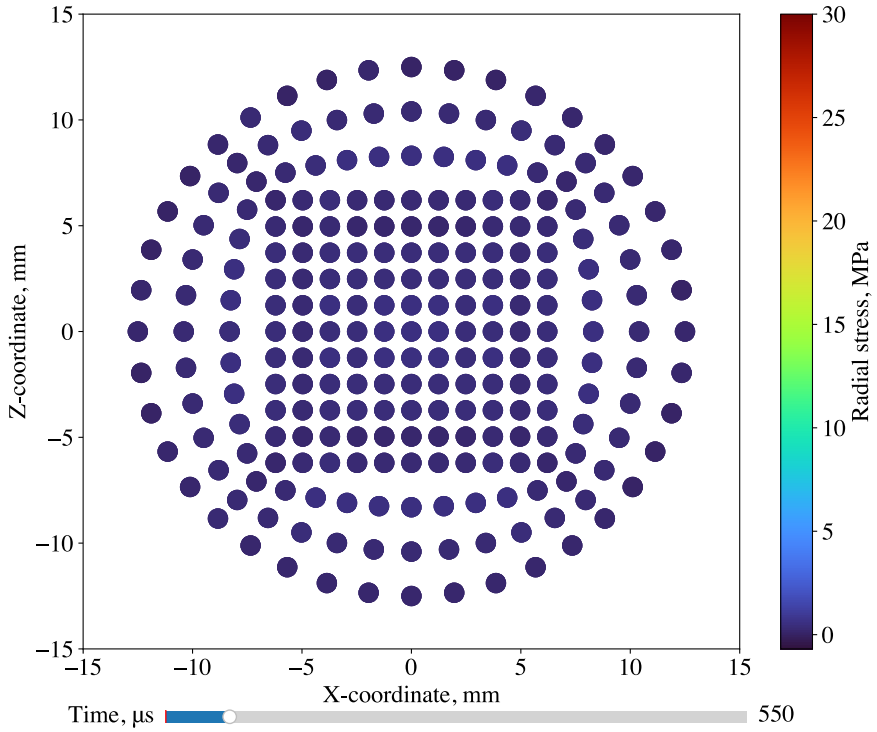

(a)

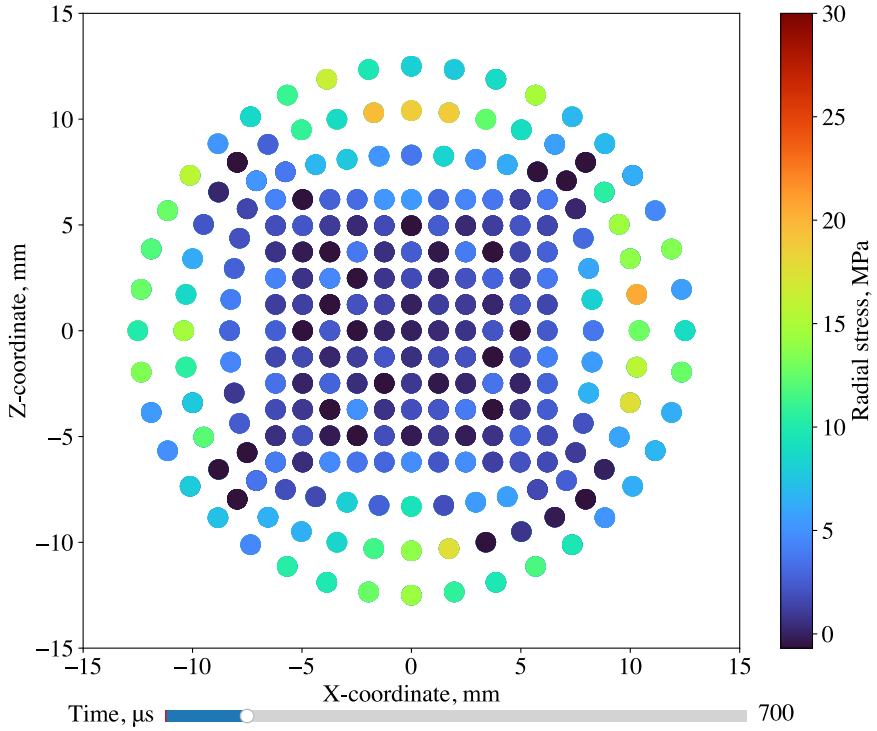

(b)

Figure 5.38: Internal radial stress distribution in the sample's central layer for the confined SHPB numerical model: (a) radial stresses at zero, and (b) maximum radial stress recorded.

5.8.2 Internal radial stress variation at x = 0

5.8.2.1 Unconfined test condition

Focusing solely on the nodes at x = 0, the variation of radial stress (z-axis) over time can be visualised in the heatmap to demonstrate radial stress variation over time. Figure 5.39 illustrates the distribution over time for the front, central and back layers under unconfined conditions, respectively. When looking at the central layer in Figure 5.39b, at around 550 μs, when the axial stress wave reaches the front interface of the sample, lateral stress gradually increases outward from the center of the sample. As previously discussed, the maximum lateral stress does not extend to the outermost nodes, as these nodes are fully extruded by the time the maximum pulse reaches the sample's edge.

Apart from the central layer, comparable stress distributions along the z-axis are observed for the front and back layers, showcasing the evolution of lateral stresses over time. This is illustrated in Figures 5.39a and 5.39c. The highest stress magnitude is observed within the back layer, attributed to its direct adjacency to the transmitted pulse, which acts as a barrier facilitating lateral stress propagation. In contrast, the front layer experiences minimal lateral stress due to its proximity to the incident bar, promoting primarily axial stress. This aligns with the behaviour observed in the internal radial stress distribution of unconfined SHPB models in Section 5.8.1, Figure 5.37.

5.8.2.2 Confined test condition

The heatmap from confined tests reveals internal reflection and subsequent superposition of the stress wave, as depicted in Figure 5.40. Initially, a wave propagates from the center to the edge of the sample, followed by an inward-travelling wave around 600 - 650 μs. Subsequently, the wave travels outward again and reaches peak lateral stress at 700 μs. This highlights how the rigid boundary prevents stress dissipation, leading to reflection of the stress wave. When these waves begin to overlap, they superimpose, resulting in a significantly higher magnitude of lateral stress. Ultimately, the superposition of internal waves leads to the concentration of radial stress, which is eventually redirected axially due to pressure buildup within the ideally sealed confining ring.

When comparing Figures 5.40a and 5.40c, the presence of the confining ring impacted the behaviour at the front and back layers of the sample. Notably, the maximum stress magnitude at the back layer is lower than at the front layer, which contrasts with conditions when sample extrusion was unrestricted. However, since the maximum lateral stress is observed in the second wave and is a direct consequence of internal reflection, the maximum stress from the initial wave remains similar to that in unconfined tests. This suggests that the tendency for stress waves to redirect laterally is unaffected by confinement, by confinement serves to encourage wave superposition. Eventually, the buildup of lateral pressure results in the stress wave being redirected onto the back interface axially. This aligns with the behaviour observed in the internal radial stress distribution of confined SHPB models in Section 5.8.1, Figure 5.38.

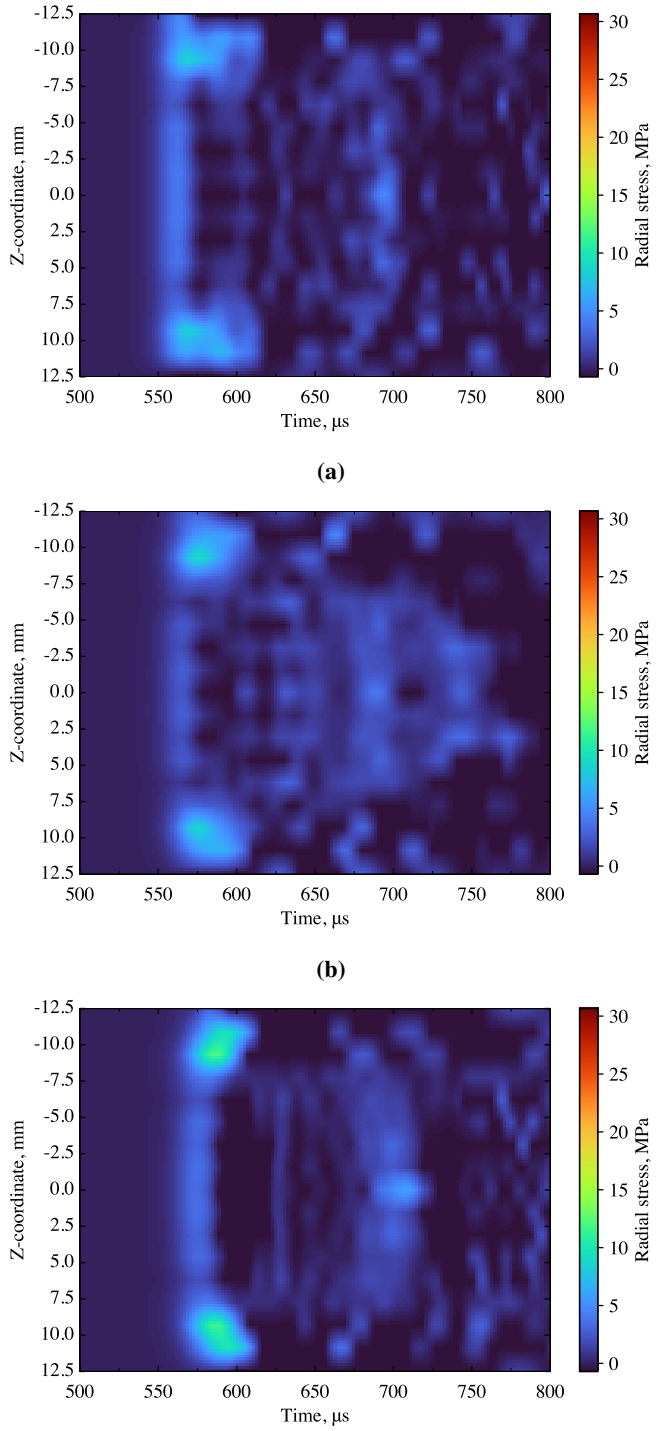

Figure 5.39: Heatmap of internal radial stress variation over time at x = 0, from unconfined SHPB numerical model for (a) front, (b) central, and (c) back layer.

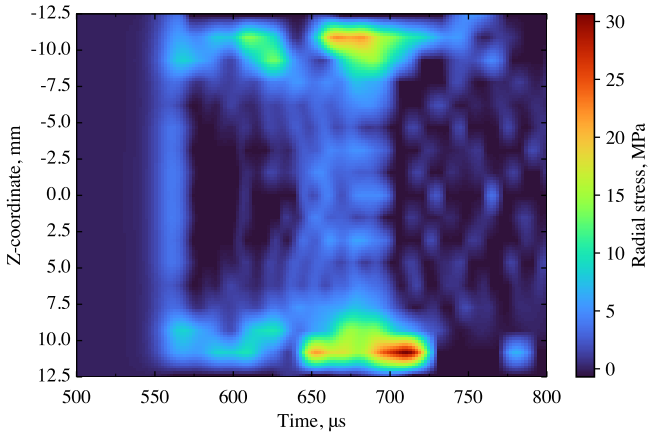

(a)

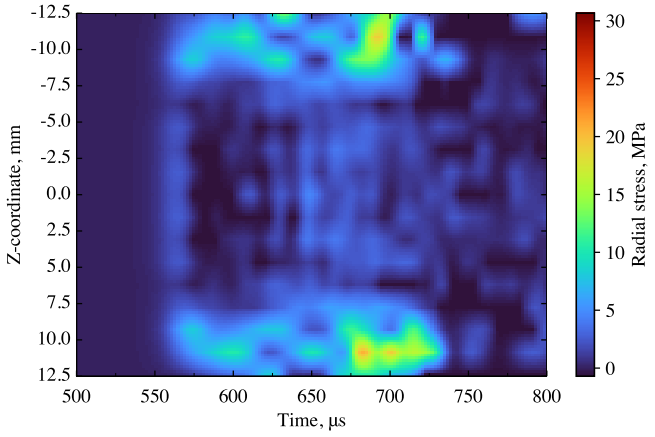

(b)

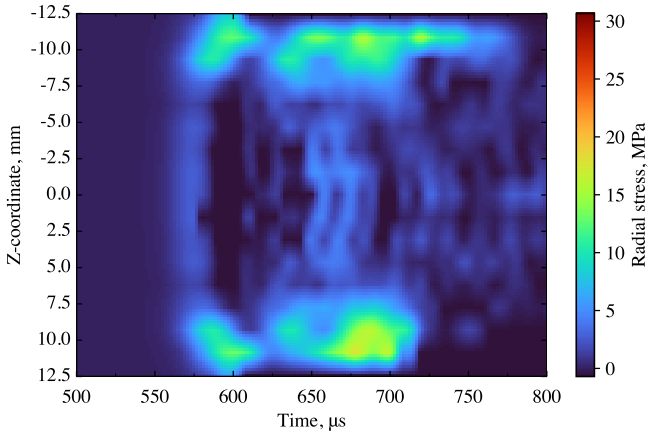

(c)

Figure 5.40: Heatmap of internal radial stress variation over time at x = 0, from confined SHPB numerical model for (a) front, (b) central, and (c) back layer.

5.9 Modelling limitations

The use of constitutive numerical models to validate experimental testing is essential. However, modern numerical modelling techniques still possesses intrinsic limitations that hinder their ability to fully emulate the behaviour of cohesive soils under high-strain-rate conditions. Notable modelling limitations of cohesive soils in LS-DYNA are as follows:

1. The difficulty in computing a compression curve due to the material's inability to endure multi-axial compression without extrusion. Since kaolin clay is strain rate dependent, no equation of state (EOS) can be determined to simulate the complete behaviour of the material under high-strain-rate conditions. Most soil specific and cohesion material models in LS-DYNA require an EOS, therefore the list of material models which could be utilised with the parameters we collected is very short, leaving `*MAT_MOHR_COULOMB` as the most suitable option. However, this material model falls short in adequately capturing the cohesion effect between the cohesive soil particles.

2. During the comparison of experimental SHPB test data and associated LS-DYNA numerical models, the impact of the material's moisture content could not be observed in the numerical model. Therefore, the phase behaviour could not be mapped out in LS-DYNA. This is due to the model's limitations in modelling cohesive soils at high-strain-rates.

3. Although SPH node modelling has been around for some time, there has been relatively little development in its application to soil depiction. This implies that this technique lacks the capabilities to model unique soil properties. LS-DYNA is unable to accurately represent the cohesion properties of cohesive soil particles. This deficiency, compounded by the lack of cohesion properties in this node modelisation tool, hinders its ability to accurately model the high-strain-rate behaviour of cohesive soils.

4. The numerical modelling of the confining ring revealed constraints related to sample extrusion, seal, vibration and contact, hence it required adjustments. Experimentally, an elastic stainless steel ring was used to obtain the radial stress behaviour of the tested specimen, but its excessive deformation compromised accuracy. Therefore, a 1/3 rigid and 2/3 elastic confining ring was created to fully confine the sample, maintain stress equilibrium, prevent sample extrusion with a tight seal, and record radial stresses without complete deformation. Nevertheless, the confining ring's perfect seal affects the model's stress results, making them greater than they should be.

Numerical modelling methods were examined to represent the high-strain-rate phase behaviour of cohesive soil observed in experimental testing. However, many limitations stem from aspects of cohesive soil behaviour that current numerical modelling techniques overlook. The creation of a sophisticated material model tailored to cohesive soil behaviour is crucial for future progress. Nonetheless, the fluid-like behaviour displayed by cohesive soils under high-strain-rates suggests that numerical modelling using SPH particles holds promise for further advancements.

5.10 Recommendations for future modelling improvements

Based on the modelling limitations identified, several recommendations can be made to improve future simulations and enhance material accuracy. These recommendations focus on addressing current challenges, refining modelling techniques, and ensuring more reliable results from LS-DYNA models. They are as follows:

1. Improved material model card
    - Develop a dedicated material model specifically for cohesive soils such as kaolin clay, capturing their unique mechanical and physical behaviours under various conditions.
    - Update the material properties to include strain-rate-dependent behaviour, incorporating viscoplasticity and non-linear strain hardening for cohesive soils.
2. Dedicated EOS adaptable to strain rate testing
    - Develop a strain-rate-sensitive EOS tailored to cohesive soils, allowing the model to account for the dynamic compaction and deformation behaviour of materials such as kaolin clay.
    - Incorporate mechanisms to adapt EOS parameters dynamically based on the specific strain rates encountered during the simulation.
3. SPH improvements for cohesive properties between particles
    - Introduce cohesive interaction models between SPH particles to replicate the bonding forces observed in cohesive soils, such as inter-particle adhesion and friction.
    - Implement advanced particle interaction algorithms that better simulate the behaviour of cohesive soils during extreme deformation.
    - Explore mesh refinement or adaptive meshing strategies to allow dynamic adjustments during high-strain-rate conditions, maintaining the sample's structural integrity and reducing computational noise.
    - Improve particle connectivity generation to ensure more accurate stress transmission and deformation patterns.
4. Optimised confining ring design
    - Introduce damping mechanisms or materials in the confining ring to mitigate excessive vibrations during high-strain-rate loading.
    - Use materials with higher damping capacities to absorb and reduce noise and unwanted resonance effects in the confining ring.

By implementing these recommendations, future modelling efforts can achieve greater accuracy and reliability in simulating the high-strain-rate behaviour of cohesive soils, bridging the gap between experimental observations and numerical predictions.

5.11 Summary

This chapter outlines the development and evaluation of the numerical models aimed at simulating the high-strain-rate phase behaviour of kaolin clay in both unconfined and fully confined SHPB experiments. Material models were carefully chosen to capture the fluid-like behaviour typical of cohesive soils, along with relevant geotechnical variables.

Initially, a 2D axisymmetric shell model was created to represent the unconfined SHPB behaviour of kaolin clay, with the *MAT_MOHR_COULOMB model proving to be fairly accurately. However, the significant volume change resulting from instantaneous sample extrusion during fully confined SHPB tests led to premature termination of model computation, preventing the recording of useful stress data.

Various numerical modelling techniques were explored to address the negative volume error, with SPH node modelling of the sample proving most effective. SPH node modelling was tailored to simulate fluids undergoing significant deformation and volume change, making it ideal for representing high-strain-rate cohesive soil behaviour. While physically confined testing typically resulted in lateral extrusion from the edges of the confining ring, the modelled confined scenario restricted lateral extrusion, amplifying the vibration effect of the steel elements due to the sample's lateral deformation. As a result, a combination of rigid and elastic elements was utilised to develop a confining ring that restricts translational movement yet remains capable of recording stress data.

The material's strain rate dependency posed challenges in modelling the SHPB tests using LS-DYNA, as no suitable material cards were available. The absence of dedicated material cards for cohesive soil modelling in LS-DYNA complicated the depiction of the observed behaviour during testing. Consequently, a general material card *MAT_MOHR_COULOMB, was used to model the kaolin clay.

In the unconfined SHPB models, the incident pulse closely matched that of the SHPB tests, validating the model setup. However, the reflected pulse exhibited considerable differences, resulting in lower front and back stress responses, attributable to the stress wave's inability to propagate through the sample. This occurred because the SPH particles dissipated instantly upon contact with the incident pulse.

In the confined SHPB models, the front, back and radial stresses are considerably higher than those obtained from the SHPB tests, since the confining ring provides a perfect seal in the model enabling the stress wave to propagate through the sample more easily. This results in considerably greater values for front, back and radial stresses. The rising trend observed for the front and back stresses in testing was also noticed in the model. The radial stresses obtained in the model, using a composite 1/3 rigid and 2/3 elastic confining ring with a perfect seal, significantly surpass those observed in testing. This is because the numerical model is a perfect test representation from which to obtain the radial stress, therefore it is unable to capture the inertial effect from the incident bar or permit sample extrusion.

Comparing the test results with the numerical model outcomes for kaolin clay samples at varying moisture contents revealed that the models failed to replicate the phase behaviour observed in experimental testing (Chapter 4). This discrepancy can be attributed to LS-DYNA's limitations in modelling cohesive soil properties accurately, leading to erroneous modelling findings. As a result, recommendations for future modelling improvements were proposed to guide the advancement of high-strain-rate cohesive soil behaviour in numerical simulations.

The FEM software LS-DYNA was used to simulate the unconfined and confined SHPB tests performed on kaolin clay samples at varying moisture contents. While modelling the test setup posed no significant challenges, clear limitations were observed in LS-DYNA when comparing experimental and numerical modelling results: there is no dedicated material card model for cohesive soils, no cohesive properties in the software and very limited use of SPH for modelling the high-strain-rate behaviour of cohesive soils. These findings underscore the existing gap in modelling the high-strain-rate behaviour of cohesive soils.

To address the identified modelling limitations, several recommendations were proposed to improve the accuracy and reliability of LS-DYNA simulations for high-strain-rate cohesive soil behaviour. These include developing a dedicated material model for cohesive soils such as kaolin clay, incorporating strain-rate-dependent properties such as viscoplasticity and non-linear strain hardening, and creating a strain-rate-sensitive Equation of State (EOS). Enhancements to SPH modelling were also suggested, including cohesive interaction models, adaptive meshing, and improved particle connectivity. Finally, optimising the confining ring design with damping mechanisms and high-damping materials was recommended to minimise noise and vibrations, bridging the gap between numerical and experimental results.

The development of numerical models led to an investigation into the internal stress propagation within the sample. Stress distribution analysis reveals that the initial radial stress wave, propagating from the centre outward, remains unaffected by confinement. However, the introduction of confinement prevents sample volume loss and facilitates the superposition of internal radial stress waves, resulting in the concentration of lateral stresses at the specimen's edge.

The research approach in this chapter highlights the significance of the numerical modelling evaluation, which aims to represent the phase behaviour observed in experimental testing. Despite its evident limitations in capturing the high-strain-rate behaviour of cohesive soils, it provides valuable insights for future modelling improvements and further development.

Chapter 6

Data-driven parametric modelling of SHPB tests on cohesive soils

6.1 Introduction

This chapter focuses on developing two data-driven parametric models using test data from SHPB experiments on kaolin clay samples. These experiments, detailed in Chapter 4, involved samples with varying moisture content levels and were conducted under both unconfined and confined conditions. Key parameters such as confinement, strain rate, and moisture content influenced the material's behaviour and, therefore, guide the design of the physics-informed parametric models. The background mathematics, methodology, and theory to design these parametric models are introduced, followed by the design method used to build and validate them. For more information on machine learning methods and tools, refer to Section 2.7 in the literature review. The methodology, design processes, and findings detailed in this chapter have been published in the International Journal of Impact Engineering (Van Lerberghe, Pasquale, Rodriguez, Barr, Clarke, Baillargeat and Chinesta 2024), and is available in Appendix A.6.

Experimental testing, while time-consuming and costly, delivers highly accurate results. Numerical modelling, though faster, faces notable limitations in accuracy, as seen in Chapter 5. Parametric modelling, by contrast, provides a valuable balance between speed and accuracy, incorporating initial test data and leveraging physics-informed principles to generate high-quality results efficiently. However, it still relies on initial test data for development and cannot operate independently.

The work in this chapter is part of a collaborative effort involving research groups from ENSAM, France, and CNRS@CREATE at NUS, Singapore, specialists in machine learning and parametric modelling. Their guidance on the selection of appropriate machine learning tools for my project was invaluable.

In this work, I led, arranged, and coordinated the project, identifying and bringing together the collaborators. I was responsible for the conceptualisation, methodology development, investigation, testing, and analysis. I also took charge of the experimental and parametric modelling efforts, optimised the models, and led the writing process. Angelo Pasquale, Sebastian Rodriguez, and Francisco Chinesta, from ENSAM, contributed to the initial model testing, analysis, model optimisation, writing, and review. Andrew D. Barr, Sam D. Clarke, and I, from the University of Sheffield, worked closely together, with Andrew and Sam providing review, writing, and supervision support. Additionally, Francisco Chinesta and Dominique Baillargeat, from CNRD@CREATE at the National University of Singapore (NUS), contributed through supervision, conceptualisation, and review.

6.2 Parametric modelling: background, methodology, and theory

Previous experimental research on kaolin clay has investigated its behaviour under various confinement, moisture content, and strain rate conditions (Van Lerberghe, Li, Barr and Clarke 2024*a*). To address the time-consuming nature of high-strain rate testing, machine learning methods now utilise collected test data to develop data-driven parametric models that supplement experimental data. These models provide a comprehensive dataset, which can be used to calibrate and assess future numerical models, offering a more integrated approach for interpreting SHPB testing. For more detailed information on the different parametric models available and their capabilities, refer to Chapter 2.7.

Now, a general procedure for constructing parametric surrogates of curves is presented, using extensive literature and reviews on state-of-the-art MOR technologies (Benner et al. 2017, Rozza et al. 2020*a*,*b*):

1. Consider a scenario where experimental data is collected, comprising of input parameters $\mathbf{p}_i$ and corresponding output curves $g(x;\mathbf{p}_i)$. Each curve represents the system's behaviour under various conditions, with $\mathbf{p}_i$ representing geometrical or material parameters. In simulation-based engineering, data $g(x;\mathbf{p}_i)$ is typically obtained through simulation software runs, with the parameters of interest $\mathbf{p}_i$ potentially including modelling features.

2. Each experimental data point can be viewed as a snapshot $(\mathbf{p}_i, g(x;\mathbf{p}_i))$, where $i = 1, 2, ..., n_s$, (n_s is the number of sampling points used for training) depicting parameter combinations and their corresponding output curves.

3. Dimensionality reduction techniques such as Principal Component Analysis (PCA) or Proper Orthogonal Decomposition (POD) are applied directly to test data to extract dominant modes of variability in the output curves $g(x;\mathbf{p}_i)$.

4. The reduced basis functions $\phi_j(x)$ are constructed by identifying the dominant modes through dimensionality reduction. These basis functions effectively capture the essential features of the output curves.

5. Using the reduced basis functions, a surrogate model $\hat{g}(x,\mathbf{p})$ is constructed to approximate the output curves $g(x;\mathbf{p}_i)$ based on the input parameters $\mathbf{p}_i$ and the domain x. This surrogate model can be formulated as:

$$\hat{g}(x,\mathbf{p}) = \sum_{j=1}^{m} \lambda_j(\mathbf{p})\phi_j(x)$$

   where $\lambda_j(\mathbf{p})$ are the coefficients of the surrogate model, which depend on the parameters $\mathbf{p}$. The reduced basis functions $\phi_j(x)$ where x is the domain variable (e.g. time or spatial coordinate), capture the dominant modes of variability, with m representing the number of retained modes and j indexing each mode or basis function.

6. Surrogate models for $\lambda_j(\mathbf{p})$ can be built by training a regression algorithm on the available dataset, to establish links between input parameters and measured output.

In polynomial regressions, addressing the challenges of high-dimensional parametric problems has led to the development of novel techniques such as the Proper Generalised Decomposition (PGD) (Ibáñez Pinillo et al. 2018, Sancarlos et al. 2023, Champaney, Chinesta and Cueto 2022). PGD, a tensor-based method, represents high-dimensional data by utilising separable representations and a greedy iterative algorithm for adaptive basis construction. It finds applications across various engineering and scientific fields, such as blast and impact dynamics in this case.

6.2.1 POD-based modes extraction

To construct the snapshots matrix for training data $\{g_i(x)\}_{i=1}^{n_s}$, for $x \in X = \{x_j\}_{j=1}^{n_x}$ utilised in this study, consider the following procedure:

$$\mathbf{S} = \begin{bmatrix} \mathbf{g}_1 & \mathbf{g}_2 & \cdots & \mathbf{g}_{n_s} \end{bmatrix} \in \mathbb{R}^{n_x \times n_s},$$

where $\mathbf{g} \in \mathbb{R}^{n_x \times 1}$ contains the evaluations of $g(x)$ over the discrete ensemble X.

Next, a reduced factorisation of the snapshots matrix is achieved through a standard truncated POD of rank r:

$$\mathbf{S} \approx \mathbf{U}\mathbf{\Sigma}\mathbf{V}^T$$

where $\mathbf{U} \in \mathbb{R}^{n_x \times r}$, $\mathbf{\Sigma} \in \mathbb{R}^{r \times r}$, $\mathbf{V} \in \mathbb{R}^{n_s \times r}$. From these, we can define the matrices of POD modes and coefficients, as follows:

$$\mathbf{\Phi} \coloneqq \mathbf{U} = \begin{bmatrix} \boldsymbol{\phi}_1 & \boldsymbol{\phi}_2 & \cdots & \boldsymbol{\phi}_r \end{bmatrix}, \; \mathbf{\Lambda} \coloneqq \mathbf{V}\mathbf{\Sigma} = \begin{bmatrix} \boldsymbol{\lambda}_1 & \boldsymbol{\lambda}_2 & \cdots & \boldsymbol{\lambda}_r. \end{bmatrix}$$

The matrix $\mathbf{\Phi}$ contains, by columns, the functions of the reduced POD basis $\{\boldsymbol{\phi}_i(x)\}_{i=1}^{r}$ evaluated at points in X, while $\mathbf{\Lambda}$ collects the projection coefficients into the reduced basis. For a generic curve $g_k(x)$ belonging to the training dataset, where $k = 1, \ldots, n_s$ and $x \in X$, its reduced counterpart is given by:

$$g_k^{(r)}(x) = \sum_{i=1}^{r} \lambda_{k,i} \phi_i(x), \tag{6.1}$$

and, in particular, its discrete form reads

$$\mathbf{g}_k^{(r)} = \mathbf{\Lambda}_{k,\bullet} \mathbf{\Phi}^T,$$

where $\mathbf{\Lambda}_{k,\bullet}$ denotes the k-th row of the matrix $\mathbf{\Lambda}$.

Now, let's consider a parametric curve dependent on d features $\bar{\mathbf{p}} \in \Omega$, denoted as $g(x; \bar{\mathbf{p}})$, where $x \in X$. From Equation (6.1) it is evident that once the reduced basis matrix $\mathbf{\Phi}$ is available, this function is projected onto this basis solely through the POD (parametric) coefficients $\{\lambda_i(\mathbf{p})\}_{i=1}^{r}$:

$$g^{(r)}(x; \bar{\mathbf{p}}) = \sum_{i=1}^{r} \lambda_i(\bar{\mathbf{p}}) \phi_i(x).$$

The equation above indicates that a reduced-order parametric metamodel for the curves can be constructed using only the set of coefficients $\{\lambda_i(\mathbf{p})\}_{i=1}^{r}$. Specifically, the following parametric function shall be constructed:

$$\mathbf{f}(\mathbf{p}) = \begin{bmatrix} \lambda_1(\mathbf{p}) \\ \lambda_2(\mathbf{p}) \\ \vdots \\ \lambda_r(\mathbf{p}) \end{bmatrix} : \Omega \subset \mathbb{R}^d \rightarrow \mathbb{R}^r,$$

from the training dataset available as $\{\mathbf{p}_k, \mathbf{\Lambda}_{k,\bullet} = (\lambda_{k,1}, \lambda_{k,2}, \ldots, \lambda_{k,r})\}_{k=1}^{n_s}$, obtained after the POD.

6.2.2 Advanced PGD-based sparse nonlinear regressions

Nonlinear regression methods such as the sparse Proper Generalised Decomposition (sPGD) are increasingly vital for managing complex parameters efficiently while preserving accuracy, complementing MOR techniques for real-world engineering problems (Ibáñez Pinillo et al. 2018, Sancarlos et al. 2023, Champaney, Chinesta and Cueto 2022). These methods have recently gained significant attraction in industry, with various approaches expanding their applicability for approximating parametric curves (Champaney, Pasquale, Ammar and Chinesta 2022*a*). For instance, sPGD can be used to predict intrusion and acceleration curves in car crash simulations (Pasquale et al. 2022*b*). These techniques are effective for virtual parametric testing of battery mechanical performance, aiding in assessing safety conditions in electric vehicles (Schmid, Pasquale, Ellersdorfer, Champaney, Raffler, Guévelou, Kizio, Ziane, Feist and Chinesta 2023, Schmid, Pasquale, Ellersdorfer, Raffler, Champaney, Ziane, Chinesta and Feist 2023). sPGD-based regressions have been used to define a hybrid twin of resin transfer moulding (RTM) process, accurately predicting the resin flow-front of a complex model throughout its entire time history (Rodriguez et al. 2023*b*).

In this section, the focus shifts to the concept behind the PGD-based regression methods for constructing metamodels dependent on d features, which are used in this study. The discussion centres on scenarios where a single-value output is measured for a given parameter choice (Champaney, Pasquale, Ammar and Chinesta 2022*a*). This setup enables the prediction of parametric curves using the coefficients $\lambda_i(\boldsymbol{p})$ corresponding to the POD modes, as previously suggested.

For each coefficient $\lambda_i(\mathbf{p})$, the challenge lies in constructing the function

$$f(p^1, \ldots, p^d) : \Omega \subset \mathbb{R}^d \rightarrow \mathbb{R},$$

which depends on d features (parameters) p^k, $k = 1, \ldots, d$, within the parametric space Ω, given a sparse sample of n_s points and their corresponding outputs.

The sparse PGD (sPGD) represents the function f using a low-rank separated representation

$$f(p^1, \ldots, p^d) \approx \tilde{f}^M(p^1, \ldots, p^d) = \sum_{m=1}^{M} \prod_{k=1}^{d} \psi_m^k(p^k), \tag{6.2}$$

constructed from rank-one updates within a greedy constructor.

Here, $\tilde{f}^M$ denotes the approximation, M the number of employed modes (sums), and ψ_m^k the one-dimensional functions pertaining to mode m and dimension k.

The functions ψ_m^k, $m = 1, \ldots, M$ and $k = 1, \ldots, d$, are derived from a standard approximation basis $\mathbf{N}_m^k$ using coefficients $\mathbf{a}_m^k$:

$$\psi_m^k(p^k) = \sum_{j=1}^{D} N_{j,m}^k(p^k) a_{j,m}^k = (\mathbf{N}_m^k)^T \mathbf{a}_m^k,$$

where D represents the number of degrees of freedom (nodes) of the chosen approximation and $\mathbf{N}_m^k$ is the vector collecting the shape functions.

In standard regression, the approximation $\tilde{f}^M$ is obtained by minimising the error function

$$\tilde{f}^M = \arg\min_{f^*} \|f - f^*\|_2^2 = \arg\min_{f^*} \sum_{i=1}^{n_s} |f(\mathbf{p}_i) - f^*(\mathbf{p}_i)|^2,$$

where $\tilde{f}^M$ takes the separated form of Equation (6.2), n_s is the number of sampling points used for training, and $\mathbf{p}_i$ are the vectors containing the input data points of the training set. It is important to note that to avoid overfitting, the number of basis functions D must satisfy $D < n_s$.

The approximation coefficients for each one-dimensional function are computed using a greedy algorithm. Given the approximation up to order $M-1$, the M-th order term is determined as

$$\tilde{f}^M = \sum_{m=1}^{M-1} \prod_{k=1}^{d} \psi_m^k(p^k) + \prod_{k=1}^{d} \psi_M^k(p^k)$$

The resulting function is expected to approximate f not only in the training set but also at any point $\mathbf{p} \in \Omega$.

The main challenge is balancing detailed approximations with limited available data while avoiding overfitting. To address this, a modal adaptivity strategy (MAS) was introduced alongside sPGD. Yet, achieving desired accuracy often leads to overfitting or premature termination of the algorithm with MAS, resulting in a PGD solution of low-order approximation functions that fails to capture the desired richness (Ibáñez Pinillo et al. 2018). Additionally, in scenarios with sparse non-zero elements in the interpolation basis, MAS struggles to accurately recognise the true model, leading to decreased accuracy.

To overcome these challenges, various regularisation methods were proposed (Sancarlos et al. 2023), combining L^1 and L^2 norms affecting coefficients $\mathbf{a}_m^k$. The L^1 norm, defined as $\|\mathbf{a}\|_1 = \sum_{i=1}^{n} |a_i|$, promotes sparsity in solutions by encouraging many coefficients to be zero. In contrast, the L^2 norm, defined as $\|\mathbf{a}\|_2 = \sqrt{\sum_{i=1}^{n} a_i^2}$, penalises larger coefficients more heavily, leading to smoother solutions. These techniques aim to enhance predictive performance beyond sPGD's capabilities or to construct parsimonious models while improving predictive accuracy.

6.3 SHPB test result summary

Using the kaolin clay samples prepared in Chapter 3, and the SHPB tests performed under both unconfined and confined conditions in Chapter 4, this section summarises the high-strain-rate phase behaviour identified in Sections 4.5.4 and 4.5.5 to develop data-driven parametric models for both test conditions.

The SHPB test signals for the incident bar, transmitter bar and confining ring were processed using the open-source Python algorithm `SHPB_Processing.py` (Van Lerberghe, Li, Barr and Clarke 2024*b*). This algorithm incorporates the subroutine `dispersion.py`, which implements Tyas and Pope's dispersion-correction approach (Tyas and Pope 2005). This ensures accurate representation of the sample's axial and radial stresses and strains during testing. For further details regarding the analysis of the signals collected from the SHPB experiments refer to Sections 4.4.6 and 4.4.7.

The behaviour of the tested kaolin clay samples can be categorised into four distinct "phases", each defined by its stress transmission characteristics, termed the "back stress" in SHPB tests (Van Lerberghe, Li, Barr and Clarke 2024*a*). These phases are delineated by the air volume ratio V_{air}/V, water volume ratio V_{water}/V, and the maximum experimental strain attained during the experiment, as illustrated in Figure 6.1a:

- **Phase 0:** Encompasses all dry specimens, positioned on the y-axis in Figure 6.1a.
- **Phase 1:** Comprises partially-saturated specimens where soil pores are primarily filled with air. The maximum moisture content for phase 1 is defined by the boundary formed by the intersection of the air and water ratio trendlines, denoted as Point A in Figure 6.1a.
- **Phase 2:** Comprises partially-saturated specimens where soil pores are primarily filled with water. The upper limit of moisture content is defined by the intersection of the air volume ratio with the max experimental strain, marked as Point B in Figure 6.1a.
- **Phase 3:** Defines experiments which begin partially-saturated, but reach full saturation during testing.

The behaviour of soil specimens vary across the four phases, depending on whether testing is unconfined or fully confined.

In unconfined conditions (Figure 6.1b), each phase exhibits a distinct stress transmission pattern, with increased moisture content correlating with reduced peak stress due to enhanced lateral movement and specimen extrusion. While moisture content minimally impacts stress transmission within each phase, back stress transmission increases with rising strain rates.

In fully confined conditions (Figures 6.1c), phases 0 and 1 primarily involve the compaction of the dry soil fraction, showcasing a similar shock absorption effect on transmitted stress. The attainment of high strains in confined SHPB tests eliminates phases 2 at higher strain rates, leading to an abrupt transition between phases 1 and 3. Upon reaching saturation, clay samples assume fluid-like behaviour with $\nu = 0.5$, resulting in a significantly heightened stress transmission.

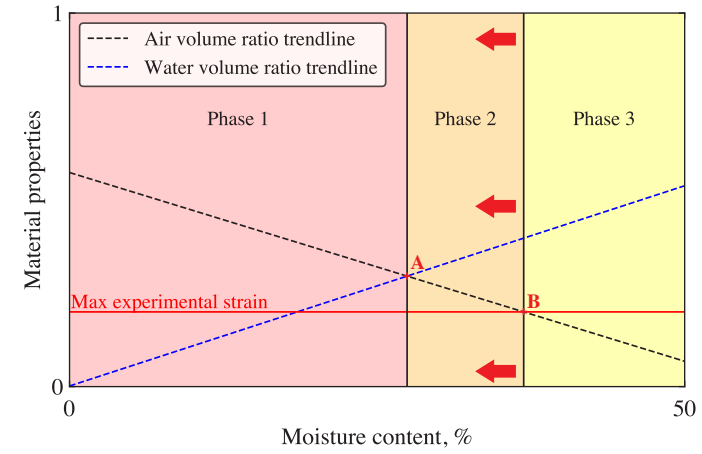

(a)

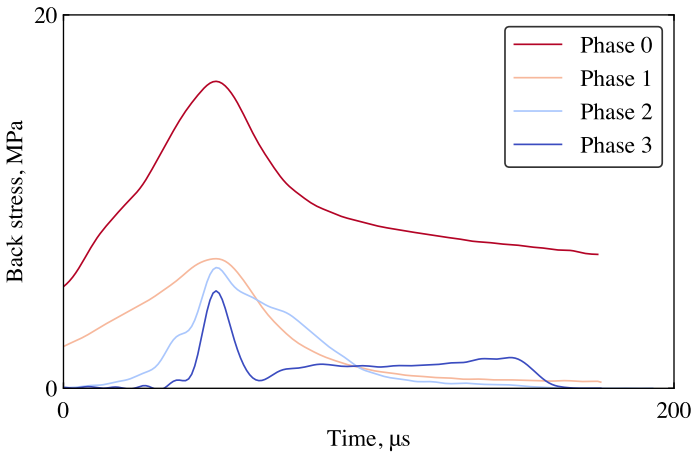

(b)

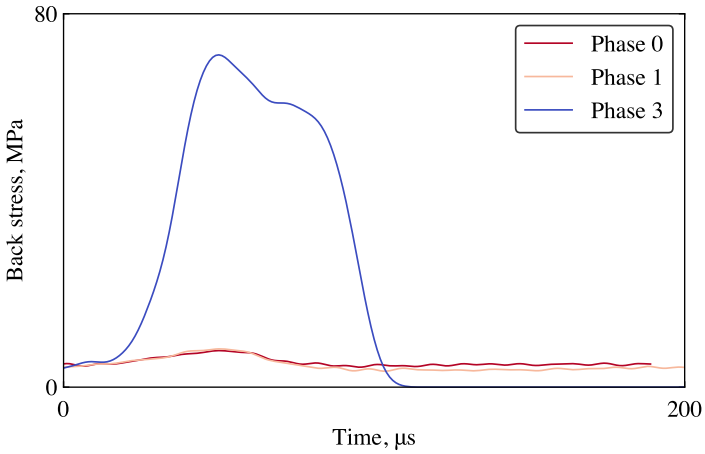

(c)

Figure 6.1: (a) Phase behaviour observed in SHPB testing of kaolin clay, defined by air and water volume ratios and maximum experimental strain. The indicative stress transmission through the clay in each phase at 2800 s^{-1} is depicted for (b) unconfined and (c) fully confined test conditions.

6.4 Data-driven classification

The classification of the data was conducted manually based on both the experimental SHPB test results, the phase diagram illustrated in Figure 6.1a and the initial sample parameters. The data obtained from the SHPB tests on the kaolin clay samples, along with their initial parameters, can be classified into five categories represented by a Russian doll model, as illustrated in Figure 6.2: SHPB testing, unconfined and confined conditions, strain rate, moisture content, and phase number.

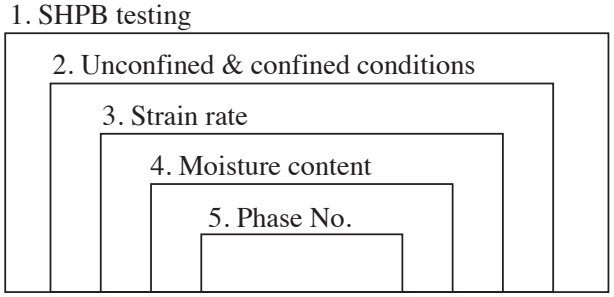

Figure 6.2: Diagram of the classification of experimental SHPB test data.

These parameters are ranked from 1 to 5, each denoting a different level of specificity in data classification. Parameter 1 encompasses all the tests, while parameter 5 represents a more specific subset. The parameters are defined as follows:

1. "SHPB testing" encompasses all tests conducted using the SHPB apparatus.
2. "Unconfined & confined conditions" categorises the tests which were performed under "unconfined" or "confined" conditions.
3. "Strain rate" indicates the tests were conducted at different strain rates: 1200, 1900, 2800 s^{-1} for unconfined and 2600, 2800 and 3100 s^{-1} for confined.
4. "Moisture content", reflects the varying moisture levels of the kaolin clay samples tested, ranging from 0 to 44 %.
5. "Phase No." assigns a specific phase number (0, 1, 2 or 3) to each moisture content, as detailed in Section 6.3.

A total of 144 SHPB experimental tests were carried out on kaolin clay samples spanning moisture contents from 0 to 44 %. Among these, 98 tests were performed under unconfined conditions, while 46 tests were conducted under fully confined conditions. The majority of the test data was utilised to develop the parametric models, with the exception of one test from each condition, which was reserved for subsequent model validation.

The insights gained into the high-strain-rate behaviour of cohesive soils, as discussed in Section 6.3, enabled the categorisation of the test data into separate confinement conditions and different phase behaviours, based on the sample's moisture content and strain rate.

This physics-informed classification, was conducted manually, guided by test findings, with the strain rate identified as the key parameter influencing the material's response. The model simplifies from a polynomial regression to a linear analysis, with "strain rate", parameter 3, as the key parameter. The analysis within each material phase number showed that variations in moisture content had no discernible impact on the overall response. Consequently, the mean response was used for the parametric models. In summary, for unconfined conditions, the strain rate was 1200, 1900, 2800 s^{-1}, with four material phases, while for confined conditions, it was 2700, 2800 and 3100 s^{-1} with 3 material phases, with phase 2 disappearing at 2700 s^{-1} under confined conditions (as confirmed in Section 4.5.5.4). Figures 6.3 and 6.4 illustrate the test distribution of the various strain rates and moisture contents employed to build the data-driven parametric models, as well as the gaps these models will address.

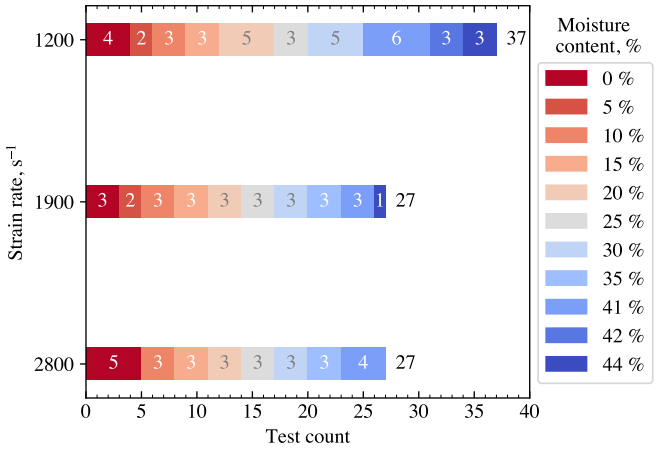

Figure 6.3: Unconfined SHPB test distribution of strain rates and moisture contents used for the parametric model.

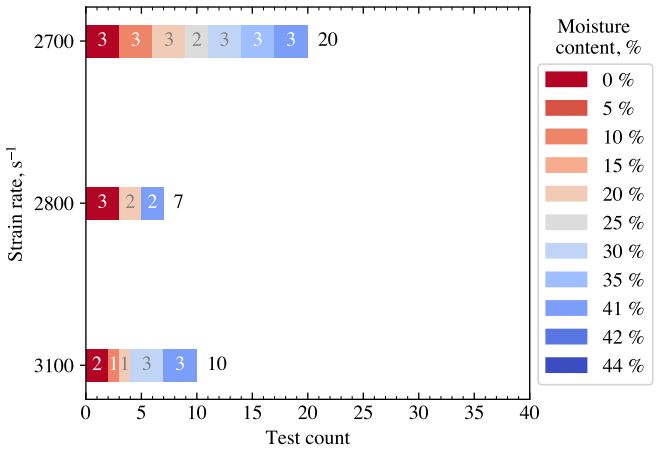

Figure 6.4: Confined SHPB test distribution of strain rates and moisture contents used for the parametric model.

6.5 Parametric model

With the data classified into corresponding SHPB test conditions and phase numbers based on strain rate and moisture content, attention shifts to the parametric model. Figure 6.5 details the structure of the parametric model used for training the test data, comprised of inputs, a surrogate model, and outputs.

The input section focuses on the model's input parameters: the Design of Experiments (DOE) and Quantity of Interest (QOI). The DOE represents the parameter the model trains on, which in this case, is the key parameter: strain rate. Three strain rate values are utilised for each confinement condition. The QOI refers to the mean data properties of interest used for training against the DOE. For unconfined SHPB testing, there are five QOIs: strain, front stress, back stress, mid stress and time. Confined SHPB testing includes six QOIs: strain, front stress, mid stress, back stress and radial stress and time.

Data training for each model is facilitated by the surrogate model, made of two sections: POD mode extraction and sPGD regression. Since there is only one parameter, strain rate, POD mode extraction focuses on a single mode, mapping the data's curve behaviour along this parameter. Subsequently, sPGD regression utilises this information to predict the data's behaviour based on this relationship along the set parameter.

The POD modes extraction and sPGD regression methodology used to build these data-driven parametric models are detailed in Sections 6.2.1 and 6.2.2, respectively. These sections clearly outline the steps used to design the surrogate models, emphasising the use of core mathematical principles. Notably, no internal Python libraries such as `TenserFlow` or `Keras` were used; instead, the models were built using the Python libraries `scipy` and `numpy`.

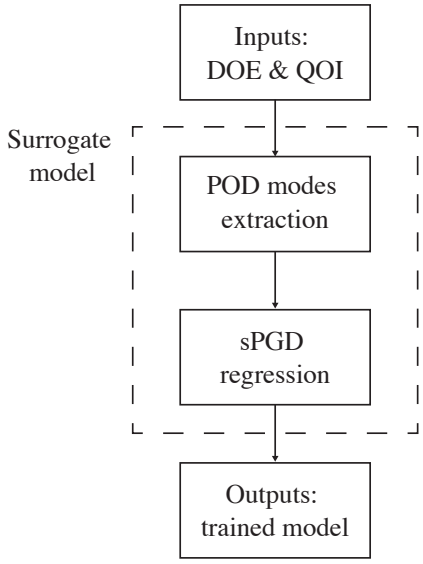

Figure 6.5: POD_sPGD flowchart.

After passing through the surrogate model, the training data is saved, resulting in the creation of four different models for each phase number, as illustrated in Figure 6.6.

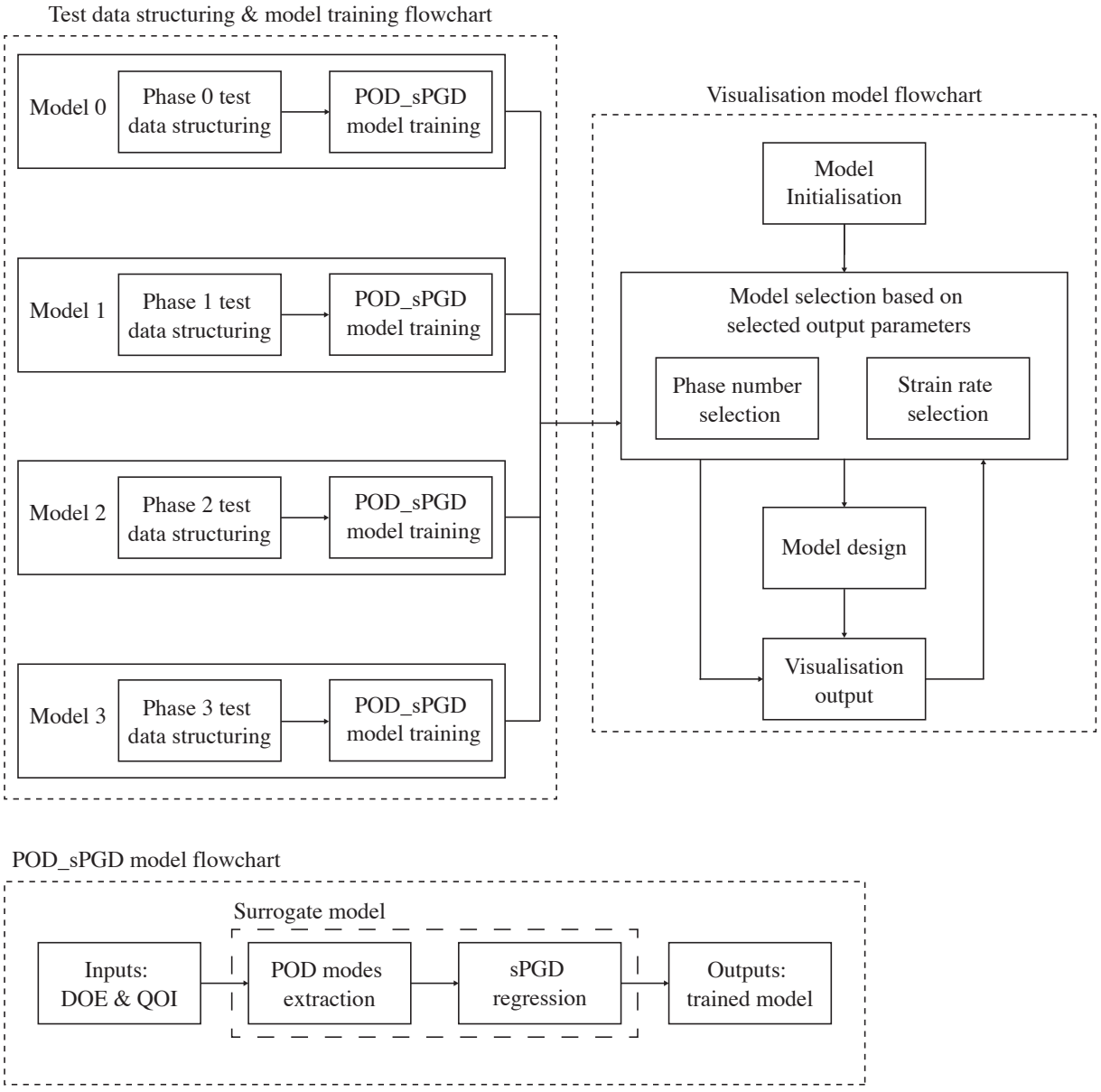

Figure 6.6: Overall design flowchart of the data-driven parametric models.

6.6 Visualisation model

After training the tests data using the POD_sPGD model, the trained model results are saved according to their respective phase number. This process is illustrated in Figure 6.6, termed as the test data structuring and model training flowchart.

This trained data is utilised for the visualisation model, as depicted in the visualisation flowchart shown in Figure 6.6. The visualisation model consists of a four sections: model initialisation, model selection based on selected output parameters, model design and visualisation output. Model initialisation establishes the input parameters and widget architecture. The model selection section is made of the phase number and strain rate selection functions. It established the relationship between the trained POD_sPGD models for each phases number and the corresponding moisture content ranges obtained from testing. The model design encompasses interactive functionalities, while the visualisation output updates the visual plots based on selected moisture content and strain rate. As the selected strain rate changes, the model representing the data remains the same. However, altering moisture content prompts a transition between different material phase number, resulting in a change of the model number selected to represent the data.

The flowchart depicted in Figure 6.6 guides the creation of two widgets for each SHPB test condition, using the trained mean data. These final interactive representations, are displayed in Figure 6.7 and 6.8. The unconfined SHPB test model features four plots, representing the four QOIs: strain, front stress, back stress and mid stress over time. Conversely, the confined SHPB test model includes five plots, representing the five QOIs: strain, front stress, mid stress, back stress and radial stress over time.

The plot axes in Figures 6.7 and 6.8 adjust responsively based on the selected moisture content, corresponding to a specific phase at a given strain rate. The y-axis dynamically adjusts to accommodate the maximum potential value.

Confidence patches, depicting the 90% confidence interval based on the standard deviation of the test data, are included in Figures 6.7 and 6.8 in light grey for both unconfined and confined SHPB test conditions. They are especially crucial for unconfined SHPB tests due to potential errors associated with testing.

The illustrations in Figures 6.7 and 6.8 show the final design of these tools. They feature sliders for strain rate and moisture content, facilitating adjustments between the different phase behaviours of cohesive soil. The sliders are user-friendly, allowing for quick and interactive changes. The selected values for moisture content and strain rate are displayed on the right hand side of each slider.

Additionally, a point picking option is available above the sliders, enabling selection of specific moisture content and strain rate values, with the complete selected ranges next to them. Both options provide immediate visualisation of cohesive soil responses under the selected parameters, offering instant information.

These interactive visuals were developed using the open-source Python library `matplotlib`, allowing for easy modification and tailoring to specific user requirements. Leveraging a widely available programming library in Python ensures versatility and accessibility, empowering engineers to rapidly and efficiently utilise the appropriate visualisation model for threat protection.

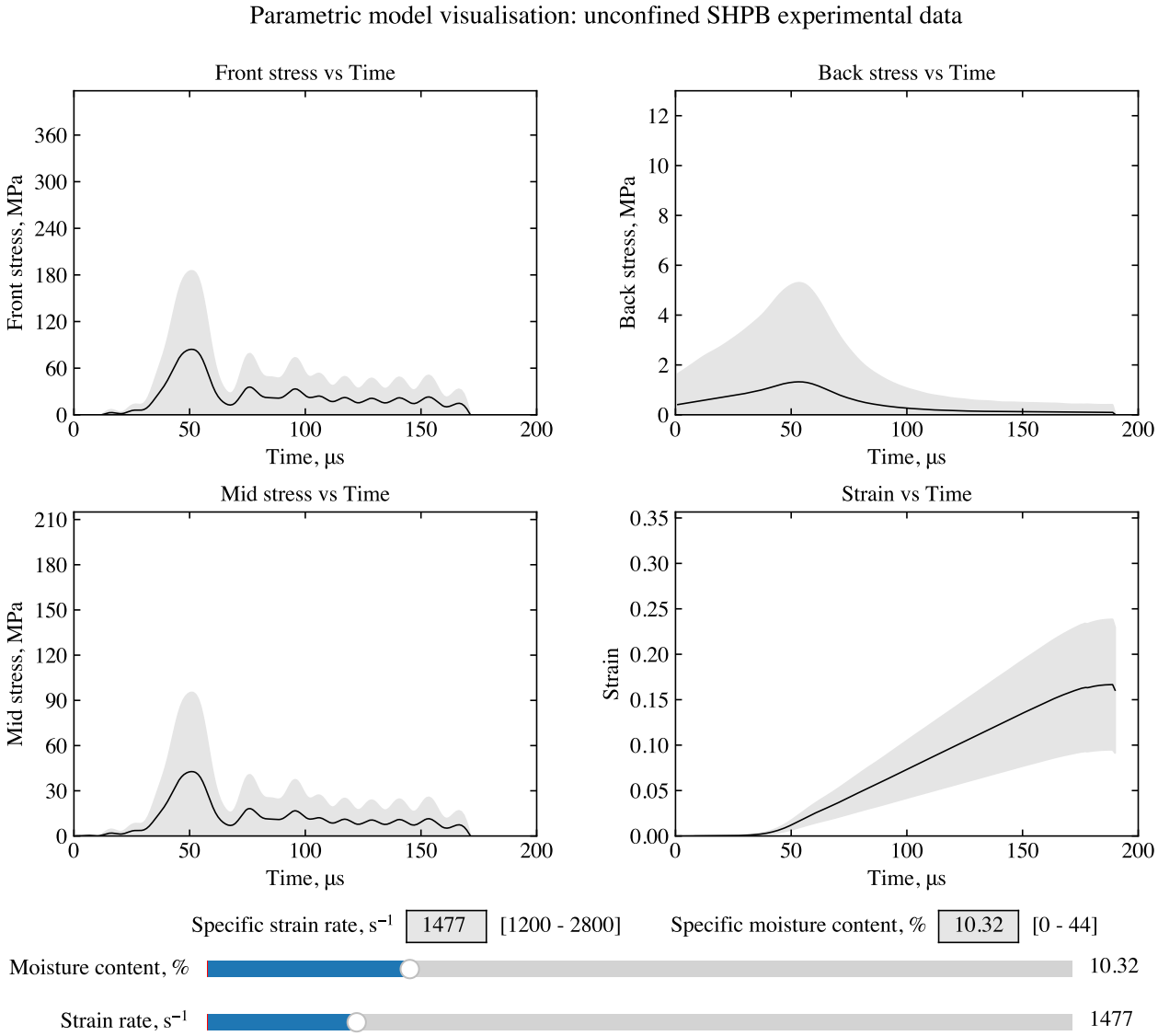

Figure 6.7: Parametric model visualisation of unconfined SHPB experimental data.

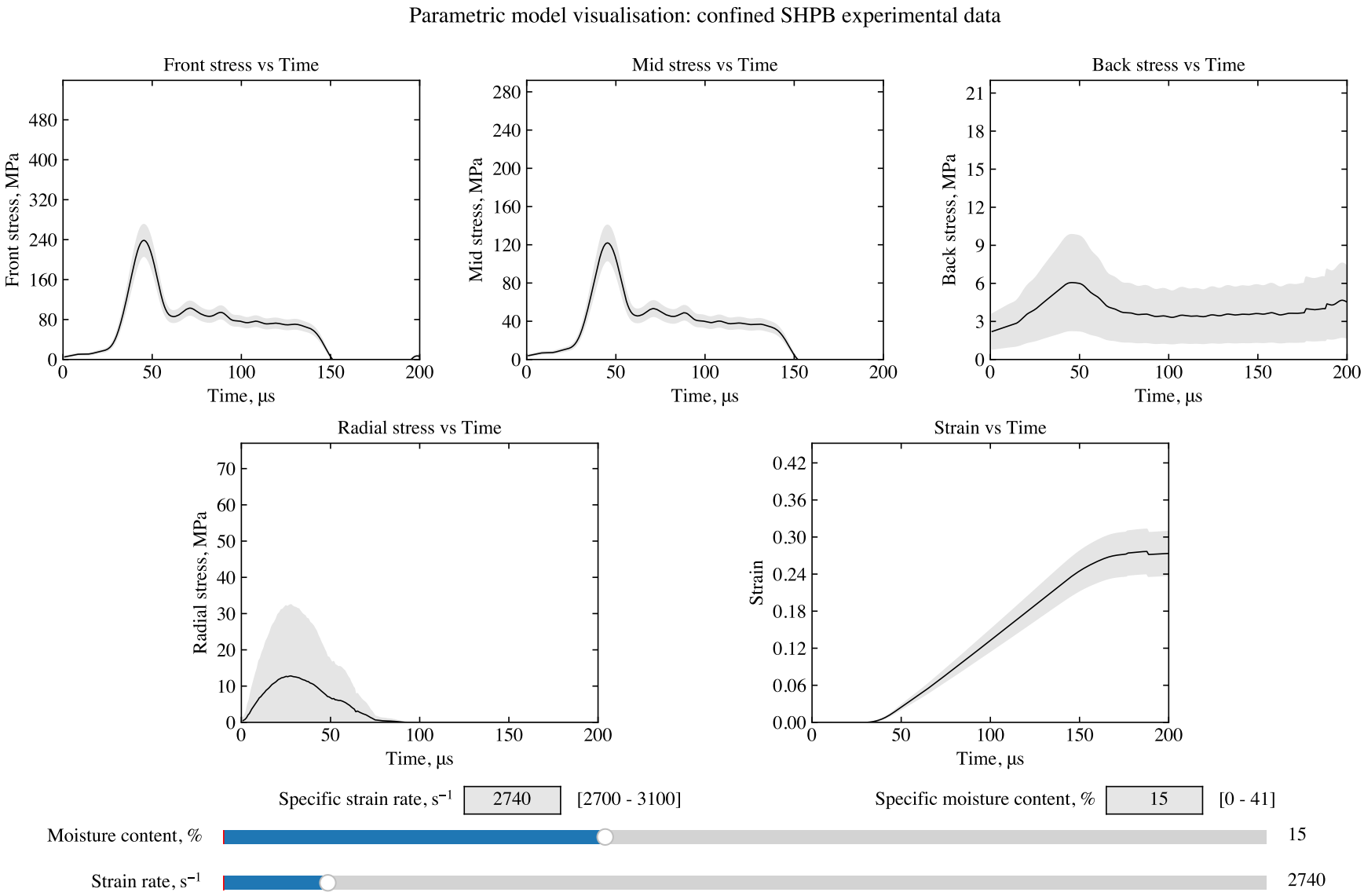

Figure 6.8: Parametric model visualisation of confined SHPB experimental data.

6.7 Model validation

To validate the data-driven parametric models, a comparative evaluation against a random SHPB test is imperative. This involves testing a kaolin clay sample with a specific moisture content under both unconfined and confined conditions using the SHPB apparatus, at a specific strain rate. The test results in red are compared against the model predictions in black (Figure 6.9 and 6.10).

The omitted unconfined SHPB test was conducted on a sample with a moisture content of 11.32 % at a speed of 12.0 m/s, corresponding to a strain rate of 1996 s^{-1}. The confined SHPB test involved a sample with a moisture content of 21.36 % at a speed of 20.0 m/s, resulting in a strain rate of 2976 s^{-1}.

The comparative results between the data-driven parametric models and the additional SHPB tests are depicted in Figures 6.9 and 6.10, where the supplementary tests are plotted in red on the interactive visual representations. When qualitatively comparing the newly performed tests and the data-driven parametric models on the interactive illustrations, the predicted representation exhibits remarkable accuracy, closely resembling the expected material response seen in testing. In both test conditions, the maximum amplitude is slightly higher, which is expected as the model represents the mean behaviour. The confidence interval around the black line is crucial, indicating the potential range of sample behaviour.

To enhance the model validation process, a quantitative comparison was conducted between the experimental data and the model predictions for both unconfined and confined SHPB test conditions, as shown in Figure 6.9 and 6.10. Metrics such as the coefficient of determination (R^2) and root mean square error (RMSE) were computed for each plot, comparing the model's predictions to the experimental results (Table 6.1). This evaluation provides objective evidence of the model's accuracy and reliability, enabling a thorough assessment of its performance in predicting the high-strain-rate behaviour of cohesive soils.

	Unconfined SHPB data: model vs experimental results				
	Front stress	*Back stress*	*Mid stress*	*Strain*	*Radial stress*
R^2	0.73	0.87	0.70	0.97	–
RMSE	9.4	12.5	10.2	4.4	–
	Confined SHPB data: model vs experimental results				
	Front stress	*Back stress*	*Mid stress*	*Strain*	*Radial stress*
R^2	0.71	0.76	0.68	0.99	0.59
RMSE	11.1	12.8	11.5	2.2	26.8

Table 6.1: Comparison of experimental and parametric model results (versus time): R² and RMSE values.

As depicted in Table 6.1, R^2 values are close to 1, indicating a strong correlation between the model and experimental data, while RMSE values are near 0 and less than 10-20% of the data range, demonstrating a high level of agreement between the model and the validation test data. This demonstrates the model's high accuracy and minimal variance between the predictions and the actual data. Notably, a single R^2 value is measured, as the comparison is made along the y-axis, with both curves sharing the same x-range.

This consistency across various test conditions reinforces reliability, enabling engineers to make informed decisions based on accurate assessments of high-strain-rate behaviour. The precision not only validates the models but also enhances their applicability in real-world scenarios, ensuring they effectively guide the design and implementation of solutions to complex engineering challenges.

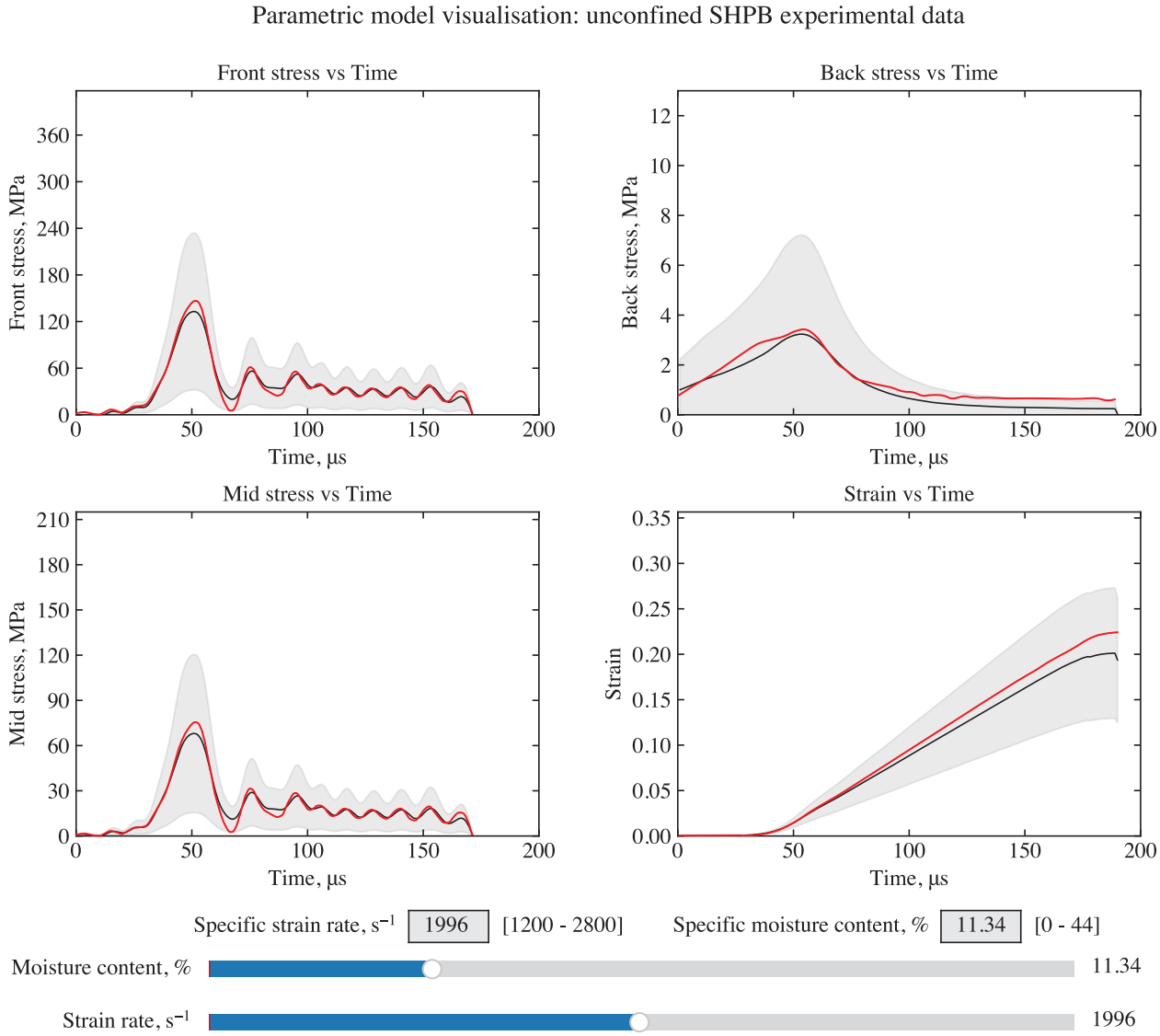

Figure 6.9: Parametric model validation: comparison of an unconfined SHPB test (in red) and its data-driven parametric model.

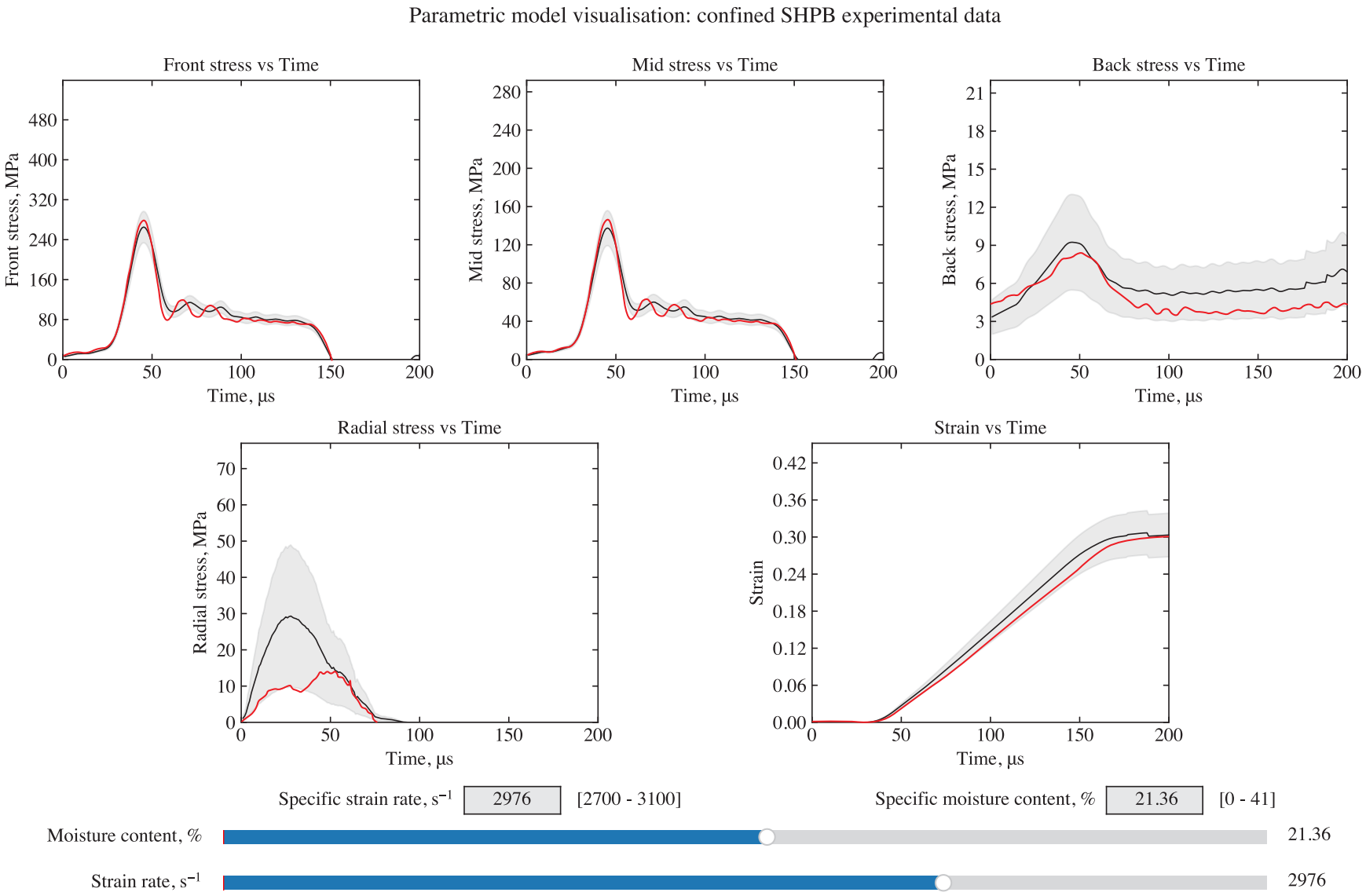

Figure 6.10: Parametric model validation: comparison of a confined SHPB test (in red) and its data-driven parametric model.

6.8 Phase transition equations: phase 2 to phase 3 boundary

In Chapter 4, the analysis of phase 2 behaviour reveals a reduction in unconfined and confined diagrams as strain rate increases. Initially, the development of a clear trendline was hindered by testing limitations and a lack of available data. This lack of clarity made it difficult to define the precise relationship between strain rate and the transition between phase 2 and phase 3. However, with the development of the parametric models, it became possible to identify specific boundaries between these phases at defined strain rates, facilitating the development of distinct trendlines, as shown in Figure 6.11a and 6.11b.

The methodology used to derive the equations for phase 2's evolution involved using both unconfined and confined parametric models. These models helped formulate equations that describe the diminishing behaviour of phase 2 as strain rate increases. Initially, challenges arose due to a lack of sufficient experimental data points, making it difficult to establish a clear trend. However, the introduction of these parametric models allowed for the augmentation of the data, adding new points and significantly improving the model's accuracy.

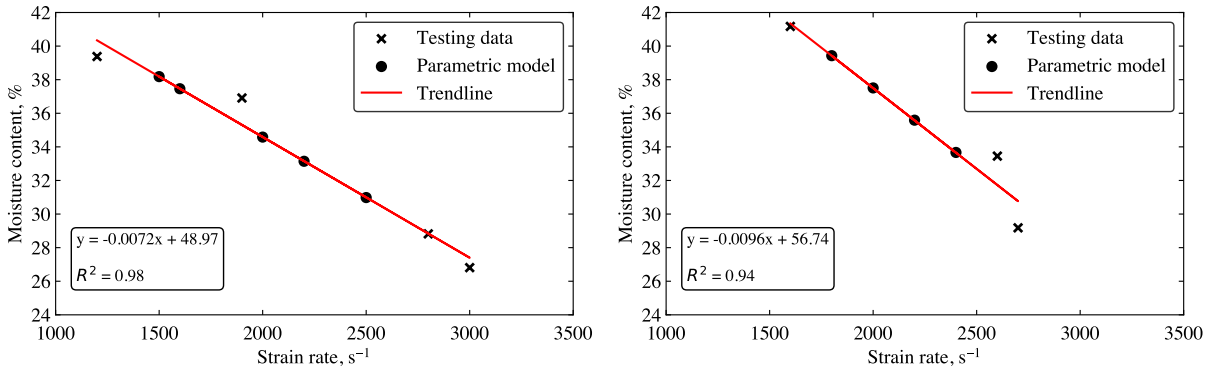

Figure 6.11: Phase 2 variations for (a) unconfined, and (b) confined tests, with trendline equations and R^2 values.

A critical aspect of this methodology was the recognition of the four phases outlined in the unconfined parametric model and the identification of the strain rate at which phase 2 ceases to exist, as discussed in Section 4.5. With this information, integrating relevant data points into the analysis became a straightforward process.

By utilising the trendline equations in Figures 6.11a and 6.11b, when inputing a strain rate value, the moisture content at which the phase 2-phase 3 boundary moves to can be determined. It is important to remember that the phase 2 to phase 3 boundary disappears in both unconfined and confined SHPB tests at strain rates of 3000 and 2700 s^{-1}, respectively (Section 4.5.4 and 4.5.5).

The development of the phase 2 equations utilised parametric modelling to bridge gaps in the initial data and enhance the overall understanding of the relationship between strain rate and phase transitions observed in experimental testing. By systematically identifying and integrating new data points, the methodology effectively captured the dynamics of phase 2, providing a robust foundation for future analyses and applications.

6.9 Discussion

Experimental SHPB tests were performed on kaolin clay samples, covering a range of moisture contents from 0 to 44 %. These tests were conducted under both unconfined and confined conditions, totalling 144 experiments, with 2 tests reserved for model validation. Of these, 98 tests were completed under unconfined conditions, while 46 tests were carried out under confined conditions. Analysis of the results revealed distinct phase behaviours of cohesive soils under high-strain-rate conditions, guiding the development of the parametric models.

Numerous constitutive models in LS-DYNA have been evaluated for modelling the high-strain-rate behaviour of cohesive soils, but they showed significant limitations (Van Lerberghe, Li, Barr and Clarke 2024*a*). As an alternative, parametric modelling options were explored, with the POD-sPGD method chosen to build these data-driven models. While these models are often viewed as simple predictive tools, their true benefit lies in supplementing existing experimental data, providing a more comprehensive dataset for calibrating and assessing future numerical models. This approach bridges the gap between Split-Hopkinson Pressure Bar (SHPB) testing and numerical simulations, emphasising the need for both. Parametric modelling offers a robust method to better integrate SHPB test data with numerical models, improving our ability to interpret and calibrate high-strain-rate behaviour.

In contrast to traditional machine learning approaches, such as artificial neural networks (ANNs), the parametric modelling approach using Proper Orthogonal Decomposition (POD) combined with the sPGD method does not require intensive training cycles, validation processes, or hyper parameter tuning. Unlike ANNs, which rely on iterative training over multiple epochs and the optimisation of loss functions such as mean squared error (MSE), the POD-sPGD method directly leverages experimental data to construct a reduced-order model without the need for cumbersome training schemes. This provides a clear advantage in terms of efficiency, making it more suitable for applications where large-scale training datasets or computationally intensive processes are impractical. This distinction underscores the simplicity and computational efficiency of POD-based approaches in comparison to traditional machine learning techniques, offering a streamlined yet powerful alternative for generating accurate models from limited experimental data.

The parametric models developed in this study were designed without reliance on implemented machine learning Python libraries, ensuring transparency and avoiding a black box scenario. Instead, the machine learning model was developed based on mathematical principles, with the coupling of POD modes extraction and sPGD regression methods. The foundation for building these models was laid upon novel SHPB test data.

The development of the models was guided by physics-informed classification of test data. Clear delineation of test data into different phase numbers based on confinement, moisture content, and strain rate behaviour eliminated the need for classification algorithms. Constructed through POD modes extraction and sPGD regression algorithms, the surrogate model played a vital role in producing trained data representing each phase number observed in material testing. The model's architecture was predominantly shaped by the strain rate, identified as the key parameter.

A vital aspect for understanding the trained data from the parametric models is a clear visual representation. To fulfil this need, interactive illustrations were crafted for both testing scenarios, offering high responsiveness and user-friendliness. These depictions offer instantaneous responses and harness the trained data from the parametric model.

Model validation involved comparing the trained model data, depicted in black, with a distinct SHPB test, highlighted in red. Unconfined tests demonstrated notable accuracy, with confined tests, though fewer, also displaying considerable precision. Unconfined tests featured larger confidence intervals due to their susceptibility to testing variations and errors, whereas confined tests showcased smaller confidence intervals owing to their high consistency. Further refinement of the confined parametric model can be achieved through additional testing. Nonetheless, at this stage, the model proves sufficiently precise, offering significant time and cost savings compared to traditional testing. Overall, the parametric model effectively predicts the high-strain-rate behaviour of cohesive soils under unconfined and confined conditions within the tested range.

In the current model representations, stress-time plots were generated, as this approach is more aligned with practical, on-site applications and better suited for evaluating the model's effectiveness. However, if needed, the validation model can also be adapted to use strain, instead of time, allowing for the generation of stress-strain curves.

Using the unconfined and confined parametric models, equations were developed to describe the diminishing evolution of phase 2 as strain rate increases. Initially, determining these equations was challenging using only experimental test data, due to insufficient data points to establish a clear trendline behaviour. Now, with the parametric models in place, the trendline behaviour can be augmented with new data points. This addition significantly enhance the ability to accurately model the evolution of phase 2 as strain rate increases. Given that the unconfined parametric model consists of four phases and the strain rate at which phase 2 disappears is known (Section 4.5), finding and integrating these points into the analysis was straightforward. For example, in the parametric model, a new strain rate was selected between two known strain rates with a defined phase 2-phase 3 moisture content boundary.

The moisture content slider was then adjusted until the behaviour changed from phase 2 to phase 3, at which point the moisture content was recorded. Applying the same principles for confined testing using the same trendline behaviour and only experimental tests, another phase 2 equation was developed (Section 6.8). It is worth noting that tests conducted under confinement at 12 and 18 m/s featured four phases, whereas those at 20 and 22 m/s had only three phases.

The machine learning tools (i.e. the POD and sPGD) used in the development of these data-driven parametric models face several limitations. Their performance is highly dependent on the quality of the data collected, and their efficiency is influenced by the quantity of available data based on the chosen experimental approach. In this case, the limited number of tests conducted for each moisture content and strain rate under different confinement conditions has an impact on the accuracy and robustness of the models. Additional testing would further improve the quality of these models.

The data-driven methods employed in this chapter can be applied to a wide range of scenarios, provided that data has been collected and key parameters influencing the collected outputs have been identified. Naturally, the more comprehensive the dataset and the greater the number of influential parameters, the more fine-tuning the model will require for optimal performance.

6.10 Summary

Experimental SHPB tests were conducted on kaolin clay samples, covering a range of moisture contents from 0 to 44%, under both unconfined and fully confined conditions. Through these tests, the degree of confinement, moisture content and strain rate were identified as the significant factors influencing the specimen's behaviour. This dataset served as the foundation for testing and training the parametric models.

Utilising cutting-edge machine learning polynomial regression techniques such as the POD and sPGD, engineers can now access two separate data-driven parametric models, offering rapid predictive capabilities for the behaviour of cohesive soils under various loading conditions and material parameters.

The work undertaken in manually classifying the data using the phase behaviour diagram was instrumental, as it demonstrated the feasibility of organising the findings within each phase number under specific confinement conditions and strain rates. Moreover, given the similar behaviour observed among test results within each phase number, the mean behaviour was used and represented. Strain rate emerged as the key parameter within each individual phase, effectively simplifying the complexity of the problem from nonlinear to linear. The POD analysis was therefore conducted along a single mode with strain rate as the key parameter, and sPGD modelling was executed within each distinct phase number, for each confinement state.

All tests, except for one from each test condition, were utilised for model construction, while the reserved tests were set aside for validation, allowing for comparisons with actual experiments, underscoring the accuracy of the two data-driven parametric models.

Interactive visual representations were tailored for each test condition, enriching the user experience and streamlining the utilisation of these data-driven parametric models to empower engineers to respond promptly and effectively to threats.

Using these data-driven parametric models, the phase behaviour equation for the reduction of phase 2 from the unconfined and confined SHPB tests can now be determined. Initially, identifying this behaviour equation was challenging due to limitations in sample creation and the fact that only three strain rates were tested, complicating the identification of a trend behaviour. However, with these parametric models, specific values and behaviours can now be accurately determined, resolving these limitations and allowing for the equation to be obtained.

For future endeavours, expanding the scope to include lower and higher strain rates would be beneficial, providing a more comprehensive understanding of the behaviour of cohesive soils at high-strain-rates. Nonetheless, the current results already offer substantial time and cost savings. This would include applications such as designing effective soil-filled barriers without the need for additional extensive experimental testing.

It is envisioned that these models will empower engineers to safeguard personnel and infrastructure from a variety of threats through the rapid assessment of cohesive soil properties. The POD-sPGD approach offers remarkable versatility and adaptability compared to traditional machine learning models such as ANNs, allowing for quick adjustments to reflect new data without extensive training or hyper parameter tuning. This efficiency makes the models ideal for practical applications, such as designing soil-filled barriers and enhancing infrastructure protection.

Chapter 7

Summary, conclusions & future work

7.1 Summary

This thesis set out to achieve several objectives:

1. Verify the impact of moisture content on the undrained shear strength behaviour of cohesive soils, at low strain rates;
2. Investigate the high-strain-rate behaviour of cohesive soils, with regard to their strain rate, moisture content and confinement conditions;
3. Evaluate current constitutive finite element models in LS-DYNA to assess their effectiveness in modelling the high-strain-rate behaviour of cohesive soils; and
4. Develop data-driven parametric models using high-strain-rate tests on cohesive soils to predict their behaviour under various strain rate, moisture content and confinement scenarios.

To begin, a comprehensive material characterisation of the chosen cohesive soil, kaolin clay, was conducted. This was followed by meticulous sample preparation and a detailed test programme, laying the groundwork for both quasi-static and high-strain-rate experimental testing. The objective of these tests is to assess the material's response under different moisture content, confinement, and strain rates.

The quasi-static behaviour of cohesive soils was examined using fully saturated kaolin clay samples to confirm the impact of moisture content on undrained shear strength behaviour. This was corroborated by UU TXC tests and static oedometer tests. Dynamic oedometer tests performed on saturated kaolin clay highlighted a stress behaviour akin to fluids under dynamic loading conditions. This observation prompted a deeper exploration into the influence of moisture and its overall impact on stress propagation within cohesive soils.

Afterwards, high-strain-rate tests were performed on kaolin clay in both unconfined and confined conditions using a SHPB apparatus. Due to the inherent impedance mismatch between incident and transmitter signals, a specialised processing algorithm, `SHPB_Processing.py`, was developed to accurately assess experimental findings. This algorithm enabled rapid and accurate analysis of the signals from the 144 SHPB tests performed on the kaolin clay specimens. Its pulse alignment functionality was crucial for aligning stresses and strains at their peak values, ensuring clear evaluation. As a result, the pulses were trimmed to focus on the core physical behaviour observed in each phase.

The examination of cohesive soil samples under high-strain-rate loading unveiled distinct phase behaviours, which were found to be correlated with material-specific parameters and experimental test conditions, as illustrated in Figure 7.1. Moisture content emerges as the primary determining factor in defining each phase. Even in fully confined testing, the same distinct material phases were observed. However, the addition of the confining ring caused lateral stress to redirect, concentrating it back towards the axial direction and the rear of the sample interface.

The design and development of the phase behaviour diagram forms the cornerstone of this research, as it directly links the high-strain-rate experimental results with the physical and material properties of the soil. This correlation provided a foundation for developing the FEM numerical model, evaluating its accuracy, and guiding the creation of the parametric models.

Modern numerical modelling techniques using FEM software LS-DYNA were evaluated to develop a constitutive cohesive soil model capable of replicating the high-strain-rate material phase behaviour observed in experimental testing for kaolin clay. Various material models were considered, but the inability to obtain a representative EOS and incorporate cohesive properties meant that no model fully captured the behaviour of cohesive soils. The extreme deformation and sudden volume changes induced by high-strain-rate loading posed a critical challenge, particularly with the occurrence of the negative volume error during numerical modelling.

Despite exploring different methods, the use of SPH node modelling emerged as the optimal approach, given its ability to handle extreme deformation and simulate the fluid-like behaviour characteristic of cohesive soils. Validations of the model against experimental results demonstrated a reasonable degree of accuracy, despite inherent numerical limitations. The numerical model also enabled the investigation of internal sample stresses, revealing that the effect of the confining ring had a limited impact on the initial radial wave. This finding supported the concept of stress redirection caused by lateral pressure and the subsequent superposition of internal stress waves. However, it is important to note that the phase behaviour developed during experimental testing could not be replicated in the numerical model.

Using advanced machine learning polynomial regression techniques such as the POD and sPGD with data collected from experimental SHPB tests, two data-driven parametric models have been developed, enabling rapid prediction of cohesive soil behaviour under varied loading conditions and material parameters. The SHPB tests on kaolin clay samples revealed confinement, moisture content, and strain rate as key factors influencing specimen behaviour, serving as the basis for training and testing the parametric models. Data classification efforts demonstrated the feasibility of organising findings within each phase number under specific confinement conditions. Strain rate emerged as the primary parameter, simplifying the problem's complexity, with models validated against actual experiments to underscore their accuracy. Interactive representations were customised for each test condition. The current model results offer substantial time and cost savings, empowering engineers to swiftly assess cohesive soil properties for protecting personnel and infrastructure from diverse threats.

While often viewed as simple predictive tools, their true benefit lies in supplementing existing experimental data, creating a more comprehensive dataset for calibrating and assessing future numerical models. This approach bridges the gap between SHPB testing and numerical simulations, underscoring the necessity of both. Parametric modelling effectively integrates SHPB test data with numerical models, improving our interpretation and calibration of high-strain-rate behaviour.

In contrast to traditional machine learning methods such as artificial neural networks (ANNs), the parametric modelling approach using POD and sPGD does not require extensive training, validation, or hyper parameter tuning. Instead of relying on iterative training and optimisation, POD-sPGD directly leverages experimental data to construct a reduced-order model, offering greater efficiency and suitability for scenarios with limited data and computational resources. This makes POD-based approaches a simpler, more efficient alternative to conventional machine learning techniques.

An exhaustive summary of each chapter of this thesis has been conducted, successfully achieving all five of the main objectives set at the beginning of this research project. The respective findings from each chapter of this thesis were structured and submitted for publication, as indicated in Table 7.1.

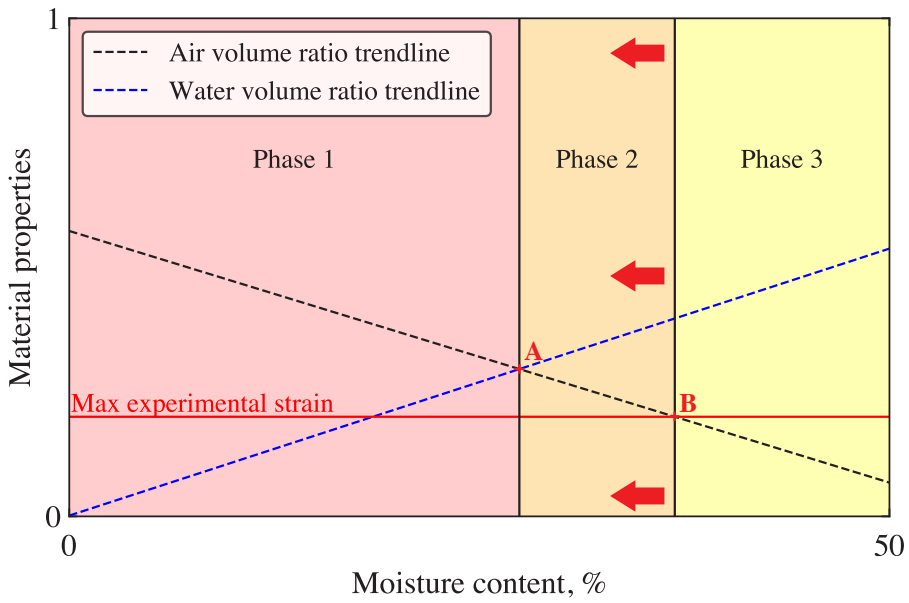

Figure 7.1: Summary diagram of the high-strain-rate phase behaviour exhibited by kaolin clay.

Thesis chapter	*Published in*
Chapter 3 - Material characterisation, specimen preparation, and test programme	Paper 2
Chapter 4 - Strain rate dependence in cohesive soils	Paper 1 & 2
Chapter 5 - Numerical modelling of high-strain-rate SHPB tests on cohesive soils	Paper 2, 4 & 5
Chapter 6 - Data-driven parametric modelling of SHPB tests on cohesive soils	Paper 3

Table 7.1: Overview of thesis chapters and associated publications.

7.2 Conclusions

7.2.1 Material characterisation, sample preparation and testing programme

- Detailed material characterisation of the cohesive soil chosen for this study, kaolin clay, ensured the reproducibility of the thesis's findings and deepened our understanding of the intrinsic material properties crucial for developing constitutive numerical models.
- A comprehensive sample preparation and test programme facilitated the meticulous analysis of how factors such confinement, moisture content, and strain rate influenced the behaviour of cohesive soils at low and high strain rates.

7.2.2 Quasi-static testing

- Well-established quasi-static static tests, such as the unconsolidated undrained TXC and static oedometer tests, on kaolin clay samples with varying moisture contents highlighted the clear impact of moisture content on the behaviour of cohesive soils at low-strain-rates.
- Dynamic oedometer test revealed that cohesive soils, particularly kaolin clay, exhibited results consistent with fluid-like behaviour.

7.2.3 Impact of confinement

For unconfined SHPB tests on cohesive soils:

- Despite the superposition of incident and reflected pulses indicating axial stress wave propagation through the sample from the incident pressure bar, the minimal magnitude of recorded back stresses suggests limited axial stress propagation through kaolin clay at high-strain-rates.
- During testing, a substantial loss of volume is observed due to sample extrusion, indicating radial stress propagation of the sample under high-strain-rate axial loading conditions.

For confined SHPB tests on cohesive soils:

- Rigid, fully confined SHPB test results exhibit greater back stress levels compared to unconfined SHPB test results.
- Measuring the circumferential strain of the steel confining ring during lateral deformation of the sample revealed significant radial stresses.
- The increased back stress observed in fully confined SHPB tests is attributed to the redirection of radial stresses caused by the confining ring. The rigid boundary intensified the concentration of radial stresses at the edge of the sample boundary and directed radial stresses towards the transmitter bar, where they were measured as back stress.

7.2.4 Phase behaviour and influence of moisture content

Drawing on evidence from axial stress propagation in SHPB testing:

- Under high-strain-rate conditions, cohesive soils propagated stress laterally rather than transmit stress axially through the sample, a phenomenon strongly affected by the moisture content in the samples.
- Distinct phase behaviours were identified within specific moisture content ranges, with boundaries dependent on the air-volume ratio, water-volume ratio and maximum experimental strain.
- The behaviour within each phase closely correlated with the moisture content in the specimens, emphasising the significance of moisture content in governing the high-strain-rate behaviour of cohesive soils.

Impact of confinement on moisture content behaviour:

- Different radial stresses were noted for identical phases in fully confined testing, demonstrating how moisture content encourages lateral stress propagation and its effects on radial stresses.
- The magnitude of radial stresses is significantly lower in unconfined tests compared to fully confined tests. This is attributed to the concentration of radial stresses directly on the surface of the sample, preventing lateral deformation and limiting any opportunity for volume loss from sample extrusion.
- The Poisson's ratio measured for the saturated cohesive soil specimens tested under fully confined high-strain-rate conditions was 0.5, identical to that of a fluid.

7.2.5 Strain rate effects

- Experimental SHPB testing revealed that at higher strain rates, unconfined tests exhibited higher magnitudes of axial stresses, while fully confined tests showed increased magnitudes of both axial and radial stresses.
- At a specific strain rate, in unconfined SHPB tests, the back stresses decreased with increasing moisture content, while in fully confined SHPB tests, both the back and radial stresses increased with increasing moisture content.
- Distinct phase behaviour persists at different moisture contents even at higher strain rates, with phase 2 decreasing as strain rate increases due to greater maximum experimental strain.
- The effects of moisture content and confinement remained consistent for strain rates tested within 10^3 s^{-1}. Although the magnitudes of back and radial stress pulses naturally increased with higher strain rates, the overall behaviour remained unchanged.
- Clear strain rate dependence of the cohesive soil material, with different stress responses based on the tested strain rate.

7.2.6 Numerical modelling

- The challenge of obtaining an accurate material card in LS-DYNA, coupled with the absence of an equation of state to model the phase behaviour of cohesive soils, complicates the selection of a suitable material card. *MAT_MOHR_COULOMB was chosen as it most accurately represents the material's behaviour based on the parameters gathered from experimental testing.
- The parameters in *MAT_MOHR_COULOMB were derived from quasi-static testing to map the Mohr-Coulomb curve. However, these parameters could not be adjusted to accommodate the sample's dry or partially saturated behaviour due to experimental limitations.
- Given the cohesive soil's fluid-like behaviour, SPH modelling emerges as the optimal choice. This preference arises from the material's propensity for significant deformation and abrupt volume alterations.
- The current material models lack the capability to incorporate cohesion properties, resulting in a larger portion of stress being reflected at the interface between the sample and the incident bar. This limitation undermines the reliability of the numerical model results.
- Numerical models using LS-DYNA successfully reproduced the high-strain-rate behaviour of saturated kaolin clay with reasonable accuracy. However, the phase behaviour observed in experimental testing failed to be captured in the model.
- The internal radial stress behaviour of the sample was found to be consistent between the unconfined and fully confined SHPB models, irrespective of confinement. This suggests an inherent tendency of the material to propagate stress laterally.
- Radial stress concentration was observed at the edge of the sample within the confining ring, ultimately resulting in the redirection of radial stress axially.

7.2.7 Parametric modelling

- Cutting-edge machine learning polynomial regression methods such as the POD and sPGD were utilised to develop two data-driven parametric models for predicting the high-strain-rate behaviour of cohesive soils using experimental SHPB test results.
- Interactive visual illustrations tailored for each SHPB test conditions were designed, enriching user experience and streamlining the utilisation of these data-driven parametric models.
- Comparative quantitative and qualitative analysis with experimental tests underscored the accuracy of the two data-driven parametric models, empowering engineers to respond promptly and effectively to threats.

7.3 Future work

The conclusions detailed above have answered all the main objectives set at the beginning of this thesis, and have subsequently dealt with the problems encountered during this research project. However, there are still areas that warrant further exploration:

7.3.1 Material phase behaviour

- To evaluate the high-strain-rate behaviour of cohesive soils, kaolin clay was chosen because of its ideal, representative, widely available material characteristics. Further high-strain-rate research can be conducted by selecting another cohesive soil material, such as adobe or London clay, as mentioned in Chapter 2, to validate the phase behaviour and findings found in this research project.
- To further understand the behaviour of cohesive soils, it is essential to investigate the effect of strain rate under various levels of confinement. While this research project focused on unconfined and fully confined testing conditions at high-strain-rates, exploring different levels of confinement, such as partial lateral confinement, could provide valuable insights. Research on this subject has been undertaken in Li, Van Lerberghe, Barr and Clarke (2024) and Li (2024), yet significant questions still remain unanswered.

7.3.2 Signal processing

- The development of `SHPB_Processing.py` has been notably effective in processing the SHPB tests data, particularly in cases where stress equilibrium is not achieved, as observed in this instance. Although significant optimisation iterations have enhanced the pulse alignment function for incident and transmitted pulses, aligning the front and back stress pulses still requires manual adjustments, especially when their shapes differ significantly. Further optimisation of the algorithm is necessary to improve the pulse alignment system.
- Given the open-source Python algorithm `SHPB_Processing.py` was designed to process high-strain-rate test data under conditions lacking stress equilibrium, it theoretically possesses the capability to be adapted for a wider range of high-strain-rate impact test setups. However, further calibration and optimisation based on test parameters would be necessary for this adaptation.

7.3.3 Numerical modelling

- The current LS-DYNA numerical model fails to capture the distinctive phase behaviours observed at different moisture contents in experimental testing. Despite modifications to the current material model, `*MAT_MOHR_COULOMB`, including variations in bulk density and Poisson's ratio, attempts to adjust the moisture content yielded no significant changes, with all numerical models at the same striker velocity exhibiting nearly identical behaviour. Future work focusing on developing a dedicated material model in LS-DYNA, particularly in SPH modelling of high-strain-rate cohesive soils, would be highly beneficial to obtain a more accurate constitutive numerical model.

- Another one of the key limitations in current numerical models is the inability of soils material models to adequately consider the effect of suction. This is crucial when dealing with cohesive soils, where the presence of water significantly influences soil behaviour, especially in high-strain-rate scenarios. The inherent cohesion between particles creates an internal suction force that prevents immediate detachment of individual particles. While some LS-DYNA material models allow for inputting a cohesion parameter, these models are not optimised for cohesive soils due to the challenges of establishing an equation of state for these materials at high-strain-rates. Therefore, the development of an updated material model optimised for cohesive soils, while also accounting for the effects of water and cohesion is essential for accurately depicting its high-strain-rate behaviour.

7.3.4 Parametric modelling

- Numerous constitutive models in LS-DYNA have been evaluated for simulating the high-strain-rate behaviour of cohesive soils, yet these models exhibit significant limitations (Van Lerberghe, Li, Barr and Clarke 2024*a*). To address this, parametric modelling approaches were explored, with the POD-sPGD method selected to develop data-driven models. While typically viewed as predictive tools, the true value of these models lies in enhancing experimental datasets, offering a more robust foundation for calibrating and validating future numerical simulations. This integration bridges the gap between Split-Hopkinson Pressure Bar (SHPB) testing and computational modelling, reinforcing the importance of combining both. Future work should focus on refining parametric modelling techniques to help improve the calibration of high-strain-rate behaviour in numerical simulations, ensuring a more accurate interpretation of experimental data.

- The two data-driven parametric models in Chapter 6, developed using high-strain-rate experimental test data on cohesive soils under varying moisture content and different confinement conditions, empower engineers to respond rapidly and efficiently to threats. Conducting additional tests at lower and higher strain rates will enable these models to offer a more comprehensive representation of cohesive soil behaviour, thereby enhancing quality and reliability of these models. Additionally, leveraging the machine learning methodology employed to create these parametric models and applying it to other scenarios utilising experimental test data could prove valuable.

Bibliography

Abbey, S., Eyo, E. U. and Ng'ambi, S. (2019), 'Swell and microstructural characteristics of high-plasticity clay blended with cement', *Bulletin of Engineering Geology and the Environment* pp. 1–12.

Akers, S. A., Reed, P. A., Ehrgott Jr, J. Q. et al. (1986), 'WES high-pressure uniaxial strain and triaxial shear test equipment'.

Anantanasakul, P., Yamamuro, J. A. and Lade, P. V. (2012), 'Three-dimensional drained behavior of normally consolidated anisotropic kaolin clay', *Soils and foundations* **52**(1), 146–159.

Arlery, M., Gardou, M., Fleureau, J. and Mariotti, C. (2010), 'Dynamic behaviour of dry and water-saturated sand under planar shock conditions', *International Journal of Impact Engineering* **37**(1), 1–10.

Aubert, J.-E., Fabbri, A., Morel, J.-C. and Maillard, P. (2013), 'An earth block with a compressive strength higher than 45 mpa!', *Construction and Building Materials* **47**, 366–369.

Bagheri, M. and Rezania, M. (2021), 'Geological and geotechnical characteristics of london clay from the isle of sheppey', *Geotechnical and Geological Engineering* **39**, 1701–1713.

Bancroft, D. (1941), 'The velocity of longitudinal waves in cylindrical bars', *Physical Review* **59**(7), 588.

Barr, A. (2016*a*), 'dispersion.m - A MatLab script for phase angle and amplitude correction of pressure bar signals'.

Barr, A. (2023), 'phasevelocity.m - A Matlab script to calculate the frequency-dependent phase velocity and radial variation of elastic waves in cylindrical bars'.

Barr, A. D. (2016*b*), Strain-rate effects in quartz sand, PhD thesis, University of Sheffield.

Barr, A., Rigby, S. and Clayton, M. (2020), 'Correction of higher mode pochhammer–chree dispersion in experimental blast loading measurements', *International Journal of Impact Engineering* **139**, 103526.

Bauer, E. (1960), History and development of the atterberg limits tests, *in* 'Papers on Soils 1959 Meetings', ASTM International.

Benner, P., Ohlberger, M., Cohen, A. and Willcox, K. (2017), *Model Reduction and Approximation*, Society for Industrial and Applied Mathematics, Philadelphia, PA.
URL: *https://epubs.siam.org/doi/abs/10.1137/1.9781611974829*

Benner, P. et al. (2020), *Snapshot-based methods and algorithms*, Walter de Gruyter GmbH & Co KG.

Bishop, A. and Henkel, D. (1957), 'The measurement of soil properties in the triaxial test, arnold'.

Borzacchiello, D., Aguado, J. V. and Chinesta, F. (2019), 'Non-intrusive sparse subspace learning for parametrized problems', *Archives of Computational Methods in Engineering* **26**, 303–326.

Bragov, A., Grushevsky, G. and Lomunov, A. (1996), 'Use of the kolsky method for confined tests of soft soils', *Experimental Mechanics* **36**, 237–242.

Bragov, A., Lomunov, A., Sergeichev, I., Tsembelis, K. and Proud, W. (2008), 'Determination of physicomechanical properties of soft soils from medium to high strain rates', *International Journal of Impact Engineering* **35**(9), 967–976.

Breiman, L. (2001), 'Random forests', *Machine Learning* **45**, 5–32.

Brown, P. W. and Clifton, J. R. (1978), 'Adobe i: the properties of adobe', *Studies in conservation* **23**(4), 139–146.

BSI (1990*a*), 'BS 1377-2: 1990: Methods of test for soils for civil engineering purposes – Part 2: Classification tests'.

BSI (1990*b*), 'BS 1377-5: 1990: Methods of test for soils of civil engineering purposes – Part 5: Compressibility, permeability and durability tests'.

BSI (1990*c*), 'BS 1377-8: 1990: Methods of test for soils for civil engineering purposes – Part 8: Shear strength tests (effective stress)'.

Busch, C. L. and Tarefder, R. A. (2017), 'Evaluation of appropriate material models in ls-dyna for mm-ale finite element simulations of small-scale explosive airblast tests on clay soils', *Indian Geotechnical Journal* **47**(2), 173–186.

Calatan, G., Hegyi, A., Dico, C. and Mircea, C. (2017), 'Experimental research on the recyclability of the clay material used in the fabrication of adobe bricks type masonry units', *Procedia Engineering* **181**, 363–369.

Casagrande, A. (1948), 'Classification and identification of soils', *Transactions of the American Society of Civil Engineers* **113**(1), 901–930.

Casini, F., Vaunat, J., Romero, E. and Desideri, A. (2012), 'Consequences on water retention properties of double-porosity features in a compacted silt', *Acta Geotechnica* **7**(2), 139–150.

Champaney, V., Chinesta, F. and Cueto, E. (2022), 'Engineering empowered by physics-based and data-driven hybrid models: A methodological overview', *International Journal of Material Forming* **15**.

Champaney, V., Pasquale, A., Ammar, A. and Chinesta, F. (2022*a*), 'Parametric curves metamodelling based on data clustering, data alignment, pod-based modes extraction and pgd-based nonlinear regressions', *Frontiers in Materials* **9**, 904707.

Champaney, V., Pasquale, A., Ammar, A. and Chinesta, F. (2022*b*), 'Parametric curves metamodelling based on data clustering, data alignment, pod-based modes extraction and pgd-based nonlinear regressions', *Frontiers in Materials* **9**, 904707.

Chen, J.-Y. and Lien, F.-S. (2018), 'Simulations for soil explosion and its effects on structures using sph method', *International Journal of Impact Engineering* **112**, 41–51.

Chinesta, F., Cueto, E., Abisset-Chavanne, E., Duval, J. L. and Khaldi, F. E. (2020), 'Virtual, digital and hybrid twins: a new paradigm in data-based engineering and engineered data', *Archives of computational methods in engineering* **27**, 105–134.

Chinesta, F., Cueto, E. and Guévelou, S. (2022), 'Material forming digital twins: the alliance between physics-based and data-driven models', *Key Engineering Materials* **926**, 3–14.

Chinesta, F., Huerta, A., Rozza, G. and Willcox, K. (2017), 'Model reduction methods', *Encyclopedia of Computational Mechanics Second Edition* pp. 1–36.

Chinesta, F., Keunings, R. and Leygue, A. (2013), *The proper generalized decomposition for advanced numerical simulations: a primer*, Springer Science & Business Media.

Chinesta, F., Leygue, A., Bordeu, F., Aguado, J. V., Cueto, E., González, D., Alfaro, I., Ammar, A. and Huerta, A. (2013), 'Pgd-based computational vademecum for efficient design, optimization and control', *Archives of Computational methods in Engineering* **20**, 31–59.

Chow, S. H., O'Loughlin, C. D., Zhou, Z., White, D. J. and Randolph, M. F. (2020), 'Penetrometer testing in a calcareous silt to explore changes in soil strength', *Géotechnique* **70**(12), 1160–1173.

Chree, C. (1889), 'The equations of an isotropic elastic solid in polar and cylindrical co-ordinates their solution and application', *Transactions of the Cambridge Philosophical Society* **14**, 250.

Christ, M. and Kim, Y.-C. (2009), 'Experimental study on the physical-mechanical properties of frozen silt', *KSCE Journal of Civil Engineering* **13**, 317–324.

Church, P., Cornish, R., Cullis, I., Gould, P. and Lewtas, I. (2014), 'Using the split hopkinson pressure bar to validate material models', *Philosophical Transactions of the Royal Society A: Mathematical, Physical and Engineering Sciences* **372**(2023), 20130294.

Colagrossi, A. and Landrini, M. (2003), 'Numerical simulation of interfacial flows by smoothed particle hydrodynamics', *Journal of computational physics* **191**(2), 448–475.

Cundall, P. A. and Strack, O. D. (1979), 'A discrete numerical model for granular assemblies', *geotechnique* **29**(1), 47–65.

Davies, E. and Hunter, S. (1963), 'The dynamic compression testing of solids by the method of the split hopkinson pressure bar', *Journal of the Mechanics and Physics of Solids* **11**(3), 155–179.

Davies, R. (1948), 'A critical study of the hopkinson pressure bar', *Philosophical Transactions of the Royal Society of London. Series A, Mathematical and Physical Sciences* **240**(821), 375–457.

Davison, L. and Atkinson, J. (1990), 'Continuous loading oedometer testing of soils', *Quarterly Journal of Engineering Geology and Hydrogeology* **23**(4), 347–355.

De Boer, R. (2005), *The engineer and the scandal*, Springer.

Degirmenci, N. (2008), 'The using of waste phosphogypsum and natural gypsum in adobe stabilization', *Construction and Building Materials* **22**(6), 1220–1224.

Donaghe, R. T., Chaney, R. C., Silver, M. L. et al. (1988), Advanced triaxial testing of soil and rock, ASTM.

Doygun, O. and Brandes, H. (2020), 'High strain damping for sands from load-controlled cyclic tests: Correlation between stored strain energy and pore water pressure', *Soil Dynamics and Earthquake Engineering* **134**, 106134.

Eremeyev, V., Balandin, V., Bragov, A., Konstantinov, A. Y., Igumnov, L. et al. (2023), 'Experimental study and numerical simulation of the dynamic penetration into dry clay', *Continuum Mechanics and Thermodynamics* **35**(2), 457–469.

Felice, C., Brown, J., Gaffney, E. and Olsen, J. (1985), Investigation into the high strain-rate behavior of compacted sand using the split-hopkinson pressure bar technique, Technical report, Air Force Inst. of Tech., Wright-Patterson AFB, OH (USA); Los Alamos ....

Felice, C. W. (1986), The response of soil to impulse loads using the split-hopkinson pressure bar technique, Technical report, AIR FORCE WEAPONS LAB KIRTLAND AFB NM.

Fiserova, D. (2006), 'Numerical analysis of buried mine explosions with emphasis on effect of soil properties on loading'.

Follansbee, P. and Frantz, C. (1983), 'Wave propagation in the split hopkinson pressure bar'.

Frew, D., Forrestal, M. and Chen, W. (2005), 'Pulse shaping techniques for testing elastic-plastic materials with a split hopkinson pressure bar', *Experimental mechanics* **45**(2), 186.

Friedman, J. H. (2001), 'Greedy function approximation: A gradient boosting machine', *The Annals of Statistics* **29**(5), 1189–1232.
URL: *http://www.jstor.org/stable/2699986*

Gasparre, A. (2005), 'Advanced laboratory characterisation of london clay'.

Gasparre, A., Nishimura, S., Coop, M. and Jardine, R. (2011), The influence of structure on the behaviour of london clay, *in* 'Stiff Sedimentary Clays: Genesis and Engineering Behaviour: Géotechnique Symposium in Print 2007', Thomas Telford Ltd, pp. 67–79.

Germaine, J. T. and Ladd, C. C. (1988), 'Triaxial testing of saturated cohesive soils', *Advanced triaxial testing of soil and rock, ASTM STP* **977**, 421–459.

Ghnatios, C., Kestelyn, X., Denis, G., Champaney, V. and Chinesta, F. (2023), 'Learning data-driven stable corrections of dynamical systems—application to the simulation of the top-oil temperature evolution of a power transformer', *Energies* **16**(15), 5790.

Ghnatios, C., Rodriguez, S., Tomezyk, J., Dupuis, Y., Mouterde, J., Da Silva, J. and Chinesta, F. (2024), 'A hybrid twin based on machine learning enhanced reduced order model for real-time simulation of magnetic bearings', *Advanced Modeling and Simulation in Engineering Sciences* **11**(1), 3.

Goodfellow, I., Bengio, Y. and Courville, A. (2016), *Deep Learning*, MIT Press.

Gorham, D. (1983), 'A numerical method for the correction of dispersion in pressure bar signals', *Journal of Physics E: Scientific Instruments* **16**(6), 477.

Gray III, G. T. (2000), 'Classic split hopkinson pressure bar testing', *ASM handbook* **8**, 462–476.

Hallquist, J. O. et al. (2007), 'Ls-dyna keyword user's manual', *Livermore Software Technology Corporation* **970**, 299–800.

Hastie, T., Tibshirani, R. and Friedman, J. (2001), *The Elements of Statistical Learning*, Springer Series in Statistics, Springer New York Inc., New York, NY, USA.

Head, K. H. and Epps, R. J. (1980), *Manual of soil laboratory testing*, Vol. 1, Pentech Press London.

Hopkinson, B. (1914), 'X. a method of measuring the pressure produced in the detonation of high, explosives or by the impact of bullets', *Philosophical Transactions of the Royal Society of London. Series A, Containing Papers of a Mathematical or Physical Character* **213**(497-508), 437–456.

Ibáñez Pinillo, R., Abisset-Chavanne, E., Ammar, A., González, D., Cueto, E., Huerta, A., Duval, J. and Chinesta, F. (2018), 'A multidimensional data-driven sparse identification technique: The sparse proper generalized decomposition', *Complexity* **2018**, 1–11.

Ibáñez, R., Abisset-Chavanne, E., Ammar, A., González, D., Cueto, E., Huerta, A., Duval, J. L. and Chinesta, F. (2018), 'A multidimensional data-driven sparse identification technique: the sparse proper generalized decomposition', *Complexity* **2018**(1), 5608286.

Ibánez, R., Abisset-Chavanne, E., Chinesta, F., Huerta, A. and Cueto, E. (2019), 'A local multiple proper generalized decomposition based on the partition of unity', *International Journal for Numerical Methods in Engineering* **120**(2), 139–152.

Ihmsen, M., Bader, J., Akinci, G. and Teschner, M. (2011), Animation of air bubbles with sph, *in* 'International Conference on Computer Graphics Theory and Applications', Vol. 2, SCITEPRESS, pp. 225–234.

ISO (2002), '14688-1: 2002: Geotechnical investigation and testing – Identification and classification of soil – Part 1: Identification and description', *British Standards Institution* .

Jamo, H. U. and Abdu, S. (2014), 'Structural analysis and surface morphology of kaolin', *Science World Journal* **9**(3), 33–37.

Kafodya, I., Okonta, F. and Kloukinas, P. (2019), 'Role of fiber inclusion in adobe masonry construction', *Journal of Building Engineering* **26**, 100904.

Karajan, N., Han, Z., Teng, H. and Wang, J. (2014), On the parameter estimation for the discrete-element method in ls-dyna®, *in* 'Proceedings of the 13th International LS_DYNA Users Conference, Dearborn, MI, USA', pp. 8–10.

King, C. et al. (1981), 'The stratigraphy of the london clay and associated deposits'.

Kolsky, H. (1949), 'An investigation of the mechanical properties of materials at very high rates of loading', *Proceedings of the physical society. Section B* **62**(11), 676.

Kolsky, H. (1963), 'Stress waves in solids. Dover Books on Physics, New York'.

Konstantinov, A., Bragov, A., Igumnov, L., Eremeyev, V., Balandin, V. V. et al. (2022), 'Experimental study and identification of a dynamic deformation model of dry clay at strain rates up to 2500 s-1', *Journal of Applied and Computational Mechanics* **8**(3), 981–995.

Krayterman, D. (2022), 'Investigation of arbitrary lagrangian–eulerian (ale) modeling and alternative material formulations of roma plastilina ballistic clay using ls-dyna numerical model'.

Lade, P. V. (2016), *Triaxial testing of soils*, John Wiley & Sons.

Leo Breiman, Jerome Friedman, C. J. S. R. O. (1984), *Classification and Regression Trees*, Chapman and Hall/CRC.

L'Eplattenier, P. and Caldichoury, I. (2016), A coupled 3d/2d axisymmetric method for simulating magnetic metal forming processes in ls-dyna, *in* '7th International Conference on High Speed Forming, April 27th-28th 2016, Dortmund, Germany'.

Li, K. S. O. (2024), Understanding rate effects in cohesive soils, PhD thesis, University of Sheffield.

Li, K. S. O., Van Lerberghe, A. and Barr, A. (2024), 'SHPB_Processing.py - An open-source Python algorithm for correcting stress wave dispersion in split-Hopkinson pressure bar experiments'.

Li, K. S. O., Van Lerberghe, A., Barr, A. D. and Clarke, S. D. (2024), 'Impact of partial lateral confinement on high-strain-rate behaviour of cohesive soils - submitted for publication in the journal of Experimental Mechanics, currently under review'.

Li, K. S. O., Van Lerberghe, A., Barr, A. D., Clarke, S. D. and Dennis, A. A. (2024), 'Split-hopkinson pressure bar testing of water with partial lateral confinement - submitted for publication in the journal of Experimental Mechanics, currently under review'.

Liu, K., Chen, S. and Voyiadjis, G. (2019), 'Integration of anisotropic modified cam clay model in finite element analysis: Formulation, validation, and application', *Computers and Geotechnics* **116**, 103198.

LSTC (2021), 'Ls-dyna keyword user's manual', *LSTC Co., Livermore, CA* .

Luo, H., Cooper, W. L. and Lu, H. (2014), 'Effects of particle size and moisture on the compressive behavior of dense eglin sand under confinement at high strain rates', *International Journal of Impact Engineering* **65**, 40–55.

Ma, Q.-Y. (2010), 'Experimental analysis of dynamic mechanical properties for artificially frozen clay by the split hopkinson pressure bar', *Journal of Applied Mechanics and Technical Physics* **51**(3), 448–452.

Martin, B., Kabir, M. E. and Chen, W. (2013), 'Undrained high-pressure and high strain-rate response of dry sand under triaxial loading', *International Journal of Impact Engineering* **54**, 51–63.

Mohd Yusoff, S. A. N., Bakar, I., Wijeyesekera, D. C., Zainorabidin, A. and Madun, A. (2015), Comparison of geotechnical properties of laterite, kaolin and peat, *in* 'Applied Mechanics and Materials', Vol. 773, Trans Tech Publ, pp. 1438–1442.

Monroy, R., Zdravkovic, L. and Ridley, A. (2010), 'Evolution of microstructure in compacted london clay during wetting and loading', *Géotechnique* **60**(2), 105–119.

Muñoz, P., Letelier, V., Muñoz, L. and Bustamante, M. (2020), 'Adobe bricks reinforced with paper & pulp wastes improving thermal and mechanical properties', *Construction and Building Materials* **254**, 119314.

Nakase, A. and Kamei, T. (1983), 'Undrained shear strength anisotropy of normally consolidated cohesive soils', *Soils and foundations* **23**(1), 91–101.

Nemat-Nasser, S., Isaacs, J. B. and Starrett, J. E. (1991), 'Hopkinson techniques for dynamic recovery experiments', *Proceedings of the Royal Society of London. Series A: Mathematical and Physical Sciences* **435**(1894), 371–391.

Nowamooz, H. and Masrouri, F. (2008), 'Hydromechanical behaviour of an expansive bentonite/silt mixture in cyclic suction-controlled drying and wetting tests', *Engineering Geology* **101**(3-4), 154–164.

Oka, F., Kodaka, T., Suzuki, H., Kim, Y. S., Nishimatsu, N. and Kimoto, S. (2010), 'Experimental study on the behavior of unsaturated compacted silt under triaxial compression', *Soils and foundations* **50**(1), 27–44.

Oluwatuyi, O. E., Ojuri, O. O. and Khoshghalb, A. (2020), 'Cement-lime stabilization of crude oil contaminated kaolin clay', *Journal of Rock Mechanics and Geotechnical Engineering* **12**(1), 160–167.

O'Sullivan, C. (2015), 'Advancing geomechanics using dem', *Geomechanics from micro to macro* p. 21.

Pantelidou, H. and Simpson, B. (2007), 'Geotechnical variation of london clay across central london', *Géotechnique* **57**(1), 101–112.

Pasquale, A., Champaney, V., Kim, Y., Hascoët, N., Ammar, A. and Chinesta, F. (2022*a*), 'A parametric metamodel of the vehicle frontal structure accounting for material properties and strain-rate effect: application to full frontal rigid barrier crash test', *Heliyon* **8**(12).

Pasquale, A., Champaney, V., Kim, Y., Hascoët, N., Ammar, A. and Chinesta, F. (2022*b*), 'A parametric metamodel of the vehicle frontal structure accounting for material properties and strain-rate effect: application to full frontal rigid barrier crash test', *Heliyon* **8**, e12397.

Pochhammer, L. (1876), 'Ueber die fortpflanzungsgeschwindigkeiten kleiner schwingungen in einem unbegrenzten isotropen kreiscylinder.', *Journal für die reine und angewandte Mathematik* **1876**(81), 324–336.

Powrie, W. (2018), *Soil mechanics: concepts and applications*, CRC Press.

Rigby, S. E., Barr, A. D. and Clayton, M. (2018), 'A review of pochhammer–chree dispersion in the hopkinson bar', *Proceedings of the Institution of Civil Engineers-Engineering and Computational Mechanics* **171**(1), 3–13.

Rigby, S., Fuller, B. and Tyas, A. (2018), Validation of near-field blast loading in ls-dyna, *in* 'Proceedings of the 5th International Conference on Protective Structures', International Association of Protective Structures.

Rodriguez, S., Monteiro, E., Mechbal, N., Rebillat, M. and Chinesta, F. (2023*a*), 'Hybrid twin of rtm process at the scarce data limit', *International Journal of Material Forming* **16**(4), 40.

Rodriguez, S., Monteiro, E., Mechbal, N., Rébillat, M. and Chinesta, F. (2023*b*), 'Hybrid twin of rtm process at the scarce data limit', *International Journal of Material Forming* **16**.

Ross, C. A., Nash, P. T. and Friesenhahn, G. J. (1986), Pressure waves in soils using a split-hopkinson pressure bar, Technical report, Southwest Research Institute San Antonio TX.

Rozza, G., Hess, M., Stabile, G., Tezzele, M., Ballarin, F., Gräßle, C., Hinze, M., Volkwein, S., Chinesta, F., Ladeveze, P., Maday, Y., Patera, A., Farhat, C., Grimberg, S., Manzoni, A., Quarteroni, A., Buhr, A., Iapichino, L. and Kutz, J. (2020*a*), *Model Order Reduction: Volume 3: Applications*, De Gruyter.

Rozza, G., Hess, M., Stabile, G., Tezzele, M., Ballarin, F., Gräßle, C., Hinze, M., Volkwein, S., Chinesta, F., Ladeveze, P., Maday, Y., Patera, A., Farhat, C., Grimberg, S., Manzoni, A., Quarteroni, A., Buhr, A., Iapichino, L. and Kutz, J. (2020*b*), *Volume 2 Snapshot-Based Methods and Algorithms*, De Gruyter.

Sancarlos, A., Champaney, V., Cueto, E. and Chinesta, F. (2023), 'Regularized regressions for parametric models based on separated representations', *Advanced Modeling and Simulation in Engineering Sciences* **10**.

Schmid, A., Pasquale, A., Ellersdorfer, C., Champaney, V., Raffler, M., Guévelou, S., Kizio, S., Ziane, M., Feist, F. and Chinesta, F. (2023), 'Pgd based meta modelling of a lithium-ion battery for real time prediction', *Frontiers in Materials (Computational Materials Science)* **10**.

Schmid, A., Pasquale, A., Ellersdorfer, C., Raffler, M., Champaney, V., Ziane, M., Chinesta, F. and Feist, F. (2023), 'Mechanical characterization of li-ion cells and the calibration of numerical models using proper generalized decomposition', *Proceedings of the ASME 2023 International Mechanical Engineering Congress and Exposition IMECE2023* .

Sharma, V., Marwaha, B. M. and Vinayak, H. K. (2016), 'Enhancing durability of adobe by natural reinforcement for propagating sustainable mud housing', *International Journal of Sustainable Built Environment* **5**(1), 141–155.

Shibusawa, S. and Oida, A. (1992), 'Transient load test system for evaluating dynamic soil behavior hierarchies by differences in the period of motion', *Journal of terramechanics* **29**(2), 161–171.

Shin, Y., Lee, M., Lam, K. and Yeo, K. (1998), 'Modeling mitigation effects of watershield on shock waves', *Shock and Vibration* **5**(4), 225–234.

Skempton, A. (1960), 'Terzaghi's discovery of effective stress', *From theory to practice in soil mechanics: Selections from the writings of Karl Terzaghi* pp. 42–53.

Skempton, A. and Terzaghi, K. (1960), 'From theory to practice in soil mechanics'.

Smola, A. and Schölkopf, B. (2004), 'A tutorial on support vector regression', *Statistics and Computing* **14**(3), 199–222.

Song, B. and Chen, W. (2004), 'Dynamic stress equilibration in split hopkinson pressure bar tests on soft materials', *Experimental mechanics* **44**(3), 300–312.

Stephens, R. C. (2013), *Strength of materials: theory and examples*, Elsevier.

Tyas, A. and Pope, D. J. (2005), 'Full correction of first-mode pochammer–chree dispersion effects in experimental pressure bar signals', *Measurement science and technology* **16**(3), 642.

Tyas, A. and Watson, A. (2000), 'Experimental evidence of pochammer-chree strain variations in elastic cylinders', *Experimental mechanics* **40**(3), 331–337.

Tyas, A. and Watson, A. J. (2001), 'An investigation of frequency domain dispersion correction of pressure bar signals', *International Journal of Impact Engineering* **25**(1), 87–101.

Van Lerberghe, A. and Barr, A. (2023*a*), 'dispersion.py - A Python algorithm for phase angle and amplitude correction of pressure bar signals'.

Van Lerberghe, A. and Barr, A. (2023*b*), 'phase_velocity.py - A Python algorithm for calculating frequency-dependent phase velocity and radial variation of elastic waves in cylindrical bars'.

Van Lerberghe, A. and Li, K. S. O. (2023), 'gauge_factor.py - A Python algorithm for calculating the gauge factor of the input bar for split-Hopkinson pressure bar experiments.'.

Van Lerberghe, A., Li, K. S. O., Barr, A. D. and Clarke, S. D. (2024*a*), 'High strain rate behaviour of cohesive soils - submitted for publication in the International Journal of Impact Engineering, currently under review'.

Van Lerberghe, A., Li, K. S. O., Barr, A. D. and Clarke, S. D. (2024*b*), 'An open-source algorithm for correcting stress wave dispersion in split-hopkinson pressure bar experiments - submitted for publication in Experimental Mechanics, currently under review'.

Van Lerberghe, A., Pasquale, A., Rodriguez, S., Barr, A. D., Clarke, S. D., Baillargeat, D. and Chinesta, F. (2024), 'Data-driven parametric modelling of split-hopkinson pressure bar tests on cohesive soils - submitted for publication in the international journal of Impact Engineering, currently under review'.

Venkatramaiah, C. (1995), *Geotechnical engineering*, New Age International.

Veyera, G. E. (1994), Uniaxial stress-strain behavior of unsaturated soils at high strain rates, Technical report, Wright Lab Tyndall Afb Fl.

Ward, W., Samuels, S. and Butler, M. E. (1959), 'Further studies of the properties of london clay', *Geotechnique* **9**(2), 33–58.

Warren, J., Kerr, S., Tyas, A., Clarke, S., Petkovski, M., Jardine, A., Church, P., Gould, P. and Williams, A. (2013), 'Briefing: Uk ministry of defence force protection engineering programme', *Proceedings of the Institution of Civil Engineers-Engineering and Computational Mechanics* **166**(3), 119–123.

White, W. A. (1949), 'Atterberg plastic limits of clay minerals', *American Mineralogist: Journal of Earth and Planetary Materials* **34**(7-8), 508–512.

Williams, E. M., Akers, S. A. and Reed, P. A. (2006), Laboratory characterization of sam-35 concrete, Technical report, ENGINEER RESEARCH AND DEVELOPMENT CENTER VICKSBURG MS GEOTECHNICAL AND ....

Yang, R., Chen, J., Yang, L., Fang, S. and Liu, J. (2017), 'An experimental study of high strain-rate properties of clay under high consolidation stress', *Soil Dynamics and Earthquake Engineering* **92**, 46–51.

Yoshinaka, R. and Kazama, H. (1973), 'Micro-structure of compacted kaolin clay', *Soils and Foundations* **13**(2), 19–34.

Appendix A

Publications

A.1 Introduction

This appendix contains copies of the papers submitted to international conferences and academic journals during this research project.

A.2 Blast attenuation in cohesive soils.

Van Lerberghe, A., Barr, A. D., Clarke, S. D., & Kerr, S. L. (2022). Blast attenuation in cohesive soils.

An abstract introducing the work which will be undertaken to investigate the high-strain-rate behaviour of cohesive soils using a split-Hopkinson pressure bar (SHPB) under both unconfined and confined conditions, submitted to the 3rd International Conference on Impact Loading of Structures and Materials (ICILSM). The abstract with the work presented at the conference is included in its entirety below as reference.

3rd International Conference on Impact Loading of Structures and Materials
ICILSM 2022

Blast Attenuation in Cohesive Soils

Arthur van Lerberghe[a], Sam Clarke[a], Andrew D. Barr[a] & Stephen L. Kerr[b].

[a]*University of Sheffield, UK*
[b]*Defence science and technology laboratory (Dstl), UK*

Abstract

Soil-filled wire and geotextile gabions are commonly used to construct defensive infrastructure in military bases, where the attenuating properties of soil are used to protect personnel and key assets from the effects of blast and fragmentation. The behaviour of cohesive soils in these extreme loading environments is unknown, and so designers require data at these high pressures and strain rates in order to develop robust soil constitutive models and adapt to new threats. Currently, the cohesive soils mostly used in experimental testing are kaolin clay, adobe clay, London clay and silt. The dry density, moisture content and Atterberg limits of these soils are contrasted between numerous different literature sources. The results reveal a lack of consistency in the recording of the parameters necessary to convincingly understand the material's performance under different loading conditions. Testing at high strain rates, a characteristic of blast and impact events, has required the development of specialised experimental methods such as the Split-Hopkinson pressure bar. Yet, no extensive applications have been conducted on cohesive soils. Additionally, testing at low strain rates using triaxial and oedometer apparatuses are important to understand the overall behaviour of cohesive soils, creating a complete soil profile of the material. This work will focus on presenting an overview of the current work which has been completed using low and high strain rate tests on cohesive soil samples, highlighting initial findings, and introducing future work opportunities.

A.3 High strain rate testing of cohesive soils.

Van Lerberghe, A., Barr, A. D., Clarke, S. D., & Kerr, S. L. (2023). High strain rate testing of cohesive soils.

A paper presenting the initial research conducted on the high-strain-rate testing of cohesive soils, submitted to the 6th International Conference on Protective Structures (ICPS6). The paper with the work presented at the conference is included in its entirety below as reference.

6th International Conference on Protective Structures (ICPS6)
14 – 17 May 2023, Auburn University USA

HIGH STRAIN RATE TESTING OF COHESIVE SOILS

A. van Lerberghe
Department of Civil and Structural Engineering, University of Sheffield, South Yorkshire, UK,
avanlerberghe1@sheffield.ac.uk

S. D. Clarke, A. D. Barr
Department of Civil and Structural Engineering, University of Sheffield, South Yorkshire, UK,
sam.clarke@sheffield.ac.uk & a.barr@sheffield.ac.uk

S. L. Kerr
Defense Science and Technology Laboratory (Dstl), Porton Down, Wiltshire, UK

ABSTRACT
Soil-filled wire and geotextile gabions are the most commonly used defensive infrastructure in military bases, where the attenuating properties of soils are employed to safeguard key assets from the effects of blast and fragmentation. Due to recent conflicts being extensively in arid regions, considerable knowledge has been acquired by engineers on the behaviour of cohesionless soils, under various loading conditions. However, very little is known of the behaviour of cohesive soils, such as clays and silts, under extreme loading environments. This lack of knowledge is critical for fortification designers, which require data at these high pressures and strain rates in order to develop robust constitutive soil models and adapt to new threats. Testing at high strain rates, a key attribute of blast and impact events, has required the development of specialized experimental methods such as the split-Hopkinson pressure bar. Experimental applications of this testing method are applied on cohesive soil samples with different moisture contents, to evaluate its effect. The results demonstrated a similar response in stress and strain for all specimens, highlighting the impact of moisture content in governing the overall behaviour of cohesive soil samples.

Keywords: Split-Hopkinson pressure bar, high strain rate testing, cohesive soils, kaolin clay

INTRODUCTION

This paper describes the current fundamental soils research conducted in the Dstl-sponsored Force Protection Engineering (FPE) programme. Its role is to investigate protective materials that can be utilized by military fortification engineers [1]. The FPE research programme aims to strengthen the knowledge of how materials used perform under various loading conditions. FPE structures today are designed through a collaboration of different methods: traditional testing, numerical modelling and experimental trials. Nevertheless, full scale tests using explosives and firearms to comprehend their behaviour against explosive and ballistic threats are scarce, especially in published literature. One of the main goals of the FPE programme is to sufficiently understand the relative performance of protective materials, to develop robust numerical models and provide suitable solutions to defend against future threats, rapidly and economically.

Currently, soil-filled wire and geotextile gabions (e.g. Hesco Concertainers) are among the most popular systems used to build defensive structures for military bases. They serve the purpose of protecting personnel and assets from the impact of blasts and fragmentation. The characteristics of soil make it a highly effective defence material against such hazards, and readily available in many locations, hence sizeable protective structures can be built quickly and cheaply. Still, soil is a variable material, with a high strain rate behaviour not fully understood. Due to recent conflicts being in arid regions, sand was the dominant soil used to build protective structures, however, what happens when sand is no longer available? This is where cohesive soils such as clay and silt can be useful.

A fortification engineer, building in an unfamiliar location will require data, which is representative of the local soil in order to understand its relative performance. The large variability of cohesive soils available makes it necessary to centre the study on a highly researched, idealised, representative soil: kaolin clay. Blast effects in cohesive soils is a vast, new, daunting subject due to the extremely limited knowledge available. The high saturation and very small particle size of cohesive soils makes it challenging to evaluate at high strain rates due to the resulting undrained loading conditions. A constitutive model will need to represent these characteristics, at high pressures and high strain rates, neither of which have been attempted before for cohesive soils, specifically kaolin clay. In comparison, cohesionless soils, such as sands, have been extensively examined at high strain rates, using the split-Hopkinson pressure bar (SHPB) [2, 3, 6, 8-10]. The larger particle size, drained behaviour and ease in sample preparation makes cohesionless samples much easier to test at high strain rates.

Recent work at the University of Sheffield aims to clarify the effects of strain rate and moisture content on kaolin clay through dynamic one-dimensional compression tests. Consequently, the main objective of this paper is to investigate the high strain-rate behaviour of undrained kaolin clay with regard to varying moisture content. Dynamic tests were performed to axial stresses of 200 MPa using a SHPB. Kaolin clay samples were confined during high strain rate SHPB testing with a steel confining ring, where the axial and lateral stresses were recorded to study the response at high strain rates.

MATERIAL CHARACTERISATION

The material tested was a white fine uniform CLAY (CL), as shown in Figure 1. For simplification, the soil selected will be referred to as ‘kaolin clay’. Kaolin clay samples were made using powdered Speswhite kaolin clay. A sieve analysis of the kaolin clay was carried out to assess the particle size distribution of the soil tested, the results are presented in Figure 2. An overview of the soil properties is shown in Table 1.

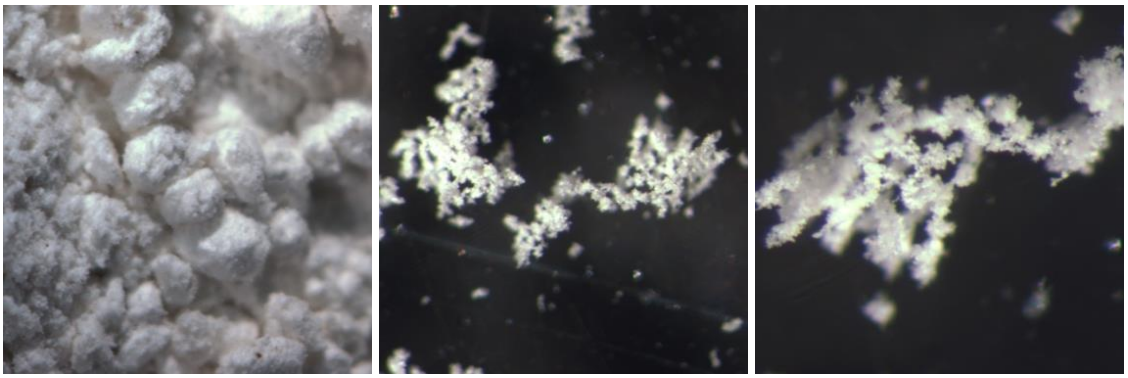

Figure 1. Optical microscope images (Left) 13X, (Center) 50X & (Right) 100X.

Table 1. Overview of kaolin clay soil properties

Primary mineral	Particle density	D_{10}	D_{60}	Coefficient of uniformity, C_u
Kaolinite	2.65 Mg/m^3	1.30 μm	3.70 μm	2.85

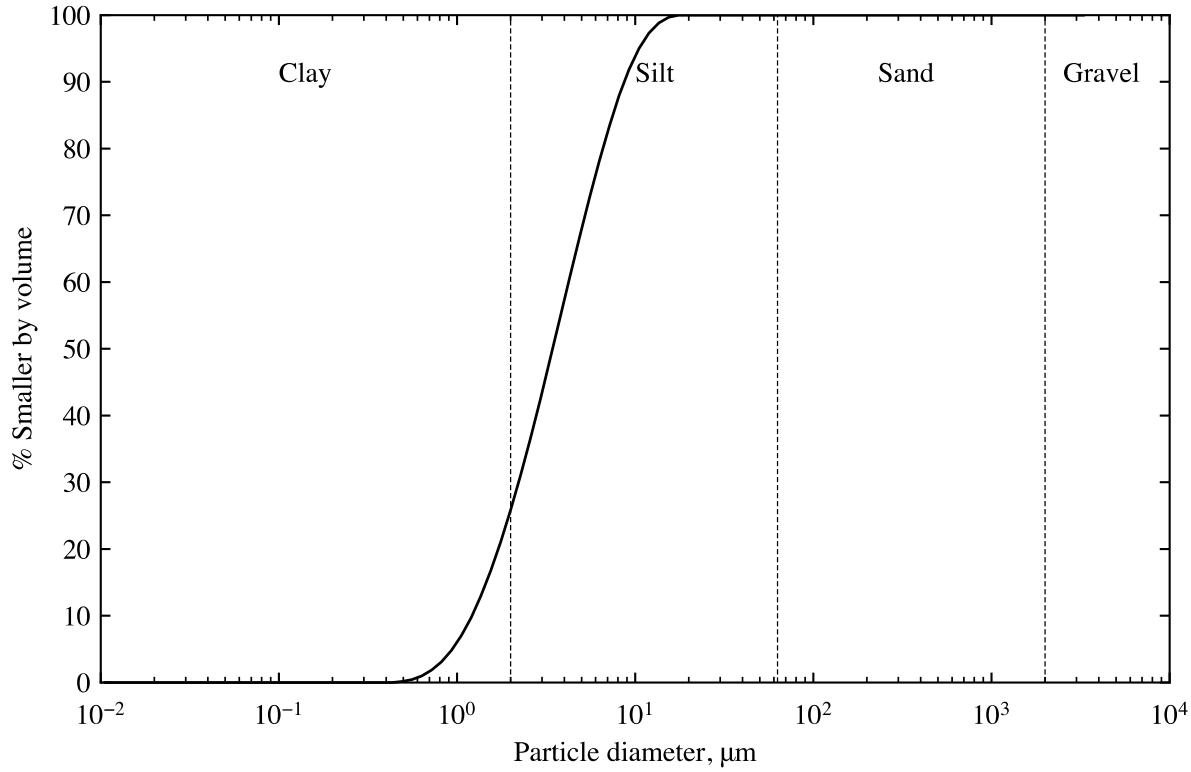

Figure 2. Initial particle size distribution of the kaolin clay.

In total, 9 kaolin clay samples were tested at moisture contents of 41.63%, 42.35% and 44.10% under confined high-strain one-dimensional compression tests, using a SHPB apparatus and a steel confining ring. They were mixed with water at a 1:1 ratio and consolidated using a Rowe cell to create solid homogenous samples at confining pressures of 400 kPa, 500 kPa & 600 kPa. The moisture content plays an important role in the behaviour of cohesive soils, much more that in cohesionless soils because of the undrained conditions of the samples, hence the Atterberg limits are crucial in this study. The specimens were stored in sealed plastic bags until testing. A summary of the material properties is shown in Table 2.

Table 2. Summary of kaolin clay sample material properties.

Soil properties	Units	Kaolin clay sample 1	Kaolin clay sample 2	Kaolin clay sample 3
Consolidation pressure	kPa	400	500	600
Bulk density, ρ	Mg/m^3	1.742	1.786	1.807
Dry density, ρ_d	Mg/m^3	1.210	1.248	1.273
Liquid Limit, LL	%	40	40	40
Plastic Limit, PL	%	25	25	25
Plastic Index, PI	%	15	15	15

TESTING PROGRAMME

The goal of this study is to assess the sensitivity of kaolin clay samples to high strain rates and to observe how any variation in response is affected by changes in moisture content. Details of the kaolin clay samples used for confined SHPB testing are in Table 2. An overview of the testing programme is in Table 3.

Table 3. Kaolin clay testing programme.

Sample details	Strain rate, s^{-1}	Moisture content, %	Test number, No.
Kaolin clay sample 1 Confined to 400 kPa	10^3	44.10	3
Kaolin clay sample 2 Confined to 500 kPa	10^3	42.35	3
Kaolin clay sample 3 Confined to 600 kPa	10^3	41.63	3

HIGH STRAIN RATE TESTING

Experiment layout

The high strain rate tests were performed using a SHPB apparatus, composed of 3 stainless steel bars and a confining ring. The stainless-steel striker, incident and transmitter bars are each 25 mm in diameter, and 400 mm, 2500 mm and 1500 mm in length, respectively. The bars are held in alignment using linear bearing fixed on a channel section. Two semi-conductor strain gauges, in a half bridge arrangement, were placed on both incident and transmitter bars, to ensure only longitudinal waves were recorded. Figure 3 shows the SHPB rig used, noting the positions of the strain gauges, dimensions and naming convention.

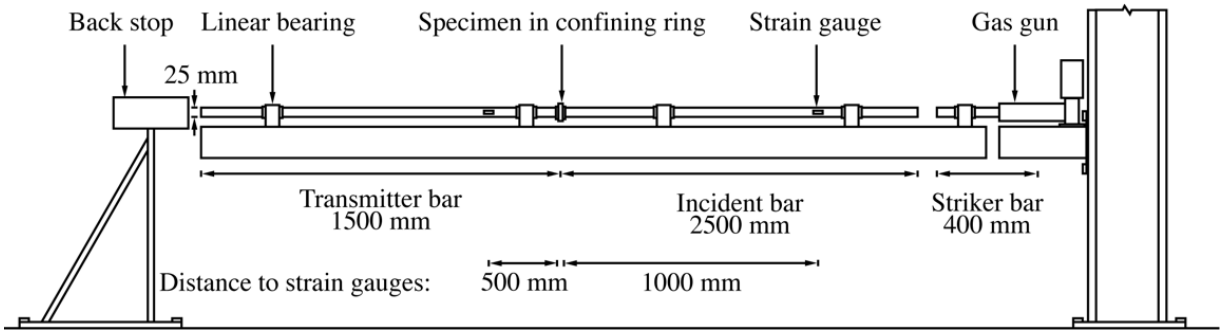

Figure 3. Schematic of the SHPB set-up prepared for the confined tests.

The individual bars were calibrated using the incident signal from the impact of the striker of known velocity (calculated using high-speed photography) and comparing it to the theoretical strain in the bar (1):

$$\varepsilon_b = \frac{v_s}{2c_0} \tag{1}$$

Where ε_b is the longitudinal strain in the bar, v_s is the velocity of the striker bar on impact and c_0 is the longitudinal wave speed in the bar.

Confining ring

Kaolin clay specimens were held in a steel confining ring with a 25 mm internal diameter and 35 mm external diameter over a length of 5 mm, as depicted in Figure 4. A semi-conductor strain gauge on the outside surface of the confining ring records the circumferential strain of the ring, as shown in Figure 5.

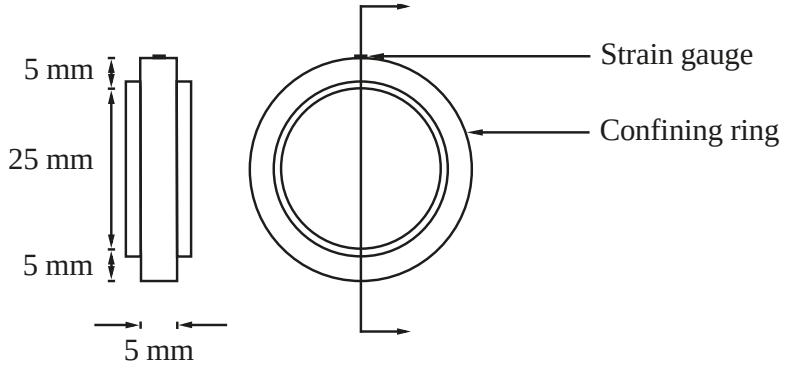

Figure 4. Gauged steel confining ring.

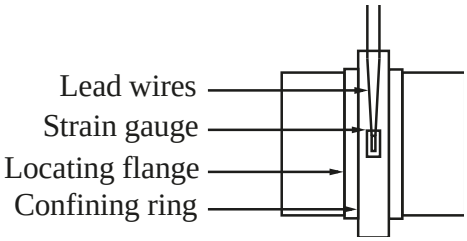

Figure 5. Strain gauge layout on a confining ring.

Using thick wall pipe theory, the average internal pressure in the sample could be linked to circumferential strain using expression (2):

$$P_i = \frac{{r_o}^2 - {r_i}^2}{2{r_i}^2} E\varepsilon_\theta \quad (2)$$

Where P_i is the internal radial pressure exerted on the specimen by the confining ring, E is the ring Young's modulus, ε_θ is the circumferential strain measured on the outside of the ring and r_o and r_i are the outer and inner radii of the ring [3].This allowed both axial and radial stresses, and strains within the sample to be recorded.

Test procedure

A kaolin clay sample with a nominal length of 5 mm, and a 25 mm diameter, was prepared by carefully placing it inside the confining ring and tamping it down using a 25 mm diameter bar, to uniformly spread the sample, filling all the gaps. The weight of the specimen was recorded prior to its installation inside the confining ring. The confining ring with the kaolin clay sample was then placed at the end of the incident bar, where the specimen in the confining ring was brought in contact with the end of the transmitter bar, as illustrated in Figure 6.

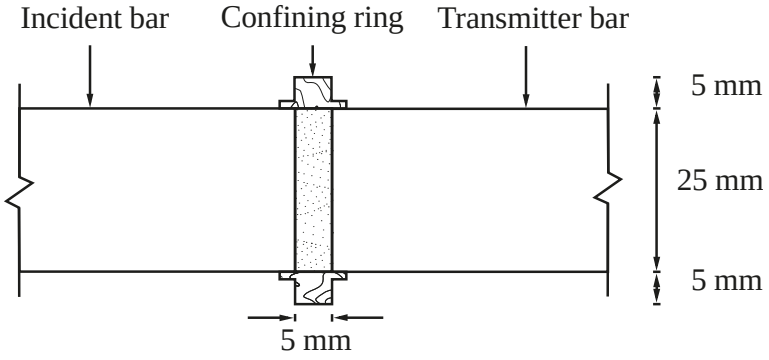

Figure 6. Axial section of the steel confining ring and kaolin clay sample set up on the SHPB.

Small sample lengths are required to achieve stress equilibrium, therefore precise measurement of the initial length is needed to ensure the high accuracy of density calculations [4]. Incident and transmitter bars were marked with perpendicular lines. The distance between the inside edges of these lines was measured using a travelling microscope fitted with a digital dial gauge (Figure 7). Measurements of before and after the kaolin clay specimen was inserted provided an initial length of the specimen with an accuracy of ±10 μm.

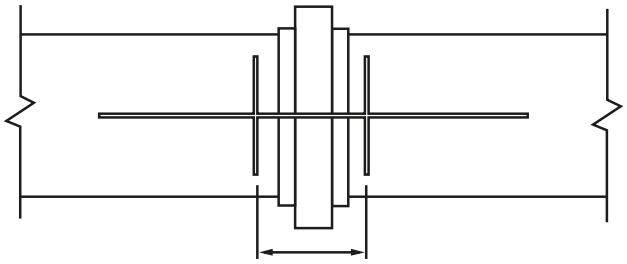

Figure 7. Axial elevation showing markings used for specimen measurements on the SHPB.

The test sequence for the SHPB tests with the confining ring on the kaolin clay samples is as follows:

1) A nylon piston was inserted into the barrel of the gas gun at a depth of 120 mm.
2) The barrel was screwed onto the gas gun, and a 0.1 mm brass diaphragm was fitted between the reservoir and the barrel.
3) The striker bar was inserted into the barrel until it was in contact with the piston.
4) Wheatstone bridges were balanced to correct for any temperature-induced strain in the bars and confining ring, and the oscilloscope was primed.
5) The reservoir of the gas gun was filled until the diaphragm ruptured, initiating the test.

The attention to detail in the set-up of the SHPB apparatus and in the measurement recording of the kaolin clay samples resulted in highly repeatable tests, as shown in the results section of this paper.

Dispersion correction is applied to the results obtained from the confined SHPB tests, conducted on the kaolin clay samples. This was completed using a specifically designed algorithm, *process_SHPB*, written in Python, for free open source access. The algorithm is available on ORDA, and GitHub, at the following:

- ORDA link: [https://doi.org/10.15131/shef.data.21973325.v1]
- GitHub link: [https://github.com/ArthurVL-maker/Process_SHPB.git]

Process_SHPB.py is the main algorithm which processes all the SHPB test data, from which the subroutines *dispersion.py* and *dispersion_factors.py* are called.

The subroutine *dispersion.py* uses an adaptation of Tyas and Pope's (2005) [5] dispersion-correction approach to verify that the inferred axial stress and strain data appropriately represent the specimen behaviour. It utilises the subroutine *dispersion_factors.py*, which includes a precalculated, normalized look-up table of phase velocity factors, m1, m2, v_ratio and norm_freq. These factors were calculated for a Poisson's ratio of 0.29, based on the steel bars used in the SHPB tests. More tables can be generated using the calculation method outlined in Tyas and Pope (2005) [5], which the python algorithm *phase_velocity.py* accomplishes successfully. The aforementioned script is available on ORDA and GitHub, at the following:

- ORDA link: [https://doi.org/10.15131/shef.data.22010999.v1]
- GitHub link: [https://github.com/ArthurVL-maker/Phase_velocity.git]

All the results are saved and named appropriately in the results folder titled, *Processed_Data*. This processing algorithm was developed from a MATLAB script created by Barr (2016) [6].

RESULTS & DISCUSSION

One-dimensional strain conditions were assumed in the sample, the maximum radial strain and maximum axial strain were recorded, where a Poisson's ratio of 0.5 was calculated. The typical strain and strain rate development as well as axial stress and radial stress development are shown in Figure 8 & 9. Figure 8 shows a consistent strain rate, throughout testing. Figure 9 shows high similarities between the axial stress and radial stress behaviour of the sample, through time, with a maximum stress of 200 MPa.

The high strain rate confined SHPB tests show no significant change in stiffness with increased moisture content. In Figure 10 & 11, the maximum axial stress is the same regardless of the dry density or strain of the sample tested. Also, in Figure 12, the compaction behaviour is identical, with a maximum axial stress reached regardless of the void ratio of the sample. Consequently, with a Poisson's ratio of 0.5, similar axial and radial stresses and an identical compaction path, the kaolin clay samples are behaving as a fluid, where the moisture of the fully saturated samples govern its behaviour.

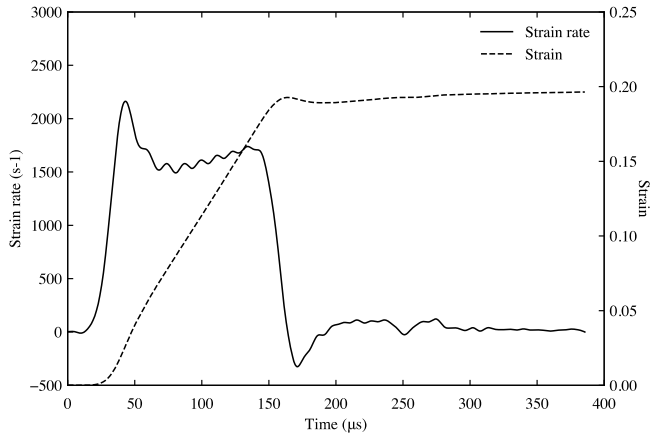

Figure 8. Typical strain and strain rate developments in confined SHPB tests on kaolin clay.

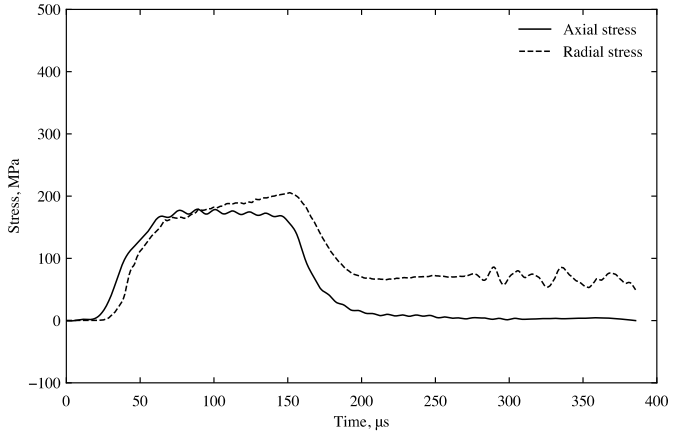

Figure 9. Typical axial stress and radial stress developments in confined SHPB tests on kaolin clay.

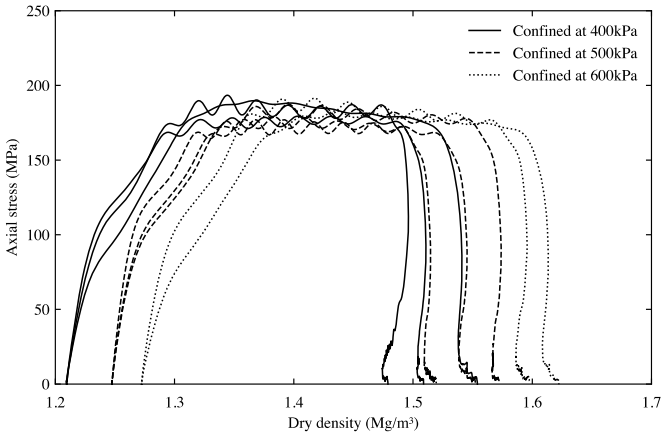

Figure 10. Axial stress-dry density data for confined SHPB tests with varying moisture content.

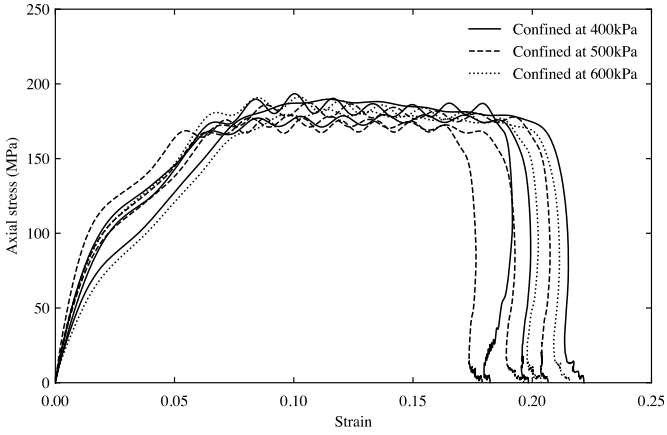

Figure 11. Axial stress-strain data for confined SHPB tests with varying moisture content.

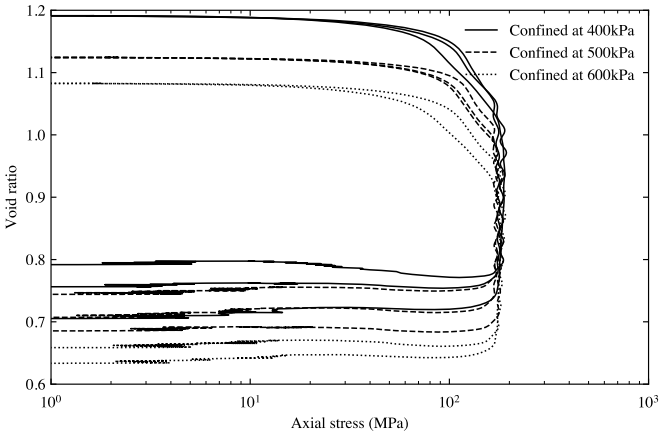

Figure 12. Void ratio-axial stress data for confined SHPB tests with varying moisture content.

CONCLUSIONS

High strain rate dynamic tests using a SHPB were carried out on kaolin clay samples to axial stresses of 200 MPa. Both axial and radial stresses and strains were recorded. The samples were made from Speswhite kaolin clay powder, which was mixed at a 1:1 ratio with water and consolidated with a Rowe cell at 400 kPa, 500 kPa & 600 kPa. Fully saturated undrained kaolin clay samples were prepared at moisture contents of 41.63%, 42.35% and 44.10%.

As these clay samples were fully saturated and loaded in undrained conditions, changes in consolidation pressure and moisture content had no effect on the overall strength of the soil. Regardless of the moisture content of the kaolin clay sample tested, its response was the same throughout.
This can be observed graphically using the results collected: the strain and strain rate development as well as the axial stress and radial stress development was identical for all kaolin clay samples. This observation is also noticeable for the axial stress vs strain and axial stress vs dry density. Additionally, a Poisson's ratio of 0.5 was calculated from these dynamic test results. In conclusion, the results observed from the tests show the behaviour the kaolin clay acting as a fluid.

High strain rate tests on sands are abundant, in which a similar observation was made regarding the significant impact of moisture content on the soil's behaviour [2, 3, 6, 8-10]. This paper highlights the high strain rate testing complexity of cohesive soils, due to their very fine particle size, undrained behaviour and fluid response in dynamic testing.

ACKNOWLEDGMENTS

The authors wish to thank Dstl for funding this research, which is part of the FPE research project [1].

REFERENCES

1. Warren, J., Kerr, S., Tyas, A., Clarke, S., Petkovski, M., Jardine, A., Church, P., Gould, P. and Williams, A., 2013. Briefing: UK ministry of defence force protection Engineering programme. *Proceedings of the Institution of Civil Engineers-Engineering and Computational Mechanics*, *166*(3), pp.119-123.
2. Bragov, A.M., Lomunov, A.K., Sergeichev, I.V., Tsembelis, K. and Proud, W.G., 2008. Determination of physicomechanical properties of soft soils from medium to high strain rates. *International Journal of Impact Engineering*, *35*(9), pp.967-976.
3. Stephens, R.C., 2013. *Strength of materials: theory and examples*. Elsevier
4. Barr, A., Clarke, S.D., Petkovski, M., Tyas, A., Warren, J. and Kerr, S., 2014, September. Quasi-static and high-strain-rate experiments on sand under one-dimensional compression. In *Proceedings of the Hopkinson Centenary Conference* (pp. 1-15). Fraunhofer EMI.
5. Tyas, A. and Pope, D.J., 2005. Full correction of first-mode Pochammer–Chree dispersion effects in experimental pressure bar signals. *Measurement science and technology*, *16*(3), p.642
6. Barr, A.D., 2016. *Strain-rate effects in quartz sand* (Doctoral dissertation, University of Sheffield).
7. Ross, C.A., Nash, P.T. and Friesenhahn, G.J., 1986. *Pressure waves in soils using a split-Hopkinson pressure bar*. SOUTHWEST RESEARCH INST SAN ANTONIO TX.
8. Luo, H., Cooper, W.L. and Lu, H., 2014. Effects of particle size and moisture on the compressive behavior of dense Eglin sand under confinement at high strain rates. *International Journal of Impact Engineering*, *65*, pp.40-55.
9. Veyera, G.E., 1994. *Uniaxial stress-strain behavior of unsaturated soils at high strain rates*. Wright Lab Tyndall Afb Fl.

A.4 An open-source algorithm for correcting stress wave dispersion in split-Hopkinson pressure bar experiments

Van Lerberghe, A., Li, K. S. O., Barr, A. D., & Clarke, S. D. (2024). An open-source algorithm for correcting stress wave dispersion in split-Hopkinson pressure bar experiments.

A paper detailing the dispersion correction capabilities and the implementation of the signal processing algorithm, submitted for publication to the MDPI journal Sensors. The journal paper is included in its entirety below as reference.

MDPI

Article

An Open-Source Algorithm for Correcting Stress Wave Dispersion in Split-Hopkinson Pressure Bar Experiments

Arthur Van Lerberghe [1]*, Kin Shing O. Li [1], Andrew D. Barr [1] and Sam D. Clarke [1]

[1] School of Mechanical, Aerospace & Civil Engineering, University of Sheffield, S1 3JD, Sheffield, UK
* Correspondence: avanlerberghe1@sheffield.ac.uk

Abstract: Stress wave dispersion can result in the loss or distortion of critical high-frequency data during high-strain-rate material tests or blast loading experiments. The purpose of this work is to demonstrate the benefits of correcting stress wave dispersion in split-Hopkinson pressure bar experiments under various testing situations. To do this, an innovative computational algorithm, `SHPB_Processing.py`, is created. Following the operational run through of `SHPB_Processing.py`'s capabilities, it is used to process test data acquired from split-Hopkinson pressure bar tests on aluminium, sand and kaolin clay samples, under various testing conditions. When comparing dispersion corrected and simple time shifting data obtained from SHPB experiments, accounting for dispersion removes spurious oscillations and improves the inferred measurement at the front of the specimen. The precision of the stress and strain results gathered from its application emphasises its importance through the striking contrast between its application and omission. This has a significant impact on the validity, accuracy and quality of the results. As a result, in the future, this tool can be utilised for any strain rate testing situation with cylindrical bars that necessitates dispersion correction, confinement or stress equilibrium analysis.

Keywords: Signal processing; dispersion correction; high-strain-rate testing; stress waves; split-Hopkinson pressure bar; material applications; open-source algorithm.

1. Introduction

Traditionally, a Hopkinson pressure bar (HPB) is used to quantify a transitory pulse generated by the impact of near-field blast events or bullets. The split-Hopkinson pressure bar (SHPB), also known as the Kolsky bar, has been widely utilised to measure dynamic material properties such as stress-strain and strain rate-strain curves of versatile materials at strain rate ranging from 10^2 to 10^4 s^{-1}. The shape of the elastic wave in SHPB and HPB distorts as it travels; this phenomenon is referred to as dispersion [1].

From the standpoint of medium particle motion, the physical origin of dispersion is inertia in the lateral motion associated with the axial disturbance. From the standpoint of wave propagation, a high-frequency wave component that constitutes the total elastic wave is slower than a lower-frequency wave component [2].

The wave profile is typically assessed at the interim axial position of the bar, using strain gauges. In the case of the HPB, the front surface of the bar is the location of interest where an impact pulse enters the bar, whereas in the case of the SHPB, the specimen location is of interest. Consequently, the measured wave profiles in HPB and SHPB must be corrected to obtain the wave profiles at the locations of interest, a procedure known as dispersion correction [1,3].

One dimensional wave theory assumes that all longitudinal waves in the bar propagate at a velocity c_0. The theory also demands that plane transverse sections of the bar remain plane, and that the stresses act uniformly across these sections. However, as a wave travels along the bar, it will expand and contract radially with compressive and tensile axial strains in accordance with the bar's Poisson's ratio. This radial motion alters the stress distribution over the bar cross-section, causing plane sections to become distorted [2].

Citation: Van Lerberghe, A.; Li, K.S.O.; Barr, A.D.; Clarke, S.D. An Open-Source Algorithm for Correcting Stress Wave Dispersion in Split-Hopkinson Pressure Bar Experiments. *Sensors* **2024**, *1*, 0. https://doi.org/

Received:
Revised:
Accepted:
Published:

The consequence of this deviation from the idealised conditions can be seen in the three-dimensional wave equations developed by Pochhammer [4] and Chree [5], which Bancroft [6] applied to the case of longitudinal waves in a cylindrical bar. Instead of travelling uniformly at a velocity c_0, longitudinal wave were proven to propagate at a specific velocity c_ω which is a function of wavelength and the bar's diameter, one-dimensional wave speed and Poisson's ratio, as depicted in Equation 1:

$$(x-1)^2\varphi(ha) - (\beta x - 1)[x - \varphi(\kappa a)] = 0 \tag{1}$$

where

$$\begin{aligned} \beta &= (1-2\nu)/(1-\nu) \\ x &= (c_\omega/c_0)^2(1+\nu) \\ h &= \gamma(\beta x - 1)^{\frac{1}{2}} \\ \kappa &= \gamma(2x-1)^{\frac{1}{2}} \\ \varphi(y) &= yJ_0(y)/J_1(y) \end{aligned}$$

and with c_ω as the phase velocity, c_0 as the one-dimensional elastic wave velocity, a as the bar radius, ν as the Poisson's ratio, γ as the wave number, $2\pi/\lambda$, λ as the wave length and J_n(y) as the Bessel function of the first kind, of order n.

This equation has an infinite number of roots, each of which corresponds to a particular mode of propagation in the bar, the first of which are shown in Figure 1. This suggests that low-frequency waves propagate at approximately c_0, but phase velocity drops with increasing frequency, especially when the wavelength matches the bar diameter.

The complex waveforms generated during a SHPB experiment contain an extensive range of frequency components, and as a result of this frequency dependency, the stress disperses as it propagates down the bar. This phenomenon is depicted in Figure 2, which displays the dispersion of a trapezoidal wave in a stainless-steel pressure bar. Dispersion of the stress pulse is accompanied by the frequency-dependent fluctuation in stress and strain throughout the bar cross-section [7]. As illustrated in Figure 3, when the frequency of the forcing function rises, strains recorded on the bar surface decrease in comparison to strains measured at the bar axis. These phase velocity and amplitude effects mean that a strain signal recorded on the bar's surface may not represent the mean strain and stress on the bar face in contact with the specimen, some distance away.

Standard practice, as discussed by Gray III [8] in the ASM handbook, assumes that simply timeshifting all the signals collected from SHPB testing is a suitable strategy, however this method can result in severe errors and inaccuracies.

Previous work by Shin [1,3,9] developed dispersion-related MATLAB and Excel scripts to process SHPB test data. These algorithms focused on phase velocity corrections but not amplitude correction. While useful for many applications, experiments with high-frequency components, or a large diameter, will experience significant stress and strain variation over the bar cross-section, making amplitude correction desirable for accurately evaluating specimen behaviour [10].

The current work seeks to develop an algorithm capable of solving the issues associated with dispersion in SHPB experiments. To accomplish this, the key theory of dispersion correction, stress wave equilibrium and confinement analysis in SHPB experiments is addressed first. Then, the aforementioned tool, `SHPB_Processing.py`, is presented with all its functionalities and subroutines. Finally, it is applied to SHPB test data collected, demonstrating its practical importance.

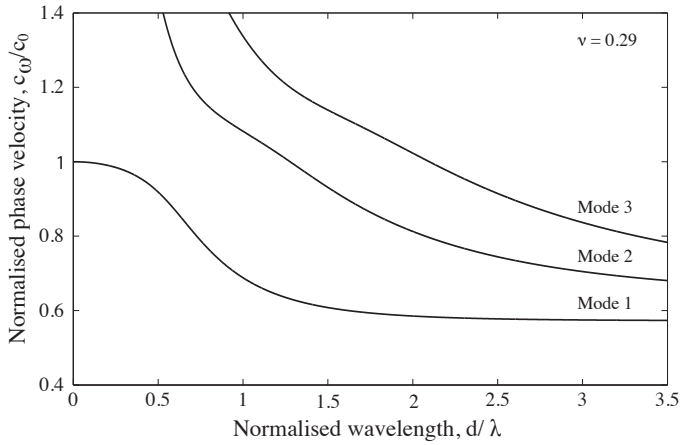

Figure 1. Relationship of phase velocity to wavelength for the first 3 modes of propagation of a longitudinal wave in a stainless-steel cylindrical bar for $\nu = 0.29$ [7].

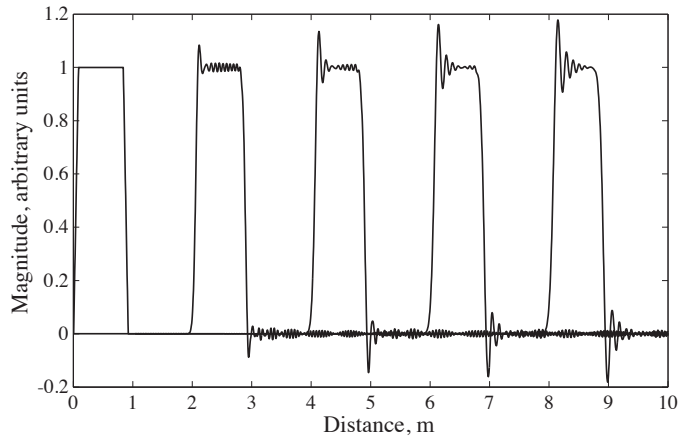

Figure 2. Dispersion of a trapezoidal wave in a cylindrical stainless-steel pressure bar, with recordings at 2 m increments [7].

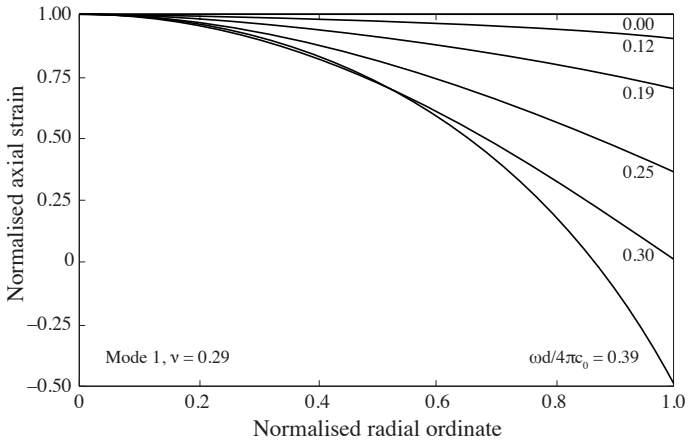

Figure 3. Distribution of axial strain over a stainless-steel ($\nu = 0.29$) bar cross section for an infinite duration single frequency forcing function [7], after [11].

2. Dispersion correction in SHPB experiments

At higher frequencies ($a/\lambda > 0.05$), the errors mentioned above become considerable, but they can be addressed using the method outlined by Tyas and Pope [10], where corrections are applied to the amplitudes and phase angles of each frequency component of the signal.

2.1. Phase angle correction

The first correction made to the SHPB signals is the adjustment of the phase angle to account for the dispersion of each frequency component over the distance between the strain gauge and the bar end. This is accomplished, according to Gorham [12] and Follansbee and Frantz [13], by computing the phase velocity c_ω, of each component using Bancroft's [6] equation (Equation 1) and then applying a phase shift, θ'_ω , as portrayed in Equation 2:

$$\theta'_\omega = \left(\frac{c_0}{c_\omega} - 1\right)\frac{\omega z}{c_0} \tag{2}$$

where ω is the component's angular frequency, and z is the distance over which the correction is performed, positive in the direction of wave propagation.

Barr et al. [14] conducted tests to understand how energy is distributed between higher modes of propagation, concluding that the frequency content in common SHPB experiments only requires consideration of the first mode of propagation.

2.2. Amplitude correction

The second correction to the SHPB signals involves applying factors to the amplitude of the frequency components. Tyas and Watson [11] established the factors M_1 and M_2 to account for the radial variation of strain and Young's modulus, respectively, derived from Davies' [15] investigation of these radial effects. Using these factors, the strain measurement obtained on the bar's surface can be utilised to calculate the mean axial stress and strain acting over the entire cross-section. In a SHPB experiment, phase angle (dispersion) correction transforms a bar surface measurement at the strain gauge to a bar surface measurement at the specimen interface, the amplitude correction transforms this bar surface measurement into the mean strain and stress experienced across the face of the specimen.

The factors are defined in Equations 3 and 4 as follows:

$$M_1 = \frac{2\left(1 + \frac{1-\beta x}{x-1}\right)}{\varphi(ha) + \frac{1-\beta x}{x-1}\varphi(\kappa a)} \tag{3}$$

$$M_2 = E\left(\frac{c_\omega}{c_0}\right)^2 \tag{4}$$

where details of the variables in Equations 3 and 4 are the same as in Equation 1, with E being the Young's modulus.

Figure 4 shows the fluctuation of M_1 and M_2 with normalised wavelength for a stainless-steel bar with a Poisson's ratio of 0.29. Due to the discontinuity in M_1 at a/λ = 0.375, which corresponds to the point where the strain recorded on the surface of the bar falls to zero, the reciprocal of M_1 is displayed; at even higher frequencies, the recorded strain has the opposite sign to the mean cross-sectional response. As the adjustments applied at a/λ = 0.375 require multiplying a low-magnitude signal by a very large correction factor, noise in the signal is likely to affect the accuracy of the result significantly. This effectively establishes an upper limit on the frequency range that can be corrected: according to Tyas and Watson [11], the approach can be used at normalised wavelengths below $a/\lambda \approx 0.3$.

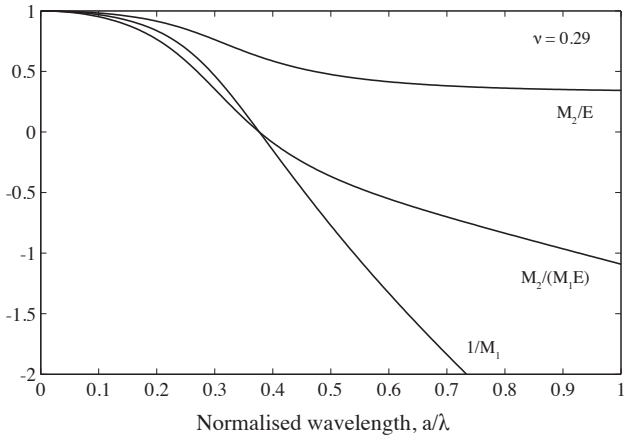

Figure 4. Variation of factors M_1 and M_2 in a cylindrical stainless-steel bar for $\nu = 0.29$ [7].

3. SHPB_Processing.py

`SHPB_Processing.py` is an open-source Python algorithm for high-strain-rate SHPB signal processing. This function includes a subroutine titled `dispersion.py` that is optimised to process raw signal strain data using dispersion correction (Section 4).

This function, `SHPB_Processing.py`, is designed to take strain gauge input data from high-strain-rate SHPB tests and, by specifying the additional input variables defined in Table 1, determine axial and radial (if confinement specified) stress developments of the sample, its strain and strain rate history variations through impact, and other related parameters derived from these output variables.

The following command line is necessary to run this algorithm:

```
SHPB_Processing(csv_path, sample_data, confinement, signal_channels,
                signal_amp, disp_correction, alignment, speedtrap)
```

The optimal approach to running this function is detailed below, with Figure 5 depicting this as a concise flowchart:

1. Calculate stress wave speed and gauge factors of the cylindrical bars used for SHPB testing using the `gauge_factor.py` script, available on GitHub and ORDA [16].
2. Use `phase_velocity.py` to calculate the dispersion factors required to perform the dispersion correction of the collected SHPB signals using `dispersion.py` based on the material properties of the cylindrical bar used for SHPB testing. The algorithm `phase_velocity.py` is available on GitHub and ORDA.
3. The algorithm `SHPB_Processing.py` is ready to be run, with `dispersion.py`, to effectively process the SHPB test data with dispersion correction, based on the input parameters chosen. The results are returned in a designated Processed data folder. `Dispersion.py` is available on GitHub and ORDA.

The full source code for `SHPB_Processing.py` is available on GitHub and ORDA [17].

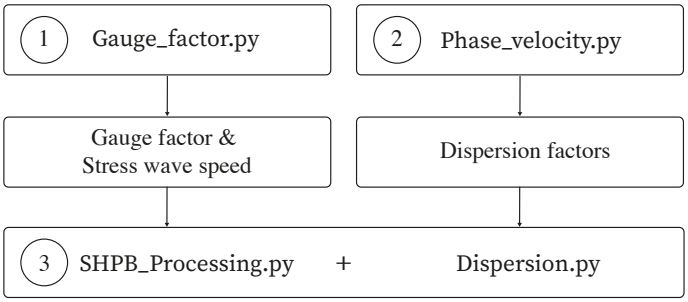

Figure 5. Flowchart illustrating the steps to run `SHPB_Processing.py` efficiently.

Table 1. Input and output variables used in `SHPB_Processing.py`.

Inputs	**Description**
`csv_path`	File directory containing CSV file with raw test data.
`sample_data`	Array containing the initial length, mass, and dry mass of the sample, i.e. [initial length, mass, dry mass].
`confinement`	Confinement mechanism applied, i.e. 'None', 'Ring', or 'Reservoir'.
`signal_channels`	Oscilloscope channel numbers used to record raw data, i.e. [in_bar_gauge_channel, out_bar_gauge_channel, ring_gauge_channel or reservoir_gauge_channel].
`signal_amp`	Strain gauge amplification applied to strain gauge measurement, i.e. [in_bar_gauge_amp, out_bar_gauge_amp, ring_gauge_amp].
`disp_correction`	Apply dispersion correction or simple time shift processing for signal data, i.e "True" for dispersion correction using `dispersion.py`.
`alignment`	Specify alignment mode for aligning stress waves at sample interfaces, i.e. 'start' aligns the start of incident and transmitted pulse, 'end' aligns the end, and 'mid' aligns the median time of the pulse. Integer/float values greater than 1 align the peaks of the incident and transmitted pulse to specific times. Float values between 0 and 1 align the incident and transmitted pulse on a specific fraction of the max value.
`speedtrap`	Specify speed trap data to determine striker bar velocity, i.e 'True' for speed trap velocity calculation.
Outputs	**Description**
Processed data folder	Folder with all the CSV processed data files, and test log for history monitoring.

The function's operation can be summarised as follows:

1. The oscilloscope data from SHPB strain gauges are read.
2. The striker bar velocity is determined based on raw speed trap data.
3. The raw data file prepared for correction and confinement analysis via pulse detection and signal reformatting.
4. The correction ('True' for dispersion correction, or 'False' for simple time shift) and confinement ('None', 'Ring' or 'Reservoir') requirements are applied on strain data collected based on input specifications.
5. The incident, reflected and transmitted pulses are detected using the trigger and wave speed propagation in the bars used during SHPB testing.
6. The pulse end is marked when the sample strain reaches its maximum.
7. The dispersion-corrected stresses and strains for each wave are calculated using `dispersion.py`, details of which are present below. For simple timeshifting, simple signal restructuring is conducted.
8. The axial stresses and strains in the specimen are calculated using the incident, reflected and transmitted wave signals.
9. Based on strain gauge strain, the sample strain is determined from the displacement of the pressure bars.
10. Based on the confinement type selected, 'None', 'Ring' or 'Reservoir', the following will happen:
    (a) For a SHPB test with 'None' as the confinement type, no radial stresses or strains are calculated for the specimen.
    (b) For a SHPB test with 'Ring' as the confinement type, using thick-walled pipe theory, the radial stress and strain in the specimen is calculated from the circumferential strain in the ring.
    (c) For a SHPB test with 'Reservoir' as the confinement type, pressure data collected from the gauge in the reservoir is used to calculate the specimen's radial stress and strain.
11. The specimen density and dry density are calculated for 'Ring' and 'Reservoir' confinement types.
12. All results are saved as csv files into the Processed data folder, along with the test log.

4. Dispersion.py

4.1. A Python function for dispersion correction

`Dispersion.py` is an open-source Python algorithm that has been developed to automate the application of phase angle and amplitude corrections to SHPB signals as part of the main processing of `SHPB_Processing.py`. This substitutes basic time shifting of signals with manipulation of individual frequency components. The capabilities of this function are described in this section, with the complete source code for `dispersion.py` and its accompanying subroutine available on GitHub and ORDA [18].

4.2. Frequency domain in Python

The fast Fourier transform (FFT) is an algorithm used to convert a signal into the frequency domain. This technique portrays a signal as the sum of a sequence of sinusoidal waves of varying frequencies and amplitudes. FFT is implemented in Python using the `numpy` library and `fft` function, which takes any regularly-sampled signal and returns amplitude and phase information with frequency as a matrix of complex vectors of the form $z = z_r + iz_i$. At a given frequency, the amplitude, A (Equation 5), and phase angle, θ (Equation 6), of the Fourier component are calculated as:

$$A = \sqrt{z_r^2 + z_i^2} \tag{5}$$

$$\theta = \tan^{-1}\left(\frac{z_i}{z_r}\right) \tag{6}$$

These relationships are illustrated in Figure 6a, where z and its complex conjugate $\bar{z}$ are represented in the complex plane, and in Figure 6b, where these values are utilised to represent the amplitude and phase angle of a specific sinusoid.

The Fourier component can be reconstituted using the relationship in Equation 7 once suitable corrections have been applied to the amplitude and phase angle, as seen below:

$$z = A\cos(\theta) + iA\sin(\theta) = Ae^{i\theta} \tag{7}$$

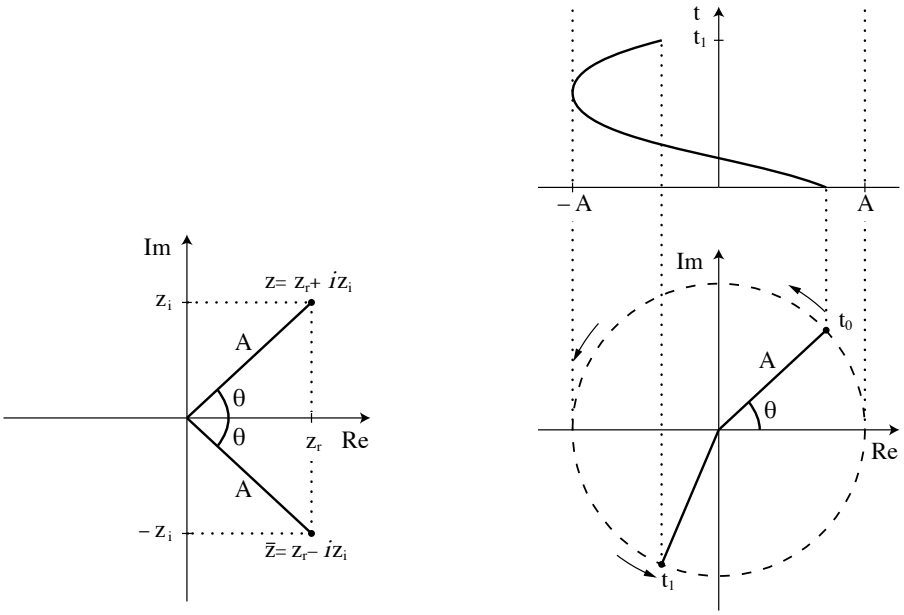

(a) **(b)**

Figure 6. A Fourier component z in the complex plane with (a) relationship to amplitude and phase angle and (b) description of a sinusoid [7].

4.3. Correction bandwidth

The FFT is an algorithm to efficiently compute the discrete Fourier transform (DFT) of a signal. The DFT calculates frequency components at a finite number of values, which depend on the original signal's sampling rate and length. If a signal is sampled N times at a frequency f, the lowest readable frequency is equal to f/N, describing a single wave occupying the sampling window (Figure 7a). Higher frequencies are multiples of the fundamental frequency, all the way up to the highest readable frequency, or Nyquist frequency, which equates to $f/2$ (Figure 7b). This limit is set because at least two samples are necessary for each period to prevent aliasing, as shown in Figure 7c. Due to undersampling, two different sinusoids can be fitted to the sample data. The oscilloscope's sample rate ($f/2$ = 500 kHz in the current tests) limits the highest readable frequency, although the frequency resolution can be improved by raising N, either by increasing the recording duration, or by zero-padding the input signal.

The `fft` function will generate an N-length frequency domain vector $X(\omega)$, given an N-length time-domain vector $x(t)$. As a result of the aliasing explained above, the second half of $X(\omega)$ is the complex conjugate of the first half, reflected about the Nyquist frequency, as seen in Figure 8. This means that modifications only need to be individually applied to the first $N/2 + 1$ bins in $X(\omega)$, which may then be reflected to complete the vector.

As stated in section 2.2, the very low strain signals measured on the surface of the bar at wavelengths below $a/\lambda \approx 0.3$, impose an additional frequency limit. For example, for a 25 mm diameter stainless-steel bar, adjustments can only be successfully made between 39 μHz and 94 kHz in the current SHPB set up. Figure 9 depicts a frequency-domain portrayal of a typical experimental incident pulse in the form of a modified periodogram. Power is measured in logarithmic units, with a charge of 10 dB denoting an order of magnitude shift in the power of the signal. The periodogram, as explained above, indicates that the power of the signal recorded on the surface of the bar rapidly decreases to zero between 94 kHz and 110 kHz. Since dispersion correction can only be implemented at frequencies below 94 kHz, for this setup, the signal is sent through a low-pass filter to remove the higher frequencies.

In Figure 10, the power at these frequencies is orders of magnitude smaller, and so little information is lost in filtering.

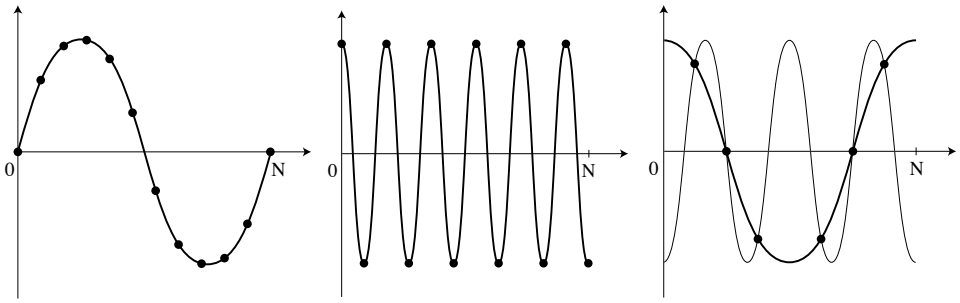

Figure 7. Frequency limitations in the FFT with (a) minimum frequency and (b) maximum frequency for a signal where N = 12 and (c) aliasing at higher frequencies [7].

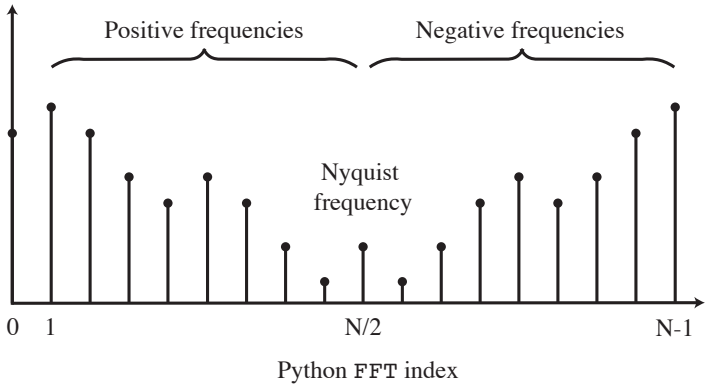

Figure 8. Composition of the frequency-domain vector produced by `fft` in Python [7].

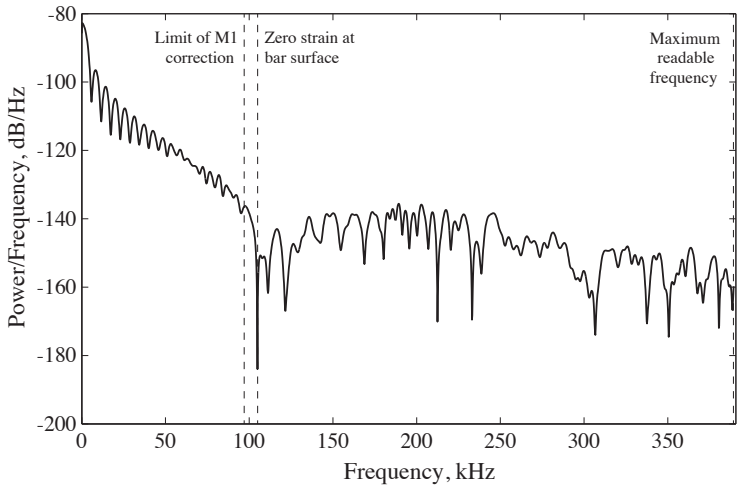

Figure 9. Power spectral density for experimental incident wave, from a 25 mm stainless-steel bar with a Poisson's ratio of 0.29, and maximum frequency limits imposed by the strain gauge data and FFT [7].

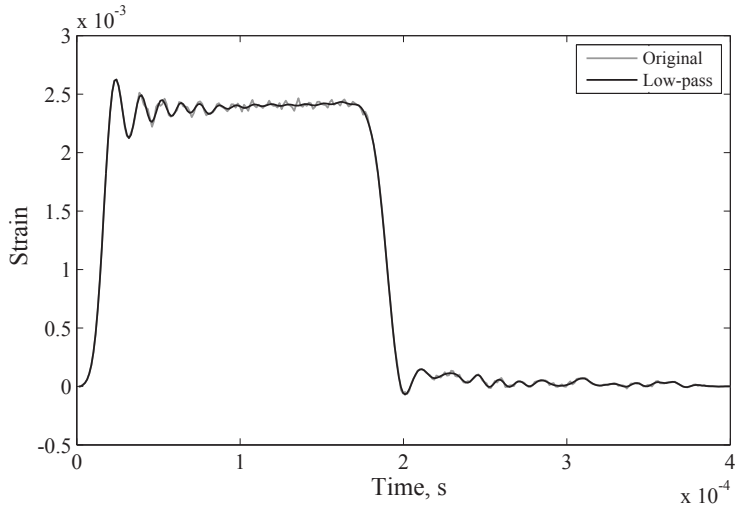

Figure 10. This experimental setup's incident wave and result of low-pass filtering of frequencies above 94 kHz [7].

4.4. Operation of dispersion.py

When the option for dispersion correction is selected in `SHPB_Processing.py`, the open-source Python algorithm `dispersion.py` is called as a subroutine during the processing of the SHPB signals collected from testing.

The function `dispersion.py` was created to automate the application of phase angle and amplitude correction factors generated by `dispersion_factors.py`, to SHPB pressure bar signals obtained from the experiments, manipulating frequency components and correcting the effects of dispersion over a specified propagation length.

The programme `dispersion_factors.py` is a mandatory subroutine of `dispersion.py`. After isolating the incident, reflected, and transmitted waves, `dispersion.py` is used to infer the stress and strains at the bar-specimen interface for each wave using the following command, which includes input and output variables defined in Table 2. Values for ν may be found from mill specification sheets, and c_0 from strain measurements of a low frequency content wave oscillating in a bar of known length. Alternatively, these can be calculated using an iterative method, such as that developed in Shin [1].

The following command line is necessary to run this algorithm:

`dispersion (x, fs, a, c0, E, z)`

Table 2. Input and output variables used in in `dispersion.py`.

Inputs	**Description**
`x`	Zero-padded strain signal in time domain (1xN numeric).
`fs`	Sampling frequency, Hz.
`a`	Bar radius, m.
`c0`	One-dimensional wave velocity of the bar, m/s.
`E`	Young's modulus of the bar, GPa.
`z`	Distance to apply correction over, positive in direction of propagation, m.
Outputs	**Description**
`x_strain`	Dispersion-corrected strain signal.
`x_stress`	Dispersion-corrected stress signal, MPa

This subroutine adapts Tyas and Pope's [10] dispersion-correction approach to ensure that the inferred axial stress and strain data accurately depicts the specimen behaviour.

The function's operation can be summarised as follows:

1. FFT is used to convert the strain signal to a frequency-domain signal.
2. The frequency components above the M_1 correction cut-off are removed using an ideal low-pass filter.
3. Below the Nyquist frequency, for each of the remaining components:
   (a) The `disperion_factors.py` function is used to calculate the required phase shift as well as the factors M_1 and M_2. To reduce computation time, this method employs a pre-calculated, normalised look-up table generated by `phase_velocity.py`.
   (b) Equation 7, factors M_1 and the phase angle correction θ'_ω are used to rebuild a dispersion-corrected strain component, as shown below in Equation 8:

$$z_\varepsilon = M_1 A e^{i(\theta - \theta'_\omega)} \tag{8}$$

   where A is the original amplitude of the component and θ is the original phase angle.

(c) A dispersion-corrected stress component is similarly reconstructed using factors M_1 and M_2, as well as the phase angle correction, θ'_ω, as illustrated in Equation 9 below:

$$z_\sigma = M_1 M_2 A e^{i(\theta - \theta'_\omega)} \quad (9)$$

4. Frequency components above the Nyquist frequency are formed by taking the complex conjugate of these adjusted stress and strain components.
5. The frequency-domain stress and strain signals are transformed back to the time domain using the inverse FFT, `ifft()`, from the numpy library, and returned as output variables `x_strain` and `x_stress`.

These corrected pressure bar stresses and strains are used in `SHPB_Processing.py` to infer the behaviour of the SHPB specimen.

4.5. Operation of dispersion_factors.py

The Python algorithm, `dispersion_factors.py`, is a subroutine of the programme `dispersion.py`. The dispersion factors utilised in this script are calculated using the algorithm `phase_velocity.py`, with a Poisson's ratio of 0.29, which is based on the property of the Hopkinson bars used for testing in this case.

Afterwards, `dispersion_factors.py` loads the four dispersion factor files, `m1`, `m2`, `norm_freqs` and `v_ratios`, before calculating the amplitude and phase angle corrections required to account for dispersion at a specific frequency.

The following command line is necessary to run this algorithm, with details of the input and output variables are outlined in Table 3:

```
dispersion_factors (f,a,c0,z)
```

Table 3. Input and output variables used in `dispersion_factors.py`.

Inputs	**Description**
`f`	Frequency, Hz.
`a`	Bar radius, m.
`c0`	One-dimensional wave velocity of the bar, m/s.
`z`	Distance to apply correction over, m.
Outputs	**Description**
`angle_mod`	Phase angle correction, rad.
`m1`	Correction for variation in response across bar cross-section.
`m2`	Correction for variation in ratio of axial stress and axial strain (dynamic Young's modulus).

The corrected `angle_mod`, `m1` and `m2` factors are then used in `dispersion.py` to apply the appropriate signal phase shift to obtain the adjusted strain and stress. It was inspired by a MATLAB script created by Barr [19].

4.6. Operation of phase_velocity.py

`Phase_velocity.py`, is an independent open-source function available on GitHub and ORDA [20]. Its objective is to find the first root of Bancroft's equation [6] using the bisection method, for a defined Poisson's ratio, and over a defined range of normalised wavelength (d/L). The result is the normalised phase velocity, c_p/c_0, which corresponds to the first mode of propagation for longitudinal waves in an elastic cylindrical bar.

Normalised wavelengths are also converted to normalised frequency, fa/c_0. Normalised phase velocities are then used to calculate Tyas and Wilson's [11] factors M_1 and M_1, which account for wavelength-dependent radial variations in strain and Young's modulus, respectively.

The following command line is necessary to run this algorithm, with details of the input and output variables outlined in Table 4:

```
phase_velocity (nu, l_ratios)
```

Table 4. Input and output variables used in `phase_velocity.py`.

Inputs	**Description**
`nu`	Poisson's ratio of bar material used for SHPB tests.
`l_ratios`	Normalised wavelength range to calculate the first root of **(alias?)** equation.
Outputs	**Description**
`dispersion_factors`	Folder which includes 4 .pickle files containing the dispersion factors `m1`, `m2`, `norm_freqs` and `v_ratios`.

The factors `m1`, `m2`, `norm_freqs` and `v_ratios` are then used in `dispersion_factors.py` and `dispersion.py` by association to carry out the dispersion correction of the acquired SHPB signals, as a functionality of the main processing script `SHPB_Processing.py`. It was inspired by a MATLAB script created by Barr [21].

5. Practical applications

5.1. SHPB testing

A split-Hopkinson pressure bar apparatus consisting of two stainless-steel pressure bars, an incident and transmitted bar, was utilised for testing. The gauge locations on the incident and transmitter bars required to process the data were placed at a distance of 1000 mm and 500 mm, respectively, from the sample front and back interfaces. On each bar, a pair of Kyowa KSP-2-120-E4 semiconductor strain gauges were used to record the signals.

5.2. Kaolin clay

A 25 mm kaolin clay sample was tested using a SHPB apparatus configuration detailed in section 5.1 under unconfined conditions. The sample had an initial length of 5.357 mm, a mass of 4.466 g and a dry mass of 3.167 g. The raw signal data for the incident and transmitter bars were recorded on channels 7 and 8. The incident and transmitter bars were amplified by a factor of 10 and 100, respectively. Dispersion correction was applied. The signals were aligned at the start, and the speed of the striker bar was measured. The data was processed using `SHPB_Processing.py` with the following command line:

```
SHPB_Processing (csv file, [5.357, 4.466, 3.167], 'None', [7, 8, 5], [10, 100, 1],
                 True, 'start', True)
```

5.3. Sand

A 25 mm medium sand sample was tested using a SHPB apparatus configuration detailed in section 5.1 under confined conditions. The sample had an initial length of 4.726 mm, a mass of 3.50 g and a dry mass of 3.50 g. The raw signal data for the incident and transmitter bars were recorded on channels 1 and 2. The raw signal for the confining ring was measured on channel 3. The incident and transmitter bars were amplified by a factor of 10. Dispersion correction was applied. The signals were aligned at the start, and the speed of the striker bar fired by the gas gun was measured. The data was processed using `SHPB_Processing.py` with the following command line:

```
SHPB_Processing (csv file, [4.726, 3.50, 3.50], 'Ring', [1, 2, 3], [10, 10, 1],
                 True, 'start', True)
```

5.4. Aluminium

A 12 mm aluminium sample was tested using the SHPB apparatus configuration detailed in section 5.1 under unconfined conditions. The sample had an initial length of 5.000 mm, a mass of 1.530 g and a dry mass of 1.530 g. The raw signal data of the incident bars were recorded on channels 1 and 2. The incident and transmitter bars were amplified by a factor of 1. Dispersion correction was applied. The signals were aligned at the start, and the speed of the striker bar was not measured. The data was processed using `SHPB_Processing.py` with the following command line:

```
SHPB_Processing (csv file, [5.000, 1.530, 1.530], 'None', [1, 2], [1, 1], True, 'start', True)
```

5.5. Comparative analysis of the SHPB tested scenarios

With all three SHPB tests processed with the algorithm `SHPB_Processing.py`, its capabilities are evident since different materials with distinctly different behaviours were run successfully. In each case, the dispersion correction adds 1000 mm of wave propagation to the incident wave, and removes 1000 mm of wave propagation from the reflected wave, taking the frequency dependence of phase velocity into account as described above. As the specimen front stress is calculated by the superposition of the incident and reflected waves, the inferred front stress is greatly improved as a result: Figures 11, 12 and 13 highlight the benefits of dispersion correction vs simple time shifting analysis. It is clear that when dispersion correction is applied to the incident and reflected waves there are substantially fewer spurious oscillations in the inferred sample front stress, which leads to more accurate axial stress data and an enhanced understanding of specimen behaviour.

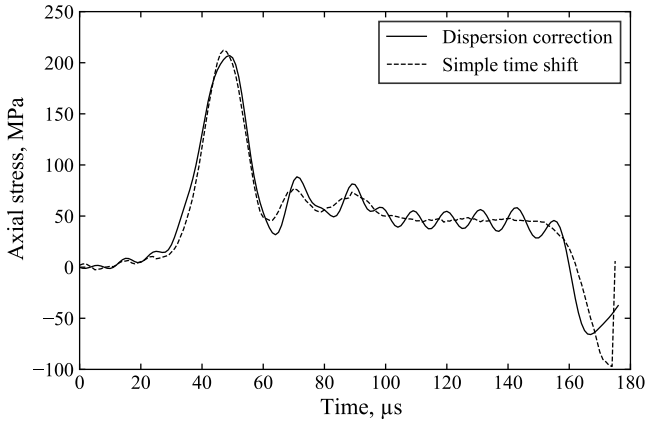

Figure 11. Dispersion vs. time shift analysis of front stress in unconfined SHPB test on kaolin clay.

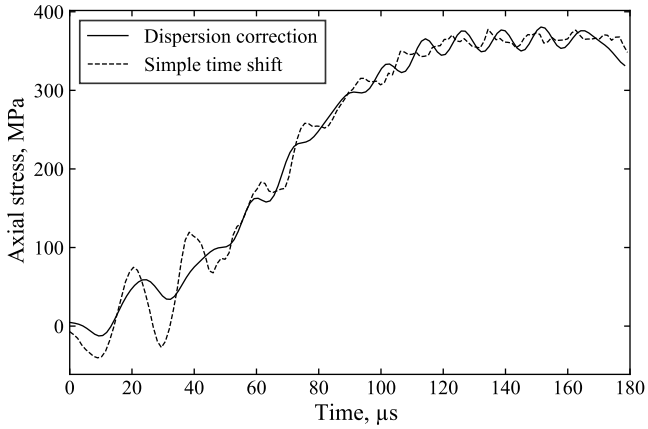

Figure 12. Dispersion vs. time shift analysis of front stress in confined SHPB test on sand.

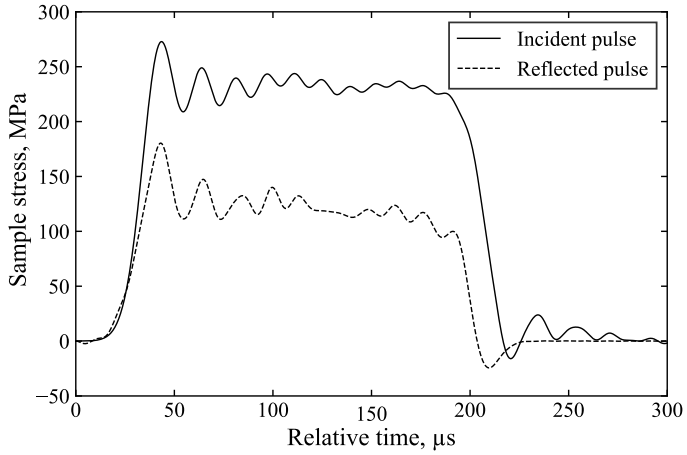

(a)

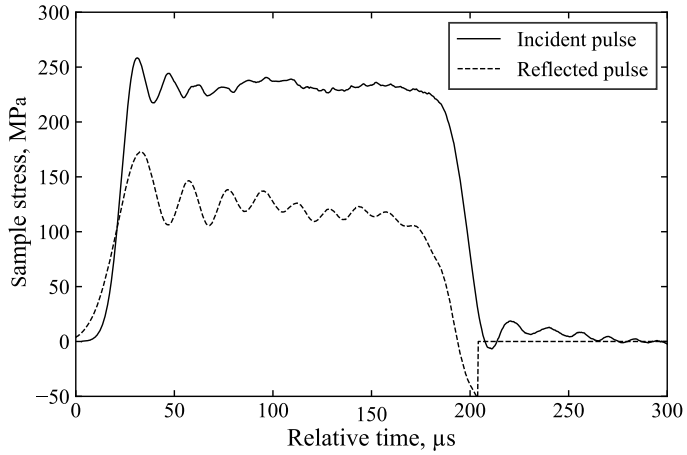

(b)

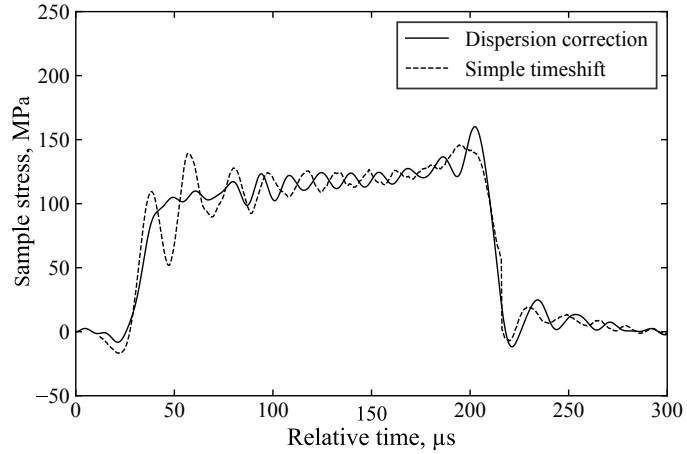

(c)

Figure 13. Processed results of the unconfined SHPB test on aluminium with (a) dispersion correction of the incident and reflected pulses, (b) simple time shifting of the incident and reflected pulses and (c) dispersion correction vs simple time shifting of the front stress.

5.6. Stress wave equilibrium

The stress difference between the front and back stress normalised by their mean was plotted for all cases, as shown in Figures 14a, 14b and 14c, to demonstrate that even if stress waves do not achieve equilibrium, `SHPB_Processing.py` still runs successfully and produces accurate results.

In the ideal circumstance stress equilibrium is achieved during SHPB testing, the length of the pulses detected at the specimen's front and back bar interfaces (i.e. front and back stresses) will be the same. However, there are instances, more commonly in cases where the stress wave does not fully propagate through the specimen, causing a considerable portion to propagate laterally.

Stress equilibrium during a SHPB test can be represented by Equation 10, provided that the deformation of the specimen is uniform and that the axial propagation of the stress wave has been taken into account.

$$\varepsilon_i(t) = \varepsilon_r(t) + \varepsilon_t(t) \tag{10}$$

The ability in `SHPB_Processing.py` to set an alignment to manage the front and back stresses means this function is able to account for cases where stress equilibrium may not be fully obtained, but an estimation of the axial stress can still be determined, though with the caveat that it should be coupled with further experimental testing or numerical modelling in order to be utilised for material characterisation.

6. Discussion

The algorithm `SHPB_Processing.py` is the main function which performs data processing of the signals obtained from the SHPB tests. It is composed of the subroutine, `dispersion.py`, which carries out the dispersion correction of the signals acquired from the experiments. Another function titled `dispersion_factors.py` is used in this subroutine. The programme `dispersion_factors.py` reformats the dispersion correction factors computed by `phase_velocity.py`. These factors are determined using the Poisson's ratio of the cylindrical bar used during SHPB experiments. They can easily be obtained for any material. This function and associated subroutines can be used independently.

As seen in the section of this paper devoted to the script, it has a broad range of capabilities, including confinement, signal amplification, dispersion correction or simple timeshifting, signal alignment, striker speed measurement, test log monitoring and data saving. Furthermore, because the input and output signals in the Hopkinson pressure bars are mapped independently, the script runs effectively regardless of whether stress wave equilibrium is attained or not. Since the code focuses on SHPB data processing, as the name suggests, it makes the procedure more efficient.

The script's practical applications were evaluated using SHPB tests with aluminium, kaolin clay and sand samples. An unconfined aluminium sample, an unconfined kaolin clay sample and a confined medium sand sample were tested with a SHPB apparatus. Most of the script's functionalities were employed to examine these SHPB experiments, most notably, `dispersion.py`, which contrasted dispersion corrected and simple time shift results, demonstrating the importance of this script for reliable data analysis.

As demonstrated in the current work, practical applications of `SHPB_Processing.py` on aluminium, kaolin clay and sand sample data collected from SHPB tests were carried out to illustrate its efficiency, accuracy and broad range of application.

Two of the algorithm's three confinement possibilities were tested, confined and unconfined SHPB experiments, as seen in the practical application section. A SHPB test using a partial lateral confinement apparatus would be extremely valuable for testing data processing quality. This programme has the advantage of working under various testing conditions regardless of whether stress wave equilibrium is attained during SHPB testing.

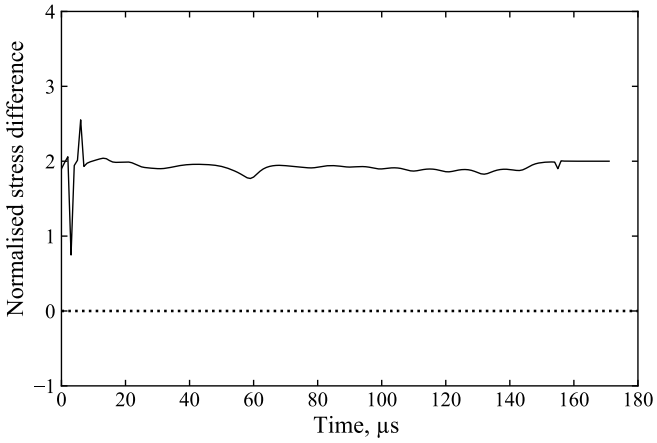

(a)

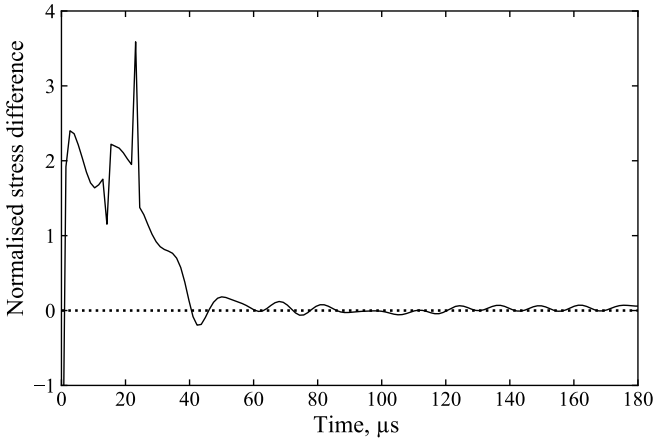

(b)

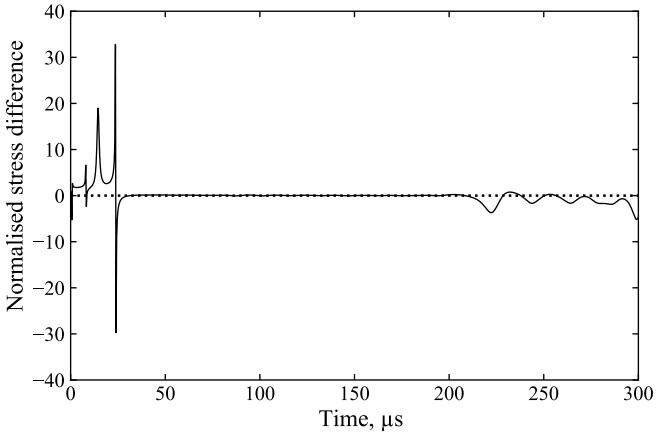

(c)

Figure 14. Stress wave difference between front and back stress, normalised by their mean, for (a) an unconfined SHPB test on kaolin clay, (b) a confined SHPB test on medium sand, and (c) an unconfined SHPB test on aluminium.

The code was run on a SHPB set up with stainless-steel pressure bars (Poisson's ratio of 0.29). Yet, SHPB testing with aluminium or polymer bars, which also require dispersion correction, would be extremely valuable to study the script's performance.

7. Conclusions

The essential theory behind dispersion correction and its importance for SHPB experiments were thoroughly investigated. To address this, an invaluable computational tool was created, `SHPB_Processing.py`, with independent subroutines to complement the script's already extensive array of functionalities. Practical applications of this function on SHPB tests conducted on aluminium, kaolin clay and sand samples demonstrate the improved quality of the results, illustrating the immense potential of this open-source algorithm for future applications.

Code availability

The algorithms developed in this paper are open-source and accessible on GitHub and ORDA at the following links:

- `gauge_factor.py`: GitHub and ORDA
- `phase_velocity.py`: GitHub and ORDA
- `SHPB_Processing.py`: GitHub and ORDA
- `dispersion.py & dispersion_factors.py`: GitHub and ORDA

Author Contributions: Conceptualisation, A.V.L., K.S.O.L., A.D.B. and S.D.C.; Software development, A.V.L. and K.S.O.L.; Formal analysis, A.V.L. and K.S.O.L.; Validation, A.V.L., K.S.O.L. and A.D.B.; Visualisation, A.V.L., K.S.O.L. and A.D.B.; Writing—original draft preparation, A.V.L.; Writing—review and editing, A.V.L., K.S.O.L., A.D.B. and S.D.C.; Supervision, A.D.B. and S.D.C. All authors have read and agreed to the published version of the manuscript.

Funding: This research was funded by the Engineering and Physical Sciences Research Council (EPSRC), and the Defence Science and Technology Laboratory (Dstl).

Informed Consent Statement: Not applicable.

Data Availability Statement: The data presented in this study are available upon request from the authors.

Conflicts of Interest: The authors declare that they have no conflict of interest.

References

1. Shin, H. Pochhammer–Chree equation solver for dispersion correction of elastic waves in a (split) Hopkinson bar. *Proceedings of the Institution of Mechanical Engineers, Part C: Journal of Mechanical Engineering Science* **2022**, *236*, 80–87. https://doi.org/https://doi.org/10.1177/0954406220980509.
2. Kolsky, H. Rader. 1963. Stress Waves in Solids. *Dover Publications, Inc., New York, NY* **1963**, *21*, 140–145.
3. Shin, H. Manual for Calibrating Sound Speed and Poisson's Ratio of (Split) Hopkinson Bar via Dispersion Correction Using Excel® and Matlab® Templates. *Data* **2022**, *7*, 55. https://doi.org/https://doi.org/10.3390/data7050055.
4. Pochhammer, L. Ueber die Fortpflanzungsgeschwindigkeiten kleiner Schwingungen in einem unbegrenzten isotropen Kreiscylinder. **1876**. https://doi.org/https://doi.org/10.1515/crll.1876.81.324.
5. Chree, C. The equations of an isotropic elastic solid in polar and cylindrical co-ordinates their solution and application. *transactions of the Cambridge Philosophical Society* **1889**, *14*, 250.
6. Bancroft, D. The velocity of longitudinal waves in cylindrical bars. *physical Review* **1941**, *59*, 588. https://doi.org/https://doi.org/10.1103/PhysRev.59.588.
7. Barr, A.D. Strain-rate effects in quartz sand. PhD thesis, University of Sheffield, 2016.
8. Gray III, G.T. Classic split-Hopkinson pressure bar testing. *ASM Handbook, Mechanical testing and evaluation* **2000**, *8*, 462–476.
9. Shin, H. Sound speed and Poisson's ratio calibration of (split) Hopkinson bar via iterative dispersion correction of elastic wave. *Journal of Applied Mechanics* **2022**, *89*, 061007. https://doi.org/https://doi.org/10.1115/1.4054107.
10. Tyas, A.; Pope, D.J. Full correction of first-mode Pochammer–Chree dispersion effects in experimental pressure bar signals. *Measurement science and technology* **2005**, *16*, 642. https://doi.org/https://doi.org/10.1088/0957-0233/16/3/004.
11. Tyas, A.; Watson, A.J. An investigation of frequency domain dispersion correction of pressure bar signals. *International Journal of Impact Engineering* **2001**, *25*, 87–101. https://doi.org/https://doi.org/10.1016/S0734-743X(00)00025-7.

12. Gorham, D. A numerical method for the correction of dispersion in pressure bar signals. *Journal of Physics E: Scientific Instruments* **1983**, *16*, 477. https://doi.org/https://doi.org/10.1088/0022-3735/16/6/008.
13. Follansbee, P.; Frantz, C. Wave propagation in the split Hopkinson pressure bar **1983**. https://doi.org/https://doi.org/10.1115/1.3225620.
14. Barr, A.; Rigby, S.; Clayton, M. Correction of higher mode Pochhammer–Chree dispersion in experimental blast loading measurements. *International Journal of Impact Engineering* **2020**, *139*, 103526. https://doi.org/https://doi.org/10.1016/j.ijimpeng.2020.103526.
15. Davies, R. A critical study of the Hopkinson pressure bar. *Philosophical Transactions of the Royal Society of London. Series A, Mathematical and Physical Sciences* **1948**, *240*, 375–457. https://doi.org/https://doi.org/10.1098/rsta.1948.0001.
16. Van Lerberghe, A.; Li, K.S.O. gauge_factor.py - A Python algorithm for calculating the gauge factor of the input bar for split-Hopkinson pressure bar experiments. **2023**. https://doi.org/10.15131/shef.data.23523927.v1.
17. Li, K.S.O.; Van Lerberghe, A.; Barr, A. SHPB_Processing.py - An open-source Python algorithm for correcting stress wave dispersion in split-Hopkinson pressure bar experiments **2023**. https://doi.org/10.15131/shef.data.24570565.v1.
18. Van Lerberghe, A.; Barr, A. dispersion.py - A Python algorithm for phase angle and amplitude correction of pressure bar signals **2023**. https://doi.org/10.15131/shef.data.24570034.v1.
19. Barr, A. dispersion.m - A MatLab script for phase angle and amplitude correction of pressure bar signals **2016**. https://doi.org/10.15131/shef.data.3996876.v1.
20. Van Lerberghe, A.; Barr, A. phase_velocity.py - A Python algorithm for calculating frequency-dependent phase velocity and radial variation of elastic waves in cylindrical bars **2023**. https://doi.org/10.15131/shef.data.22010999.v1.
21. Barr, A. phasevelocity.m - A Matlab script to calculate the frequency-dependent phase velocity and radial variation of elastic waves in cylindrical bars **2023**. https://doi.org/10.15131/shef.data.21982604.v1.

A.5 High strain rate behaviour of cohesive soils

Van Lerberghe, A., Li, K. S. O., Barr, A. D., & Clarke, S. D. (2024). High-strain-rate behaviour of cohesive soils.

A paper documenting the high-strain-rate response of cohesive soils and describing the effects of moisture content and strain rate, submitted for publication to the International journal of Impact Engineering. The journal paper is included in its entirety below as reference.

High strain rate behaviour of cohesive soils

Arthur Van Lerberghe[a,*], Kin Shing O. Li[a], Andrew D. Barr[a], Sam D. Clarke[a]

[a]*Department of Civil & Structural Engineering, University of Sheffield, Mappin Street, Sheffield, S1 3JD, UK*

Abstract

Soil-filled wire and geotextile gabions are essential components of defensive infrastructure in military bases, leveraging the attenuating properties of soils to safeguard personnel and critical assets against blast and fragmentation effects. However, understanding the behaviour of cohesive soils under extreme loading conditions remains largely unexplored, presenting a crucial knowledge gap for design engineers tasked with developing robust soil constitutive models to address evolving threats. This study investigates the response of cohesive soils, focusing primarily on kaolin clay due to its homogeneity, widespread availability and consistent properties. Through high strain rate experimental testing of kaolin clay specimens, using the split-Hopkinson pressure bar (SHPB) apparatus, both unconfined and confined conditions are explored across varying moisture contents, spanning the spectrum from unsaturated to fully saturated states. The analysis of the experimental results uncovers the strain rate dependence of cohesive soils and identifies distinct phase behaviour for transmitted and radial stresses influenced by factors such as strain rate, moisture content and confinement. Utilising LS-DYNA, and the finite element method (FEM), the SHPB tests are modelled for comparison against experimental findings. While LS-DYNA, supplemented by Smooth Particle Hydrodynamics (SPH) node modelling, provides valuable insights, significant disparities between modelled and practical results underscore the challenges inherent with the accuracy in simulating the behaviour of cohesive soils. Nonetheless, this comprehensive exploration of cohesive soil's high strain rate behaviour yields critical insights for engineers, enabling them to adapt defensive strategies to diverse threats and loading scenarios effectively.

Keywords: High strain rate testing, Split-Hopkinson pressure bar, Cohesive soils, Kaolin clay, LS-DYNA modelling, Smooth particle hydrodynamics

1. Introduction

Fortification engineers face a daunting challenge: ensuring the resilience of defensive structures worldwide. Soil-filled wire and geotextile gabions, exemplified by Hesco Concertainer, stand as stalwart solutions, offering protection against the destructive forces of blast and fragmentation. The versatility and availability of soil make it an attractive defence material, facilitating the rapid and cost-effective construction of robust-barriers. However, despite its ubiquity, the high strain rate behaviour of soil remains enigmatic, especially in the context of emerging threats and evolving landscapes. As conflicts shift from sandy terrains to regions where sand may not be readily available, the need to understand and harness the potential of cohesive soils such as clay and silt becomes imperative. These cohesive materials, found across the globe, constitute the terrestrial and aquatic strata, offering promising alternative for fortifications in diverse settings.

In navigating unfamiliar terrain, fortification engineers require precise data to assess the performance of local soils and adapt their designs accordingly. The development of constitutive models capable of accommodating new soils and emerging threats necessitates comprehensive studies on soil behaviour under extreme loading conditions. In this regard, the focus on kaolin clay, a well-researched and representative soil, provides a foundation for quantitative insights into its mechanical response. By preparing kaolin clay samples at varying moisture contents and testing them under both unconfined and confined conditions using the SHPB apparatus, this study aims to elucidate the effects of strain rate, moisture content and confinement on cohesive soils.

Blast attenuation and cohesive soils are expansive fields. The unique characteristics of cohesive soils, including their undrained behaviour, variable saturation states, and very fine particle size, pose significant challenges in evaluating their response at high strain rates. Unlike cohesionless soils, like sand, which have been extensively studied under high strain rates conditions [1–6], cohesive soils, particularly kaolin clay, remains largely unexplored in this context. This study aims to bridge this gap by delving into new frontiers of understanding, thereby paving the way for more resilient and adaptive fortification designs.

The contemporary SHPB apparatus, named after Bertram Hopkinson, originated from his method to measure the pressure generated by bullet impacts or explosive detonations [7]. Initially, the Hopkinson pressure bar consisted of a long steel bar transmitting pressure from the impact, with a shorter bar serving as a momentum trap, allowing inference of pressure wave magnitude and duration.

*Corresponding author.

Email address: avanlerberghe1@sheffield.ac.uk (Arthur Van Lerberghe)

Herbert Kolsky expanded upon this design by incorporating two bars in series, separated by a material specimen. This configuration facilitated recording of stress pulses in each bar, enabling calculation of the dynamic stress-strain response of the specimen [8]. This system, known as the split-Hopkinson pressure bar (SHPB) or Kolsky bar, remains fundamentally unchanged. By employing one-dimensional wave theory, stress pulses measured in the bars provide insights into the stress and strain histories of the two ends of the specimen [9].

Several studies utilising the SHPB apparatus have investigated the high strain rate behaviour of cohesive soils, with tests conducted up to 2500 s^{-1}, under both unconfined and confined conditions, at different moisture contents. However, these studies lacked detailed material characterisation and sample preparations of their chosen cohesive soil. This included factors such as moisture content, particle size distribution and Atterberg limits, which hindered the reproducibility of their findings and restricted comparative possibilities with other studies [10–13].

For instance, SHPB tests conducted on dry clay samples provided some insights into the effects of moisture content on cohesive soils at high strain rates [10–13]. However, artificially frozen clay samples compromised the inherent properties of moisture content in cohesive soils, rendering the results incomparable with other SHPB tests on cohesive soils [11].

Confined SHPB tests on dry clay samples were conducted, with steel jackets of different thicknesses [10], and utilising gauged steel cylindrical cages [13]. These results provided some information on the effect of confinement at high strain rates by measuring the radial stress behaviour of the sample. Yet, no comparison was made with unconfined SHPB tests on the same soil samples to determine the effect of confinement.

In contrast, high strain rate SHPB testing on cohesionless soils is more comprehensive, with clearly defined material properties prior to investigating the impact of strain rate, moisture content and lateral confinement [1–6]. This further underscores the untapped potential of novel research in comprehensively addressing the behaviour of cohesive soils at high strain rates, an area that remains largely unexplored.

Full scale trials of blast and ballistic events entail considerable costs and time investments. Consequently, numerical techniques serve as invaluable tools for modelling these events. Explosions, blast effects, and impacts are commonly simulated using dynamic software such as LS-DYNA, which incorporates the Finite Element Method (FEM) [14].

The reliability and accuracy of material models are paramount and must be verified against experimental data [15]. Typically, this involves developing a material model based on experimental properties and then comparing the results obtained from physical experiments to those of more complex simulations. Discrepancies between the experimental and modelled data indicate inaccuracies in the material model. Adjusting the inputs until the outputs align with experimental data is not a viable solution, as the model may fail to predict future material responses under different test configurations.

In FEM-based modelling, soil is often treated as a continuum with homogeneous bulk properties [16]. Since individual particles are not explicitly modelled in continuum approaches, constitutive models are employed to capture crucial bulk properties, which are typically derived from geotechnical tests.

LS-DYNA offers various modelling approaches to create constitutive numerical models for dynamic impacts on soils. These include Lagrangian with material erosion and/or mesh adaptivity, Arbitrary Lagrangian-Eulerian (ALE), and Smooth Particle Hydrodynamics (SPH) [14]. Additionally, LS-DYNA provides a range of built-in material cards for simulating soil behaviour, from basic models with compressibility curves and yield surfaces to more complex models incorporating pore water effects, strain softening & hardening, and strain effects [14].

While most finite element (FE) studies using LS-DYNA in the literature focus on buried explosives, only as small number address SHPB modelling of soils, with an even smaller subset dedicated to cohesive soils.

LS-DYNA has been employed to model high strain rate experiments on cohesive soils, including unconfined and confined SHPB tests, utilising material cards such as `*MAT_SOIL_AND_FOAM`, `*MAT_PSEUDO_TENSOR`, `*MAT_FHWA_SOIL`, `*MAT_GEOLOGIC_CAP_MODEL` as well as `*MAT_MOHR_COULOMB`. Experimental data is used to build ALE numerical models and comparing their results to collected test data, yielding limited accuracy [13, 17, 18].

These studies highlight critical issues: the lack of clear material characterisation of the investigated cohesive soil, the absence of soil shear strength data at high pressures during modelling, and evident limitations in modelling the behaviour of cohesive soils across all saturation levels

Furthermore, SPH modelling, an innovative meshless Lagrangian numerical technique for modelling fluid equations of motion under high strain rate effects, has never been utilised in LS-DYNA for the modelling of SHPB experiments on cohesive soils. Given the dynamic nature of SHPB tests and the complex material behaviour of cohesive soils, this presents an ideal opportunity for exploration [19].

2. Material characterisation

The soil selected is defined using EN ISO 14688–1:2002 [20], as white fine CLAY (CL). For brevity, it is referred to as 'kaolin clay'. Table 1 provides an overview of the kaolin clay material properties, which are derived using the methods described in sections 2.1, 2.2, 2.3, 2.4 and 2.5.

Soil properties	Units	Value
Primary mineral	–	Kaolinite
Particle density, ρ_s	$Mg.m^{-3}$	2.65
Liquid Limit, LL	%	40
Plastic Limit, PL	%	25
Plastic Index, PI	%	15
D_{50}	μm	0.74
Particle sphericity	–	Low – Medium
Angularity	–	Subrounded – Subangular
Surface texture	–	Smooth

Table 1: Overview of the kaolin clay material properties.

2.1. Particle size mineralogy

X-ray diffraction (XRD) was carried out on the kaolin clay to establish the constituent minerals. In XRD an incident X-ray beam undergoes diffraction due to the regular atomic structure of a crystalline specimen. By measuring the intensity of diffraction at different incident angles, θ, a distinct diffraction pattern is obtained. This pattern can be compared to a database of known patterns to identify the phases present in the specimen. Phase analysis was carried out using a PANalytical Aeris diffractometer and the ICDD's Diffraction File (PDF-4+).

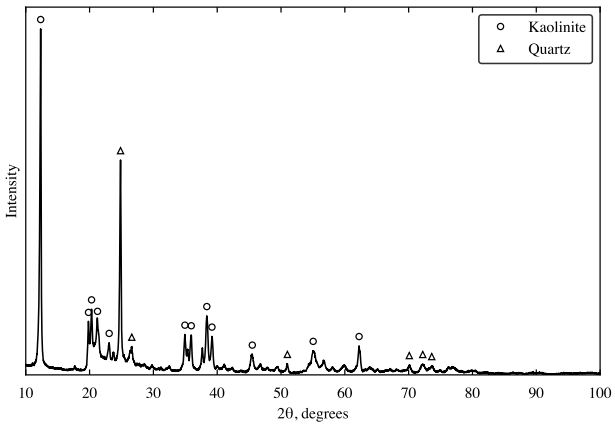

Figure 1: X-ray diffraction data of the kaolin clay soil.

Figure 1 shows the diffraction pattern of the kaolin clay. As expected, kaolinite is the primary mineral, followed by quartz.

2.2. Particle size distribution

The particle size distribution (PSD) of the kaolin clay is assessed using the data sheet provided by the supplier, IMERYS. Figure 2 depicts the cumulative PSD of the kaolin clay. The D_{50} of this well-graded impermeable soil is 0.74 μm, and the clay and silt contents are calculated to be 80 % and 20 %, respectively. The soil is therefore characterised as CLAY (CL).

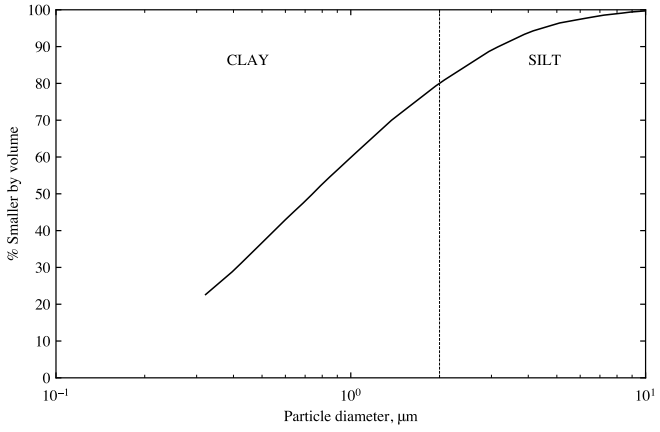

Figure 2: Cumulative particle size distribution of the kaolin clay soil.

2.3. Particle density

The particle density, denoted as ρ_s, represents the density of the solid mineral particles. It is used with the bulk dry density, ρ_d, to determine the void ratio of a soil using the following relationship:

$$e = \frac{\rho_s}{\rho_d} - 1 \tag{1}$$

The particle density, ρ_s, of the kaolin clay was calculated to be 2.65 Mg.m^{-3}, using the method described in BS 1377–2:1990 §8.2 [21] , which is the density of kaolinite.

2.4. Atterberg limits

To ensure sample consistency, Atterberg limits must be consistent across all soil samples. The fall cone test was used to obtain consistent Atterberg limit values for the different kaolin clay samples [21]. The liquid limit, LL, plastic limit, PL, and plastic index, PI are 40 %, 25 % and 15 %, respectively [21]. The values of which are above the A-line, confirming the soil selected is a CLAY (CL) [22].

2.5. Particle shape

The shape of the kaolinite-sized particles in the soil are assessed qualitatively with a scanning electron microscope (SEM), using the descriptors provided in EN ISO 14688–1:2002 [20]. The kaolin clay soil was gold (Au) coated before being inserted into the SEM. Using Figure 3, the kaolin clay particles vary from low to medium sphericity, are subrounded to subangular, and have smooth surface texture.

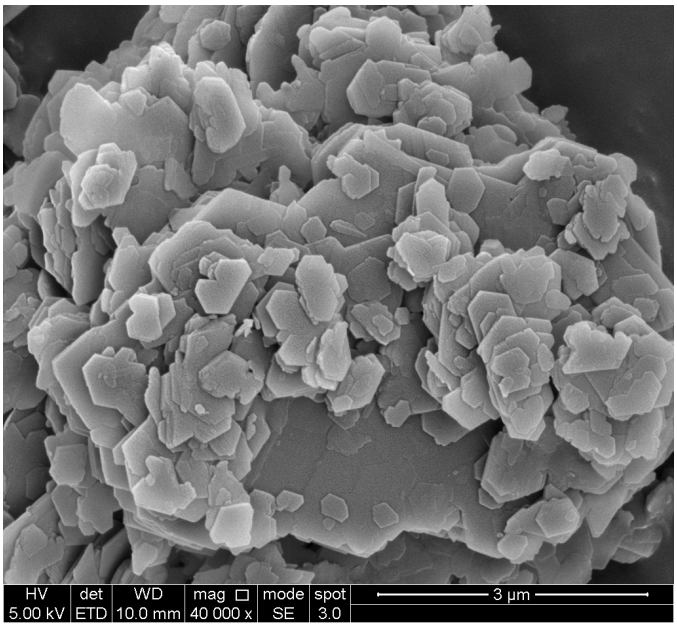

Figure 3: SEM imagery of kaolin clay at 40,000x magnification.

3. Specimen preparation

Kaolin clay samples are made using powdered speswhite kaolin clay. The powder was mixed with water at a 1:1 ratio to create a kaolin slurry, which was then placed in a pressurised cylindrical Rowe cell to consolidate the kaolin clay to 600 kPa. This approach was employed to create a consolidated, fully saturated, kaolin clay wheel, with a corresponding moisture content of 44 %, as determined after preparation using the material characterisation tests indicated in section 2.

A controlled drying procedure was utilised to study the effect of moisture content in kaolin clay samples at high strain rates. Specimens with moisture content levels of 0, 5, 10, 15, 20, 25, 30, 35, 41, 42 and 44 % were prepared, covering all saturation levels from unsaturated to fully saturated.

The kaolin clay samples used for both unconfined and confined SHPB testing are prepared using the following procedure:

1. Cylindrical kaolin clay samples with varying moisture content are made using a 25 mm stainless-steel cylinder slicer. The specimen's have a nominal length of 5 mm and a diameter of 25 mm. The initial weight of the kaolin clay specimen is recorded immediately after it has been sliced.
2. Samples are air dried in a temperature-controlled setting at 20 degrees Celsius, and weighed at regular intervals to measure their current moisture content based on their initial wet weight and current weight.
3. Cut and air-dried samples are wrapped in polyvinylidene chloride to minimise changes in moisture content between sample preparation and testing. The samples are prepared and tested in different laboratories, hence they are stored in sealed plastic bags until required for testing.

4. Experimental setup

The SHPB experimental set up consists of a typical pressure bar arrangement consisting of a striker, an incident and a transmitter bar each 25 mm in diameter and 350 mm, 2500 mm and 1500 mm long, respectively, as represented in Figure 4.

For confined SHPB testing, the experimental set up includes an additional steel confining ring shown in Figure 5a, which houses the kaolin clay sample and slots in between the incident and transmitter bars, as illustrated in Figure 5b.

Signals from the pressure bar strain gauges are recorded using a TiePie Handyscope four-channel digital oscilloscope with a 14-bit A-D resolution, a sample frequency of 1 MHz, and a record length of 131.072 kSa. The material's axial stress response is monitored using a pair of Kyowa KSP-2-120-E4 strain gauges mounted on the incident and transmitter bars. The radial stress response is measured using a single strain gauge mounted on the outside of the confining ring. Strain gauge signals are collected from the incident and transmitter bars using a half Wheatstone bridge configuration (Figure 6). Strain gauge signal from the confining ring is acquired using a quarter Wheatstone bridge configuration (Figure 7).

5. Testing procedure

This experimental testing procedure was used on kaolin clay samples to demonstrate the SHPB's ability to test cohesive soils under unconfined and confined conditions, as well as to validate that the chosen design set up produces reliable measurements.

Prior to testing, the samples are weighed to three decimal places using an RS Pro weighing scale, with an accuracy of 0.001 g. The samples' thickness is measured using a digital calliper at three different locations and averaged to account for any sample inconsistencies, with an accuracy of 0.01 mm. These parameters are required to process the experimental data.

Unconfined SHPB testing on kaolin clay samples was conducted using the following procedure:

1. Supports surrounding the incident and transmitter bars are bolted down to the channel of the SHPB setup.
2. A kaolin clay sample 5 mm in nominal length and 25 mm in diameter was placed in between the incident and transmitter bars, inside a glass polymer containment box.
3. The lid of the containment box is closed, ready for testing.

For confined SHPB testing, a similar testing procedure was followed, where the confining ring was inserted onto the incident bar before the prepared specimen is gently placed in between the incident and transmitter bars. After which, the confining ring is slid back over the specimen, ready for testing.

In both cases, loading was achieved by hitting the incident bar with a steel striker bar fired from a gas gun at varied speeds, with speeds measured using a speed trap at the exit of the gas gun barrel, to achieve different strain rates.

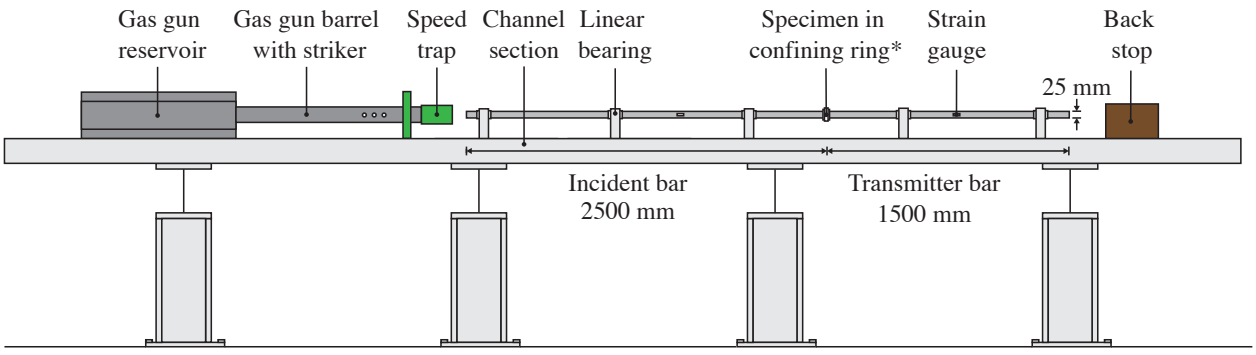

Figure 4: Schematic diagram of the SHPB experimental setup with the confining ring [* removed for unconfined SHPB tests].

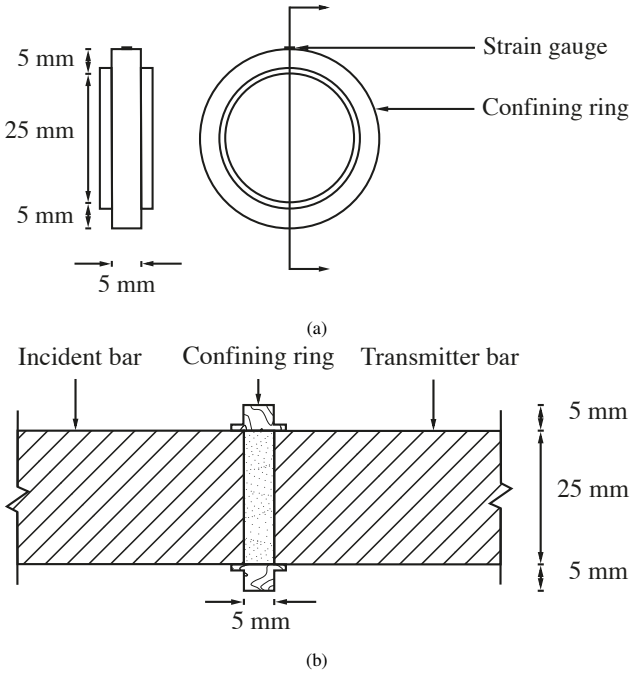

Figure 5: Diagrams showing (a) the confining ring for confined SHPB testing and (b) the confining ring with the sample inside, ready for testing.

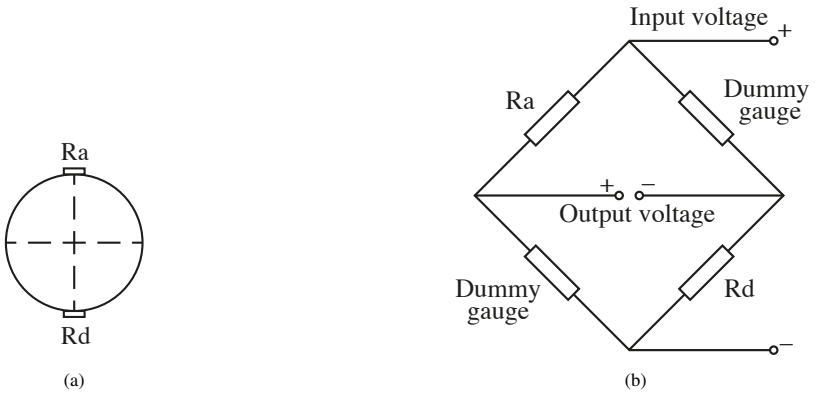

Figure 6: Pressure bars (a) strain gauge arrangement, and (b) half Wheatstone bridge configuration.

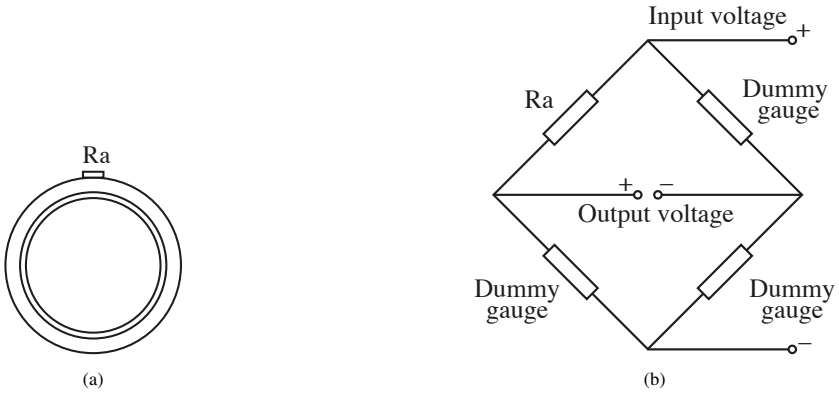

Figure 7: Confining ring (a) strain gauge arrangement, and (b) quarter Wheatstone bridge configuration.

6. Test programme

For unconfined SHPB testing, the test programme began with tests at 8, 12 and 16 m/s on kaolin clay samples with varying moisture content ranging from 0 to 44 %. Additional tests were carried out at 18, 20 and 22 m/s to evaluate the effects of kaolin clay at higher strain rates. Under unconfined conditions, the strain rate is on average 1200, 1900 and 2770 s^{-1}, for 8, 12 and 16 m/s, over approximately 150 μs, as shown in Figure 8.

For confined SHPB testing, the test programme began with tests at 12 m/s on kaolin clay samples with varying moisture content ranging from 0 to 41 % for behavioural comparison with the unconfined SHPB tests. Then, tests were carried out at 18, 20 and 22 m/s. Under confined conditions, the strain rate is on average 2600, 2800 and 3100 s^{-1}, for 18, 20 and 22 m/s, over approximately 150 μs, as shown in Figure 9.

At these high strain rate conditions, the specimen's axial and radial stresses and strains are measured.

The test speed utilised during SHPB testing is setup-specific and depends on the gas gun configuration selected, whereas the strain rate is what the sample experiences during testing.

7. Signal processing

Incident bar, transmitter bar and confining ring signals gathered during SHPB tests on kaolin clay samples with varying moisture contents, are processed using the open-source Python algorithm `SHPB_Processing.py` [23], available on ORDA [24]. This code incorporates the subroutine `dispersion.py`, which implements Tyas and Pope's dispersion-correction approach. This ensures accurate representation of the sample's axial and radial stresses and strains during testing [25].

Figures 10 and 11 show the front stress for a typical unconfined and confined SHPB test, computed using dispersion correction and simple time shifting. The 'front' stress pertains to the incident bar-clay sample interface, while the 'back' stress corresponds to the clay sample-transmitter bar interface. These figures illustrate how the dispersion-corrected approach reduces stress wave amplitude, eliminating initial fluctuations and preventing inaccurate inferences about the kaolin clay specimen's behaviour during SHPB testing. The amplitude difference between unconfined and confined SHPB tests is due to radial stresses being redirected axially by the confining ring.

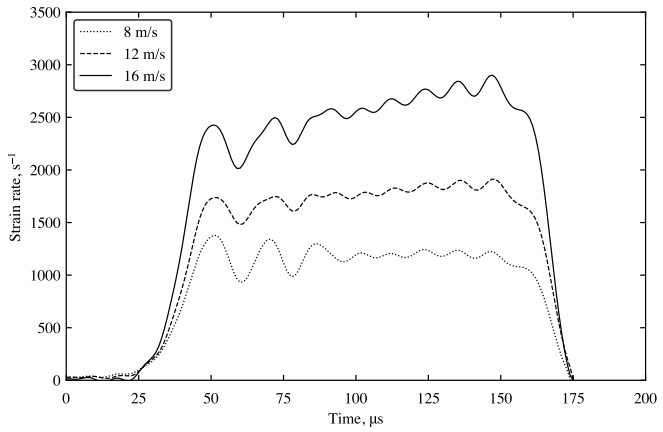

Figure 8: Strain rate variation during unconfined SHPB testing on kaolin clay.

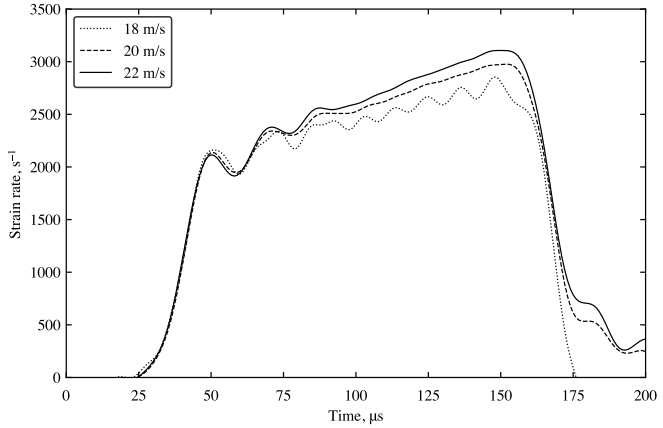

Figure 9: Strain rate variation during confined SHPB testing on kaolin clay.

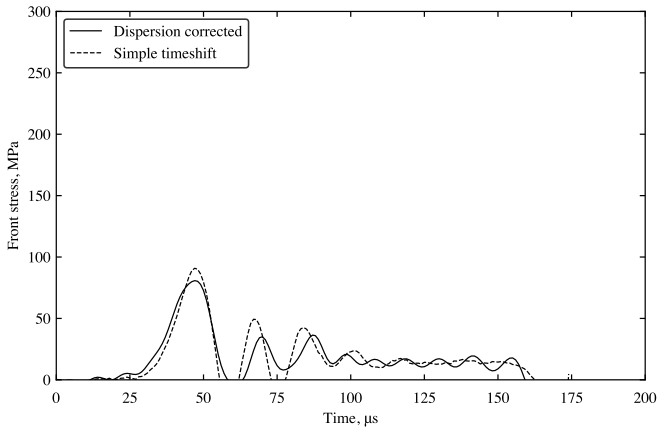

Figure 10: Front stress computed using dispersion correction and simple timeshifting, for a typical unconfined SHPB tests on kaolin clay.

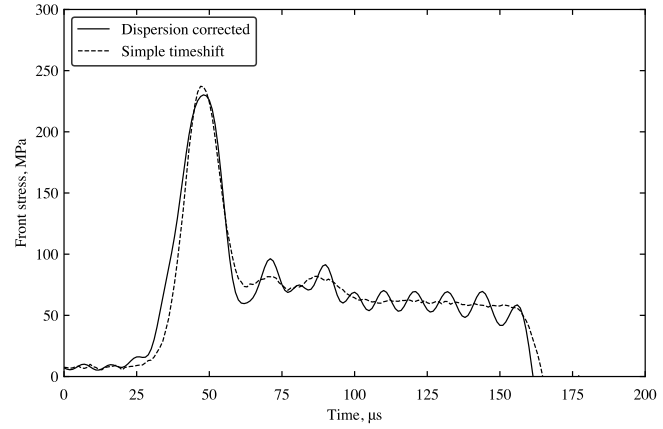

Figure 11: Front stress computed using dispersion correction and simple timeshifting, for a typical confined SHPB test on kaolin clay.

8. Experimental results

8.1. Sample material properties

After the completion of unconfined and confined SHPB tests, the main sample properties for this study being the volume of air in the sample, V_{air}, volume of water in the sample, V_{water}, and total volume of the sample V are calculated in order to physically comprehend how the composition of air, water and soil in the sample evolved during testing.

The air volume ratio in the sample is derived by dividing the total volume of air in the sample (V_{air}) by its entire volume (V), using Equation 2:

$$Air\ volume\ ratio = \frac{V_{air}}{V} \tag{2}$$

The water volume ratio in the sample was computed by dividing the total volume of water in the sample (V_{water}) by the total volume of the sample (V), using Equation 3:

$$Water\ volume\ ratio = \frac{V_{water}}{V} \tag{3}$$

8.2. Unconfined SHPB test results

Unconfined SHPB tests were performed on kaolin clay samples with moisture content levels ranging from 0 to 44 %, to cover all saturation stages: dry, partially-saturated and fully saturated. Initially, the samples were tested at 8, 12, 16 m/s, corresponding to strain rates of 1200, 1900 and 2770 s^{-1}. The sample's strain, front, back and mid stresses were determined using the signal processing technique in section 7.

Figures 12, 13, 14 and 15 show that in a typical unconfined SHPB test at a moisture content of 0 %, increasing the strain rate correlates with higher material strain, front, back and mid stresses. Figure 14 portrays kaolin clay's strain rate dependency. A crucial discovery in our understanding of the high strain rate behaviour of cohesive soils.

At the same strain rate, the material's strain and front stress behaviour are consistent across all moisture contents. However, the back stress behaviour is dependent on the strain rate and moisture content of the tested kaolin clay sample, where it exhibits four distinct phase behaviours, as displayed in Figure 16. This means that the material's mid stress for a specific strain rate and moisture content, is the sole product of the resulting back stress.

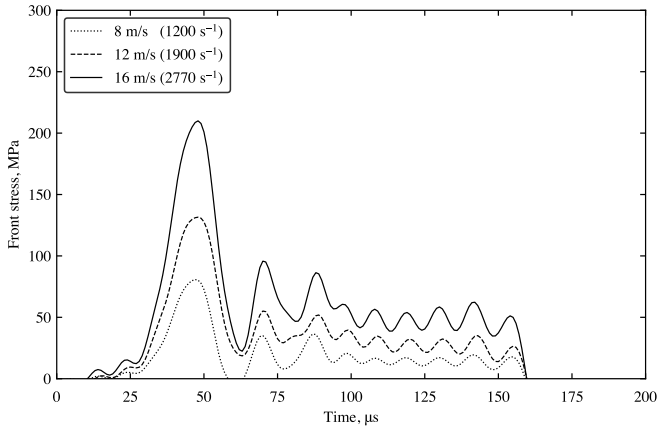

Figure 12: Typical front stress versus time behaviour for an unconfined SHPB tests on kaolin clay, at a moisture content of 0 % and different strain rates.

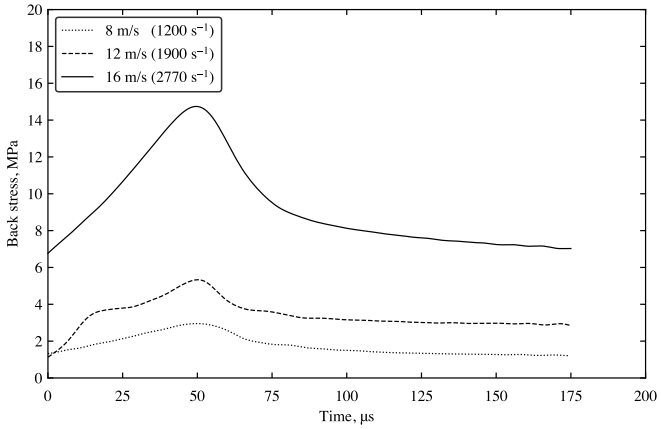

Figure 13: Typical back stress versus time behaviour for an unconfined SHPB tests on kaolin clay, at a moisture content of 0 % and different strain rates.

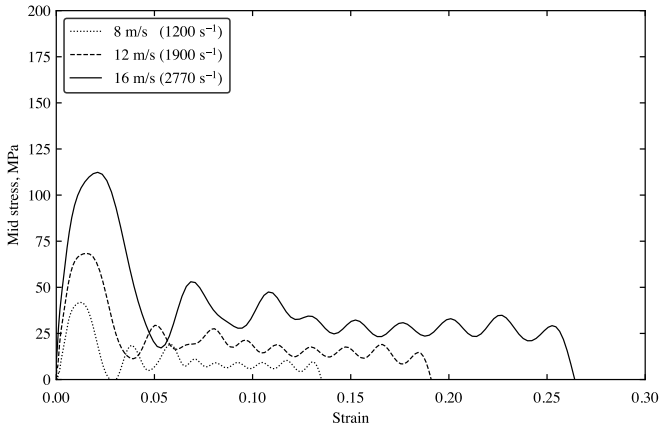

Figure 14: Typical mid stress versus strain behaviour for an unconfined SHPB tests on kaolin clay, at a moisture content of 0 % and different strain rates.

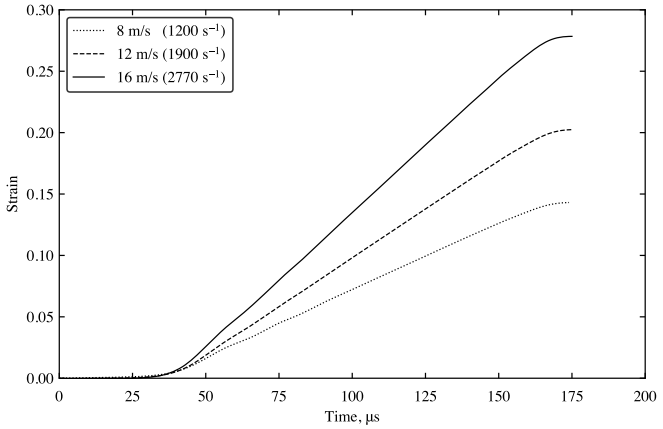

Figure 15: Typical strain versus time behaviour for an unconfined SHPB tests on kaolin clay, at a moisture content of 0 % and different strain rates.

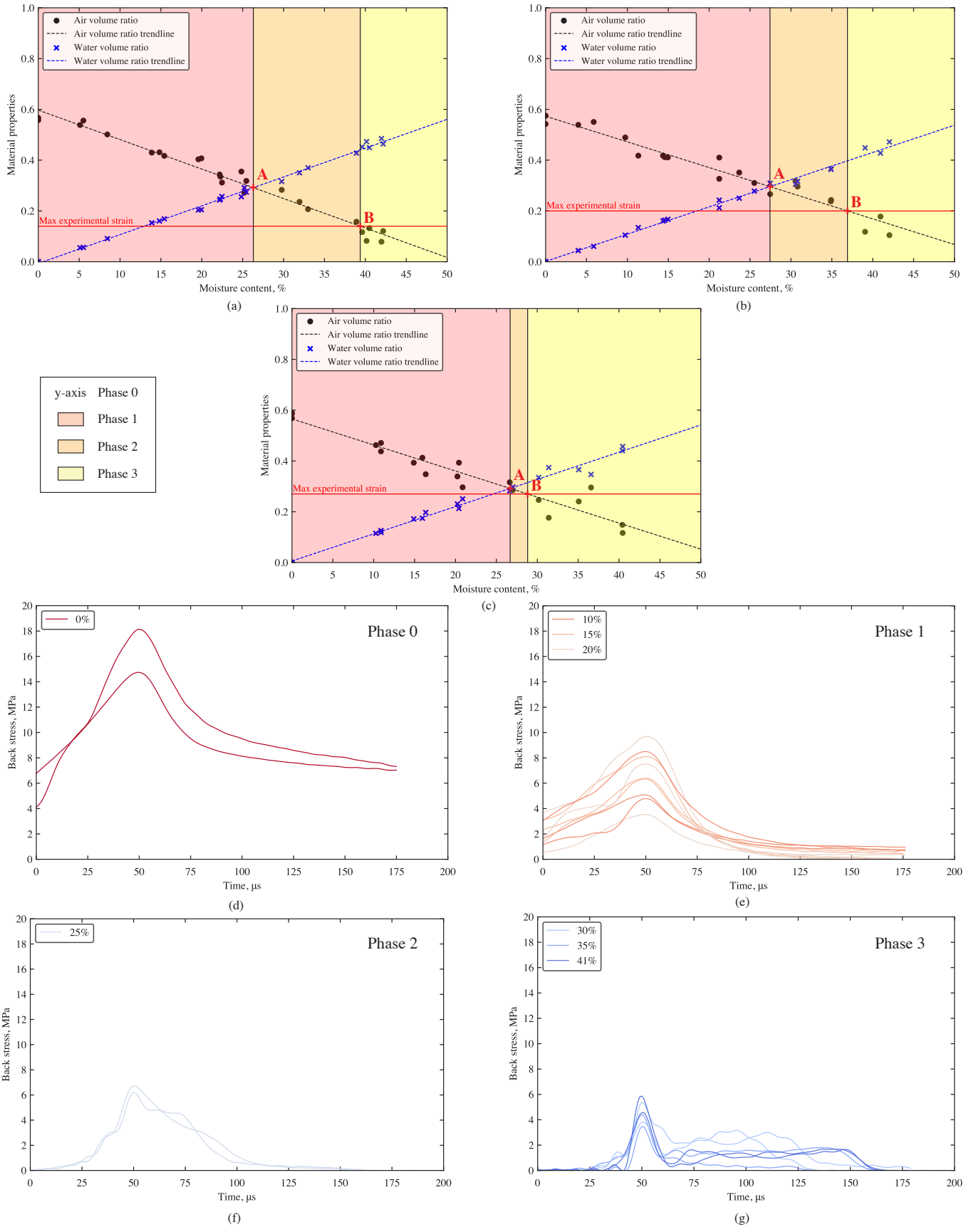

Figure 16: Unconfined SHPB testing of kaolin clay with (a) the phase behaviour at 8 m/s (1200 s^{-1}), (b) phase behaviour at 12 m/s (1900 s^{-1}) and (c) phase behaviour at 16 m/s (2770 s^{-1}), as well as the associated back stress at 16 m/s (2770 s^{-1}) for (d) Phase 0, (e) Phase 1, (f) Phase 2 and (g) Phase 3.

The four phases, seen in Figures 16a, 16b and 16c, dependent on the sample's material properties, are defined as follows:

- **Phase 0:** This phase includes the tests located on the y-axis of Figures 16a, 16b and 16c. Samples are dry, with a moisture content of 0 %. The sample no longer contains any water; it is dry, consisting mainly of air and kaolin clay. Since there is no moisture to encourage lateral extrusion of the sample in this phase, the back stress is the highest, and a larger proportion of the stress wave travels axially towards the transmitter bar. The back stress does not return to zero because the sample consolidates, leaving a thin dry kaolin disk between the bars (Figure 16d).

- **Phase 1:** This phase is shown in red in Figures 16a, 16b and 16c. Samples in this phase are partially-saturated throughout the test, and the soil pores are primarily filled with air. It encompasses tests with a moisture content above 0 % and the intersection of the air and water volume trendlines (Point A). The back stress during this phase has a distinct shape, with a magnitude significantly lower than in phase 0, and returns close to zero after reaching its peak as the sample almost entirely extruded during testing. In phase 1, moisture content has no effect on the back stress behaviour of the kaolin clay samples (Figure 16e).

- **Phase 2:** This phase is shown in orange in Figures 16a, 16b and 16c. Samples in this phase are partially-saturated throughout the test but the soil pores are primarily filled with water. The range of this phase varies depending on the strain rate of the tests and correlated between the theoretical and final experimental strains. This phase spans from Point A to the intersection of the air volume ratio and the maximum experimental strain experienced by the sample during testing (Point B). In phase 2, moisture content has no effect on the back stress behaviour of the kaolin clay samples (Figure 16f).

- **Phase 3:** This phase is shown in yellow in Figures 16a, 16b and 16c. Samples in this phase become fully saturated during testing. This phase includes tests with a moisture content higher than the intersection of the air volume ratio and the maximum experimental strain experienced by the sample during testing (Point B). During this phase, the back stress first consists of an initial peak before levelling off and gradually decreasing back down to zero. This is due to the fast extrusion of the kaolin clay sample, which is behaving as a fluid. Within phase 3, moisture content has no effect on the back stress behaviour of the kaolin clay samples (Figure 16g).

Figures 16a, 16b and 16c show that as strain rate rises, phase 1 and 3 increase, while phase 2 decreases. This is due to the increase in the max experimental strain the sample experiences during unconfined SHPB testing. Additional tests performed at 18, 20 and 22 m/s have phase 2 disappearing, as the max experimental strain achieved a strain of 0.29, at the intersection of the two trendlines.

8.3. Confined SHPB test results

Applying the same processing methodology used for unconfined SHPB tests (section 7), the sample's stress and strain data from the confined SHPB tests can be obtained. The confining ring is employed to investigate the effects of strain rate and moisture content and determine if the previously observed phase behaviour in unconfined testing persists under rigid lateral confinement.

Figures 17, 18, 19, 20 and 21 display the strain, radial, front, back and mid stresses for a typical confined SHPB test on kaolin clay, with 0 % moisture content at different strain rates. These figures illustrate how the stress and strain responses of the sample increase with higher strain rates, while the moisture content remains constant. At a given strain rate, strain and front stress remain consistent regardless of the moisture content of the sample. However, radial and back stresses vary depending on the sample's moisture content, directly impacting the mid stress response (Figure 22). The mid stress versus strain response is displayed in Figure 20. This confirms earlier findings from unconfined SHPB tests, highlighting the strain rate and moisture content dependence of cohesive soils (see section 8.2).

Similar to the findings in unconfined SHPB tests, moisture content in the sample significantly influences the high strain rate behaviour of back and radial stresses. Figure 22 illustrates the distinct differences in stress propagation attributed to the phase behaviour of radial and back stresses. The rigid lateral confinement provided by the confining ring acts as a barrier, restricting lateral propagation and redirecting stress axially. Additionally, the confining ring ensures stress wave equilibrium during testing and allows precise recording of radial stresses without deformation at high strain rates.

For fully saturated kaolin clay samples, a Poisson's ratio of 0.5 is calculated using confined SHPB test results, and gradually reduces as the sample's moisture content falls. Nevertheless, as the phase behaviour evolves from 4 to 3 phases, as seen in Figure 22, the confining ring is unable to completely seal the sample inside. Therefore, the radial stress obtained is solely a product of the high incident stresses caused by the speed of the striker bar as it impacts the sample, causing it to extrude.

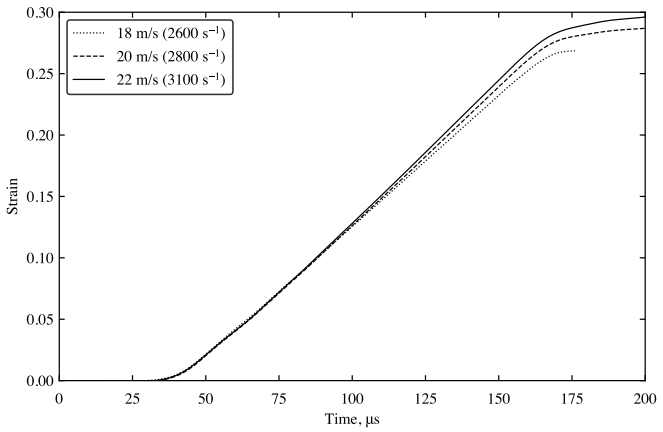

Figure 17: Typical strain versus time behaviour for a confined SHPB tests on kaolin clay, at a moisture content of 0 % and different strain rates.

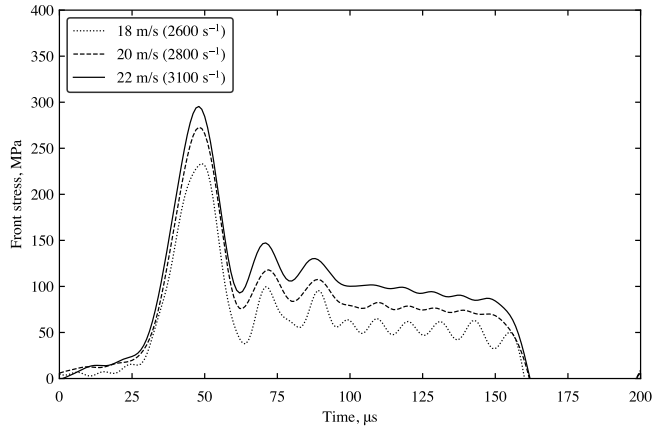

Figure 18: Typical front stress versus time behaviour for a confined SHPB tests on kaolin clay, at a moisture content of 0% and different strain rates.

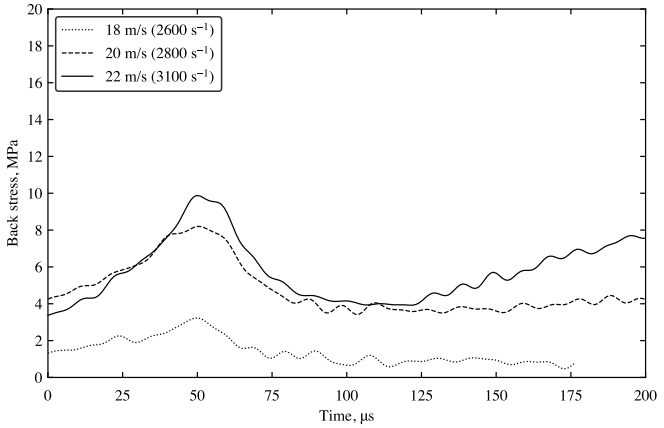

Figure 19: Typical back stress versus time behaviour for a confined SHPB tests on kaolin clay, at a moisture content of 0% and different strain rates.

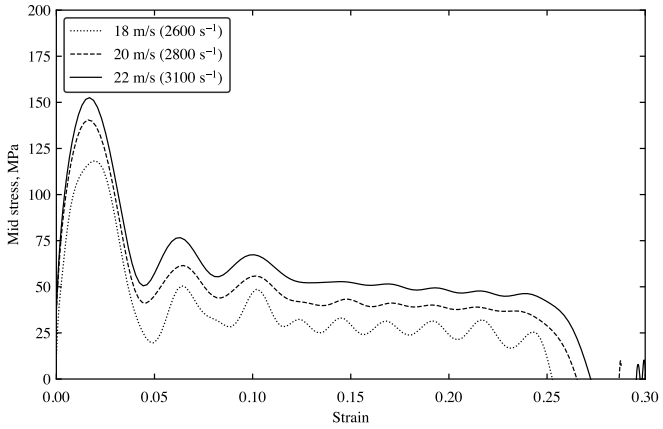

Figure 20: Typical mid stress versus strain behaviour for a confined SHPB tests on kaolin clay, at a moisture content of 0% and different strain rates.

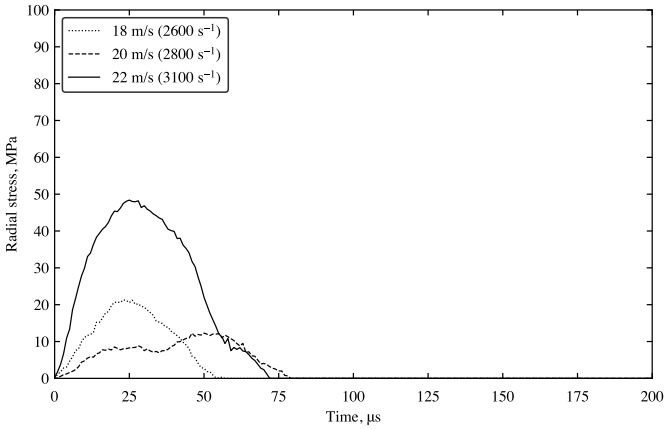

Figure 21: Typical radial stress versus time behaviour for a confined SHPB tests on kaolin clay, at a moisture content of 0% and different strain rates.

Confined SHPB tests include four phases at 18 m/s (i.e 2600 s^{-1}) and three phases at 20 and 22 m/s (i.e. 2800 and 3100 s^{-1}, respectively), as seen in Figures 22a, 22b and 22c.

In phases 0 and 1, back and radial stresses behave similarly. The back stress starts at zero, increases to a maximum, then slowly decreases before levelling off, never returning to zero (Figures 22d and 22e). The radial stress reaches a similar maximum then returns to zero after 50 μs (Figures 22g and 22h).

This occurs for phase 0 and 1, since the volume of water in the sample is less than its total volume of air and soil. During testing, since samples in phase 0 and 1 have a large volume of air voids, they are compacted upon impact. The sample's compaction throughout testing generates a shock absorption effect, dampening the stress wave. As a result, just a fraction of the stress wave propagates through the sample onto the transmitted bar interface. This phenomenon is caused by the confining ring. This instrument provides a rigid lateral confinement around the sample, forcing it to consolidate, resulting in a high radial stress and a totally compacted sample at the end of testing.

It is crucial to note that at the same strain rate, 2700 s^{-1}, under unconfined conditions, a SHPB test requires a striker speed of 12 m/s. Hence, speed is relative to our own test setup whereas strain rate is what the sample exhibits during testing.

Phase 2 manifests only in the confined SHPB tests at 18 m/s (equivalent to 2600 s^{-1}). However, it completely vanishes when the sample's maximum experimental strain reaches 0.29, occurring at a strain rate of 2700 s^{-1} (Point B equals Point A), a finding empirically validated. Consequently, Phase 2 is conspicuously absent at higher velocities of 20 and 22 m/s (i.e. 2800 and 3100 s^{-1}, respectively), as shown in Figures 22a, 22b and 22c.

Figures 22f and 22i illustrate the discernible back and radial stress behaviours characteristic of phase 3 compared to other phases. Beyond a strain rate of 2700 s^{-1}, following the disappearance of phase 2, the impact of the incident bar, the effect of inertia, becomes significant enough to prompt the sample extrusion, irrespective of confinement.

Similar to unconfined experiments, once the moisture content surpasses the threshold for the specimen to achieve full saturation, the water content ratio dictates the sample's behaviour, leading to complete lateral extrusion.

In theory, the confining ring forms a tight seal around the pressure bars, ostensibly preventing sample extrusion. However, in practice, kaolin clay particles still undergo extrusion beyond a certain strain rate due to the substantial impact caused. The confining ring's influence on stress wave propagation in cohesive soils is underscored by several intrinsic factors.

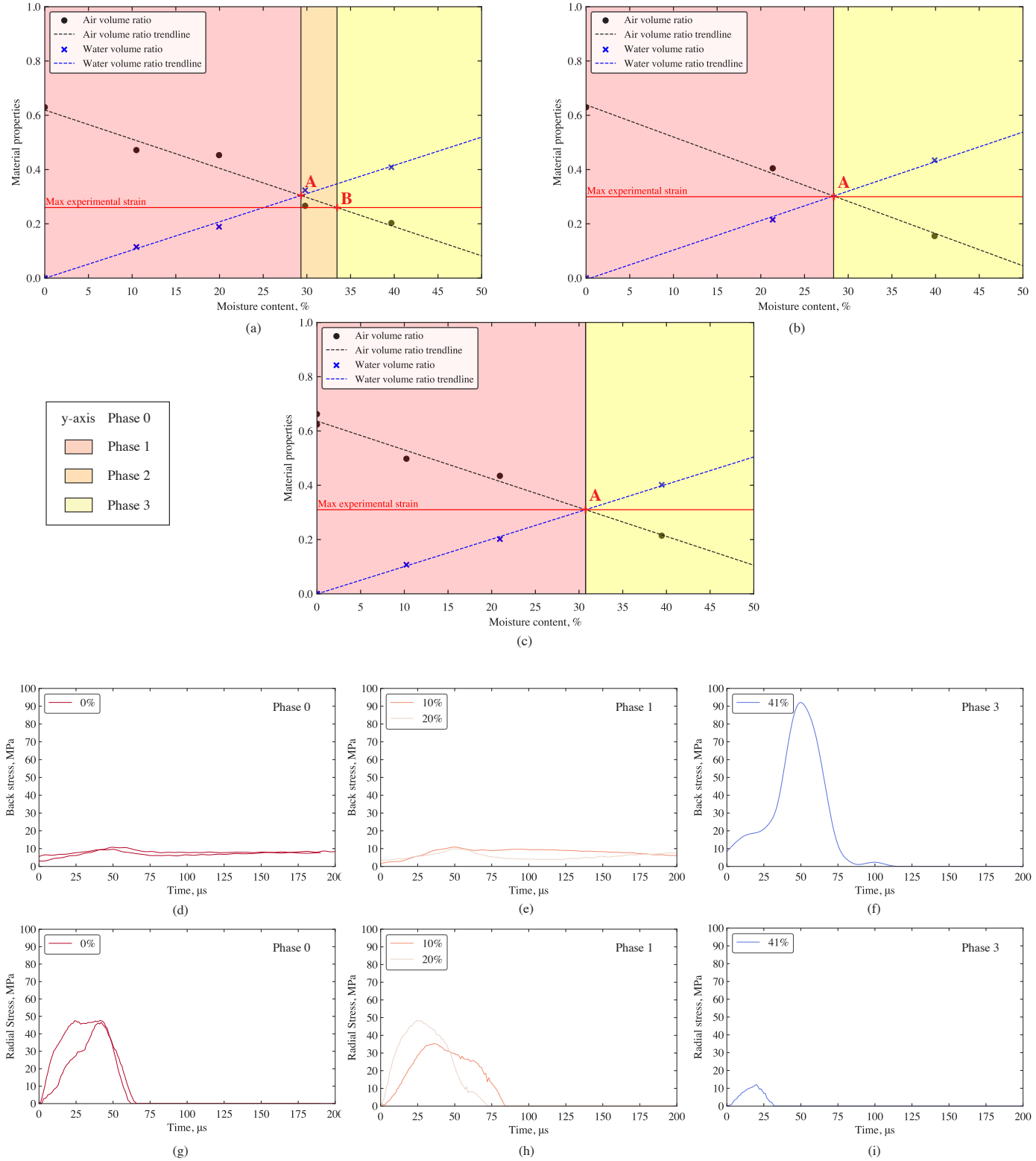

Figure 22: Confined SHPB testing of kaolin clay with (a) phase behaviour at 18 m/s (2600 s^{-1}), (b) phase behaviour at 20 m/s (2800 s^{-1}) and (c) phase behaviour at 22 m/s (3100 s^{-1}), as well as the associated back stress at 20 m/s (2800 s^{-1}) for (d) Phase 0, (e) Phase 1, and (f) Phase 3, and radial stress at 20 m/s (2800 s^{-1}) for (g) phase 0, (h) phase 1, and (i) phase 3.

*MAT_MOHR_COULOMB

$#	mid	ro	gmod	rnu		phi	cval	psi
	X	x1	1.3E7	x2		0.08075	55759.4	0.0
$#		nplanes		lccpdr	lccpt	lccjdr	lccjt	lcsfac
		0		0	0	0	0	0
$#	gmoddp	gmodgr	lcgmep	lcphiep		lcgmst	cvalgr	aniso
	0.0	0.0	0.0	0.0		0.0	0.0	1.0

[x1 and x2 are adjusted based on the material properties of the sample tested.]

Table 2: Material card for *MAT_MOHR_COULOMB, calibrated for use with kaolin clay [14].

9. Numerical modelling of SHPB tests

9.1. Model setup

The numerical model of the setup is shown in Figure 23. It was created using the FEM software LS-DYNA, in order to compare numerical and experimental SHPB test results on kaolin clay samples. The striker (yellow in Figure 23), incident (blue in Figure 23) and transmitter (green in Figure 23) bars are modelled as 3D solid Lagrangian meshes. The confining ring (orange and pink in Figure 24b) is also modelled this way. SPH node modelisation was used for the kaolin clay sample.

Figure 24a depicts the 5 mm SPH kaolin clay sample section numerically simulated between the incident and transmitter bars. A more detailed representation of the confining ring with the SPH sample slotted inside is illustrated in Figure 24b. A fixed sample length of 5 mm was chosen, and the model's bulk density was changed to match the precise sample length tested using the SHPB apparatus.

When examined at high strain rates, kaolin clay exhibits high deformation and fluid-like behaviour, hence SPH is chosen as the most suitable option over traditional ALE or Lagrangian meshing procedures. Consequently, there are no problems associated with excessive distortion or negative volume errors.

The contact interface between the SPH-modelled kaolin clay sample and the two Lagrangian pressure bars (i.e. incident and transmitter bar) was represented in LS-DYNA using the automated nodes-to-surface contact interaction. The contact interface between the SPH-modelled kaolin clay sample and the inside of the confining ring was modelled in this similar manner, using automated nodes-to-surface contact interaction.

The interfaces between the striker-incident bar, and incident-transmitter bar are modelled using manual surface-to-surface contact interactions.

9.2. Model material cards

The stainless-steel pressure bars are modelled as linear elastic using the *MAT_ELASTIC, with a density, Young's modulus and Poisson's ratio of ρ = 7666 kg.m^{-3}, E = 222 GPa and ν = 0.29, respectively. To mirror the experimental tests, the model's striker bar velocity was set to the associated striker speed used in experimental testing: 8, 12, 16 m/s for unconfined SHPB tests and 18, 20, 22 m/s for confined SHPB tests.

The confining ring used for SHPB testing is made of stainless-steel. It was initially modelled as linear elastic using *MAT_ELASTIC, however, this led to a lot vibration and noise interference with the numerical data. A fully rigid confining ring was modelled using the *MAT_RIGID to remove these interferences associated with the contact between the pressure bars and the confining ring. This resulted in no radial stress data being recorded. Therefore, a combination of rigid and elastic elements were utilised to model the confining ring to be able to collect radial stress data (orange and pink in Figure 24b).

The kaolin clay sample made using SPH was modelled with *MAT_MOHR_COULOMB, which has a bulk density (ro), elastic shear modulus (gmod), Poisson's ratio (rnu), angle of friction (phi) and cohesion factor (cval). The bulk density (ro) and Poisson's ratio (rnu) vary depending on the moisture content of the kaolin clay sample examined. These parameters are established using standard quasi-static tests, and are summarised in Table 2.

Figure 23: LS-DYNA SHPB model set up with the confining ring [The confining ring is removed for unconfined SHPB modelisation].

(a) (b)

Figure 24: LS-DYNA zoom-in on modelling for (a) the unconfined SHPB setup, and (b) the confined SHPB setup.

9.3. *Comparison between unconfined SHPB tests and corresponding LS-DYNA numerical models*

The material card *MAT_MOHR_COULOMB incorporates the bulk density, ρ, and Poisson's ratio, ν, based on the moisture content of the sample being modelled. These parameters are designated as x1 and x2 in Table 2.

Table 3 provides a comprehensive overview of the inputs utilised in LS-DYNA to model the unconfined SHPB tests, along with the corresponding results, specifically the maximum front and back stresses within the model. Twelve distinct unconfined SHPB model setups were executed, each with varying input parameters, such as striker speed, moisture content, bulk density (ρ) and Poisson's ratio (ν).

Test number 6 highlighted a critical issue: inputing a Poisson's ratio of 0.5 in the *MAT_MOHR_COULOMB material card resulted in failure. A crucial parameter for accurately simulating the fluid-like behaviour of kaolin clay under high moisture content and high strain rates (Table 3).

Test results also indicated that inputing a Poisson's ratio of 0.40, 0.44 or 0.49 yielded identical maximum front and back stresses as noticed across tests no. 1, 2 and 3. Similarly, the variation in bulk density within the sample, intended to simulate different moisture content levels, had no effect on the output, as demonstrated by the consistent maximum front and back stresses observed in tests 2, 4 and 5 (Table 3).

The incident and reflected pulses as well as the back stress obtained from the LS-DYNA numerical models are compared against the experimental SHPB test data collected, as illustrated in Figures 25, 26 and 27.

Figures 25 and 26 juxtapose the typical experimental and numerical incident and reflected pulses obtained for a striker speed of 8 m/s (1200 s^{-1}). The shape of the incident pulse in the numerical model still mirrors a similar pattern to the experimental results. However, there is a notable difference in the reflected pulse behaviour. While experimentally, the incident pulse propagates through the sample, in the LS-DYNA numerical model, the incident pulse is completely reflected, indicating that the stress wave is unable to propagate through the SPH sample in the model. As a result, the computed front stress is significantly lower than the experimental results.

Figure 27 illustrates a notable disparity between the back stress in LS-DYNA and the experimental back stress. This disparity arises because the incident pulse is entirely reflected upon contact with the sample. Upon impact from the incident bar, the SPH particles in LS-DYNA eject both axially and laterally as the stress wave propagates through the kaolin clay sample. Consequently, the particle cohesion properties of the specimen do not contribute to the stress wave's propagation into the transmitted bar.

Despite the limitations in LS-DYNA in modelling cohesive soils at high strain rates, tests number 2, 4, 5, 7, 8, 9, 10, 11 and 12, conducted at speeds of 8, 12 and 16 m/s, demonstrated that as the strain rate increases so does the maximum front and back stresses. This indicates that these LS-DYNA models still adequately capture the effect of strain rate in cohesive soils at high strain rate.

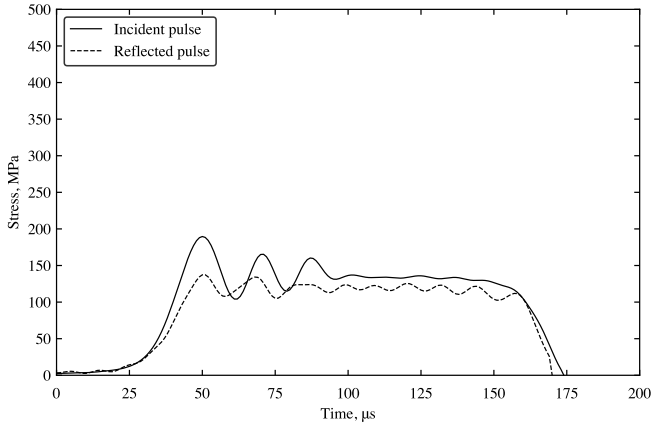

Figure 25: Typical stress behaviour from the incident and reflected pulses of an unconfined SHPB experimental test, at 8 m/s (1200 s^{-1}).

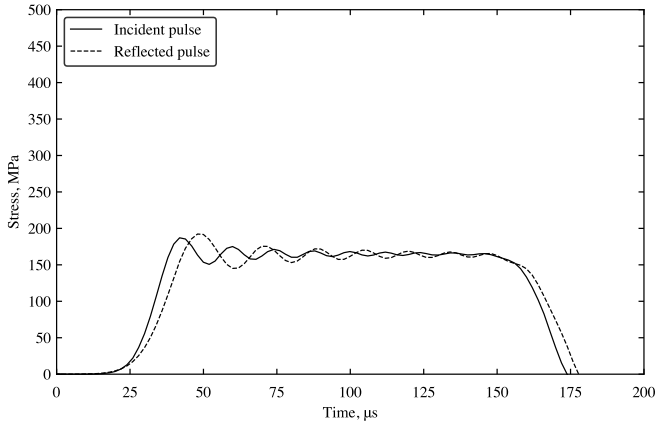

Figure 26: Typical stress behaviour from the incident and reflected pulses of an unconfined SHPB tests in LS-DYNA, at 8 m/s (1200 s^{-1}).

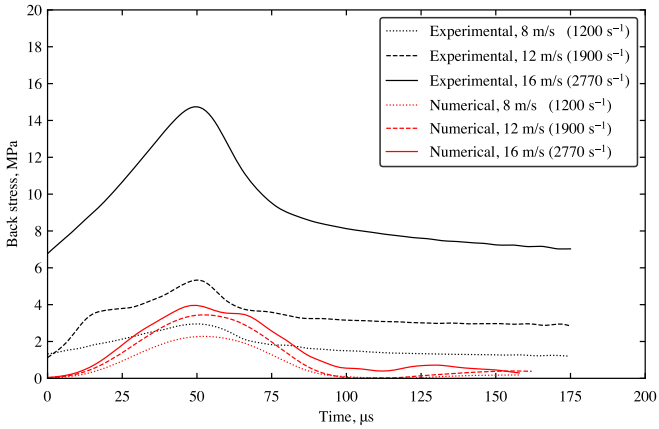

Figure 27: Comparison of back stress from the experimental unconfined SHPB tests and corresponding numerical LS-DYNA models on kaolin clay at a moisture content of 0% and different strain rates.

Test No.	Striker speed m/s	Moisture content %	ρ (ro) kg.m^{-3}	ν (rnu)	Max front stress MPa	Max back stress MPa	Max radial stress MPa
UNCONFINED SHPB MODELLING							
1	8	0	934	0.40	21.4	2.3	–
2	8	0	934	0.44	21.4	2.3	–
3	8	0	934	0.49	21.4	2.3	–
4	8	20	1087	0.44	21.4	2.3	–
5	8	41	1296	0.44	21.4	2.3	–
6	8	41	1296	0.50	FAIL	FAIL	–
7	12	0	934	0.44	32.8	3.4	–
8	12	20	1087	0.44	32.8	3.4	–
9	12	41	1296	0.44	32.8	3.4	–
10	16	0	934	0.44	44.8	4.0	–
11	16	20	1087	0.44	44.8	4.0	–
12	16	41	1296	0.44	44.8	4.0	–
CONFINED SHPB MODELLING							
13	18	0	934	0.40	324.4	394.3	509.0
14	18	0	934	0.44	324.4	394.3	509.0
15	18	0	934	0.49	324.4	394.3	509.0
16	18	20	1087	0.44	324.4	394.3	509.0
17	18	41	1296	0.44	324.4	394.3	509.0
18	18	41	1296	0.50	FAIL	FAIL	FAIL
19	20	0	934	0.44	365.1	432.6	624.0
20	20	20	1087	0.44	365.1	432.6	624.0
21	20	41	1296	0.44	365.1	432.6	624.0
22	22	0	934	0.44	410.3	481.3	674.0
23	22	20	1087	0.44	410.3	481.3	674.0
24	22	41	1296	0.44	410.3	481.3	674.0

['–': Data not recorded, 'FAIL': LS-DYNA model failed to run]

Table 3: Summary of the LS-DYNA modelling inputs and outputs.

9.4. *Comparison between confined SHPB tests and corresponding LS-DYNA numerical models*

The same material card is used to model the confined SHPB tests in LS-DYNA, *MAT_MOHR_COULOMB. Similarly to the unconfined SHPB models, Table 3 provides an overview of the inputs utilised in LS-DYNA to model the confined SHPB tests, along with the corresponding outputs, specifically the maximum front, back and radial stresses from the model.

Tests 13 to 24, detailed in Table 3, echo the findings of unconfined SHPB models, confirming that Poisson's ratio does not influence the results, with the model failing to run for a Poisson's ration of 0.5. Furthermore, adjustments in moisture content through variations in bulk density, observed in model tests 13 to 24, do not alter the material's behaviour in the model.

Figures 28 and 29 depict the incident and reflected pulses in the experimental tests and numerical model. The front stress behaviour in the LS-DYNA numerical model resembles that observed in the SHPB tests, albeit with a higher magnitude due to the sample containment seal in the numerical model setup of the confining ring (Table 3).

Back and radial stresses are shown in Figures 30 and 31. The magnitudes of these stresses are considerably higher than those obtained from experimental testing. This is primarily due the confining ring's influence in LS-DYNA and its modelling approach, since the confining ring effectively seals the SPH specimen inside, preventing extrusion during testing. Nevertheless, the model does not accurately reflect the genuine behaviour of cohesive soils, as neither moisture content nor Poisson's ratio affects the model outputs.

The back stress results from the numerical models show an increasing trend, consistent with observations from SHPB testing. Additionally, the radial stress results from the models exhibit also an increasing trend as speed increases (Table 3).

When the sample is fully saturated, with a Poisson's ratio of 0.5, the model fails to run due to limitations of *MAT_MOHR_COULOMB, necessitating the used of *MAT_NULL to model the fluid-like behaviour of the material. Since there is no sample extrusion in the numerical model, the front, back and radial stress results show higher values than in the experimental SHPB tests (Table 3). The perfect seal of the ring in the model alters the sample's radial stress behaviour, as there is no inertia effect from the incident bar impacting the sample. Hence, the radial stress does not fall due to excessive sample extrusion from the ring, before rising again, as seen in testing.

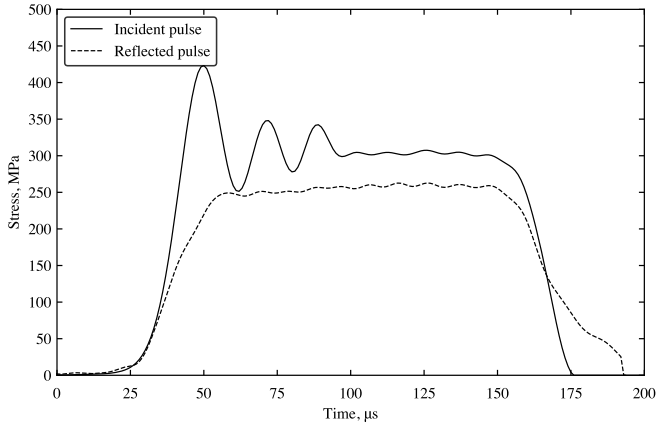

Figure 28: Typical stress behaviour from the incident and reflected pulses of an confined SHPB experimental test, at 18 m/s (2600 s^{-1}).

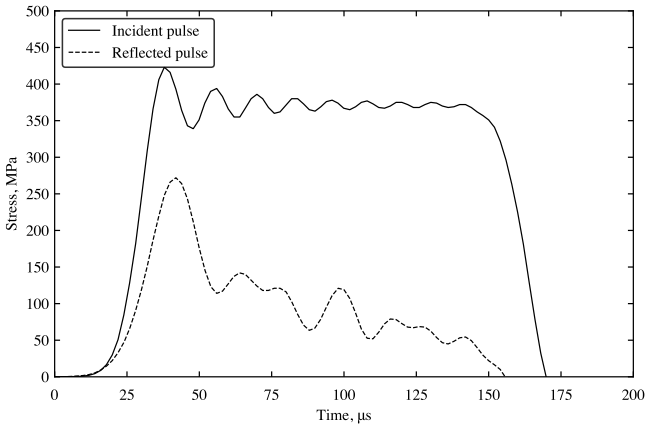

Figure 29: Typical stress behaviour from the incident and reflected pulses of an confined SHPB tests in LS-DYNA, at 18 m/s (2600 s^{-1}).

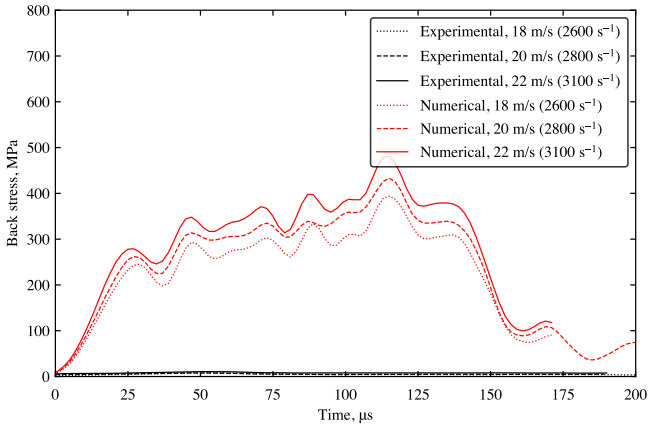

Figure 30: Comparison of back stress from the experimental confined SHPB tests and corresponding numerical LS-DYNA models on kaolin clay at a moisture content of 0% and different strain rates.

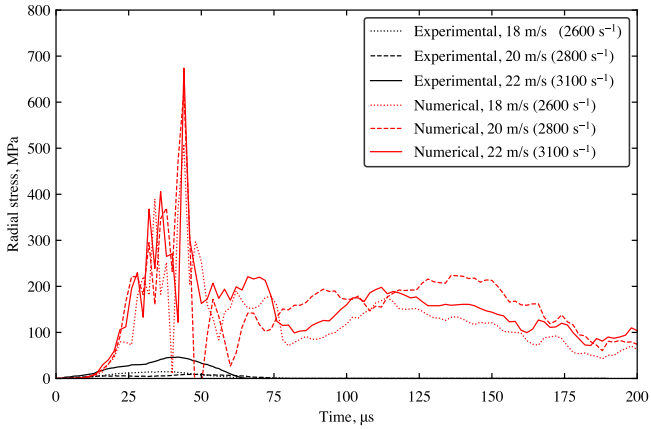

Figure 31: Comparison of radial stress from the experimental confined SHPB tests and corresponding numerical LS-DYNA models on kaolin clay at a moisture content of 0% and different strain rates.

9.5. LS-DYNA modelling limitations

Notable LS-DYNA modelling limitations are as follows:

1. The difficulty in computing a compression curve due to the material's inability to endure multi-axial compression without extrusion. Since kaolin clay is strain rate dependent, no equation of state (EOS) can be determined to simulate the complete behaviour of our material under high strain rates conditions. Most soil specific and cohesion material models in LS-DYNA require an EOS, therefore the list of material models which could be utilised with the parameters we collected is very short, leaving `*MAT_MOHR_COULOMB` as the most suitable option.
2. During the comparison of experimental SHPB test data and associated LS-DYNA numerical models, the impact of the material's moisture content could not be observed in the numerical model. Therefore, the phase behaviour could not be mapped out in LS-DYNA. This is due to the model's limitations in modelling cohesive soils at high strain rates.
3. The development of the SPH node modelisation technique in LS-DYNA is limited. LS-DYNA is unable to accurately represent the cohesion properties of cohesive soil particles. The deficiency, compounded by the lack of cohesion properties in this node modelisation tool, hinders the ability to accurately model the high strain rate behaviour of cohesive soils [26].
4. The numerical modelling of the confining ring revealed constraints related to sample extrusion, seal, vibration and contact, hence it required adjustments. Experimentally, an elastic stainless-steel ring was used to obtained the radial stress behaviour of the tested specimen, but its excessive deformation compromised accuracy. Therefore, a half rigid, half elastic confining ring was created to fully confine the sample, maintain stress equilibrium, prevent sample extrusion with a tight seal, and record radial stresses without complete deformation. Nevertheless, the perfect seal of the confining ring affects the stress results produced from the model, making them greater than they should be.

10. Discussion

The effect of moisture content on the behaviour of cohesive soils was thoroughly investigated through SHPB tests conducted under both confined and unconfined conditions, revealing an inherent phase behaviour. This phase behaviour significantly impacts the use of cohesive soils, as moisture content directly affects the material's ability to propagate stress. Moisture content levels in phase 1 yielded the most effective results in preventing stress wave propagation in confined test cases, while in unconfined test cases, phase 4 was the most effective.

In unconfined SHPB testing, phase 4 sees the behaviour of the material governed by the water volume in the specimen. In unconfined testing scenarios, stress propagation through the material is primarily limited by moisture content, while any remaining stress propagates laterally as the specimen extrudes. However, implementing this in practice poses challenges due to the difficulty in transporting and moulding the material into specific structures.

In confined SHPB testing, phase 1 sees the material's physical behaviour dictated by the soil, as the volume of soil in the sample exceeds that of water. In contrast to other phases, where the water volume ratio is either nonexistent (phase 0) or dominant (phases 2 and 3), phase 1 sees the water volume in the sample aiding to the material's strengthening. In cases where a confining ring restricts lateral propagation, stress is redirected axially, resulting in an increase in axial stress, as seen in phase 4 for confined SHPB tests. When phase 2 disappears, radial stress initially drops but then rises again due to inertia effects from the incident bar, resulting in sample extrusion. This indicates that the confining ring is unable to contain the sample at such high strain rate levels. Moreover, differing speed and strain rate between unconfined and confined SHPB tests underscored confinement's impact kaolin clay's high strain rate behaviour. The stress-strain analysis of the sample revealed a clear strain rate dependence of the material at high strain rates.

Given the high strain rate conditions of this research, SPH node modelisation was chosen to model the kaolin clay sample, due to its suitability for high-impact high-deformation scenarios. However, the material's strain rate dependency posed challenges in modelling the SHPB tests using LS-DYNA, as no suitable material cards were available. The absence of dedicated material cards for cohesive soil modelling in LS-DYNA complicated the depiction of observed behaviour during testing. Consequently, a general material card `*MAT_MOHR_COULOMB`, was used to model the kaolin clay.

In the unconfined SHPB models, the incident pulse closely matched that of the SHPB tests, validating the model setup. However, the reflected pulse exhibited considerable differences, resulting in lower front and back stress responses, attributable to the stress wave's inability to propagate through the sample. The SPH particles dissipated instantly upon contact with the incident pulse. In the confined SHPB models, the front, back and radial stresses are considerably higher than those obtained from the SHPB tests, since the confining ring provides a perfect seal in the model enabling the stress wave to propagate through the sample more easily, resulting in considerably greater values. The rising trend observed for the front and back stresses in testing was also noticed in the model. The radial stresses obtained in the model, using a composite half-rigid, half-elastic confining ring with a perfect seal, significantly surpass those observed in testing. This is because the numerical model is a perfect test representation from which to obtain the radial stress, therefore it is unable to capture the inertial effect from the incident bar.

Comparing the tests to the numerical models for kaolin clay samples with varying moisture contents, it was observed that the variation in moisture content in model failed to demonstrate the same phase behaviour. The discrepancy can be attributed to LS-DYNA's limitations in modelling cohesive soil properties accurately, leading to erroneous modelling findings.

In conclusion, cohesive soils' ability to limit stress propagation is clearly influenced by moisture content and confinement. The SHPB test derived back stress indicates the stress that can propagate through the sample, with moisture content acting as a dampener that impedes lateral stress propagation. Confinement restricts lateral extrusion, redirecting radial stress axially and consequently affecting stress transmission through the sample.

11. Summary

In this study, the high strain rate behaviour of cohesive soils was investigated using the SHPB apparatus. A comprehensive material characterisation analysis was conducted on the chosen cohesive soil, kaolin clay. High strain rate SHPB tests were performed on kaolin clay samples with different moisture content levels under both unconfined and confined conditions. The experimental results emphasise the novelty of this research, revealing that strain rate, moisture content and confinement all influence the behaviour of cohesive soils at high strain rates. The presence of a soil phase behaviour based on the sample's moisture content was identified, as evidenced by the back stress for the unconfined SHPB tests and the radial and back stresses for the confined SHPB tests.

The FEM software LS-DYNA was used to simulate the unconfined and confined SHPB tests performed on kaolin clay samples at varying moisture contents. While modelling the test setup posed no significant challenges, clear limitations were observed in LS-DYNA when comparing experimental and numerical results: there is no dedicated material card model for cohesive soils, no cohesive properties in the software and very limited use of SPH for modelling the high strain rate behaviour of cohesive soils. These findings underscore the existing gap in modelling the high strain rate behaviour of cohesive soils.

Future endeavours in this field will initially focus on developing data-driven parametric models using all the experimental test data collected. This will enable the prediction of the unconfined and confined behaviour of cohesive soils, at high strain rates within the explored range, thereby saving considerable time and costs. Subsequently, in light of the discussed modelling limitations, there is a clear need for improvements in modelling the high strain rate behaviour of cohesive soils. To address this, experimental test data will be utilised to develop a hybrid twin model that incorporates all SHPB test results, enriching the numerical model.

Furthermore, the effect of confinement was explored by comparing a free-field unconfined scenario with a rigid confined SHPB test scenario. However, an intermediate case remains unexplored, which would assess the impact of confining pressure on lateral and axial stress propagation. This avenue presents an opportunity for further investigation.

Author statement

Arthur Van Lerberghe: Conceptualisation, Methodology, Investigation, Testing, Analysis & Writing. **Kin Shing O. Li:** Conceptualisation, Modelling & Analysis. **Andrew D. Barr:** Conceptualisation, Supervision & Review. **Sam D. Clarke:** Conceptualisation, Supervision & Review.

Acknowledgements

This research was funded by the Engineering and Physical Sciences Research Council (EPSRC), and the Defence Science and Technology Laboratory (Dstl).

Declaration of competing interest

The authors declare that they have no known competing financial interest or personal relationships that could have appeared to influence the work reported in this paper.

References

[1] C. A. Ross, P. T. Nash, G. J. Friesenhahn, Pressure waves in soils using a split-hopkinson pressure bar, Tech. rep., Southwest Research Institute San Aantonio TX (1986).

[2] G. E. Veyera, Uniaxial stress-strain behavior of unsaturated soils at high strain rates, Tech. rep., Wright Lab Tyndall Afb Fl (1994).

[3] G. T. Gray III, Classic split hopkinson pressure bar testing, ASM handbook 8 (2000) 462–476.

[4] A. Bragov, A. Lomunov, I. Sergeichev, K. Tsembelis, W. Proud, Determination of physicomechanical properties of soft soils from medium to high strain rates, International Journal of Impact Engineering 35 (9) (2008) 967–976. doi:https://doi.org/10.1016/j.ijimpeng.2007.07.004.

[5] H. Luo, W. L. Cooper, H. Lu, Effects of particle size and moisture on the compressive behavior of dense eglin sand under confinement at high strain rates, International Journal of Impact Engineering 65 (2014) 40–55. doi:https://doi.org/10.1016/j.ijimpeng.2013.11.001.

[6] A. D. Barr, Strain-rate effects in quartz sand, Ph.D. thesis, University of Sheffield (2016).

[7] B. Hopkinson, X. a method of measuring the pressure produced in the detonation of high, explosives or by the impact of bullets, Philosophical Transactions of the Royal Society of London. Series A, Containing Papers of a Mathematical or Physical Character 213 (497-508) (1914) 437–456. doi:https://doi.org/10.1098/rsta.1914.0010.

[8] H. Kolsky, An investigation of the mechanical properties of materials at very high rates of loading, Proceedings of the physical society. Section B 62 (11) (1949) 676. doi:https://doi.org/10.1088/0370-1301/62/11/302.

[9] H. Kolsky, Stress waves in solids. Dover Books on Physics, New York (1963). doi:https://doi.org/10.1016/0022-460X(64)90008-2.

[10] A. Bragov, G. Grushevsky, A. Lomunov, Use of the kolsky method for confined tests of soft soils, Experimental Mechanics 36 (1996) 237–242. doi:https://doi.org/10.1007/BF02318013.

[11] Q.-Y. Ma, Experimental analysis of dynamic mechanical properties for artificially frozen clay by the split hopkinson pressure bar, Journal of Applied Mechanics and Technical Physics 51 (3) (2010) 448–452. doi:https://doi.org/10.1007/s10808-010-0060-8.

[12] R. Yang, J. Chen, L. Yang, S. Fang, J. Liu, An experimental study of high strain-rate properties of clay under high consolidation stress, Soil Dynamics and Earthquake Engineering 92 (2017) 46–51. doi:https://doi.org/10.1016/j.soildyn.2016.09.036.

[13] A. Konstantinov, A. Bragov, L. Igumnov, V. Eremeyev, V. V. Balandin, et al., Experimental study and identification of a dynamic deformation model of dry clay at strain rates up to 2500 s-1, Journal of Applied and Computational Mechanics 8 (3) (2022) 981–995. doi:https://doi.org/10.22055/jacm.2022.39321.3387.

[14] J. O. Hallquist, et al., Ls-dyna keyword user's manual, Livermore Software Technology Corporation 970 (2007) 299–800.

[15] P. Church, R. Cornish, I. Cullis, P. Gould, I. Lewtas, Using the split hopkinson pressure bar to validate material models, Philosophical Transactions of the Royal Society A: Mathematical, Physical and Engineering Sciences 372 (2023) (2014) 20130294. doi:https://doi.org/10.1098/rsta.2013.0294.

[16] P. A. Cundall, O. D. Strack, A discrete numerical model for granular assemblies, geotechnique 29 (1) (1979) 47–65. doi:https://doi.org/10.1680/geot.1979.29.1.47.

[17] C. L. Busch, R. A. Tarefder, Evaluation of appropriate material models in ls-dyna for mm-ale finite element simulations of small-scale explosive airblast tests on clay soils, Indian Geotechnical Journal 47 (2) (2017) 173–186. doi:https://doi.org/10.1007/s40098-016-0196-4.

[18] V. Eremeyev, V. Balandin, A. Bragov, A. Y. Konstantinov, L. Igumnov, et al., Experimental study and numerical simulation of the dynamic penetration into dry clay, Continuum Mechanics and Thermodynamics 35 (2) (2023) 457–469. doi:https://doi.org/10.1007/s00161-023-01189-w.

[19] J. L. Lacome, Smooth particle hydrodynamics (sph): a new feature in ls-dyna, in: 6th international LS-DYNA users conference, 2000, pp. 7–30.

[20] ISO, 14688-1: 2002: Geotechnical investigation and testing – Identification and classification of soil – Part 1: Identification and description, British Standards Institution (2002).

[21] BSI, BS 1377-2: 1990: Methods of test for soils for civil engineering purposes – Part 2: Classification tests (1990).

[22] A. Casagrande, Classification and identification of soils, Transactions of the American Society of Civil Engineers 113 (1) (1948) 901–930. doi:https://doi.org/10.1061/TACEAT.0006109.

[23] A. Van Lerberghe, K. S. O. Li, A. D. Barr, S. D. Clarke, An open-source algorithm for correcting stress wave dispersion in split-hopkinson pressure bar experiments - submitted for publication in Experimental Mechanics, currently under review (2024).

[24] K. S. O. Li, A. Van Lerberghe, A. Barr, SHPB_Processing.py - An open-source Python algorithm for correcting stress wave dispersion in split-Hopkinson pressure bar experiments (2024). doi:10.15131/shef.data.24570565.v1.

[25] A. Tyas, D. J. Pope, Full correction of first-mode pochammer–chree dispersion effects in experimental pressure bar signals, Measurement science and technology 16 (3) (2005) 642. doi:https://doi.org/10.1088/0957-0233/16/3/004.

[26] K. S. O. Li, A. Van Lerberghe, A. Barr, S. D. Clarke, A. A. Dennis, Split-hopkinson pressure bar testing of water with partial lateral confinement - submitted for publication in Measurement Science and Technology, currently under review (2024).

A.6 Data-driven parametric modelling of split-Hopkinson pressure bar tests on cohesive soils

Van Lerberghe, A., Pasquale, A., Rodrigues, S., Barr, A. D., Clarke, S. D., Baillargeat, D., & Chinesta, F. (2024). Data-driven parametric modelling of split-Hopkinson pressure bar tests on cohesive soils

A paper presenting de development of two data-driven parametric models using SHPB test data on cohesive soils, submitted for publication to the International journal of Impact Engineering. The journal paper is included in its entirety below as reference.

Data-driven parametric modelling of split-Hopkinson pressure bar tests on cohesive soils

Arthur Van Lerberghe[a,*], Angelo Pasquale[b], Sebastian Rodriguez[b], Andrew D. Barr[a], Sam D. Clarke[a], Dominique Baillargeat[c], Francisco Chinesta[b,c]

[a] *Department of Civil & Structural Engineering, University of Sheffield, Mappin Street, Sheffield, S1 3JD, UK*
[b] *PIMM Lab, Arts et Métiers Institute of Technology, 151 Boulevard de l'Hôpital, Paris, 75013, France*
[c] *CNRS@CREATE Ltd, 1 Create Way, #08-01 CREATE Tower, Singapore, 138602, Singapore*

Abstract

Soil-filled wire and geotextile gabions stand as vital bulwarks in military bases, harnessing soil's innate capacity to absorb shock and safeguard both personnel and critical assets from blast and fragmentation effects. Yet, the dynamic response of cohesive soils under extreme loads remains largely unexplored, leaving engineers grappling with a significant void in knowledge as they strive to fortify structures against emerging threats. This paper considers the high-strain-rate behaviour of kaolin clay using the split Hopkinson pressure bar in both confined and unconfined configurations, with a range of moisture contents representing dry, partially-saturated and saturated conditions. Analysis of the results indicates distinct phase behaviours in transmitted and radial stress based on strain rate, moisture content and confinement. Leveraging cutting-edge machine learning models such as the Proper Orthogonal Decomposition (POD) and sparse Proper Generalised Decomposition (sPGD), data-driven parametric models were developed based on the experimental data. These models enable the prediction of cohesive soil behaviour at specified strain rate and moisture content, enabling engineers to rapidly predict soil behaviour in response to new threats and ground conditions.

Keywords: Data-driven parametric modelling, Physics informed machine learning, Curve metamodeling, High-strain-rate testing, Split-Hopkinson pressure bar, Cohesive soils

1. Introduction

Fortification engineers rely on soil-filled barriers like Hesco Concertainers for blast protection, yet cohesive soil's high-strain-rate behaviour remains elusive despite its widespread use. Understanding cohesive soils such as clay and silt is crucial for the design of fortifications, due to their global presence and potential as alternatives where sandy soils are less common.

Precise data on local soils are vital for fortification engineers to adapt designs, urging comprehensive studies on soil behaviour under extreme loading conditions. Focusing on kaolin clay offers a foundation for understanding its response to strain rate, moisture, and confinement variations through SHPB tests. The complexities of cohesive soils, including their undrained behaviour and fine particle size, pose challenges compared to cohesionless soils such as sand [1–6], necessitating new research to inform resilient fortification designs and bridge existing knowledge gaps.

Experimental research on kaolin clay has explored its behaviour under varied confinement, moisture content and strain rate conditions [7]. Overcoming the limitations of time-consuming high-strain rate testing, machine learning methods leverage collected test data to construct data-driven parametric models capable of predicting cohesive soil behaviour.

Various machine learning algorithms can be utilised for regression tasks. Linear regression assumes a relationship between input features and the target variable, while polynomial regression extends this concept by considering polynomial relationships. Regularised regressions, such as Ridge and Lasso, add penalty terms to prevent overfitting and induce sparsity in models [8]. Support vector Regression (SVR) [9] extends support vector machines (SVMs) for regression tasks, while decision trees [10] and random forest regression [11] split the data and combine trees to improve accuracy. Gradient boosting [12] builds weak learners sequentially, correcting errors, and deep learning techniques [13], like artificial neural networks, learn complex relationships for regression.

Polynomial regression techniques, employed in computational mechanics [14] and structural deformation [15], have yet to be applied in the field of blast and impact dynamics. This study aims to utilise SHPB test data and machine learning tools to rapidly predict the high-strain-rate behaviour of cohesive soils under diverse loading conditions and material properties.

2. Parametric modelling: background, method & theory

Model Order Reduction (MOR) is a branch within computational science dedicated to simplifying intricate mathematical models, often represented by systems of differential equations or transfer functions, while preserving their fundamental be-

*Corresponding author.
Email addresses: avanlerberghe1@sheffield.ac.uk (Arthur Van Lerberghe), angelo.pasquale@ensam.eu (Angelo Pasquale), sebastian.rodriguez_iturra@ensam.eu (Sebastian Rodriguez), a.barr@sheffield.ac.uk (Andrew D. Barr), francisco.chinesta@ensam.eu (Francisco Chinesta)

haviour. MOR aims to reduce the computational burden associated with simulating or analysing such models by generating simplified versions, known as reduced-order models (ROMs), that adequately represent the system's dynamics with sufficient accuracy.

Through the reduction of degrees of freedom in the model, MOR facilitates faster simulations, optimisation, and control design, all while maintaining fidelity. This proves advantageous for systems characterised by high-dimensional or parametric descriptions encountered in scientific environments.

Now, a general procedure for constructing parametric surrogates of curves is presented, using extensive literature and detailed reviews on state-of-the-art MOR technologies [16–18]:

1. Consider a scenario where experimental data is collected, comprising of input parameters $\mathbf{p}_i$ and corresponding output curves $g(x;\mathbf{p}_i)$. Each curve represents the system's behaviour under various conditions, with $\mathbf{p}_i$ representing geometrical or material parameters. In simulation-based engineering, data $g(x;\mathbf{p}_i)$ is typically obtained through simulation software runs, with the parameters of interest $\mathbf{p}_i$ potentially including modelling features.
2. Each experimental data point can be viewed as a snapshot $(\mathbf{p}_i, g(x;\mathbf{p}_i))$, where $i = 1, 2, ..., n_s$, (n_s is the number of sampling points used for training) depicting parameter combinations and their corresponding output curves.
3. Dimensionality reduction techniques such as Principal Component Analysis (PCA) or Proper Orthogonal Decomposition (POD) are applied directly to test data to extract dominant modes of variability in the output curves $g(x;\mathbf{p}_i)$.
4. The reduced basis functions $\phi_j(x)$ are constructed by identifying the dominant modes through dimensionality reduction. These basis functions effectively capture the essential features of the output curves.
5. Using the reduced basis functions, a surrogate model $\hat{g}(x,\mathbf{p})$ is constructed to approximate the output curves $g(x;\mathbf{p}_i)$ based on the input parameters $\mathbf{p}_i$ and the domain x. This surrogate model can be formulated as:

$$\hat{g}(x,\mathbf{p}) = \sum_{j=1}^{m} \lambda_j(\mathbf{p})\phi_j(x)$$

   where $\lambda_j(\mathbf{p})$ are the coefficients of the surrogate model, which depend on the parameters $\mathbf{p}$.
6. Surrogate models for $\lambda_j(\mathbf{p})$ can be built by training a regression algorithm on the available dataset, to establish links between input parameters and measured output.

In polynomial regressions, addressing the challenges of high-dimensional parametric problems has led to the development of novel techniques such as the Proper Generalised Decomposition (PGD) [19–21]. PGD, a tensor-based method, represents high-dimensional data by utilising separable representations and a greedy iterative algorithm for adaptive basis construction. It finds applications across various engineering and scientific fields, such as blast and impact dynamics in this case.

2.1. POD-based modes extraction

To construct the snapshots matrix for training data $\{g_i(x)\}_{i=1}^{n_s}$, for $x \in X = \{x_j\}_{j=1}^{n_x}$ utilised in this study, consider the following procedure:

$$\mathbf{S} = \begin{bmatrix} \mathbf{g}_1 & \mathbf{g}_2 & \dots & \mathbf{g}_{n_s} \end{bmatrix} \in \mathbb{R}^{n_x \times n_s},$$

where $\mathbf{g} \in \mathbb{R}^{n_x \times 1}$ contains the evaluations of $g(x)$ over the discrete ensemble X.

Next, a reduced factorisation of the snapshots matrix is achieved through a standard truncated POD of rank r:

$$\mathbf{S} \approx \mathbf{U}\mathbf{\Sigma}\mathbf{V}^T$$

where $\mathbf{U} \in \mathbb{R}^{n_x \times r}$, $\mathbf{\Sigma} \in \mathbb{R}^{r \times r}$, $\mathbf{V} \in \mathbb{R}^{n_s \times r}$. From these, we can define the matrices of POD modes and coefficients, as follows:

$$\mathbf{\Phi} \coloneqq \mathbf{U} = \begin{bmatrix} \boldsymbol{\phi}_1 & \boldsymbol{\phi}_2 & \dots & \boldsymbol{\phi}_r \end{bmatrix}, \ \mathbf{\Lambda} \coloneqq \mathbf{V}\mathbf{\Sigma} = \begin{bmatrix} \boldsymbol{\lambda}_1 & \boldsymbol{\lambda}_2 & \dots & \boldsymbol{\lambda}_r. \end{bmatrix}$$

The matrix $\mathbf{\Phi}$ contains, by columns, the functions of the reduced POD basis $\{\boldsymbol{\phi}_i(x)\}_{i=1}^{r}$ evaluated at points in X, while $\mathbf{\Lambda}$ collects the projection coefficients into the reduced basis. For a generic curve $g_k(x)$ belonging to the training dataset, where $k = 1, \dots, n_s$ and $x \in X$, its reduced counterpart is given by:

$$g_k^{(r)}(x) = \sum_{i=1}^{r} \lambda_{k,i}\phi_i(x), \tag{1}$$

and, in particular, its discrete form reads

$$\mathbf{g}_k^{(r)} = \mathbf{\Lambda}_{k,\bullet}\mathbf{\Phi}^T,$$

where $\mathbf{\Lambda}_{k,\bullet}$ denotes the k-th row of the matrix $\mathbf{\Lambda}$.

Now, let's consider a parametric curve dependent on d features $\bar{\mathbf{p}} \in \Omega$, denoted as $g(x;\bar{\mathbf{p}})$, where $x \in X$. From Equation (1) it is evident that once the reduced basis matrix $\mathbf{\Phi}$ is available, this function is projected onto this basis solely through the POD (parametric) coefficients $\{\lambda_i(\mathbf{p})\}_{i=1}^{r}$:

$$g^{(r)}(x;\bar{\mathbf{p}}) = \sum_{i=1}^{r} \lambda_i(\bar{\mathbf{p}})\phi_i(x).$$

The equation above indicates that a reduced-order parametric metamodel for the curves can be constructed using only the set of coefficients $\{\lambda_i(\mathbf{p})\}_{i=1}^{r}$. Specifically, the following parametric function shall be constructed:

$$\mathbf{f}(\mathbf{p}) = \begin{bmatrix} \lambda_1(\mathbf{p}) \\ \lambda_2(\mathbf{p}) \\ \vdots \\ \lambda_r(\mathbf{p}) \end{bmatrix} : \Omega \subset \mathbb{R}^d \to \mathbb{R}^r,$$

from the training dataset available as $\{\mathbf{p}_k, \mathbf{\Lambda}_{k,\bullet} = (\lambda_{k,1}, \lambda_{k,2}, \dots, \lambda_{k,r})\}_{k=1}^{n_s}$, obtained after the POD.

2.2. Advanced PGD-based sparse nonlinear regressions

Nonlinear regression methods such as the sparse Proper Generalised Decomposition (sPGD) are increasingly vital for managing complex parameters efficiently while preserving accuracy, complementing MOR techniques for real-world engineering problems [19–21]. These methods have recently gained significant attraction in industry, with various approaches expanding their applicability for approximating parametric curves [15]. For instance, sPGD can be used to predict intrusion and acceleration curves in car crash simulations [22]. These techniques are effective for virtual parametric testing of battery mechanical performance, aiding in assessing safety conditions in electric vehicles [23, 24]. sPGD-based regressions have been used to define a hybrid twin of resin transfer moulding (RTM) process, accurately predicting the resin flow-front of a complex model throughout its entire time history [25].

In this section, the focus shifts to the concept behind the PGD-based regression methods for constructing metamodels dependent on d features, which are used in this study. The discussion centres on scenarios where a single-value output is measured for a given parameter choice [15]. This setup enables the prediction of parametric curves using the coefficients $\lambda_i(\boldsymbol{p})$ corresponding to the POD modes, as previously suggested.

For each coefficient $\lambda_i(\mathbf{p})$, the challenge lies in constructing the function

$$f(p^1, \ldots, p^d) : \Omega \subset \mathbb{R}^d \to \mathbb{R},$$

which depends on d features (parameters) p^k, $k = 1, \ldots, d$, within the parametric space Ω, given a sparse sample of n_s points and their corresponding outputs.

The sparse PGD (sPGD) represents the function f using a low-rank separated representation

$$f(p^1, \ldots, p^d) \approx \tilde{f}^M(p^1, \ldots, p^d) = \sum_{m=1}^{M} \prod_{k=1}^{d} \psi_m^k(p^k), \qquad (2)$$

constructed from rank-one updates within a greedy constructor. Here, $\tilde{f}^M$ denotes the approximation, M the number of employed modes (sums), and ψ_m^k the one-dimensional functions pertaining to mode m and dimension k.

The functions ψ_m^k, $m = 1, \ldots, M$ and $k = 1, \ldots, d$, are derived from a standard approximation basis $\mathbf{N}_m^k$ using coefficients $\mathbf{a}_m^k$:

$$\psi_m^k(p^k) = \sum_{j=1}^{D} N_{j,m}^k(p^k) a_{j,m}^k = (\mathbf{N}_m^k)^T \mathbf{a}_m^k,$$

where D represents the number of degrees of freedom (nodes) of the chosen approximation and $\mathbf{N}_m^k$ is the vector collecting the shape functions.

In standard regression, the approximation $\tilde{f}^M$ is obtained by minimising the error function

$$\tilde{f}^M = \arg\min_{f^*} \|f - f^*\|_2^2 = \arg\min_{f^*} \sum_{i=1}^{n_s} |f(\mathbf{p}_i) - f^*(\mathbf{p}_i)|^2,$$

where $\tilde{f}^M$ takes the separated form of Equation (2), n_s is the number of sampling points used for training, and $\mathbf{p}_i$ are the vectors containing the input data points of the training set. It is important to note that to avoid overfitting, the number of basis functions D must satisfy $D < n_s$.

The approximation coefficients for each one-dimensional function are computed using a greedy algorithm. Given the approximation up to order $M-1$, the M-th order term is determined as

$$\tilde{f}^M = \sum_{m=1}^{M-1} \prod_{k=1}^{d} \psi_m^k(p^k) + \prod_{k=1}^{d} \psi_M^k(p^k)$$

The resulting function is expected to approximate f not only in the training set but also at any point $\mathbf{p} \in \Omega$.

The main challenge is balancing detailed approximations with limited available data while avoiding overfitting. To address this, a modal adaptivity strategy (MAS) was introduced alongside sPGD. Yet, achieving desired accuracy often leads to overfitting or premature termination of the algorithm with MAS, resulting in a PGD solution of low-order approximation functions that fails to capture the desired richness [19].

Additionally, in scenarios with sparse non-zero elements in the interpolation basis, MAS struggles to accurately recognise the true model, leading to decreased accuracy.

To overcome these challenges, various regularisation methods were proposed [20], combining L^2 and L^1 norms affecting coefficients $\mathbf{a}_m^k$. These techniques aim to enhance predictive performance beyond sPGD's capabilities or to construct parsimonious models while improving predictive accuracy.

3. Split-Hopkinson pressure bar testing of cohesive soils

3.1. Material characterisation

The soil chosen is defined as white fine CLAY (CL) according to EN ISO 14688–1:2002 [26], and referred to as 'kaolin clay' for brevity. Table 1 outlines the material properties of the kaolin clay, derived using the methods detailed below.

Soil properties	Units	Value
Primary mineral	–	Kaolinite
Particle density, ρ_s	Mg.m^{-3}	2.65
Liquid limit, LL	%	40
Plastic limit, PL	%	25
Plastic Index, PI	%	15
D_{50}	μm	0.74
Particle sphericity	–	Low – Medium
Angularity	–	Subrounded – Subangular
Surface texture	–	Smooth

Table 1: Overview of the kaolin clay material properties.

The kaolin clay's particle size distribution (PSD) was assessed using IMERYS' supplier-provided data sheet. Figure 1 shows the cumulative PSD, revealing a D_{50} of 0.74 μm. With 80 % clay and 20 % silt, the soil is classified as CLAY (CL).

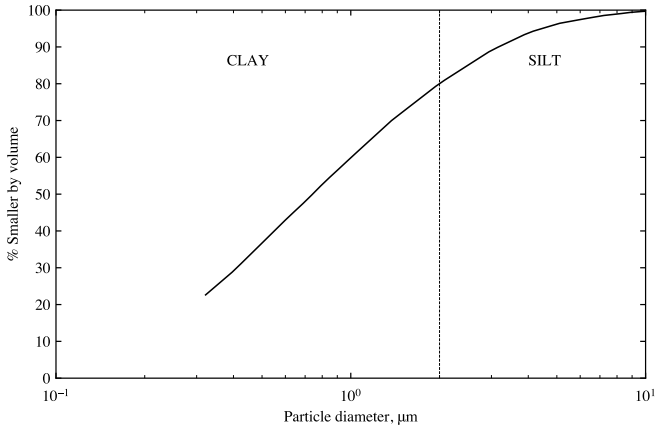

Figure 1: Cumulative particle size distribution of the kaolin clay soil.

The particle density, ρ_s, represents the density of the solid mineral particles. Together with the bulk dry density, ρ_d, it determines the soil's void ratio using the relationship:

$$e = \frac{\rho_s}{\rho_d} - 1$$

The kaolin clay's particle density, ρ_s, was determined to be 2.65 Mg.m^{-3}, following the method outlined in BS 1377–2:1990 §8.2 [27] , which is the density of kaolinite.

X-ray diffraction (XRD) was conducted on the kaolin clay to identify its constituent minerals. In XRD, an incident X-ray beam diffracts due to the specimen's regular atomic structure. By measuring diffraction intensity at various incident angles, θ, a unique diffraction pattern is obtained. This pattern was compared to a database of known patterns for phase identification. Phase analysis utilised a PANalytical Aeris diffractometer and the ICDD's Diffraction File (PDF-4+). Figure 2 displays the diffraction pattern of the kaolin clay, revealing primarily kaolinite with some quartz present.

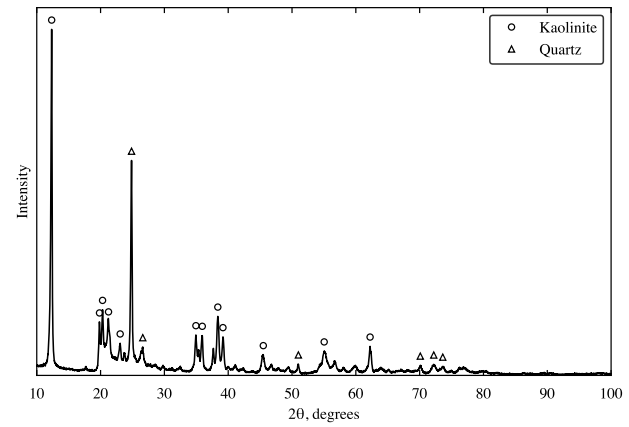

Figure 2: X-ray diffraction data of the kaolin clay soil.

Sample consistency is vital, hence Atterberg limits must be consistent across all soil samples. The fall cone test was used to obtain the Atterberg limits of kaolin clay [27]. The liquid limit (LL), plastic limit (PL), and plastic index (PI) are 40 %, 25 % and 15 %, respectively [27]. These values surpass the A-line, confirming the soil's classification as CLAY (CL) [28].

Kaolinite-sized particles in the soil were qualitatively assessed using a scanning electron microscope (SEM), employing descriptors from EN ISO 14688–1:2002 [26]. Before insertion into the SEM, the kaolin clay soil undegoes gold (Au) coating. Figure 3 illustrates the kaolin clay particles, revealing variations from low to medium sphericity, with subrounded to subangular shape, and smooth surface texture.

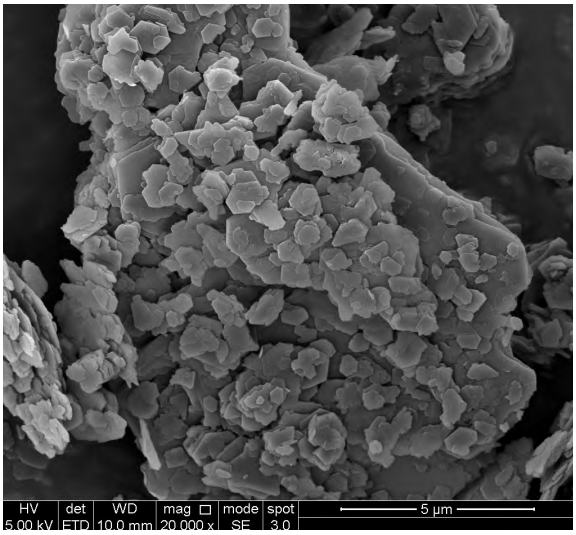

Figure 3: SEM imagery of kaolin clay at 20,000x magnification.

3.2. Specimen preparation

Kaolin clay samples were prepared using powdered speswhite kaolin clay, mixed with water at a 1:1 ratio to form a slurry. The slurry was consolidated in a pressurised cylindrical Rowe cell to 600 kPa, resulting in a fully saturated kaolin clay wheel with a 44 % moisture content. Controlled drying was employed to study the effect of moisture content on the high-strain-rate behaviour of kaolin clay. Specimens with moisture content levels ranging from 0 to 44 % were prepared, covering all saturation levels, from unsaturated to fully saturated [7]. For both unconfined and confined SHPB testing, the following procedure was followed to prepare the specimens:

1. Cylindrical kaolin clay samples with varying moisture content are made using a 25 mm stainless-steel cylinder slicer. The specimens have a nominal length of 5 mm and a diameter of 25 mm. The initial weight of the kaolin clay specimen is recorded immediately after it has been sliced.
2. Samples are air dried in a temperature-controlled setting at 20 degrees Celsius, and weighed at regular intervals to measure their current moisture content based on their initial wet weight and current weight.
3. Cut and air-dried samples are then wrapped in polyvinylidene chloride to minimise changes in moisture content between sample preparation and testing. The samples are prepared and tested in different laboratories, hence they are stored in sealed plastic bags until required for testing.

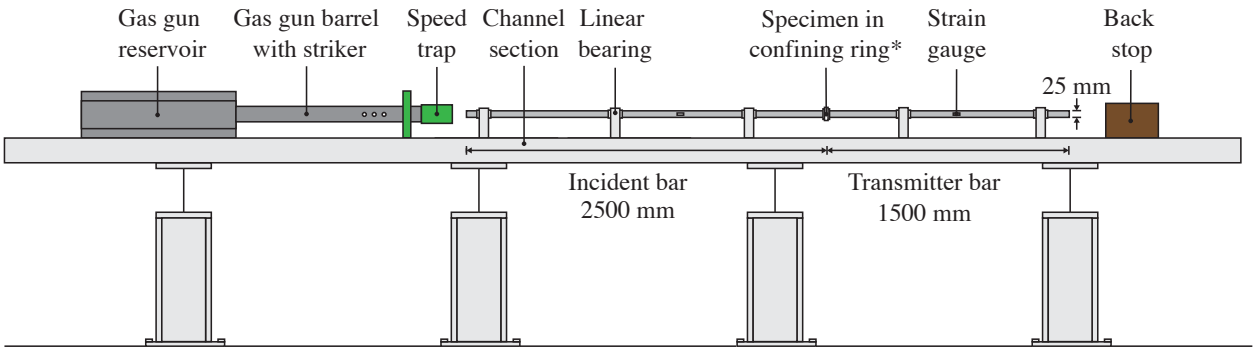

Figure 4: Schematic diagram of the SHPB experimental setup with the confining ring [* removed for unconfined SHPB tests].

3.3. Experimental setup

The SHPB experimental setup features a conventional pressure bar arrangement comprising a striker bar (350 mm), an incident bar (2500 mm) and a transmitter bar (1500 mm), each with a diameter of 25 mm (Figure 4). For confined SHPB testing, a steel confining ring (Figure 5a) was used to encase the sample between the incident and transmitter bars (Figure 5b).

Pressure bar strain gauges signals were captured using a TiePie Handyscope four-channel digital oscilloscope with a 14-bit A-D resolution, a sampling frequency of 1 MHz, and a record length of 131.072 kSa. The material's axial stress response was monitored using a pair of Kyowa KSP-2-120-E4 strain gauges mounted on the incident and transmitter bars, while the radial stress was measured using a single strain gauge mounted on the outside of the confining ring. Strain gauge signals were collected from the incident and transmitter bars using a half Wheatstone bridge configuration, and from the confining ring using a quarter Wheatstone bridge configuration [7].

3.4. Test programme

For unconfined SHPB testing, tests commenced at 8, 12 and 16 m/s on kaolin clay samples with moisture content ranging from 0 to 44 %. Subsequent tests were conducted at 18, 20 and 22 m/s to assess the impact of higher strain rates. Correspondingly, peak average strain rates of 1200, 1900 and 2800 s^{-1}, were achieved for 8, 12 and 16 m/s, respectively [7].

For confined SHPB testing, tests started at 12 m/s on kaolin clay samples with moisture content ranging from 0 to 41 % for behavioural comparison with the unconfined SHPB tests. Then, tests at 18, 20 and 22 m/s were conduced. Under confined conditions, the average peak strain rates were 2600, 2800 and 3100 s^{-1}, for 18, 20 and 22 m/s, respectively [7].

Under both testing conditions, the specimen's axial and radial stresses and strains are measured.

It is important to note that the test speed in these SHPB experiments is setup-specific, while the strain rate reflects what the sample experiences during testing.

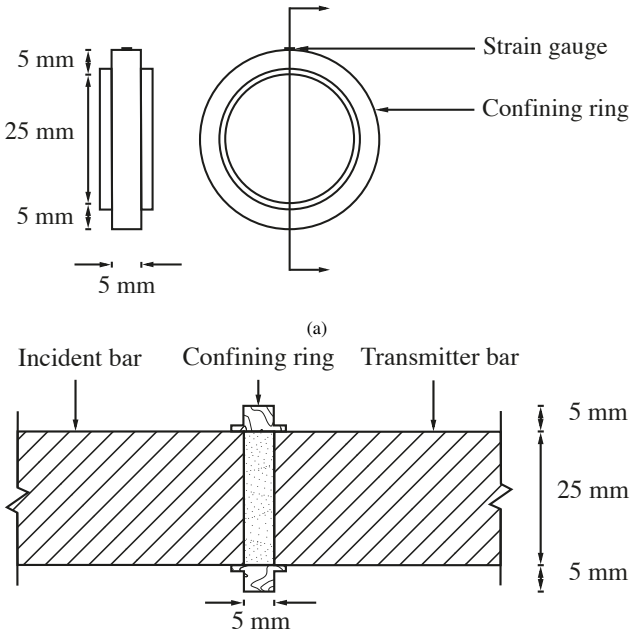

Figure 5: Diagrams showing (a) the confining ring for confined SHPB testing and (b) the confining ring with the sample inside, ready for testing.

3.5. Testing results

The SHPB test signals for the incident bar, transmitter bar and confining ring were processed using the open-source Python algorithm `SHPB_Processing.py` [29]. This algorithm incorporates the subroutine `dispersion.py`, which implements Tyas and Pope's dispersion-correction approach [30]. This ensures accurate representation of the sample's axial and radial stresses and strains during testing.

The behaviour of the tested kaolin clay samples can be categorised into four distinct "phases", each defined by its stress transmission characteristics, termed the "back stress" in SHPB tests [7]. These phases are delineated by the air volume ratio V_{air}/V, water volume ratio V_{water}/V, and the maximum experimental strain attained during the experiment, as illustrated in Figure 6a:

- **Phase 0:** Encompasses all dry specimens, positioned on the y-axis in Figure 6a.
- **Phase 1:** Comprises partially-saturated specimens where soil pores are primarily filled with air. The maximum moisture content for phase 1 is defined by the boundary formed by the intersection of the air and water ratio trendlines, denoted as Point A in Figure 6a.
- **Phase 2:** Comprises partially-saturated specimens where soil pores are primarily filled with water. The upper limit of moisture content is defined by the intersection of the air volume ratio with the max experimental strain, marked as Point B in Figure 6a.
- **Phase 3:** Defines experiments which begin partially-saturated, but reach full saturation during testing.

The behaviour of soil specimens vary across the four phases, depending on whether testing is unconfined or fully confined.

In unconfined conditions (Figure 6b), each phase exhibits a distinct stress transmission pattern, with increased moisture content correlating with reduced peak stress due to enhanced lateral movement and specimen extrusion. While moisture content minimally impacts stress transmission within each phase, back stress transmission increases with rising strain rates.

In fully confined conditions (Figures 6c), phases 0 and 1 primarily involve the compaction of the dry soil fraction, showcasing a similar shock absorption effect on transmitted stress. The attainment of high strains in confined SHPB tests eliminates phases 2 at higher strain rates, leading to an abrupt transition between phases 1 and 3. Upon reaching saturation, clay samples assume fluid-like behaviour with $\nu = 0.5$, resulting in a significantly heightened stress transmission.

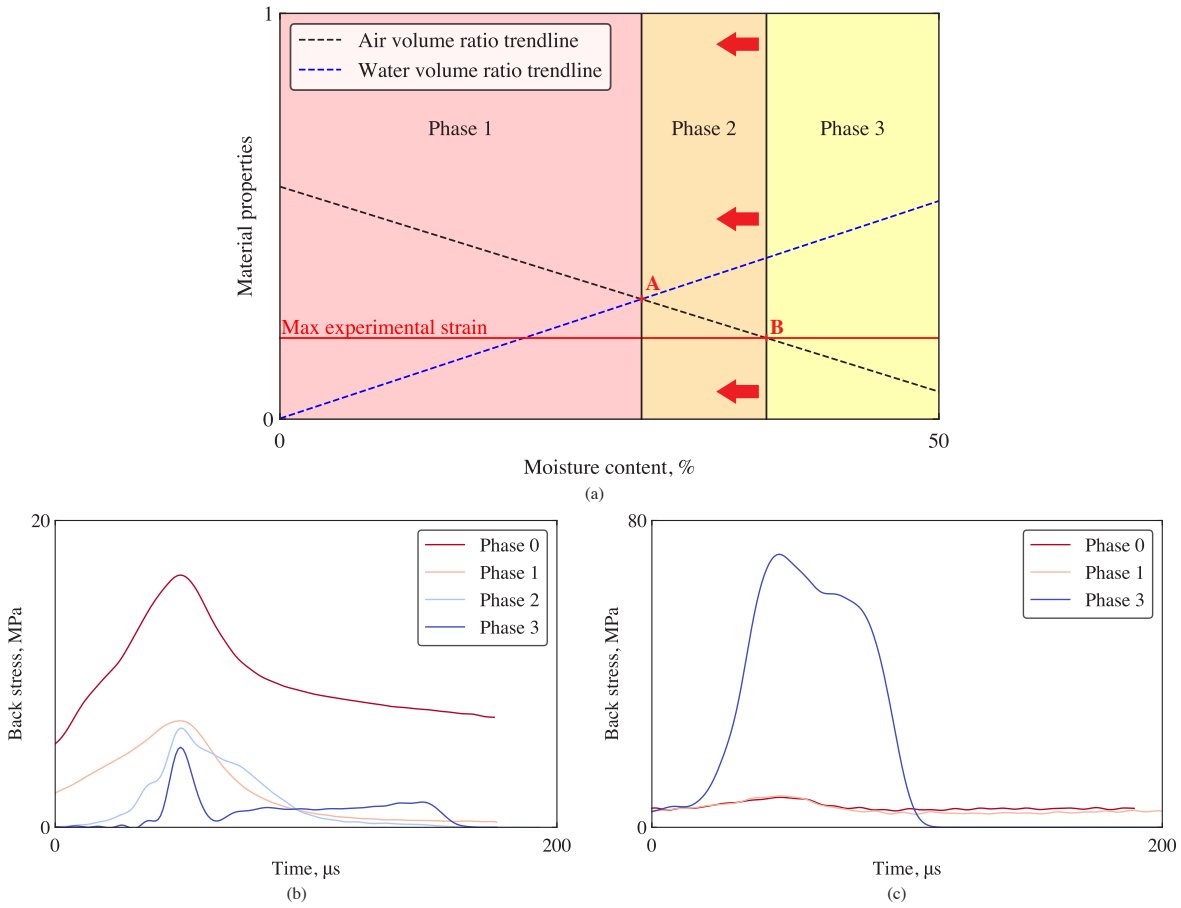

Figure 6: (a) Phase behaviour observed in SHPB testing of kaolin clay, defined by air and water volume ratios and maximum experimental strain. The indicative stress transmission through the clay in each phase at 2800 s^{-1} is depicted for (b) unconfined and (c) fully confined test conditions.

4. Development of data-driven parametric models

4.1. Data-driven classification

The classification of the data was conducted based on both the experimental test results and the initial sample parameters.

The data obtained from the SHPB tests on the kaolin clay samples, along with their initial parameters, can be classified into five categories represented by a Russian doll model, as illustrated in Figure 7: SHPB testing, unconfined and confined conditions, strain rate, moisture content, and phase number.

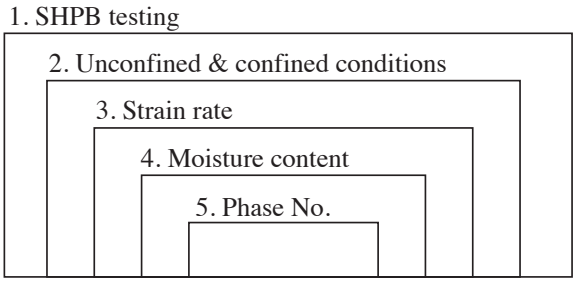

Figure 7: Diagram of the classification of experimental SHPB test data.

These parameters are ranked from 1 to 5, each denoting a different level of specificity in data classification. Parameter 1 encompasses all the tests, while parameter 5 represents a more specific subset. The parameters are defined as follows:

1. "SHPB testing" encompasses all tests conducted using the SHPB apparatus.
2. "Unconfined & confined conditions" categorises the tests which were performed under "unconfined" or "confined" conditions.
3. "Strain rate" indicates the tests were conducted at different strain rates: 1200, 1900, 2800 s^{-1} for unconfined and 2600, 2800 and 3100 s^{-1} for confined.
4. "Moisture content", reflects the varying moisture levels of the kaolin clay samples tested, ranging from 0 to 44 %.
5. "Phase No." assigns a specific phase number (0, 1, 2 or 3) to each moisture content, as detailed in Section 3.5.

A total of 144 SHPB experimental tests were carried out on kaolin clay samples spanning moisture contents from 0 to 44 %. Among these, 98 tests were performed under unconfined conditions, while 46 tests were conducted under fully confined conditions. The majority of the test data was utilised to develop the parametric models, with the exception of one test from each condition, which was reserved for subsequent model validation.

The insights gained into the high-strain-rate behaviour of cohesive soils, as discussed in Section 3.5, enabled the categorisation of the test data into separate confinement conditions and different phase behaviours, based on the sample's moisture content and strain rate. This physics-informed classification, was conducted manually, guided by test findings, with the strain rate identified as the key parameter influencing the material's response. The model simplifies from a polynomial regression to a linear analysis, with "strain rate", parameter 3, as the key parameter. The analysis within each material phase number showed that variations in moisture content had no discernible impact on the overall response. Consequently, the mean response was used for the parametric models. In summary, for unconfined conditions, the strain rate was 1200, 1900, 2800 s^{-1}, with four material phases, while for confined conditions, it was 2700, 2800 and 3100 s^{-1} with 3 material phases, with phase 2 disappearing at 2700 s^{-1} under confined conditions.

4.2. Parametric model

With the data classified into corresponding SHPB test conditions and phase numbers based on strain rate and moisture content, attention shift to the parametric model. Figure 8 details the structure of the parametric model used for training the test data, comprising inputs, a surrogate model, and outputs.

The input section focuses on the model's input parameters: the Design of Experiments (DOE) and Quantity of Interest (QOI). The DOE represents the parameter the model trains on, which in this case, is the key parameter: strain rate. Three strain rate values are utilised for each confinement condition. The QOI refers to the mean data properties of interest used for training against the DOE. For unconfined SHPB testing, there are five QOIs: strain, front stress, back stress, mid stress and time. Confined SHPB testing includes six QOIs: strain, front stress, mid stress, back stress and radial stress and time.

Data training for each model is facilitated by the surrogate model, made of two sections: POD mode extraction and sPGD regression. Since there is only one parameter, strain rate, POD mode extraction focuses on a single mode, mapping the data's curve behaviour along this parameter. Subsequently, sPGD regression utilises this information to predict the data's behaviour based on this relationship along the set parameter.

After passing through the surrogate model, the training data is saved, resulting in the creation of four different models for each phase number, as illustrated in Figure 9.

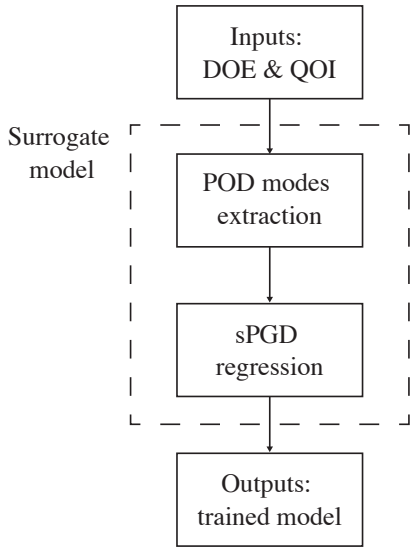

Figure 8: POD_sPGD flowchart.

4.3. Visualisation model

After training the tests data using the POD_sPGD model, the trained model results are saved according to their respective phase number. This process is illustrated in Figure 9, termed as the test data structuring and model training flowchart.

This trained data is utilised for the visualisation model, as depicted in the visualisation flowchart shown in Figure 9. The visualisation model consists of a four sections: model initialisation, model selection based on selected output parameters, model design and visualisation output. Model initialisation establishes the input parameters and widget architecture. The model selection section is made of the phase number and strain rate selection functions. It established the relationship between the trained POD_sPGD models for each phases number and the corresponding moisture content ranges obtained from testing. The model design encompasses interactive widget functionalities, while the visualisation output updates the visual plots based on selected moisture content and strain rate. As the selected strain rate changes, the model representing the data remains the same. However, altering moisture content prompts a transition between different material phase number, resulting in a change of the model number selected to represent the data.

The flowchart depicted in Figure 9 guides the creation of two widgets for each SHPB test condition, using the trained mean data. These final interactive widgets, are displayed in Figure 10 and 11. The unconfined SHPB test model features four plots, representing the four QOIs: strain, front stress, back stress and mid stress over time. Conversely, the confined SHPB test model includes five plots, representing the five QOIs: strain, front stress, mid stress, back stress and radial stress over time.

The plot axes in Figures 10 and 11 adjust responsively based on the selected moisture content, corresponding to a specific phase at a given strain rate. The y-axis dynamically adjusts to accommodate the maximum potential value.

Confidence patches, depicting the 90% confidence interval based on the standard deviation of the test data, are included in Figures 10 and 11 in light grey for both unconfined and confined SHPB test conditions. They are especially crucial for unconfined SHPB tests due to potential errors associated with testing.

The widgets in Figures 10 and 11, feature sliders for strain rate and moisture content, facilitating adjustments between the different phase behaviours of cohesive soil. The sliders are user-friendly, allowing for quick and interactive changes. The selected values for moisture content and strain rate are displayed on the right hand side of each slider. Additionally, a point picking option is available above the sliders, enabling selection of specific moisture content and strain rate values, with the complete selected ranges next to them. Both options provide immediate visualisation of cohesive soil responses under the selected parameters, offering instant information.

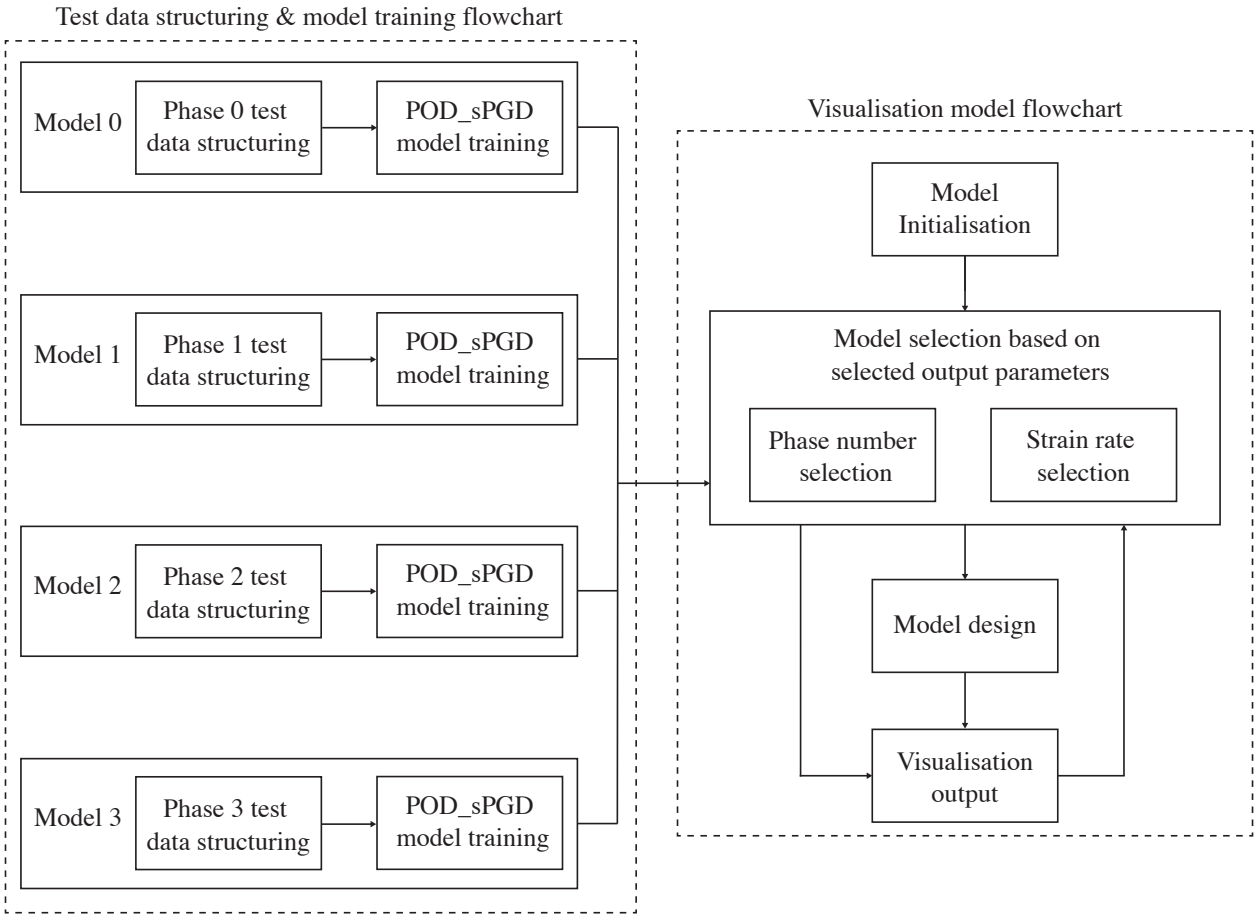

Figure 9: Overall design flowchart of the data-driven parametric models.

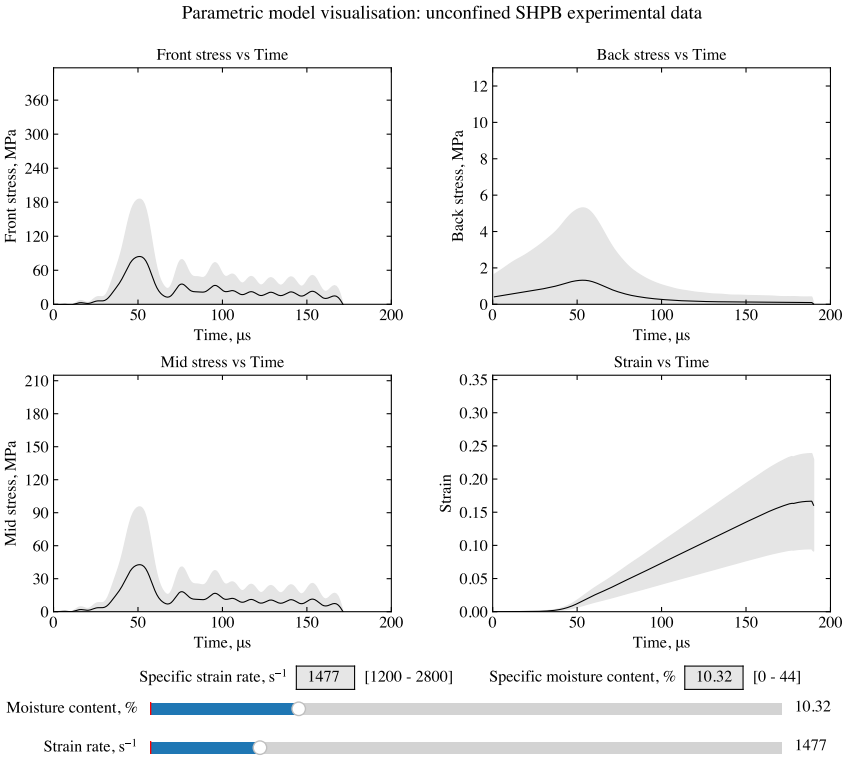

Figure 10: Parametric model visualisation widget for unconfined SHPB experimental data.

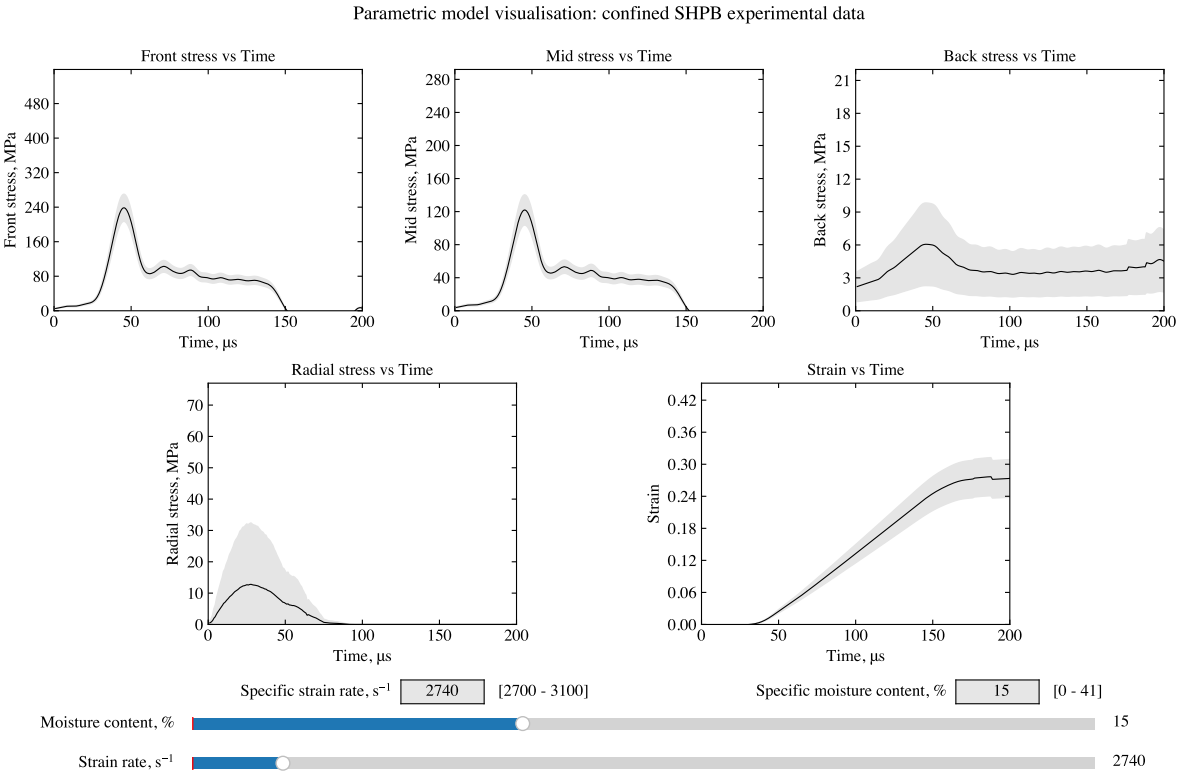

Figure 11: Parametric model visualisation widget for confined SHPB experimental data.

4.4. Model validation

To validate the data-driven parametric models, a comparative evaluation against a random SHPB test is imperative. This involves testing a kaolin clay sample with a specific moisture content under both unconfined and confined conditions using the SHPB apparatus, at a specific strain rate. The test results in red are compared against the model predictions.

The additional unconfined SHPB test was conducted on a kaolin clay sample with a moisture content of 11.32 % at a speed of 12.0 m/s, corresponding to a strain rate of 1996 s^{-1}. Similarly, the confined SHPB test involved a kaolin clay sample with a moisture content of 21.36 % at a speed of 20.0 m/s, resulting in a strain rate of 2976 s^{-1}.

The comparative results between the data-driven parametric models and the additional SHPB tests are depicted in Figures 12 and 13, where the supplementary tests are plotted in red on the interactive visual widgets. When comparing the newly performed tests and the data-driven parametric models on the visual widgets, the predicted representation exhibits remarkable accuracy, closely resembling the expected material response seen in testing. In both test conditions, the maximum amplitude is slightly higher, which is expected as the model represents the mean behaviour. The confidence interval around the black line is crucial, indicating the expected range of sample behaviour. Therefore, it is prudent to base designs on the maximum value.

These data-driven parametric models are suitable for direct use, given their fast, reliable and accurate capabilities in predicting the high-strain-rate behaviour of cohesive soils under both unconfined and confined conditions.

5. Discussion

Experimental SHPB tests were performed on kaolin clay samples, covering a range of moisture contents from 0 to 44 %. These tests were conducted under both unconfined and confined conditions, totalling 144 experiments, with 2 tests reserved for model validation. Of these, 98 tests were completed under unconfined conditions, while 46 tests were carried out under confined conditions. Analysis of the results revealed distinct phase behaviours of cohesive soils under high-strain-rate conditions, guiding the development of the parametric models.

The parametric models developed in this study were designed without reliance on implemented machine learning Python libraries, ensuring transparency and avoiding a black box scenario. Instead, the machine learning model was developed based on mathematical principles, with the coupling of POD modes extraction and sPGD regression methods proving invaluable in creating these parametric models. The foundation for building these models was laid upon novel SHPB test data.

The development of the models was guided by physics-informed classification of test data. Clear delineation of test data into different phase numbers based on confinement, moisture content, and strain rate behaviour eliminated the need for classification algorithms. Constructed through POD modes extraction and sPGD regression algorithms, the surrogate model played a vital role in producing trained data representing each phase number observed in material testing. The model's architecture was predominantly shaped by the strain rate, identified as the key parameter.

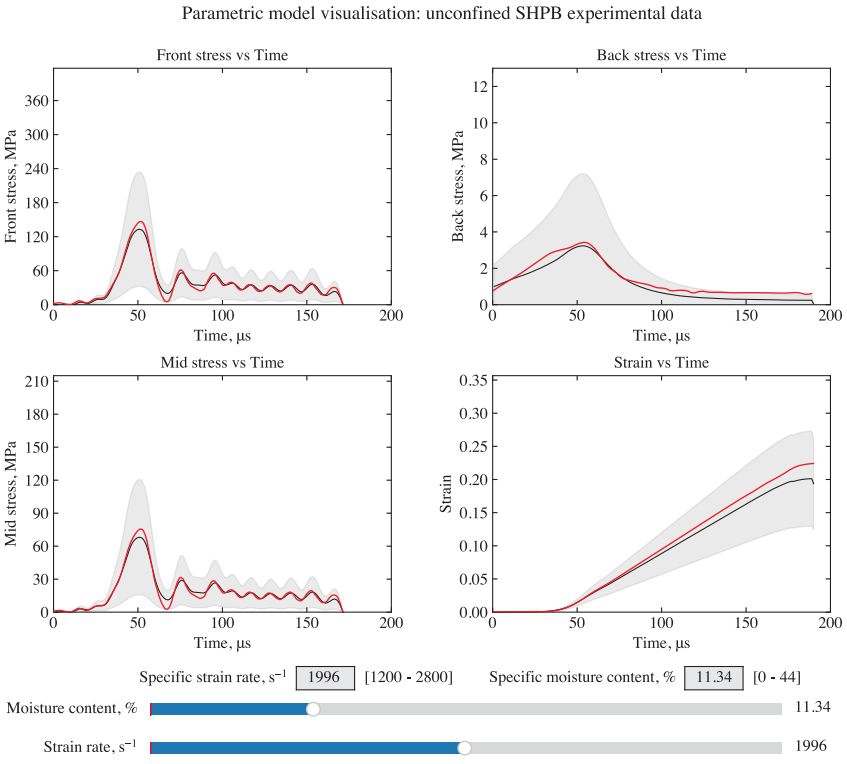

Figure 12: Parametric model validation: comparison of an unconfined SHPB test (in red) and its data-driven parametric model.

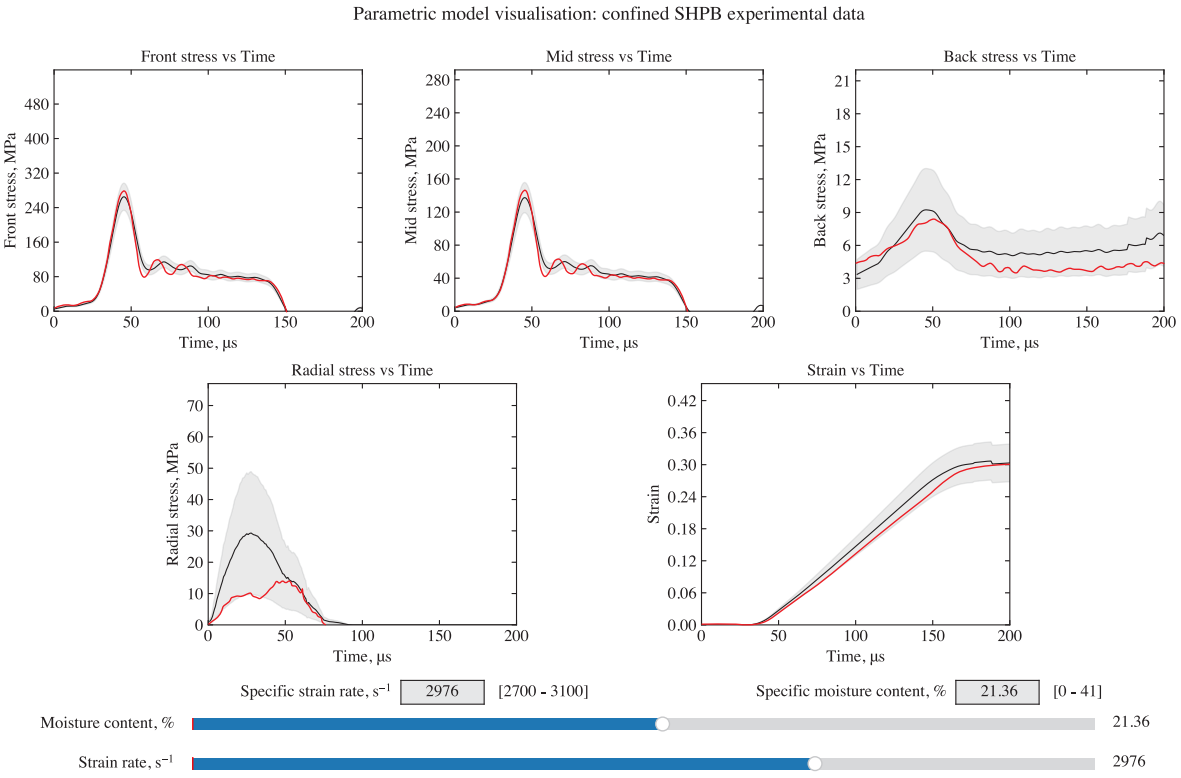

Figure 13: Parametric model validation: comparison of a confined SHPB test (in red) and its data-driven parametric model.

A vital aspect for understanding the trained data from the parametric models is a clear visual representation. To fulfil this need, interactive widgets were crafted for both testing scenarios, offering high responsiveness and user-friendliness. These widgets offer instantaneous responses and harness the trained data from the parametric model.

Model validation involved comparing the trained model data, depicted in black, with a distinct SHPB test, highlighted in red. Unconfined tests demonstrated notable accuracy, with confined tests, though fewer, also displaying considerable precision. Unconfined tests featured larger confidence intervals due to their susceptibility to testing errors, whereas confined tests showcased smaller confidence intervals owing to their high consistency. Further refinement of the confined parametric model can be achieved through additional testing. Nonetheless, at this stage, the model proves sufficiently precise, offering significant time and cost savings compared to traditional testing. Overall, the parametric model effectively predicts the high-strain-rate behaviour of cohesive soils under unconfined and confined conditions within the tested range.

6. Summary

Utilising cutting-edge machine learning polynomial regression techniques such as the POD and sPGD, engineers can now access two separate data-driven parametric models, offering rapid predictive capabilities for the behaviour of cohesive soils under various loading conditions and material parameters.

Experimental SHPB tests were conducted on kaolin clay samples, covering a range of moisture contents from 0 to 44%, under both unconfined and fully confined conditions. Through these tests, the degree of confinement, moisture content and strain rate were identified as the significant factors influencing the specimen's behaviour. This dataset served as the foundation for testing and training the parametric models.

The work undertaken in classifying the data was instrumental, as it demonstrated the feasibility of organising the findings within each phase number under specific confinement conditions and strain rates. Moreover, given the similar behaviour observed among test results within each phase number, the mean behaviour was used and represented. Strain rate emerged as the key parameter within each individual phase, effectively simplifying the complexity of the problem from nonlinear to linear. The POD analysis was therefore conducted along a single mode with strain rate as the key parameter, and sPGD modelling was executed within each distinct phase number, for each confinement state.

All tests, except for one from each test condition, were utilised for model construction, while the reserved tests were set aside for validation, allowing for comparisons with actual experiments, underscoring the accuracy of the two data-driven parametric models.

Interactive visual widgets were tailored for each test condition, enriching the user experience and streamlining the utilisation of these data-driven parametric models to empower engineers to respond promptly and effectively to threats.

For future endeavours, expanding the scope to include lower and higher strain rates would be beneficial, providing a more comprehensive understanding of the behaviour of cohesive soils at high-strain-rates. Nonetheless, the current results already offer substantial time and cost savings. This would include applications such as designing effective soil-filled barriers without the need for additional extensive experimental testing.

It is envisioned that these models will empower engineers to safeguard personnel and infrastructure from a variety of threats through the rapid assessment of cohesive soil properties.

Author statement

Arthur Van Lerberghe: Conceptualisation, Methodology, Investigation, Testing - Experimental & Parametric model, Analysis, Model optimisation & Writing. **Angelo Pasquale:** Conceptualisation, Initial model testing, Analysis, Model optimisation & Writing. **Sebastian Rodriguez:** Conceptualisation, Initial model testing, Analysis, Model optimisation, Writing & Review. **Andrew D. Barr:** Writing & Review. **Sam D. Clarke:** Supervision & Review. **Dominique Baillargeat:** Conceptualisation, Supervision & Review. **Francisco Chinesta:** Conceptualisation, Supervision & Review.

Acknowledgements

This research was funded by the Engineering and Physical Sciences Research Council (EPSRC), and the Defence Science and Technology Laboratory (Dstl).

Authors also acknowledge the support of the ESI Group through its research chair CREATE-ID at Arts et Métiers ParisTech. This research is part of the program DesCartes and is supported by the National Research Foundation, Prime Minister's Office, Singapore under its Campus for Research Excellence and Technological Enterprise (CREATE) program.

Declaration of competing interest

The authors declare that they have no known competing financial interest or personal relationships that could have appeared to influence the work reported in this paper.

References

[1] C Allen Ross, Phillip T Nash, and Gerard J Friesenhahn. Pressure waves in soils using a split-hopkinson pressure bar. Technical report, Southwest Research Institute San Aantonio TX, 1986.

[2] George E Veyera. Uniaxial stress-strain behavior of unsaturated soils at high strain rates. Technical report, Wright Lab Tyndall Afb Fl, 1994.

[3] George T Gray III. Classic split hopkinson pressure bar testing. *ASM handbook*, 8:462–476, 2000.

[4] AM Bragov, AK Lomunov, IV Sergeichev, K Tsembelis, and WG Proud. Determination of physicomechanical properties of soft soils from medium to high strain rates. *International Journal of Impact Engineering*, 35(9):967–976, 2008.

[5] Huiyang Luo, William L Cooper, and Hongbing Lu. Effects of particle size and moisture on the compressive behavior of dense eglin sand under confinement at high strain rates. *International Journal of Impact Engineering*, 65:40–55, 2014.

[6] Andrew D Barr. *Strain-rate effects in quartz sand*. PhD thesis, University of Sheffield, 2016.

[7] Arthur Van Lerberghe, Kin Shing Oswald Li, Andrew D. Barr, and Sam D. Clarke. High strain rate behaviour of cohesive soils - submitted for publication in the International Journal of Impact Engineering, currently under review. 2024.

[8] Trevor Hastie, Robert Tibshirani, and Jerome Friedman. *The Elements of Statistical Learning*. Springer Series in Statistics. Springer New York Inc., New York, NY, USA, 2001.

[9] AJ. Smola and B. Schölkopf. A tutorial on support vector regression. *Statistics and Computing*, 14(3):199–222, 2004.

[10] Charles J. Stone R.A. Olshen Leo Breiman, Jerome Friedman. *Classification and Regression Trees*. Chapman and Hall/CRC, 1984.

[11] L Breiman. Random forests. *Machine Learning*, 45:5–32, 10 2001.

[12] Jerome H. Friedman. Greedy function approximation: A gradient boosting machine. *The Annals of Statistics*, 29(5):1189–1232, 2001.

[13] Ian Goodfellow, Yoshua Bengio, and Aaron Courville. *Deep Learning*. MIT Press, 2016. http://www.deeplearningbook.org.

[14] Angelo Pasquale, Victor Champaney, Youngtae Kim, Nicolas Hascoët, Amine Ammar, and Francisco Chinesta. A parametric metamodel of the vehicle frontal structure accounting for material properties and strain-rate effect: application to full frontal rigid barrier crash test. *Heliyon*, 8(12), 2022.

[15] Victor Champaney, Angelo Pasquale, Amine Ammar, and Francisco Chinesta. Parametric curves metamodelling based on data clustering, data alignment, pod-based modes extraction and pgd-based nonlinear regressions. *Frontiers in Materials*, 9:904707, 06 2022.

[16] Peter Benner, Mario Ohlberger, Albert Cohen, and Karen Willcox. *Model Reduction and Approximation*. Society for Industrial and Applied Mathematics, Philadelphia, PA, 2017.

[17] Gianluigi Rozza, Martin Hess, Giovanni Stabile, Marco Tezzele, Francesco Ballarin, Carmen Gräßle, Michael Hinze, Stefan Volkwein, Francisco Chinesta, Pierre Ladeveze, Yvon Maday, Anthony Patera, Charbel Farhat, Sebastian Grimberg, Andrea Manzoni, Alfio Quarteroni, Andreas Buhr, Laura Iapichino, and J. Kutz. *Model Order Reduction: Volume 3: Applications*. De Gruyter, 2020.

[18] Gianluigi Rozza, Martin Hess, Giovanni Stabile, Marco Tezzele, Francesco Ballarin, Carmen Gräßle, Michael Hinze, Stefan Volkwein, Francisco Chinesta, Pierre Ladeveze, Yvon Maday, Anthony Patera, Charbel Farhat, Sebastian Grimberg, Andrea Manzoni, Alfio Quarteroni, Andreas Buhr, Laura Iapichino, and J. Kutz. *Volume 2 Snapshot-Based Methods and Algorithms*. De Gruyter, 12 2020.

[19] Rubén Ibáñez Pinillo, Emmanuelle Abisset-Chavanne, Amine Ammar, David González, Elías Cueto, Antonio Huerta, Jean Duval, and Francisco Chinesta. A multidimensional data-driven sparse identification technique: The sparse proper generalized decomposition. *Complexity*, 2018:1–11, 11 2018.

[20] Abel Sancarlos, Victor Champaney, Elias Cueto, and Francisco Chinesta. Regularized regressions for parametric models based on separated representations. *Advanced Modeling and Simulation in Engineering Sciences*, 10, 03 2023.

[21] Victor Champaney, Francisco Chinesta, and Elias Cueto. Engineering empowered by physics-based and data-driven hybrid models: A methodological overview. *International Journal of Material Forming*, 15, 05 2022.

[22] Angelo Pasquale, Victor Champaney, Youngtae Kim, Nicolas Hascoët, Amine Ammar, and Francisco Chinesta. A parametric metamodel of the vehicle frontal structure accounting for material properties and strain-rate effect: application to full frontal rigid barrier crash test. *Heliyon*, 8:e12397, 12 2022.

[23] Alexander Schmid, Angelo Pasquale, Christian Ellersdorfer, Victor Champaney, Marco Raffler, Simon Guévelou, Stephan Kizio, Mustapha Ziane, Florian Feist, and Francisco Chinesta. Pgd based meta modelling of a lithium-ion battery for real time prediction. *Frontiers in Materials (Computational Materials Science)*, 10, 08 2023.

[24] Alexander Schmid, Angelo Pasquale, Christian Ellersdorfer, Marco Raffler, Victor Champaney, Mustapha Ziane, Francisco Chinesta, and Florian Feist. Mechanical characterization of li-ion cells and the calibration of numerical models using proper generalized decomposition. *Proceedings of the ASME 2023 International Mechanical Engineering Congress and Exposition IMECE2023*, 11 2023.

[25] Sebastian Rodriguez, Eric Monteiro, Nazih Mechbal, Marc Rébillat, and Francisco Chinesta. Hybrid twin of rtm process at the scarce data limit. *International Journal of Material Forming*, 16, 06 2023.

[26] ISO. 14688-1: 2002: Geotechnical investigation and testing – Identification and classification of soil – Part 1: Identification and description. *British Standards Institution*, 2002.

[27] BSI. BS 1377-2: 1990: Methods of test for soils for civil engineering purposes – Part 2: Classification tests, 1990.

[28] Arthur Casagrande. Classification and identification of soils. *Transactions of the American Society of Civil Engineers*, 113(1):901–930, 1948.

[29] Arthur Van Lerberghe, Kin Shing Oswald Li, Andrew D. Barr, and Sam D. Clarke. An open-source algorithm for correcting stress wave dispersion in split-hopkinson pressure bar experiments - submitted for publication in Experimental Mechanics, currently under review. 2024.

[30] Andrew Tyas and Dan J Pope. Full correction of first-mode pochammer–chree dispersion effects in experimental pressure bar signals. *Measurement science and technology*, 16(3):642, 2005.

A.7 Split-Hopkinson pressure bar testing of water, with partial lateral confinement

Li, K. S. O., Van Lerberghe, A., Barr, A. D., Dennis, A. A.,& Clarke, S. D. (2024). Split-Hopkinson pressure bar testing of water with partial lateral confinement.

A paper on the application of the partial lateral confinement apparatus to conduct SHPB testing on water, submitted for publication to the journal of Experimental Mechanics. The journal paper is included in its entirety below as reference.

Split-Hopkinson pressure bar testing of water with partial lateral confinement

Kin Shing Oswald Li[1*], Arthur Van Lerberghe[1], Andrew D. Barr[1], Adam A. Dennis[1], Sam D. Clarke[1]

[1*]Department of Civil & Structural Engineering, University of Sheffield, Mappin Street, Sheffield, S1 3JD, , UK.

*Corresponding author(s). E-mail(s): ksoli1@sheffield.ac.uk;
Contributing authors: avanlerberghe1@sheffield.ac.uk; a.barr@sheffield.ac.uk; a.a.dennis@sheffield.ac.uk; sam.clarke@sheffield.ac.uk;

Abstract

Background: For the first time, the high-strain-rate behaviour of water is investigated experimentally and validated to LS-DYNA numerical simulations, using Smooth Particle Hydrodynamics (SPH).
Objective: This paper presents the application of a modified split-Hopkinson pressure bar (SHPB) fitted with a partial lateral confinement apparatus on a water specimen.
Method: The lateral confinement is provided by a water reservoir surrounding the specimen. A pressure transducer is installed in the reservoir wall to measure lateral stresses, and a dispersion correction algorithm, `SHPB_Processing.py`, is utilised to obtain accurate measurements of axial and radial stresses and strains.
Results: Experimental results underscore the capability of the modified apparatus to assess triaxial behaviour of water under high-strain rates. Comparisons with numerical modelling reveal that cohesion between water particles is non-existent, highlighting an intrinsic limitation in numerical modelling.
Conclusion: These results highlight the capability to perform characterisation of fluids under high-strain rates. While limitations in numerical modelling still exist, numerical modelling and experimental testing using the modified apparatus can be applied to characterise fluid behaviour in the future.

Keywords: High-strain-rate testing, split-Hopkinson pressure bar, partial lateral confinement, LS-DYNA, SPH, water

1 Introduction

The split Hopkinson pressure bar (SHPB) is a common tool used for characterising the behaviour of materials under high strain-rate conditions, ranging from 102 $s^{-}1$ to 104 $s^{-}1$. Soils testing employing the SHPB are commonly performed by confining a soil specimen in a rigid tube or ring, limiting lateral displacement. These uniaxial strain experiments are effective for characterising soil compaction response at different strain rates [1–3], as well as comparing soils with different moisture contents [3, 4], initial densities [5, 6] and particle size distributions [7], but have never been used to characterise the behaviour of liquids.

Several authors have developed methods that allow lateral confinement to alter throughout a SHPB test to generate a triaxial stress state. Pierce and Charlie [8] used a steel tube lined

with a membrane to investigate the wave speed of partially saturated sands, at varying confining stresses of 0 kPa and 310 kPa. While the steel tube prevented lateral strains from developing, water pressure applied between the tube and membrane provided additional confining stress, which was also transmitted along the pressure bars via a piston assembly on the transmitter bar. Bailly et al [9] employed brass confining rings to imitate approximately elastic (near perfectly plastic) behaviour at high strain rates. The material specimen would initially be laterally confined within the rings and deform in uniaxial strain until the radial stress reached the yield point in the ring, at which point the specimen would begin to laterally deform at a quasi-constant confining stress.

Other authors have modified the traditional triaxial cell (CTC) for high-strain-rate testing. Christensen et al [10] used a large pressure vessel to conduct triaxial tests on sandstone to confining stresses of 207 MPa. The specimen and pressure bars were enclosed in the pressure vessel, which had a hole at one end to facilitate loading of the incident bar, which was secured with a collar. Frew et al [11] improved the triaxial SHPB further by incorporating pressure vessels around both the specimen and transmitter bar ends, allowing hydrostatic loading to be followed by a high strain rate deviatoric phase. This modified apparatus was utilised by Martin et al [12] to test the shear response of sand at confining stresses between 25 MPa and 150 MPa, as well as strain rates of 500 s-1 and 1000 s-1.

Barr et al [13] pioneered a modified SHPB experiment setup involving a partial lateral confinement reservoir that allows a confining stress to build passively during high-strain-rate axial loading. This method combines aspects of unconfined SHPB experiments (usually with a thin membrane) and fully confined SHPB experiments (often with a steel ring) to provide a more comprehensive picture of soil behaviour during high-strain-rate events. This is especially pertinent to blast and impact events, as research into the strain rate dependent behaviour of soils exhibited during high-strain-rates prompts its application in buried explosive scenarios.

The current work seeks to utilise the SHPB set up pioneered by Barr et al [13] to investigate high-strain-rate effects of liquids, specifically water. This paper will investigate the high-strain-rate effects of water through the employment of the modified SHPB with partial lateral confinement.

2 Experimental setup

The modified SHPB is made up of a standard pressure bar arrangement which consists of a striker, an incident and a transmitter bar, 25 mm in diameter, with a 350 mm, 2500 mm and 1500 mm length, respectively, as shown in Figure 1. In addition, as illustrated in Figure 2, a 600 mm long steel water reservoir is set on linear bearings and centred around the specimen. When the pressure bars are in place, the annular gap present throughout the length of the reservoir is filled with water at atmospheric pressure, as depicted in Figure 2. The sample tested is water, therefore the entire reservoir is filled with water, and the radial stress response, σ_r, is measured by a pressure transducer mounted on the reservoir's wall. The axial stress response, σ_a, is measured with Kyowa KSP-2-120-E4 semiconductor strain gauges on the pressure bars, set up in pairs for the Wheatstone bridge arrangement.

The reservoir length was designed so that the time required for a stress wave initiated at the specimen surface to travel to and from the reservoir's end exceeds the loading duration in the specimen, guaranteeing that inward-travelling waves from the boundary do not interfere with

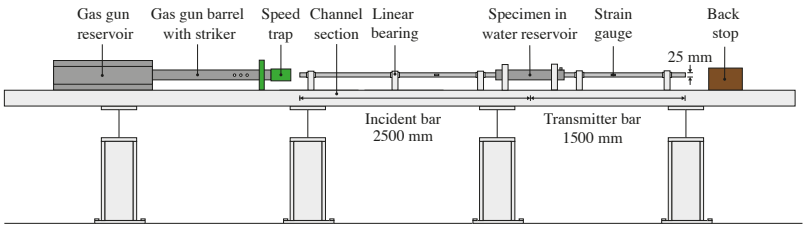

Fig. 1: Schematic of the partially confined SHPB apparatus: Bar and reservoir configuration.

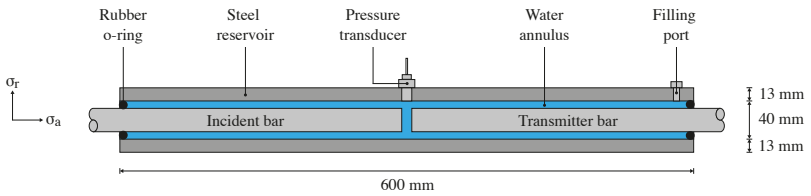

Fig. 2: Schematic of the partially confined SHPB apparatus: water reservoir section with axial/radial axis convention.

pressure measurements [13]. This simplifies the seal between the reservoir and the pressure bars, which are only needed to keep the water at atmospheric pressure.

3 Sample methodology

The application of this testing method was carried out on water to illustrate the capacity of the partially-confined SHPB and to validate that the chosen design results in reliable fluid pressure measurements. The water density tested was 1.0 Mg m^{-3}. Preparation of the sample was as follows:

1. Supports were installed on the channel around the incident and transmitter bars of the SHPB setup, prior to installing the steel reservoir providing lateral confinement for the sample.
2. The incident bar was placed into position, approximately 5 mm from the transmitter bar, this was measured as the change in length between the end of the transmitter bar and the final support. It was checked again before all supports were bolted down, and the test launched.
3. The water reservoir is translated into the centre of the setup, and the pressure port is aligned with the centre of the specimen.
4. The incident bar's linear bearing, closest to the steel reservoir, is re-adjusted to its initial test position and bolted back down.
5. O-rings were inserted on either side of the water reservoir to seal its ends.
6. The reservoir was filled with water using a filling port and sealed by fitting the pressure transducer and filling port bolt. The transducer used in the experiment was a Kulite HKM-375-2500, calibrated by the manufacturer to perform linearly to a pressure of 25 MPa.
7. Measurement of the length between the two Hopkinson pressure bars was done one last time between the end of the transmitter bar and the final support (Figure 3).

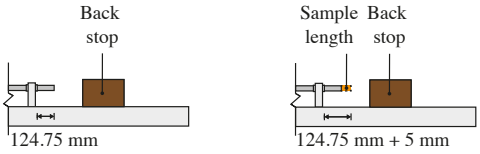

Fig. 3: Schematic of sample measurements process before and after installation inside reservoir.

The method was carried out in the same manner as a standard SHPB experiment. Loading was done by striking the incident bar with a stainless-steel striker bar fired from a gas gun, at varying velocities. Tests were conducted at 16 m/s and 20 m/s, where speeds were recorded using a speed trap placed at the exit of the gas gun barrel.

Signals from the pressure bar strain gauges and pressure transducer were recorded using a TiePie Handyscope four-channel digital oscilloscope using 14-bit A-D resolution and a sample frequency of 1 MHz, with a record length of 131.072 kSa.

From these tests, conducted at two different speeds, a broad range of strain rate was captured, as shown in Figure 4, where the strain rate increases to 2095 $s^{-}1$ and 4844 $s^{-}1$, over approximately 150 μs. Under these high-strain-rate conditions, both the axial and radial stresses of the specimen were measured.

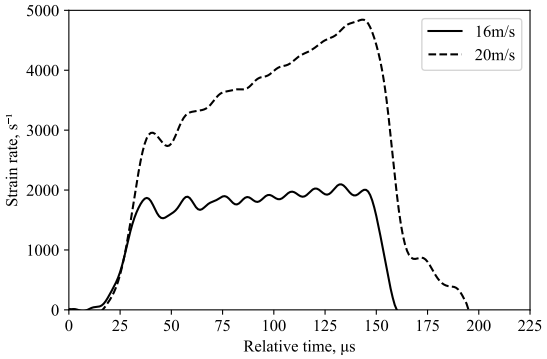

Fig. 4: Variation of strain rate during partially-confined SHPB experiments on water.

4 Signal processing

When processing signals from SHPB experiments, it is frequently believed that longitudinal stress waves in the pressure bars travel one-dimensionally at a common velocity c_0, and hence measurements recorded at strain gauges are frequently simply translated to the end of the bar using a suitable time delay [14]. In actuality, stress waves travel at a certain phase velocity, c_p, which is a function of frequency, bar diameter, one-dimensional wave speed and Poisson's ratio [15], as illustrated in Figure 5 [3].

As the frequency of a wave grows, the phase velocity drops, resulting in signal dispersion as it propagates down the bar. The dispersion of the stress pulse is accompanied by a frequency-dependent variation in stress and strain across the bar cross-section, so a signal recorded on the surface of the bar at some distance from the specimen will not accurately reflect the stresses the specimen was subjected to, and therefore cannot be used to accurately determine specimen response.

The pressure bar signals were processed using an open-source Python algorithm, `SHPB_Processing.py`, with specific functionalities for partial lateral confinement testing using SHPB setups [16]. It uses an implementation of Tyas and Pope's dispersion-correction approach via a subroutine titled `dispersion.py`, to verify that the inferred measures of axial stress and strain appropriately depict the specimen behaviour [17]. In this script the method utilised is as follows:

1. Fast Fourier transform (FFT) is used to transfer the time-domain strain signal to the frequency domain.
2. To account for the dispersion over the distance between the strain gauge and the bar end, the phase angle of each frequency component is corrected using the relationship illustrated in Figure 5.
3. The amplitude of each frequency component is corrected using the factors M1 and M2, which account for the fluctuation of strain and Young's modulus over the bar cross section, respectively. These are derived from Davies' analysis of the radial effects in a cylindrical pressure bar [18].
4. Using the inverse FFT, the signal is then converted back into the time domain.

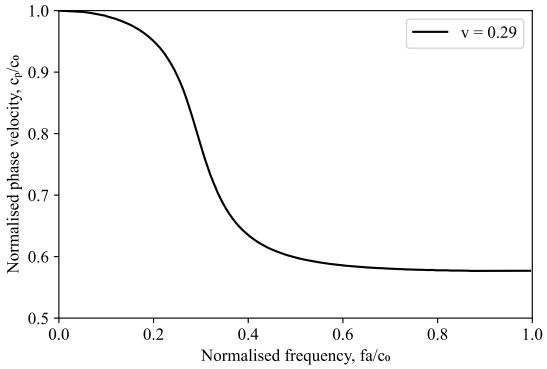

Fig. 5: Phase velocity frequency relationship for the first mode of propagation of a longitudinal wave [3].

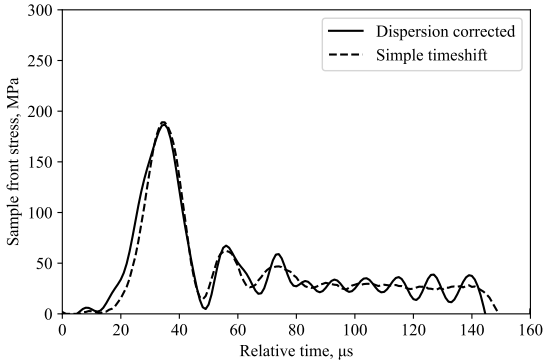

Fig. 6: Partially confined SHPB test on water: front stress computed using dispersion correction and simple timeshifting.

The dispersion adjustment is especially crucial in determining the stress transmitted into the specimen from the incident bar since it is determined from the sum of the incident and reflected waves, both of which contain considerable high-frequency components.

The incident and reflected stress waves measured at the incident bar strain gauge are assumed to maintain their shape as they are translated along the time axis using simple timeshifting whereas in the corrected method the dispersion associated with 1000 mm travel in the bar is added to the incident wave and removed from the reflected wave.

Figure 6 shows how the dispersion-corrected approach minimises the amplitude of the stress wave and eliminates an initial fluctuation in stress, which would have led to incorrect inferences about the specimen's behaviour. In this case, dispersion effects are minimal.

5 Numerical modelling

5.1 Model setup

The numerical modelisation of the arrangement in Figure 7 was carried out using the explicit finite element code in LS-DYNA [19], in order to compare numerical and experimental results. A more detailed representation of the water sample and confinement reservoir are shown in Figure 8. The model was created in 3D, where the striker bar (yellow in Figure 7), incident bar (blue in Figure 7) transmitter bar (green in Figure 7) and steel reservoir (grey in Figure 7) were modelled as Lagrangian solid mesh. SPH node modelisation was used to model the water sample (red in Figure 8) [20–23].

For simplicity, the steel reservoir is modelled as a rigid steel boundary material, assuming that the fluid pressures generated will not be large enough to cause significant radial strains in the reservoir. The rubber rings were replaced with a boundary constraint to prevent the water from exiting the reservoir from the ends.

Automatic nodes-to-surface contact were selected for contact representation between the water sample made with SPH nodes and the lagrangian members of the incident and transmitter bars. Automatic nodes-to-surface contact was also utilised between the water sample and the steel reservoir. Manual surface-to-surface contact adjustments were made between lagrangian members in the model, such as between the striker and incident bars, and between the incident and transmitter bars.

5.2 Model material cards

The three steel pressure (striker, incident and transmitter) bars were modelled as linear elastic materials (`*MAT_ELASTIC`) with a density, Young's modulus and Poisson's ratio of $\rho = 7850$ kg m^{-3}, $E = 168$ GPa, $\nu = 0.29$ respectively based on existing known properties of steel.

For all analyses, to match the experimental tests conducted, the striker bar was given an initial impact velocity of 16 m/s or 20 m/s similar to match the speeds tested experimentally. The steel reservoir was modelled as rigid (`*MAT_RIGID`), with a density, Young's modulus and Poisson's ratio of $\rho = 7850$ kg m^{-3}, $E = 168$ GPa, $\nu = 0.29$ respectively. The SPH water sample that encompassed the water annulus and the gap between the pressure bars was modelled using the linear polynomial equation of state (EOS):

$$P = C_0 + C_1\mu + C_2\mu^2 + C_3\mu^3 + (C_4 + C_5\mu + C_6\mu^2)E \quad (1)$$

where C_0, C_1, C_2, C_3, C_4, C_5 and C_6 are constants, $\mu = \rho/\rho_0$ - 1, ρ and ρ_0 are the current and initial densities of the fluid, and E is the specific internal energy of the fluid. Table 1, displays the properties used to implement the null material card (`*MAT_NULL`), which only requires density, and equation of state parameters utilised in this work for water. To pressurise the water to atmospheric conditions (101 kPa atmospheric pressure), the initial internal energy of the water, E_0, was set as 205.36 kPa.

Fig. 7: LS-DYNA SHPB partial lateral confinement model set up.

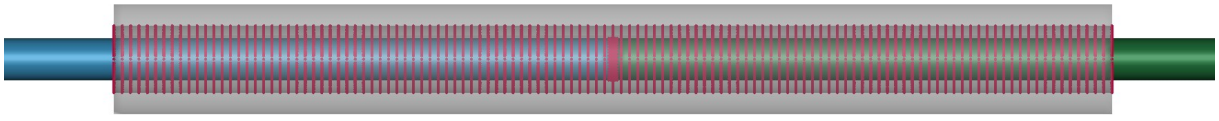

Fig. 8: LS-DYNA cross section zoom-in on the sample inside the partial lateral confinement SHPB set up.

Table 1: Material model and equation of state (EOS) parameters for water (SI units) [20].

MAT_NULL							
1000							
EOS_LINEAR_POLYNOMIAL							
C_0	C_1	C_2	C_3	C_4	C_5	C_6	E_9
0.0	2.190E9	9.224E9	8.767E9	0.4934	1.3937	0.0	205.36E3

6 Results

Figure 9 display the typical stress difference between axial and radial stress, illustrating the viability of the current configuration in assisting with the triaxial response of a liquid. The near zero stress difference indicates the translation of axial stress into radial stress when subject to loading, a property that aligns with the Poisson's ratio of water.

Figures 10 and 11 show that the experimental and numerical incident pulses have the same amplitude at the same gauge locations, but the reflected pulses are very different.

Tests were performed using the modified SHPB fitted with the partial lateral confinement reservoir on water, at 16 m/s and 20 m/s. Figures 12 and 13 show similarities in terms of response behaviour, with a logical increase in amplitude associated with its higher test speed.

Figures 12 and 13 depict the experimentally measured front, back and radial stresses. The radial stress directly adjacent to the water in between the pressure bars was calculated by taking into account the transit time of the radial stress wave through the water annulus (5.1 μs, assuming a wave speed in water of 1482 m/s). The recorded radial stress shows a radial stress wave with peaks that align relatively well with front and back stresses, indicating that the lateral response recorded with the pressure transducer is a direct result of the axial loading from the SHPB test.

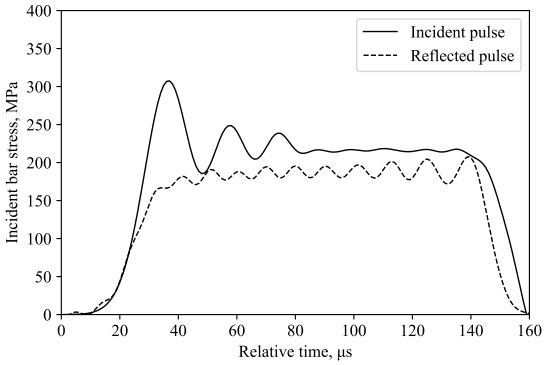

Fig. 10: Typical behaviour of a partially confined SHPB experimental test on water at 16 m/s: incident and reflected pulses from the incident bar.

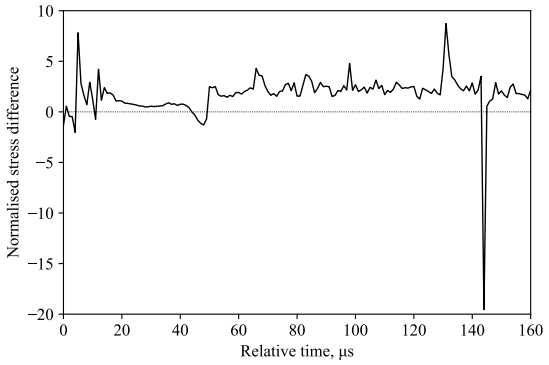

Fig. 9: Typical response of a partially confined SHPB test on water showing axial and radial stress difference normalised by their mean.

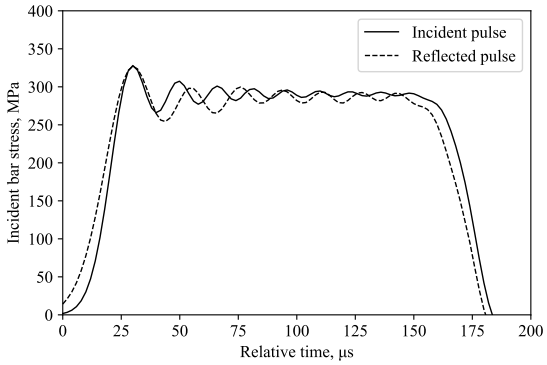

Fig. 11: Typical behaviour of a partially confined SHPB LS-DYNA model on water at 16 m/s: incident and reflected pulses from the incident bar.

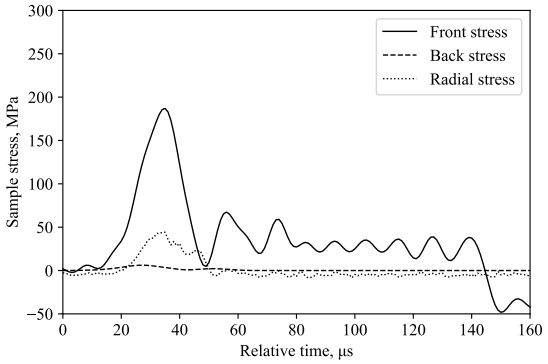

Fig. 12: Partially confined SHPB test on water at 16 m/s: front, back and radial stresses.

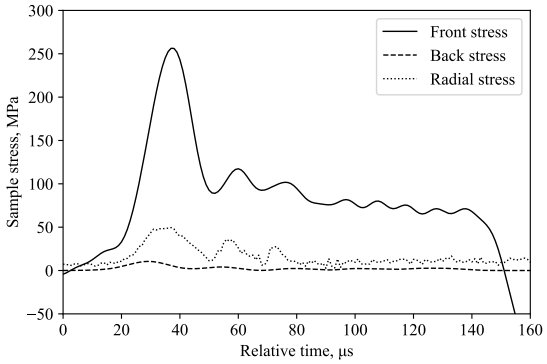

Fig. 13: Partially confined SHPB test on water at 20 m/s: front, back and radial stresses.

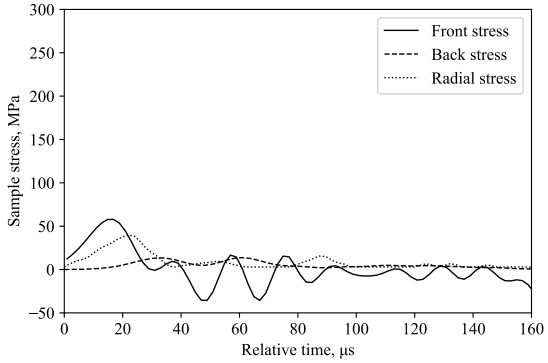

Fig. 14: Partially confined SHPB LS-DYNA model on water at 16 m/s: front, back and radial stresses.

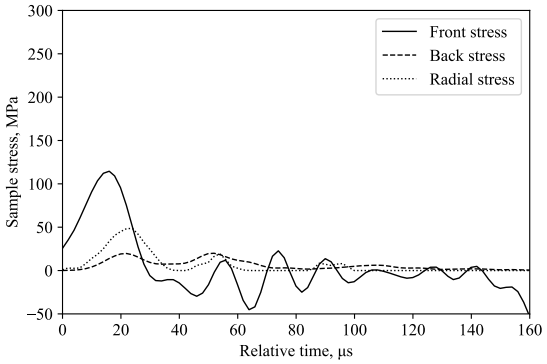

Fig. 15: Partially confined SHPB LS-DYNA model on water at 20 m/s: front, back and radial stresses.

Looking at the Poisson's ratio, experimentally at 16 m/s, the maximum front, back and radial stress recorded are 180, 5 and 46 MPa, respectively, resulting in a Poisson's ratio of 0.5 (Figure 12), when the axial stress ($[180 + 5]/2 = 92.5$ MPa) is divided by the radial stress (46 MPa). Since the theoretical Poisson's ratio for water is 0.5, this indicates that the axial and radial stress data obtained by employing this modified SHPB setup exhibit a degree of accuracy reflected in theory.

At higher striker speeds, the incident bar's inertia and the partial lateral confinement steel reservoir will have an impact on the front, back and radial stresses, as seen in Figure 13. This will have an effect on the Poisson's ratio of the water specimen, progressively lowering its value.

The back stress values differ by 60-80 %, radial stress values differ by 11-13 %, and the front stress values differ by 76-105 %, when comparing numerical and experimental stresses at 16 m/s and 20 m/s (Figures 12, 13, 14 & 15).

7 Discussion

The capabilities of the modified SHPB with the implementation of the lateral confinement apparatus allow for high-strain-rate testing on water to explore its axial and lateral responses. The results collected from the experimental tests and numerical model in LS-DYNA, revealed a significant difference in front stress, leading to a considerable lower axial stress. This is due to the numerical model's lack of cohesion between SPH particles when modelling a fluid like water, as evidenced by the two key arguments below:

1. The water sample in the modified SHPB with the lateral confinement apparatus, was modelled in LS-DYNA using SPH. This was done in the same manner as other research projects which have modelled water, for blast and high impact tests [21]. They used *MAT_NULL and the EOS linear polynomial, as shown in Table 1. However, *MAT_NULL only uses the initial density of the fluid. It does not include any cohesion parameters, which is a fundamental property of fluids. Water itself is a highly cohesive material. Consequently, omitting this will have a considerable impact on the numerical results.
2. When comparing modelling and experimental test results, the radial stress is within 10-13 % of the experimental values obtained, however, the back and front stresses are more than 60-80 % and 75-105 % away, respectively, from what it should be, experimentally. The radial stress is measured with a pressure transducer, while the front and back stresses are measured at the strain gauge location on the incident and transmitter bars in the model. Hence, the value obtained at these points is from the stress wave as it propagates through the SPH water particles, and hits the transmitter bar interface and pressure transducer. The significant difference in front and back stresses is due to the instant extrusion of the water sample upon contact from the incident pulse.

There is no cohesion between the SPH particles. The particles are instantaneously displaced in both horizontal and vertical directions, due to the impact of the stress wave considerably changing the size and shape of the specimen. There is no medium for the wave to propagate through. As a result, the water sample is unable to compact sufficiently to let the stress wave propagate through before extruding from in-between the Hopkinson pressure bars.

When comparing experimental and model outputs, it is evident the model is under predicting the stress results. This indicates that adding cohesion properties to this model would intuitively improve the specimen's ability to withstand the stress wave passing through it.

Material cards that consider cohesion in LS-DYNA include *MAT_PSEUDO_TENSOR, *MAT_CONCRETE_DAMAGE, *MAT_FHWA_SOIL, *MAT_MOHR_COULOMB, *MAT_DRUCKER_PRAGER and *MAT_JOINTED_ROCK. However, the material cards *MAT_PSEUDO_TENSOR, *MAT_CONCRETE_DAMAGE, *MAT_FHWA_SOIL and *MAT_JOINTED_ROCK can not be used since they are made for steel, concrete, rock and soils, with some requiring an EOS and other parameters which can not be obtained for water. The material cards *MAT_MOHR_COULOMB and *MAT_DRUCKER_PRAGER had obtainable parameters, but showed the same behaviour as *MAT_NULL.

SPH parameters were explored in LS-DYNA, and it was discovered that there was no option to change the cohesion parameter for fluid modelling. Viscosity was evaluated in the numerical model and showed no effect on improving SPH particle cohesiveness, as it simply slowed their lateral and transverse movements.

The ability to evaluate the high-strain-rate behaviour of liquids and record both their lateral and axial stress responses fills a gap in present research that previously restricted SHPB testing to fluid materials.

Also, since high-strain testing on water can be directly used to compare the effect of saturation and actual water, the influence of water content on other materials such as soils can be better understood. The specific effect of soil parameters such as particle size or density can be examined more thoroughly by comparing high-strain and quasi-static triaxial tests on fully saturated soils.

8 Conclusion

An innovative testing methodology for partially-confined SHPB experiments has been used to test water at high-strain-rates, where the specimen is contained in a long sleeve reservoir. A pressure transducer in the wall of the reservoir is used to measure the radial stress of the specimen.

Experimental results showed a clear correlation between the increase of the strain rate and the amplitude of the radial and axial stresses. To compare with the experimental data collected from the tests, LS-DYNA numerical modelling of tests with and SPH water sample was undertaken. Although radial and back stresses were measured and represented in the numerical model with reasonable accuracy, substantial modelling constraints were discovered when looking at the front stress obtained from the model. This was due

to a failure to account for the cohesion qualities of the SPH particles in the numerical model, which fluids naturally have.

The material card `*MAT_NULL`, which is commonly used to depict water in LS-DYNA, only requires its initial density; however, this material card does not account for the highly cohesive properties of water particles, an intrinsic property of fluids.

As a result, improvements to the existing model are required, such as creating a new material card in LS-DYNA that incorporates cohesion as a parameter for fluids and upgrading the modelling representation of SPH to account for cohesion between particles.

Experimentally, in addition to its capabilities for testing soils, this apparatus can be used to accurately characterise liquid materials at high strain-rates, which was previously impossible.

Future test series using this new apparatus will aim to define strain rate dependency as well as further investigate the influence of radial inertia observed in current tests. Furthermore, the results of high strain-rate water characterisation can be utilised to characterise very fine, undrained, fully saturated soils under high strain rate conditions.

Acknowledgements. This research was funded by the Engineering and Physical Sciences Research Council (EPSRC), and the Defence Science and Technology Laboratory (Dstl).

Declarations

Conflict of interest. The authors declare that they have no conflict of interest.

References

[1] Bragov, A.M., Lomunov, A.K., Sergeichev, I.V., Tsembelis, K., Proud, W.G.: Determination of physicomechanical properties of soft soils from medium to high strain rates. International Journal of Impact Engineering **35**(9), 967–976 (2008) https://doi.org/10.1016/j.ijimpeng.2007.07.004

[2] Song, B., Chen, W., Luk, V.: Impact compressive response of dry sand. Mechanics of Materials **41**(6), 777–785 (2009) https://doi.org/10.1016/j.mechmat.2009.01.003

[3] Barr, A.D., Clarke, S.D., Petkovski, M., Tyas, A., Rigby, S.E., Warren, J., Kerr, S.: Effects of strain rate and moisture content on the behaviour of sand under one-dimensional compression. Experimental Mechanics **56**(9), 1625–1639 (2016) https://doi.org/10.1007/s11340-016-0200-z

[4] Martin, B.E., Chen, W., Song, B., Akers, S.A.: Moisture effects on the high strain-rate behavior of sand. Mechanics of Materials **41**(6), 786–798 (2009) https://doi.org/10.1016/j.mechmat.2009.01.014

[5] Lu, H., Luo, H., Komaduri, R.: Dynamic compressive response of sand under confinements. Society for Experimental Mechanics - SEM Annual Conference and Exposition on Experimental and Applied Mechanics 2009 **2**(January), 1046–1052 (2009)

[6] Luo, H., Lu, H., Cooper, W.L., Komanduri, R.: Effect of Mass Density on the Compressive Behavior of Dry Sand Under Confinement at High Strain Rates. Experimental Mechanics **51**(9), 1499–1510 (2011) https://doi.org/10.1007/s11340-011-9475-2

[7] Huang, J., Xu, S., Hu, S.: Effects of grain size and gradation on the dynamic responses of quartz sands. International Journal of Impact Engineering **59**, 1–10 (2013) https://doi.org/10.1016/j.ijimpeng.2013.03.007

[8] Pierce, S.J., Charlie, W.A.: High-intensity Compressive Stress Wave Propagation Through Unsaturated Sands. PhD thesis, Colorado State University (1990)

[9] Bailly, P., Delvare, F., Vial, J., Hanus, J.L., Biessy, M., Picart, D.: Dynamic behavior of an aggregate material at simultaneous high pressure and strain rate: SHPB triaxial tests. International Journal of Impact Engineering **38**(2-3), 73–84 (2011) https://doi.org/10.1016/j.ijimpeng.2010.10.005

[10] Christensen, R.J., Swanson, S.R., Brown, W.S.: Split-hopkinson-bar tests on rock under confining pressure. Experimental Mechanics **12**(11), 508–513 (1972) https://doi.org/10.1007/BF02320747

[11] Frew, D.J., Akers, S.A., Chen, W., Green, M.L.: Development of a dynamic triaxial Kolsky bar. Measurement Science and Technology **21**(10) (2010) https://doi.org/10.1088/0957-0233/21/10/105704

[12] Martin, B.E., Kabir, M.E., Chen, W.: Undrained high-pressure and high strain-rate response of dry sand under triaxial loading. International Journal of Impact Engineering **54**, 51–63 (2013) https://doi.org/10.1016/j.ijimpeng.2012.10.008

[13] Barr, A.D., Clarke, S.D., Rigby, S.E., Tyas, A., Warren, J.A.: Design of a split Hopkinson pressure bar with partial lateral confinement. Measurement Science and Technology **27**(12) (2016) https://doi.org/10.1088/0957-0233/27/12/125903

[14] Gray, T.G.: Classic Split-Hopkinson Pressure Bar Testing. In: Mechanical Testing and Evaluation, pp. 462–476. ASM International, ??? (2000). https://doi.org/10.31399/asm.hb.v08.a0003296

[15] Bancroft, D.: The Velocity of Longitudinal Waves in Cylindrical Bars. Physical Review **59**(7), 588–593 (1941) https://doi.org/10.1103/PhysRev.59.588

[16] Van Lerberghe, A., Li, K., Barr, A., Clarke, S.: An open-source algorithm for correcting stress wave dispersion in split-Hopkinson pressure bar experiments. Submitted for publication in Experimental Mechanics (2024)

[17] Tyas, A., Pope, D.J.: Full correction of first-mode Pochammer-Chree dispersion effects in experimental pressure bar signals. Measurement Science and Technology **16**(3), 642–652 (2005) https://doi.org/10.1088/0957-0233/16/3/004

[18] Davies, R.M.: A critical study of the Hopkinson pressure bar. Philosophical Transactions of the Royal Society of London. Series A, Mathematical and Physical Sciences **240**(821), 375–457 (1948) https://doi.org/10.1098/rsta.1948.0001

[19] Livermore Software Technology Corporation: LS-DYNA Theory Manual, California, USA (2023)

[20] Shin, Y.S., Lee, M., Lam, K.Y., Yeo, K.S.: Modeling mitigation effects of watershield on shock waves. Shock and Vibration **5**(4), 225–234 (1998) https://doi.org/10.1155/1998/782032

[21] Varas, D., Artero-Guerrero, J.A., Pernas-Sánchez, J., López-Puente, J.: Numerical modelling of the fluid structure interaction using ALE and SPH: The Hydrodynamic Ram phenomenon. 11th European LS-Dyna Conference (2017)

[22] Jianming, W., Na, G., Wenjun, G.: Abrasive waterjet machining simulation by SPH method. International Journal of Advanced Manufacturing Technology **50**(1-4), 227–234 (2010) https://doi.org/10.1007/s00170-010-2521-x

[23] Anghileri, M., Castelletti, L.M.L., Tirelli, M.: Fluid-structure interaction of water filled tanks during the impact with the ground. International Journal of Impact Engineering **31**(3), 235–254 (2005) https://doi.org/10.1016/j.ijimpeng.2003.12.005

A.8 Impact of confinement on high-strain-rate behaviour of cohesive soils

Li, K. S. O., Van Lerberghe, A., Barr, A. D., & Clarke, S. D. (2024). Impact of confinement on high-strain-rate behaviour of cohesive soils.

A paper showcasing the capabilities of the partial lateral confined SHPB apparatus in assisting with the characterisation of cohesive soils and exploring the effects of confining pressure, submitted for publication to the journal of Experimental Mechanics. The journal paper is included in its entirety below as reference.

Impact of confinement on high-strain-rate behaviour of cohesive soils

Kin Shing Oswald Li[1*], Arthur Van Lerberghe[1], Andrew D. Barr[1], Sam D. Clarke[1]

[1*]Department of Civil & Structural Engineering, University of Sheffield, Mappin Street, Sheffield, S1 3JD,UK.

*Corresponding author(s). E-mail(s): ksoli1@sheffield.ac.uk;
Contributing authors: avanlerberghe1@sheffield.ac.uk; a.barr@sheffield.ac.uk; sam.clarke@sheffield.ac.uk;

Abstract

Background: Traditional free field unconfined and rigid confined split-Hopkinson pressure bar (SHPB) testing lay the groundwork for understanding high-strain-rate behaviour of cohesive soils, however the impact of confinement on triaxial response remains primarily uncharacterised.
Objective: This paper presents the application of a modified SHPB apparatus equipped with a partial lateral confinement (PLC) reservoir on cohesive soils, focusing on kaolin clay. It validates the method using LS-DYNA modelling to explore the effects of confinement and lateral stress development during the deviatoric phase by comparing with results under different confinement mechanisms.
Method: The kaolin clay sample is encased within a latex membrane and tested using the PLC apparatus where radial stresses are measured using a pressure transducer. LS-DYNA numerical simulations are used to validate experimental findings, particularly for cohesive soils exhibiting fluid-like behaviour and extreme deformation under high-strain-rates.
Results: Experimental results highlight the PLC apparatus' capability to characterise triaxial behaviour of kaolin clay under high-strain-rates. While limitations exist with modelling cohesive soils, numerical simulations were crucial in understanding the mechanisms that occur as a product of increasing confining pressure. Comparison with unconfined and confined SHPB results underscore the effects of confinement and its ability to encourage the build-up and redirection of internal lateral stresses.
Conclusions: The experimental and numerical results underline the significance of confinement in influencing cohesive soil behaviour, highlighting the capabilities of the PLC apparatus for characterisation of triaxial behaviour when subject to high-strain-rates.

Keywords: high-strain-rate testing, split-Hopkinson pressure bar, partial lateral confinement, cohesive soils, kaolin clay, LS-DYNA, smoothed particle hydrodynamics, confinement effects,

1 Introduction

A key property of cohesive soils is its innate ability to retain larger amounts of water compared to other common geomaterials used in fortification engineering. When subject to extremely high and immediate loading such as that from blast or fragmentation, the material may respond differently due to the lateral inertia applying a confining pressure. Hence, it is important to identify the effect of confinement on the ability of cohesive soils to withstand extreme pressures.

Free field unconfined and rigidly confined split-Hopkinson pressure bar (SHPB) experiments are a common method of characterising the high-strain-rate behaviour of soils within a range from 10^2 s^{-1} to 10^4 s^{-1} [1–5].

While the presence of a rigid confining ring has been shown to have an effect on the resultant stress transmitted through a kaolin clay specimen [6], it is necessary to investigate whether this effect is consistent when lateral strains are permitted. It becomes critical for triaxial behaviour under high-strain-rates to be evaluated when confining pressure is not limited by confinement. Unconfined SHPB tests allow for free field high-strain-rate tests to be conducted, but does not enable for radial stresses to be precisely examined. Hence, a method which permits the development of lateral strain but also enables the measurement of generated radial stresses would provide crucial insight into cohesive soil behaviour.

In contrast to experiments where the hydrostatic pressure is applied before the axial loading [7], this employment of a partial lateral confined (PLC) SHPB apparatus allows the confining pressure on the specimen to develop during the deviatoric phase. As the sample is loaded axially, the inertia of the water annulus resists radial deformation that occurs in response to the behaviour of the sample. The aims for PLC experimental testing on kaolin clay are to:

- Demonstrate the capability of the modified SHPB apparatus for high-strain-rate testing on cohesive soils.
- Assess the effects of confinement by comparing material behaviour from PLC, unconfined, and confined conditions.

Several authors have devised methods to introduce lateral confinement during SHPB tests, aiming to achieve a triaxial stress state. Pierce et al. [8] utilized a steel tube lined with a membrane to investigate wave speed in partially saturated sands under varying confining stresses. Bailly et al. [9] employed brass confining rings to simulate elastic behaviour at high strain rates. Gong et al. [10] utilized a modified SHPB setup to study compressive strength relationships in sandstone. Additionally, adaptations of the conventional triaxial cell (CTC) were made by Christensen et al. [11] and Frew et al. [12] to investigate sandstone and sand responses under high-strain-rates. This paper employs the modified SHPB with PLC, as pioneered by Barr et al. [13], to comprehensively understand soil behaviour during high-strain events.

Unconfined and confined SHPB tests have been fundamental in the understanding of high-strain-rate behaviour of kaolin clay. A key discovery was the identification of distinct phase behaviours corresponding to specific moisture content thresholds. Notably, the high-strain-rate behaviour of cohesive soils are influenced by internal moisture, leading to a tendency for stress to propagate laterally rather than axially through the sample when subject to high-strain-rate loading [6]. While radial stresses under rigid confinement has been investigated, the PLC SHPB apparatus allows radial stresses to be measured when lateral deformation of the sample is permitted. This novel avenue bridges the gap between conventional free field unconfined SHPB testing for solid materials, and rigid confined SHPB testing typically used in soil testing. Ultimately uncovering the effects of confinement on material behaviour under high-strain-rate conditions.

Experimental testing with the PLC apparatus was focus on various saturation levels and striker speeds. Although radial deformation was allowed to develop under this modified setup, the radial inertia caused by the development of hydrostatic pressure means the lateral confining pressure wass still greater than in free field unconfined tests, hence a difference in strain rate is expected.

Replicating full-scale physical testing of blast or ballistic conditions is time-consuming and costly. Therefore, the development of comprehensive numerical models to simulate experimental testing serves as invaluable tools for characterizing material behaviour. Numerical modelling has been completed to develop models for unconfined and confined SHPB test conditions with reasonable accuracy using LS-DYNA. Although various geometrical techniques were considered [14], the fluid-like nature of cohesive soils makes SPH node modelling ideal [15]. However, intrinsic numerical limitations associated with depicting cohesion properties still prevents the model from fully characterizing physical behaviour. Hence, the `MAT_MOHR_COULOMB` material model has been chosen to represent the sample material due to its lack

of requirement for an Equation of State (EOS) and its ability to represent known parameters [6].

2 Material characterisation

The cohesive geomaterial selected for stuy in the paper is kaolin clay, defined using EN ISO 14688-1:2002 soil descriptions as 'White fine kaolin clay.' The focus of this work was to investigating the sensitivity of strain rate effects to changes in soil properties of kaolin clay [6]. A summary of the characterisation tests conducted and soil properties of kaolin clay are shown in Table 1.

Table 1: Summary of material characterisation tests and findings for kaolin clay.

Properties	*Findings*	*Tests*
Primary mineral	Kaolinite	XRD diffraction
D_{50}	0.748 μm	Data sheet
Particle density	2.65 Mgm^{-3}	Pycnometer test
Particle sphericity	Low-Medium	SEM
Angularity	SR-SA	SEM
Surface texture	Smooth	SEM
Liquid limit	39.51%	Fall cone test
Plastic limit	25%	Fall cone test
Plastic index	14.89%	Fall cone test

The scanning electron microscope (SEM) was used to determine the particle shape based on soil descriptions from EN ISO 1468801:2002. Kaolin clay was coated with gold and placed into the SEM for imaging, as shown in Figure 1.

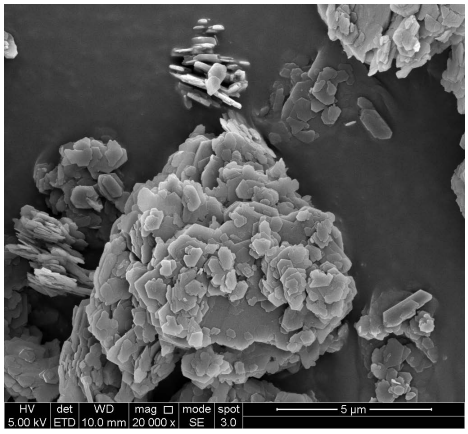

Fig. 1: Electron microscope images of kaolin clay under magnification of 20000x

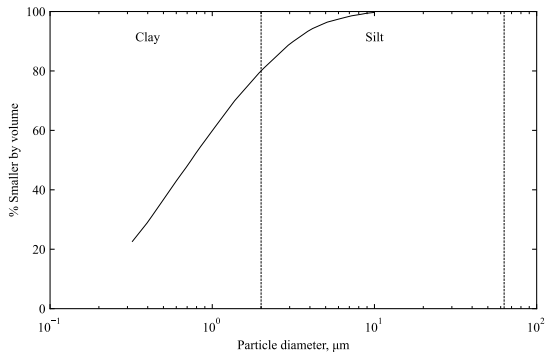

Fig. 2: Cumulative particle size distribution histogram of kaolin clay.

The particle size distribution (PSD) of the kaolin clay was obtained from the data sheet provided by the supplier (Imerys Performance Minerals). The data sheet for the kaolin clay supplied specified that the particle size of up to 83% of the material was less than $2\mu m$ (particle size range for clay). The cumulative particle size distribution graph for the selected soil is shown in Figure 2.

3 Specimen preparation

Kaolin clay specimens were prepared using powdered speciwhite kaolin clay, which were sieved and mixed with water then consolidated to 600kPa to create a solid homogenous kaolin clay sample using a Rowe cell.

To investigate the effects of moisture content and by extension saturation ratio, an air drying procedure was undergone in order to obtain moisture contents at the levels: 0%, 20%, and 45%, providing a range of saturation levels from dried, partially saturated, and fully saturated specimens that can be compared with unconfined and confined tests. Kaolin clay samples at varying moisture contents were prepared with the intent for use in all SHPB testing using the following procedure:

1. Saturated samples are cut with a stainless-steel, cylindrical cutting tool to diameters of 25 mm and nominal lengths of 5 mm.
2. Specimens are air-dried in a 20 °C temperature controlled room, and weighed at regular intervals until they reach the desirable moisture content.
3. After air-drying, specimens were wrapped in polyvinyl chloride to prevent further changes in moisture content.

4 Unconfined and confined behaviour of cohesive soils

Existing SHPB tests have been conducted on kaolin clay under both unconfined and confined conditions to reveal the effects of moisture content and saturation on the intrinsic stress propagation capabilities of cohesive soils when subject to high-strain-rate loading. Experimental results demonstrated the existence of four unique behavioural phases with boundaries correlating to levels of moisture content. While the magnitude of recorded stresses within each phase do not show a conclusive relationship, the pattern of stresses recorded at the back of the sample interface (back stress) generally decrease as the moisture content phase increases when lateral deformation is unrestricted as seen in Figure 3 [6].

The boundaries within each of the phases have been observed to be a direct effect of intrinsic material properties and experimental conditions – namely air-volume ratio, water-volume ratio, and peak average experimental strain. Phase 0 refers to fully dried samples. Phase 1 refers to samples with a lesser composition of moisture than solids and air. Phase 3 refers to samples with a high volume ratio of water. Phase 2, a variable phase, sees increases in average peak experimental strain correlating with reductions in boundary 3 (B3), phase 2 disappears if average peak experimental strain equals boundary 2 (B2). Boundaries for phases 1-3 are represented in Figure 4.

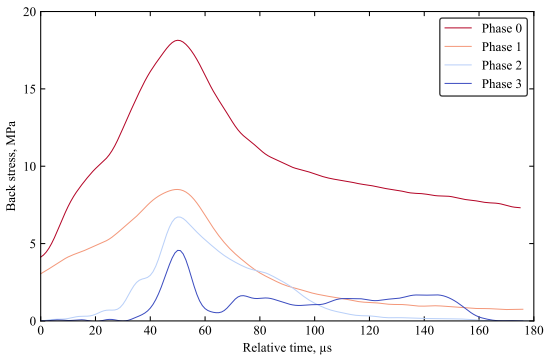

Fig. 3: Typical back stress corresponding to each of the four moisture content phases for unconfined SHPB testing on kaolin clay.

When a steel confining ring was added to restrict lateral sample deformation, radial stresses was able to be monitored by recording the circumferential strain of the ring during loading. This evidently had a direct result on the recorded back stress as the confining ring redirected lateral stresses axially as the concentration of internal radial stresses created a build-up of pressure. The result is an effect directly opposite to unconfined tests where higher back stress was associated with higher moisture content phases as seen in Figure 5. This was supported with radial stress measurements, where a comparable increase was generally observed with higher moisture content phases as seen in Figure 6.

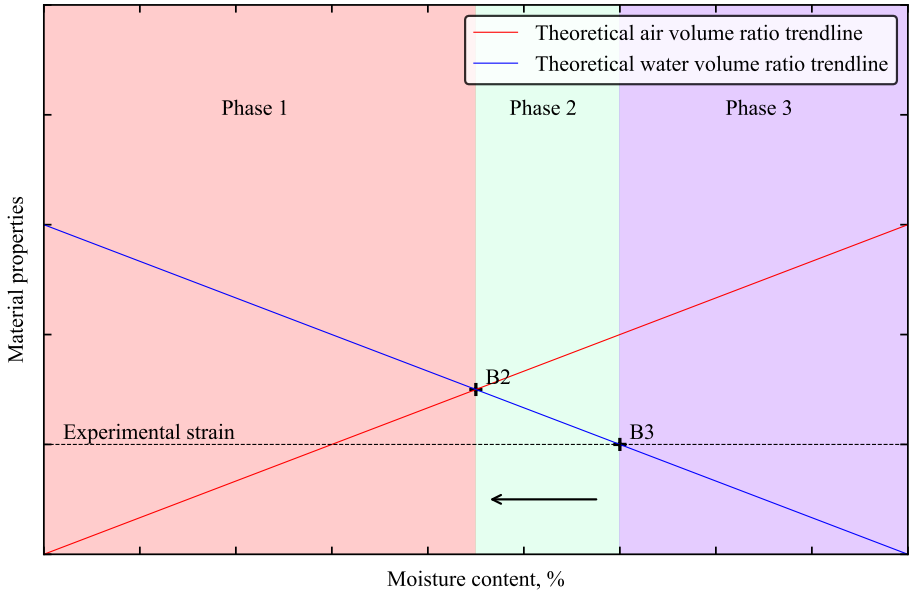

Fig. 4: General phase behaviour of kaolin clay under high-strain-rate, governed by material properties.

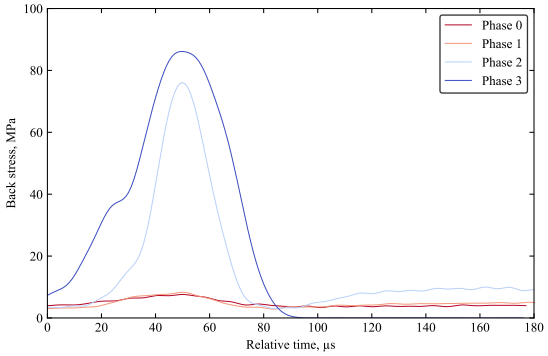

Fig. 5: Typical back stress corresponding to each of the four moisture content phases for confined SHPB testing on kaolin clay.

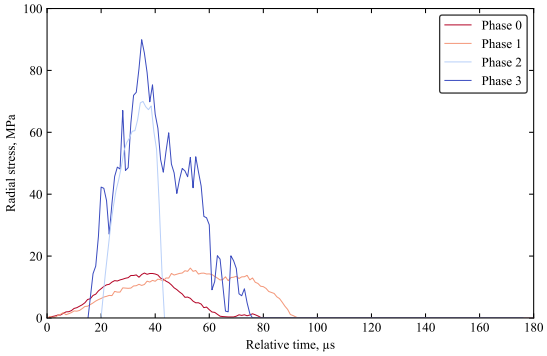

Fig. 6: Typical radial stress corresponding to each of the four moisture content phases for confined SHPB testing on kaolin clay.

4.1 Evaluation of numerical model

The initial setup of the SHPB apparatus for both confinement arrangements are similar to previous models for SHPB tests [6]. SPH node modelling has been identified to be optimal for modelling high-strain-rate behaviour of cohesive soils due to its fluid-like nature [16–18]. Numerical stresses at the locations of instrumental stress readings were shown to exhibit a considerable degree of accuracy in relation to experimental results, albeit with the main limitation of the inability to depict cohesive behaviour within individual particles [6].

Figure 7 shows a comparison between experimental and numerical back stresses from unconfined SHPB tests. While the effects of strain rate are represented to a reasonable degree of accuracy, the numerical model failed to capture the unique phase behaviour at various moisture contents.

The confined SHPB model shows a much greater disparity between experimental and numerical results (Figure 8). The confining ring in the numerical model served the purpose to effectively limit sample extrusion, ultimately resulting in the build-up of lateral stress within the sample volume and the subsequent translation of the amplified stress towards the axial direction. Physical factors prevented this from occurring in experimental testing, where movement of the ring induced by axial stress propagation along the pressure bars inevitably results in sample extrusion. The effect of confinement that facilitates this behaviour is further investigated with the introduction of PLC SHPB tests, which enable the exploration of behaviour within free field and fully sealed confinement conditions.

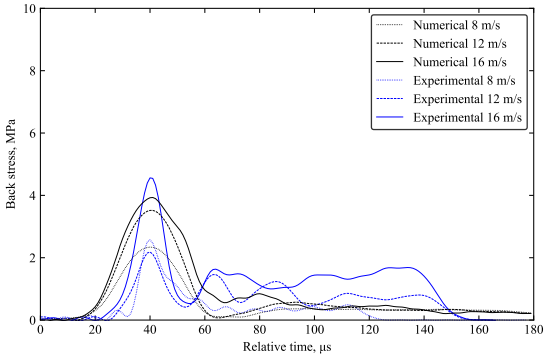

Fig. 7: Comparison between back stress from experimental and numerical model for unconfined SHPB tests on saturated kaolin clay

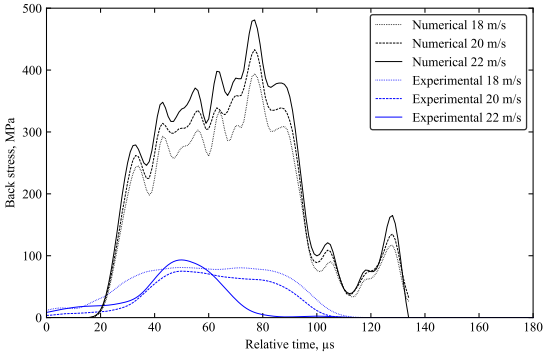

Fig. 8: Comparison between back stress from experimental and numerical model for confined SHPB tests on saturated kaolin clay

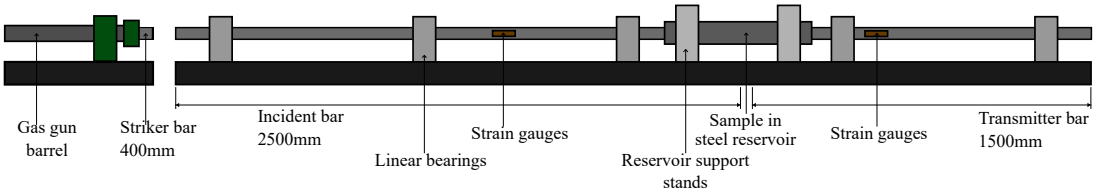

Fig. 9: Schematic of the partially lateral confined SHPB apparatus.

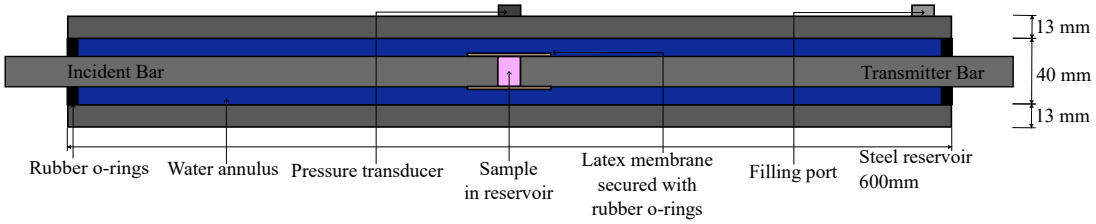

Fig. 10: Schematic of the partially lateral confined SHPB apparatus: water reservoir section.

5 Experimental setup

The modified SHPB is made up of a standard SHPB arrangement which consists of a striker, an incident and a transmitter bar, 25 mm in diameter, with a 400 mm, 2500 mm and 1500 mm length, respectively, as shown in Figure 9. In addition, as illustrated in Figure 10, a 600 mm long steel water reservoir was set on linear bearings and centred around the specimen. A 0.05 mm thick latex membrane was enveloped over the sample and both incident and transmitter bars, then secured by small rubber o-rings, this preserves the saturation level of the sample and prevents water from contaminating the sample prior to loading.

The reservoir was filled with water, and radial response was measured by a pressure transducer mounted on the walls of the reservoir which detects changes in water pressure during the deviatoric phase. The pressure transducer used was the Kulite HKM-375-2500, which has been calibrated prior to testing and by the manufacturer to perform linearly to a pressure of 25MPa. The axial response was measured with Kyowa KSP-2-120-E4 semiconductor strain gauges on the pressure bars, set up in half-Wheatstone bridge arrangements.

The reservoir length was designed so the time required for a stress wave at the specimen surface to travel to and from the reservoir's end exceeds the loading duration in the specimen, ensuring that stress waves from the boundary do not interfere with pressure measurements. This simplifies the seal between the reservoir and pressure bars, which was only needed to maintain reservoir pressure during the initial radial pulse.

To facilitate use of the water reservoir for PLC testing, reservoir support stands were installed for precise manual reservoir alignment and accessible removal of the water reservoir before and after testing. The ball bearings were loosely screwed onto the aluminium frame and capable of being manually adjusted to ensure the reservoir was centred between the pressure bars prior to testing. Figure 11 shows a simplified schematic of the water reservoir stand.

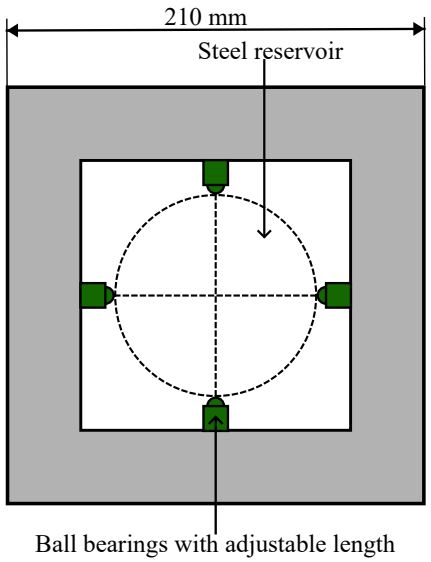

Fig. 11: Simplified schematic of the reservoir support stand used for PLC SHPB tests.

6 Sample methodology

The initiation process of PLC tests follow a similar procedure to traditional SHPB tests, however fitting of the sample in preparation for testing with the water reservoir is crucial to ensure sample measurements were accurately obtained. Sample radius and mass were recorded prior to the loading of the sample. The procedure to load the sample into the apparatus is as follows:

1. Both reservoir support stands is secured onto the channel prior to installation of the water reservoir and fitting of the sample.
2. Linear bearing support closest to specimen interface on incident bar is moved leftwards.
3. Water reservoir is slotted in between the reservoir support stands and in between the incident and transmitted pressure bars.
4. Water reservoir is slid to the left onto the incident bar, in the space of the vacated linear bearing support.
5. Small plastic o-rings are slid onto the incident and transmitted bars and latex membrane is slid onto the incident bar.
6. Sample is carefully placed in between the incident and transmitted pressure bars.
7. Latex membrane is carefully slid over to fully encompass the specimen and sealed onto the pressure bars with the small o-rings.
8. Water reservoir is centred between the incident and transmitter bars, and pressure transducer port is aligned directly on top of the specimen.
9. Linear bearing support is slid back rightwards.
10. Ball bearings on reservoir support stand are manually adjusted to ensure the water reservoir is centred on both pressure bars.
11. Larger o-rings are used to seal the two open ends of the water reservoir.
12. The reservoir is slowly filled with water through the filling port and the pressure transducer is secured onto the pressure port.
13. Measurement of the sample length is performed based on the distance between the end of the transmitted bar and the final linear bearing support (Figure 12)

The test then proceeded like a traditional SHPB tests, with axial loading being provided by firing the striker bar onto the incident bar. Striker bar speeds were recorded using a speed trap installed on the edge of the gas gun barrel.

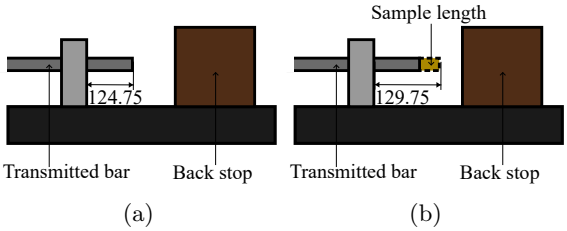

Fig. 12: Sample measurement process a) before and b) after installation within reservoir.

7 Test programme

The purpose of experimental tests was to characterise the effects of confinement, thus the validation of material behaviour revealed from previous testing was crucial. The unique phase behaviour observed during high-strain-rate testing of kaolin clay was investigated via tests at various moisture content levels. The test programme for PLC SHPB testing on kaolin clay was focused around tests at a striker bar speed of 16 m/s, which corresponds to an average peak strain rate of 2500 s^{-1}. Additional tests on saturated kaolin clays at 12 and 20 m/s were conducted to assess the effects of strain rate, which correspond to average peak strain rates of 1900 and 3000 s^{-1} (Figure 13).

The moisture contents selected for testing were based on material behaviour revealed from existing unconfined and confined SHPB testing. Tests were conducted to validate the existence of these phase boundaries, after which the results were compared with existing unconfined and confined behaviour in order to evaluate the holistic effect of confinement and the triaxial behaviour of cohesive soils under high-strain-rate loading.

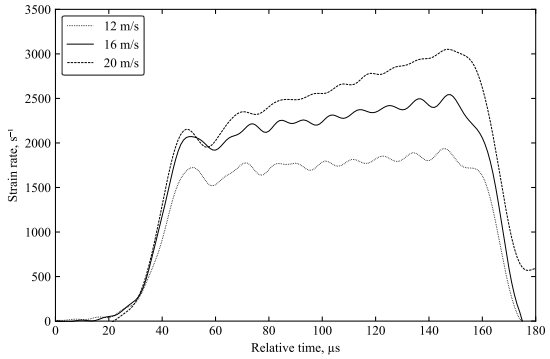

Fig. 13: Typical strain rate variation for PLC SHPB tests on kaolin clay at 12, 16, and 20 m/s, corresponding to an average peak strain of 1800, 2500, and 3000 s^{-1}.

8 Signal processing

A computational algorithm, `SHPB_processing.py` was used to process a variety of SHPB tests [19].

The key elements of the algorithm can be subdivided into the following functionalities:

- Pulse detection via automatic trigger and optimisation for stress equilibrium
- Adjustment of stresses for confinement modes
- Dispersion correction method [20, 21] (with the inclusion of the subroutine `dispersion.py`)

The transit time through the water annulus has been considered when processing pressure transducer data by accounting for the time required to travel through the medium of fluid within the annulus. Thus the time for the stress pulse, t_{transit}, to travel through the reservoir annulus can be given by:

$$t_{\text{transit}} = \frac{l_{\text{reservoir}}}{v_{\text{fluid}}} \tag{1}$$

where $l_{\text{reservoir}}$ is the thickness of the reservoir annulus, and v_{fluid} is the wave speed of the fluid in the annulus. The recorded radial stress obtained from processing pressure transducer signal is then timeshifted by the transit time (Equation 1) to acquire the radial stress at the surface of the specimen, with the assumption that the fluid wave speed for water is 1482 m/s, as shown in Figure 14.

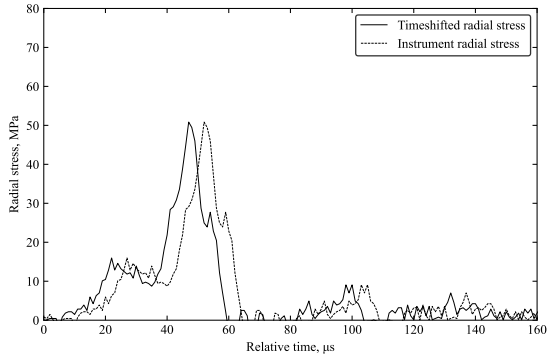

Fig. 14: Example of instrument radial stress from pressure transducer and timeshifted radial stress by accounting for transit time through water.

9 Experimental results

Experimental tests were conducted with the PLC SHPB apparatus to uncover the effects of moisture content under confinement mechanism in between free field and fully rigidly confined conditions. Tests were structured around validating the strain and moisture content effects in cohesive soils under high-strain-rates. Ultimately leading to a viable comparison with existing confinement modes and to reveal the effects of confinement.

Sample stress is determined by taking the average of stresses on the front and back interfaces of the specimen. Back stress is the main component that undergoes drastic change when moisture content is varied, while front stress remains relatively constant for the same striker bar speeds. Typical front stresses are shown in Figure 15.

9.1 Moisture content and strain rate effects

Cohesive soils such as kaolin clay, with no initial confining pressure, tend to propagate stress laterally and result in limited axial transmission of stress towards the back sample interface.

Although strain rate affects magnitudes of stresses within moisture content phases, pulse shapes remain consistent in unconfined and confined SHPB tests. Thus, the behaviour within each of the phases was inferred to be similar, albeit with varying magnitudes. Back and radial stresses for saturated kaolin clay samples at various strain rates are seen in Figures 16 and 17 respectively, where increases in strain rate corresponded with increases in both radial and axial stress.

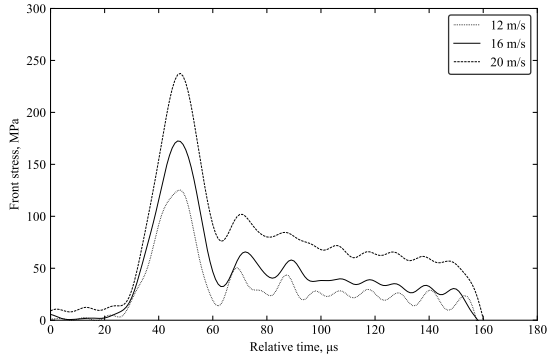

Fig. 15: Typical front stress variation for PLC SHPB tests at 12, 16, and 20 m/s.

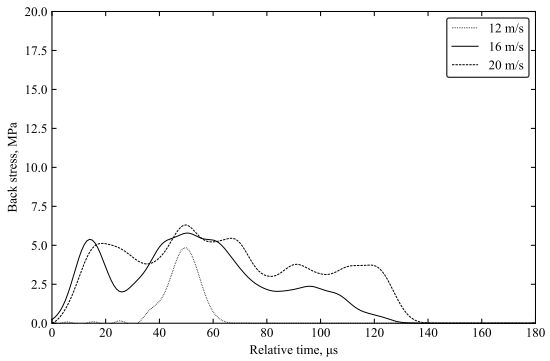

Fig. 16: Typical back stress from partially confined SHPB test on saturated kaolin clay 12, 16, and 20 m/s

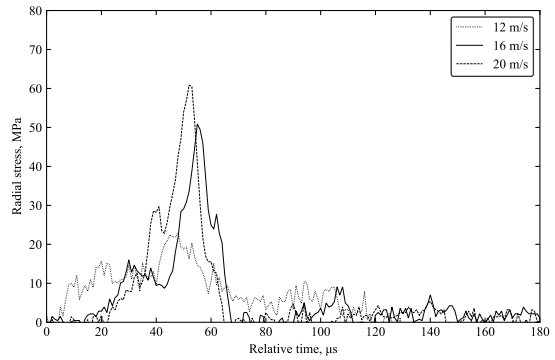

Fig. 17: Typical radial stress from partially confined SHPB test on saturated kaolin clay at 12, 16, and 20 m/s

As highlighted from unconfined and confined tests, unique variations in wave propagation behaviour occur within specific moisture content boundaries. The existence of these phases were validated with the modified apparatus for saturated, partially saturated, and dried kaolin clay samples (Figure 18). The advantage of the PLC SHPB setup is its ability to characterise lateral behaviour without restricting lateral deformation, prompting the development of lateral stresses to be monitored while the sample deforms under different saturation phases. The similarities in phase behaviour to unconfined tests emphasises the freedom for the sample to deform laterally, yet pressure readings allow for lateral deformation under limited confinement to be characterised.

An overview of the findings within each moisture content phase based on PLC SHPB testing is as follows:

Phase 0 (0%): Axial stress during phase 0 retains the same characteristics of unconfined tests where back stress does not return to zero as energy is being used to consolidate the dry sample by filling in existing air gaps. Axial stress propagation is greatest in this phase due to the lack of moisture forcing lateral propagation, naturally inducing a much lower radial pulse due to a lesser degree of lateral propagation. While a radial pulse is still visible, the noise recorded by the pressure transducer reaches up to 3 MPa and overlaps up to 50% of the recorded radial pulse as seen in Figure 18b. Hence, other than the interpolation that radial stress is at a minimum, it is not feasible to reach accurate conclusions from tests at low moisture contents at this time.

Phase 1 (0% to B2): The presence of moisture means that there is a lesser degree of consolidation due to a portion of the stress being propagated laterally, hence back stress gradually returns to zero. The greater degree of saturation within the sample causes a portion of the stress to propagate laterally. Hence the magnitude of the recorded radial stresses show a considerable increase from phase 0 as seen in Figure 18d.

Phase 3 (B3 to full saturation): This phase exhibits the least axial stress propagation, the high volume of water in saturated samples induces maximum lateral stress propagation and the least amount of back stress as moisture dictates the majority of high-strain-rate behaviour within this phase. The capability of the apparatus to measure radial stresses in saturated kaolin clay samples is demonstrated. This phase invokes the greatest magnitude of radial stress, evident from Figure 18f, where a distinct radial stress pulse is observed.

While tests have not been conducted explicitly within phase 2, consistency between characteristics of other phases from existing unconfined and confined tests indicate similar behaviours exist.

The presence of unique phase behaviour demonstrates the capability of the modified apparatus to characterise radial effects under limited confined conditions, providing a vital perspective to the lateral wave propagation effects that occur under conditions similar to unconfined SHPB tests.

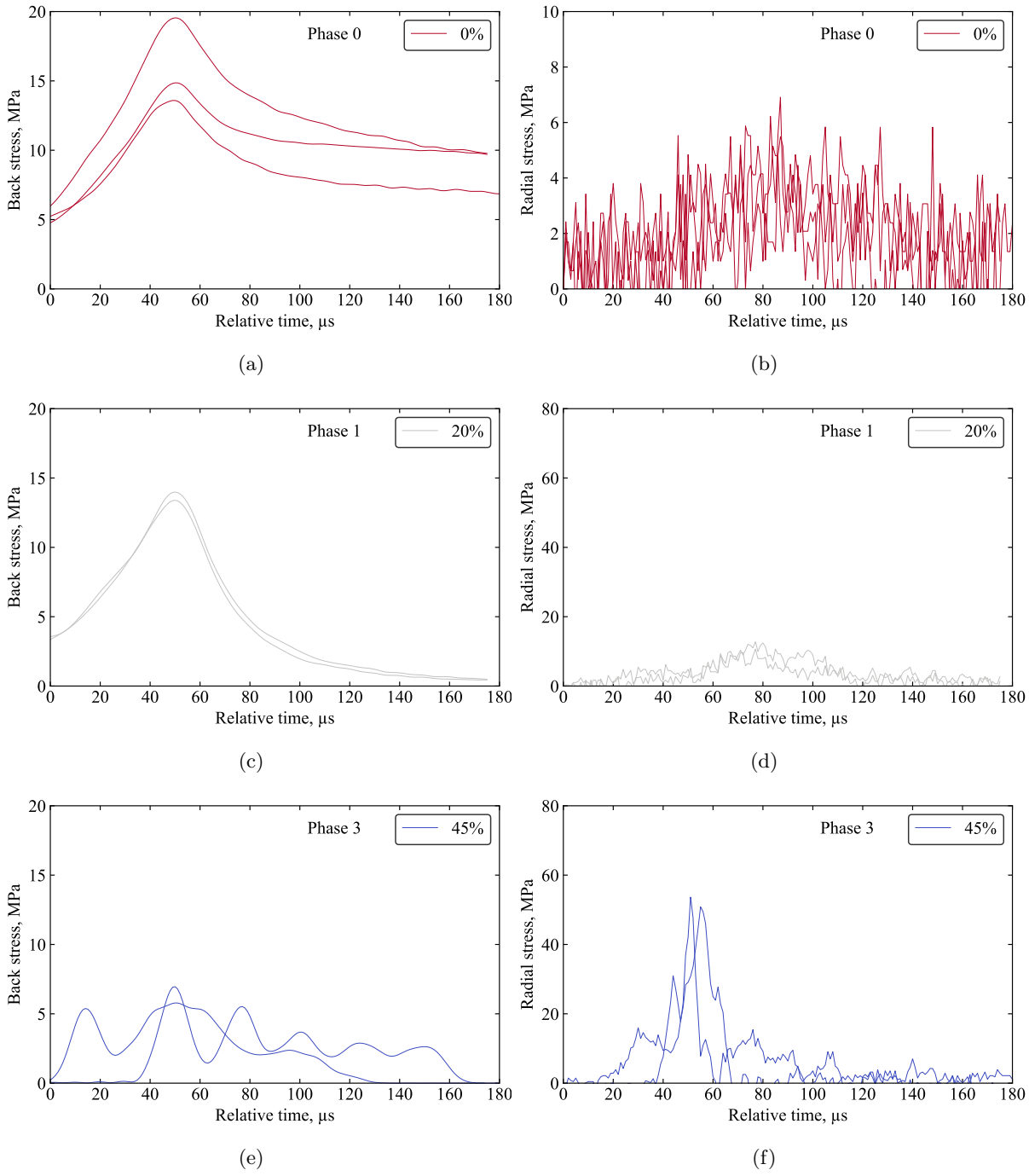

Fig. 18: Back and radial stress for PLC testing on kaolin clay at 16 m/s at phase 0 (a, b), phase 1 (c, d), and phase 3 (e, f).

9.2 Similarities to water

The PLC apparatus was optimised for tests without soil samples, creating an environment that emulates high-strain-rate impact testing of water. Results were obtained by measuring axial stresses from pressure bar gauge readings and radial stresses from water pressure changes [22].

There is a notable similarity between experimental results of water and saturated kaolin clay (Figure 19). The same effect is observed where axial stress from the incident bar fails to propagate through the sample (or water medium) onto the interface of the transmitted bar. This is coupled with changes in water pressure to indicate lateral transferral of stress during the deviatoric phase.

This emphasises that the build-up of pressure within the internal sample boundaries is what ultimately leads to the redirection of lateral stress back towards the axial direction. Similar to the effect of water applying a subsequent pressure in all directions when subject to dynamic compression.

9.3 Comparison with unconfined and confined SHPB testing

To compare the effect of the PLC with existing SHPB results, the pulses from the three confinement modes are visualised in Figure 20 [6]. The magnitude of back stress pulse greatly resemble unconfined tests, albeit to a slightly greater magnitude. This indicates that the same effect occurs, where stresses were mostly being forced laterally rather that being propagated axially towards the transmitter bar.

The disparity in radial stress compared to confined tests can be attributed to no lateral stress build-up due to the absence of initial confining pressure. The replication of a free field environment within the reservoir prompts lateral stresses to dissipate without being concentrated directly on the surface of the specimen.

After sample deformation occurs, the confining pressure begins to develop and results in increased water pressrure. This effectively leads to a greater degree of axial transmission compared to unconfined tests. This shows that the tendency to propagate stress laterally is an intrinsic property of cohesive soils such as kaolin clay, but the addition of a confining pressure acts to concentrate and redirect lateral stress towards the axial direction.

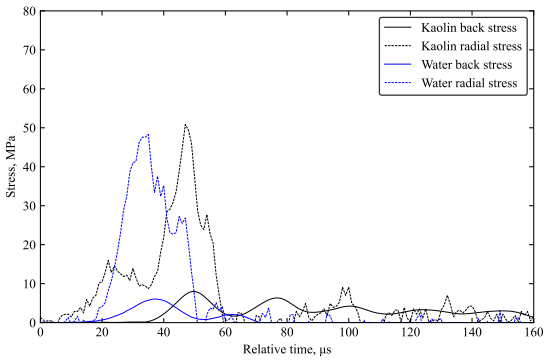

Fig. 19: Typical back and radial stresses from partially confined SHPB tests on water and saturated kaolin clay at 16 m/s.

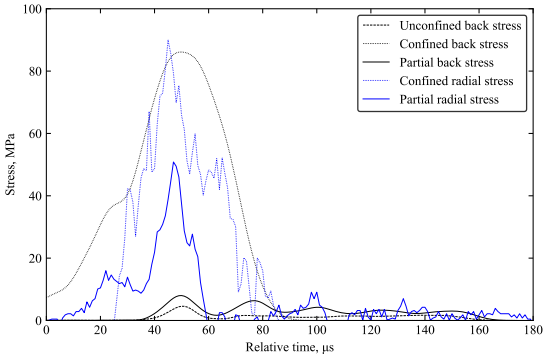

Fig. 20: Typical back and radial stress from unconfined, confined, and partial confined SHPB tests.

9.4 Triaxial stress state

Radial stress data obtained from PLC SHPB tests on kaolin allows for the triaxial stress state to be evaluated. The difference between sample axial and radial stresses for confined and PLC SHPB tests on kaolin clay is shown in Figures 21 and 22.

Moisture content evidently has the same effect regardless of confinement, such that each phase typically experiences smaller differences in axial and radial stresses. The concentration of radial stresses experienced under confined conditions emphasises the triaxial stress state, where in addition to the initial axial stress wave, the confinement mechanism serves to provide a confining pressure to restrict lateral deformation. This ultimately enables stress to propagate through to the back of the sample, unlike what occurs in unconfined SHPB tests.

This is juxtaposed with PLC testing, where the confining pressure is allowed to passively develop instead. The measured radial stresses corresponds to the confining pressure that develops as the sample is strained axially. The magnitude of the stress difference was much lower compared to when a stainless-steel confining ring was present. Consequently, this corresponds to a significantly reduced amount of stress that was able to propagate through the sample.

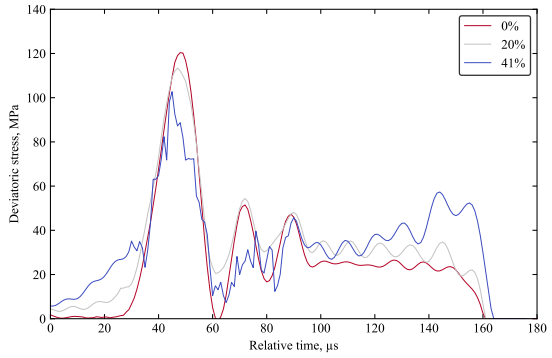

Fig. 21: Axial and radial stress difference from confined SHPB tests on kaolin clay at varying moisture contents.

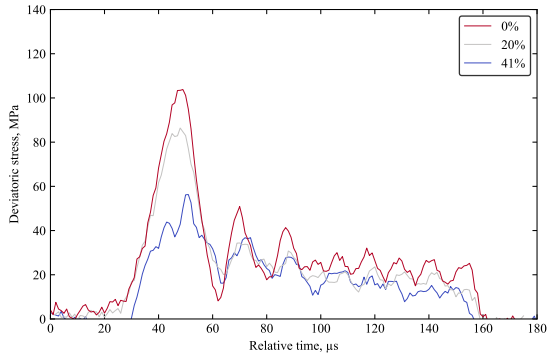

Fig. 22: Axial and radial stress difference from PLC SHPB tests on kaolin clay at varying moisture contents.

10 Numerical modelling

10.1 Model setup

The numerical modelling of the arrangement was carried out using the explicit finite element code in LS-DYNA to compare numerical and experimental results as seen in Figure 23. The initial setup of the SHPB apparatus is similar to previous models for unconfined SHPB tests [6], with the addition of a steel reservoir and water annulus (Figure 24). Similarly, SPH nodes were generated to represent clay specimen due to its ability to emulate fluid-like behaviour under high-strain-rates.

Two separate SPH node parts have been tested to represent both the SPH sample and the water annulus. However, the methods to define contact interactions between two separate SPH "fluids" with unique densities lead to computational errors because these densities are defined over quantities of SPH particles, causing interactions at boundary elements to not behave as they would in real-life [23]. Hence only the SPH specimen was modelled as SPH nodes.

All pressure bars were modelled as an elastic material, `MAT_ELASTIC` with steel properties. While the kaolin clay sample was modelled as `MAT_MOHR_COULOMB` with parameters obtained from existing testing. The reservoir was modelled as a rigid material, `MAT_RIGID`, as fluid pressures were assumed to not be significant enough to cause deformation of the steel reservoir. The water annulus was modelled with the null material card, `MAT_NULL`, with the input parameters and equation of state of water [24]. The rubber o-rings were replaced with a boundary constraint to restrict expulsion of the water annulus.

Contact interactions between all Lagrangian model parts were manually designated by specifying interaction surfaces to reduce computation time. But all SPH node to Lagrangian interactions were defined automatically by the `CONTACT_AUTOMATIC_NODE_TO_SURFACE` contact algorithm in order to enhance accuracy regarding sample behaviour [25].

Fig. 23: LS-DYNA SHPB partial lateral confinement model set up containing the incident bar (blue), transmitted bar (green), striker bar (yellow), and water reservoir (grey). Sample and water annulus are modelled inside the water reservoir.

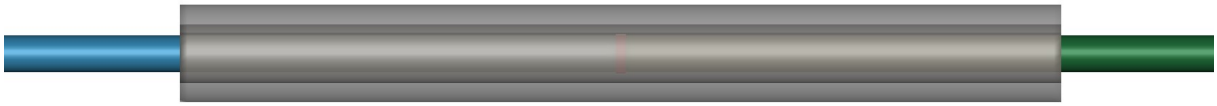

Fig. 24: LS-DYNA cross section zoom-in on the sample inside the partial lateral confinement SHPB set up containing the incident bar (blue), transmitted bar (green), water reservoir (grey), water annulus within reservoir, and the sample (red).

10.2 Comparison between experimental and numerical results

Figure 25 shows the difference in back stress between experimental results and the numerical model. Even though qualitative observation show similar behaviour, the back stress from the numerical model is nearly twice as high as experimental results. This can be attributed back to the lack of cohesion modelling capabilities as the numerical model is not limited by the rubber o-rings to create a sealed environment within the water annulus. The boundary constraints in the numerical model prevent the leakage of water without interfering with the movement of the pressure bars, creating a perfect condition where both axial and radial stresses can develop within the reservoir. While this was the idealistic environment when the apparatus was conceptualised, in actuality, multiple factors affect the development of lateral confining pressure, notably the movement of the o-rings when stress wave passes through the pressure bars start to create leakage and disrupts the internal water pressure.

Figure 26 shows the difference in radial stress between the numerical model and typical experimental results. Evidently, a similar peak and pulse pattern can be inferred, but the numerical model experienced significantly lower lateral stresses. This is primarily a result of the lack of the capability to model cohesion properties, resulting a much higher reflected pulse in the model. In turn, this culminates in a much lower portion of stress that actually gets transmitted through the sample both radially and axially.

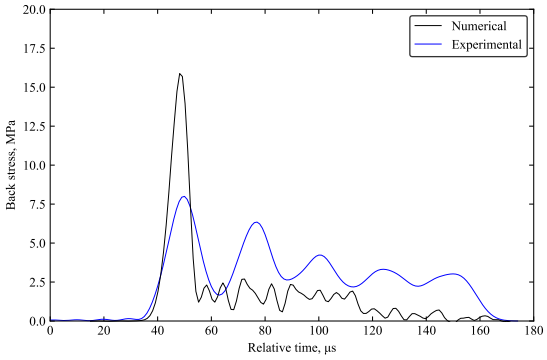

Fig. 25: Comparison between back stress from experimental and numerical model for PLC SHPB test on saturated kaolin clay.

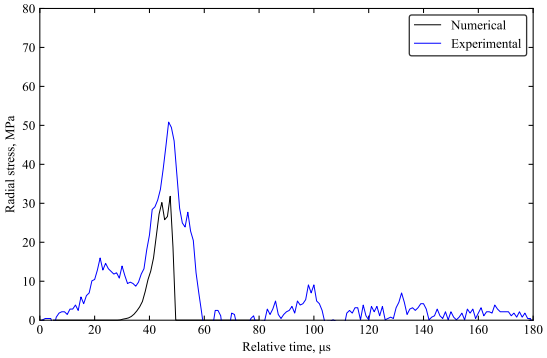

Fig. 26: Comparison between radial stress from experimental and numerical model for PLC SHPB test on saturated kaolin clay.

The primary limitation in modelling cohesive soils is the inability to accurate depict cohesive properties for materials of which an equation of state cannot be obtained. When changes were made to the Poisson's ratio (to values closer to the experimentally determined value of 0.5) and bulk density was varied to represent the material properties of kaolin clay at different moisture content, no changes was observed in the model results. This indicates that while the model is able to visualise changes in strain rate and general behaviour, further development is necessary to prompt comprehensive modelling of cohesive soil behaviour under high-strain-rate.

Overall, while the numerical model enhances understanding of high-strain-rate behaviour, the inherent drawbacks of numerical modelling cohesive soils still limit comprehensive reflection of physical conditions with LS-DYNA.

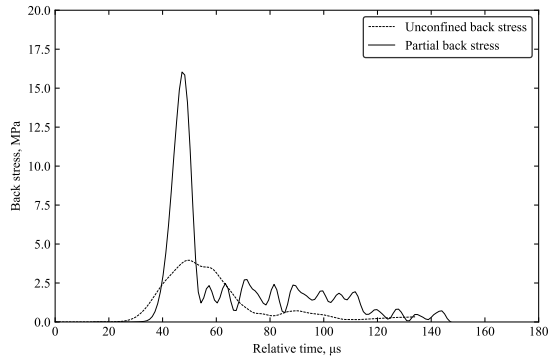

Fig. 27: Comparison between back stress from numerical model for unconfined, PLC SHPB test on saturated kaolin clay.

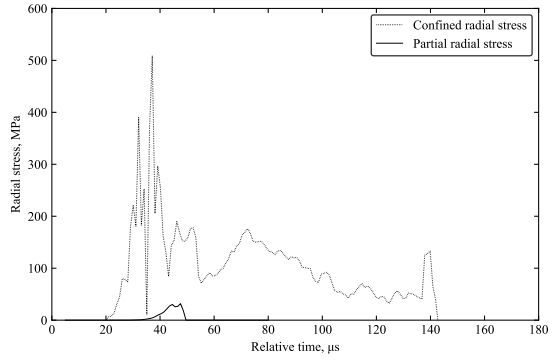

Fig. 28: Comparison between radial stress from numerical model for confined, and PLC SHPB test on saturated kaolin clay.

10.3 Comparison against unconfined and confined numerical models

While the same material limitations exist between the unconfined, confined, and PLC SHPB numerical model, the juxtaposition between the three confinement modes allows for the effects of confinement to be magnified by developing idealistic situations at the three different lateral pressure modes.

Figure 27 shows the difference in back stress experienced by the numerical model under unconfined and PLC conditions, the back stress for confined cases is significantly larger than both of these magnitudes and so has not been shown. The ability for the PLC sample to deform laterally is evident due to its similarity to unconfined cases, the lack of rigid confinement to redirect stress back towards the axial direction like results in a significantly lesser back stress unlike confined cases.

The radial effects of confinement can be visualised in Figure 28 depicting the radial stresses obtained from the confining ring and the water pressure directly adjacent to the sample. Evidently, a significant disparity is observed as the model for the confining ring acts as a perfect seal, and forces all lateral stress to be concentrated on the ring. This indicates that the confinement mechanism directly affects axial transmission as internal radial stresses of the specimen are wrapped and redirected towards the back interface according to the degree of confinement. Thus a system with limited confinement such as the PLC depicts low measured radial stresses and equally low axial back stresses.

While there are obvious physical differences between the three confinement modes, the PLC approach can be considered to be a combination of the unconfined and confined cases. Comparison with high-strain-rate behaviour under different confinement conditions reveal that increasing the initial confining pressure induces an increase in both recorded back and radial stress. This indicates that confinement increases the degree of which radial stresses become concentrated on both the sample radial edges and back interface, however further investigation of internal stress propagation is crucial in understanding the intrinsic mechanisms.

11 Internal stress distribution

Numerical modelling allows for the stresses at exact locations to be monitored, thus the internal lateral stress distribution during the deviatoric phase can be investigated. By only considering stresses at $x = 0$, the lateral stress distribution for individual sample layers can be visualised as heatmaps for unconfined and confined conditions.

The same method was applied to investigate radial stresses distribution within the sample during loading in a PLC SHPB test. The heatmap for internal radial stresses within the sample is shown in Figure 29 with the water annulus modelled as water at 1000 kg/m^3. It was observed that while the maximum stresses are similar to unconfined tests, a second pulse develops as a result of confining pressure developing as the sample deforms laterally.

The initial radial pulse from the centre to the edge of the sample was similar in both unconfined and confined confinement cases as shown in Figures 30a and 31a. The rigid confinement mechanism caused the subsequent concentration of radial stress during rigidly confined SHPB tests as a result of internal stress wave superposition. This emphasises that resistance to lateral deformation from confining pressure creates a build-up of internal radial stress, of which is eventually redirected axially to the direction of the transmitter bar.

In order to validate the effects of confinement in promoting the amplification of radial stress via wave reflection, the density of the "water" was modified in the PLC numerical model to alter the effective inertia of the reservoir annulus. Figure 30b shows the heatmap when the fluid density was set to 1 kg/m^3, which theoretically resembles a fluid medium with limited resistance like free-field SHPB tests. Evidently, the subsequent reflected wave disappears, coinciding with preconceived behaviour from unconfined SHPB tests.

Contrarily, the density of water was increased to create an effect of greater confinement as the energy required to displace elements of the water annulus were now comparatively greater. Multiple model iterations were developed at various densities to assess the maximum velocity of adjacent fluid elements during lateral deformation of the sample, as summarised in Table 2.

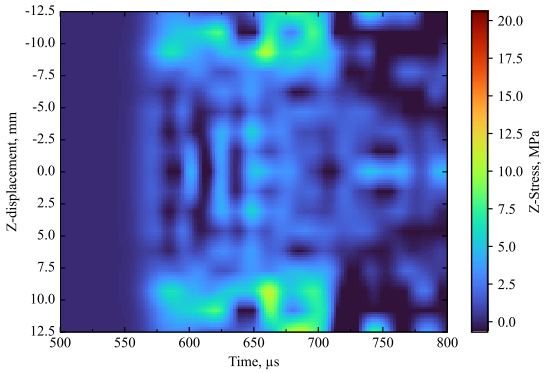

Fig. 29: Heatmap describing internal radial stress distribution from numerical model of PLC SHPB tests, with water modelled as 1000 kg/m^3.

Table 2: Summary of numerical model iterations and required energy to displace confining elements.

Material	*Density, kg/m^3*	*Mass, kg*	*Peak radial velocity, m/s*	*Kinetic energy, J*
Steel	7850	3.42×10^{-5}	0.0822	1.16×10^{-7}
Water	1	1.98×10^{-8}	28.90	8.26×10^{-6}
Water	1000	1.98×10^{-5}	8.08	6.45×10^{-4}
Water	5000	9.88×10^{-5}	2.81	3.90×10^{-4}
Water	1×10^{7}	0.20	8.37×10^{-3}	6.92×10^{-6}
Water	2×10^{7}	0.40	4.73×10^{-3}	4.42×10^{-6}
Water	6×10^{7}	1.19	1.70×10^{-3}	1.71×10^{-6}
Water	1×10^{8}	1.98	1.01×10^{-3}	1.01×10^{-6}
Water	9×10^{8}	17.79	1.23×10^{-4}	1.35×10^{-7}
Water	1×10^{9}	19.77	1.15×10^{-4}	1.31×10^{-7}
Water	1.1×10^{9}	21.71	1.06×10^{-4}	1.22×10^{-7}
Water	2.5×10^{9}	49.4	6.57×10^{-5}	1.07×10^{-7}

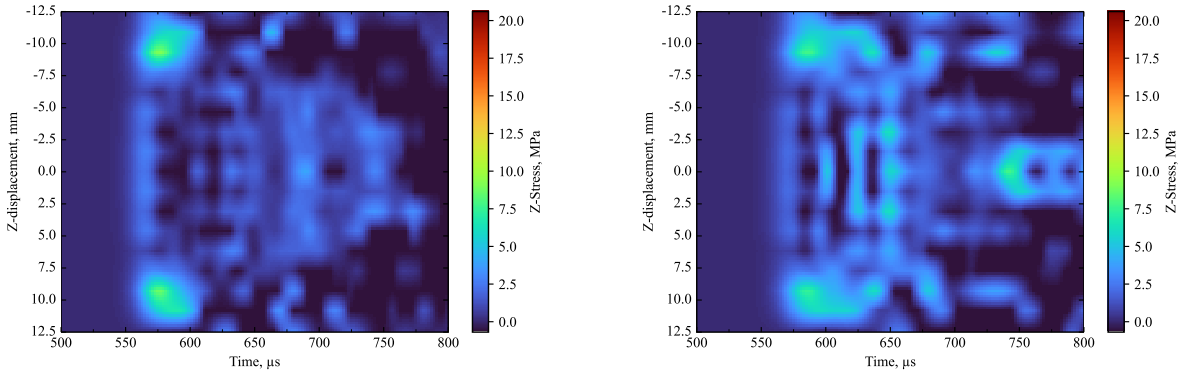

(a) (b)

Fig. 30: Heatmaps describing internal radial stress distribution from numerical models of a) unconfined SHPB and b) PLC SHPB with equivalent water annulus density (1 kg/m^3).

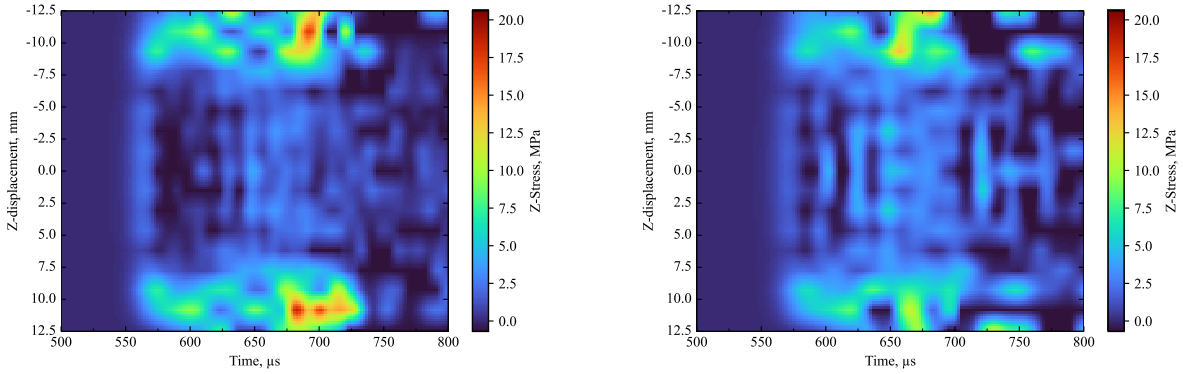

(a) (b)

Fig. 31: Heatmaps describing internal radial stress distribution from numerical models of a) confined SHPB and b) PLC SHPB with equivalent water annulus density (1.1×10^9 kg/m^3).

While the initial pulse remained the same regardless of density, the magnitude of the subsequent pulse increases as the density of the fluid annulus increases. This corroborates the notion that increasing confinement encourages pulse reflection and the build-up of internal lateral stress.

To compare the confinement conditions with the numerical model with a steel confining ring, the corresponding energy required to displace a fluid element with a defined volume from rest, E, is derived for each density, ρ, to reveal a power-law relationship expressed by:

$$E = 0.3542\rho^{-0.727} \tag{2}$$

The r^2 value for Equation 2 was determined to be 0.951, indicating an excellent relationship.

As such, the density of the modelled fluid with an equivalent energy to the elastic steel confining ring is determined to be 1.1×10^9 kg/m^3. The heatmaps illustrating the PLC numerical model with a fluid annulus modelled with this density can be compared to the results from the confined model in Figure 31.

Evidently, the lateral stresses found in the second pulse exhibit similarities in peak stress. Intrinsic differences between material behaviour explain the difference between the two models, notably the difference in compressibility between the water modelled as a null material and steel modelled as an elastic material, resulting in the pulse with a steel confining ring maintaining its peak magnitude for a longer duration as the stress wave travels within elastic steel ring elements.

This emphasises the effects of confinement in cohesive soils when subject to high-strain-rate loading, where the confining pressure prompts the internal reflection of radial stress and culminates in the concentration of radial stress in eventual internal radial waves. This intensification of radial stress ultimately results in the axial redirection of amplified radial stress.

12 Discussion

Due to the ability of cohesive soils to retain a larger proportion of moisture, the effect of moisture content is vital in dictating material behaviour. When subject to high-strain-rate axial loading, moisture forces the stress to propagate laterally, this typically creates volume loss as an after effect of the loading. This is supported by testing with the PLC SHPB apparatus, where it is evident that when under no confinement conditions, lateral stress remains at its greatest, and the opposite is true for the recorded back stress.

However, while experimental results have provided an idea of the effect of confinement, apparatus limitations prevent the full characterisation of confinement effects without numerical modelling. From numerical models on confined SHPB tests, a fully rigid ring demonstrates the ability to fully translate lateral stress into axial stress at the back of the specimen interface by creating a condition that prevents volume loss. Comparison to PLC modelling reveal a similar effect, where a larger portion of radial stress is observed.

Hence it can be said that the confinement of lateral pressure creates an effect of stress redistribution back towards the axial axis. PLC SHPB tests reveal lateral confining pressure is the primary factor that prompts this behaviour, such that confinement urges the build-up of lateral pressure within the sample boundaries. This behaviour is consistent even at varying strain rates, with increasing strain rate corresponding with increased recorded stress pulses.

This is supported by further numerical modelling of PLC tests, where the propagation of radial stress within the sample were monitored during loading. By varying the density of the fluid annulus, the model was able to recreate confinement environments that resemble both unconfined and confined scenarios. This provides evidence of the effects of confinement on stress wave propagation behaviour, such that the development of confining pressure results in radial wave reflection at the sample edge. The subsequent superposition of the internal radial waves culminates in the concentration of lateral pressure, of which is ultimately redirected towards the back sample interface.

Intrinsic limitations associated with modelling cohesive soils under high-strain conditions still persist and hinder comprehensive modelling of physical behaviour. Other than the lack of an accurate material model to depict cohesive soil behaviour, there are also idealistic differences that inherent cause the numerical model to differ from experimental conditions. A prime instance of this is the ability to create perfect boundary conditions. Large rubber o-rings were utilised to seal the water reservoir and ideally create a condition of controlled pressure within the water annulus, yet still allow for the pressure bars to move and propagate stress during loading. The subsequent effect of loading typically involves the water seal being broken immediately, invoked by lateral movement of the rubber o-rings by the sudden pressure change and movement of the pressure bars. While the effect may not be as noticeable given only the initial radial pulse is of primary concern, numerical modelling allows for an idealistic scenario where the pressure in the water annulus can be fully controlled without hindering the stress propagation through the pressure bars.

13 Conclusion

Overall, the PLC SHPB apparatus is a suitable method in experimentally determining high-strain-rate effects of cohesive soils. This is especially valuable due to the tendency for cohesive soils to exhibit lateral stress propagation when subject to high-strain-rate loading. However, if radial stresses are limited due to lack of sample moisture, inaccuracies start to arise due to presence of noise. Further developments of the apparatus would be the addition of an amplification capability and higher accuracy pressure transducers to reduce the noise intake and also increase accuracy of pressure readings if pressure readings are low.

By validating material behaviour from PLC SHPB testing to results from unconfined and confined SHPB testing, high-strain-rate behaviour within these two confinement modes were compared. The supplementation of numerical modelling was crucial in enhancing the holistic effect of confinement by creating idealistic conditions that allow the comparison between the various confinement modes. From which it was discovered that increasing confining pressure encourages internal stress wave reflection and the concentration of stress within the sample, but that the initial radial stress wave remained unaffected by the effects of confinement.

Even though the numerical models provided valuable insight of the internal mechanisms during loading, the limitations of modern numerical modelling techniques in replicating the behaviour of cohesive soils under high-strain-rates was still apparent. The lack of an appropriate material model that accounts for the properties of cohesion is a primary factor in the disparities between numerical and experimental results, and an avenue that requires explicit future development.

Acknowledgements. This research was funded by the Engineering and Physical Sciences Research Council (EPSRC), and the Defence Science and Technology Laboratory (Dstl).

Declarations

Conflict of interest. The authors declare that they have no conflict of interest.

References

[1] Song, B., Chen, W., Luk, V.: Impact compressive response of dry sand. Mechanics of Materials - MECH MATER **41**, 777–785 (2009) https://doi.org/10.1016/j.mechmat.2009.01.003

[2] Barr, A., Clarke, S., Petkovski, M., Tyas, A., Rigby, S., Warren, J., Kerr, S.: Effects of strain rate and moisture content on the behaviour of sand under one-dimensional compression. Experimental Mechanics **56** (2016) https://doi.org/10.1007/s11340-016-0200-z

[3] Luo, H., Lu, H., Cooper, W.L., Komanduri, R.: Effect of Mass Density on the Compressive Behavior of Dry Sand Under Confinement at High Strain Rates. Experimental Mechanics **51**(9), 1499–1510 (2011) https://doi.org/10.1007/s11340-011-9475-2

[4] Martin, B.E., Chen, W., Song, B., Akers, S.A.: Moisture effects on the high strain-rate behavior of sand. Mechanics of Materials **41**(6), 786–798 (2009)

[5] Konstantinov, A., Bragov, A., Igumnov, L., Eremeyev, V., Balandin, V.V., Balandin, V.V.: Experimental Study and Identification of a Dynamic Deformation Model of Dry Clay at Strain Rates up to 2500 s-1. Journal of Applied and Computational Mechanics **8**(3), 981–995 (2022)

[6] Van Lerberghe, A., Li, K., Barr, A., Clarke, S.: High strain rate behaviour of cohesive soils. Submitted for publication in International Journal of Impact Engineering (2024)

[7] Bragov, A.M., Lomunov, A.K., Sergeichev, I.V., Tsembelis, K., Proud, W.G.: Determination of physicomechanical properties of soft soils from medium to high strain rates. International Journal of Impact Engineering **35**(9), 967–976 (2008) https://doi.org/10.1016/j.ijimpeng.2007.07.004

[8] Pierce, S.J., Charlie, W.A.: High-intensity Compressive Stress Wave Propagation Through Unsaturated Sands. PhD thesis, Colorado State University (1990)

[9] Bailly, P., Delvare, F., Vial, J., Hanus, J.L., Biessy, M., Picart, D.: Dynamic behavior of an aggregate material at simultaneous high pressure and strain rate: SHPB triaxial tests. International Journal of Impact Engineering **38**(2-3), 73–84 (2011) https://doi.org/10.1016/j.ijimpeng.2010.10.005

[10] Gong, F.-Q., Si, X.-F., Li, X.-B., Wang, S.-Y.: Dynamic triaxial compression tests on sandstone at high strain rates and low confining pressures with split hopkinson pressure bar. International Journal of Rock Mechanics and Mining Sciences **113**, 211–219 (2019) https:

//doi.org/10.1016/j.ijrmms.2018.12.005

[11] Christensen, R.J., Swanson, S.R., Brown, W.S.: Split-hopkinson-bar tests on rock under confining pressure. Experimental Mechanics **12**(11), 508–513 (1972) https://doi.org/10.1007/BF02320747

[12] Frew, D.J., Akers, S.A., Chen, W., Green, M.L.: Development of a dynamic triaxial Kolsky bar. Measurement Science and Technology **21**(10) (2010) https://doi.org/10.1088/0957-0233/21/10/105704

[13] Barr, A.D., Clarke, S.D., Rigby, S.E., Tyas, A., Warren, J.A.: Design of a split Hopkinson pressure bar with partial lateral confinement. Measurement Science and Technology **27**(12) (2016) https://doi.org/10.1088/0957-0233/27/12/125903

[14] Livermore Software Technology Corporation: LS-DYNA Theory Manual, California, USA (2023)

[15] Lacome, J.L.: Smooth particle hydrodynamics (sph): a new feature in ls-dyna. In: 6th International LS-Dyna Users Conference, Detroit, USA (2000)

[16] Varas, D., Lopez-Puente, J., Artero-Guerrero, J., Pernas-Sanchez, J.: Numerical modelling of fluid structure interaction using ale and sph: The hydrodynamic ram phenomenon. In: 11th European LS-DYNA Conference (2017)

[17] Anghileri, M., Castelletti, L.M.L., Tirelli, M.: Fluid-structure interaction of water filled tanks during the impact with the ground. International Journal of Impact Engineering **31**(3), 235–254 (2005) https://doi.org/10.1016/j.ijimpeng.2003.12.005

[18] Jianming, W., Na, G., Wenjun, G.: Abrasive waterjet machining simulation by SPH method. International Journal of Advanced Manufacturing Technology **50**(1-4), 227–234 (2010) https://doi.org/10.1007/s00170-010-2521-x

[19] Van Lerberghe, A., Li, K., Barr, A., Clarke, S.: An open-source algorithm for correcting stress wave dispersion in split-Hopkinson pressure bar experiments. Submitted for publication in Experimental Mechanics (2024)

[20] Tyas, A., Pope, D.J.: Full correction of first-mode pochammer–chree dispersion effects in experimental pressure bar signals. Measurement science and technology **16**(3), 642 (2005)

[21] Gray, T.G.: Classic Split-Hopkinson Pressure Bar Testing. In: Mechanical Testing and Evaluation, pp. 462–476. ASM International, ??? (2000). https://doi.org/10.31399/asm.hb.v08.a0003296

[22] Li, K., Van Lerberghe, A., Barr, A., Dennis, A., Clarke, S.: Split-Hopkinson pressure bar testing of water with partial lateral confinement. Submitted for publication in Experimental Mechanics (2024)

[23] Ihmsen, M., Bader, J., Akinci, G., Teschner, M.: Animation of air bubbles with sph. In: International Conference on Computer Graphics Theory and Applications, vol. 2, pp. 225–234 (2011). https://doi.org/10.5220/0003322902250234 . SCITEPRESS

[24] Shin, Y.S., Lee, M., Lam, K.Y., Yeo, K.S.: Modeling mitigation effects of watershield on shock waves. Shock and Vibration **5**(4), 225–234 (1998) https://doi.org/10.1155/1998/782032

[25] Xu, J., Wang, J.: Interaction methods for the sph parts (multiphase flows, solid bodies) in ls-dyna. In: Proceedings of the 13th International LS-DYNA Users Conference, Detroit, MI, USA, pp. 8–10 (2014)

Appendix B

Experimental test log

B.1 Introduction

This appendix presents the measurements taken during the SHPB tests of the kaolin clay samples, covering trials for both unconfined and fully confined. It serves as a condensed version of the original test log used to document all the SHPB trials conducted during the experimental testing phase of this thesis.

The dry mass of each sample was determined based on their weight before air-drying, while the wet mass was measured just before insertion of the sample between the Hopkinson pressure bars on the SHPB apparatus. Moisture content levels aimed for testing are noted, with actual moisture content calculated based on the wet and dry mass of each sample. The tested samples all had a diameter of 25 mm. The methods for measuring specimen length and wet mass are detailed in Section 4.4.3, along with the experimental procedures for unconfined and fully confined SHPB tests.

B.2 Unconfined SHPB test log

This section contains test logs for unconfined SHPB tests on kaolin clay specimens. Table B.1 shows the pressure-depth combinations for each striker bar velocity used and references the individual logs.

Striker bar velocity, m/s	*Gas gun pressure, PSI*	*Striker bar depth, mm*	*Table No.*
8	14	600	B.2
12	28	600	B.3
16	48	600	B.4
18	60	600	B.5
20	72	600	B.6
22	86	600	B.7

Table B.1: Summary of the unconfined SHPB tests conducted on kaolin clay specimens and their test parameters.

Moisture content, %	*Actual moisture content, %*	*Length, mm*	*Wet mass, g*	*Dry mass, g*
10.00	8.71	3.261	5.330	3.000
20.00	22.47	3.880	5.650	3.168
15.00	14.82	3.541	5.800	3.084
5.00	5.52	2.965	5.580	2.810
30.00	33.74	4.256	5.790	3.182
41.00	39.37	4.556	5.680	3.269
42.00	40.59	4.227	5.660	3.007
44.00	42.47	4.163	5.410	2.922
15.00	13.88	3.360	5.440	2.950
20.00	22.27	3.659	5.500	2.993
30.00	32.99	3.765	5.140	2.831
10.00	7.24	3.036	5.680	2.831
5.00	5.11	3.057	5.500	2.908
41.00	40.15	4.829	5.960	3.446
42.00	39.86	4.765	5.770	3.407
44.00	42.18	4.115	5.360	2.894
30.00	33.39	4.048	5.760	3.035
0.00	0.00	3.345	5.860	3.345
25.00	25.20	4.248	5.980	3.393
20.00	19.95	3.598	5.950	3.000
30.00	31.95	4.199	5.910	3.182
25.00	25.44	3.851	5.800	3.070
20.00	22.18	3.871	5.890	3.168
30.00	29.77	3.838	5.670	2.957
25.00	24.84	3.692	5.850	2.957
20.00	19.58	3.503	5.730	2.929
10.00	8.45	3.253	5.660	3.000
41.00	39.61	4.150	5.300	2.973
15.00	15.41	3.697	5.950	3.203
42.00	40.49	4.086	5.340	2.908
44.00	41.97	4.237	5.260	2.984
0.00	0.00	3.175	5.633	3.175
41.00	40.26	4.498	6.740	3.207
41.00	38.91	4.455	5.943	3.207
0.00	0.00	3.809	6.620	3.809
41.00	39.90	4.625	6.220	3.306
0.00	0.00	3.107	5.927	3.107

Table B.2: Unconfined SHPB experimental test log for tests performed at 8 m/s.

Moisture content, %	*Actual moisture content, %*	*Length, mm*	*Wet mass, g*	*Dry mass, g*
0.00	0.00	3.051	5.520	3.051
41.00	40.77	4.326	6.130	3.073
30.00	27.46	4.034	5.730	3.165
25.00	25.50	3.937	5.860	3.137
20.00	21.23	3.871	5.697	3.193
15.00	14.55	3.416	5.400	2.982
10.00	11.32	3.500	5.397	3.144
25.00	23.68	3.609	5.627	2.918
20.00	20.25	3.586	5.040	2.982
15.00	14.94	3.800	6.023	3.306
10.00	9.74	3.210	5.540	2.925
30.00	30.56	3.948	6.167	3.024
41.00	40.97	4.590	6.350	3.256
44.00	42.05	4.111	5.253	2.894
20.00	21.25	3.589	6.030	2.960
10.00	11.63	3.360	4.873	3.010
15.00	14.34	3.603	5.743	3.151
25.00	24.98	3.947	5.550	3.158
30.00	30.81	4.140	6.277	3.165
41.00	39.06	4.215	5.377	3.031
0.00	0.32	3.149	6.007	3.149
35.00	34.91	4.089	5.927	3.031
35.00	35.35	3.921	5.130	2.897
5.00	3.99	2.866	5.083	2.756
35.00	34.90	3.993	5.747	2.960
0.00	0.00	3.019	5.073	3.019
5.00	5.89	3.112	5.810	2.939

Table B.3: Unconfined SHPB experimental test log for tests performed at 12 m/s.

Moisture content, %	*Actual moisture content, %*	*Length, mm*	*Wet mass, g*	*Dry mass, g*
0.00	0.00	2.805	5.250	2.805
35.00	36.57	3.947	6.210	2.890
30.00	30.16	3.927	5.537	3.017
25.00	27.03	3.572	5.190	2.812
20.00	20.43	3.548	5.753	2.946
15.00	16.35	3.822	5.550	3.285
41.00	38.34	4.846	6.410	3.503
25.00	26.66	3.383	5.123	2.671
20.00	20.87	3.655	5.130	3.024
15.00	14.90	3.369	5.180	2.932
30.00	31.41	4.029	5.243	3.066
35.00	35.08	3.951	5.713	2.925
0.00	0.00	3.183	5.747	3.183
0.00	0.00	3.148	6.220	3.148
10.00	10.28	3.272	5.397	2.967
41.00	41.43	4.506	6.023	3.186
35.00	36.31	3.833	5.257	2.812
30.00	31.29	4.192	5.617	3.193
25.00	25.04	3.561	4.487	2.848
0.00	0.00	3.411	6.080	3.411
41.00	40.45	4.524	5.807	3.221
10.00	10.89	3.533	5.967	3.186
15.00	15.97	3.449	5.540	2.974
20.00	20.26	3.568	5.303	2.967
41.00	40.39	4.414	5.877	3.144
10.00	10.88	3.353	5.327	3.024
0.00	0.00	3.149	5.847	3.149

Table B.4: Unconfined SHPB experimental test log for tests performed at 16 m/s.

Moisture content, %	*Actual moisture content, %*	*Length, mm*	*Wet mass, g*	*Dry mass, g*
0.00	0.00	3.309	6.753	3.309
20.00	20.63	3.435	6.033	2.848
41.00	39.90	4.388	6.583	3.137

Table B.5: Unconfined SHPB experimental test log for tests performed at 18 m/s.

Moisture content, %	*Actual moisture content, %*	*Length, mm*	*Wet mass, g*	*Dry mass, g*
0.00	0.00	3.378	6.923	3.413
20.00	22.04	3.914	6.463	3.202

Table B.6: Unconfined SHPB experimental test log for tests performed at 20 m/s.

Moisture content, %	*Actual moisture content, %*	*Length, mm*	*Wet mass, g*	*Dry mass, g*
20.00	21.75	3.836	6.377	3.151
25.00	24.48	3.694	5.470	2.967

Table B.7: Unconfined SHPB experimental test log for tests performed at 22 m/s.

B.3 Confined SHPB test log

This section contains test logs for confined SHPB tests on kaolin clay specimens. Table B.8 shows the pressure-depth combinations for each striker bar velocity used and references the individual logs.

Striker bar velocity, m/s	*Gas gun pressure, PSI*	*Striker bar depth, mm*	*Table No.*
12	28	600	B.11
18	60	600	B.12
20	72	600	B.9
22	86	600	B.10

Table B.8: Summary of the confined SHPB tests conducted on kaolin clay specimens and their test parameters.

Moisture content, %	*Actual moisture content, %*	*Length, mm*	*Wet mass, g*	*Dry mass, g*
0.00	0.00	3.247	6.470	3.247
0.00	0.00	3.662	7.123	3.662
0.00	0.00	3.344	6.940	3.344
20.00	21.36	3.781	6.300	3.115
20.00	21.63	3.858	6.393	3.172
41.00	39.65	4.656	6.347	3.334
41.00	39.89	4.368	5.843	3.123

Table B.9: Confined SHPB experimental test log for tests performed at 20 m/s.

Moisture content, %	*Actual moisture content, %*	*Length, mm*	*Wet mass, g*	*Dry mass, g*
0.00	0.00	3.137	7.140	3.137
0.00	0.00	3.351	6.847	3.351
10.00	10.24	3.318	5.857	3.010
20.00	20.94	3.657	6.393	3.024
30.00	30.22	3.901	6.093	2.996
30.00	30.47	4.028	6.383	3.087
30.00	30.66	3.951	6.077	3.024
41.00	38.08	4.117	5.813	2.982
41.00	38.60	4.279	5.827	3.087
41.00	39.46	4.109	5.897	2.946

Table B.10: Confined SHPB experimental test log for tests performed at 22 m/s.

Moisture content, %	*Actual moisture content, %*	*Length, mm*	*Wet mass, g*	*Dry mass, g*
0.00	0.00	3.357	6.907	3.357
0.00	0.00	3.344	6.877	3.344
0.00	0.00	3.461	6.913	3.461
20.00	21.54	3.735	6.407	3.073
20.00	21.94	3.842	6.270	3.151
20.00	22.25	3.912	6.483	3.200
41.00	39.02	4.625	6.287	3.327
41.00	39.61	4.930	6.877	3.531
41.00	39.81	4.750	6.447	3.397

Table B.11: Confined SHPB experimental test log for tests performed at 12 m/s.

Moisture content, %	*Actual moisture content, %*	*Length, mm*	*Wet mass, g*	*Dry mass, g*
0.00	0.00	3.257	6.760	3.257
0.00	0.00	3.273	6.507	3.273
0.00	0.00	3.121	6.493	3.121
10.00	10.48	3.115	5.243	2.819
10.00	11.85	3.193	5.743	2.855
10.00	11.94	3.314	5.620	2.960
20.00	19.47	3.402	5.373	2.848
20.00	19.94	3.610	6.467	3.010
20.00	20.85	3.501	5.450	2.897
25.00	24.44	3.798	6.013	3.052
25.00	26.11	3.769	6.080	2.989
30.00	28.98	4.000	5.787	3.101
30.00	29.80	4.181	6.040	3.221
30.00	30.16	4.211	5.350	3.235
35.00	33.66	4.136	6.090	3.094
35.00	34.30	4.099	5.910	3.052
35.00	35.81	4.365	6.353	3.214
41.00	38.10	4.244	6.003	3.073
41.00	39.67	4.184	5.927	2.996
41.00	40.34	4.224	6.060	3.010

Table B.12: Confined SHPB experimental test log for tests performed at 18 m/s.

Appendix C

Striker bar speed tests

C.1 Introduction

This appendix provides setup-specific speed trap data used to calibrate the new SHPB gas gun. Various combinations of gas gun pressure and striker bar depth were tested to achieve desired striker bar velocities. A relations between gas gun pressure and striker bar depth was established to help determine precise pressure-depth combinations for achieving desired striker bar speeds during SHPB testing.

C.2 Speed test log

Tables C.1, C.2, C.3 and C.4 provide a comprehensive log of pressure and striker depth combinations tested with the new gas gun as part of the new SHPB setup. These tests aimed to determine the relationship between gas gun reservoir pressures (in PSI) and striker depths (in mm) necessary to achieve various speeds (in m/s). The pressure indicates the reading on the main pressure gauge after pressurising the new gas gun reservoir, while striker bar depth refers to the insertion depth of the striker bar within the gas gun barrel. Striker bar velocities were precisely measured using a speed trap equipped with two laser detectors positioned at the open end of the barrel. The striker itself was a cylindrical stainless steel bar, measuring 25 mm in diameter and 350 mm in length.

Based on the test data, power regression equations were formulated from the plotted trendlines for each variation of striker bar depth, establishing a relationship between the gas gun pressure, p, and acquired striker bar velocity, v_s, as illustrated in Figure C.1. Table C.5 displays the equations of four trendlines, each corresponding to a specific striker bar depth. All R^2 values surpass 0.99, indicating a near-perfect fit to the experimental data. The designated striker bar velocities for SHPB testing, as utilised throughout this thesis, are derived based on these equations. Consequently, using these equations, the necessary pressure in PSI for a specific striker depth in mm can be determined in order to achieve the desired striker speed in m/s.

Pressure, PSI	*Striker depth, mm*	*Striker bar velocity, m/s*
12	200	4.04
14	200	4.35
16	200	4.52
18	200	4.93
24	200	5.92
30	200	6.63
50	200	8.86
40	200	7.85
42	200	7.98
60	200	9.57
64	200	9.86
65	200	10.00
66	200	10.12

Table C.1: SHPB gas gun test log: pressure - striker bar depth - velocity combinations (striker depth = 200 mm).

Pressure, PSI	*Striker depth, mm*	*Striker bar velocity, m/s*
12	400	5.92
20	400	8.08
30	400	10.03
40	400	11.65
42	400	12.05
50	400	13.11
56	400	13.99
60	400	14.51
64	400	15.08

Table C.2: SHPB gas gun test log: pressure - striker bar depth - velocity combinations (striker depth = 400 mm).

Pressure, PSI	*Striker depth, mm*	*Striker bar velocity, m/s*
12	600	7.37
14	600	8.14
16	600	8.61
20	600	10.07
28	600	12.05
36	600	13.62
38	600	14.12
46	600	15.68
48	600	15.91
50	600	16.56
60	600	18.00
65	600	18.80
72	600	20.04
86	600	22.00

Table C.3: SHPB gas gun test log: pressure - striker bar depth - velocity combinations (striker depth = 600 mm).

Pressure, PSI	*Striker depth, mm*	*Striker bar velocity, m/s*
12	800	8.25
16	800	9.95
20	800	11.56
22	800	12.14
28	800	14.04
30	800	14.39
38	800	16.00

Table C.4: SHPB gas gun test log: pressure - striker bar depth - velocity combinations (striker depth = 800 mm).

Striker depth, mm	*Pressure-velocity trendline equation*	R^2 *values*
200	$v_s = 1.0205\ p^{0.5485}$	0.9983
400	$v_s = 1.5279\ p^{0.5509}$	0.9992
600	$v_s = 1.8938\ p^{0.5514}$	0.9993
800	$v_s = 1.9836\ p^{0.582}$	0.9932

Table C.5: Summary of the different striker depths, associated trendline equations and R^2 values.

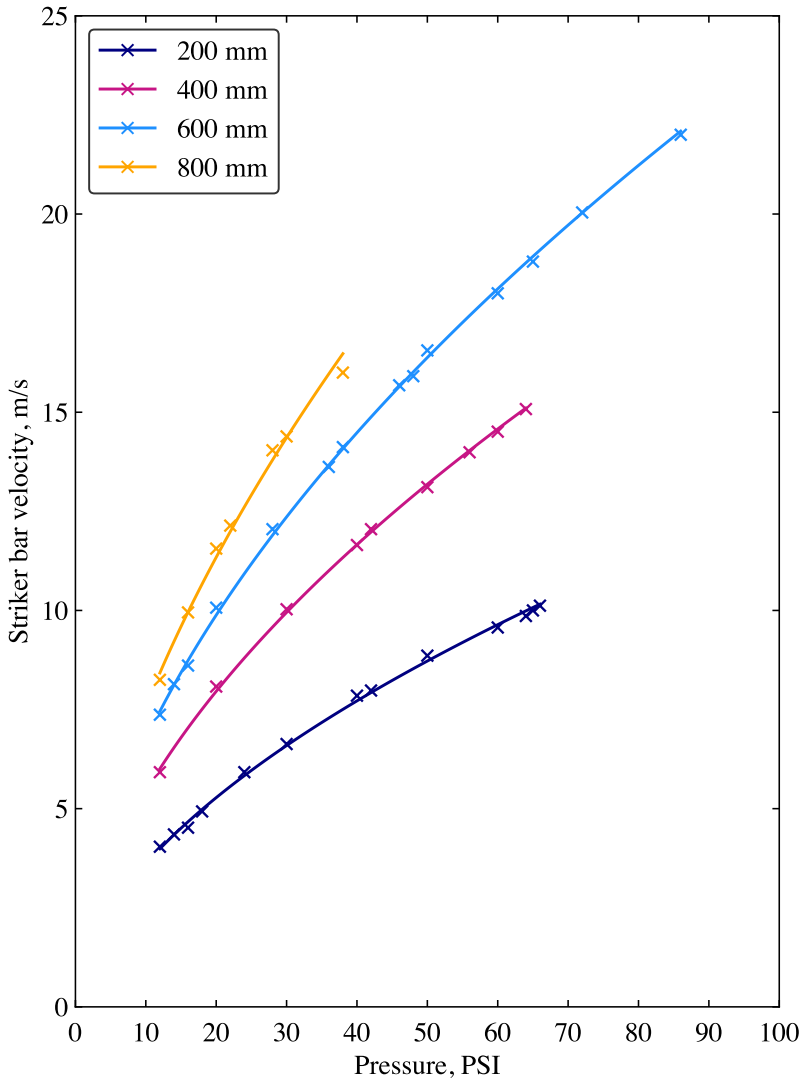

Figure C.1: Pressure-striker bar velocity combinations: power regression trendlines for different striker bar depths.

Appendix D

LS-DYNA material cards

D.1 Introduction

This appendix includes the LS-DYNA material cards and other pertinent keyword files utilised in the numerical modelling of SHPB experiments conducted in this study. A thorough explanation of their implementation is provided in Chapter 5.

D.2 Material cards

```
*MAT_ELASTIC
Stainless steel pressure bar
$#      mid     ro      e       pr      da      db      not used
        X       7666.0  1.68E11 0.29    0.0     0.0     0.0
```

Table D.1: Material card for *MAT_ELASTIC, calibrated to represent stainless steel pressure bars

```
*MAT_NULL
Water
$#      mid     ro      pc      mu      terod   cerod   ym      pr
        X       1000.0  0.0     0.0     0.0     0.0     0.0     0.0
```

Table D.2: Material card for *MAT_NULL, calibrated to represent water.

```
*MAT_NULL
Air
$#      mid     ro      pc      mu      terod   cerod   ym      pr
        X       1.225   0.0     0.0     0.0     0.0     0.0     0.0
```

Table D.3: Material card for *MAT_NULL, calibrated to represent air at atmospheric pressure.

```
*MAT_MOHR_COULOMB
Kaolin clay sample
$#      mid     ro      gmod    rnu             phi     cval    psi
        X       1296.0  1.3E7   0.44            0.08075 55759.4 0.0

$#              nplanes         lccpdr  lccpt   lccjdr  lccjt   lcsfac
                0               0       0       0       0       0

$#      gmoddp  gmodgr  lcgmep  lcphiep         lcgmst  cvalgr  aniso
        0.0     0.0     0.0     0.0             0.0     0.0     1.0
```

Table D.4: Material card for *MAT_MOHR_COULOMB, calibrated to represent kaolin clay.

```
*MAT_RIGID
Rigid steel
$#      mid     ro      e       pr      n       couple  m       alias
        X       7666.0  1.68E11 0.29    0.0     0.0     0.0     0.0

$#      cmo     con1    con2
        1.0     7       7

$#      a1      a2      a3      v1      v2      v3
        0.0     0.0     0.0     0.0     0.0     0.0
```

Table D.5: Material card for *MAT_RIGID, calibrated to represent rigid steel.

D.3 Contact cards

```
*CONTACT_AUTOMATIC_NODES_TO_SURFACE
$#      cid     title
        X       N−S

$#      ssid    msid    sstyp   mstyp   sboxid  mboxid  spr     mpr
        X       X       4       3       0       0       0       0

$#      fs      fd      dc      vc      vdc     penchk  bt      dt
        0.0     0.0     0.0     0.0     0.0     0       0       1E20

$#      sfs     sfm     sst     mst     sfst    sfmt    fsf     vsf
        5.0     5.0     0.0     0.0     1.0     1.0     1.0     1.0
```

Table D.6: Contact card for *CONTACT_AUTOMATIC_NODES_TO_SURFACE, calibrated for SPH node to Lagrangian solid surface interactions.

```
*CONTACT_AUTOMATIC_SURFACE_TO_SURFACE
$#      cid     title
        X       S−S

$#      ssid    msid    sstyp   mstyp   sboxid  mboxid  spr     mpr
        X       X       3       3       0       0       0       0

$#      fs      fd      dc      vc      vdc     penchk  bt      dt
        0.0     0.0     0.0     0.0     0.0     0       0       1E20

$#      sfs     sfm     sst     mst     sfst    sfmt    fsf     vsf
        1.0     1.0     0.0     0.0     1.0     1.0     1.0     1.0
```

Table D.7: Contact card for *CONTACT_AUTOMATIC_SURFACE_TO_SURFACE, calibrated for interactions between Lagrangian solid element surfaces.

D.4 Equation of state (EOS) cards

```
*EOS_LINEAR_POLYNOMIAL
EOS Water
$#      eosid    c0       c1       c1       c1       c1       c1       c1
        X        0.0      2.19E9   9.22E9   8.77E9   0.4934   1.3937   0.0

$#      e0       v0
        205360.0 1.0
```

Table D.8: EOS card for *EOS_LINEAR_POLYNOMIAL, calibrated to depict the behaviour of water.

```
*EOS_LINEAR_POLYNOMIAL
EOS Air
$#      eosid    c0       c1       c1       c1       c1       c1       c1
        X        0.0      0.0      0.0      0.0      0.0      0.0      0.0

$#      e0       v0
        253400.0 0.0
```

Table D.9: EOS card for *EOS_LINEAR_POLYNOMIAL, calibrated to to depict the behaviour of air at atmospheric pressure.